# Control of Crystallisation Using Surface Topography

by

Phillip Alan Lee

Submitted in accordance with the requirements for the degree of Doctor of Philosophy

The University of Leeds

Faculty of Mathematics and Physical Sciences

School of Chemistry

April 2017

The candidate confirms that the work submitted is his/her own and that appropriate credit has been given where reference has been made to the work of others.

## Acknowledgements

First and foremost, I would like to thank my supervisor, Prof. Fiona Meldrum for providing me with the opportunity to pursue this PhD after having completed my undergraduate degree. I am sincerely thankful for the input and feedback she has given me during my PhD. Despite her busy schedule, she made time to keep informed about my research and accompany me to various meetings and conferences for which I'm very grateful. I would also like to thank Hugo Christenson for his help throughout my project, his geniality and his open door.

Next, I would like to thank Mark Holden, for our countless interesting discussions about both science and various other topics. His input helped me to develop my ideas and theories about my research, and also aided in deepening my understanding of my research area. Our conversations greatly improved my confidence both as a researcher and as a person.

Giles Crowley, for his patience and guidance, as well as his kindness in welcoming me as one of the Unilever team and for providing me with many opportunities during my research.

I would also like to thank the people that helped guide me throughout my research and build me into the researcher that I am today. Yi-Yeoun, for supervising me during my undergraduate degree and helping me throughout my PhD. Li Chen and Mark Rosamond, for help in the cleanroom and their immense knowledge about microfabrication. Rob Menzel and Chris Smith for their time and help during my graphene research, as well as Lesley Neve, Ben Johnson and Guixin Wang.

It would be impossible not to mention my research group as well and to thank them for their friendliness and entertainment. Mark L, Clara, Dave, Muling, Bart, Johannes, Yunwei, Shunbo, Joe, Angela and Alex.

On a personal level, special thanks goes to my Mum, for being the strongest person I know and despite having been dealt a bad hand in life, she is still the kindest and most loving person that I have ever met. Her warmth is felt not only by friends and family, but also by complete strangers. My Dad, for developing my love of science from a young age and for cultivating my interests in a range of other subjects and hobbies as well. I am indebted to you for giving up almost every one of your weekends when I was a child to take me to football. My brothers and sisters, Alexander, Aurelia, Aprillia and Daniil. By far the funniest people that I know, our memories together are my most treasured. My Granny, Grandad Lee, Gran and Grandad, all my uncles and Aunts, especially my Auntie Anna and Uncle John, thank you.

Helmut Cölfen and Malcolm Povey, thank you very much for agreeing to be my viva assessors, I enjoyed the experience far more than I had expected to and found our discussion thoroughly interesting; it was a great experience I will never forget.

I would like to thank the EPSRC and Unilever for funding, as well as Alex Ashcroft, Pat Unwin and Parky for their contribution.

Last, and definitely not least, special thanks goes to my girlfriend, Aly. The most beautiful person that I know, inside and out. There is no way that I could've done this without you, I am forever grateful. Thank you for keeping me sane, for everything you have ever done for me, and for making me stick at it when I felt as though doing a PhD was the worst idea I had ever had.

**Abstract**

The purpose of this research project was to realise the control of crystallisation using surface topography. Calcium carbonate crystallisation was primarily used as this is a model system for crystallisation studies. The first experimental chapter involves the precipitation of calcium carbonate on a plasma-treated poly(dimethylsiloxane) (PPDMS) substrate. Exposure to atmospheric air-plasma results in oxidation of the surface of the poly(dimethylsiloxane), causing a superficial silica-like ($SiO_x$) surface layer to form. Cracks in this surface, which arise because of its rigidity compared to the underlying bulk, were found to act as effective nucleation sites for calcium carbonate precipitation. Crystals were often observed only at the cracks and were absent elsewhere on the substrate. The surface chemistry was altered using a carboxylate terminated alkylthiol self-assembled monolayer (SAM), formed from the monomer 16-mercaptohexadecanoic acid. The presence of this monomer on the PPDMS substrate caused a significant increase in crystal population and enhanced the localising effect of the cracks. Further control of crystallisation was achieved by varying the initial ion ratio ($Ca^{2+}$:$CO_3^{2-}$) and by the presence of magnesium ions in solution. The substrate also proved effective at causing the localised precipitation of other inorganic materials: strontium carbonate, barium carbonate, manganese carbonate, basic copper carbonate and calcium oxalate. Through the application of contact masks or a tensile stress during plasma-treatment, it was possible to control the distribution of the cracks across the surface and therefore pattern the crystallisation of calcium carbonate. The second research chapter is a quantitative analysis of the system discussed in the first chapter. Here, an image analysis software, ImageJ, was used to obtain data from electron micrographs of the PPDMS substrate after crystallisation. Calcium carbonate had been precipitated on the PPDMS substrate once the surface chemistry had been modified using a variety of differently terminated alkylthiol SAMs. The research revealed that not only is it possible to control crystal populations at the surface features, but also the crystal polymorph. In the third research chapter, silicon wafers that had been spincoated with reduced-graphene oxide were used as substrates for calcium carbonate precipitation. Interestingly, the vast majority of crystals that had formed on these wafers were aragonite, a metastable phase of calcium carbonate. In order to understand why this was so, a series of investigations followed that were aimed at

elucidating if it was a topographical effect or due to the presence of impurities. The data suggested that the large proportion of aragonite was due to topographical effects. The final research chapter involved cleanroom microfabrication techniques common to the semiconductor industry to construct surface structures on silicon wafers that were used as substrates. Crystallisation was locallised to these features, proving that it is possible to design surface topographies that can be used to control crystallisation.

## Table of Contents

**List of Figures**

**List of Tables**

# 1 Introduction

Crystals are ubiquitous in the world around us, from the chocolate and ice cream we consume, to the medications prescribed to us by our doctors; they even exist inside our bodies as the inorganic component of bone and the otoliths within our ear that help us to balance. Naturally occurring crystals have fascinated mankind for millennia because of their beautiful, symmetrical and regular forms. Wars have been financed by and fought over crystals, with diamonds a poignant example, but also natural resources of industrial importance from which crystalline materials can be derived, such as ores that provide us with metals. Crystals are of critical importance to modern civilisation, as many technological systems rely on an understanding of their formation and growth. Information, communication, energy, transportation, medical and safety technologies are all heavily dependent upon our ability to fabricate crystals with tailored properties.

Phase change begins with nucleation, which can be considered as the birth of a new material from another. Nucleation is a widespread phenomenon, and is involved in the formation of black holes, the eruption of volcanoes, as well as the development of decompression sickness in divers [1]. It is of course, a necessary step in the formation of crystals. Nucleation is initiated as particles come together to form infinitesimally small entities, known as nuclei. Their formation is stochastic and their survival is dependent upon the environment into which they were born, with the vast majority shrinking back into nonexistence. Their persistence beyond that of a transient entity can be greatly enhanced by their formation in contact with a foreign surface; a speck of dust or the wall of a container will often suffice. The interaction between the nucleus and the surface reduces the energy barrier to nucleation that must be overcome for the nucleus to grow. An understanding of how surfaces can achieve this can aid us in obtaining materials without the need for soluble chemical additives, which can be expensive, toxic and may even restrict the application of the material if it is incorporated into the final product.

A surface can promote nucleation not only by the formation of favourable interactions between the nucleus and substrate, but also through its surface topography. The topography can be considered as the microscopic features of a surface, where the equivalent on a landscape would be its plains, valleys and mountains. In this thesis I study a number of

different systems that prove that surface topography is an effective tool for the control of crystallisation.

After an Introduction (Chapter 1), my first research chapter presents work where surface fractures that have been induced in a flexible polymer act as preferential nucleation sites for crystallisation. By varying the surface chemistry of this material, it was possible to greatly enhance the crystal population present at the features, and the substrate was effective at influencing crystallisation for other inorganic systems. Chapter 3 is a quantitative analysis of the system found in Chapter 2, where image analysis software has been used to extract data regarding the properties of the crystals from scanning electron micrographs. Chapter 4 involves the use of reduced-graphene oxide as a surface coating on a silicon wafer. The resultant surface topography promotes the formation of a metastable polymorph. In Chapter 5, I have used cleanroom microfabrication techniques to construct microstructures that are capable of localising the formation of crystals. Finally, Chapter 6 provides a suggestion as to why the substrates are effective, and Chapter 7 discusses the work as a whole and summarises the research chapters.

## 1.1 Crystallisation

### 1.1.1 Crystals and Polymorphs

A crystal at its simplest is a material comprising a regular array of repeating units. These may be ions, molecules or particles, but the crystals that they form all possess long range order due to this regular arrangement of constituents. The entire lattice can be reconstructed by applying a repetitive translation in three-dimensions of the unit cell, which is the smallest repeatable unit. In theory, a single crystal has a continuous lattice, where the only boundaries are the edges of the material. However, in reality, a single crystal rarely exists as impurities are incorporated causing the crystal lattice to become tilted, twisted or shifted to varying extents. This can cause the formation of grain boundaries. A polycrystalline material on the other hand is one that is composed of many small crystals, where grain boundaries are considered as the interfaces between crystallites and the lattice planes show no coherence from one crystallite to the next. Amorphous materials lack structural periodicity and as such have no long range order [2].

Polymorphs are materials with the same chemical composition, but they possess different structures and thus exhibit different properties. A polymorph may be crystalline or amorphous and a compound may have only a few polymorphs, or many, though polymorphism is a common trait of the solid state. It has been rigorously studied and is of critical importance in many fields, where crystal polymorphs may have sufficiently different chemical and physical properties such that obtaining one over another is cause for concern. For example, in pharmaceuticals, the bioavailability of polymorphs may differ (a result of the different solubilities) and therefore their efficacy. Hence, careful consideration of the synthetic procedures involved must be exercised as even a tiny amount of a low energy, inactive polymorph has been found to convert huge batches of the active form into this medically useless material [3]. Polymorphs can transform into each other by either a displacive or reconstructive transformation. A displacive transformation involves only minor adjustments to the crystal lattice, such as small alterations to the angle between subunits, instead of the breaking or formation of bonds. This is possible because the structures of the two polymorphs are quite similar. A reconstructive transformation takes place if the structures are quite different. This involves breaking the bonds, reordering the constituents and forming new bonds. Consideration of polymorphic transformations and the conditions under which they occur can be vital. For example, the structural integrity of a component may deteriorate as it

slowly transforms into another polymorph. This occurs in tin pest, where the ductile β-form of tin transforms to the α-form at low temperature and an associated volume increase causes once continuous structures to be reduced to a powder [4].

## 1.1.2 Classical Crystallisation

### 1.1.2.1 Supersaturation

Supersaturation can be considered as the thermodynamic driving force for crystallisation and is a prerequisite for the phase change to occur. Simply put, crystals form to lower the free energy of the system and as such the free energy difference between the current state and the equilibrium state is what propels the phase change [5]. This is described by the change in Gibbs free energy:

$$\Delta G = \Delta H - T\Delta S \qquad \text{Equation 1}$$

where ΔG is the free energy difference between the solid and the supersaturated liquid, ΔH and ΔS are the associated enthalpy and entropy changes, respectively, and T is the temperature. As with all thermodynamic processes, if ΔG < 0, then the phase change will occur spontaneously.

A solution is supersaturated when the activity product of the reactants surpasses the equilibrium solubility product. This is described by the equations below. For a given reaction, the activity product, AP, is:

$$aA + bB + nN \ldots \rightarrow A_aB_b \ldots N_n \qquad \text{Equation 2}$$

$$AP = [A]^a[B]^b \ldots [N]^n \qquad \text{Equation 3}$$

And the solubility product, $K_s$, which is unique to each material:

$$K_s = [A]_e^a[B]_e^b \ldots N_e^n \qquad \text{Equation 4}$$

Where the subscript 'e' indicates that this is the activity at equilibrium. Therefore, in order for crystallisation to take place AP > $K_s$ must be true. For crystallisation from solution (which will only be considered in this thesis), the concentration of the compound in solution is an approximation of its activity. Hence, supersaturation can be considered as the ratio between the supersaturated concentration and the equilibrium concentration.

$$S = \frac{c}{c*} \qquad \text{Equation 5}$$

where c is the solution concentration and c* is the equilibrium concentration at the given temperature. If S > 1, then the solution is supersaturated with respect to the compound. The saturation index, SI, is often quoted in this thesis and is a convenient representation of the supersaturation:

$$SI = \log AP - \log K_s \qquad \text{Equation 6}$$

Again, a value greater than unity for SI indicates a supersaturated solution.

Although supersaturation is required for crystallisation, its existence does not guarantee that a phase change will occur. This can be explained by consideration of how the new phase forms. Once supersaturation has been achieved, nucleation will take place, which involves the ions in solution coming together to form clusters. However, the small volume and large surface area of these embryonic nuclei causes them to be unstable and the vast majority have exceedingly small lifetimes. In order for the new phase to exist beyond a small number of units, it is necessary for a nucleus to overcome the energy barrier to nucleation.

#### 1.1.2.2 Homogeneous Nucleation

If we consider that a nucleus is composed of z number of particles, then $z_s$ of these will exist at the surface and $z_b$ will be located in the bulk. Therefore, we can write the free energy of the cluster as the sum of the free energies of the bulk ($g_b$) and surface particles ($g_s$):

$$g_z = z_b g_b + z_s g_s \qquad \text{Equation 7}$$

We must also consider the interfacial tension, γ, which arises because particles in the bulk have their interactions fully and homogeneously satisfied, whereas those at the surface do not (Figure 1).

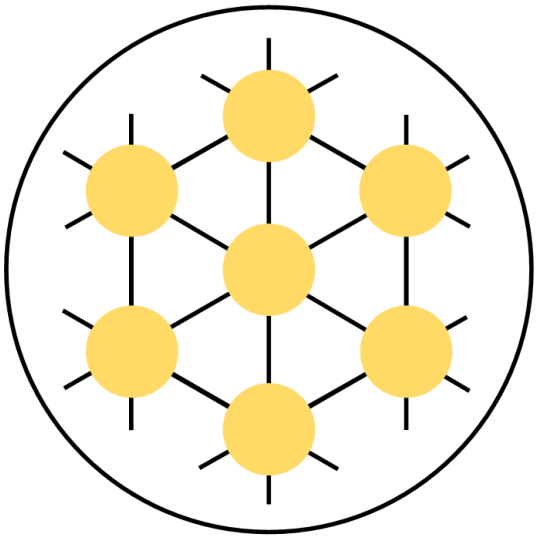

**Figure 1: A cluster of particles during nucleation**

The interfacial tension can be written as:

$$\gamma = (g_s - g_b)z_s/A \qquad \text{Equation 8}$$

where A is the cluster surface area. If we assume that the molecules form a spherical cluster, then $z^{2/3}$ number of particles will be situated at the surface. Using this, we can write the free energy of the cluster in terms of the chemical potential:

$$g_z = z\mu_b + \beta\gamma z^{2/3} \qquad \text{Equation 9}$$

in which β is an area shape factor that is dependent on the nucleus shape and $\mu_b$ is the chemical potential of a particle in the bulk of the cluster. For the nucleation of one mole of substance, the change in Gibbs energy is:

$$\Delta G = g_z - z\mu, \qquad \mu = \mu^o + k_B T ln(c)\ , \quad \text{assuming } c = a_{ss} \qquad \text{Equations 10, 11}$$

In equation 10, μ is the chemical potential of monomers in solution, in equation 11 $\mu^o$ is the standard chemical potential of the monomers and c is the concentration of the supersaturated solution. As mentioned above, c (at low concentration) can be considered equal to the activity of the supersaturated solution ($a_{ss}$). By combining equations 9, 10 and 11 we get:

$$\Delta G = \left(z\mu_b + \beta\gamma z^{\frac{2}{3}}\right) - z(\mu^o + k_B T ln(c)) \qquad \text{Equation 12}$$

Then, at equilibrium the chemical potential of particles in the bulk of the nucleus is the same as those in the solution:

$$\mu_b = \mu^o + \text{kTln(c*)}\text{ , assuming c* = } a_{eq} \qquad \text{Equation 13}$$

we can combine equations 12 and 13 to get:

$$\Delta G = -zk_BTlnS + \beta\gamma z^{2/3} \qquad \text{Equation 14}$$

Equation 14 represents the Gibbs free energy change for homogeneous nucleation, that is, nucleation that occurs away from any solid surfaces. The positive term represents the surface contribution of the nucleus and acts to destabilise the nucleus due to the energetic cost of forming a new interface. The negative term is stabilising and originates from the bulk of the nucleus and decreases the Gibbs free energy as the formation of bonds in the interior is favourable. Small objects have a large surface area to volume ratio and so ΔG will initially be positive as the surface term dominates. Therefore initial growth of the cluster will be unfavourable, though the volume term will increase with cluster size faster than the surface term (as volume is a cubic function compared to surface area which is quadratic). Once a sufficient number of particles constitute the nucleus, the surface and volume terms will be equal. This is known as the critical cluster size, $z_c$, and the value of ΔG that this occurs at is the homogeneous energy barrier to nucleation, ΔG*. Beyond this size, further growth of the nucleus is thermodynamically favourable as it causes a decrease in the free energy (Figure 2).

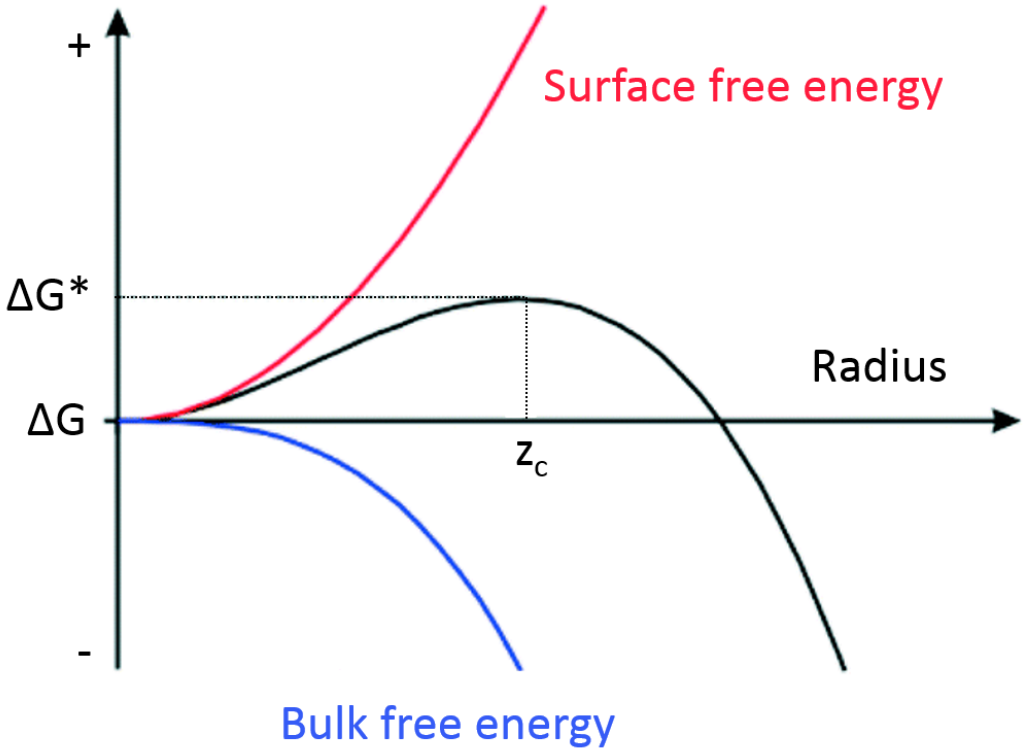


**Figure 2: Graph of the change in free energy with cluster size**

The likelihood of forming a critical cluster is dependent upon this energy barrier, with high supersaturations associated with a decrease in the barrier and large interfacial tensions associated with an increase. Hence, a solution may be supersaturated, but if the energy barrier is too large, then no nuclei will grow past the critical size [7].

#### 1.1.2.3 Heterogeneous Nucleation

Thus far, homogeneous nucleation has been described, which involves the formation of a continuous interface between the nucleus and the solution. This is energetically expensive, [8] and much more frequent in occurrence is heterogeneous nucleation. This involves the formation of the new phase in contact with another surface. Since this route of formation occurs more readily, the associated energy barrier, ΔG', must be smaller than for homogeneous nucleation, ΔG*:

$$\Delta G' = \phi \Delta G^* \qquad \text{Equation 15}$$

Where ϕ is a factor with a value less than unity. Heterogeneous nucleation is more prevalent than homogeneous as the interactions between the ions in the nucleated phase and the substrate are often stronger than the bonds of solvation [9]. The interfacial tension plays a critical role in the Gibbs free energy of a nucleus forming via homogeneous nucleation and is a destabilising term. Therefore, if this contribution can be minimised, then the barrier to

nucleation can also be reduced. Through decreasing the area of the nucleus' interface that is in contact with the solution and replacing this with an interface that provides more favourable interactions, nucleation becomes significantly more probable. Figure 3 shows three phases in contact and the associated interfacial energies.

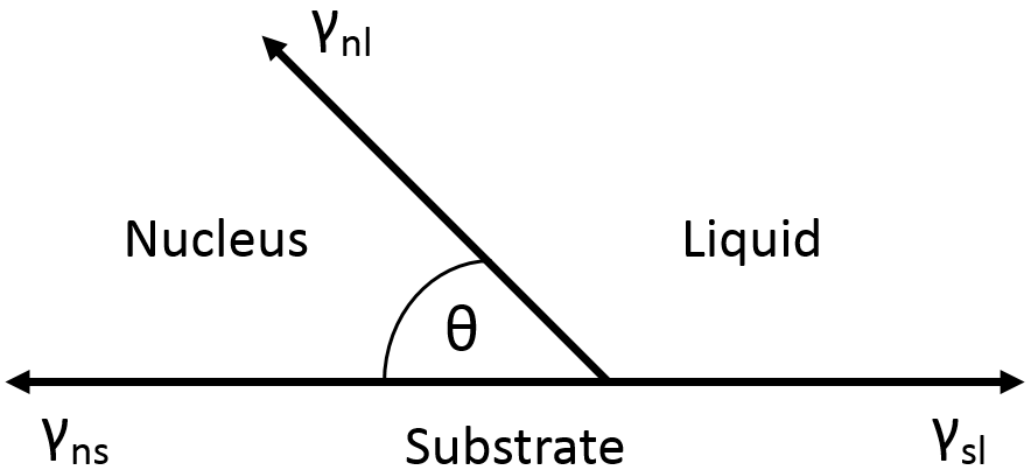


**Figure 3: Interfacial energy diagram for three phases in contact**

θ is the contact angle between the nucleus and the substrate and corresponds to the angle of wetting in a liquid-solid system. The interfacial tensions are as follows:

- $\gamma_{ns}$: Interfacial tension between nucleus and substrate.
- $\gamma_{nl}$: Interfacial tension between nucleus and liquid.
- $\gamma_{sl}$: Interfacial tension between substrate and liquid.

The relationship between these is described by Equation 16:

$$cos\theta = \frac{\gamma_{sl} - \gamma_{ns}}{\gamma_{nl}} \qquad \text{Equation 16}$$

Hence, the contact angle is a direct result of how favourable the interactions between the phases are. Smaller contact angles are found in systems where the interfacial tension between the nucleus/substrate and nucleus/liquid is small. This can be rationalised by considering that in order to form the nucleus on the substrate, it is necessary to form two new interfaces (nucleus/substrate and nucleus/liquid) alongside the liquid/substrate interface. Hence, large values of $\gamma_{sl}$ make the formation and growth of a nucleus more likely. The factor ϕ, of Equation 17, is related to the contact angle by:

$$\phi = \frac{(2 + cos\theta)(1 - cos\theta)^2}{4} \qquad \text{Equation 17}$$

This means that if the contact angle is 180°, then there will be no decrease in the energy barrier to homogeneous nucleation, as ϕ = 1 and ΔG' = ΔG*. If the contact angle is less than 180°, then ϕ < 1 and the heterogeneous nucleation event will be more favourable than the homogeneous event. Contact angle values of 0° occur when there is complete affinity between the nucleus and substrate, for example between a surface composed of a material with the same structure and composition as the nucleus (for example seed crystals), and nucleation on such a substrate would proceed without an energy barrier [1, 2, 5, 7, 8, 10].

#### 1.1.2.4 Crystal Growth

The surface of a crystal can be approximated by stacked cubes that represent the growth units. The flat surfaces are referred to as terraces, the edge of a raised partial layer is a step, and the corner of an incomplete step a kink site. Surface and edge vacancies may also exist (Figure 4).

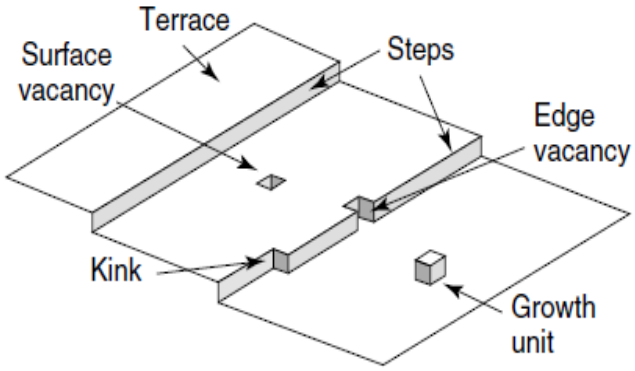


**Figure 4: Schematic of the growth sites of a crystal surface**

At the kink, the growth unit forms bonds in three different directions, as opposed to forming one or two on the terraces or at a step edge, respectively. Since there are more interactions formed at kink sites, growth units that exist here are more likely to remain a part of the crystal and so the growth rate, at a given solute concentration, scales with the kink density and thus can be controlled by blocking kinks or roughening steps [12]. A number of energy barriers must be overcome in order for the growth unit to reach the kink site. The growth unit must undergo partial desolvation to join the terrace, diffuse across the surface of the crystal to find

a step and then further desolvation is required to enter the kink. As the growth units join on to the crystal at the kink sites, the step is propagated and the crystal grows [13].

In order for a crystal to grow, there must be a net addition of growth units to the crystal. The flux of molecules attaching to the surface is determined by the solution concentration, whereas the flux away from the surface is dependent on the strength of bonds between incorporated growth units. Therefore, c*eteris paribus*, a crystal with a high solubility will grow more quickly than a sparingly soluble crystal if both are grown at the same supersaturation [9]. In early crystallisation studies, experimentalists often observed crystals growing at rates far larger than predicted at low supersaturation. Researchers realised that in order for these crystals to grow so quickly, there must be highly active growth structures on their surfaces of the type that are not eliminated by further growth. Such an imperfection that matches this description is a screw dislocation. This can be considered as a spiral of growth units emanating from the surface. The dislocation creates a step, and as growth units attach to this, they cause a second step edge to be formed. The steps advance towards the face edge, generating more steps as they do so and propagating the screw dislocation (Figure 5).

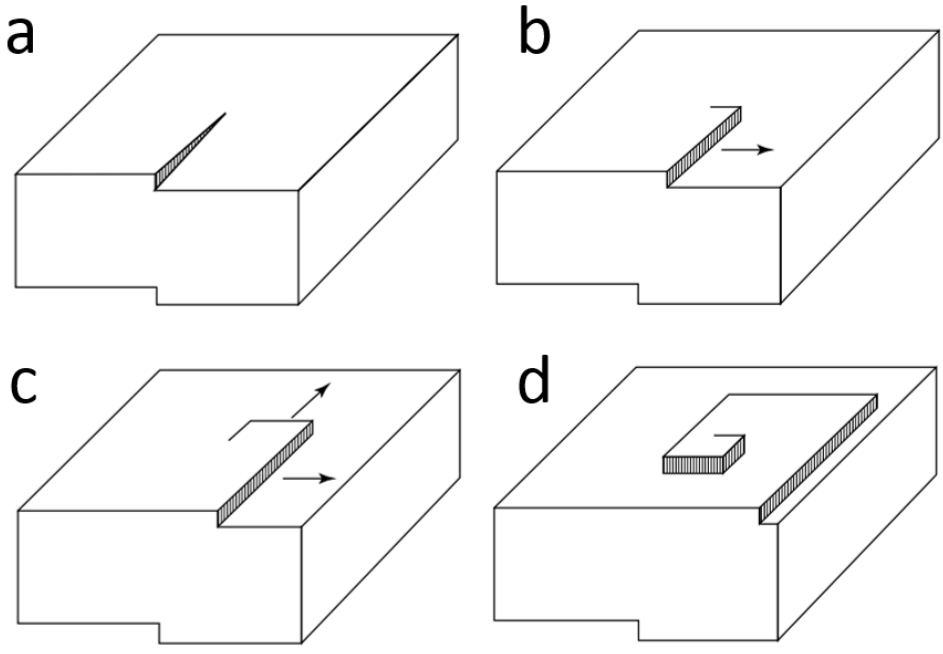


**Figure 5: Schematic of the propagation of steps via a growth spiral**

### 1.1.3 Ostwald's Step Rule

Crystallisation is known to not always proceed via a single step, but instead can progress from supersaturation to equilibrium in stages [15]. For example, it may be that the final stable phase is obtained via a series of metastable phases with intermediate energy barriers between the parent and final phase. Research has shown that a huge variety of systems exhibit this behaviour, including many proteins, colloids, minerals and polymeric solutions [16, 17]. Known as Ostwald's Step rule, it suggests that it is not necessarily the most stable phase that will form first, but the one with the free energy closest to the initial state (smallest energy barrier) (Figure 6).

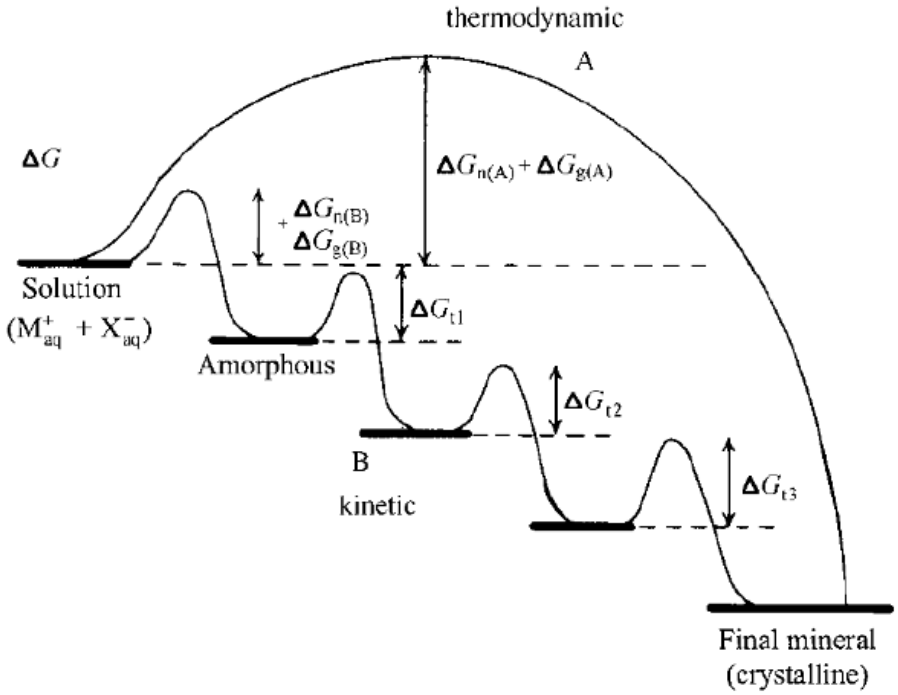


**Figure 6: Schematic illustration of different pathways by which a phase transformation may occur**

This crystallisation route is common in biomineralisation, where the phase transformation proceeds in a stepwise manner, rather than in a single step. In biological systems, additives play a central role in controlling crystallisation, where they modify the solubility of the phases and the free energies of activation of interconversion by binding to the crystal surface and, in some instances, subsequent incorporation [18]. Figure 6 illustrates this, where the large energy barrier involving direct transformation of the solution to the final mineral (Pathway A) is circumvented and instead a series of transformations involving smaller energy barriers occurs (Pathway B). This is made possible by shifting the driving force from one that is thermodynamic to one that is kinetic. A less dense and less organised phase forms first, such

as an amorphous precursor. The amorphous phase may then convert to the next phase by a dissolution-reprecipitation mechanism or by nucleation of the new phase at the surface or in the interior and subsequent conversion of the old phase as it grows. Although the transformation progresses in the order of increasing thermodynamic stability, it does not necessarily mean that all phases will appear along the pathway [19].

### 1.1.4 Non-classical Crystallisation Pathways

#### *1.1.4.1 Multistep Nucleation Theories*

Classical nucleation theory (CNT) is based on a number of assumptions. CNT was developed to describe the condensation of a liquid from a vapour, and was then extended to describe the formation of a solid from melt or solution. It assumes that the nucleus has the same density, structure and composition as the most stable phase, which may not be the case. This section covers briefly some of the theories that have been proposed that aim to address the shortcomings of classical nucleation theory.

A simplification of CNT is that the nucleus is spherical in shape and the interface is defined by a single interfacial energy [20]. Of course, this will not be true if the nucleus is faceted and composed of crystal faces with different surface energies. Further, it also considers the interface as a planar surface that represents a sharply defined boundary between the nucleating phase and the mother phase with a thickness that is small compared to the size of the nucleus [21]. Diffuse Interface Theory (DIT) addresses this, and instead treats the interface as several molecular layers and applies a surface tension that is related to this thickness, and is strongly curvature dependent [22, 23]. DIT has proven effective at describing the nucleation of a number of materials, including metals, oxide glasses and hydrocarbon liquids.

The assumption that the surface tension of a highly curved surface is the same as that of a planar surface is known as the capillary approximation [24]. It also assumes that ions/molecules in the centre of the nucleus behave like those at the interface. Another complication of CNT is that nucleation involves not only a change in density as ions come together to form the nucleus, but also a change in the local periodic structure [25]. CNT suggests that both the clustering of the particles and their reorganisation into that of the new phase occurs simultaneously, and as such, it is the density parameter that defines the old and the new phase. Density Fluctuation theory accounts for this by describing a nucleus as a

function of two structural parameters, a critical structured size and a coinciding density change [26].

In a two-step nucleation mechanism, large density fluctuations within the solution permit the formation of dense liquid clusters. These form first as they have a lower interfacial free energy, resulting in a lower nucleation barrier as compared to the crystalline phase [27]. The elevated local supersaturation within the cluster provides the ideal environment for the nucleation of a second, crystalline phase. This was first observed experimentally by Zhang and Liu, where they used a colloidal system to visualise nucleation on the macroscale [28-30]. Two-step nucleation has since been observed on the microscale using AFM to track the crystallisation of S-layer proteins [31], and has been suggested as the nucleation pathway for many protein systems since. Once formed, the clusters undergo internal rearrangements, producing a small number of crystal nuclei. These are unstable and are continuously dissolving and reforming. As the growth of the dense liquid continues, the number of nuclei increases until they eventually merge into a mature, stable crystalline nucleus. This process involves two energy barriers that represent the cluster formation and the internal rearrangement.

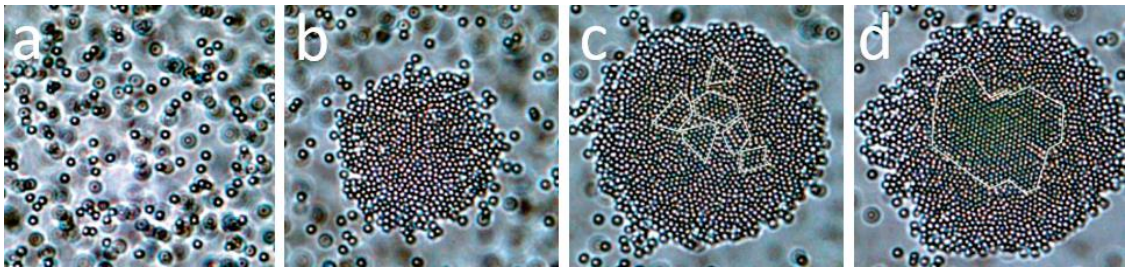


**Figure 7: Two-step nucleation pathway in a colloidal model system**

Prenucleation clusters (PNC's), considered as amorphous multi-ion clusters that are neutral in charge, were first proposed by Gebauer *et al* in 2008 [32]. Calcium carbonate PNC's were detected using analytical ultracentrifugation combined with calcium ion activity measurements. Since then, they have been observed both experimentally and by nucleation modelling studies in a wide range of systems [33-39]. The structure of $CaCO_3$ PNC's with a size between 0.6 - 1.1 nm and 2 nm is believed to be an ionic polymer of alternating calcium and carbonate ions [40], rather than the compact agglomeration that may be expected. The PNC's are dynamic arrangements of ions, held together by ionic interactions, and they exist as linear/branched chains or rings. The formation of these dynamically ordered liquid-like oxyanion polymers (DOLLOPs) is driven primarily by entropy [41]. The association of the ions into clusters causes the release of water molecules from their hydration layers. As such, the

water transfers from a crystalline state, where it has limited translational and rotational freedom, to the liquid state, where it is free in solution. Therefore, in order for an entropic driving force to exist, it is necessary that there are fewer bound water molecules per ion when the ions are in a clustered state compared to the free state.

In the classical view, metastable clusters are continuously forming and redissolving, and in order for their growth to become favourable they must surpass the energy barrier to nucleation. The growth proceeds via the addition of individual ions to the cluster. Conversely, the formation of prenucleation clusters is thought to involve an energy barrier that is negligible compared to the thermal energy [42]. The PNC's represent the initial step in phase separation, they then merge to form amorphous calcium carbonate that subsequently crystallises. Therefore, crystallisation via PNC's as described follows Ostwald's Step Rule, as the free energy barrier to nucleation of the metastable phases is smaller than the barrier associated with the most stable phase [43]. Since the energy barrier for the metastable phases will be small, their nucleation rate is greater than the more stable phases and so they form first then convert to further polymorphs (Figure 8). Although the transformation progresses in the order of increasing thermodynamic stability, it does not necessarily mean that all phases will appear along the pathway [19]. Crystallisation in this manner is said to be under kinetic control (proceeds via a series of metastable phases to the final crystalline phase) rather than thermodynamic control (direct nucleation of the most stable phase).

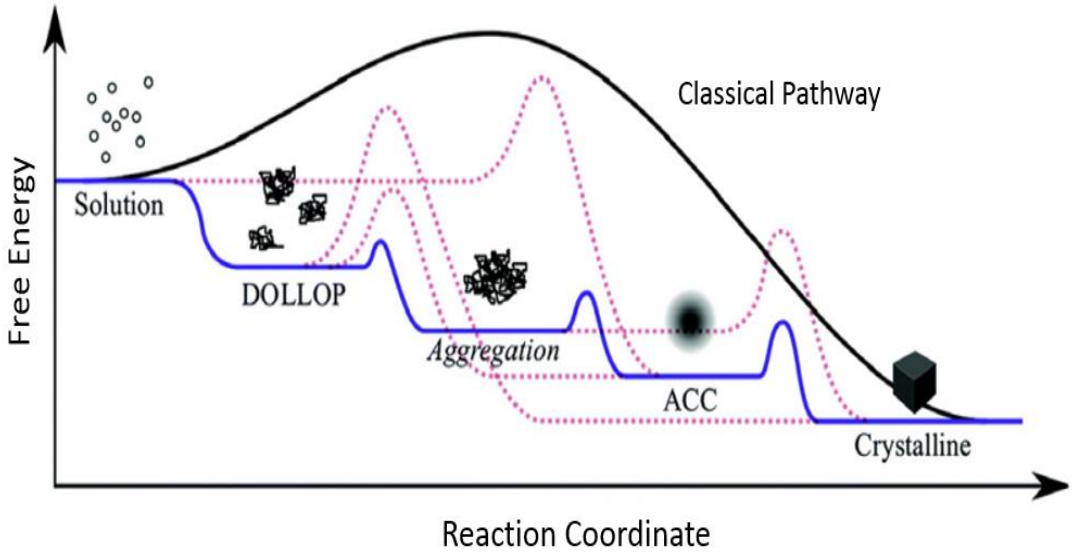


**Figure 8: Free energy diagram of crystallisation under kinetic (blue line) or thermodynamic control (black line)**

However, the stability of prenucleation clusters with respect to the free ions is still debated. Some studies have suggested that they are metastable with respect to the monomers (they are uphill from the monomers in the free energy diagram) [44], whilst others have suggested that the free energy minimum sits below that of the free ions [32, 40, 45]. Regardless, the role that they play in crystallisation is diverse and not restricted to a single pathway, as evidenced by the large number of mechanisms that have been proposed [44-48].

#### *1.1.4.2 Non-classical Aggregation-based Growth*

Crystal growth according to the classical model occurs through the continual addition of individual ions to the crystal. However, it is now known that this is not the case for all systems, and in particular biominerals and their biomimetic counterparts that involve the use of additives [49]. Growing evidence suggests that in some systems, crystal growth proceeds through the assembly of primary nanoparticles (amorphous or crystalline nuclei). There are two mechanisms that have been proposed for aggregation based crystal growth, both of which result in a superstructure composed of iso-oriented single crystal particles. These are oriented attachment and mesocrystal formation (Figure 9).

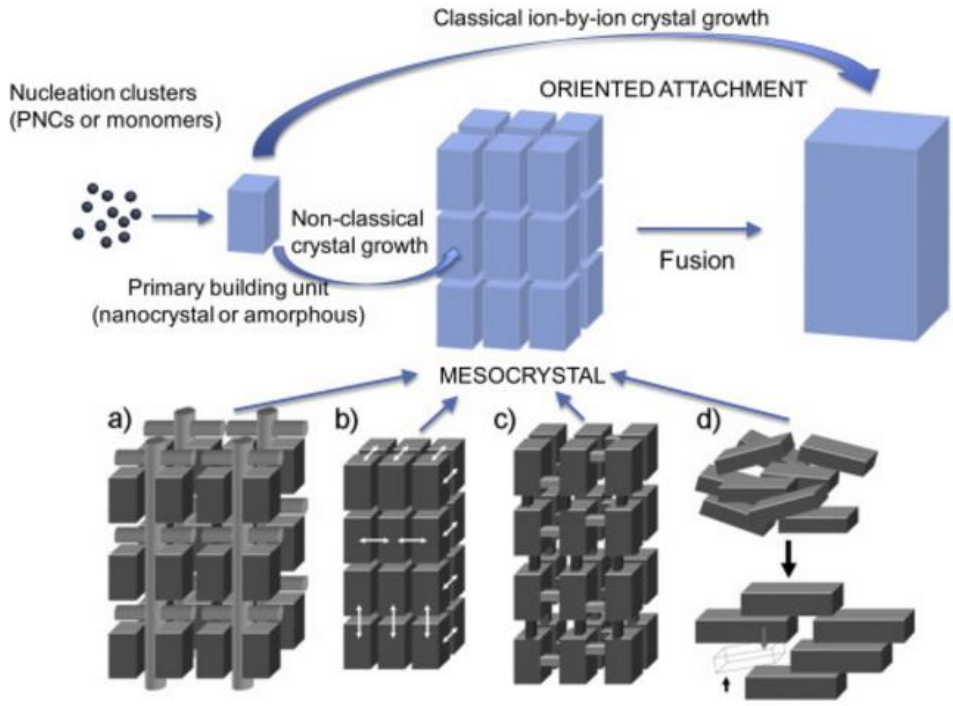


**Figure 9: Schematic representation of classical crystal growth and non-classical crystal growth**

The driving force for the assembly of the primary nanoparticles is a reduction in the surface energy, and once in proximity to one another, their thermal energy allows them to reorient themselves to find the lowest-energy configuration, represented by a corresponding lattice match. The first observation of crystal growth via oriented attachment was of the self-assembly of iron oxide and titania nanoparticles made by Penn and Banfield [50]. More recently, Li *et al* used a HRTEM fluid cell to observe the oriented attachment of iron oxyhydroxide nanocrystals in solution [51]. Oriented attachment may also occur via an amorphous precursor. This was described by Rodriguez-Navarro *et al*, where amorphous calcium carbonate particles were able to assemble into a superstructure due to the presence of calcitic mid-range order within these subunits [52]. This provided sufficient anisotropy to allow the formation of 1D, 2D and 3D ACC structures that were most likely guided by dipole-dipole interactions.

Mesocrystals are defined as “mesoscopically structured crystals” and the term therefore encompasses a broad range of materials since the classification is based on their structure rather than the formation mechanism [49, 53]. They can be considered as “colloidal crystals made up of individual crystalline nanoparticles arranged in crystallographic register via mesoscale aggregation and alignment” [43]. They *may* diffract as single crystals and can

exhibit other single crystal properties (such as birefringence). Some might have a significantly larger surface area than a single crystal at an identical volume because of the exposure of surfaces between the individual subunits, the spacing of which is maintained by the presence of amorphous organic or inorganic layers. However, this is not true for all mesocrystals as the interspace can be inaccessible if completely obstructed by interstitial matter. Another feature that differentiates them from single crystals is a much shorter coherence length (smaller crystallite size), caused by the presence of the iso-oriented subunits [43]. It is also necessary that these subunits have nanoscale sizes, though their alignment need not be perfect and as such not all mesocrystals will diffract as single crystals [53].

There are a number of currently known methods of mesocrystal formation. Nanoparticle alignment by an organic matrix (Figure 9a) occurs when the arrangement of the crystalline subunits is dictated by a biological template. This formation route is dominant in biominerals. The process may occur as the crystals are formed elsewhere and then aligned along the matrix, or alternatively they can nucleate on the matrix, which dictates their orientation as they grow. Another mechanism is by physical fields, such as dipole/electric/magnetic fields, or polarisation forces (Figure 9b). The assembly can occur in the absence of additives, though the interactions that guide the arrangement should be anisotropic. Mineral bridges can facilitate mesocrystal formation (Figure 9c) and these are connections between particles that help transmit the crystallographic alignment between subunits. Spatial constraints can cause the formation of mesocrystals. Their orientation is restricted as the free space reduces, forcing them to pack into an ordered array that efficiently fills the constricted area/volume (Figure 9d). Mesocrystal formation guided by the face-selective adsorption of macromolecules has also been proposed. If the faces of a crystal have sufficiently different charge then preferential adsorption of a macromolecule to specific faces may occur. When in proximity to one another, the interactions between macromolecules and the minimisation of unfavorable interactions may promote mesocrystal formation. Finally, it has also been suggested that mesocrystals can be an intermediate state towards oriented attachment. In this scenario, the displacement of stabilising molecules between nanocrystallites will precede the crystallographic fusion of subunits. This may happen if the stabilisation between the units is not sufficient, and so is driven by the elimination of the interior surfaces.

## 1.2 Calcium Carbonate

Calcium carbonate ($CaCO_3$) is a naturally abundant material that makes up approximately 4% of the Earth's crust and deposits can be found in rocks around the world [54]. It is a common biomineral and is the main constituent of pearls, eggshells and the shells of sea organisms. By incorporation of organic additives, organisms have been able to produce calcium carbonate based materials that have long fascinated researchers [55]. Further, the structures are formed with great control under physiological conditions, a far cry from the high temperatures and toxic environments often used by man to form materials with similar function. Hierarchical structuring is common in biominerals and imparts properties that far exceed those of the inorganic material alone. Alongside its prevalence and success in nature, calcium carbonate has found applications in a diverse range of fields, including construction, agriculture, plastics, paints, papers, adhesives, food and pharmaceuticals [56]. The wide range of uses of this material and the endeavour of scientists to understand and emulate biominerals has meant that a large body of research exists regarding this material. As such, calcium carbonate is often considered as a model system. This is the reason why it has been used extensively throughout this thesis.

Calcium carbonate is only sparingly soluble in pure water. However, the presence of $CO_2$ has a strong influence on the equilibrium of $CaCO_3$ solutions and the solubility of this salt is dictated by the presence of this gas. The existence of simultaneous chemical equilibria of a large number of chemical species ($CO_3^{2-}$ , $HCO_3^-$ , $CO_2$, $Ca^{2+}$, $H_2O$, $H_2CO_3$ etc) across the solid, liquid and gas phases increases the complexity of the system. By consideration of the following chemical equilibria, the solubility of calcium carbonate under a variety of conditions can be explained.

$$Ca^{2+} + 2HCO_3^- \rightleftharpoons Ca^{2+} + CO_3^{2-} + CO_{2(aq)} + H_2O \qquad \text{Equation 18}$$

$$CO_{2(aq)} + H_2O \rightleftharpoons H_2CO_3 \rightleftharpoons HCO_3^- + H^+ \qquad \text{Equation 19}$$

$CO_2$ is able to determine the solubility of calcium carbonate as it alters the quantity of species present in solution. A decrease in the partial pressure of $CO_2$ above the solution will cause aqueous carbon dioxide to be lost according to Le Châtelier's principle. This will have the effect of shifting the equilibrium in Equation 18 to the right (bicarbonate will release carbonate) and Equation 19 to the left, decreasing the concentration of carbonic acid, whilst increasing the

pH. This decreases the solubility of calcium carbonate. This is also indicative of the influence of pH on the solubility of calcium carbonate, as lower pH values (high $P_{CO_2}$) will increase the amount of $HCO_3^-$ present relative to $CO_3^{2-}$, resulting in a calcium carbonate solubility increase. The precipitation of calcium carbonate is exothermic, and so it may be supposed that an increase in temperature will drive Equation 18 to the left. However, carbon dioxide is less soluble at higher temperatures and so the equilibrium will shift to the right, hence why the solubility of $CaCO_3$ is inversely related to temperature [57, 58].

Calcium carbonate has three anhydrous polymorphs, two hydrated forms and several amorphous forms. This thesis is concerned with only the anhydrous and amorphous forms, which will be described in the following sections. In order of decreasing stability at room temperature, these are calcite, aragonite, vaterite and amorphous calcium carbonate.

### 1.2.1 Calcite

Calcite is the most thermodynamically stable form of calcium carbonate at ambient conditions. It has a solubility product at 298K of $3.31 \times 10^{-9}$ $mol^2$ $dm^{-6}$ [7]. The structure of calcite can be considered as a distorted rock salt structure. NaCl has a face-centred cubic unit cell, which can be transformed into the calcite rhombohedral unit cell by some minor modifications. The calcium ions take the place of the sodium ions, while the carbon atom at the centre of each triganol planar carbonate anion occupies the $Cl^-$ location. Hence the $Ca^{2+}$ ions are coordinated by 6 carbonate ions and exist in an octahedral environment where each nearest neighbor is an oxygen atom. Finally, by compression along the three fold symmetry axis [111], one of the body diagonals is shortened by 76.66% while the length of the cube edges are maintained, giving the calcite unit cell. The shape of this unit cell is the same as that of the macroscopic cleavage rhombohedron, though it contains 4 $CaCO_3$ units. However, in calcite there are alternating layers of carbonate ions that are oriented in opposite directions, so the rhombohedral unit cell is not a true unit cell as it does not capture this. Instead, a hexagonal unit cell is often used, which contains 6 $CaCO_3$ units. In this model, the longest axis is the *c* axis and the z coordinates are given in fractions of *c*, which correspond to the equally spaced $Ca^{2+}$ levels. Exactly halfway between these are the carbonate anions with alternating orientation (Figure 10) [59].

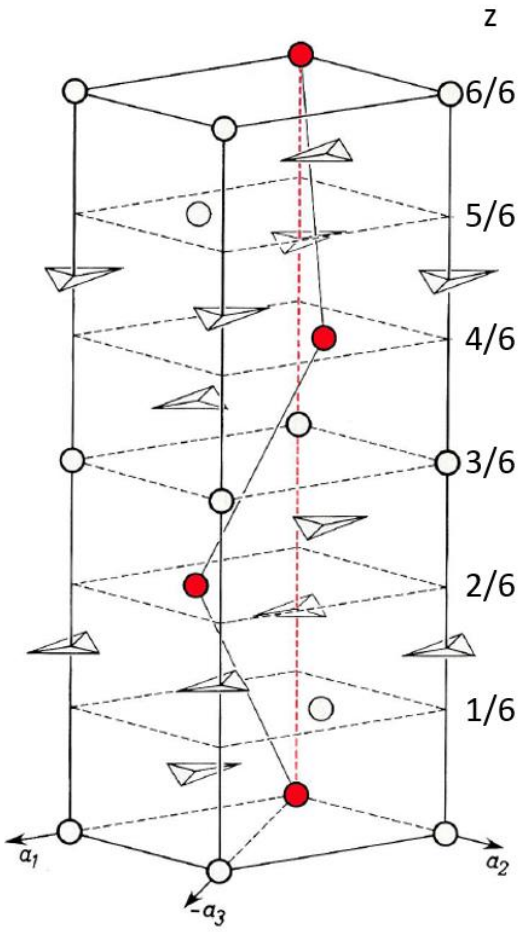


**Figure 10: Hexagonal unit cell of calcite**

### 1.2.2 Aragonite

Aragonite, is the next most stable polymorph under ambient conditions, and has a solubility product of 6.0 x $10^{-9}$ $mol^2$ $dm^{-6}$. It is metastable with respect to calcite and will eventually transform to calcite under ambient conditions. This metastability arises from the fact that each calcium ion is coordinated by 9 oxygen atoms contributed by 6 carbonate anions (three of the anions are bonded to the same calcium by two oxygens each). The calcium cation is relatively small and so this coordination is not as favourable as that found in calcite. The coordination originates from the corrugated structure of the carbonate planes that exist between those of the calcium ions. In the calcite structure, the carbonate ions are situated exactly half way between planes of $Ca^{2+}$. This is not true for the aragonite structure, where the long axis is again the *c* axis and the planes are stacked parallel to this, but the z positions of the rows of carbonates in the same layer alternate in height (Figure 11). Aragonite has a higher density than calcite, which is counterintuitive if one considers only the Ca-O distances of aragonite, which are all larger than that found in calcite. However, the difference in density

is because the average distance between oxygens of adjacent $CO_3^{2-}$ groups is shorter in aragonite, resulting in a more effective packing of the subunits overall [59].

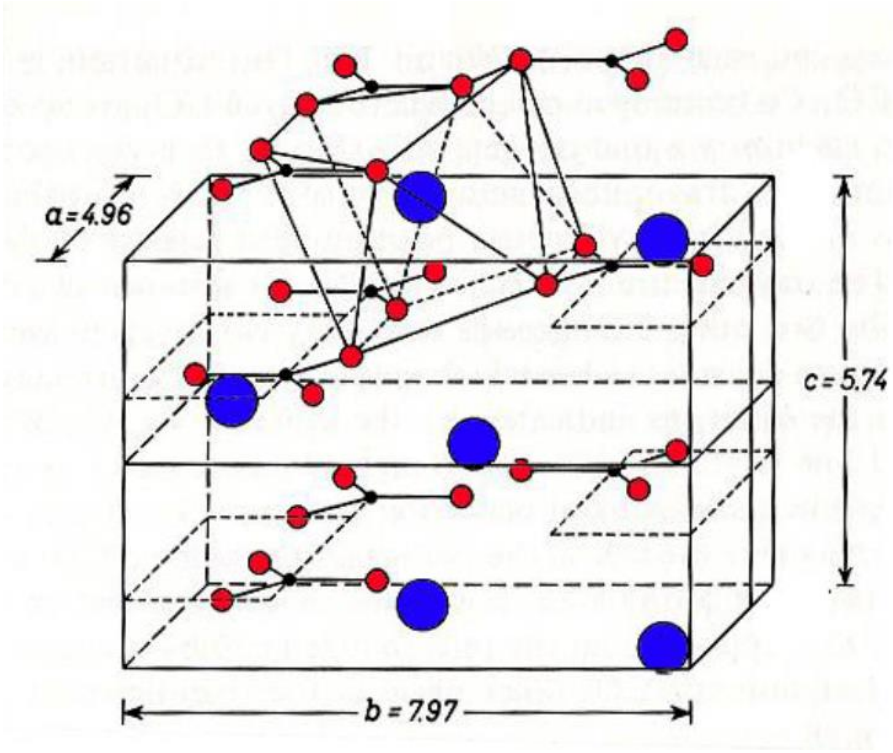


**Figure 11: Orthorhombic unit cell of aragonite**

### 1.2.3 Vaterite

Vaterite is the third modification of calcium carbonate and the least stable polymorph. Its solubility product is 1.22 x $10^{-8}$ $mol^2$ $dm^{-6}$ [7] and so it is the most soluble of the anhydrous polymorphs. In common with the calcite structure, calcium ions exist in an octahedral environment coordinated by 6 oxygens atoms. The hexagonal unit cell is again composed of alternating layers of cations and anions, though instead of possessing carbonate ions that are coplanar with the basal plane, they are parallel to the c axis. The density of vaterite is lower than calcite and aragonite, which aided in its initial identification as a separate polymorph. This is due to a more loosely packed structure [56].

There is also evidence that there are minor crystal structures that exist alongside the major hexagonal structure of the vaterite single crystal. These minor structures have not yet fully been characterised, nor is it fully understood how the minor and major structures are arranged relative to one another in space [61].

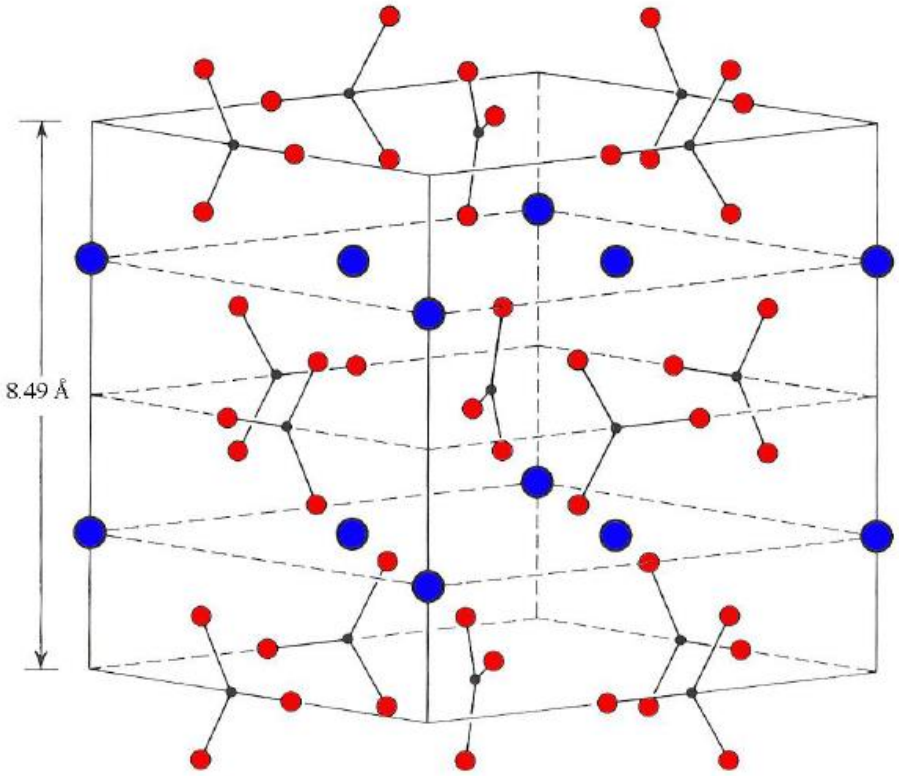


**Figure 12: Subcell of vaterite**

### 1.2.4 Amorphous Calcium Carbonate

Amorphous calcium carbonate (ACC) is the least stable form of calcium carbonate and has a solubility product of 4.0 x $10^{-6}$ $mol^2$ $dm^{-6}$ at 25°C [62]. Since ACC is amorphous, it is isotropic and has no preferred directions or specific morphological features and will exist as spheres in solution in order to minimise the interfacial energy. It readily transforms into the anhydrous polymorphs via dissolution-reprecipitation, and there is evidence to suggest that aragonite and vaterite may form via a surface nucleation event on ACC particles, followed by a solid-state transformation to the crystalline phase, though this has not yet been observed for calcite [63]. Further, there is debate regarding how many forms of ACC may exist. Initially, only one form of ACC was known [64], and then later experiments revealed that there are two forms, anhydrous and hydrous, the latter of which is more stable [65]. More recently, authors have suggested that there may also be an additional two forms of the hydrated phase [66]. There is also evidence to support the existence of proto-calcitic and proto-vateritic ACC, where the local carbonate environments of the amorphous counterparts are similar to those in their crystalline modifications [46]. The formation of crystalline phases from ACC is of significant interest, where contemporary findings indicate that in some instances conventional nucleation pathways are bypassed and non-classical nucleation may occur through the

addition of ACC prenucleation clusters [32, 67]. An alternative method that has been proposed for the formation of different polymorphs is one that is dependent on the size of the ACC particles that form on initial supersaturation. At high supersaturations, vaterite is often the most prevalent phase, which may be due to the initial prevalence of small ACC particles (approx. 70 nm diameter) with low stability that dissolve rapidly and hence produce a high local supersaturation favourable for vaterite. Calcite is typically dominant at low supersaturations, and it has been speculated that this could be because of large ACC particles (200 nm) that cause a gradual increase in the supersaturation, therefore inhibiting the formation of vaterite, leading directly to calcite [68].

## 1.3 Control of Crystallisation Using Surfaces

As described by Section 1.1.2, the interfacial tension plays a critical role in nucleation. The energy barrier to nucleation can be lowered significantly by the formation of an interface between the nucleus and a solid body, as opposed to a single, continuous interface with the solution. The control of nucleation and growth using soluble additives has been studied extensively and methods discovered from this research have been used throughout material engineering. In fact, an understanding of the processes involved has directly contributed to the accelerated advance in technology that has occurred over the past few decades, and will aid in sustaining this trend [69]. Bringing our understanding of how surfaces can control crystallisation in line with that of additives will provide another tool for the materials chemist/engineers toolbox. Surfaces can exert control through their chemistry, or through their topography, often both. Throughout this thesis, thiol self-assembled monolayers are used extensively in order to modify surface chemistry, and thus are described below. What follows is then a review of our current understanding of the influence of surface topography on crystallisation.

### 1.3.1 Thiol Self-Assembled Monolayers

The use of self-assembled monolayers (SAMs) in biomineralisation research was instigated by the understanding that biogenic inorganics are often found in contact with macromolecular matrices enriched in acidic functional groups [70-77]. Technical difficulties associated with purification and characterisation of these large, negatively charged molecules hindered the understanding of their role in biomineral formation and as such, the community gravitated towards SAMs as a model system [71].

Thiol SAMs are 2-dimensional supramolecular assemblies constructed on a solid substrate and formed from solution; the stabilising lateral interactions between molecules are what differentiate SAMs from spontaneously adsorbed molecules [78]. SAMs enable the facile production of highly specific chemical interfaces across large surface areas with regular molecular packing, making them ideal instruments in the investigation of the interaction between inorganic phases and organic surfaces. The SAMs are formed from long-chain thiol molecules that terminate in a ω-terminal group, the functionality of which can be selected (alcohol, ether, carboxylic acid, methyl, perfluorocarbon, aldehyde, amide, ester amine and nitrile) in order to impose desired chemical properties to the metal substrate [79] (Figure 13).

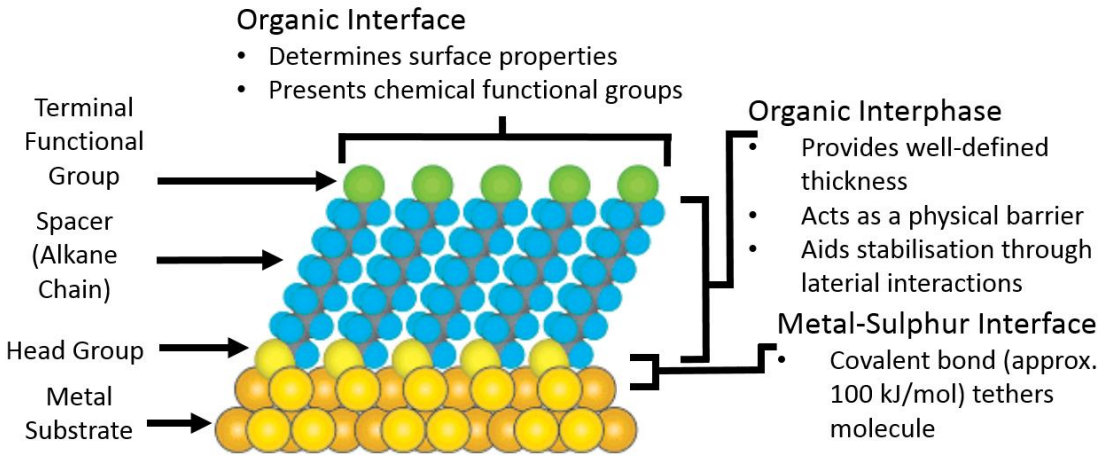


**Figure 13: Schematic representation of the structure of a thiol self-assembled monolayer**

The thiol groups bind strongly and specifically to noble metal surfaces, typically gold or silver are used, and an ordered monolayer results. The substrate on which the SAM is formed can influence the 2-dimensional arrangement of the SAM. For example, if a crystalline support such as (111) gold is used, the organisation of single chain thiols will be commensurate with the crystalline structure of the underlying gold. The thiol-gold bond is on the order of 100 kJ $mol^{-1}$, which is sufficient to make it stable in a range of solvents and temperatures [81]. A high occupancy of available sites is achieved, driven by the high free energy change that occurs on formation of the bond between the headgroup and substrate (for a gold substrate, this is on the order of -120 kcal/mol [82]).

The chemical nature of the terminal group can have a huge effect on the nucleation and growth of a material in contact with the SAM. Termini that interact specifically with the nucleating phase can significantly reduce the energy barrier to nucleation compared to SAM monomers that interact non-specifically. This was demonstrated by Aizenberg, Black and Whitesides in which they patterned a substrate with islands of carboxylic acid terminated monomers arrayed in a sea of $CH_3$ terminated monomers [83]. On exposure to a solution supersaturated with respect to calcium carbonate, crystallisation was restricted to the acidic domains (Figure 14).

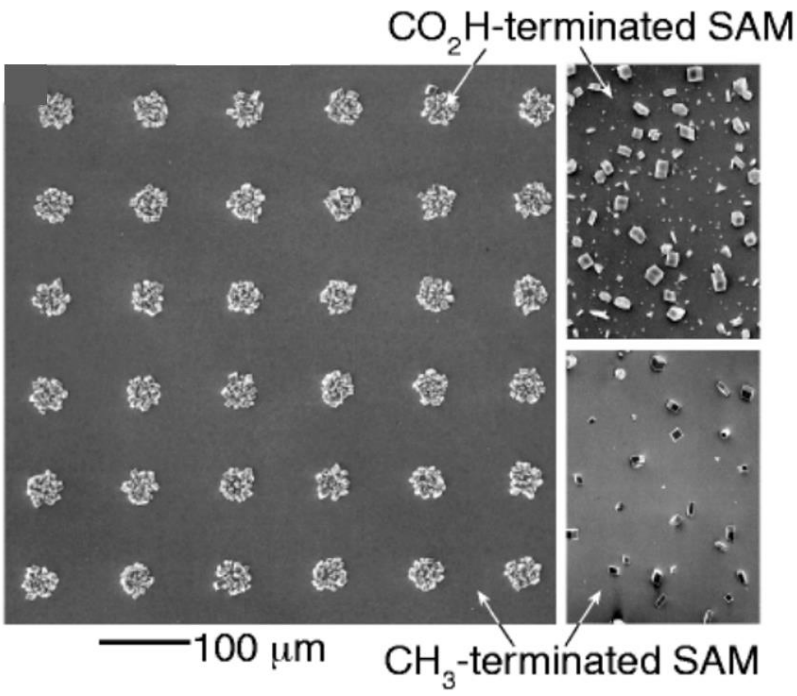


**Figure 14: SEM image of the ordered array of crystals produced by Aizenberg, Black and Whitesides**

The resultant crystal arrangements were attributed to mass transport effects caused by the favourable interactions of the carboxylate terminal groups with calcium carbonate crystals. The rate of nucleation on the polar SAM regions was much greater than that on the methyl terminated spaces. This meant that a growing crystal in the polar region would deplete the calcium and carbonate ions over the non-polar area causing undersaturation and a failure of crystals to grow in these locations.

Consideration of chain parity is also of importance when selecting thiol monomers for SAMs. This was demonstrated by De Yoreo *et al* in an investigation into the formation of calcium carbonate on monolayers formed from either odd or even chained thiol monomers that had the same terminal group [84]. They found that the chain parity determined the orientation of the terminal group. Even though both SAMs possessed carboxylate functional groups, the even-chained monomer formed a more ordered array of terminal groups and so was better able to arrange $Ca^{2+}$ ions at the interface. This resulted in a lower energy barrier to nucleation for the even-chained SAM and oriented precipitation of the heterogeneously precipitated calcite crystals. Similar conclusions were drawn by Han and Aizenberg in an earlier study [85]. The research indicates that the orientation of the terminal group is important in allowing it to interact with the nascent nucleus. This was corroborated by De Yoreo et al in a later study [86] and has been confirmed elsewhere [87, 88].

### 1.3.2 The Effect of Surface Topography on Crystallisation

Although research into the effect of surface topography on crystallisation has not been neglected, there still remains many questions to be answered. Progress has been made in recent years, with studies suggesting that angular geometries are often the most effective at promoting nucleation [10, 89-91]. However, the mechanism by which they achieve this is unclear, which is due in part to the stochastic nature of nucleation and the infinitesimally small entities involved. This makes observation of the early stages difficult. This is complicated further by the number of known nucleation pathways and the fact that a single crystalline material can follow a different route to a stable nucleus depending on the conditions. Hence, given the thermodynamic and kinetic considerations involved in nucleation, it is not unreasonable to suggest that a topographical feature that exhibits control over one system under a defined set of conditions may be ineffective when applied to another in much the same way that is observed with soluble additives. Nevertheless, scientists from a range of disciplines have investigated the interaction between crystals and surface features, and here is presented a review of the knowledge in this area thus far.

Early research into the effect of surface topography was focused on the combined effect of multiple undefined features of a substrate (i.e. surface roughness) and was constrained to fields where prevention of crystal formation was of interest [92-97]. For example, the blockage of tubings and piping by carbonate and sulphate based scale is a huge problem for the petroleum industry with regards to oil production, transportation and refinery [98]. Scale formation must be considered in any industrial process that involves the heating of water, since inorganics such as calcium carbonate, calcium sulphate, calcium phosphate (whose ionic constituents are often naturally abundant in water) exhibit an inverse temperature/solubility relationship [99]. Further, it is not uncommon for industrial plants to use cooling systems where the coolant is sea water [100-102], which must obviously be softened first.

That surface roughness can indeed enhance nucleation, and therefore scale formation, was indicated by Keysar *et al* [103]. They investigated the formation of calcite crystal deposits formed from a flow of highly supersaturated calcium carbonate solution onto steel surfaces of varying roughness. The surface asperities were often found to be the location at which nucleation occurred most readily, with growth spreading across and filling the interstitial valleys. Interestingly, Stevenson *et al* had also observed this manner of nucleation and growth half a decade earlier, but for the formation of diamond thin films via chemical vapour

deposition [104]. Accounts of nucleation and growth proceeding this way in other systems elsewhere in the literature are not to be found. Keysar *et al* suspect that in their case, this may be due to a mass transfer effect, such that the diffusion of ions is greater at convex points compared to concave points (also suggested by Stevenson *et al*). They also found that the roughness of the substrate had an effect on the morphology of the calcite scale. Calcite that had nucleated on a convex point of the roughened substrate were ordered into a fan-like structure, and the mirror image of this fan-like structure was observed in convex locations, though with a lesser degree of organisation. These structures were not observed in the samples grown on a smooth substrate (Figure 15).

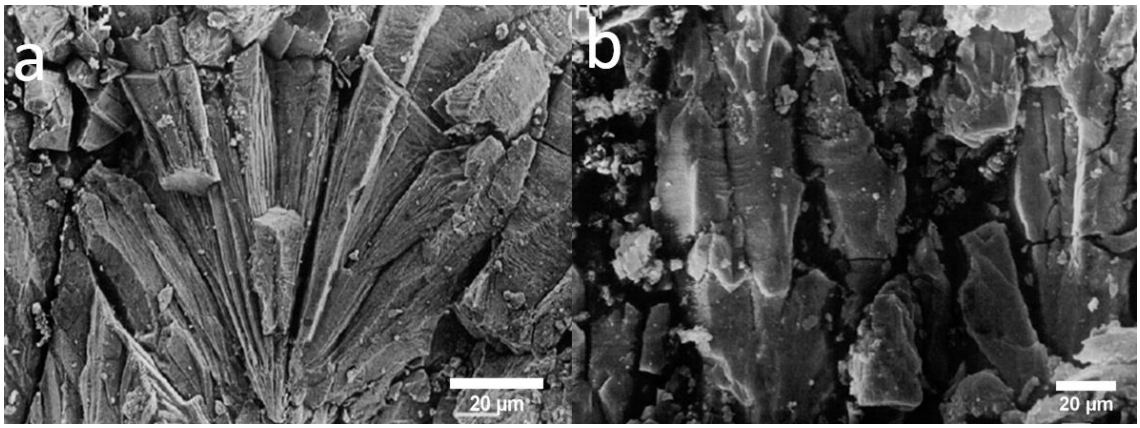


**Figure 15: Different crystal morphologies observed by Keysar *et al* [103]**

As a result of these fan-like features, the "wavy" structure of the roughened surface was maintained in the body of the deposit and the base structure was seen to be duplicated in the top surface of the scale. On the other hand, the scale formed on the smooth substrate was found to exhibit topography typical of a grainy crystalline layer. Macadam and Parsons carried out a similar investigation, in which they found that an increase in surface roughness from 0.2 micrometres to 0.8 micrometres would cause a 30% increase in nucleation rate [105].

Holbrough *et al* also carried out an investigation into the effect of surface roughness on precipitation, though they investigated the nucleation of simple organic substances nucleating from vapour onto glass microscope slides or freshly cleaved muscovite mica [89]. The surface defects were induced through abrasion of the surface with three kinds of diamond powders of different particulate sizes (<10 nm, <1 µm and 40-60 µm), after which the substrates were rinsed with Millipore water, ethanol and then blown dry with nitrogen. No obvious differences in the morphology of the crystals were observed on the mica substrate compared to the glass substrate. The nucleation density was significantly larger on scratched compared to

unscratched mica substrates, though almost indifferent on glass. The 10 nm diameter diamond powder caused significant damage to the mica surface, but left only a few isolated defects on the glass. Flakes of mica produced as a result of the abrasion were observed adhered to the mica surface, whereas the glass surface contained defined furrows. The <1 µm diamond powder caused even more mica flakes and appeared to have disrupted the atomically flat mica to a greater extent than the finer powder, whilst again creating long furrows in the glass substrate, though this time bunched together. Finally, the coarsest powder (40-60 µm particulate size) completely transformed the initially homogenous mica substrate into a landscape of disorder, with piles of mica flakes juxtaposed with deep crevices. The glass substrate exhibited broad grooves concentrated together (Figure 16).

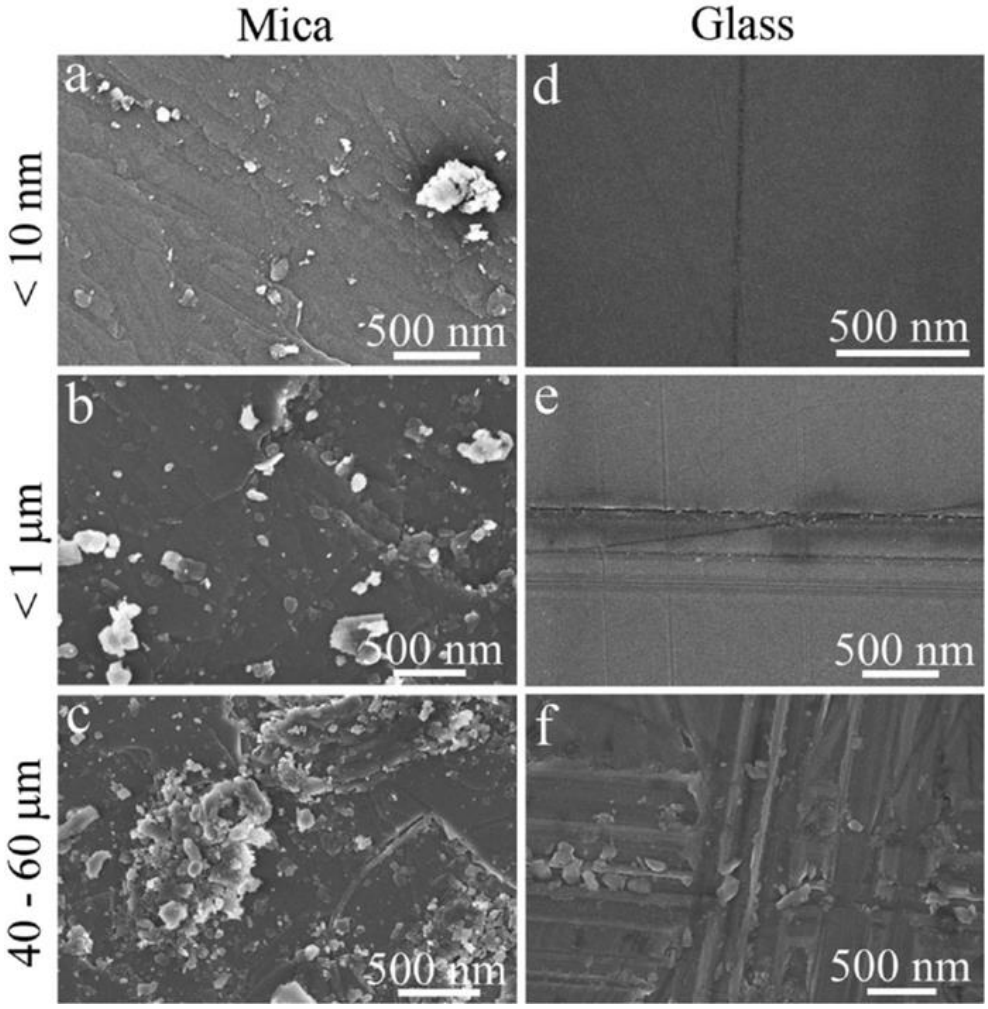


**Figure 16: SEM of the surface defects induced by the different grades of diamond powder on mica and glass substrates by Holbrough *et al***

The authors propose that the finer grades of powder generate a large number of similar nucleation sites, while the larger grain sizes cause fewer nucleation sites to form, but with greater variety. With increasing grain size used to abrade the mica, a greater number and

variety of surface defects are produced. An increase in grain diameter resulted in an increase in nucleation density on the mica substrate, while a decrease in nucleation density was observed on the glass substrate with increasing grain size. The variation in nucleation density between the substrates as a result of grain size is attributed to the dimensions of the defects produced. The fine grain powder creates defects on the glass of similar dimensions to the critical nucleus of the organic substances tested (3-8 nm), thus reducing the free energy barrier and aiding in their stabilisation. The coarser powders do not create surface defects within the size range needed to stabilise the organic nuclei, and so a reduced nucleation density is observed. Conversely, the coarse powders create many topographical features with sharp edges and vertices as a result of the separation of the mica crystal planes. These have dimensions comparable to the critical nucleus of the organic substances, and so a greater nucleation density is observed. Interestingly though, in a separate piece of research the authors conducted an investigation into the freezing of water droplets using a similar methodology and found that topography has little effect on promoting the formation of an ice nucleus [106]. They state that this is most likely because solid nuclei in the melt typically have large contact angles with the substrate, whereas the contact angle of a nucleus forming from vapour is often much smaller. Therefore the reduction in energy barrier caused by a surface feature should be much less for a nucleus forming from the melt compared to formation from vapour. Research carried out by other groups has also confirmed that nucleation can be enhanced by increasing surface roughness [107-113].

More recent is the investigation into the effect of individual surface features on crystallisation, namely surface defects. This line of research was pursued by Campbell *et al* in a study involving the crystallisation of organic molecules from vapour onto a mica substrate. It involved identification of the nucleation sites, vapourisation of the crystals and then characterisation of these surface features [91]. Rather than create surface defects through abrasion with diamond powder as before, naturally occurring cleavage defects were used. These were classified into seven groups for ease of analysis (Figure 17): flat surface, step edge, overhanging flake, cave-like opening, crack, loose fragment and uncharacterisable (too many types of defects situated in area of interest making classification impossible).

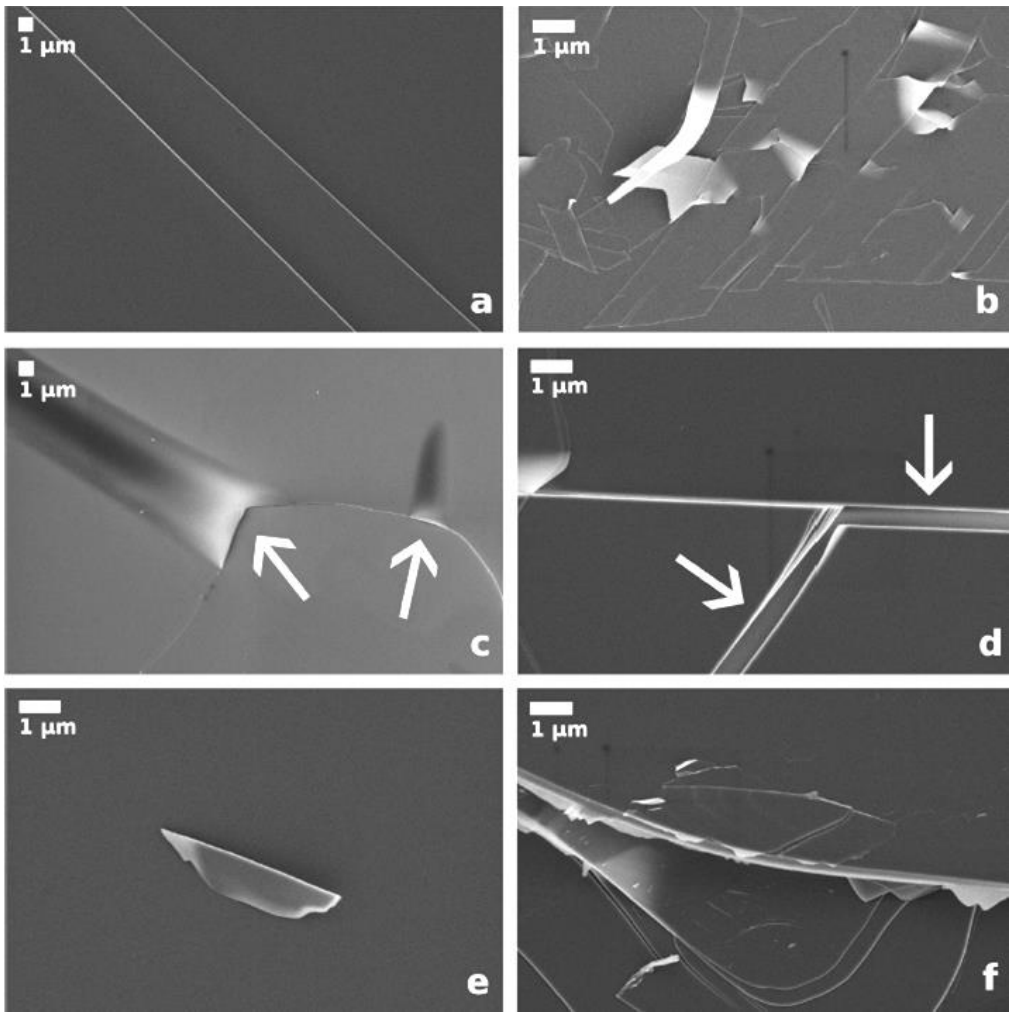


**Figure 17: Surface defects on mica substrate representative of each group as classified by Campbell *et al***

If the nucleation was random, then the majority of crystals would be observed on the flat mica surface (as mica is predominantly flat), with a smaller fraction on the step edges and even less on the remaining types of surface defects. In reality, the inverse of this was observed and for each of the organic substances tested, the same trend was exhibited by each. This can be seen in Figure 18.

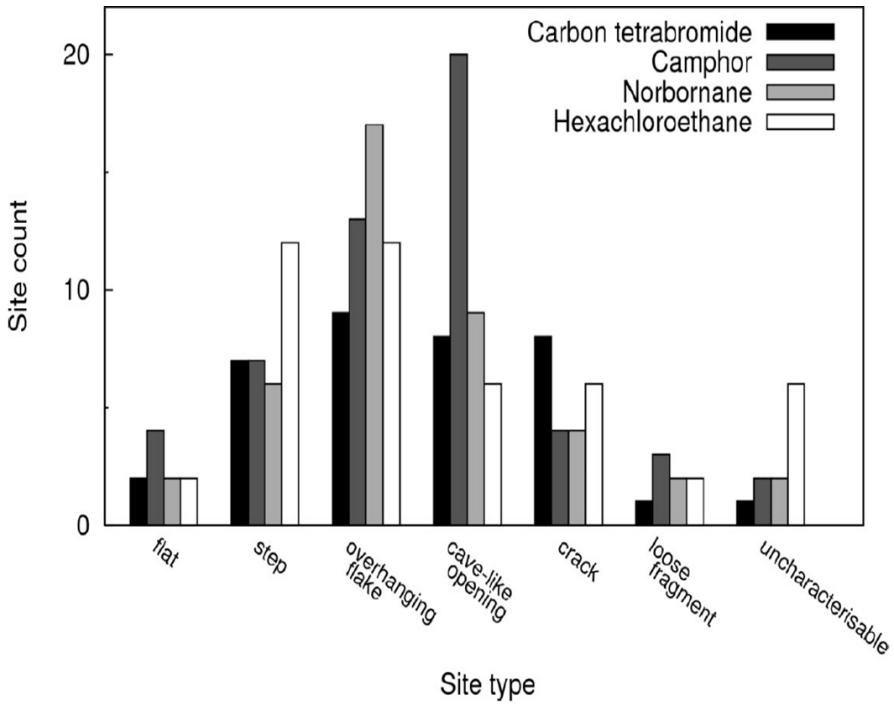


**Figure 18: Plot of Site count vs Site type by Campbell *et al***

Campbell *et al* used the interference fringes present in optical micrographs to calculate the wedge angle of several feature types (Figure 19). An angle of $1.8^{o} \pm 0.1^{o}$ for a hanging flake, $6.3^{o} \pm 0.3^{o}$ for a cave-like opening, $2.3^{o} \pm 0.1^{o}$ for loose fragment and $1.6^{o} \pm 0.2^{o}$ for a split in the surface was obtained, though the measured angles are likely to be wider than at the actual point of contact. The most popular nucleation sites were seen to be those that exhibit wedge geometries, with the more acute the angle of the wedge, the more favourable the site for nucleation. The research revealed a strong correlation between wedge geometry and the effectiveness of nucleation sites.

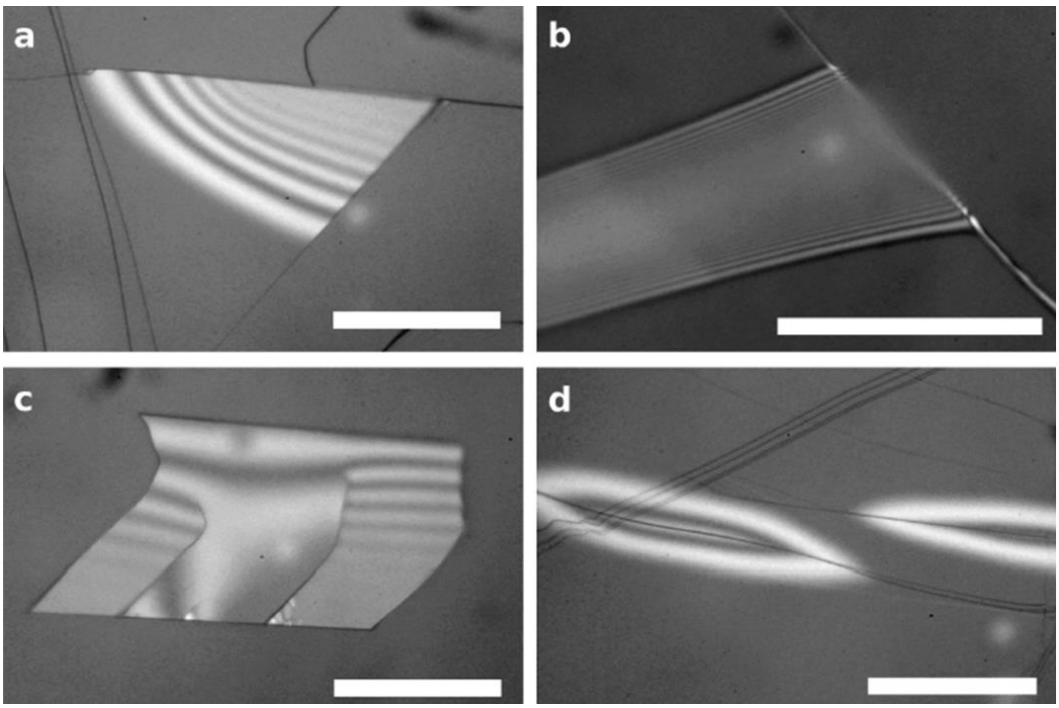


**Figure 19: Optical micrographs of several surface defects displaying infringement patterns obtained by Campbell *et al***

The results obtained by Campbell *et al* are in agreement with calculations carried out by Sholl and Fletcher [114] into the free energy of formation of an isotropic critical nucleus on a planar wedge. Sholl and Fletcher's results suggest that the nucleation barrier of a nucleus forming in an acute wedge is always lower than that of a flat surface. This barrier decreases monotonically with decreasing wedge angle, but an angle exists at which a decrease in nucleation barrier does not occur thereafter. It is also suggested that nuclei with contact angles greater than $150^{o}$ do not experience a significant reduction in the energy barrier, however if the contact angle of the system is less than $90^{o} – (\phi/2)$, in which $\phi$ is the wedge angle, then no nucleation barrier will exist for the nucleating phase and a capillary condensate will form. This method of nucleation, capillary condensation, is proposed by Campell *et al* as the crystallising route of the organic substances used in their experiment. The hypothesis is supported by the authors in work published later, in which capillary condensates are observed in mica pockets for other organic compounds [90].

A number of groups have researched the effect of nanoporous media on the crystallisation of a wide range of materials, where evidence suggests that the most effective nucleators are not only those with the appropriate surface chemistry, but also possess a pore size distribution in the range of a critical nucleus (2 to 10 nm) [115-128]. In addition, a number of simulations have been conducted into the effect of nanopore shape on heterogeneous nucleation. Page

and Sear used a computer simulation of the heterogeneous nucleation of a crystal inside a pore. The pore geometry studied was a simple rectangular slit and the simulation supported the theory that nucleation is orders of magnitude faster in a pore than on a smooth surface [129]. This was substantiated by another computer simulation carried out by Page and Sear into the effect of the wedge angle on the nucleation of a crystal [130]. Their results indicated that an interaction exists between the angle of the wedge and the intrinsic angles of the crystal lattice. This correspondence results in a value for the wedge angle at which the nucleation rate is at a maximum. Furthermore, the data suggests that by engineering an appropriate wedge angle, the crystal polymorph that forms could be selected.

The results obtained by Page and Sear are complimented by an experiment carried out by Diao *et al,* in which lithographic methods were employed to pattern polymer films with nanopores of various shapes and diameters in order to examine their effect on the nucleation of aspirin crystals [131]. A new lithographic technique was developed for the process, named Nanoparticle Imprint Lithography, which allows for the patterning of polymer surfaces with arrays of nanopores of a variety of shapes and sizes. The process uses nanoparticle arrays on quartz slides as templates onto which a mixture of monomer, crosslinker and initiator are poured and then polymerised using UV light. The imprint mould is then peeled off revealing a polymer film with nanopore surface features. By altering the nanoparticle shape, size and density, the nanopores on the substrate can be finely tuned. In addition, the process is nondestructive and so the template can be recovered and reused. The polymer used as the substrate for crystallisation was one that had the capacity to hydrogen bond to aspirin crystal faces. The shapes and sizes of the nanopores were:

- Circular pores of 15 nm, 40 nm and 120 nm diameter.
- Hexagonal pores of 15 nm diameter.
- Square pores of 120 nm diameter.

The extent to which the nanopatterned polymer films reduced the induction time of the nucleation of the aspirin crystals was perceived as a measure of their effectiveness.

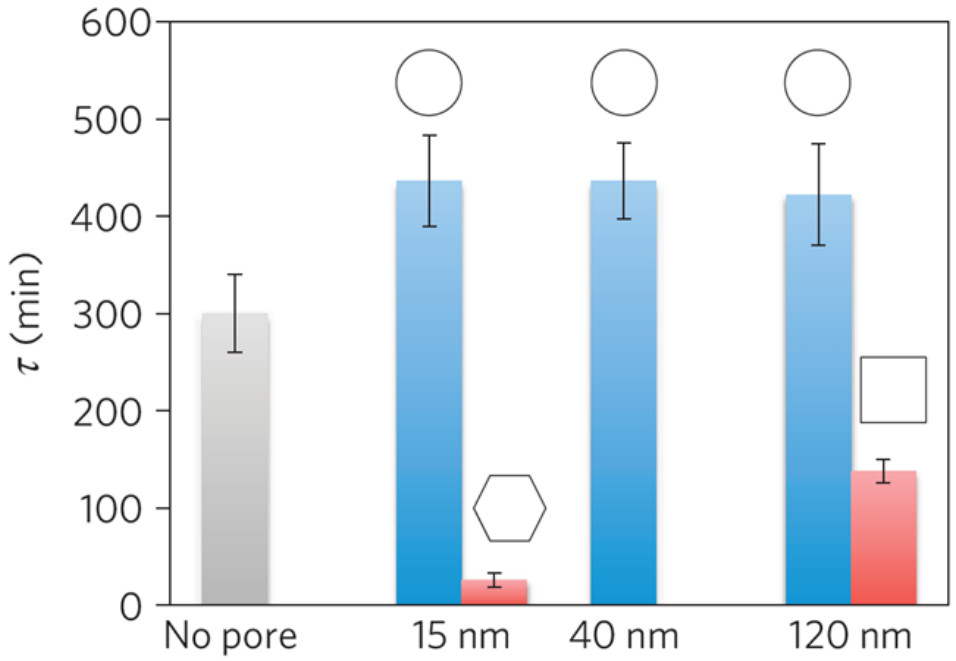


**Figure 20: Effect of nanopore shape and size on the induction time of aspirin as observed by Diao *et al***

Contrary to what might be expected, it was found that the induction time for circular nanopatterned polymer substrates was greater than that of an unpatterned substrate. Also, the diameter of the circular pores appeared to have little effect on the induction time of the aspirin crystals. On the other hand, the square and hexagonal pores resulted in a decrease in induction time relative to the nonporous substrate, with the square pores having a more pronounced effect than the hexagonal. The cause of this difference between the shapes of the pores was said to be a result of 'angle-directed nucleation'. This is a phenomenon in which the angle characteristic of the feature closely matches the intrinsic angles of the crystal lattice resulting in crystal nucleation with a minimum-strain configuration. This is manifested as a geometrical match between the substrate and the crystal and facilitated by crystal face-substrate hydrogen bonding. This hypothesis has been investigated by the same group in a number of other studies, in which their data suggests that the same may be true for the nucleation of other materials in pores with defined shapes [117, 126, 132].

Some groups have opted to investigate surface topography and crystallisation using other micro/nanofabrication techniques [133-143]. Hatton and Aizenberg used a lithographically produced topography to control the heterogeneous nucleation and growth of amorphous calcium carbonate (ACC) [144]. Their work was a development of the research carried out by Varanasi *et al* in which an array of hydrophilic tipped microposts with hydrophobic walls was

used to spatially control the condensation of water droplets. The droplets preferentially nucleated on the tips of the posts and the system was reminiscent of the method by which the Namib Desert beetle collects water in the arid conditions in which it lives [145]. Hatton and Aizenberg used a superhydrophobic silicon nanopost array, with each of the tips of the nanoposts acting as identical nucleation sites, and the liquid interface was limited to the tips of the posts (Figure 21).

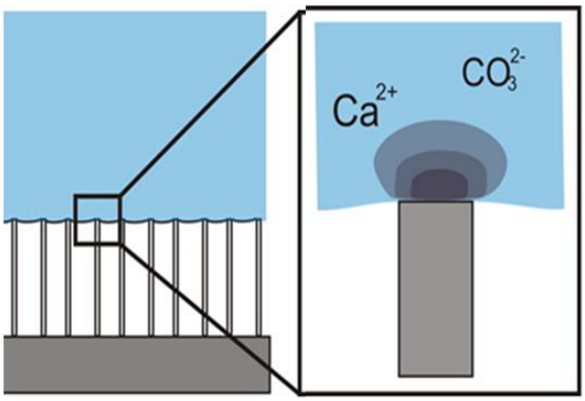


**Figure 21: Schematic of the superhydrophobic Si nanopost array used by Hatton and Aizenberg and the way in which each nanopost acts as a nucleation site**

The posts were produced on the silicon wafer by a deep reactive ion etching Bosch process and the hydrophobic coating through overnight treatment in a vacuum with (heptadecafluoro-1,1,2,2-tetrahydrododecyl)-trichlorosilane after oxygen plasma cleaning. The ACC produced on the nanoposts was monodisperse and the size of the particles was controllable through the reaction time. According to the authors, prior to these results the approximate threshold size limit to prevent an amorphous phase from recrystallisation was thought to be about 100 nm, though the particles grown by Hatton and Aizenberg were almost nine times this (Figure 22).

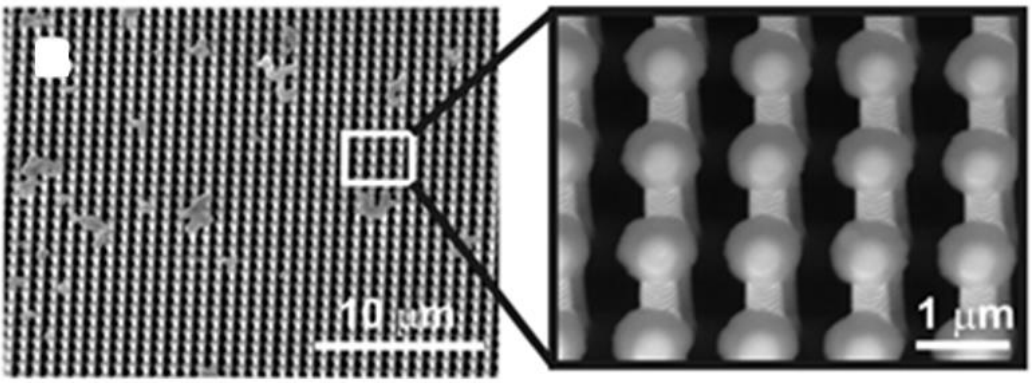


**Figure 22: Si Nanopost array capped by monodisperse amorphous $CaCO_3$ produced by Hatton and Aizenberg**

According to the authors, the technique is hypothetically applicable to a variety of crystal systems. The contact area, time of contact and tip surface chemistry may be manipulated, permitting the formation of a monodisperse array of particles. A number of other projects have demonstrated the use of topographical features to generate ordered 2D arrays of a variety of crystals varying from micrometres to nanometres in size [146-151].

Finally, although the importance of surface topography in nucleation has been demonstrated, it is still not possible to say with certainty what constitutes a good nucleation site or to describe the mechanism by which the site acts. Further, it is often difficult to decouple the effects of surface chemistry and surface topograpy and thus assign any observations to the latter.

## 1.4 References


1. Kashchiev, D., *Nucleation*. 2000: Elsevier Science.
2. Gay, P., *The Crystalline State: An Introduction*. 1972: Oliver & Boyd.
3. Bauer, J., et al., *Ritonavir: an extraordinary example of conformational polymorphism.* Pharmaceutical research, 2001. **18**(6): p. 859-866.
4. Burns, N.D., *A Tin Pest Failure.* Journal of Failure Analysis and Prevention, 2009. **9**(5): p. 461-465.
5. Brice, J.C. and J.C. Brice, *The growth of crystals from liquids*. 1973: North-Holland Pub. Co.
6. Polte, J., *Fundamental growth principles of colloidal metal nanoparticles–a new perspective.* CrystEngComm, 2015. **17**(36): p. 6809-6830.
7. Davey, R.J. and J. Garside, *From Molecules to Crystallizers*. 2000: Oxford University Press, Incorporated.
8. Mullin, J.W., *Crystallization*. 2001: Elsevier Science.
9. De Yoreo, J.J. and P.G. Vekilov, *Principles of crystal nucleation and growth.* Reviews in mineralogy and geochemistry, 2003. **54**(1): p. 57-93.
10. Campbell, J.M., *On topography and crystal nucleation*, in *School of Physics and Astronomy*. 2014, University of Leeds: Leeds. p. 232.
11. Cubillas, P. and M.W. Anderson, *Synthesis Mechanism: Crystal Growth and Nucleation*, in *Zeolites and Catalysis*. 2010, Wiley-VCH Verlag GmbH & Co. KGaA. p. 1-55.
12. De Yoreo, J. and P.G. Vekilov, *Principles of Crystal Nucleation and Growth*, in *Biomineralization*, P.M. Dove, J. De Yoreo, and S. Weiner, Editors. 2003, Mineralogical Society of America. p. 57-93.
13. Sunagawa, I., *Crystals: Growth, Morphology, & Perfection*. 2005: Cambridge University Press.
14. Cubillas, P. and M.W. Anderson, *Synthesis mechanism: crystal growth and nucleation.* Zeolites and Catalysis: Synthesis, Reactions and Applications, 2010: p. 1-55.
15. Threlfall, T., *Structural and thermodynamic explanations of Ostwald's rule.* Organic process research & development, 2003. **7**(6): p. 1017-1027.
16. Chung, S.-Y., et al., *Multiphase transformation and Ostwald's rule of stages during crystallization of a metal phosphate.* Nature Physics, 2009. **5**(1): p. 68-73.
17. Hedges, L.O. and S. Whitelam, *Limit of validity of Ostwald's rule of stages in a statistical mechanical model of crystallization.* The Journal of chemical physics, 2011. **135**(16): p. 164902.
18. Cölfen, H. and S. Mann, *Higher-order organization by mesoscale self-assembly and transformation of hybrid nanostructures.* Angewandte Chemie International Edition, 2003. **42**(21): p. 2350-2365.
19. Meldrum, F.C. and H. Cölfen, *Controlling mineral morphologies and structures in biological and synthetic systems.* Chemical reviews, 2008. **108**(11): p. 4332-4432.
20. Karthika, S., T. Radhakrishnan, and P. Kalaichelvi, *A Review of Classical and Nonclassical Nucleation Theories.* Crystal Growth & Design, 2016. **16**(11): p. 6663-6681.
21. Gránásy, L., *Diffuse interface theory for homogeneous vapor condensation.* The Journal of chemical physics, 1996. **104**(13): p. 5188-5198.
22. Gránásy, L., *Diffuse interface theory of nucleation.* Journal of non-crystalline solids, 1993. **162**(3): p. 301-303.
23. Gránásy, L., *Fundamentals of the diffuse interface theory of nucleation.* The Journal of Physical Chemistry, 1996. **100**(25): p. 10768-10770.

24. Kožíšek, Z., P. Demo, and A. Sveshnikov, *Limits of the Applicability of the Classical Nucleation Theory.* Advanced Science, Engineering and Medicine, 2015. **7**(4): p. 316-320.
25. Gunton, J., *Homogeneous nucleation.* Journal of Statistical Physics, 1999. **95**(5-6): p. 903-923.
26. Cahn, J.W. and J.E. Hilliard, *Free energy of a nonuniform system. I. Interfacial free energy.* The Journal of chemical physics, 1958. **28**(2): p. 258-267.
27. Vekilov, P.G., *Dense liquid precursor for the nucleation of ordered solid phases from solution.* Crystal growth & design, 2004. **4**(4): p. 671-685.
28. Zhang, T.H. and X.Y. Liu, *Effect of long-range attraction on growth model.* The Journal of Physical Chemistry C, 2007. **111**(3): p. 1342-1346.
29. Zhang, K.-Q. and X.Y. Liu, *In situ observation of colloidal monolayer nucleation driven by an alternating electric field.* Nature, 2004. **429**(6993): p. 739-743.
30. Zhang, T.H. and X.Y. Liu, *How Does a Transient Amorphous Precursor Template Crystallization.* Journal of the American Chemical Society, 2007. **129**(44): p. 13520-13526.
31. Chung, S., et al., *Self-catalyzed growth of S layers via an amorphous-to-crystalline transition limited by folding kinetics.* Proceedings of the National Academy of Sciences, 2010. **107**(38): p. 16536-16541.
32. Gebauer, D., A. Völkel, and H. Cölfen, *Stable prenucleation calcium carbonate clusters.* Science, 2008. **322**(5909): p. 1819-1822.
33. Gary, D.C., et al., *Two-Step Nucleation and Growth of InP Quantum Dots via Magic-Sized Cluster Intermediates.* Chemistry of Materials, 2015. **27**(4): p. 1432-1441.
34. Carcouët, C.C.M.C., et al., *Nucleation and Growth of Monodisperse Silica Nanoparticles.* Nano Letters, 2014. **14**(3): p. 1433-1438.
35. Baumgartner, J., et al., *Nucleation and growth of magnetite from solution.* Nat Mater, 2013. **12**(4): p. 310-314.
36. Schiener, A., et al., *In situ investigation of two-step nucleation and growth of CdS nanoparticles from solution.* Nanoscale, 2015. **7**(26): p. 11328-11333.
37. Fleury, B., et al., *Amorphous to Crystal Conversion as a Mechanism Governing the Structure of Luminescent YVO4:Eu Nanoparticles.* ACS Nano, 2014. **8**(3): p. 2602-2608.
38. Kellermeier, M., et al., *Amino acids form prenucleation clusters: ESI-MS as a fast detection method in comparison to analytical ultracentrifugation.* Faraday Discussions, 2012. **159**(0): p. 23-45.
39. Lupulescu, A.I. and J.D. Rimer, *In situ imaging of silicalite-1 surface growth reveals the mechanism of crystallization.* Science, 2014. **344**(6185): p. 729-732.
40. Demichelis, R., et al., *Stable prenucleation mineral clusters are liquid-like ionic polymers.* Nature communications, 2011. **2**: p. 590.
41. Kellermeier, M., et al., *Entropy Drives Calcium Carbonate Ion Association.* ChemPhysChem, 2016. **17**(21): p. 3535-3541.
42. De Yoreo, J.J., N.A. Sommerdijk, and P.M. Dove, *Nucleation pathways in electrolyte solutions*, in *New Perspectives on Mineral Nucleation and Growth*. 2017, Springer. p. 1-24.
43. Rodriguez-Navarro, C., et al., *Nonclassical crystallization in vivo et in vitro (II): Nanogranular features in biomimetic minerals disclose a general colloid-mediated crystal growth mechanism.* Journal of Structural Biology, 2016.
44. Habraken, W.J., et al., *Ion-association complexes unite classical and non-classical theories for the biomimetic nucleation of calcium phosphate.* Nature communications, 2013. **4**: p. 1507.

45. Gebauer, D., et al., *Pre-nucleation clusters as solute precursors in crystallisation.* Chemical Society Reviews, 2014. **43**(7): p. 2348-2371.
46. Gebauer, D., et al., *Proto-calcite and proto-vaterite in amorphous calcium carbonates.* Angewandte Chemie, 2010. **122**(47): p. 9073-9075.
47. Wallace, A.F., et al., *Microscopic Evidence for Liquid-Liquid Separation in Supersaturated CaCO3 Solutions.* Science, 2013. **341**(6148): p. 885-889.
48. Wolf, S.E., et al., *Carbonate-coordinated metal complexes precede the formation of liquid amorphous mineral emulsions of divalent metal carbonates.* Nanoscale, 2011. **3**(3): p. 1158-1165.
49. Song, R.Q. and H. Cölfen, *Mesocrystals—ordered nanoparticle superstructures.* Advanced materials, 2010. **22**(12): p. 1301-1330.
50. Penn, R.L. and J.F. Banfield, *Imperfect oriented attachment: dislocation generation in defect-free nanocrystals.* Science, 1998. **281**(5379): p. 969-971.
51. Li, D., et al., *Direction-specific interactions control crystal growth by oriented attachment.* Science, 2012. **336**(6084): p. 1014-1018.
52. Rodriguez-Navarro, C., et al., *Formation of amorphous calcium carbonate and its transformation into mesostructured calcite.* CrystEngComm, 2015. **17**(1): p. 58-72.
53. Sturm, E.V. and H. Cölfen, *Mesocrystals: structural and morphogenetic aspects.* Chemical Society Reviews, 2016. **45**(21): p. 5821-5833.
54. Turekian, K.K. and K.H. Wedepohl, *Distribution of the elements in some major units of the earth's crust.* Geological Society of America Bulletin, 1961. **72**(2): p. 175-192.
55. Meldrum, F.C., *Calcium carbonate in biomineralisation and biomimetic chemistry.* International Materials Reviews, 2003. **48**(3): p. 187-224.
56. Tegethoff, F.W., J. Rohleder, and E. Kroker, *Calcium Carbonate: From the Cretaceous Period Into the 21st Century*. 2001: Birkhäuser Verlag.
57. Gutzow, I. and J. Schmelzer, *The vitreous state: thermodynamics, structure, rheology, and crystallization*. 2013: Springer Heidelberg.
58. Roy, R.N., et al., *The thermodynamics of aqueous carbonate solutions II. Mixtures of potassium carbonate, bicarbonate, and chloride.* The Journal of Chemical Thermodynamics, 1984. **16**(4): p. 303-315.
59. Lippmann, F., *Sedimentary carbonate minerals*. Vol. 228. 1973: Springer.
60. Lam, S.K.R., *Calcium Carbonate Deposition in Synthetic Systems*, in *School of Chemistry*. 2008, University of Bristol: Bristol. p. 372.
61. Kabalah-Amitai, L., et al., *Vaterite crystals contain two interspersed crystal structures.* Science, 2013. **340**(6131): p. 454-457.
62. Hamm, L.M., et al., *Reconciling disparate views of template-directed nucleation through measurement of calcite nucleation kinetics and binding energies.* Proceedings of the National Academy of Sciences, 2014. **111**(4): p. 1304-1309.
63. Nielsen, M.H., S. Aloni, and J.J. De Yoreo, *In situ TEM imaging of CaCO3 nucleation reveals coexistence of direct and indirect pathways.* Science, 2014. **345**(6201): p. 1158-1162.
64. Brečević, L. and A.E. Nielsen, *Solubility of amorphous calcium carbonate.* Journal of Crystal Growth, 1989. **98**(3): p. 504-510.
65. Koga, N. and Y. Yamane, *Thermal behaviors of amorphous calcium carbonates prepared in aqueous and ethanol media.* Journal of Thermal Analysis and Calorimetry, 2008. **94**(2): p. 379-387.
66. Radha, A., et al., *Transformation and crystallization energetics of synthetic and biogenic amorphous calcium carbonate.* Proceedings of the National Academy of Sciences, 2010. **107**(38): p. 16438-16443.

67. Pouget, E.M., et al., *The initial stages of template-controlled CaCO3 formation revealed by cryo-TEM.* Science, 2009. **323**(5920): p. 1455-1458.
68. Zou, Z., et al., *Opposite particle size effect on amorphous calcium carbonate crystallization in water and during heating in air.* Chemistry of Materials, 2015. **27**(12): p. 4237-4246.
69. Markov, I.V., *Crystal growth for beginners: fundamentals of nucleation, crystal growth and epitaxy*. 2003: World scientific.
70. Addadi, L., et al., *Mollusk shell formation: a source of new concepts for understanding biomineralization processes.* Chemistry-A European Journal, 2006. **12**(4): p. 980-987.
71. Gotliv, B.A., et al., *Asprich: A novel aspartic acid-rich protein family from the prismatic shell matrix of the bivalve Atrina rigida.* ChemBioChem, 2005. **6**(2): p. 304-314.
72. Aizenberg, J., et al., *Factors involved in the formation of amorphous and crystalline calcium carbonate: a study of an ascidian skeleton.* Journal of the American Chemical Society, 2002. **124**(1): p. 32-39.
73. Albeck, S., et al., *Interactions of various skeletal intracrystalline components with calcite crystals.* Journal of the American Chemical Society, 1993. **115**(25): p. 11691-11697.
74. Weiner, S. and L. Addadi, *Acidic macromolecules of mineralized tissues: the controllers of crystal formation.* Trends in biochemical sciences, 1991. **16**: p. 252-256.
75. Herman, A., L. Addadi, and S. Weiner, *Interactions of sea-urchin skeleton macromolecules with growing calcite crystals—a study of intracrystalline proteins.* 1988.
76. Addadi, L., et al., *A chemical model for the cooperation of sulfates and carboxylates in calcite crystal nucleation: relevance to biomineralization.* Proceedings of the National Academy of Sciences, 1987. **84**(9): p. 2732-2736.
77. Addadi, L. and S. Weiner, *Interactions between acidic proteins and crystals: stereochemical requirements in biomineralization.* Proceedings of the National Academy of Sciences, 1985. **82**(12): p. 4110-4114.
78. Kondo, T., R. Yamada, and K. Uosaki, *Self-Assembled Monolayer (SAM)*, in *Organized Organic Ultrathin Films*. 2013, Wiley-VCH Verlag GmbH & Co. KGaA. p. 7-42.
79. Bhushan, B. and H. Liu, *Self-Assembled Monolayers for Controlling Adhesion, Friction and Wear*, in *Nanotribology and Nanomechanics: An Introduction*, B. Bhushan, Editor. 2005, Springer Berlin Heidelberg: Berlin, Heidelberg. p. 885-928.
80. Love, J.C., et al., *Self-assembled monolayers of thiolates on metals as a form of nanotechnology.* Chemical reviews, 2005. **105**(4): p. 1103-1170.
81. Vos, J.G., R.J. Forster, and T.E. Keyes, *Interfacial Supramolecular Assemblies*. 2003: Wiley.
82. Butt, H.J., K. Graf, and M. Kappl, *Physics and Chemistry of Interfaces*. 2006: Wiley.
83. Aizenberg, J., A.J. Black, and G.M. Whitesides, *Control of crystal nucleation by patterned self-assembled monolayers.* Nature, 1999. **398**(6727): p. 495-498.
84. Hu, Q., et al., *The thermodynamics of calcite nucleation at organic interfaces: Classical vs. non-classical pathways.* Faraday Discussions, 2012. **159**(1): p. 509-523.
85. Han, Y.-J. and J. Aizenberg, *Face-Selective Nucleation of Calcite on Self-Assembled Monolayers of Alkanethiols: Effect of the Parity of the Alkyl Chain.* Angewandte Chemie, 2003. **115**(31): p. 3796-3798.
86. Lee, J.R., et al., *Cooperative reorganization of mineral and template during directed nucleation of calcium carbonate.* The Journal of Physical Chemistry C, 2013. **117**(21): p. 11076-11085.

87. Lee, J.R., et al., *Structural development of mercaptophenol self-assembled monolayers and the overlying mineral phase during templated CaCO3 crystallization from a transient amorphous film.* Journal of the American Chemical Society, 2007. **129**(34): p. 10370-10381.
88. Lee, J.R.I., et al., *Effect of Ring Substitution Position on the Structural Conformation of Mercaptobenzoic Acid Self-Assembled Monolayers on Au(111).* Langmuir, 2006. **22**(26): p. 11134-11141.
89. Holbrough, J., et al., *Topographical control of crystal nucleation.* Crystal Growth & Design, 2012. **12**(2): p. 750-755.
90. Campbell, J.M., F.C. Meldrum, and H.K. Christenson, *Observing the formation of ice and organic crystals in active sites.* Proceedings of the National Academy of Sciences, 2016: p. 201617717.
91. Campbell, J.M., F.C. Meldrum, and H.K. Christenson, *Characterization of Preferred Crystal Nucleation Sites on Mica Surfaces.* Crystal Growth & Design, 2013. **13**(5): p. 1915-1925.
92. Jarvis, P., *Scaling processes and problems.* Plant, Cell & Environment, 1995. **18**(10): p. 1079-1089.
93. Donaldson, J., *Scale prevention and descaling.* Tube Int., 1988. **7**(1): p. 39-42.
94. Rankin, B. and W. Adamson, *Scale formation as related to evaporator surface conditions.* Desalination, 1973. **13**(1): p. 63-87.
95. Glater, J., J.L. York, and K.S. Campbell, *Scale formation and prevention*. Vol. 627. 1980: Academic Press.
96. Donaldson, J. and S. Grimes, *Lifting the scales from our pipes.* New Scientist, 1988. **117**(18): p. 43-46.
97. Merrill, D. and R.L. Sanks, *Corrosion Control by Deposition of Calcium Carbonate Films: Part 2, A Practical Approach for Operators.* American Water Works Association Journal, 1977. **69**(12): p. 634-40.
98. Chen, T., et al. *A Physical Preventive Treatment of Crystallization and Precipitation in the Petroleum Industry*. in *Canadian International Petroleum Conference*. 2001. Petroleum Society of Canada.
99. Ben, B.R. and M.L. Clarendon, *Prevention of and removal of scale formation in water systems*. 1969, Google Patents.
100. Macdonald, I.A., et al., *Industrial cooling seawater antifouling optimisation through the adoption of Pulse-Chlorination®.* Operational and environmental consequences of large industrial cooling water systems. Springer, New York, 480pp, 2012. **8**.
101. Polman, H., F. Verhaart, and M. Bruijs, *Impact of biofouling in intake pipes on the hydraulics and efficiency of pumping capacity.* Desalination and Water Treatment, 2013. **51**(4-6): p. 997-1003.
102. Bruijs, M., *Cost Effective Fouling Control in Cooling Water Intake Systems with Environmental and Operational Benefits*, in *Recent Progress in Desalination, Environmental and Marine Outfall Systems*. 2015, Springer. p. 109-118.
103. Keysar, S., et al., *Effect of Surface Roughness on the Morphology of Calcite Crystallizing on Mild Steel.* Journal of Colloid and Interface Science, 1994. **162**(2): p. 311-319.
104. Dennig, P.A. and D.A. Stevenson, *Influence of substrate topography on the nucleation of diamond thin films.* Applied physics letters, 1991. **59**(13): p. 1562-1564.
105. Macadam, J. and S. Parsons, *Calcium carbonate scale control, effect of material and inhibitors.* Water Science & Technology, 2004. **49**(2): p. 153-159.

106. Campbell, J.M., F.C. Meldrum, and H.K. Christenson, *Is ice nucleation from supercooled water insensitive to surface roughness?* The Journal of Physical Chemistry C, 2015. **119**(2): p. 1164-1169.
107. Liu, Y., et al., *Investigation of adhesion of CaCO3 crystalline fouling on stainless steel surfaces with different roughness.* International Communications in Heat and Mass Transfer, 2011. **38**(6): p. 730-733.
108. Förster, M., W. Augustin, and M. Bohnet, *Influence of the adhesion force crystal/heat exchanger surface on fouling mitigation.* Chemical Engineering and Processing: Process Intensification, 1999. **38**(4): p. 449-461.
109. Herz, A., M.R. Malayeri, and H. Müller-Steinhagen, *Fouling of roughened stainless steel surfaces during convective heat transfer to aqueous solutions.* Energy Conversion and Management, 2008. **49**(11): p. 3381-3386.
110. Lei, C., et al., *Experimental observation of surface morphology effect on crystallization fouling in plate heat exchangers.* International Communications in Heat and Mass Transfer, 2011. **38**(1): p. 25-30.
111. Cheong, W.C., P.H. Gaskell, and A. Neville, *Substrate effect on surface adhesion/crystallisation of calcium carbonate.* Journal of Crystal Growth, 2013. **363**(0): p. 7-21.
112. Bargir, S., et al., *The use of contact angle measurements to estimate the adhesion propensity of calcium carbonate to solid substrates in water.* Applied Surface Science, 2009. **255**(9): p. 4873-4879.
113. Bohnet, M., *Influence of the transport properties of the crystal/heat transfer surface interfacial on fouling behavior.* Chemical engineering & technology, 2003. **26**(10): p. 1055-1060.
114. Sholl, C. and N. Fletcher, *Decoration criteria for surface steps.* Acta Metallurgica, 1970. **18**(10): p. 1083-1086.
115. Chayen, N.E., *Turning protein crystallisation from an art into a science.* Current Opinion in Structural Biology, 2004. **14**(5): p. 577-583.
116. Saridakis, E. and N.E. Chayen, *Towards a 'universal' nucleant for protein crystallization.* Trends in Biotechnology, 2009. **27**(2): p. 99-106.
117. Diao, Y., et al., *Surface Design for Controlled Crystallization: The Role of Surface Chemistry and Nanoscale Pores in Heterogeneous Nucleation.* Langmuir, 2011. **27**(9): p. 5324-5334.
118. Veran-Tissoires, S., M. Marcoux, and M. Prat, *Salt crystallisation at the surface of a heterogeneous porous medium.* EPL (Europhysics Letters), 2012. **98**(3): p. 34005.
119. Benavente, D., et al., *Role of pore structure in salt crystallisation in unsaturated porous stone.* Journal of Crystal Growth, 2004. **260**(3–4): p. 532-544.
120. Khurshid, S., et al., *Porous nucleating agents for protein crystallization.* Nat. Protocols, 2014. **9**(7): p. 1621-1633.
121. Bolanos-Garcia, V.M. and N.E. Chayen, *New directions in conventional methods of protein crystallization.* Progress in Biophysics and Molecular Biology, 2009. **101**(1–3): p. 3-12.
122. Chayen, N.E., *Methods for separating nucleation and growth in protein crystallisation.* Progress in Biophysics and Molecular Biology, 2005. **88**(3): p. 329-337.
123. Chayen, N.E., E. Saridakis, and R.P. Sear, *Experiment and theory for heterogeneous nucleation of protein crystals in a porous medium.* Proceedings of the National Academy of Sciences of the United States of America, 2006. **103**(3): p. 597-601.
124. Scherer, G.W., *Crystallization in pores.* Cement and Concrete Research, 1999. **29**(8): p. 1347-1358.

125. Chayen, N., et al., *Porous silicon: an effective nucleation-inducing material for protein crystallization.* Journal of molecular biology, 2001. **312**(4): p. 591-595.
126. Tan, L., et al., *Control of Heterogeneous Nucleation via Rationally Designed Biocompatible Polymer Surfaces with Nanoscale Features.* Crystal Growth & Design, 2015. **15**(5): p. 2176-2186.
127. Deng, Y., X. Li, and Q. Li, *Effect of pore size on the growth of hydroxyapatite from mesoporous CaO− SiO2 substrate.* Industrial & Engineering Chemistry Research, 2009. **48**(19): p. 8829-8836.
128. Zhou, R.-B., et al., *A review on recent advances for nucleants and nucleation in protein crystallization.* CrystEngComm, 2017. **19**(8): p. 1143-1155.
129. Page, A.J. and R.P. Sear, *Heterogeneous Nucleation in and out of Pores.* Physical review letters, 2006. **97**(6): p. 065701.
130. Page, A.J. and R.P. Sear, *Crystallization Controlled by the Geometry of a Surface.* Journal of the American Chemical Society, 2009. **131**(48): p. 17550-17551.
131. Diao, Y., et al., *The role of nanopore shape in surface-induced crystallization.* Nature Materials, 2011. **10**(11): p. 867-871.
132. López-Mejías, V., A.S. Myerson, and B.L. Trout, *Geometric Design of Heterogeneous Nucleation Sites on Biocompatible Surfaces.* Crystal Growth & Design, 2013. **13**(8): p. 3835-3841.
133. Chen, H.-M., et al., *Thermally induced morphology evolution of pit-patterned Si substrate and its effect on nucleation properties of Ge dots.* Nanotechnology, 2011. **23**(1): p. 015303.
134. Ribeiro-Andrade, R., et al., *Study of growth properties of InAs islands on patterned InP substrates defined by focused ion beam.* Physica E: Low-dimensional Systems and Nanostructures, 2017. **87**: p. 59-67.
135. Cho, Y., T.S. Shim, and S. Yang, *Spatially Selective Nucleation and Growth of Water Droplets on Hierarchically Patterned Polymer Surfaces.* Advanced Materials, 2015: p. n/a-n/a.
136. Das, K., et al., *Preferential ordering of self-assembled Ge islands on focused ion-beam patterned Si (100).* Journal of Nanoparticle Research, 2012. **14**(2): p. 725.
137. Huangfu, Y., et al., *Optimal growth of Ge-rich dots on Si (001) substrates with hexagonal packed pit patterns.* Nanotechnology, 2012. **24**(3): p. 035302.
138. Yoon, T.-S., et al., *Microstructure analysis of epitaxially grown self-assembled Ge islands on nanometer-scale patterned SiO 2⁄ Si substrates by high-resolution transmission electron microscopy.* Journal of Applied Physics, 2007. **102**(10): p. 104306.
139. Portavoce, A., et al., *Mechanism of the nanoscale localization of Ge quantum dot nucleation on focused ion beam templated Si (001) surfaces.* Nanotechnology, 2006. **17**(17): p. 4451.
140. Duska, C.J. and J.A. Floroa, *Highly uniform arrays of epitaxial Ge quantum dots with interdot spacing of 50 nm.* structure, 2014. **12**: p. 17.
141. Aqua, J.-N., et al., *Growth and self-organization of SiGe nanostructures.* Physics Reports, 2013. **522**(2): p. 59-189.
142. Lee, J.Y., et al., *Filling of hole arrays with InAs quantum dots.* Nanotechnology, 2009. **20**(28): p. 285305.
143. Gherasimova, M., et al., *Controlled Nucleation of Ge Islands on Si and Self-Assembly of Nanoscale Island Clusters.* International Journal of High Speed Electronics and Systems, 2014. **23**(01n02): p. 1420003.

144. Hatton, B.D. and J. Aizenberg, *Writing on Superhydrophobic Nanopost Arrays: Topographic Design for Bottom-up Assembly.* Nano Letters, 2012. **12**(9): p. 4551-4557.
145. Varanasi, K.K., et al., *Spatial control in the heterogeneous nucleation of water.* Applied Physics Letters, 2009. **95**(9): p. -.
146. Thalladi, V.R. and G.M. Whitesides, *Crystals of Crystals: Fabrication of Encapsulated and Ordered Two-Dimensional Arrays of Microcrystals.* Journal of the American Chemical Society, 2002. **124**(14): p. 3520-3521.
147. Suh, K.Y., et al., *Single Nanocrystal Arrays on Patterned Poly(ethylene glycol) Copolymer Microstructures Using Selective Wetting and Drying.* Langmuir, 2004. **20**(15): p. 6080-6084.
148. Su, B., et al., *"Clinging-Microdroplet" Patterning Upon High-Adhesion, Pillar-Structured Silicon Substrates.* Advanced Functional Materials, 2011. **21**(17): p. 3297-3307.
149. Mishchenko, L., et al., *Spatial Control of Condensation and Freezing on Superhydrophobic Surfaces with Hydrophilic Patches.* Advanced Functional Materials, 2013. **23**(36): p. 4577-4584.
150. McCarthy, T.J. and Y. Wang, *Dip-Coating Deposition on Chemically Patterned Surfaces: A Mechanistic Analysis and Comparison with Topographically Patterned Surfaces.* Langmuir, 2014.
151. Barton, J.E. and T.W. Odom, *Mass-Limited Growth in Zeptoliter Beakers: A General Approach for the Synthesis of Nanocrystals.* Nano Letters, 2004. **4**(8): p. 1525-1528.

# 2 Crystallisation on a Plasma-treated Poly(dimethylsiloxane) Substrate

## 2.1 Introduction

The work presented in this chapter describes a method of controlling crystallisation using the surface topography of plasma-treated poly(dimethylsiloxane) substrates. Preliminary work had revealed that defects introduced to glass substrates through abrasion with diamond powder could localise the precipitation of calcium carbonate. A system that offered more control and greater efficacy was sought, and the substrate used to provide this was a plasma-treated poly(dimethylsiloxane) (PPDMS). On exposure to radio-frequency generated atmospheric air-plasma for a sufficiently long time, fractures form in the surface of PDMS due to oxidation. When used as substrate for the crystallisation of inorganics, the crystals preferentially precipitate at these surface cracks. The aim of the work presented in this chapter was to use this system to investigate the effects that surface topography can have on crystal nucleation and growth.

The majority of this chapter involves an investigation into the precipitation of calcium carbonate on plasma-treated PDMS (PPDMS), although other carbonates were investigated, as well as calcium oxalate. Plasma exposure can cause a diverse arrangement of surface fractures to occur on the surface of PPDMS, and these were documented using scanning electron microscopy (SEM) and atomic force microscopy (AFM). When used as a substrate for calcium carbonate crystallisation, the crystals showed a strong preference for the cracks. The research was progressed by modifying the surface chemistry using a carboxylate terminated thiol monolayer, with the aim of producing a chemically homogenous substrate surface. On crystallising calcium carbonate, enhanced alignment to the cracks as well as an increase in crystal populations under the same conditions were observed. The electron micrographs of these substrates illustrate how strong this preference for the surface feature was, such that crystals would only nucleate away from the cracks once they had been fully occupied. A number of other experiments were conducted including variation of the cation:anion ratio and an alternative precipitation method. The effect of magnesium ions on the crystallisation was investigated, as well as methods to control the arrangement of cracks and therefore

distribution of crystals. Finally, a method of modifying the thiol SAM post-formation and the effect that this has on crystallisation is documented, and then separately, crystallisation on a silane SAM is described. The results demonstrate that topography can indeed have a very strong effect on crystallisation and can be manipulated to control the formation of crystals.

## 2.2 Background

### 2.2.1 PDMS

Poly(dimethylsiloxane) (PDMS) is a siloxane polymer that that has been used for a huge variety of applications, most notably in microfluidics and bioengineering [1]. The molecular structure consists of a silicon-oxygen backbone with two pendant methyl groups bonded to each of the silicon atoms.

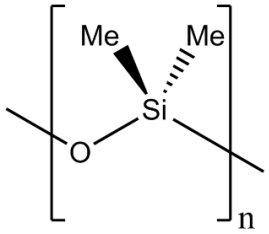


**Figure 23: The molecular structure of PDMS.**

There are a number of surface, bulk and chemical properties of PDMS that make it suitable for high tech (as well as low tech) applications; PDMS is hydrophobic and has a relatively low surface tension compared to hydrocarbon based polymers [2, 3], it has a large free volume, high thermal expansivity, high gas permeability (especially with respect to oxygen, nitrogen and water vapour), high compressibility, good thermal stability, high oxidative resistance, low chemical reactivity (except at extremes of pH), it is biocompatible and non-odorous [4]. These attributes are a direct result of fundamental properties. Intermolecular forces and backbone flexibility govern the physical behaviour of PDMS in a variety of environments, while bond energy and polarity account for the chemical consequences of the PDMS structure. The PDMS polymer chain can be considered as low intermolecular force pendant groups arrayed along a highly flexible backbone. The siloxane backbone is flexible because the energetic cost of rotation about the Si-O bond is exceptionally low at about 2.5 kJ/mol, compared to approximately 17 kJ/mol for most alkanes [5]. The bond length and bond angle also contribute to the flexibility of the backbone, with a large bond length and flat angle associated with a greater degree of flexibility. PDMS possesses both of these qualities, with the almost linear arrangement of silicon and oxygen being a result of the Si dπ –O pπ bonding interaction ($l_{Si-C}$ = 0.164 nm, $\theta_{Si-O-Si}$ = 143°, compared to $l_{C-C}$ = 0.153 nm and $\theta_{C-C-C}$ = 112° for polyethylene), as well as relatively long mainchain-pendant group silicon-carbon bonds (0.190 nm) [5, 6]. This, coupled with the low energetic cost of rotation provides PDMS with an extended flexible chain

system that allows the pendant methyl groups to be unobscured by steric hindrance and to therefore adopt the lowest surface energy configuration. Consequently, PDMS has a very low surface tension in air (15-21.8 $mN/m^2$ depending on the molecular weight, $M_n$ [7]) and a high contact angle with water ($\theta_{H2O}$ = 95 – 110$^o$) [8-11]. The bond energy and polarity are also important when considering the polymer's properties. The high thermal stability of PDMS can be attributed to the dissociation energy of the Si-O bond ($D_{Si-O}$ = 452 kJ/mol), which is significantly larger than those associated with hydrocarbon polymers ($D_{C-C}$ = 346 kJ/mol and $D_{C-O}$ = 358 kJ/mol) [12]. Remarkably, the interatomic distance between a bonded oxygen and silicon atom is less than their cumulative atomic radii, due to the polarity of this bond. Oxygen is more electronegative than silicon (3.44 and 1.90, respectively) and so the bond possesses some ionic character [13]. The resultant partial positive charge on the silicon atom also has another interesting effect. Bonded to the pendant methyl groups, it acts as an electron drain and polarises the adjacent carbon atoms. As a result of this, a methyl group bonded to a silicon atom that is part of a siloxane backbone will be more oxidative and thermally stable than one found on a hydrocarbon backbone. However, a Si-O backbone shares weaknesses with other partially ionised structures, namely a susceptibility to nucleophilic or electrophilic attack leading to hydrolysis by water, notably at extremes of pH. This effect is most evident at pH values below 2.5 and above 11.0 [4]. It is also worth noting that PDMS has the lowest glass transition temperature of any known polymer (149.3 K) [14, 15].

## 2.3 Preliminary Study into the Effect of Surface Topography on Crystallisation

### 2.3.1 Introduction

The aim of the preliminary study was to develop a facile method to generate surface features on a suitable substrate in order to control crystallisation using surface topography. Initial experiments investigated crystallisation on glass microscope slides that had been scratched with diamond powder. Two grades of diamond powder were used, along with different abrasion techniques. Calcium carbonate was precipitated on the substrates and a qualitative analysis of the location of the crystals on the surface was carried out. Finally, image analysis was conducted using ImageJ in order to obtain the average crystal populations per $mm^2$ for each sample type.

### 2.3.2 Method

Glass microscope slides were scratched using two grades of diamond powder so as to introduce surface defects in to the surface. Firstly, the glass slides were sonicated in a LeelaSonic 50 sonicator bath in Millipore water for 15 mins, then rinsed with ethanol and dried with an air jet. Using a gloved finger, 0.01 g of synthetic diamond powder, particulate size 40 - 60 micrometre diameter (Alfa Aesar) was rubbed against a glass microscope slide (76 x 25 mm) using the following techniques:

- **Longitudinally**: The diamond powder was rubbed in a motion parallel to the long axis of the slide, five times in each direction.
- **Circularly**: A separate group of slides were rubbed with a circular motion, with the diameter of the circles approximately equal to the width of the slide. Five complete revolutions for each circle were completed and four circles were drawn per slide along its length, such that the circles overlapped, but the entire slide had been abrased.
- **Cross-Hatch**: The final group of slides were abrased with a cross-hatch motion. Firstly, the finger was moved five times in each direction along the long axis. Then, starting at one end of the slide, and at the width of the pad of the index finger, the diamond powder was rubbed five times parallel to the short axis in each direction. The finger was then moved along the long axis approximately one finger pad width and then abrasion along the short axis commenced for five repetitions in each direction. This

was continued until the entire length of the slide had been scratched along the short axis, completing the cross-hatch abrasion.

Next, the slides were rinsed repeatedly in ethanol and sonicated in a bath of ethanol, then left in piranha solution (70:30 %wt sulphuric acid:hydrogen peroxide) for 2h. Lastly, the slides were washed with Milli-Q water, then ethanol and dried using an air jet. The process was repeated for diamond powder with a particulate size of <10 nm (Sigma Aldrich). Control slides, slides that had not been scratched, were also prepared. These were cleaned in the same manner as those that had been treated with diamond powder. Crystallisations were carried out using equimolar concentrations of calcium chloride (Sigma Aldrich) and sodium carbonate (Alfa Aesar) at 1, 2 and 3 mM, each with a substrate residence time of 10 minutes.

Finally, ImageJ was used to determine the crystal populations on the glass slides. This was carried out in the following manner:

- An image was loaded into ImageJ and using the line tool, a line was drawn over the scale bar to match its length.
- The scale bar was then set using Analyse > Set Scale, and the known distance set to the scale bar of the micrograph (200 μm).
- Next the image was converted to an 8-bit image using Image > Type > 8-bit.
- The threshold was changed such that only crystals were selected. This was done using the sliders to alter the maximum and minimum. The chosen values are unique to each image to ensure the vast majority of crystals are detected.
- The crystals are then counted using Analyze > Analyze Particles. In the pop-up box, a number of parameters must be set. The 'Show' box should be set to Outlines, and Display Results, Clear Results, Summarize, Exclude on Edges and Include Holes should all be selected.
- This provides the data for a single image. For each substrate at each condition, this was repeated 5 times to obtain an average number of crystals across the analysed 1.3 x $10^6$ $\mu m^2$ surface of glass. This was then converted to number of crystals per $mm^2$.

### 2.3.3 Results/Discussion

Control experiments were initially carried out using the same concentrations and residence time as those used for the diamond scratched slides. Optical micrographs of these experiments are shown below for the three chosen conditions (Figure 24).

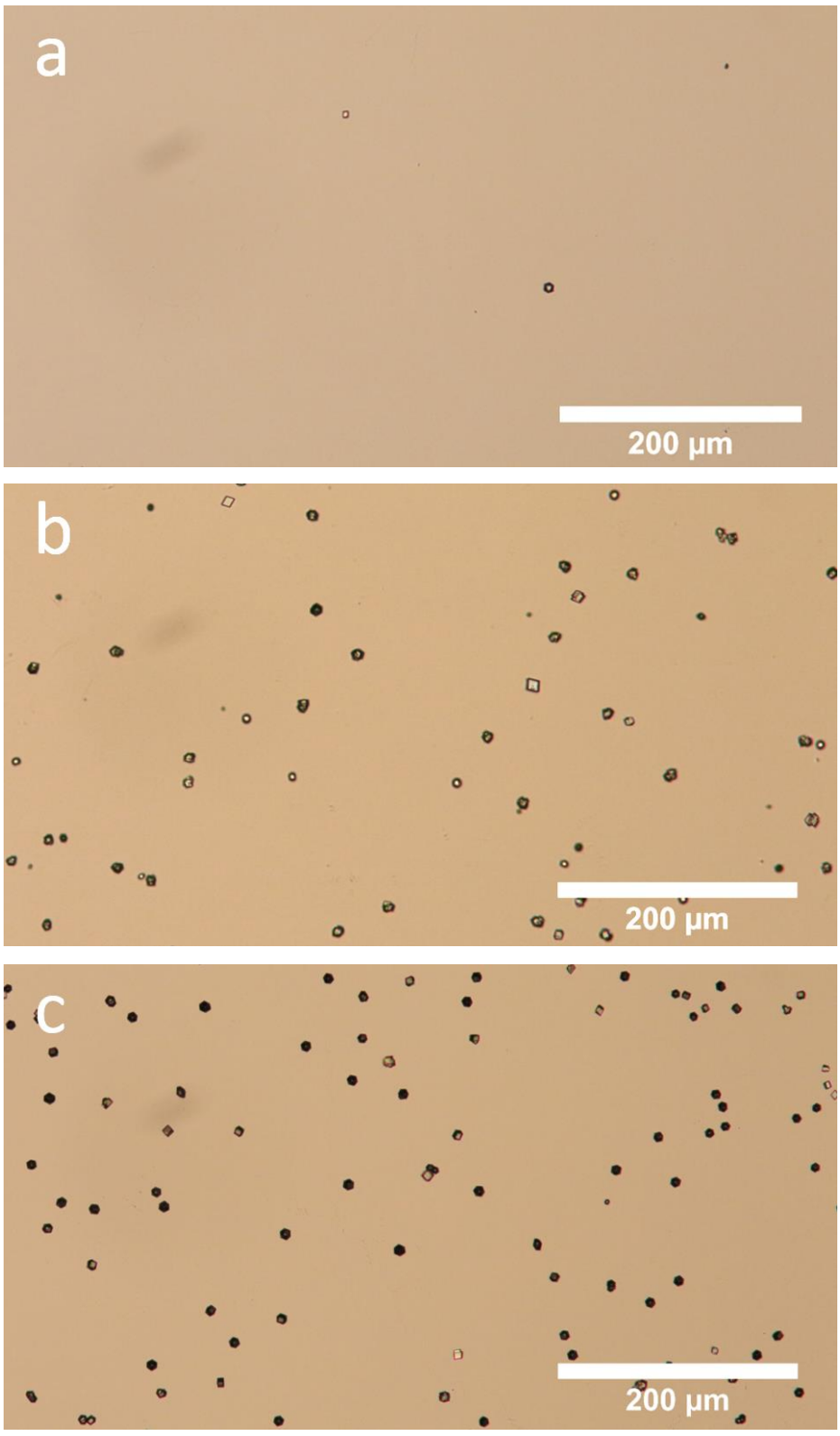


**Figure 24: Optical micrographs of calcite crystals grown on glass microscope slides**

Given the short residence time and low concentration of calcium and carbonate in solution, the crystal population on the slide exposed to $[Ca^{2+}] = [CO_3^{2-}] = 1$ mM was low. As expected, the crystal population increased with concentration and the crystals were randomly

distributed across the slide. The results for the slides scratched with 40 – 60 µm diamond powder were quite different (Figure 25).

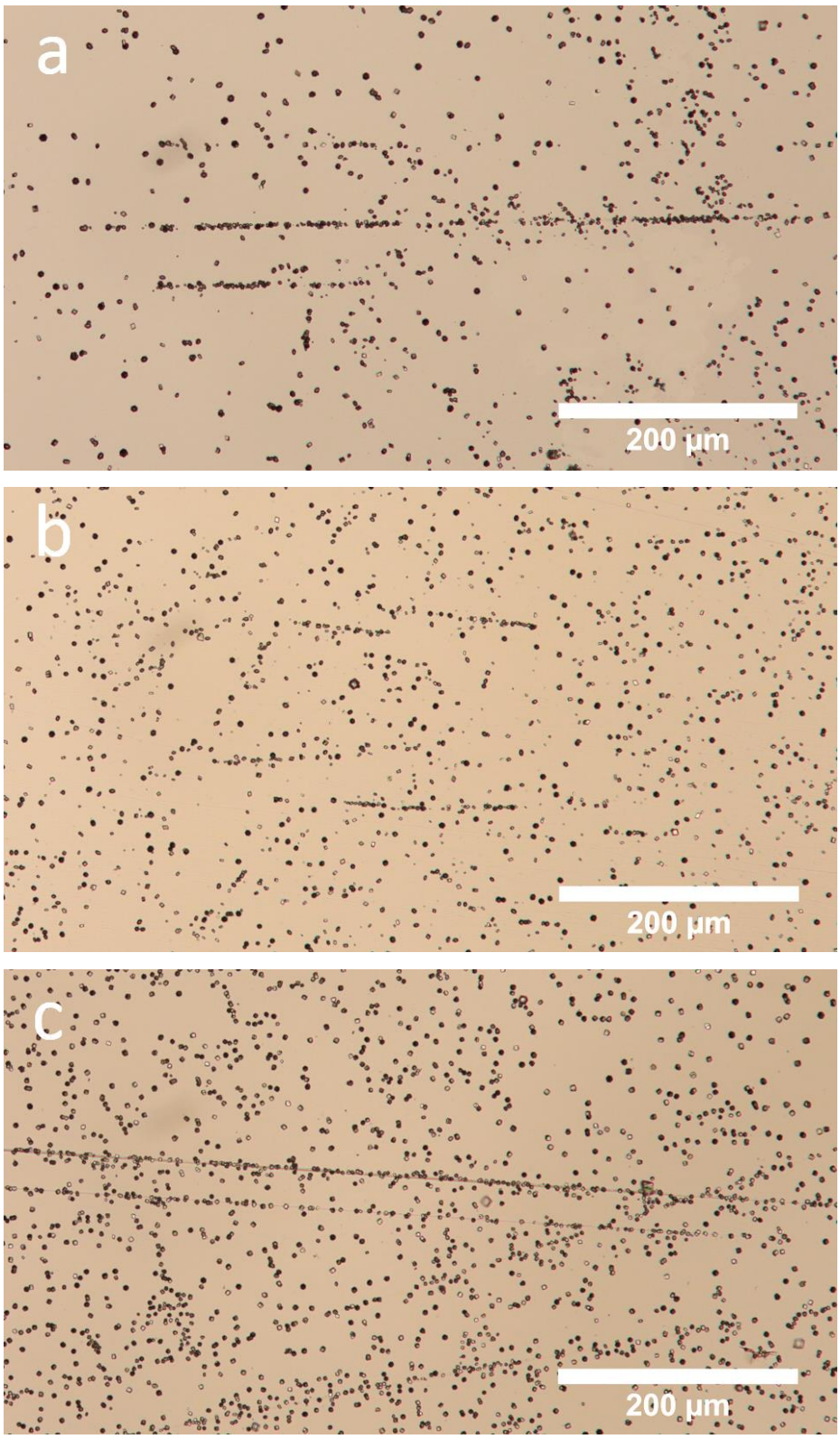


**Figure 25: Optical micrographs of calcite crystals precipitated on glass slides scratched parallel to the long axis with 40 – 60 µm diamond powder**

A significant increase in the crystal population and noticeable reduction in crystal size was observed relative to the controls at each concentration for these samples. In addition, occasional alignment of crystals was observed, most likely due to their nucleation along an

individual trench. Unexpected results were obtained for the glass slides abrased with a circular motion (Figure 26).

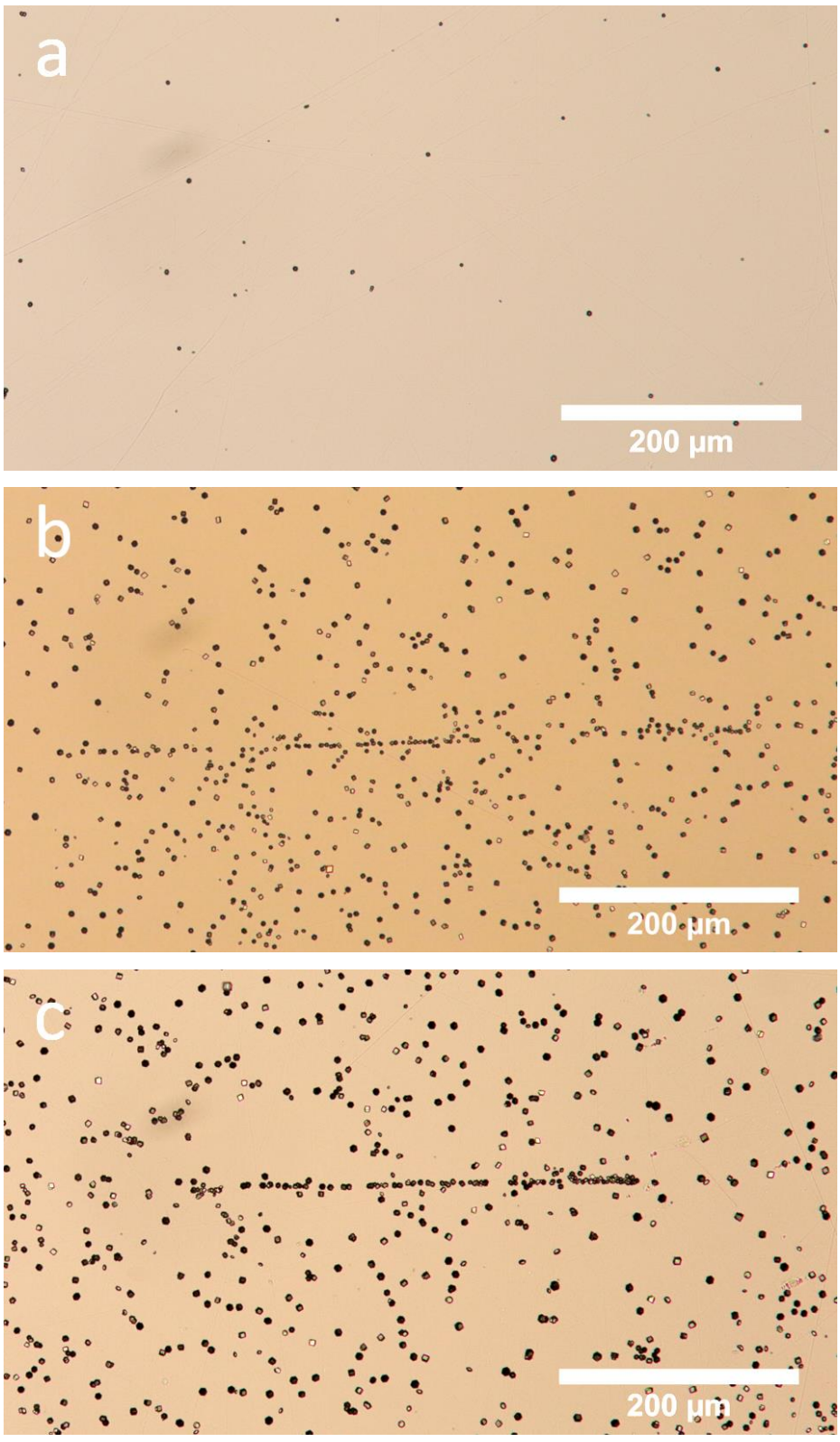


**Figure 26: Optical micrographs of calcite crystals precipitated on glass slides abrased using a circular motion with 40 – 60 µm diamond powder**

There were fewer crystals present on the circularly scratched glass slides at all conditions than on the slides scratched along their long axis, though still far more than the controls at each condition. Crystal alignment wasn't observed at 1 mM, but occasional alignment was observed

at the other two conditions. Similar results were acquired for the cross-hatch abrased slides (Figure 27).

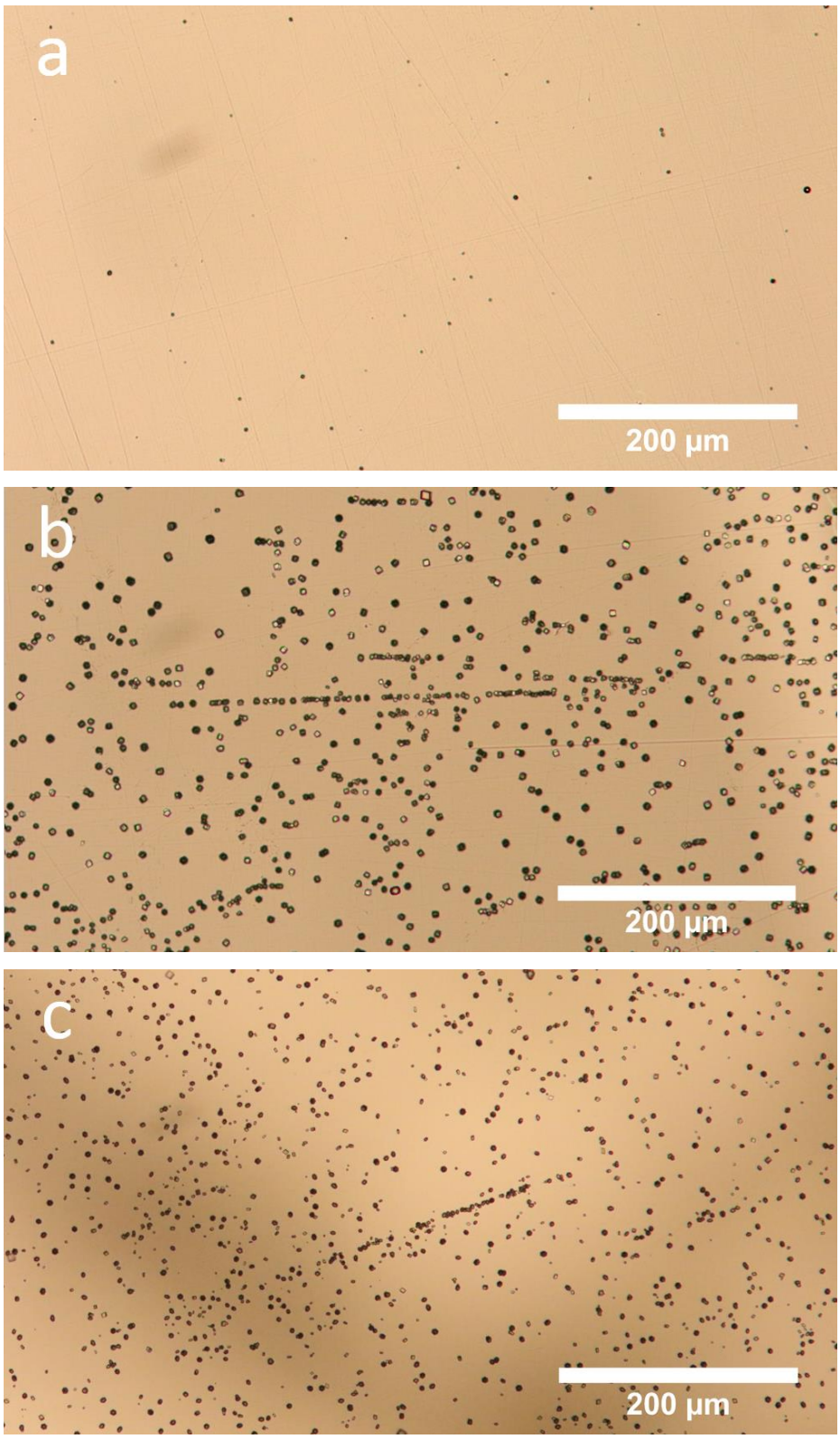


**Figure 27: Optical micrographs of glass slides scratched with 40 – 60 µm diamond powder in a cross-hatch pattern**

Again, far fewer crystals were present at all conditions than on the slides scratched along the long axis, no alignment was observed at 1 mM and occasional alignment was present at 2 and 3 mM. In contrast, the glass slides that had been scratched with 2 nm diamond powder yielded

crystal populations only slightly greater than those of the controls. In addition, there was little difference between crystal populations of slides scratched with different techniques. Representative images are provided in Figure 28.

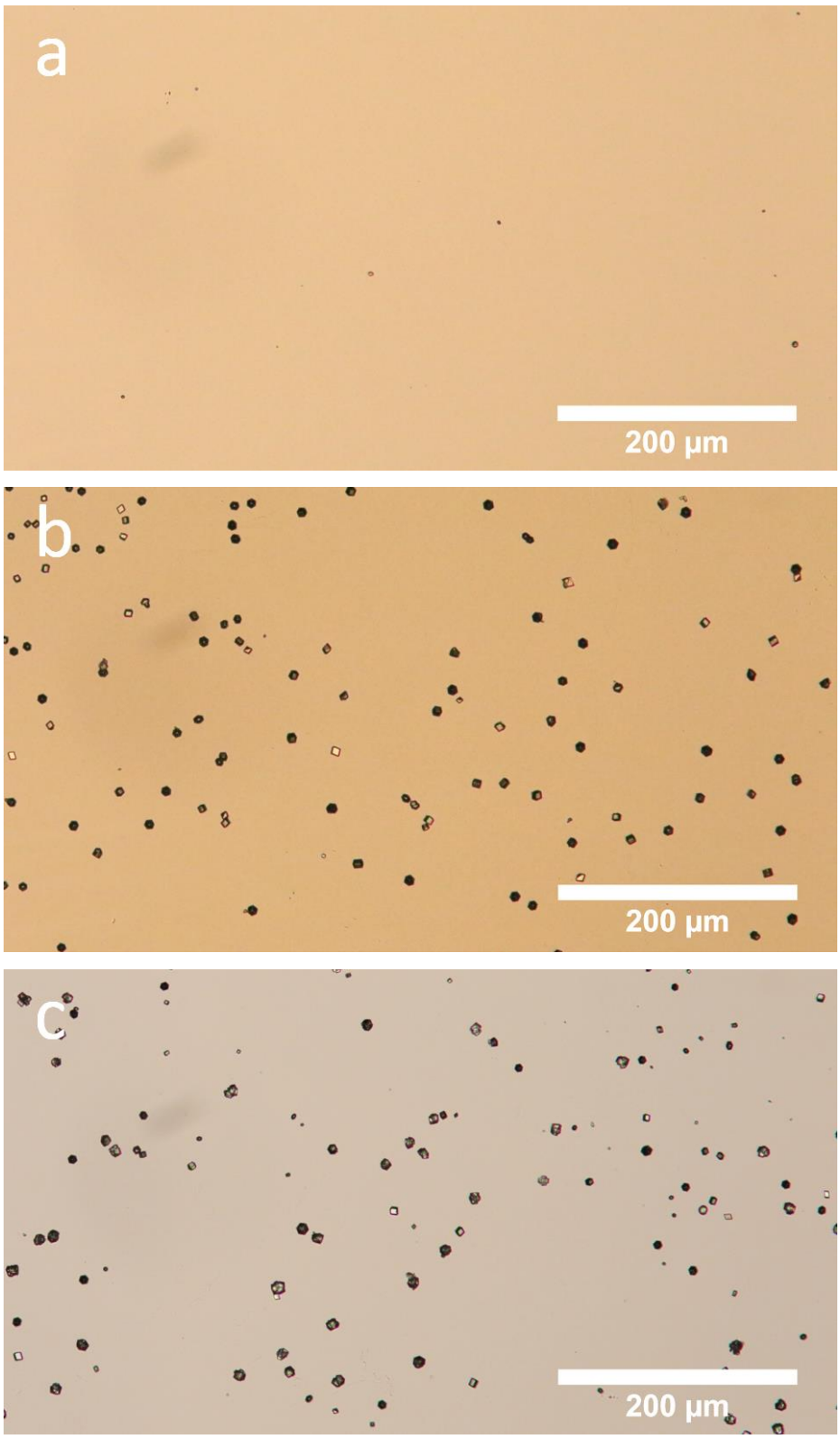


**Figure 28: Representative optical micrographs of glass slides scratched with <10 nm diamond powder**

The crystal populations on the slides scratched with <10 nm diamond powder were closer to those of the controls than those of the slides scratched with 40 – 60 µm diamond powder, with the <10 nm particulate scratched slides possessing crystal populations slightly greater

than the controls. In addition, no aligned crystals were observed. The crystal population data provided by image analysis is presented in Table 1, Table 2 and Table 3.

**Table 1: Populations of crystals at various $[Ca^{2+}] = [CO_3^{2-}]$ that precipitated on unscratched glass slides.**

| Concentration (mM) | Number of crystals per $mm^2$ precipitated on Control Glass Slides (per $mm^2$) |
|---|---|
| 1 | 21.6 ± 5.2 |
| 2 | 201.6 ± 18.6 |
| 3 | 320.4 ± 37.6 |

**Table 2: Populations of crystals at various $[Ca^{2+}] = [CO_3^{2-}]$ that precipitated on glass slides that had been scratched with a diamond powder that possessed an average particulate size of 40 – 60 µm.**

| Concentration (mM) | Number of crystals per $mm^2$ precipitated on Glass Slides Scratched with 40 – 60 µm Diamond Powder (per $mm^2$) | | |
|---|---|---|---|
| | *40-60µmLong* | *40-60µmCircular* | *40-60µmHatch* |
| 1 | 2973.6 ± 135.8 | 140.4 ± 21.6 | 198 ± 23.8 |
| 2 | 4510.8 ± 201.6 | 1947.6 ± 103.6 | 2275.2 ± 83.4 |
| 3 | 4989.6 ± 215.8 | 2332.8 ± 117.8 | 3906 ± 179.2 |

**Table 3: Populations of crystals at various $[Ca^{2+}] = [CO_3^{2-}]$ precipitated on glass slides that had been scratched with a diamond powder that possessed an average particulate size of <10 nm.**

| Concentration (mM) | Number of crystals per $mm^2$ precipitated on Glass Slides Scratched with <10 nm Diamond Powder (per $mm^2$) | | |
|---|---|---|---|
| | *<10nmLong* | *<10nmCircular* | *<10nmHatch* |
| 1 | 50.4 ± 11.2 | 57.8 ± 9.8 | 46.2 ± 8.8 |
| 2 | 385.2 ± 25.2 | 402.6 ± 36.6 | 410.6 ± 28.2 |
| 3 | 439.2 ± 34.6 | 427.6 ± 17.8 | 418.6 ± 42.8 |

The image analysis confirmed the results optical microscopy data. Between the slides scratched with 40 – 60 µm diamond powder, the slides that had been scratched parallel to the

long axis nucleated far more crystals than circular and cross hatch abrasive techniques. Though more crystals nucleated on the slides abraded with <10 nm diamond powder than in the controls, the image analysis suggested that the increase was not substantial, unlike the case with the other grade of diamond powder. In addition, the slides abrased with the smaller particulates produced crystal populations with errors that overlapped. This indicates that the abrasive techniques either all generated a similar surface topography or that something else may be causing the increase in crystal population. After inspection of the surfaces of the control and the treated glass slides in the SEM, the reason for the difference in crystallisation data between each of the samples became evident. The surface of an unscratched glass slide appears quite featureless, at least in the SEM (atomic force microscopy would provide greater topographical information), and the roughness (Ra, Roughness Average) of glass slides from the same manufacturer has been measured elsewhere as 0.3 nm [16]. Interestingly, the surface topography of the glass slides scratched with the <10 nm diamond powder was similar to the control slides. A representation of the topographies of these slides is given in Figure 29.

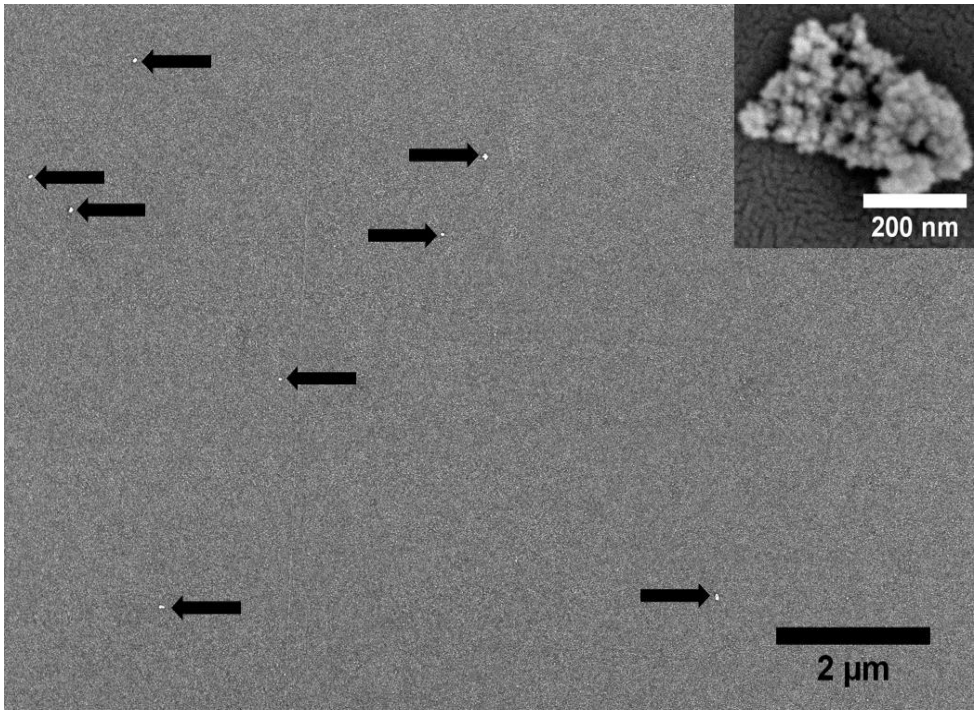


**Figure 29: SEM image of the surface of a glass slide scratched with <10 nm diamond powder**

Although there appears to be no visible surface defects made on the glass slide by the <10 nm powder and the surface seems similar to the control slides, the crystal populations on the slides scratched with this grade were slightly greater than the controls. That no perceptible defects were observed on the surface is not necessarily an indication that they did not exist

anywhere on the slide, as a similar study conducted by Holbrough *et al* observed marks caused by <10 nm diamond powder on glass in only a few isolated places [16]. On inspection, a few particulates could be seen on the surface of the glass (Figure 29 inset). It is assumed that this was residual diamond powder, though confirmation of this was difficult due to their small size and as such no EDX signal could be obtained. However, the average diameter of these particles was measured at 7.6 nm and so their size is similar to the description of the diamond powder provided by the supplier. It may be supposed that the presence of these particles, combined with any generated surface topography unseen by the SEM, was the cause of the increase in crystal population. An SEM image of agglomerations of the <10 nm powder are provided below in Figure 30.

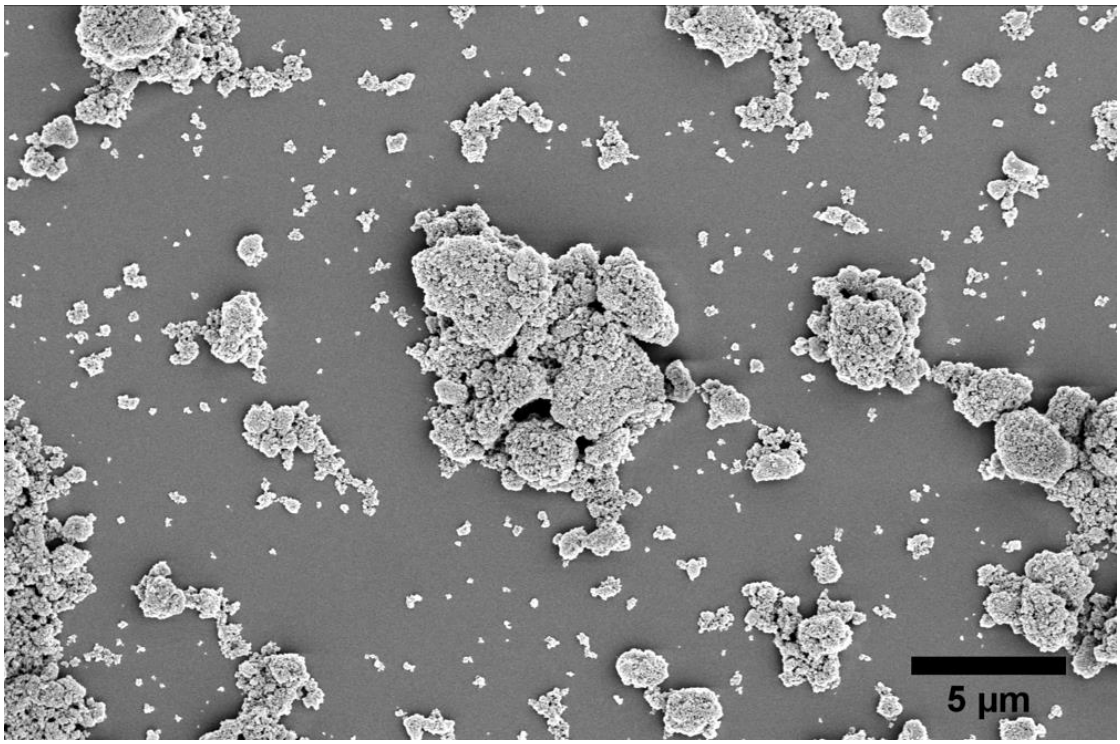


**Figure 30: SEM micrograph of agglomerations of the <10 nm diamond powder.**

The lack of surface defects after abrasion with this powder may be due to the small size of the particles and the fact that a gloved finger was used. The latex of the glove is a pliable material and this combined with the small size of the particles likely meant that not enough force could be applied to damage the surface of the glass, as the latex/finger pad deformed around the particles. Any agglomerations of diamond particles were simply spread apart into a thin coating on the glove, failing to affect the surface. In contrast, after abrasion with the 40 – 60 µm diamond powder, the glass slides possessed topographies vastly different to the slides scratched with <10 nm powder and control slides. Long furrows were present on each of the

slides, in addition to other features such as overhanging material, pits, and loose fragments (present even after thorough cleaning). The surface topographies of each abrasive technique using the 40 – 60 μm diamond powder are given below in Figure 31, along with arrows indicating an example of each of the above listed surface features. Coloured arrows have been used to highlight a single case of each feature for the sample types, where these colours indicate: red – furrow, green – overhang, blue – loose material, yellow – pit.

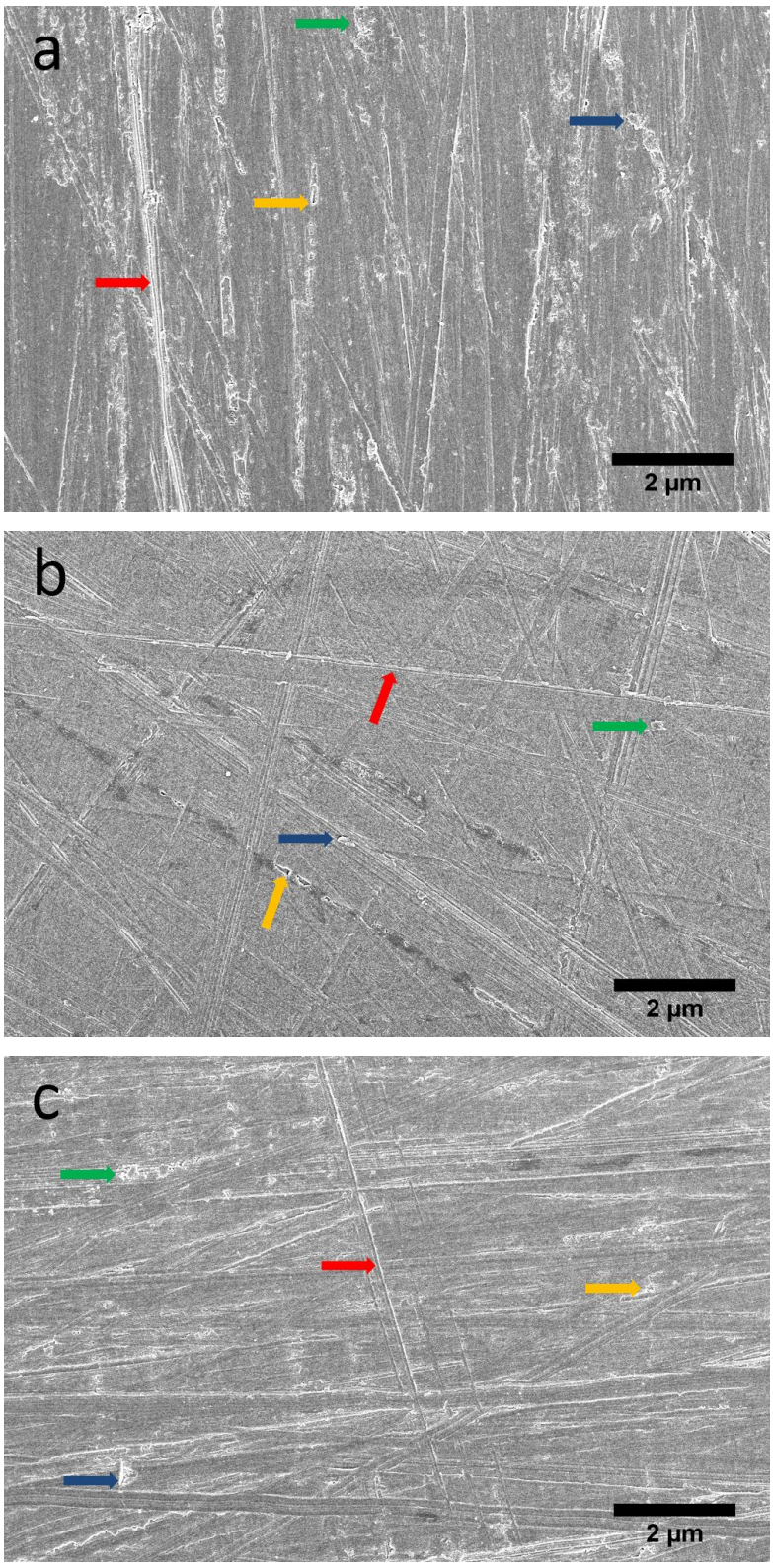


**Figure 31: SEM micrographs of glass slides scratched with 40 – 60 µm diamond powder using different abrasive motions**

No attempt at quantifying the density of the different types of defects associated with a particular abrasive technique was made, and these classifications (furrows, overhanging material, pits and loose fragments) are rather broad terms used merely for descriptive purposes. As can be seen from the SEM images, the topographies possess a far greater variety

of surface features than those described here, but quantification and analysis of these are beyond the scope of this preliminary research. However, on visual inspection of the electron micrographs, differences between the topographies are evident. The topographies of the circularly and cross-hatched scratched slides are similar, in that the dominant feature on the surface is long furrows. By comparing the crystallisation data of Figure 26 and Figure 27 and Table 2, we can see that the crystal populations were similar, with low populations at 1 mM. On the other hand, the topography generated by scratching the glass slide parallel to the long axis was much more complex. There was a wealth of overhanging material and loose fragments, as well as furrows and pits. Campbell *et al* looked into the effect of various surface defects exhibited by delaminated mica on the crystallisation of organic compounds from vapour [17]. They found that the most effective features at causing nucleation were those with acute geometries. Although the research presented here cannot confirm that the same is true for this system as the density of the various types of surface features has not been quantified, the large variety of surface sites formed on these glass slides are most likely the cause of the relative increase in crystal population; which surface feature is most effective at causing nucleation though, cannot be confirmed using the data obtained in this study. That scratching parallel to the long axis of the slide generates a more varied topography than scratching in a circular or cross-hatch motion is probably due to the fact that a greater proportion of the diamond powder is maintained on the surface for the duration of the abrasion. Because only one simple motion is employed when scratching the surface in this way (backwards and forwards), it is much easier to keep all of the applied diamond powder on the surface of the slide. As such, the presence of a greater number of diamond particles can damage the surface more effectively. An image of the 40 – 60 µm diamond powder is provided below in Figure 32.

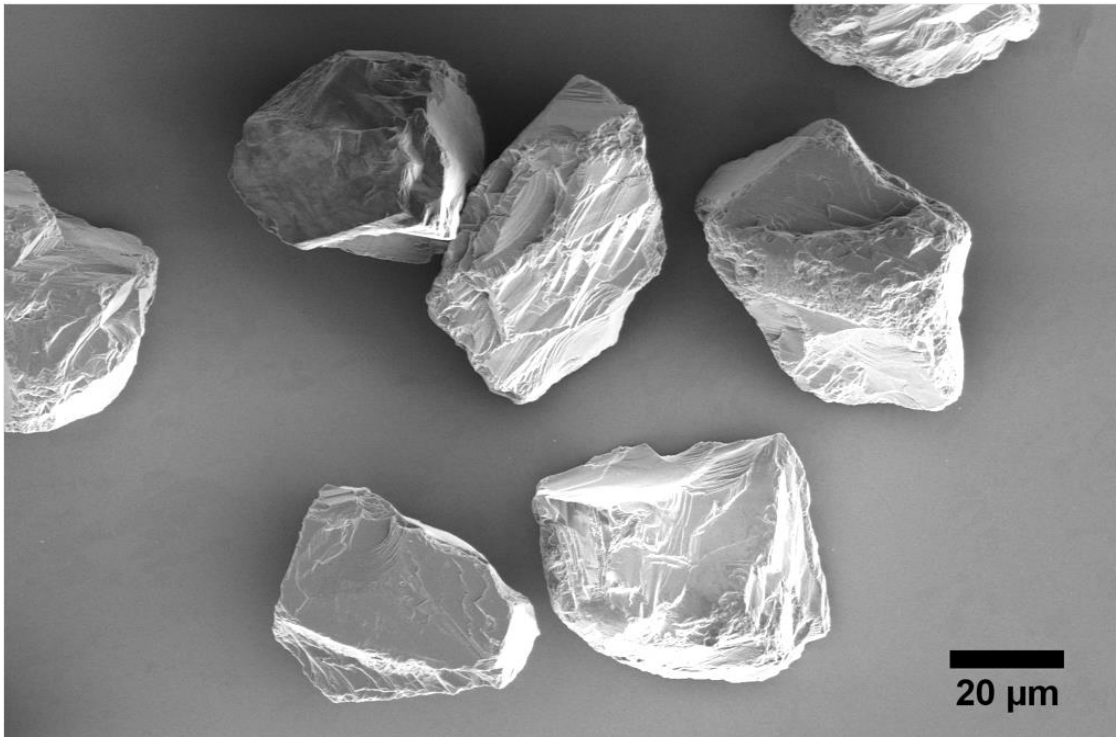


**Figure 32: SEM micrograph of the 40 – 60 µm diamond powder.**

In the case of the circularly and cross-hatch abrased techniques, some of the diamond powder is unavoidably lost from the slide as it falls off the edge during abrasion. This is because more individual movements are required to complete these techniques, but also because the width of the slide relative to the width of a finger are quite similar and so ensuring that the entire slide has been affected without losing material is difficult. In addition to the variations in crystal populations, occasional alignment was observed across all of the 40 – 60 µm diamond powder scratched slides. The most reasonable explanation for this is that the aligned crystals nucleated along a single furrow in the glass surface. However, given the ubiquity of these furrows across the surfaces of the glass, the rarity of their occurrence is surprising. This indicates that scratching glass slides with diamond powder rarely creates surface features that can cause the alignment of crystals.

### 2.3.4 Conclusion

The preliminary data presented here suggests that although the formation of surface features through abrasion with diamond powder is a crude method, the topography of a surface can certainly have an influence on crystallisation. However, the high density of scratches across the surface and the fact that alignment of crystals to the trenches was only observed a handful of times across a single substrate indicates that this method is ineffective at controlling the localised distribution of crystals on a surface. It is effective, however, at increasing the

population of crystals relative to an unscratched slide, most likely due to the introduction of a range of surface defects, including furrows, overhanging material, loose material and pits. This simple method of altering the surface topography of glass slides demonstrated the feasibility of influencing crystallisation using surface topography and as such, further research was conducted and a substrate sought that could develop this idea further.

## 2.4 Experimental Methods

The experimental methods described in the following section are those used for the main body of research in this chapter and therefore relate to the data presented in the Results/Discussion, Section 2.5.

In order to investigate the effect of surface topography on crystallisation, it was necessary to find a suitable patterning technique/substrate that provided submicron surface features that were (ideally) simple to fabricate. It was a paper by Hillborg *et al* that provided the answer [18], and although the researchers had formed microscale surface structures unintentionally in their study into the hydrophobic recovery of PDMS, their work provided the initial step for much of the research content of this thesis. Hillborg *et al* exposed PDMS to plasma generated in various ways and found that after extended exposure to a corona discharge, surface oxidation of the siloxane would be sufficient to form surface cracks (Figure 33).

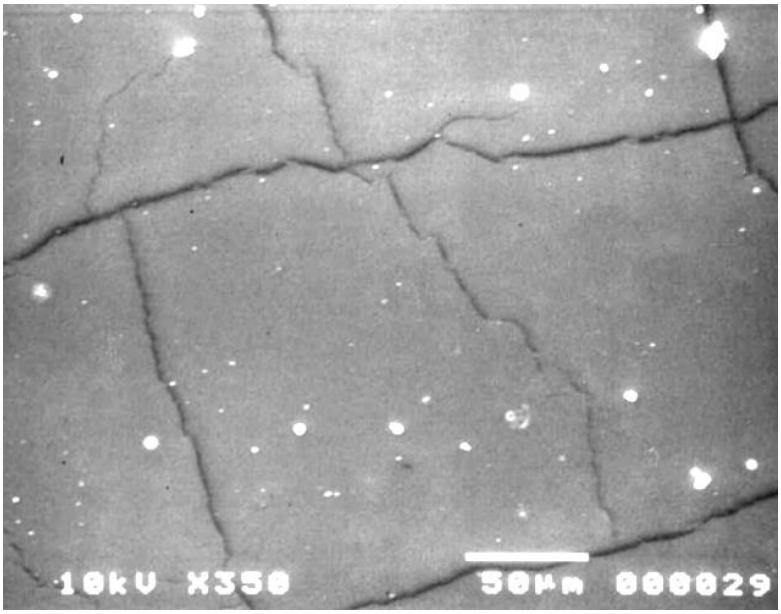


**Figure 33: Surface cracks produced by Hillborg *et al* by exposing PDMS to a corona discharge for three hours [18].**

The exposure time used by the researchers was considerably long at three hours. Research elsewhere had revealed that it was possible to introduce surface cracks in PDMS using radio frequency-generated plasma [19-21]. This method was appealing due to the accessibility of all the components (plasma cleaner and low-cost PDMS) and also its simplicity. As such, the technique was investigated and plasma-treated PDMS was used as a substrate for the study of the effect of surface topography and surface chemistry on crystallisation, with interesting results. This experimental section gives details on how the plasma-treated PDMS was made,

the crystallisation techniques, as well the methods used to modify the surface chemistry of the material and distribution of surface cracks.

## 2.4.1 Methods

### 2.4.1.1 Plasma-treated Poly(diemthylsiloxane) (PPDMS)

13g of Dow Corning Sylgard 184 Silicone Elastomer base was poured into a square petri dish with sides of 100 mm. 1.3g of the corresponding curing agent was added (10:1) and then the constituents were thoroughly mixed. This was degassed in a Nalgene 7000 $cm^3$ vacuum desiccator for 30 minutes and then placed into the oven at 60 $^oC$ overnight. Once cured, the PDMS was cut into strips of approximately 5 x 50 mm in size. These were placed into a Harrick plasma cleaner PDC-002 in air on high setting for 7 minutes. Next, the PDMS was cut using a sharp blade into rectangles approximately 5 x 3 mm in size. These substrates were then used as they are and are designated as PPDMS (Plasma-treated PDMS).

### 2.4.1.2 Thiol Self Assembled Monolayer PPDMS

In order to modify the surface chemistry of the PPDMS and to investigate its effect on crystallisation, a thiol self-assembled monolayer was used. The PPDMS substrates were coated with iridium using a Cressington 208HR High Resolution sputter coater and MTM-20 thickness controller. Iridium was sputtered to a thickness of 10 nm at a rate of 1 $Ås^{-1}$. A 16-mercaptohexadecanoic acid thiol (Sigma-Aldrich), referred to as 16COOH, was dissolved in ethanol (absolute grade) to make a 1 mM solution. The iridium coated PPDMS was then placed into a Falcon Polystyrene 50 x 9 mm petri dish, 7 ml of the SAM solution was added and the dish was sealed with the lid. The tight fit of the lid of these petri dishes prevents evaporation of the ethanol. Monolayer assembly was left to proceed for 18 hours, and then the substrates were carefully rinsed repeatedly whilst still in the petri dish using ethanol, and sonicated for 5 minutes. To dry the substrates, they were removed individually from the petri dish and placed onto Whatman 42.5 mm diameter qualitative filter papers with the treated face of the PPDMS oriented upwards and then a gentle jet of $N_2$ was used to remove excess ethanol from the surface. Crystallisation experiments were always carried out within 10 minutes of removing the substrate from solution.

### 2.4.1.3 Thiol Exchange Experiment

The literature suggests that thiol molecules that exist at features with acute/obtuse angles are more labile than those on planar surfaces [22]. As such, the monomers in these locations can

be exchanged for the monomers of another thiol, generating a surface possessing the monomers of two different thiols. An investigation into this was carried out in order to reveal any interesting effects this may have on the crystallisation of calcium carbonate as a result of this exchange taking place at the cracks of the PPDMS substrate. To execute the exchange, the thiol formation was carried out as described in Section 2.4.1.2, except that after submersion in 16-mercaptohexadecanoic acid, the substrates were washed thoroughly with ethanol and then immersed in 1 mM 11-mercaptoundecanol for 18 hours. To provide a control, separate iridium-coated substrates were submerged in an equimolar mixture of the two thiols used for the exchange, 16-mercaptohexadecanoic acid and 11-mercaptoundecanol. The SAM assembly was allowed to proceed for 18 hours, and the substrate was then washed and dried as before. To provide additional control experiments, an 11-mercaptoundecanol SAM was formed on an Ir-coated PPDMS substrate (using the same protocol as that described in Section 2.4.1.2, but with OH-terminated thiol instead of 16-mercaptohexadecanoic acid).

#### 2.4.1.4 Silane-coated PPDMS

Interesting crystallisation results were obtained by altering the surface chemistry using a thiol self-assembled monolayer, and so a silane self-assembled monolayer was also investigated to ascertain if the same effect could be achieved using this different type of monolayer. The terminal group of the thiol 16-mercaptohexadecanoic acid is of course a carboxylic acid functionality. However, in order to produce a silane that terminates in this functional group, it is necessary to deposit a C=C terminated silane and then convert this alkene group to a COOH group, as otherwise the methoxy groups and COOH groups of monomers would react with one another in solution. To form the silane coating, silanisation of the PPDMS was conducted by placing the 5 x 3 mm substrates onto a glass slide in a Nalgene 7000 $cm^3$ vacuum desiccator immediately after they had been prepared. 100 µl of the silane trimethoxy(7-octen-1-yl) was pipetted onto a separate glass slide and this was placed alongside the slide containing the substrates. The gas within the desiccator was then evacuated and after 1 hour, the substrates were removed. These were sonicated in ethanol for 5 mins within a Falcon Polystyrene 50 x 9 mm petri dish to remove any silane residue that may have accumulated on the surface. Next, the substrates were dried on filter paper with a gentle jet of air. An oxidation is required to convert the C=C group to a COOH group. As described by Moaz and Sagiv [23], this is achieved by placing a drop of 1.2 M potassium permanganate solution onto the silane-coated surface. The drop should form a thick layer over the surface and after 3 minutes, was

removed by carefully sucking it up through a pipette. The substrate was then washed thoroughly with Millipore water and used as is for crystallisation studies.

#### 2.4.1.5 Crystallisation by Direct Mixing

For $CaCO_3$ precipitation, the direct mixing method of crystallisation involved calculating the volumes of $CaCl_2$, $Na_2CO_3$ (100 mM stock solutions) and Millipore water required to obtain the desired concentrations at a total volume of 20 ml. Once these had been calculated, $CaCl_2$ solution, water, and $Na_2CO_3$ solution were mixed in this order in a cylindrical petri dish with a diameter of 60 mm and volume of 35 ml containing the samples. The samples were always oriented vertically in the petri dish (propped up against the side wall), so as to prevent crystals formed in the bulk from sedimenting on top. The petri dish lid was placed on top and once the desired residence time had passed, the samples were removed, rinsed repeatedly in ethanol and dried gently with a $N_2$ jet. In the case of the $SrCO_3$ and $BaCO_3$ crystallisations, the metal chloride was used in conjunction with sodium carbonate. In the case of $MnCO_3$ and $CuCO_3$ crystallisations, sodium bicarbonate was used. For calcium oxalate, ammonium oxalate was used instead of sodium carbonate.

#### 2.4.1.6 Initial Ion Concentrations and Saturation Indices

Throughout this research, a variety of calcium carbonate solution concentrations were used. Listed below are the initial ion concentrations and the associated saturation indices, SI (SI is defined in Section 1.1.2), for calcite, aragonite and vaterite under direct mixing, where these were calculated using Visual Minteq.

**Table 4: Reference table of initial ion concentrations in the reaction solution that the substrate is exposed to and their associated SI calculated using Visual Minteq.**

| Initial Ion Concentrations (mM) | | Saturation Index | | |
|---|---|---|---|---|
| $Ca^{2+}$ | $CO_3^{2-}$ | Calcite | Aragonite | Vaterite |
| 0.5 | 0.5 | 1.2 | 1.1 | 0.6 |
| 0.5 | 1 | 1.2 | 1.1 | 0.6 |
| 1 | 1 | 1.7 | 1.6 | 1.1 |
| 2 | 2 | 2.1 | 2.0 | 1.6 |
| 3 | 3 | 2.4 | 2.2 | 1.8 |
| 4 | 4 | 2.5 | 2.4 | 2.0 |
| 10 | 1 | 2.1 | 2.0 | 1.5 |
| 1 | 10 | 2.1 | 2.0 | 1.6 |

| | | | | |
|---|---|---|---|---|
| 3 | 15 | 2.6 | 2.5 | 2.1 |
| 15 | 3 | 2.6 | 2.5 | 2.0 |
| 0.5 | 20 | 1.9 | 1.7 | 1.3 |
| 20 | 0.5 | 1.8 | 1.7 | 1.2 |

#### 2.4.1.7 Precipitation of $CaCO_3$ in the presence of $Mg^{2+}$ ions

The direct mixing method was used for these experiments (As described in Chapter 2: Common Methods). As before, calcium chloride and sodium carbonate were mixed together. Magnesium chloride hexahydrate was used as a $Mg^{2+}$ source and added after water, but before sodium carbonate to the crystallisation dish. Three $Ca^{2+}$:$Mg^{2+}$ ratios were investigated, along with three residence times, all of which are detailed in the table below:

**Table 5: Conditions used for the $CaCO_3$ precipitation in the presence of $Mg^{2+}$ experiments.**

| **$[Ca^{2+}]$: $[Mg^{2+}]$** | **$[Ca^{2+}]$ (mM)** | **$[Mg^{2+}]$ (mM)** | **Residence time (hours)** |
|---|---|---|---|
| 1:3 | 1 | 3 | 1 |
| 1:3 | 2 | 6 | 1 |
| 1:5 | 1 | 5 | 1 |
| 1:5 | 2 | 10 | 1 |
| 1:3 | 1 | 3 | 2 |
| 1:3 | 2 | 6 | 2 |
| 1:5 | 1 | 5 | 2 |
| 1:5 | 2 | 10 | 2 |
| 1:3 | 1 | 3 | 2.5 |
| 1:3 | 2 | 6 | 2.5 |
| 1:5 | 1 | 5 | 2.5 |
| 1:5 | 2 | 10 | 2.5 |

The substrates used for this were the 16-mercaptohexadecanoic acid-coated PPDMS and also a PDMS substrate coated with the same thiol to provide a substrate without any cracks and as such act as a control experiment.

#### 2.4.1.8 Crystallisation by the Ammonia Diffusion Method

The ammonia diffusion method was also used in some experiments, which is an alternative crystallisation technique to direct mixing. Substrates were placed in the same type of petri dishes as used for the direct mixing method (60 mm diameter and 35 ml volume) and oriented vertically up against the wall of the dish to prevent sedimentation of crystals formed in the bulk solution. The solution was made-up to a volume of 20 ml at the desired calcium concentration. The petri dish was sealed with parafilm that had been perforated with needle holes and then placed in a desiccator alongside a petri dish of the same dimensions containing 3 g of ammonium carbonate. The desiccator was closed, and after the desired residence time had passed, the petri dish was taken from the desiccator and the samples removed. Once washed with ethanol, they were dried with a light jet of $N_2$.

#### 2.4.1.9 Selected Area exposure of PDMS to RF Plasma Using Contact Masks

As mentioned in the introduction to this section, control over the properties of the cracks was difficult. It was possible however, using a contact mask, to control the areas that were exposed to the RF plasma. This meant that although the size and arrangement of cracks could not be controlled, they could be forced to form only in defined areas by exposing only these regions to the plasma, whilst masking the rest of the surface.

**PDMS Mask**

The first mask that was used was formed from a piece of PDMS. An array of holes was created in a 12 x 12 x 4 mm section of PDMS using a 0.75 mm Schuco Miltex biopsy punch to form a piece of PDMS with cylindrical vacancies. This was placed in contact with a PDMS substrate and gentle pressure was applied with a gloved finger to ensure removal of trapped air. Next, the mask/substrate was placed in a Harrick plasma cleaner PDC-002 in air on high setting for 7 minutes. The mask was then carefully removed and the substrates were coated with iridium using a Cressington 208HR High Resolution sputter coater and MTM-20 thickness controller. Iridium was sputtered to a thickness of 2 nm at a rate of 1 $Å s^{-1}$. The 16COOH SAM formation was then carried out as described in Section 2.4.1.2.

**TEM Grid Mask**

The use of the PDMS mask to expose selected areas of the PDMS to RF plasma was a fairly crude method in that the distribution of holes could not be accurately controlled (as the array was made by hand), and the smallest hole punch available was 0.75 mm. To create a regular array of smaller exposed areas, a TEM grid was used as a mask. Using pointed tip tweezers,

individual copper TEM grids (Agar Scientific, 400 x 100 mesh, 3.05 mm) were placed reflective side up onto 5 x 3 mm PDMS sections, taking care not to bend the grids and therefore distort their shape. These grids possess windows that are 40 μm wide and so the exposed areas of PDMS are significantly smaller than those when the PDMS mask is used. The TEM grid/substrate was then placed in a Harrick plasma cleaner PDC-002 in air on high setting for 7 minutes, and then the TEM mask was removed and the substrate was coated with 2 nm of iridium using a Cressington 208HR High Resolution sputter coater and MTM-20 thickness controller at a rate of 1 $Å s^{-1}$. The 16COOH SAM formation was then carried out as described in Section 2.4.1.2.

#### 2.4.1.10 Wrinkle-PDMS

The masks described above provided a means of forming the cracks in defined areas, though the distribution of cracks within these areas could not be controlled. A paper by Yang *et al* described a method by which it was possible to form surface undulations by exposing the PDMS to plasma whilst under tension [24]. As described in the associated part of the Results/Discussion section of this document, the topography I obtained was quite different to that of Yang *et al*'s, but nevertheless yielded interesting results once coated with the 16-mercaptohexadecanoic acid thiol. The wrinkled plasma-treated PDMS substrates were formed by cutting a 20 x 50 mm strips of PDMS and then clamping this into a custom-made stretch jig, an image of which is provided below in Figure 34.

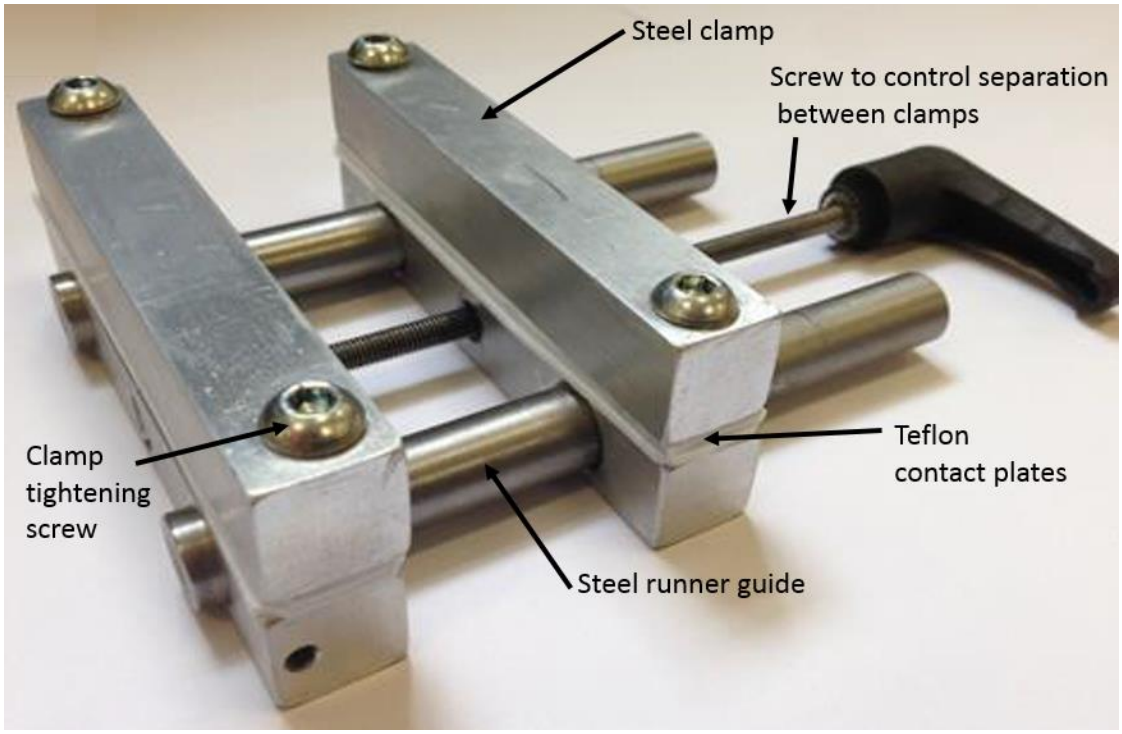


**Figure 34: Photograph of the stretch jig**

The clamps of the jig were separated until a distance of 50 mm between them was achieved (made reproducible by marking the position of the clamp on the steel runner guide using a permanent marker), giving the PDMS exposed to the plasma a length of 30 mm. The apparatus and PDMS was placed into the Harrick Plasma Cleaner on high setting for 7 minutes, such that the PDMS was exposed whilst under tension. After exposure, the tension was released by reducing the separation between the clamps and then the PDMS was cut loose (rather than unscrewing the clamps) such that only the exposed region was acquired. This PPDMS material was then cut into approximately 5 x 3 mm sections, and the carboxylate-terminated thiol deposition described in Section 2.4.1.2 was used.

#### 2.4.1.11 Scanning Electron Microscopy

Scanning electron microscopy (SEM) is a widely used characterisation technique for the analysis of micro/nanostructures. It is primarily an imaging technique that uses electrons to visualise a sample surface, though x-rays produced by the specimen can be used for chemical identification. In SEM, a beam of high energy electrons are generated, by either a field emission gun or a thermoionic source, and accelerated inside an ultra-high vacuum through a voltage difference between an anode and cathode. The difference can be as low as 0.1 kV or as high as 50 kV, though typically 3 to 10 kV are used for imaging. The electrons are demagnified using a condenser lens system, producing an electron probe with a diameter

between 1 and 10 nm, depending on the operating parameters. Deflector coils then scan the probe in a raster pattern across the sample scan area (Figure 35). Since an ultrahigh vacuum is used, the sample must be stable under these conditions. An image can be reconstructed by integrating the scanned position electron intensities, such that the intensity of a pixel on the screen corresponds to the electron count at the equivalent location on the surface.

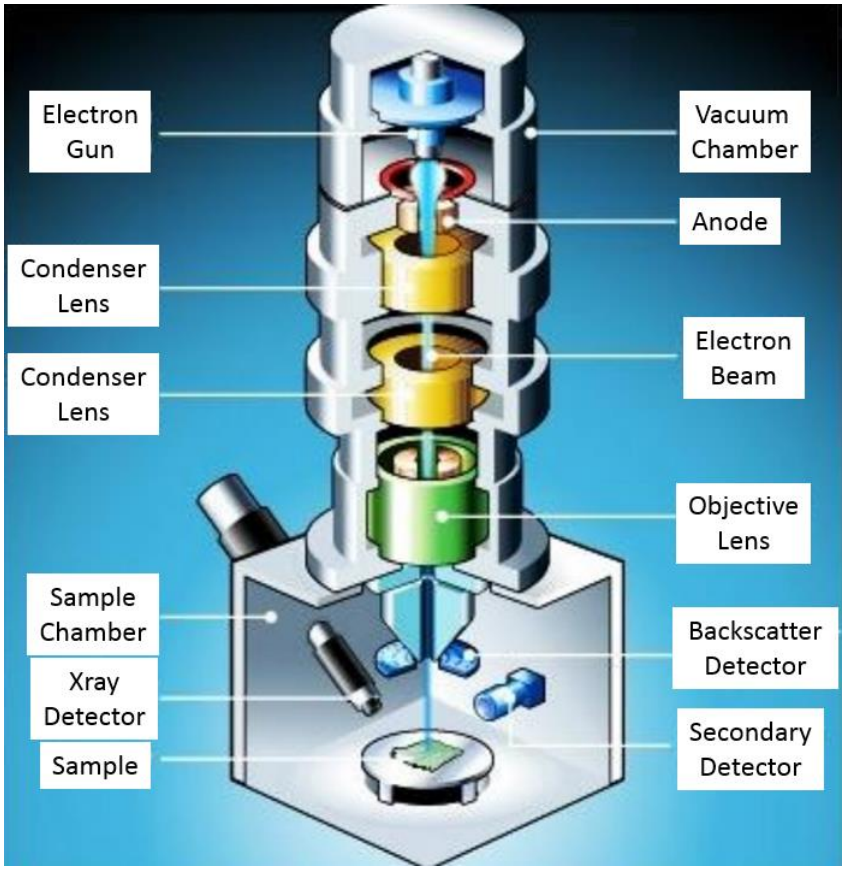


**Figure 35: Schematic of a scanning electron microscope**

An advantage of SEM is that a variety of electron-sample interactions can be used to form an image and to provide qualitative and quantitative information. The volume of the specimen that the electrons penetrate is known as the interaction volume, and this increases with beam acceleration. The radiations that are generated as a result of the primary electrons (beam electrons) must escape the specimen in order to be detected. The most commonly used imaging signal are the secondary and backscattered electrons (SE and BE, respectively), though analyses may also be performed using emitted X-rays and through cathodoluminescence.

SE's are low energy electrons that originate from the inelastic interactions of the primary and backscattered electrons with surface atoms. Since the primary electrons are more numerous

than the BE's, the majority of detected SE's have been produced by primary electrons. The SE's have a low energy, and as such are only able to escape from a region of the specimen a little larger than the beam diameter. This means that their images provide topographical information and are very sensitive to surface conditions. Once they have escaped the surface, in order to possess sufficient kinetic energy to be detected, they must first be accelerated towards the detector using a positive bias before their signal can be used to generate an image.

BE's originate from the elastic interaction of the primary electrons with the specimen atoms. They have a much higher kinetic energy than the SE's and as such can originate from much deeper in the specimen. They can be used to differentiate between areas of different chemical composition, since the number of scattered electrons emitted from the specimen for each incident electron is dependent upon the atomic number of the atoms that are being interacted with [26-28].

Scanning electron micrographs were taken using a FEI Nova NanoSEM 450 operating at between 3.0 and 10.0 kV. For all samples where it was possible to use a coating of iridium (Chapter 2, 3 and 4), secondary electrons were collected using an Everhart-Thornley detector. Otherwise, when a coating could not be deposited as the substrates must be reused (Chapter 5), the concentric back-scattered electron detector was used. The samples were mounted on an aluminium SEM stub with adhesive carbon tabs. Where necessary, the samples were sputter coated with 2 nm of iridium using a Cressington 208HR High Resolution sputter coater and MTM-20 thickness controller.

## 2.5 Results/Discussion

### 2.5.1 Introduction

As shown by the preliminary research in which glass slides were scratched with two different grades of diamond powder and various abrasive motions employed, surface topography can indeed have an effect on crystallisation. This section aims to build upon the data of the preliminary study through the use of plasma-treated poly(dimethylsiloxane) (PPDMS) as a substrate. The data below specifies how a proportion of precipitated calcium carbonate crystals were found to nucleate at the cracks of a PPDMS substrate. This alignment of crystals with these surface features could be enhanced and their populations increased under the same conditions by coating the surface with a carboxylate-terminated thiol. The effect of the $[Ca^{2+}]/[CO_3^{2-}]$ ion ratio was investigated, as well as an alternative precipitation method. A brief experiment into the effect of magnesium on precipitation of $CaCO_3$ was also conducted, followed by an investigation into the effectiveness of the substrate at influencing the crystallisation of other inorganic materials. An attempt at localising the surface features and altering their distribution was made, and afterwards a thiol exchange was attempted in which labile regions of monomer are exchanged for another with a different end-group functionality. Finally, given the success of the carboxylate-terminated thiol-coated PPDMS substrate at affecting crystallisation, a silane with a COOH-terminus was investigated as a crystallisation substrate.

### 2.5.2 Plasma-treated Poly(dimethylsiloxane) Characterisation and Use as a Crystallisation Substrate

The effect of plasma treatment on the PDMS surface was investigated using SEM and AFM techniques. Plasma treatment is a facile method of surface modification, which is often used in microfluidics to increase the hydrophilicity of the PDMS surface through the formation of silanol groups in the place of the pendant methyl groups [29]. The process may also be used to enhance adhesion of the PDMS to surfaces or to clean the surface of contaminants and impurities. The plasma is formed by an electrical discharge in low pressure air (achieved via a vacuum pump) within the chamber. This electrical discharge causes the formation of highly reactive species: ions, radicals, electrons, photons and excited molecules [30]. Oxygen radicals and hydroxyl radicals formed by the discharge (the sources of which are atmospheric oxygen and water vapour, respectively) react with the pendant methyl groups, displacing them and

forming silanol groups in their place. After plasma treatment, hydrophobic recovery occurs through the diffusion of untreated polymer chains to the surface, hydroxyl group condensation, migration of treated chains away from the surface to the bulk or pendant group reorientation of polar silanol groups away from the surface [4, 19, 29, 31, 32]. On extended plasma treatment, significant oxygen enrichment of the surface and polymer chain crosslinking occurs, leading to the formation of a silica-like ($SiO_x$) surface layer [18, 30, 33, 34]. This layer has a lower specific volume than the PDMS from which it originated, and also a different Young's modulus than the underlying PDMS. These two factors cause the formation of stress in the plane of the oxidised layer, which is relaxed by the development of surface cracks [19] (Figure 36).

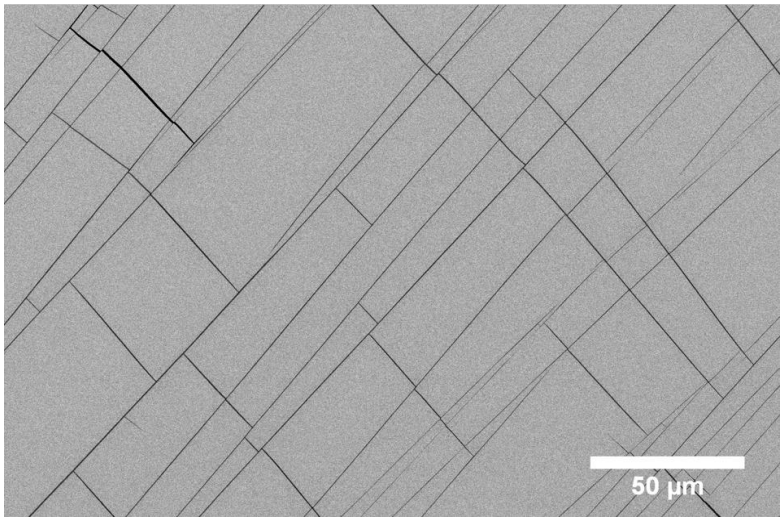


**Figure 36: SEM micrograph of a poly(dimethylsiloxane) surface after exposure to radio frequency generated plasma**

In the present research, unless stated otherwise, the PDMS substrates were exposed to plasma for 7 minutes. After treatment, the entire PDMS surface contained cracks that were tens to hundreds of microns long with widths between 0.1 and 2 µm as measured by atomic force microscopy (Figure 37).

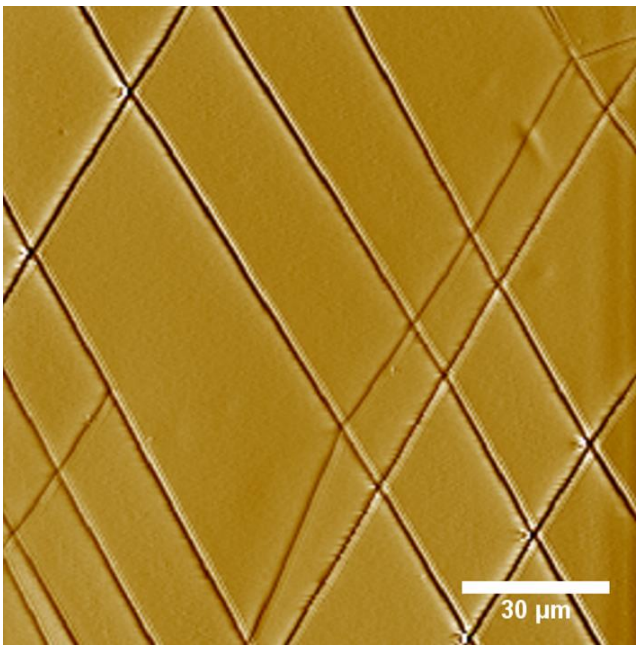


**Figure 37: Atomic force micrograph of the surface cracks of a plasma-treated poly(dimethylsiloxane).**

The trenches were between 50 and 120 nm deep relative to the adjacent terrace and were flanked on each side by a raised edge approximately 30 to 140 nm high, giving the trenches a depth from peak to trough of between 80 and 260 nm. Although the dimensions of the cracks typically existed within the specified range, the arrangement and distribution of cracks across the surface was highly variable and appeared stochastic. Grid arrangements were the most common, the elements of which are rectangles (where elements refers to the spaces defined by the cracks), though triangular elements may exist amongst these as well. Figure 36 and Figure 37 is an example of such an arrangement, as is Figure 38 below.

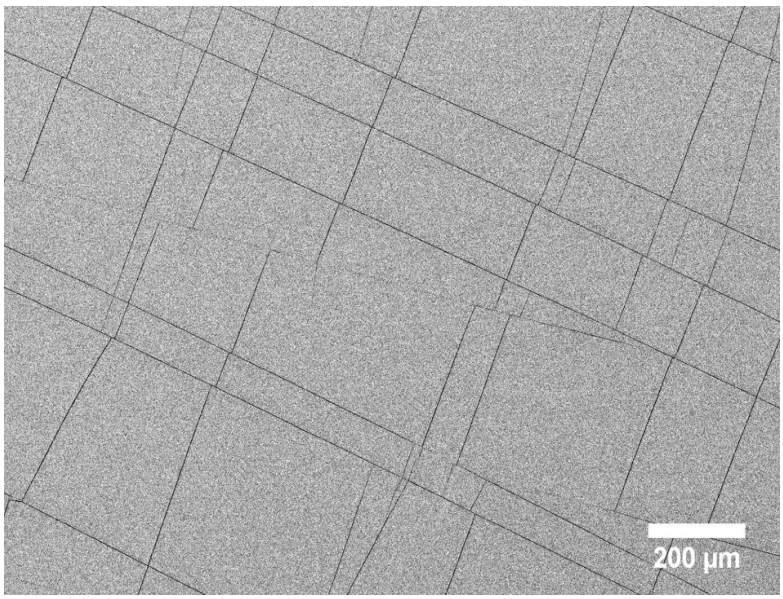


**Figure 38: An example of a grid arrangement of cracks on a PPDMS surface, taken using a scanning electron microscope.**

The density of the cracks across the surface can also differ. Figure 39a, b and c are electron micrographs of the surfaces of three different PPDMS substrates. The density of cracks across the surface varies significantly, even though all three were produced using the same methodology.

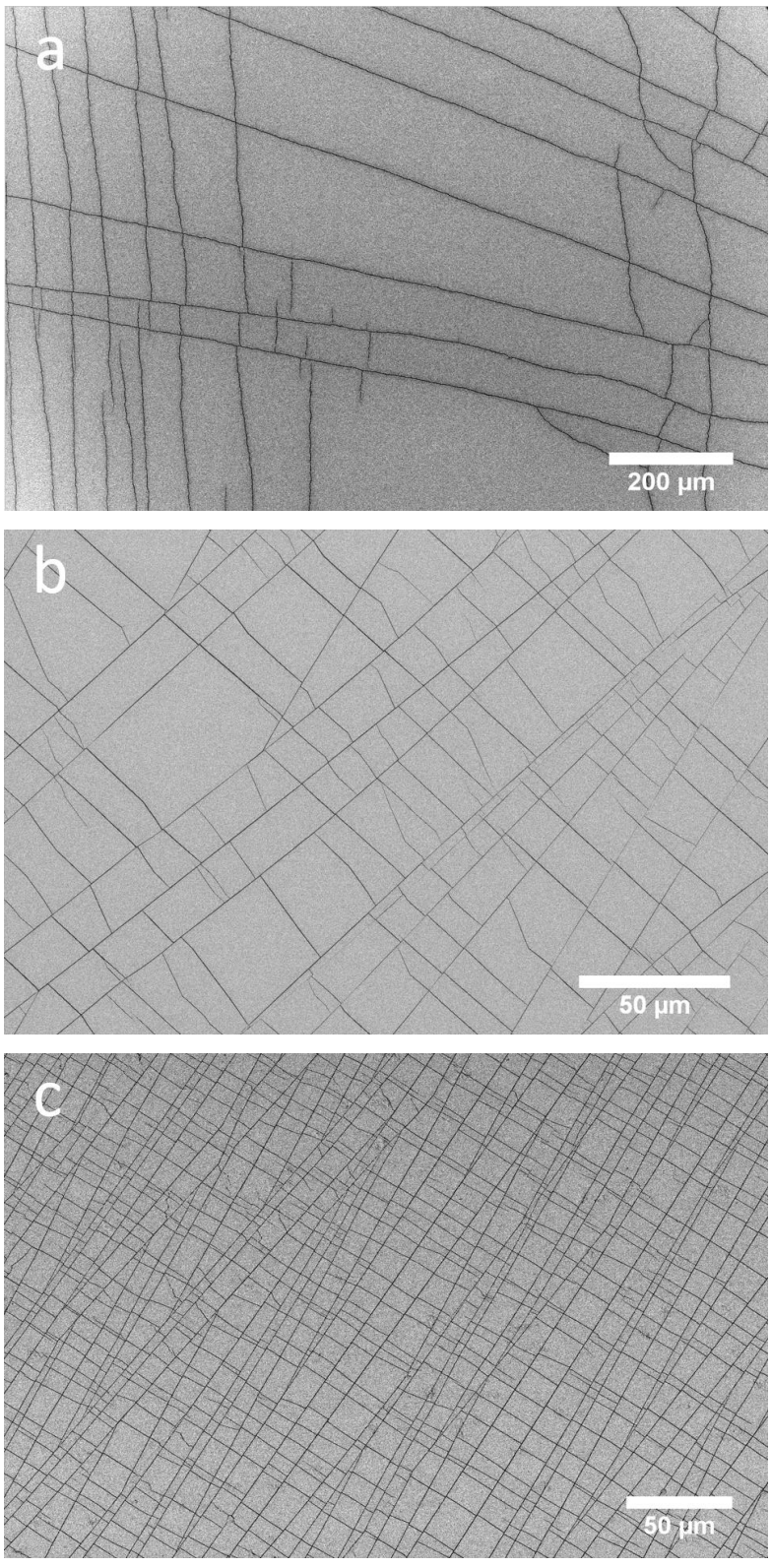


**Figure 39: Micrographs of the surface of different pieces of PPDMS**

In addition to these rectangular/triangle grid arrangements, it is also possible for the cracks to define elements that are irregular, resulting in a very different distribution of features. Examples of these arrangements are given below in Figure 40.

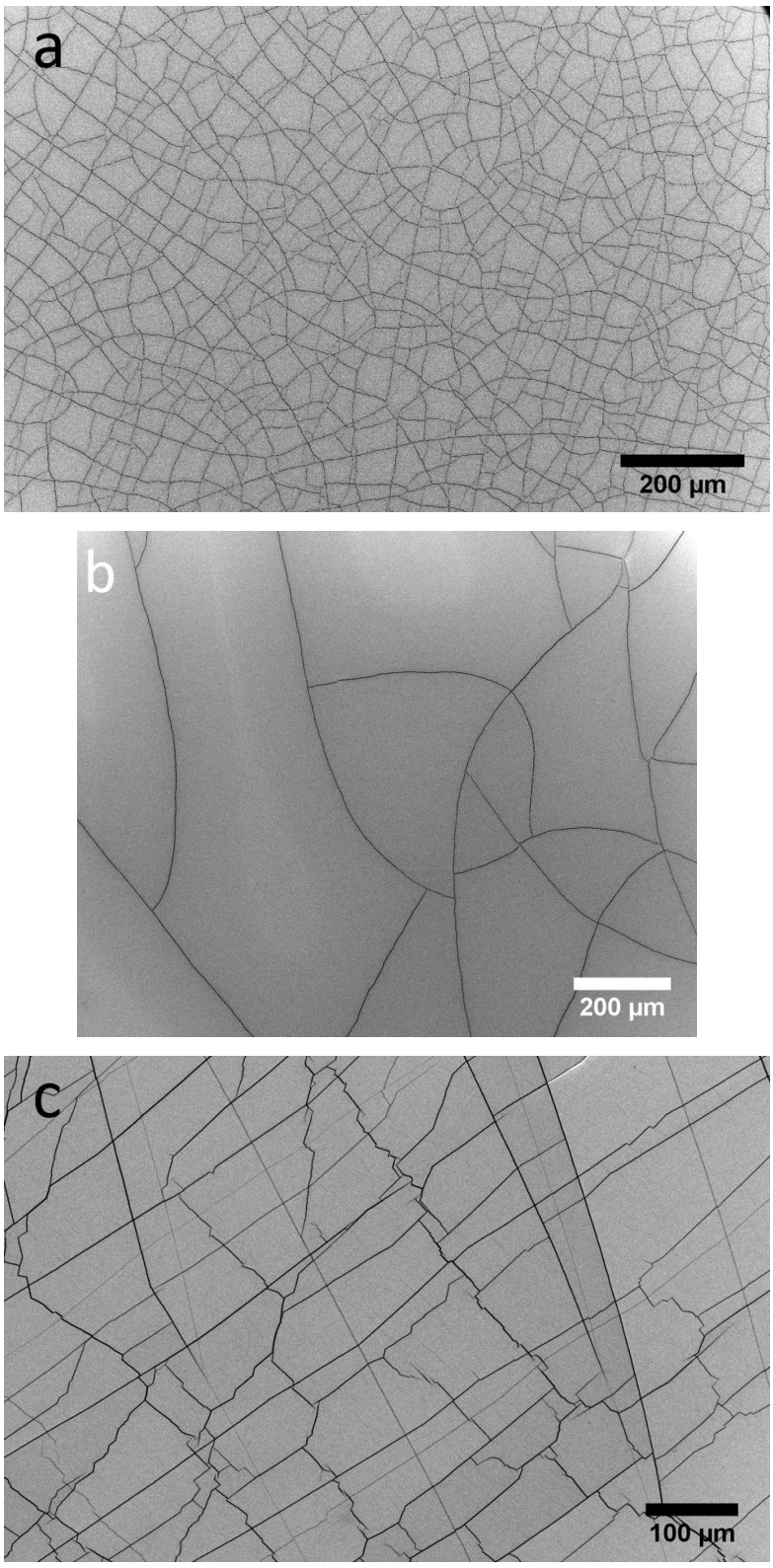


**Figure 40: Electron micrographs of PPDMS surfaces with crack arrangements very different to the rectangular grid distributions presented above**

The fact that the features are present alongside planar regions means that these substrates are ideal for investigating the effect of surface topography on crystallisation. This is because

the cracks are sufficiently spaced such that it is easy to determine whether or not the crystals formed in association with the crack, or on the adjacent flat regions. As indicated in the preliminary research, if a substrate has little topographical control over nucleation, then the precipitated material will be randomly distributed across the surface. When the cracked PPDMS samples were used as substrates for the crystallisation of calcium carbonate and then analysed in the SEM, crystals were observed at the cracks, indicating that the crystals had preferentially nucleated at these features over the terraces.

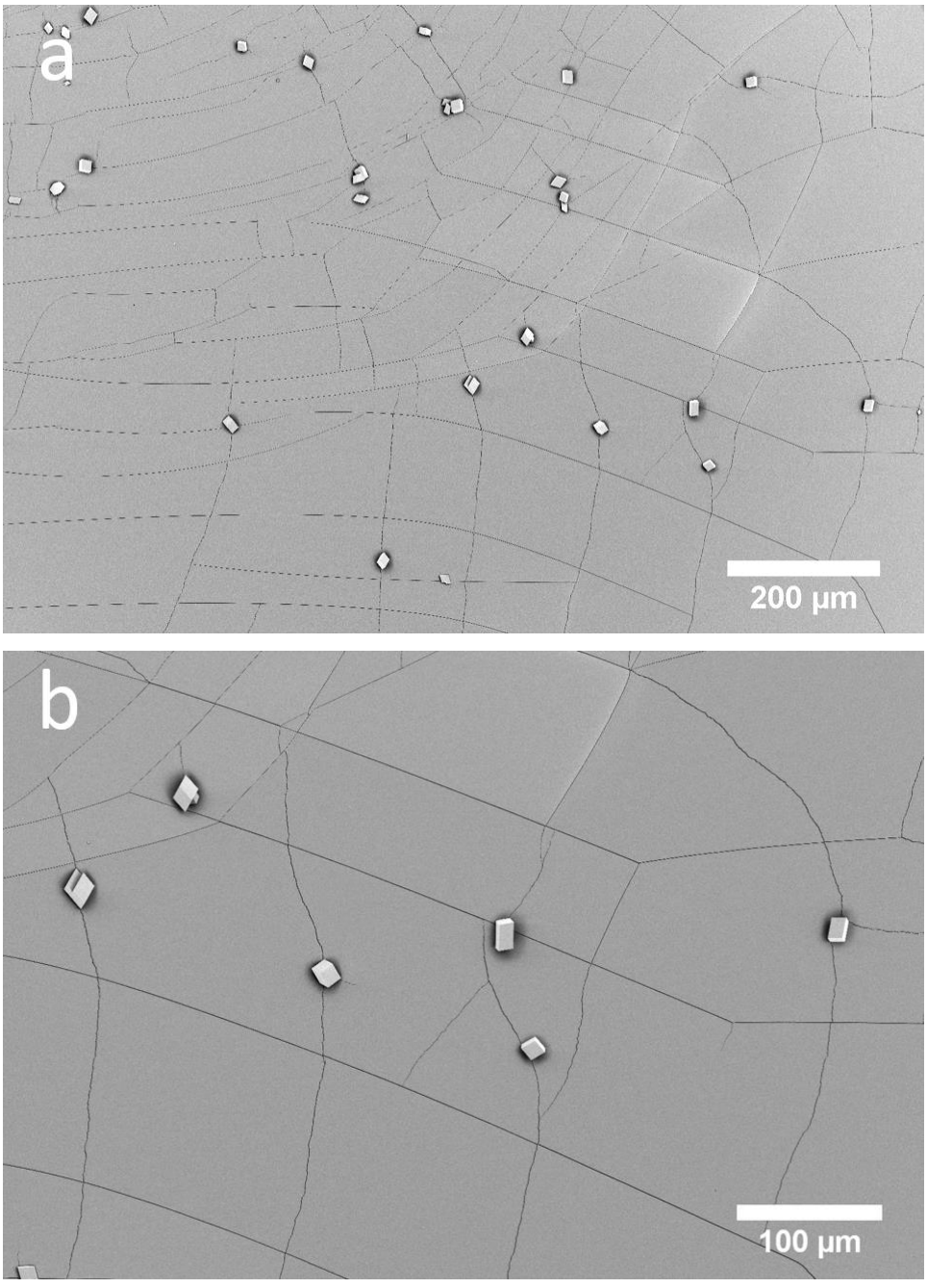

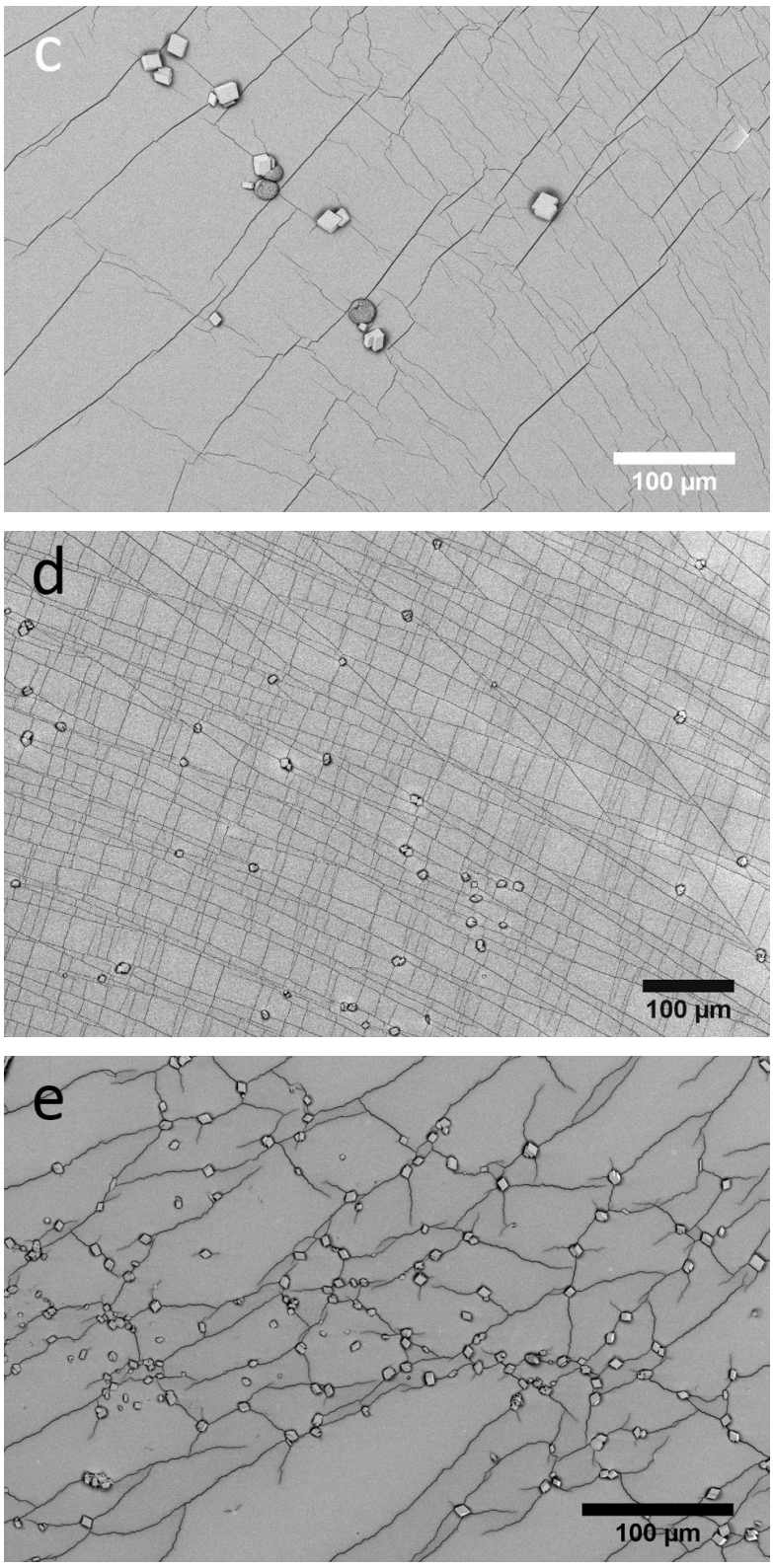


**Figure 41: Electron micrographs of calcium carbonate crystals precipitated on PPDMS substrates at varying initial concentrations**

The dominant polymorph observed on the PPDMS substrate was calcite, but occasionally vaterite or aragonite could be found (Figure 42). The crystals were all of a similar size, indicating that they had nucleated simultaneously.

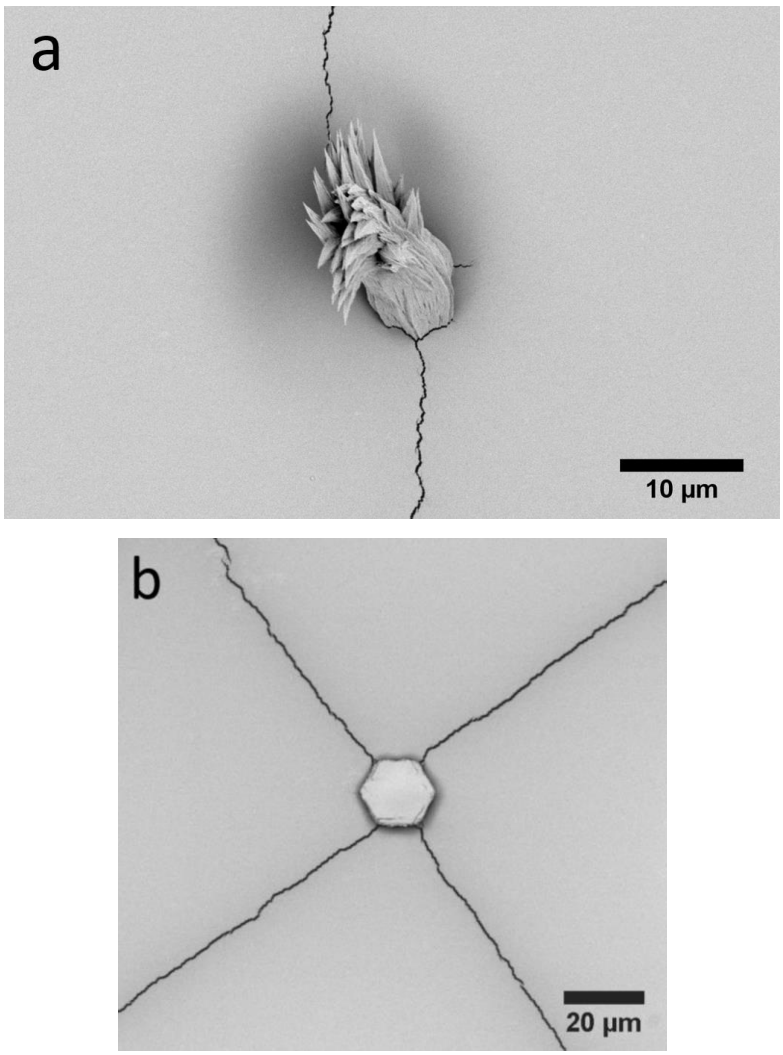


**Figure 42: Examples of (a) aragonite (b) vaterite crystals precipitated on the PPDMS substrate**

The crystals that had precipitated on the cracked PPDMS substrate were observed to have nucleated at the furrows. By tilting the stage on which the PPDMS sample was located in the scanning electron microscope, it was possible to visualise the interior of the crack in more detail. The exact location of the nucleation event within the crack is unknown, though it is likely to occur at the nanocracks that exist within the microcracks (Figure 43), which were unable to be detected by the AFM probe due to the tip lacking a high enough aspect ratio.

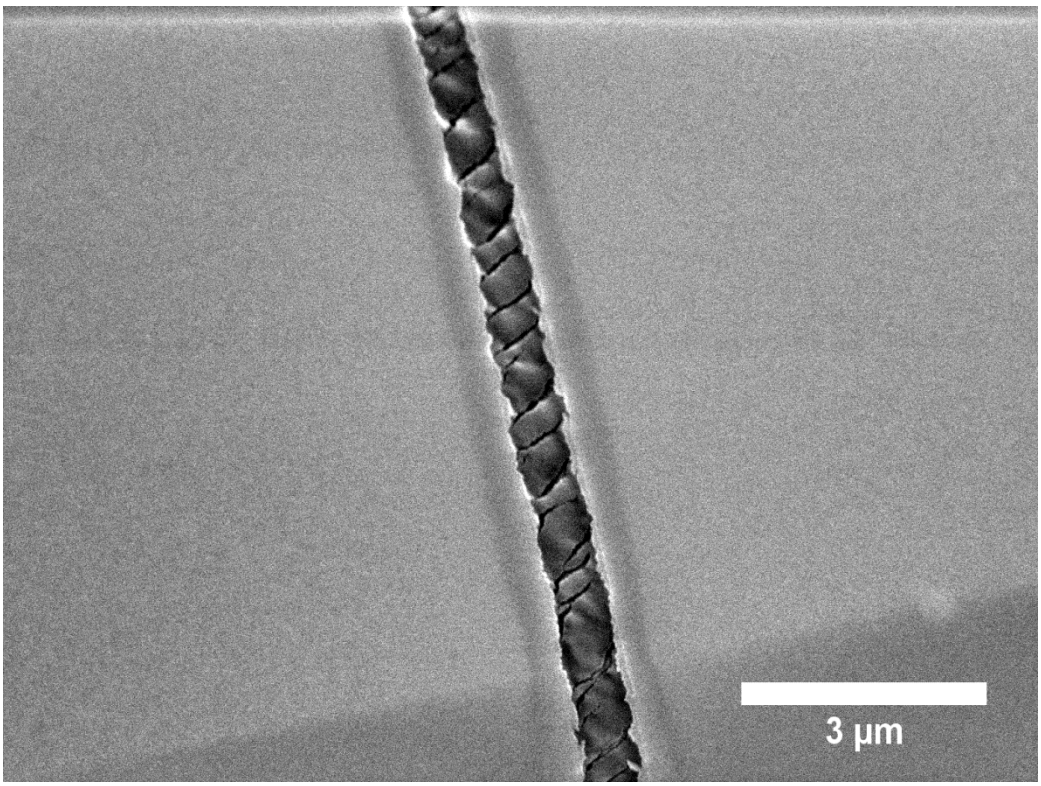


**Figure 43: SEM micrograph of an approximately 650 nm wide crack in the plasma-treated PDMS viewed at a 45° tilt angle**

Using SEM data, the nanocracks have been measured to be approximately 90 nm at their widest and <10nm at their narrowest. The reason why the nucleation event is likely to occur at the narrowest points of the nanocracks is addressed in Chapter 6.

As mentioned above, the arrangement of the cracks appeared random, in that samples made using the same methodology may have different distributions of cracks across the surface. In an attempt to understand more about how the crack density can be controlled, an investigation was conducted in which the exposure time to the RF plasma was varied. It was revealed that the surface cracks begin to form after approximately 3 minutes of exposure (Figure 44). Exposure beyond this did not influence the distribution of the cracks.

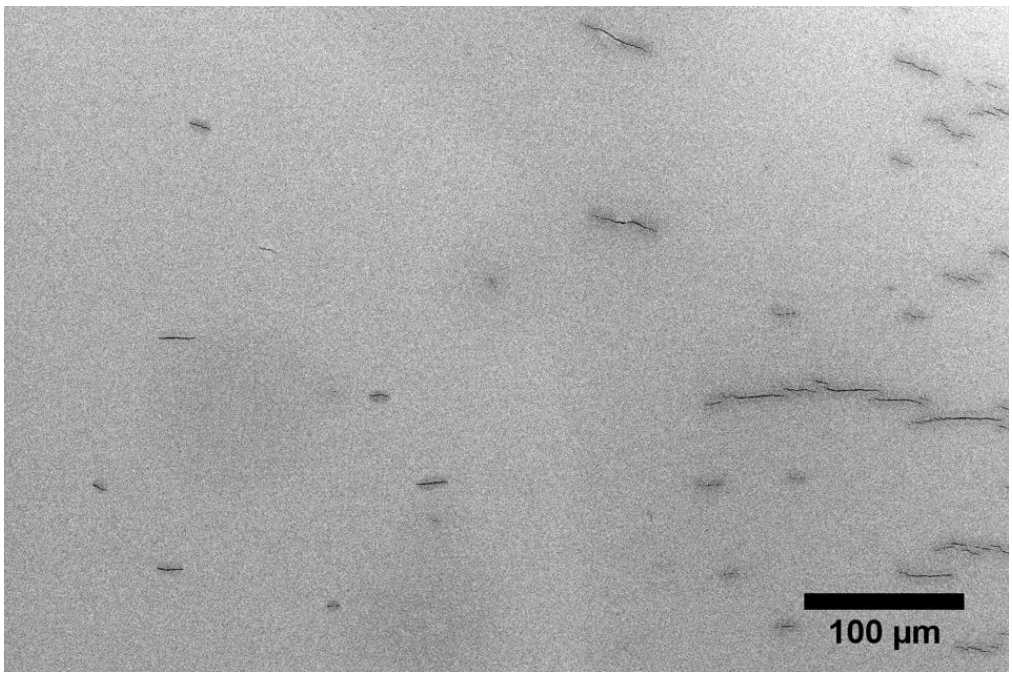


**Figure 44: Electron micrograph of the surface of a PPDMS sample after 3 minutes of exposure to RF plasma**

These short exposure time substrates were also used as substrates for the crystallisation of calcium carbonate. Although the cracks were many times shorter than those previously observed, they were still effective at nucleating calcium carbonate (Figure 45).

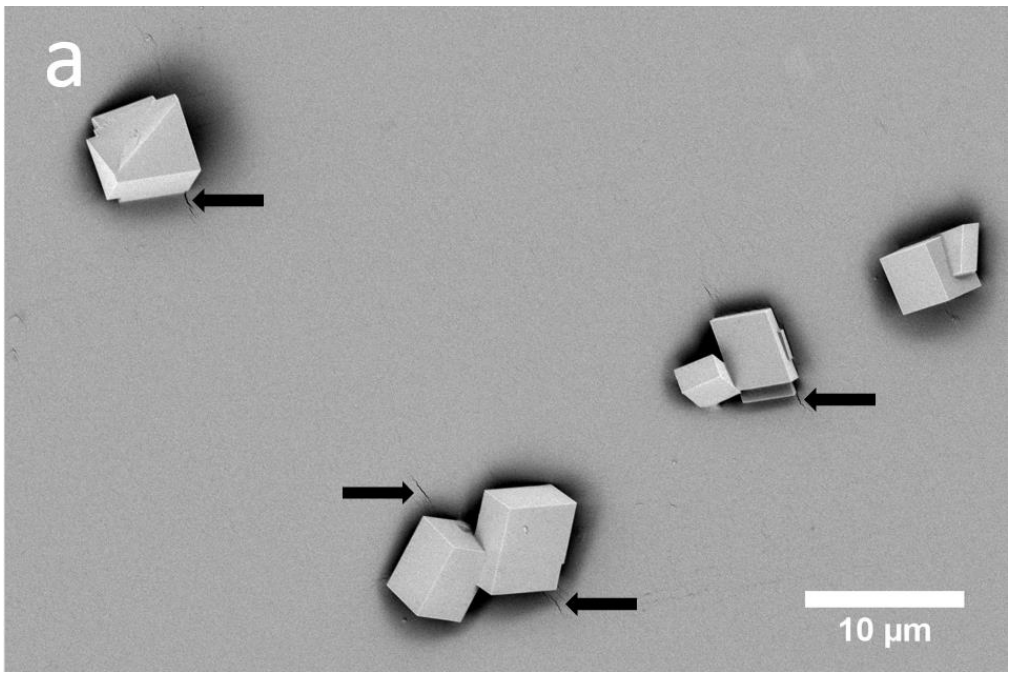
a
10 µm

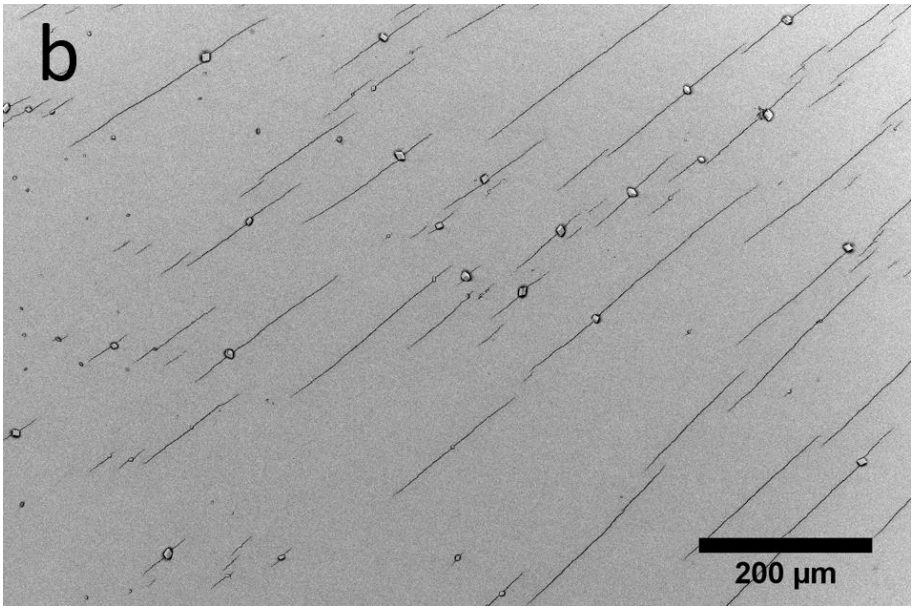
b
200 µm

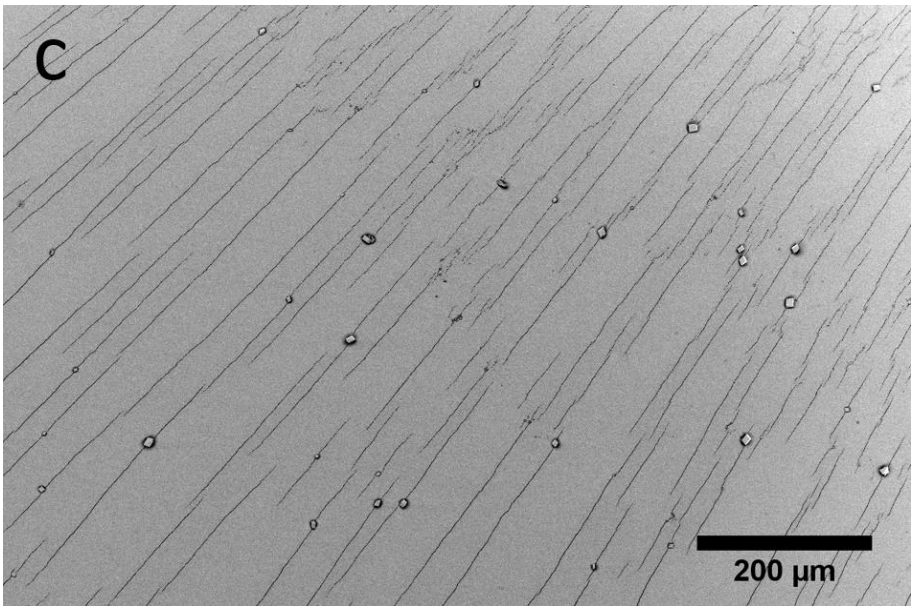
c
200 µm

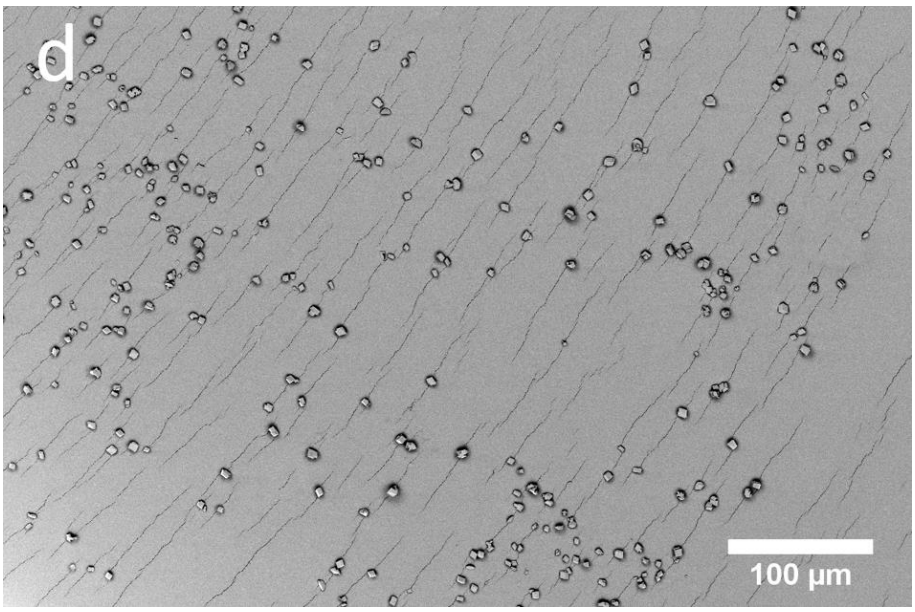


**Figure 45: SEM micrographs of calcite precipitated on PPDMS that had been exposed to varying durations of plasma treatment**

Finally, as the time taken to form the cracks had been identified, it was possible to design some control experiments. The aim was to oxidise the surface as much as possible via plasma exposure, without allowing cracks to form. This would provide substrates that would, hypothetically, have a similar surface chemistry as the cracked substrates, but would lack the surface features, therefore providing a suitable comparison for the effect of topography. However, without characterising the cracked and uncracked plasma-treated surfaces using surface sensitive analytical techniques, it is difficult to confirm this. An exposure time of 2 mins, 30 secs was used as well as similar crystallisation conditions. These substrates provide a simple comparison between crystallisation on a featureless substrate and one containing features that have been shown to influence crystallisation. Figure 46 contains electron micrographs of crystallisations carried out on these control substrates.

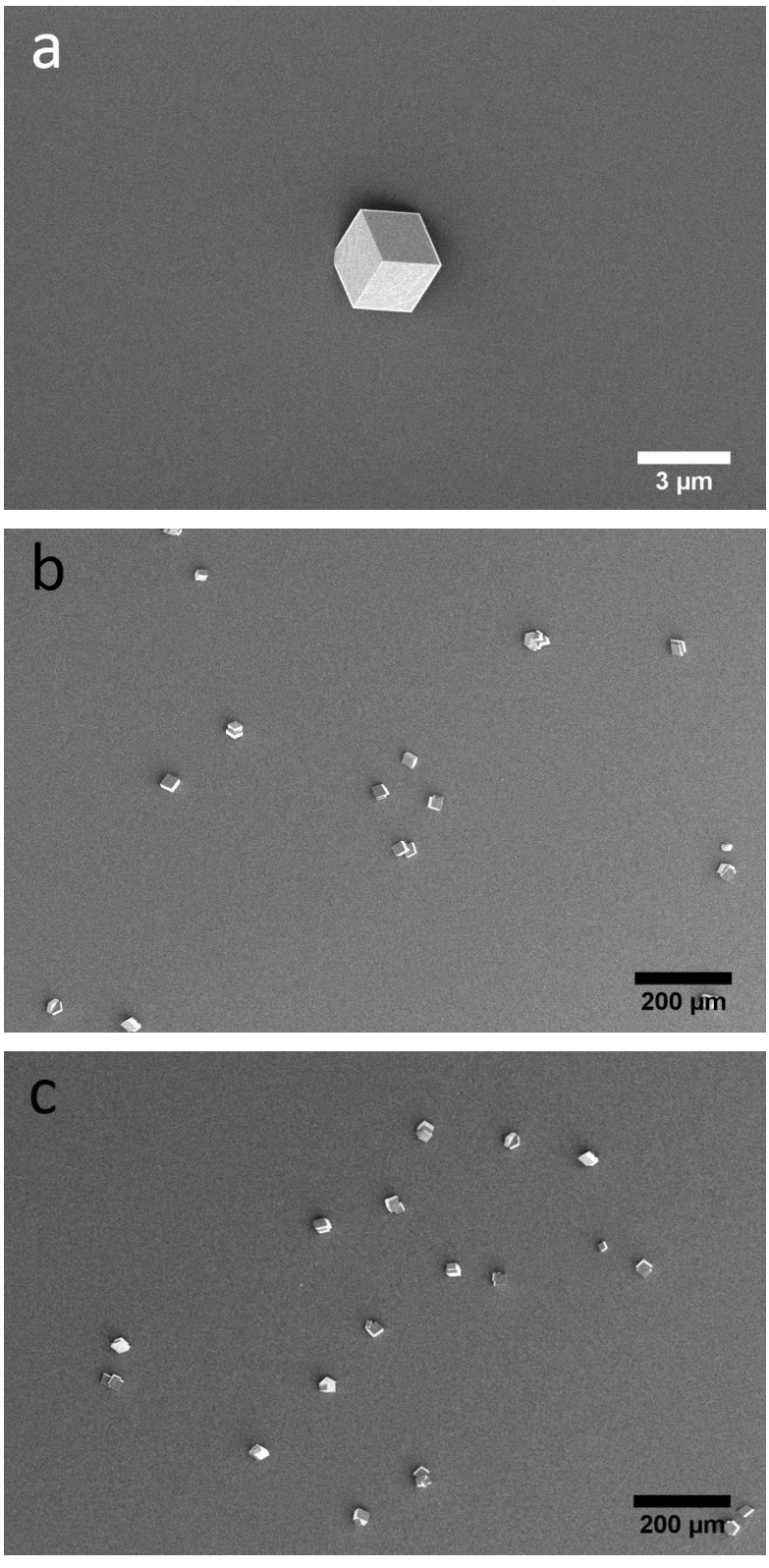
a
3 µm
b
200 µm
c
200 µm

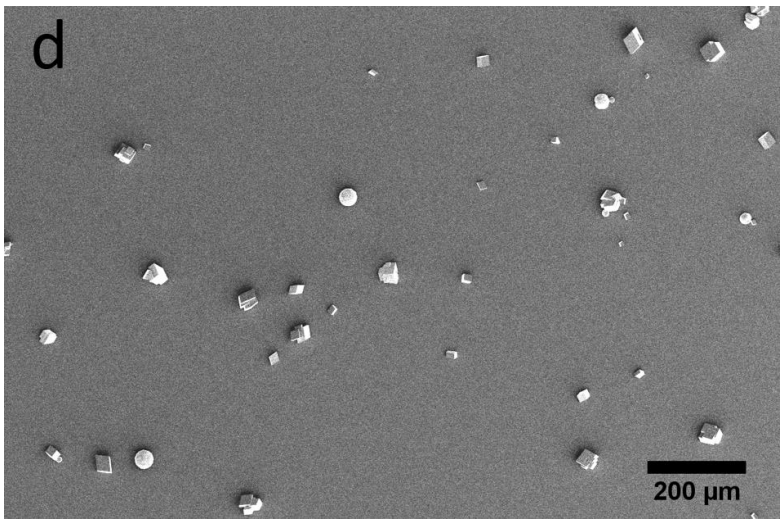


**Figure 46: Electron micrographs of calcium carbonate crystals precipitated on PDMS substrates that had been exposed to RF plasma for 2 mins and 30 secs**

On visual inspection of Figure 46, the crystal populations are significantly lower than that which would be expected for a PDMS substrate exposed to plasma for the full 7 mins, as shown in Figure 41. The crystallisation data associated with the uncracked PPDMS substrate highlight the effect that surface topography can have on crystallisation and how, by introducing the surface features with the correct geometry, crystal populations can be greatly enhanced.

### 2.5.3 Crystallisations on the Surface of Thiol Self-Assembled Monolayer-Coated PPDMS

As mentioned above, the cracks in the plasma-treated PDMS have not yet been fully characterised due to the difficulties associated with imaging such small structures. It is not known if the crack in the $SiO_x$ surface layer penetrates down to the underlying PDMS. If the PDMS is exposed, then the chemistry of the apex of the crack may be different to the walls and the rest of the exposed surface. However, the previous data showed that cracks begin to form in the surface after 3 minutes of exposure (Figure 44). This is supported by research carried out by Fritz *et al*, which suggests that the early formation of the cracks allows their internal walls to become oxidised, such that the surface chemistry may be similar inside the crack as outside on the flat terrace [19]. To overcome this uncertainty and in an attempt to homogenise the surface chemistry across the substrate (such that the chemistry in the crack is the same as that on the flat regions), the PPDMS surface was coated with a carboxylate terminated thiol (the method of which is described in Section 2.4.1.2).

#### 2.5.3.1 16COOH (16-Mercaptohexadecanoic Acid) Coated PPDMS

The carboxylate terminal functional group and its interaction with inorganic materials has received much attention in the biomineralisation community over the years, particularly with regards to calcium carbonate crystallisation. In the early/mid-1980's, it was understood that matrix molecules that are closely associated with mineral phases in living organisms often possess acidic characteristics [35-39]. In particular, aspartic acid rich protein domains were identified as playing a key role in the interaction between mineral and organic, and, due to the fact that the R-group of this amino acid involves a carboxylate functionality, research proceeded in this direction. The most common approach to studying how these proteins interacted with inorganics at the time was to extract and purify the acidic macromolecules from an appropriate source, such as a mollusk shell, and then to examine their effects on crystal growth *in vitro* [35, 40-42]. Given the prevalence of calcium carbonate across aquatic invertebrate species, a body of literature was built up regarding the interactions between carboxylate-containing molecules and this inorganic material [43-74]. As knowledge progressed and nascent technologies emerged, new ways in which crystal induction and growth regulation could be studied were harnessed. Of particular interest was the use of thiol self-assembled monolayers for crystallisation studies, a technique which quickly became a standard tool in the surface-modification tool-set across disciplines. Their ease of synthesis and similarity to extracellular immobilised macromolecules made them an attractive model for biomineralisation and so a number of papers were published in which the effect of carboxylate-terminated monolayers on calcium carbonate were detailed [75-87]. Alongside reduction in induction times and orientation effects, enhancement of crystal populations and a number of other phenomena were described. As such, combining surface modification in the form of a carboxylate thiol SAM with the cracked PDMS substrates was an enticing progression of this project.

The carboxylate thiol that was used for this research was 16-mercaptohexadecanoic acid (referred to as 16COOH), as its effects on the heterogeneous nucleation of calcium carbonate are well documented. The PPDMS samples were coated with Ir and then the SAM was formed as detailed in Section 2.4.1 The samples were used as substrates for $CaCO_3$ precipitation over a range of supersaturations with interesting results (for a table detailing the initial ion concentrations and their associated saturation indexes, refer to Table 4 of Section 2.4.1.6). Under all direct mixing conditions tested, the only polymorph observed across all 16COOH-coated PPDMS samples was calcite. Further, the crystal population was much larger than that

observed in the absence of the thiol at the same supersaturation (in reference to the uncoated cracked plasma-treated PDMS of Figure 41). The crystals exhibited a very strong preference for the cracks in the PPDMS substrate, only deviating from the cracks once the entire feature had been occupied (Figure 47).

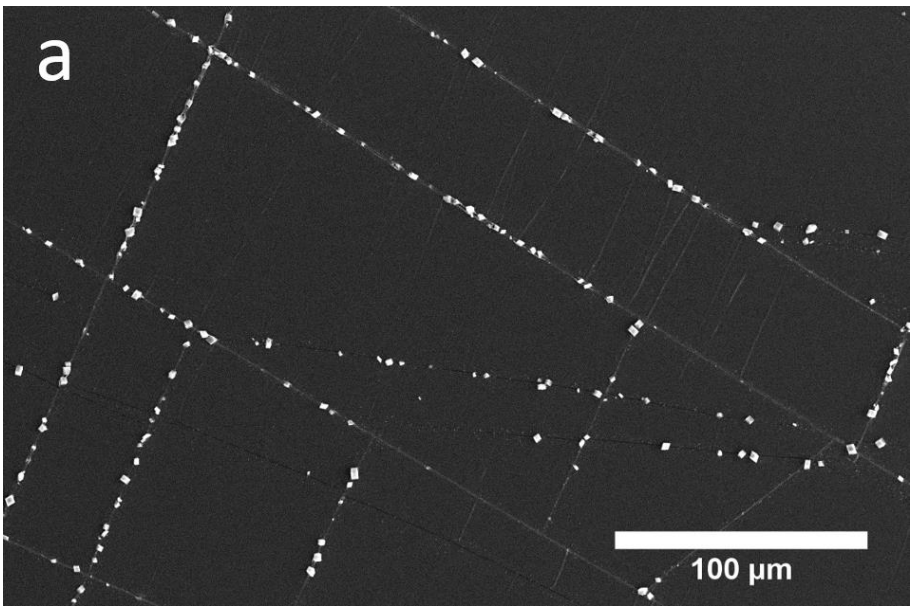
a
100 µm

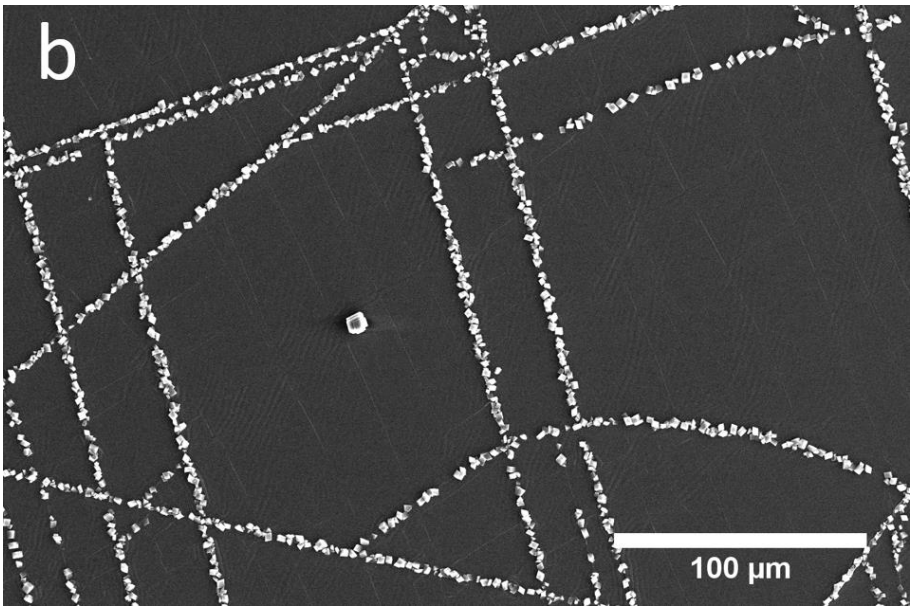
b
100 µm

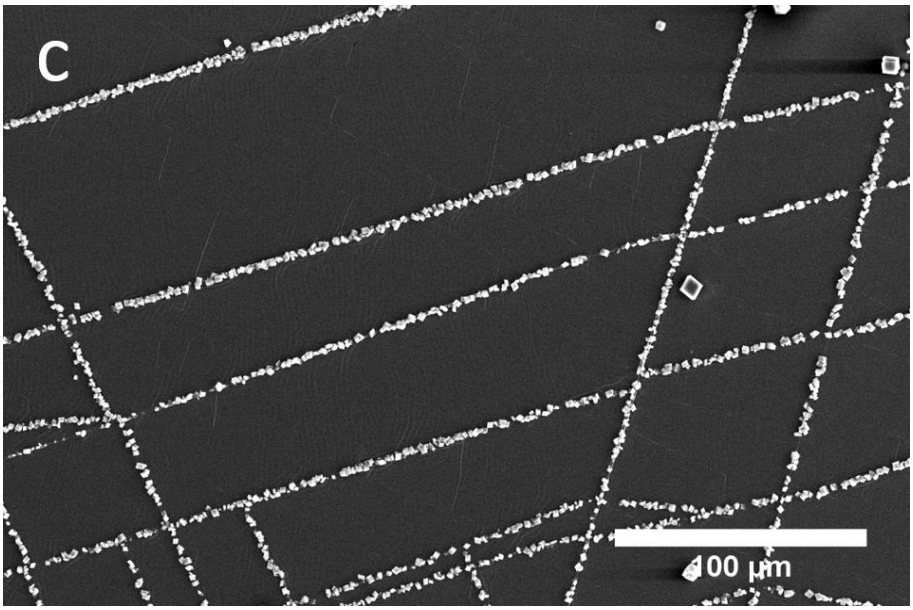
c
100 µm

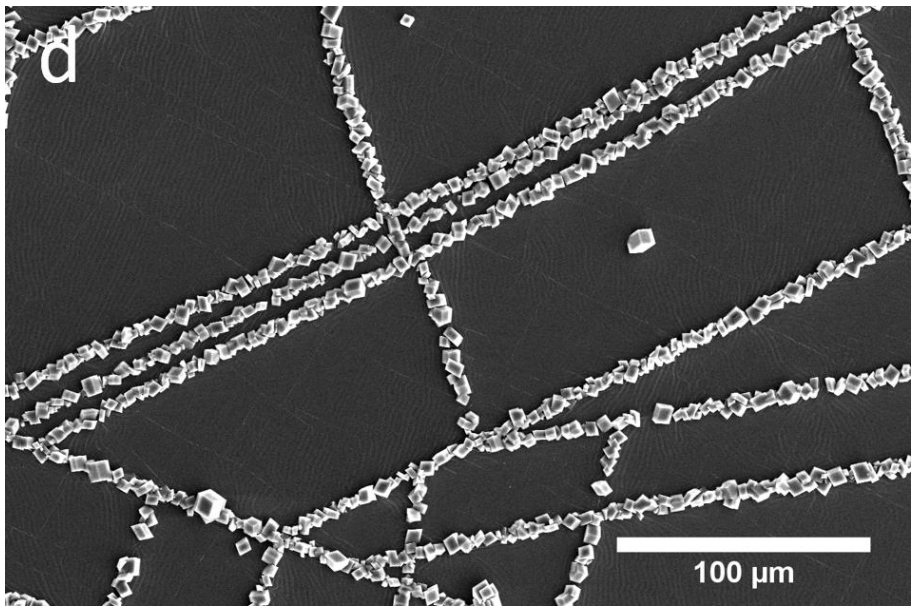
d
100 µm

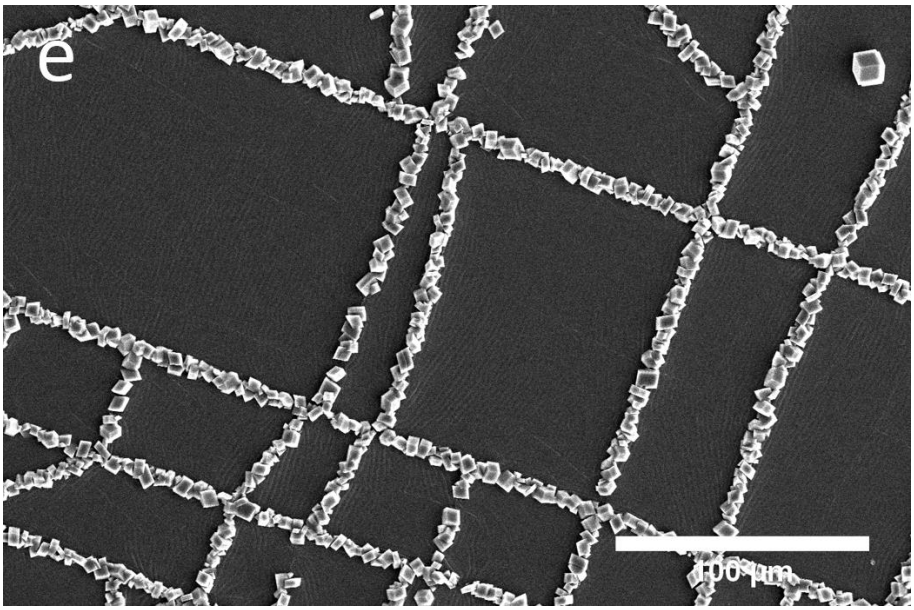
e
100 µm

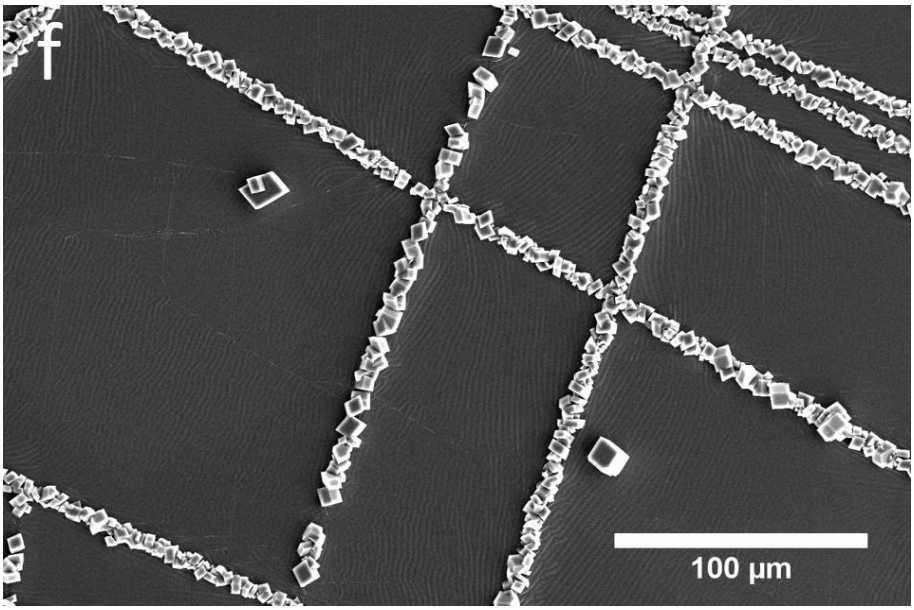
f
100 µm

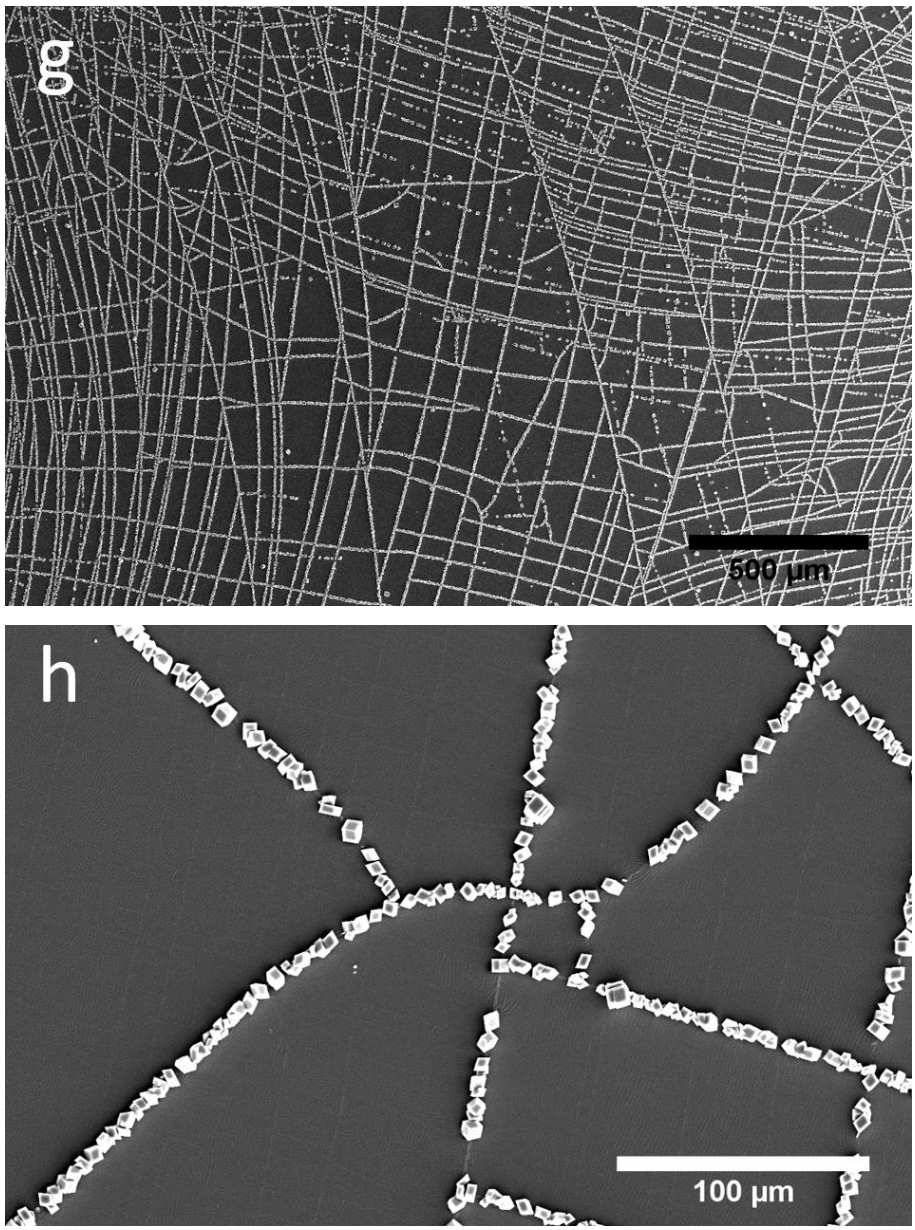
g
500 µm
h
100 µm

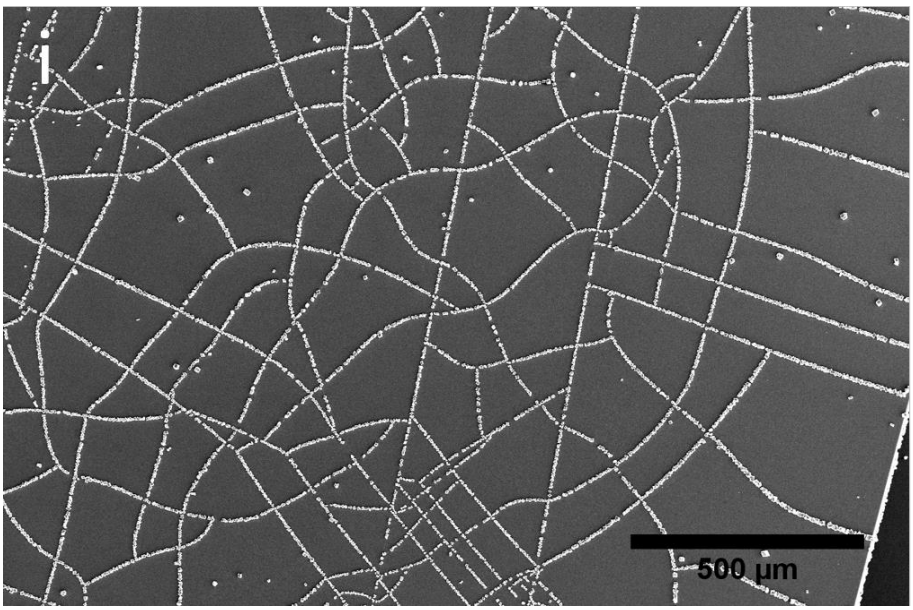


**Figure 47: SEM images of a Plasma-treated poly(dimethylsiloxane) surfaces that had been coated with a 16-mercaptohexadecanoic acid self-assembled monolayer and subsequently used as substrates for the crystallisation of calcium carbonate at various concentrations**

The crystals that were not situated on the cracks were always larger than the aligned crystals (some can be seen in Figure 47b - h), suggesting that they were able to grow to a larger size as they were not competing for growth resources with adjacent crystals, unlike those on the cracks. The close proximity of crystals to one-another within the cracks will deplete the immediate solution environment, reducing their growth rate relative to an isolated crystal and as such, their growth is likely limited by the ion flux into this region [81]. The size discrepancy was confirmed by image analysis, which determined that crystals that had nucleated on the flat terraces were 295% larger in 2-dimensional area than those that nucleated on the cracks (this value was calculated using the data from Chapter 4: Image Analysis, where this is an average across all solution conditions and substrates for the 16COOH-coated PPDMS substrate). The localisation of the crystals to the cracks as opposed to the adjacent flat areas of the PPDMS suggests that the free-energy barrier to nucleation is significantly lower in the cracks than on the terraces. Research elsewhere has suggested that for 16COOH coated gold substrates, the value of the effective interfacial energy between a calcite crystal and a 16COOH SAM is 72 mJ $m^{-2}$ (the effective interfacial energy between a calcite crystal and the solution has been calculated as 109 mJ $m^{-2}$) [88]. The effective interfacial energy associated with 16COOH-coated PPDMS may not be the same as this, as the authors used gold deposited on glass, whilst here Ir on PPDMS is used. The underlying structure of the substrate and intermediary layer play an important role in the arrangement of the SAM molecules and subsequent interfacial energy value, as stated in the literature review of Chapter 1. However,

it is evident from the data presented here that the interfacial energy between crystal and substrate is significantly lower on 16COOH-coated PPDMS than on the uncoated PPDMS, as indicated by the greater number of crystals observed at the same supersaturation after a shorter length of time (compare Figure 41c and d to Figure 47a and b). As a further comparison, control experiments were conducted by coating PDMS that had been exposed to plasma for 2 mins 30 (so as to form an uncracked, oxygen enriched surface layer) with Ir and then forming the 16COOH SAM on the surface. These were then used as crystallisation substrates, SEM images of the crystallisation data can be seen in Figure 48 where the conditions used are the same as those for Figure 47.

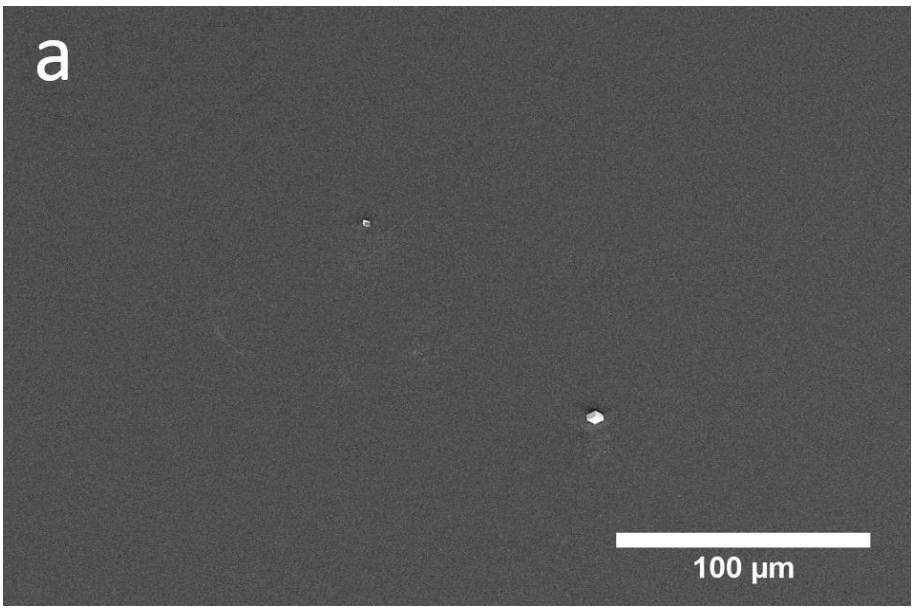
a
100 µm

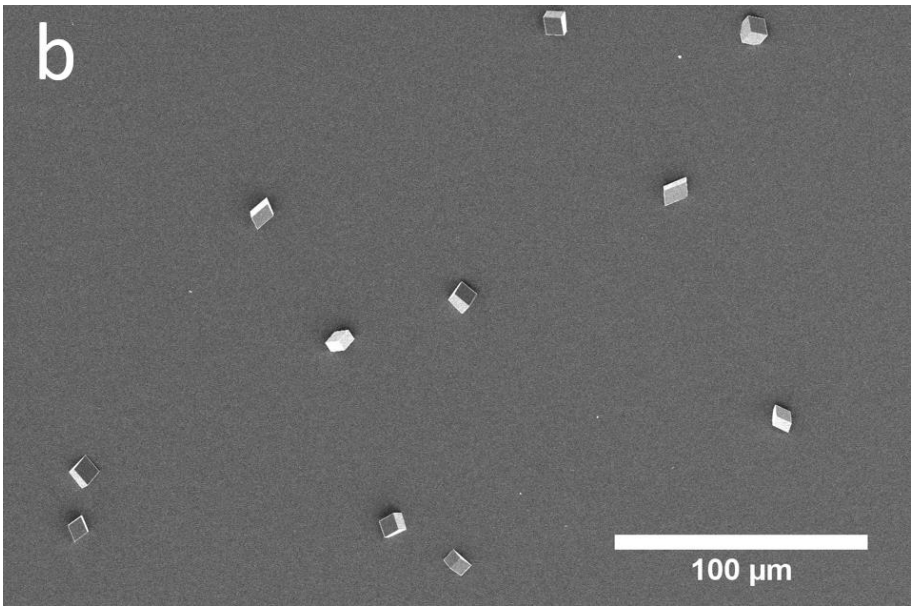
b
100 µm

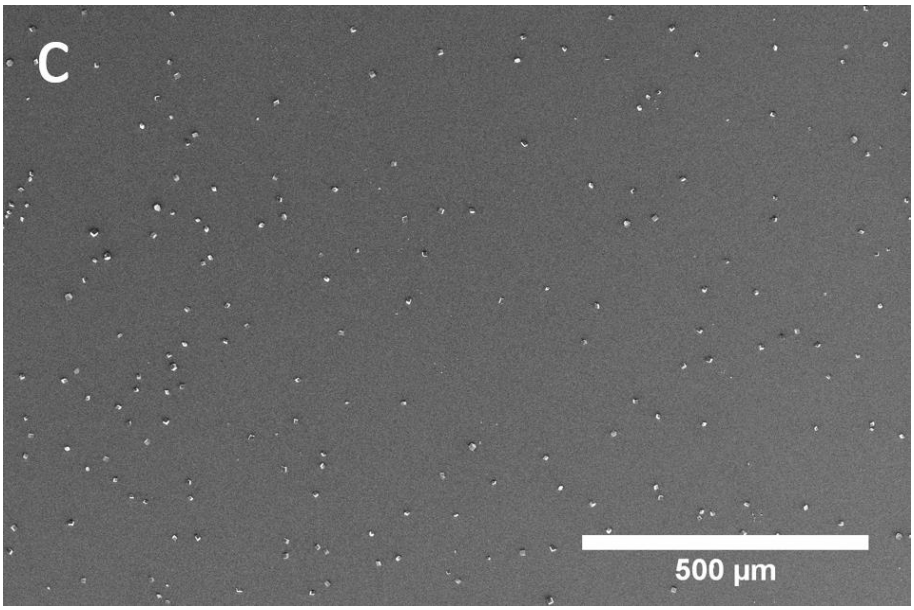
c
500 µm

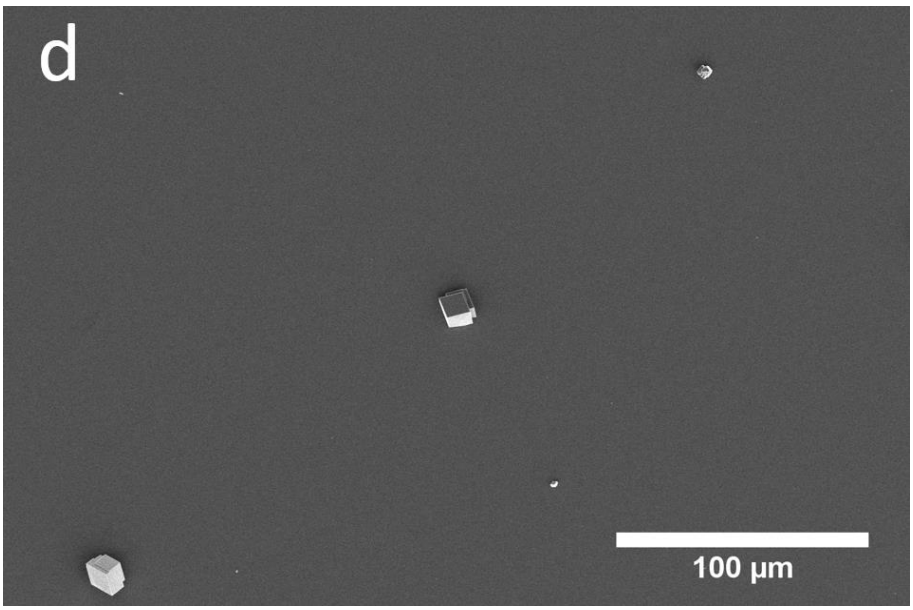
d
100 µm

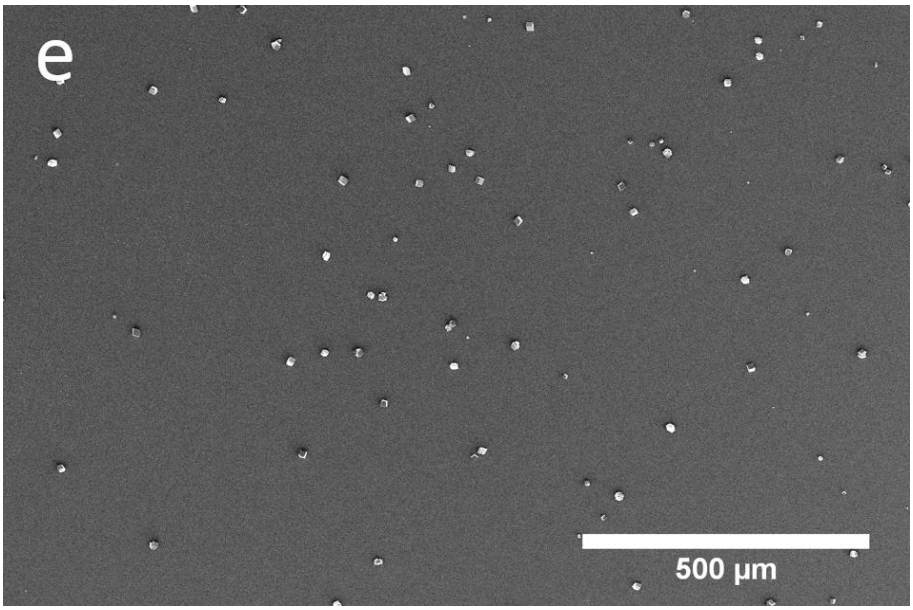
e
500 µm

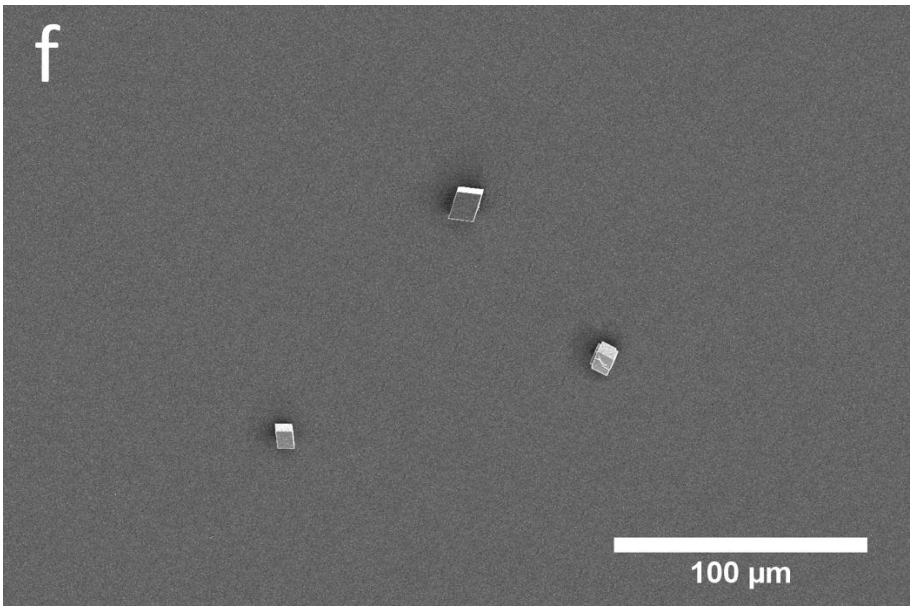
f
100 µm

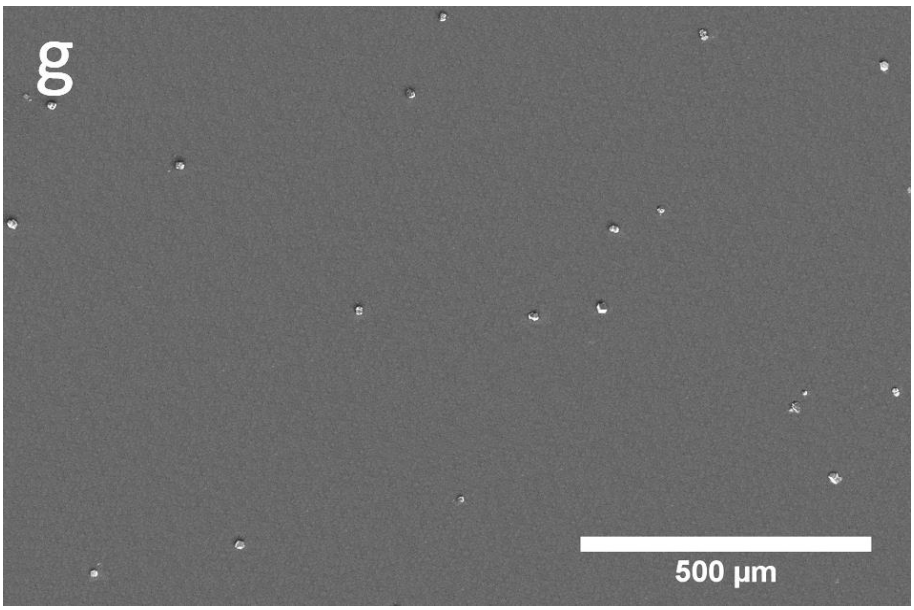


**Figure 48: Crystallisations of calcium carbonate on a 16COOH thiol coated uncracked PPDMS substrate**

As expected, at all conditions there were far fewer crystals on the substrates without cracks than those that possessed them. The difference between samples at the same concentration is quite striking. The lack of crystals on the featureless substrates is evidently a result of the absence of the cracks.

#### 2.5.3.2 Variation of the Calcium Carbonate Solution Initial Ion Ratio on 16-Mercaptohexadecanoic Acid Coated PPDMS

The effect of the initial ion ratio $[Ca^{2+}]:[CO_3^{2-}]$ on the localisation of crystals to the cracks was explored. The conditions investigated are given in Table 6, where the saturation index is defined as the ion activity product divided by the solubility product. This was calculated using Visual Minteq:

**Table 6: Initial Ion ratio of $[Ca^{2+}]:[CO_3^{2-}]$ used for the crystallisation of calcium carbonate on 16COOH coated PPDMS and uncracked 16COOH PPDMS.**

| Initial Ion Ratio | Initial Ion Concentration (mM) | | Saturation Index ($SI_{calcite}$) |
|---|---|---|---|
| $Ca^{2+}:CO_3^{2-}$ | $Ca^{2+}$ | $CO_3^{2-}$ | |
| 1:10 | 1 | 10 | 2.1 |
| 10:1 | 10 | 1 | 2.1 |
| 1:5 | 3 | 15 | 2.6 |
| 5:1 | 15 | 3 | 2.6 |
| 1:40 | 0.5 | 20 | 1.9 |
| 40:1 | 20 | 0.5 | 1.8 |

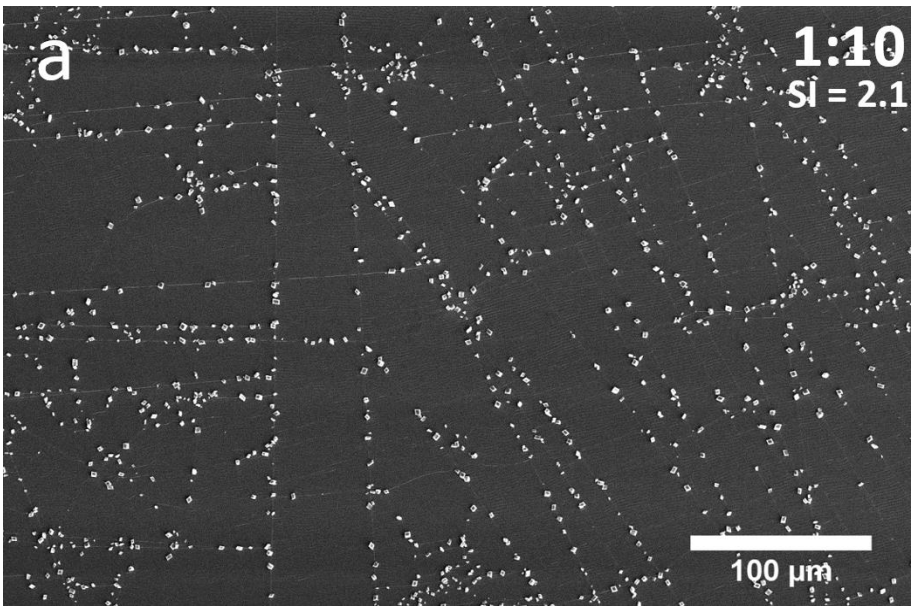
a
1:10
SI = 2.1
100 µm

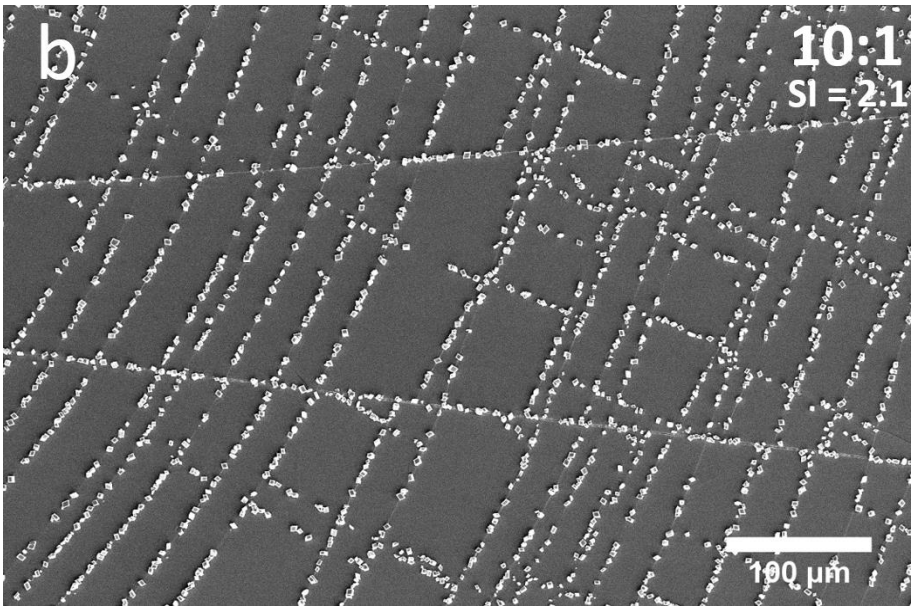
b
10:1
SI = 2.1
100 µm

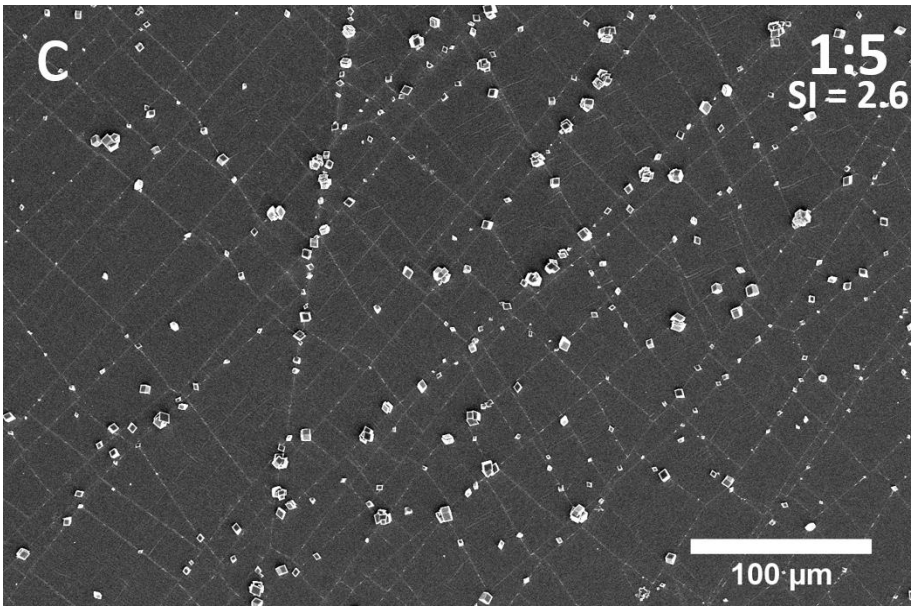
c
1:5
SI = 2.6
100 µm

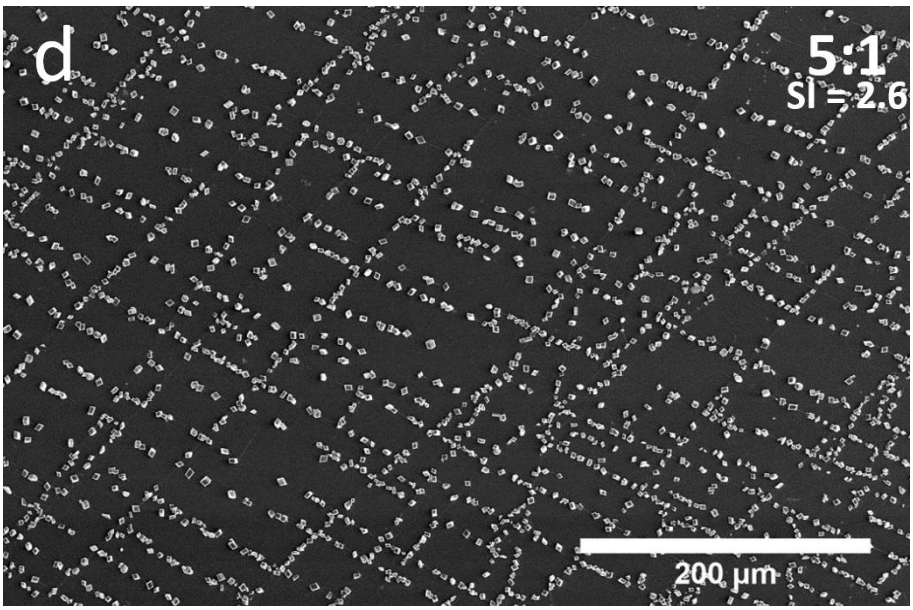
d
5:1
SI = 2.6
200 µm

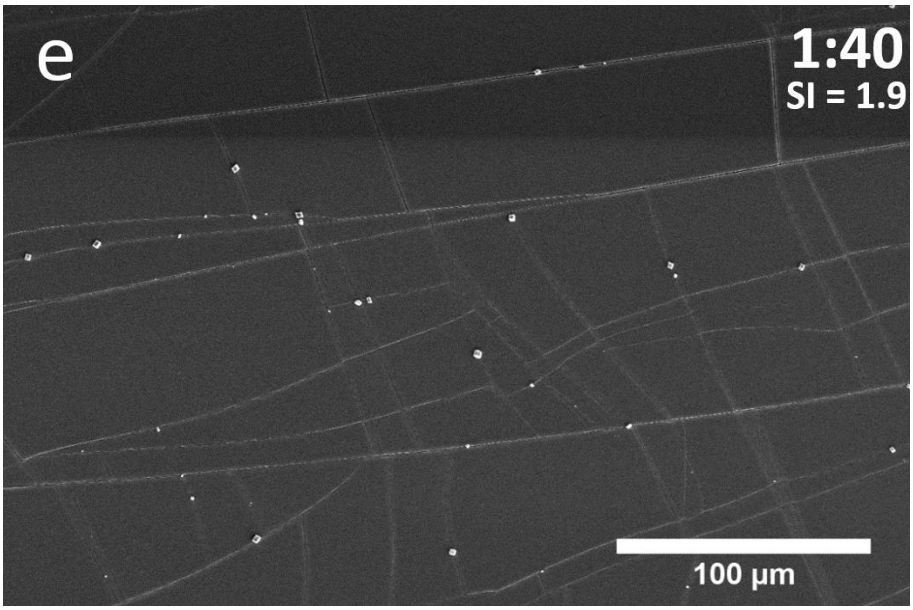
e
1:40
SI = 1.9
100 µm

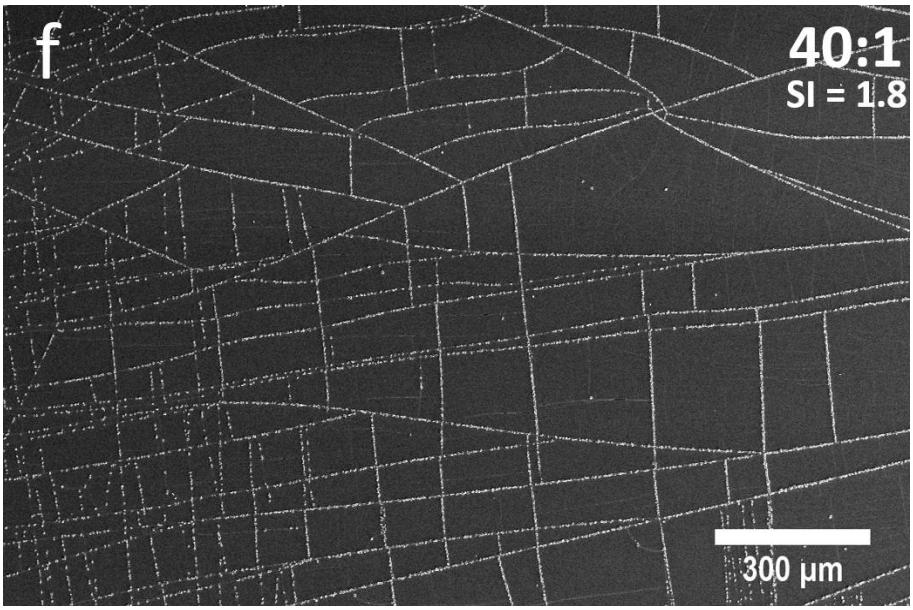
f
40:1
SI = 1.8
300 µm

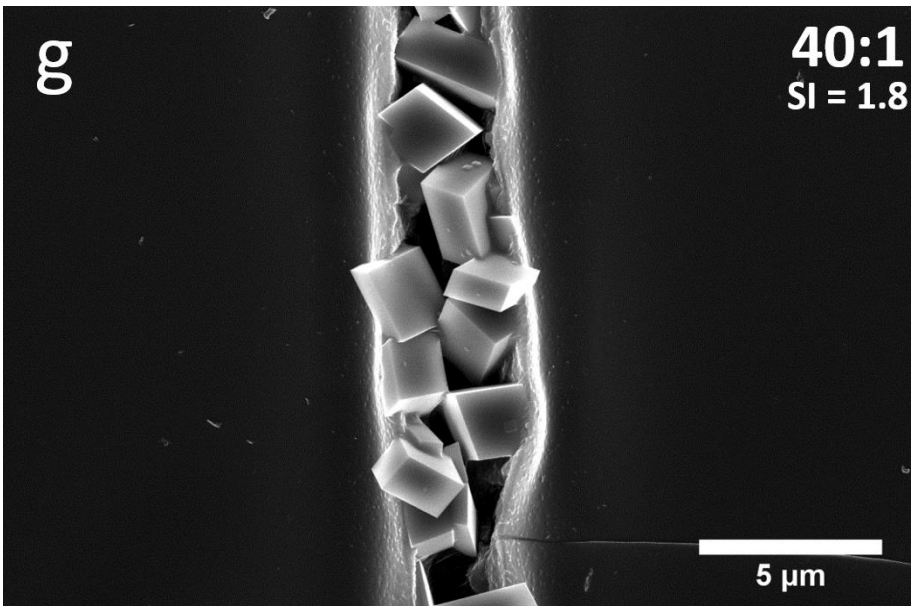


**Figure 49: SEM images of 16COOH substrates after crystallisation at various ion ratios**

The population of crystals was greater when calcium was present at a higher concentration than carbonate, and calcite was the only polymorph present in all instances. The fact that more crystals are observed when $[Ca^{2+}] > [CO_3^{2-}]$ compared to when $[CO_3^{2-}] > [Ca^{2+}]$ cannot be accounted for by the supersaturations, which are similar in each set of experiments. The difference in crystal population was most prominent in the 1:40 experiments (Figure 49e-g), with crystals filling the cracks of the $[Ca^{2+}]$ = 20.0 mM, $[CO_3^{2-}]$ = 0.5 mM, t = 10 mins substrate (Figure 49f, g), yet the cracks were sparsely populated when the ion ratio was reversed (Figure 49e). This trend can be explained by the gaseous exchange of carbon dioxide from the atmosphere into the crystallising solution. When the carbonate concentration is high, once all of the calcium ions have been consumed, the crystallisation comes to a halt. On the other hand, when the calcium concentration is much greater than the carbonate concentration, carbon dioxide in the atmosphere is able to replace the consumed carbonate according to Le Châtelier's principle, allowing the crystallisation to proceed for a longer duration of time and therefore a greater number of crystals are observed. A simple way in which this hypothesis could be confirmed was to prevent gaseous exchange occurring between the atmosphere and solution of the $[Ca^{2+}]$ = 20.0 mM, $[CO_3^{2-}]$ = 0.5 mM, t = 10 mins condition. To achieve this, the experiment was repeated and the petri dish was sealed with parafilm. The result of this can be seen below in Figure 50.

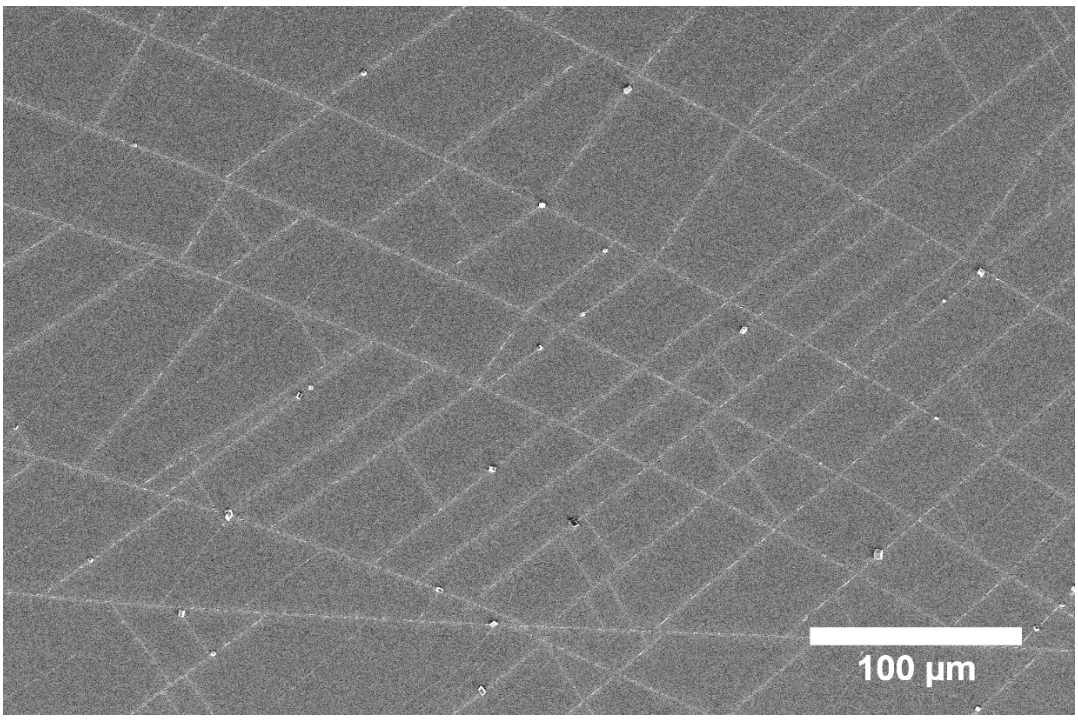


**Figure 50: SEM micrograph of a 16COOH coated PPDMS substrate after precipitation at $[Ca^{2+}]$ = 20.0 mM, $[CO_3^{2-}]$ = 0.5 mM, t = 10 mins**

The fact that very few crystals precipitated on the 16COOH coated PPDMS substrate when the vessel was hermetically sealed indicates that the observed difference in populations between high calcium and low calcium conditions was indeed due to carbon dioxide in the atmosphere dissolving in the solution. It's interesting that the rate of carbon dioxide dissolution is sufficient to cause such a huge discrepancy in crystal population given the short residence time (10 mins). However, consideration of the solution pH and the equilibria of calcium carbonate precipitation provides the answer. The stock solution pH's for 100 mM calcium chloride and 100 mM sodium carbonate were measured as 5.6 and 11.4 respectively. Immediately after mixing to obtain solution concentrations of $[Ca^{2+}]$ = 20 mM and $[CO_3^{2-}]$ = 0.5 mM, the pH was measured as 6.6. After 10 minutes, the pH had reached 9.1. Calcium carbonate precipitation is associated with an increase in pH, and carbon dioxide is more soluble in a basic aqueous solution. As the crystallisation proceeds and the pH increases, more carbon dioxide is able to dissolve into the solution and is converted to either bicarbonate or carbonate ions, therefore increasing the supersaturation with respect to calcium carbonate. Hence, if the atmosphere is in contact with the solution, a greater crystal population is observed relative to if the vessel were sealed.

To provide a comparison to the cracked substrates, the experiment was repeated using uncracked PPDMS (exposed to plasma for 2 mins 30 secs instead of the full 7 mins) coated with the 16COOH thiol.

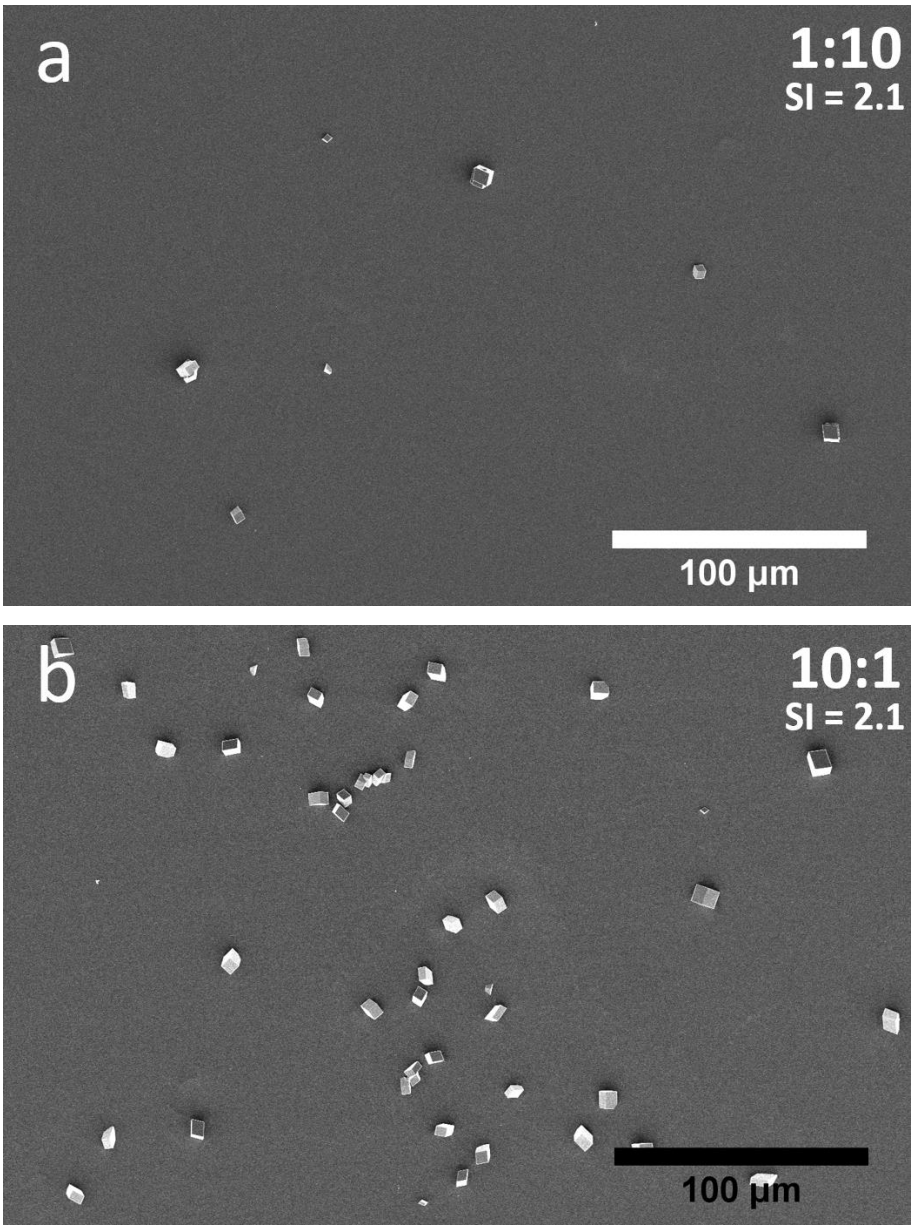

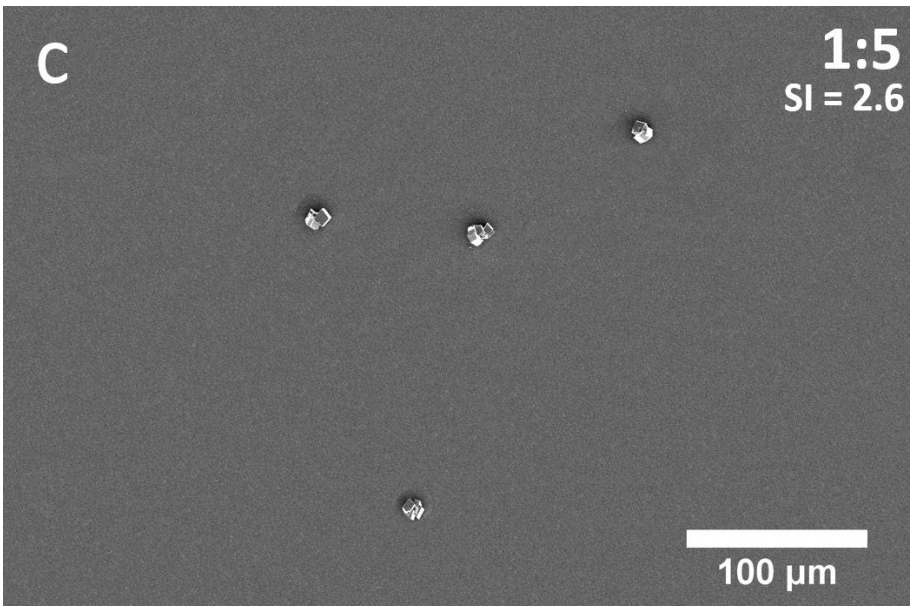
c
1:5
SI = 2.6
100 µm

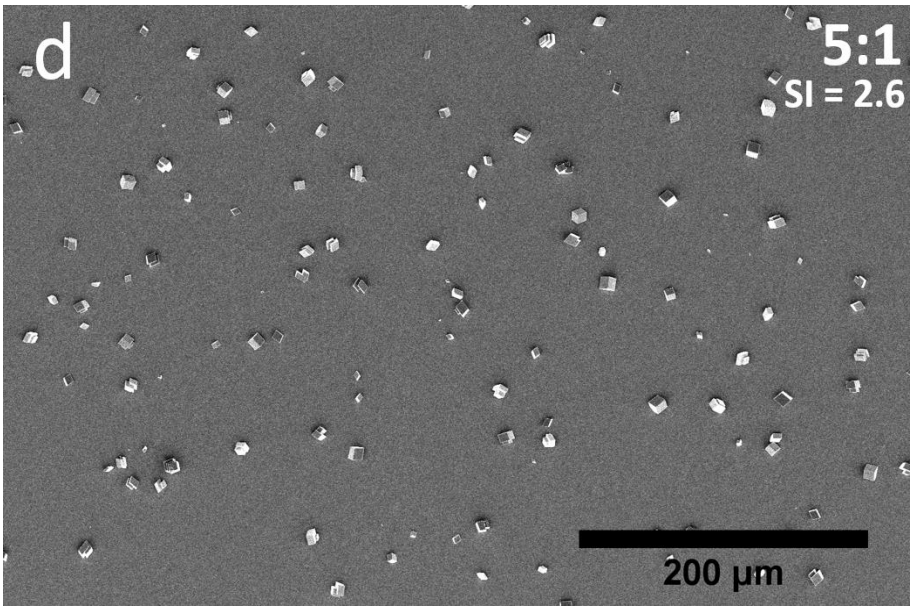
d
5:1
SI = 2.6
200 µm

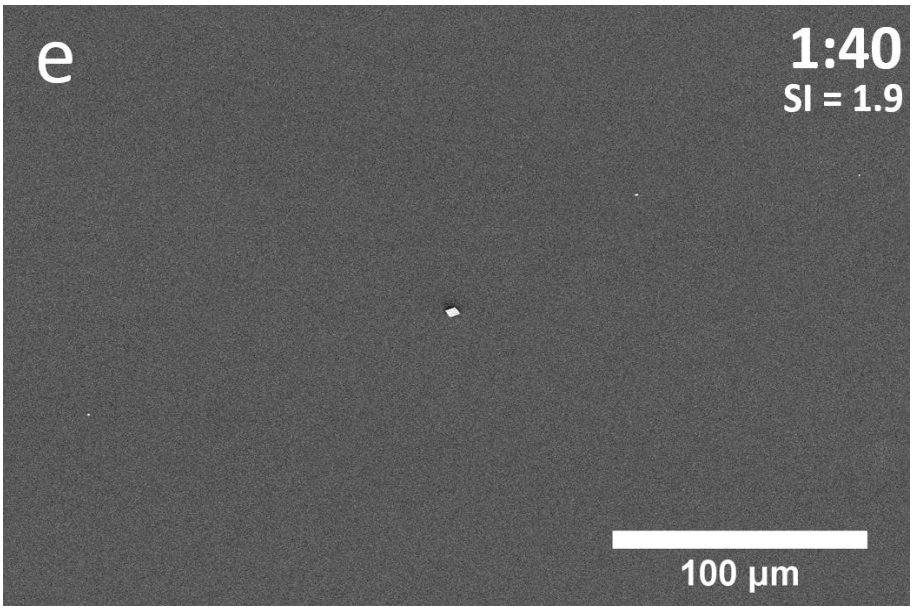
e
1:40
SI = 1.9
100 µm

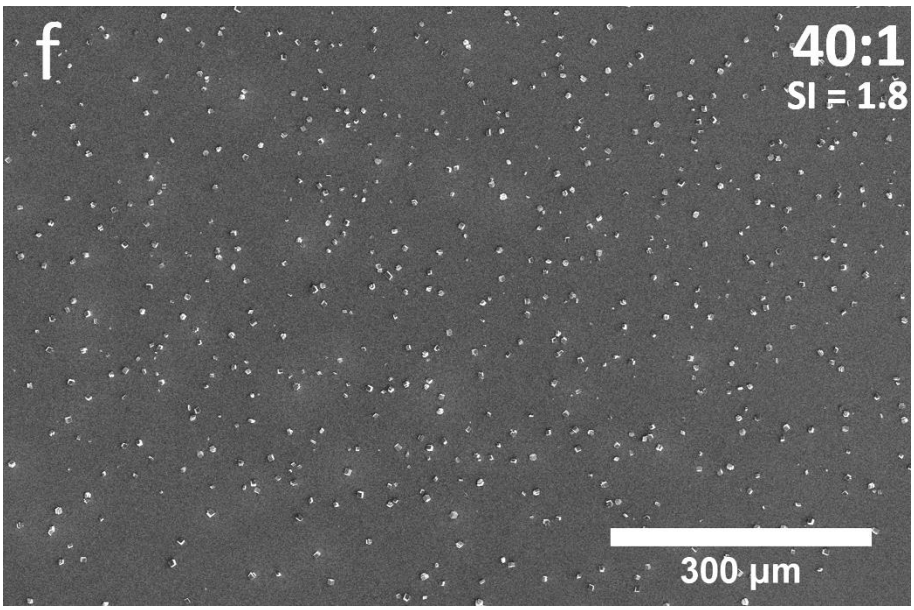


**Figure 51: Electron micrographs of calcium carbonate crystals precipitated on a 16COOH coated PPDMS substrate that had been exposed to RF plasma for 2 mins 30 seconds**

Again, the crystallisation data on the uncracked substrates was very different to that of the cracked PPDMS substrates, though the trend was the same. That is, the experiments in which the $[Ca^{2+}]$ is greater than the $[CO_3^{2-}]$, more crystals are observed on the substrate, as explained above. The observed difference in crystallisation data between Figure 49 and Figure 51 demonstrates the influence surface topography can have on nucleation and growth and show that the ion ratio can be used to control the crystallisation at the surface features.

#### 2.5.3.3 Crystallisation of Calcium Carbonate via the Ammonia Diffusion Method on 16-Mercaptohexadecanoic Acid Coated PPDMS

Another method of precipitating calcium carbonate is through the ammonia diffusion method, in which a calcium chloride solution is placed into a desiccator in the presence of ammonium carbonate, which decomposes to ammonia and carbon dioxide. Both of these gases then dissolve in the calcium chloride solution, increasing the supersaturation with respect to $CaCO_3$ and eventually causing precipitation [89]. This technique was employed for calcium chloride solutions of concentration 1, 5, and 10 mM at a residence time of 10 mins or 60 mins (Figure 52).

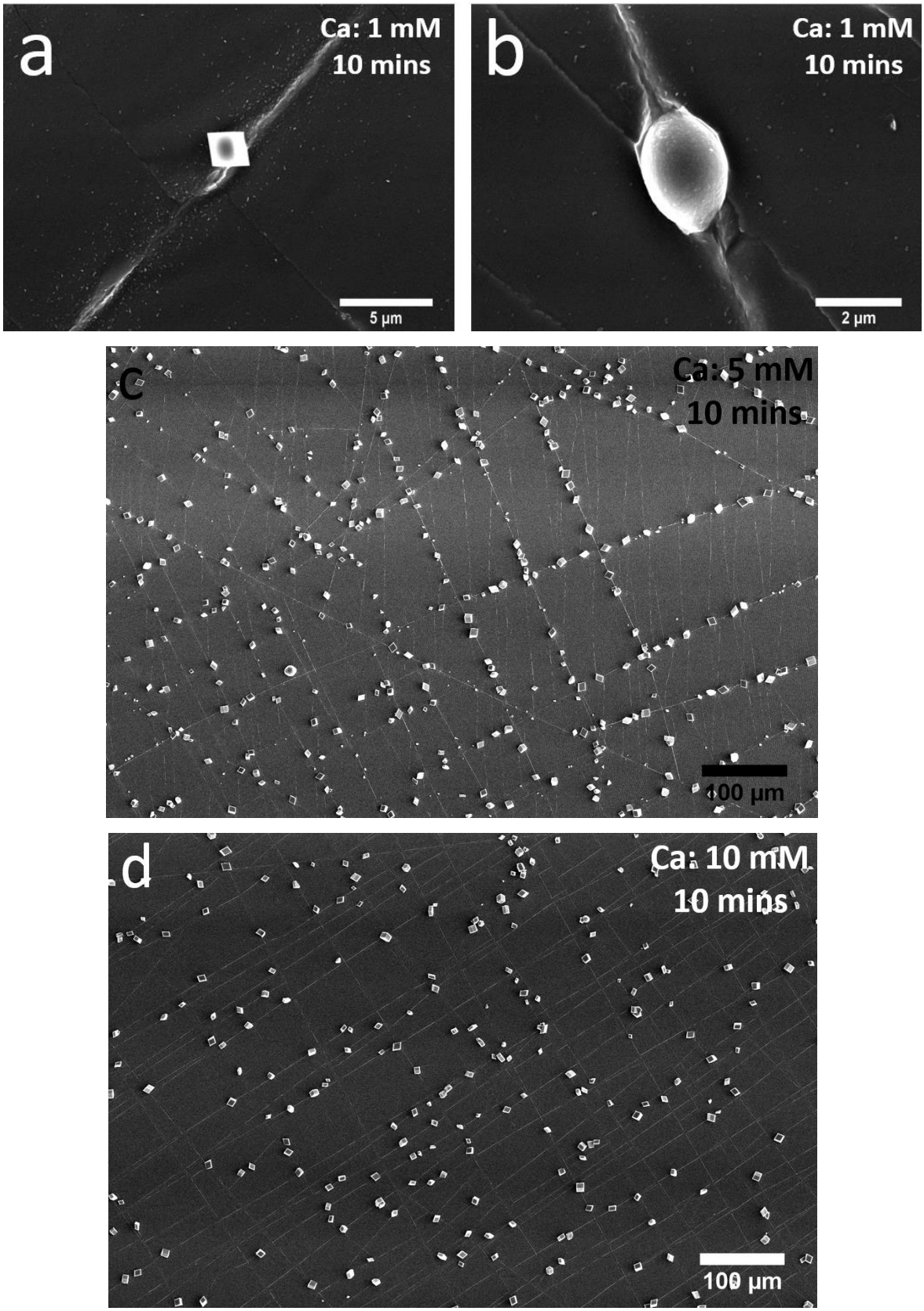
a
Ca: 1 mM
10 mins
5 µm
b
Ca: 1 mM
10 mins
2 µm
c
Ca: 5 mM
10 mins
100 µm
d
Ca: 10 mM
10 mins
100 µm

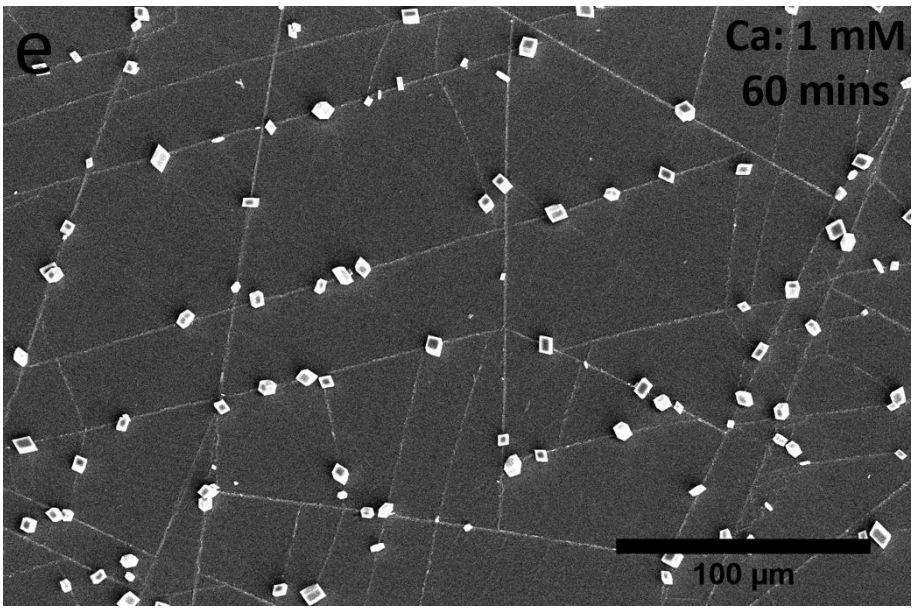
e
Ca: 1 mM
60 mins
100 µm

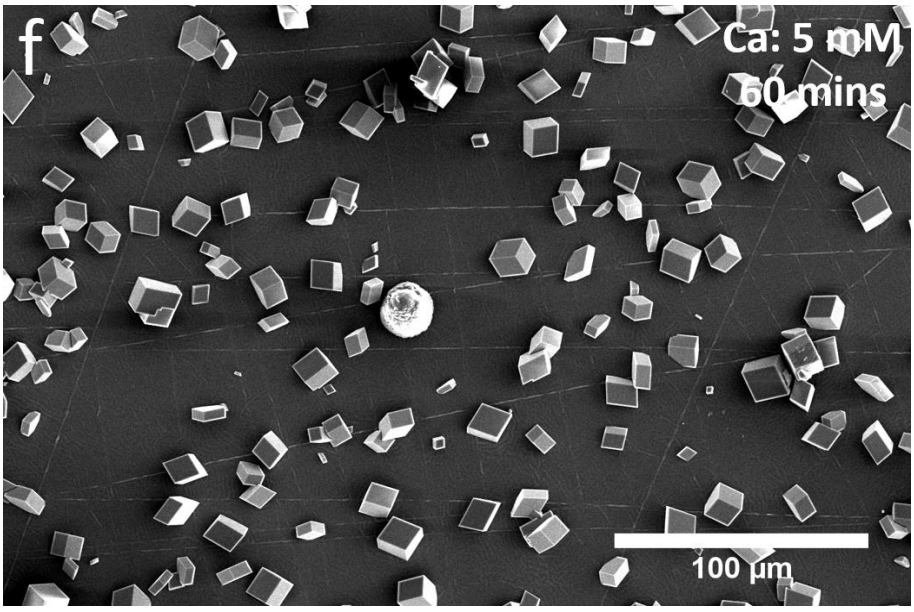
f
Ca: 5 mM
60 mins
100 µm

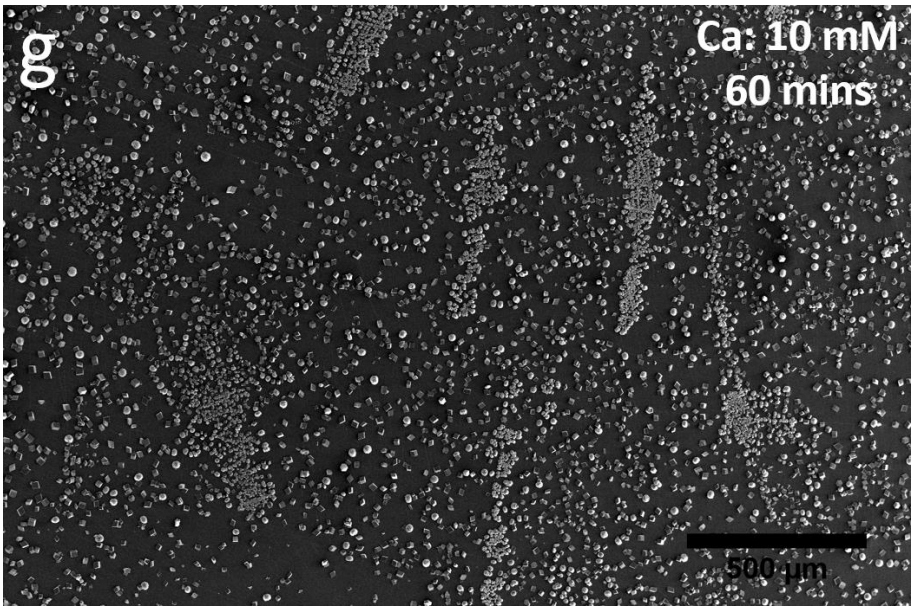
g
Ca: 10 mM
60 mins
500 µm

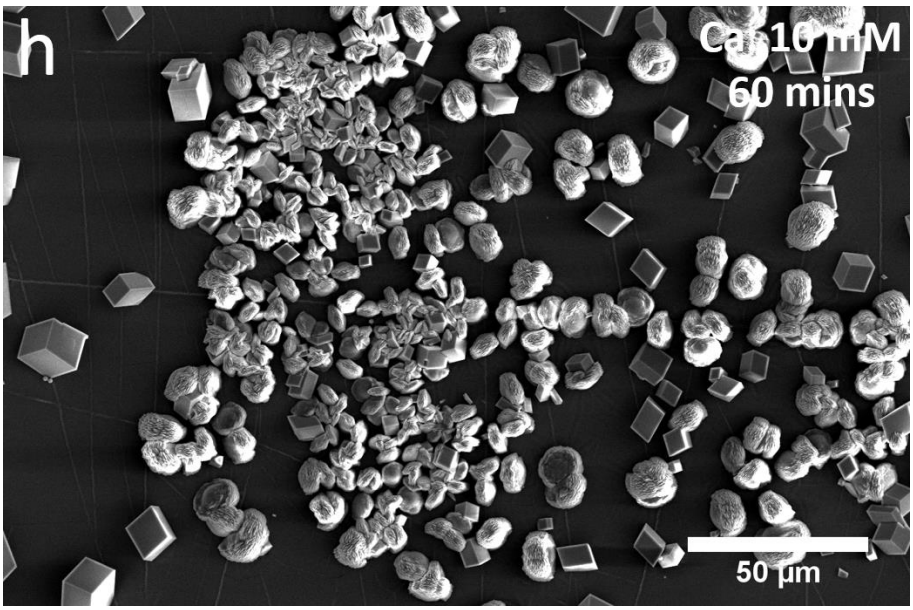


**Figure 52: SEM micrographs of the 16COOH coated PPDMS substrates after precipitation using the ammonia diffusion method at various [$Ca^{2+}$]**

Calcite and vaterite were present on all substrates (Figure 52a - e) with the proportion of vaterite increasing as the [$Ca^{2+}$] increased. Another noticeable quality was the large polydispersity of the crystal populations compared to the direct mixing method. Both of these observations can be explained by considering the solution dynamics during the experiment. The solid ammonium carbonate decomposes, releasing gaseous carbon dioxide and ammonium carbonate into the desiccator. Gas phase saturation is rapidly achieved with respect to these species and once obtained, a near constant vapour pressure is maintained. Carbon dioxide dissolves into the calcium solution, forming carbonic acid, which then deprotonates and dissociates into carbonate and bicarbonate ions. The ratio of bicarbonate to carbonate is determined by the solution pH, which is in turn initially dictated by the formation of ammonium ions from the gaseous ammonia. As more ammonium is formed, the pH increases and the ratio of bicarbonate to carbonate shifts towards carbonate. At a critical pH/supersaturation, which is about pH 8.5, calcium carbonate precipitation will start [89]. This is associated with the partial transformation of bicarbonate to carbonate. The pH continues to increase to a value of approximately pH 9.8, where it remains constant for a prolonged period of time [89]. The predominant formation of calcite at lower initial $Ca^{2+}$ solution conditions and shorter residence time (t = 10 mins) is likely due to the fact that the calcite supersaturation is surpassed before the vaterite supersaturation, which, due to the short residence time, hasn't been exceeded for long enough such that there is sufficient time for a large population of vaterite to form. On visual inspection, more crystals were present on

substrates present in the [$Ca^{2+}$] = 5 mM solution than the [$Ca^{2+}$] = 10 mM solution after 10 mins, which is evident if we compare Figure 52c and Figure 52d. This is a result of a longer induction time associated with the 10 mM condition, which occurs because of a retardation in the pH increase, therefore delaying the conversion of $HCO_3^-$ to $CO_3^-$ and hence the precipitation of calcium carbonate.

For the 60 minute experiments, alignment with the cracks was worse at 5 mM and 10 mM than at 1 mM (Figure 52e - h). At lower supersaturations, the reduction in the energy barrier associated with nucleation at the cracks is more significant because the energy barrier associated with nucleation elsewhere (such as on the flat parts of the substrate) is much larger than at the cracks. As the supersaturation increases, the energy barriers decrease and so the difference between the nucleation barrier at the crack and the barrier for nucleation elsewhere becomes smaller. As such, a greater proportion of crystals nucleate across the substrate indiscriminately at 5 and 10 mM calcium concentration. At 10 mM, more vaterite was observed, which is evidently due to a larger solution supersaturation. For comparison, the same experiment was carried out using uncracked 16COOH coated PPDMS substrates (Figure 53).

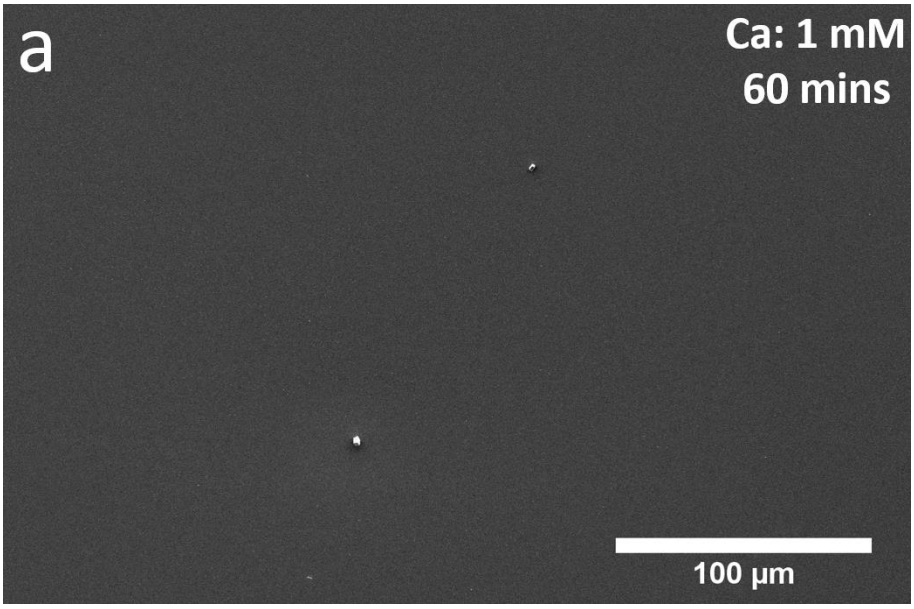

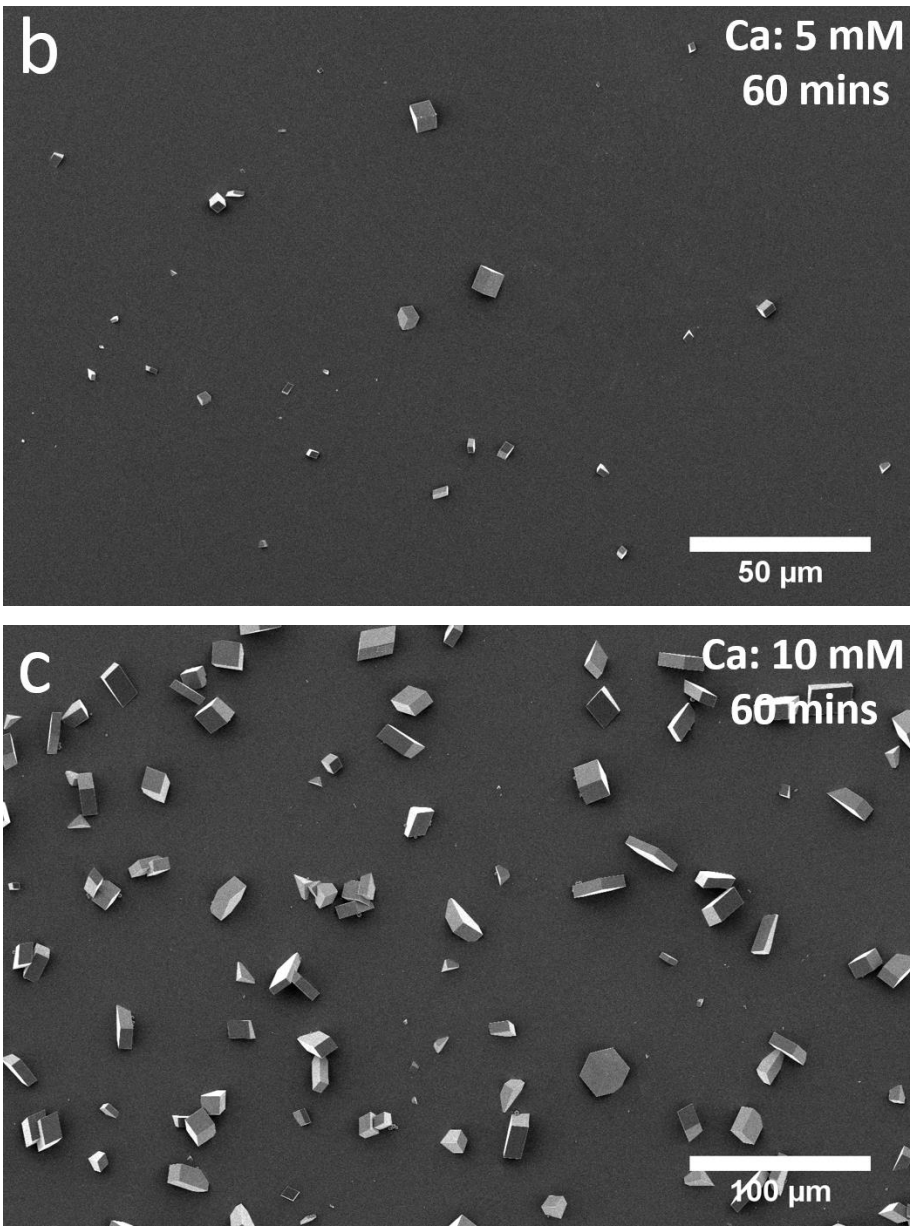


**Figure 53: SEM micrographs of the 16COOH coated uncracked PPDMS substrates after precipitation using the ammonia diffusion method at various [$Ca^{2+}$]**

No crystals were present on the substrates after a 10 minute residence time at any of the initial solution concentrations, indicating an increased induction time relative to the cracked substrates and highlighting the reduction in energy barrier associated with precipitation at these features. At 1 mM, 60 mins, the 16COOH coated uncracked PPDMS substrate was sparsely populated with crystals, and as the initial calcium concentration was increased, the crystal population also increased. At 10 mM, 60 mins, very few vaterite were observed on the uncracked substrate (Figure 53c) compared to the cracked (Figure 52g, h). Again, this highlights the decrease in energy barrier associated with the features of the cracked 16COOH coated PPDMS substrate.

#### 2.5.3.4 Effect of $Mg^{2+}$ on the Crystallisation of Calcium Carbonate on 16-Mercaptohexadecanoic Acid Coated PPDMS

The effects of additives on the localisation of calcium carbonate on 16COOH-coated PPDMS has also briefly been looked at in the present work; the chosen additive was magnesium. Magnesium is known to influence the crystallisation of $CaCO_3$ and can effect a morphological change in calcite when present in solution and also induce the formation of aragonite [60]. The aim of the experiments was to investigate how the surface topography of the 16COOH-coated PPDMS substrates might affect $CaCO_3$ precipitation in the presence of magnesium, given that thus far the substrates have demonstrated their effectiveness at promoting localised nucleation and growth. The system is also appropriate for understanding how topography can affect the induction time of crystallisation, since $Mg^{2+}$ ions are known to cause an increase in the length of time before precipitation can be detected. The presence of magnesium in the crystallising solution did not affect the localisation of the crystals to the cracks, but did have a significant influence on the morphology of the crystals, where the latter is expected at sufficiently high concentrations [90] (Figure 54).

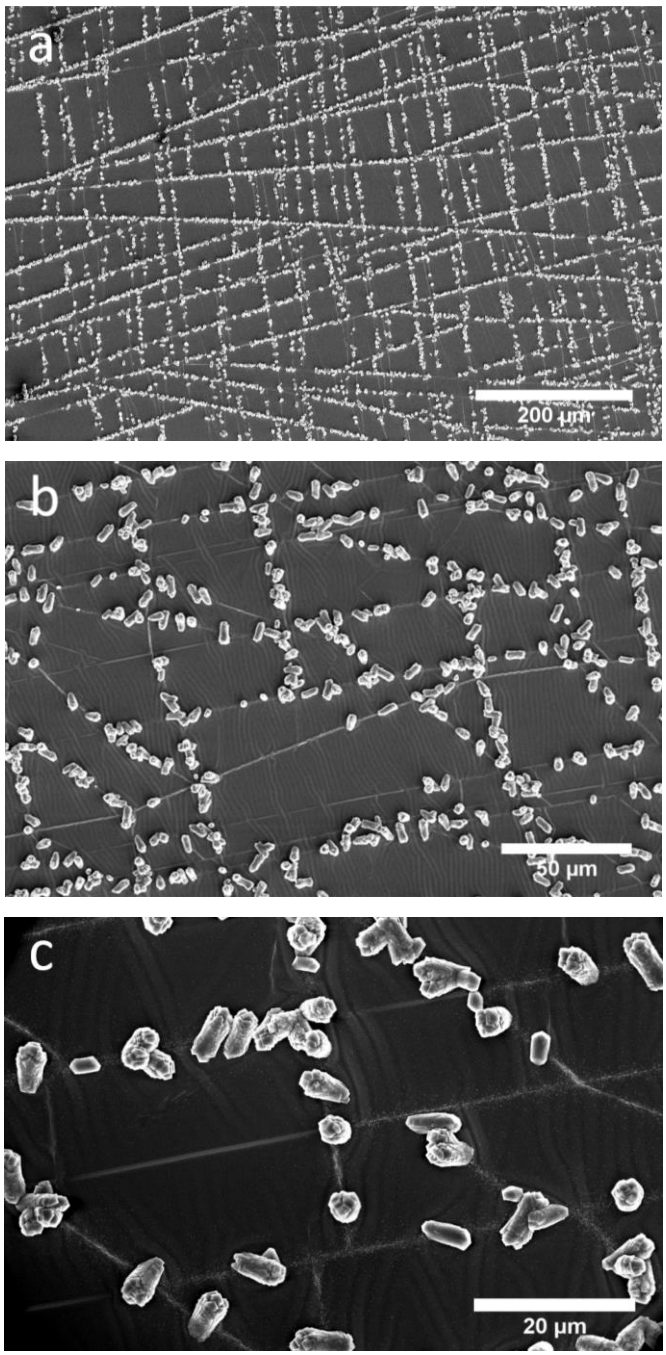


**Figure 54: SEM images of calcium carbonate crystals grown in the presence of magnesium ions**

The crystals here have been confirmed as calcite via Raman spectroscopy. This conclusion was established by the presence of peaks in the spectrum at 281, 713 and 1086 $cm^{-1}$, where the 281 $cm^{-1}$ peak is unique to calcite among the calcium carbonate polymorphs. The deviation from a rhombohedral morphology to an elongated particle with a roughened surface is caused by the differing interaction of the $Mg^{2+}$ ion with the obtuse (+) and acute (-) steps of the (104) face [91]. There exist two obtuse and two acute steps that make up the growth hillock and the

difference in the geometry of the two types of steps is a result of the orientation of the carbonate anion in each (Figure 55).

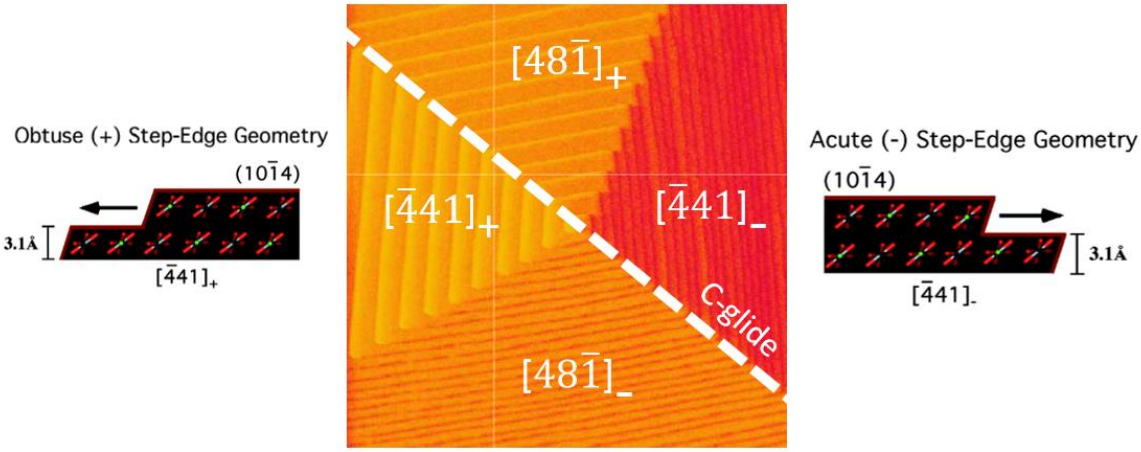


**Figure 55: Four distinct steps can be identified on the growth spirals of the {104} cleavage surface of calcite**

At the acute steps, $Mg^{2+}$ binds more strongly because of favourable coordination geometries and as such reduces the growth velocity of these steps. This causes a change in the form of the growth spiral from straight step edges to circular and the subsequent formation of a new step direction, [42$\bar{1}$] (Figure 56).

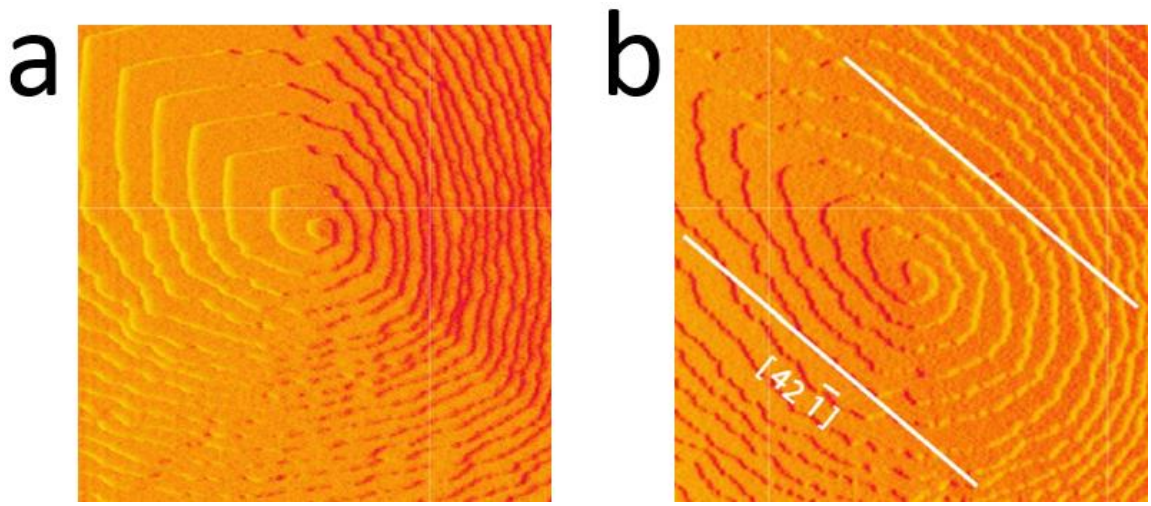


**Figure 56: AFM micrographs that illustrate the progression from straight step edges rounded, which results in the formation of circular steps and the emergence of a new step direction, [42$\bar{1}$]**

The direction of growth of this step direction is parallel to the vector [010], which leads to the creation of apparent {010} faces and elongation of the calcite crystals along the c-axis, as observed in Figure 54c.

An increase in the induction time and a decrease in the growth rate of calcite has also been described [92], which is likely due to the adsorption competition between magnesium ions and calcium ions at the crystal surface. Inhibition caused by magnesium cations is a result of the small, strongly hydrated $Mg^{2+}$ ion ($\Delta H^{o}_{hyd}$ = -1923 kJ/mol) [93] adsorbing onto active calcite growth sites. Due to the large enthalpy of hydration, carbonate ions are not able to remove the layer of water molecules that shield the magnesium ion, therefore blocking the growth site [94]. At sufficiently high concentrations, magnesium ions can inhibit the nucleation and growth of calcite, such that aragonite forms instead [95, 96]. This is dictated by the activity of magnesium in solution [97]. Based on these observations, experiments were carried out with the intent of obtaining aragonite aligned to the cracks (Figure 57).

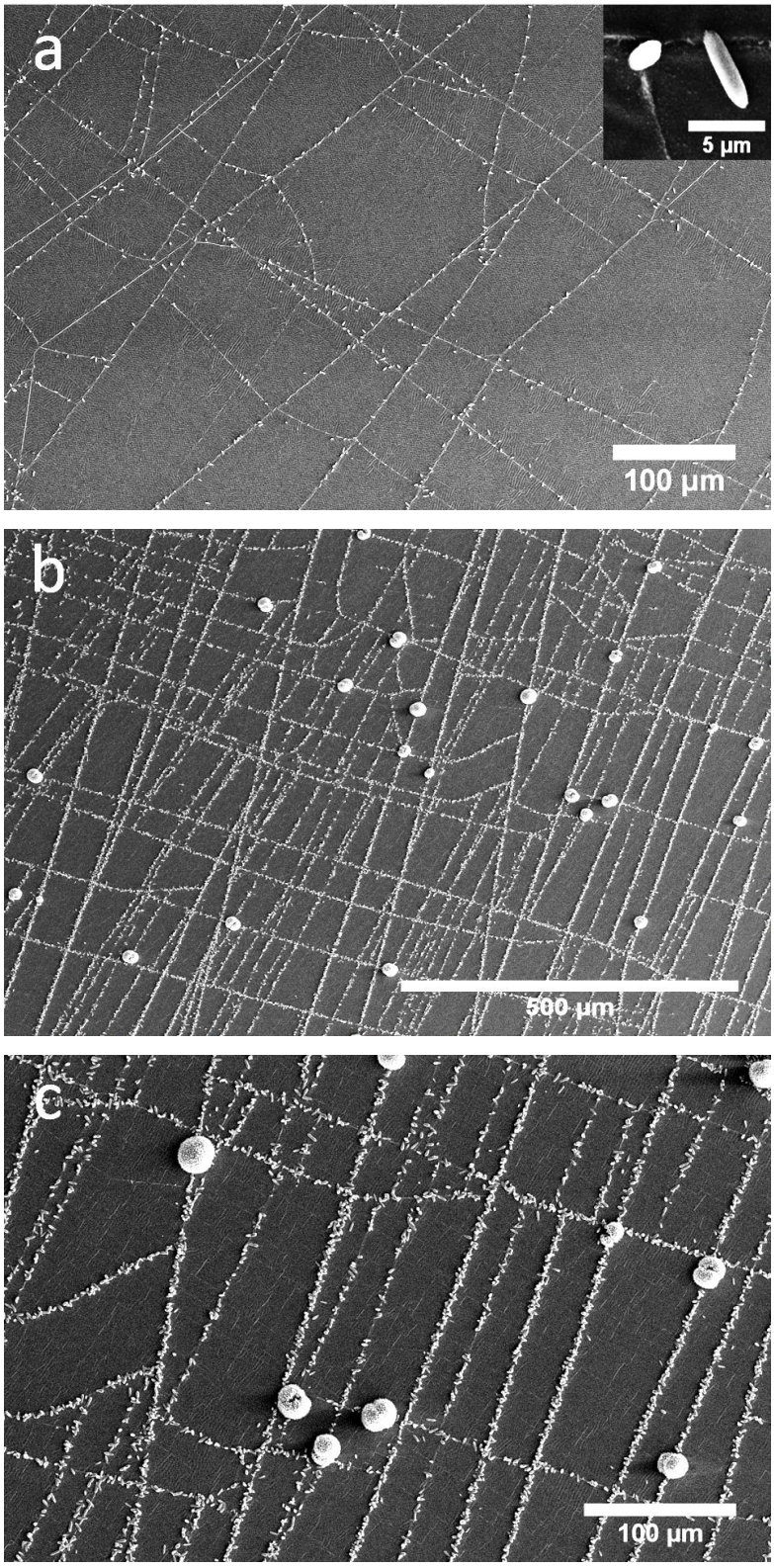


**Figure 57: SEM micrographs of calcium carbonate crystals precipitated onto a 16COOH-coated PPDMS substrate in the presence of $Mg^{2+}$ ions**

A range of $Ca^{2+}$:$Mg^{2+}$ conditions were investigated as well as residence times (Section 2.4.1.7). However, of these, only [$Ca^{2+}$] = [$CO_3^{2-}$] = 2.0 mM, [$Mg^{2+}$] = 6.0 mM, t = 150 mins produced

aragonite. At the same conditions, but shorter residence time (120 mins), calcite was present in the absence of aragonite (Figure 57a). Results obtained by Wada *et al* suggest that magnesium is not incorporated in significant quantities into the aragonite spherulite, in contrast to calcite crystals which can accommodate magnesium in the crystal lattice [98]. The authors also observe an increase in the calcite induction time as the concentration of $Mg^{2+}$ in solution increases. Elsewhere in the literature, researchers have proposed that at a sufficiently high calcium to magnesium ratios, the precipitation of calcite can be inhibited, and as such, only aragonite will form [95, 96, 99]. Based on this, it is possible to explain why aragonite forms subsequent to calcite in the case presented here. When the precipitation is initiated, the ratio of $Ca^{2+}$:$Mg^{2+}$ is 1:3, as stated. Although magnesium is incorporated into the growing calcite crystals, it is not incorporated at a large enough mole ratio within the calcite lattice to significantly reduce the concentration within solution. Therefore, as the calcite precipitation progresses, the calcium to magnesium ratio gradually increases. Eventually, the ratio is high enough such that calcite nucleation and growth becomes inhibited, causing only aragonite to precipitate. Therefore, only calcite is observed after 120 mins (Figure 57a), yet both calcite and aragonite are found after 150 mins (Figure 57b-c). This explanation is supported by the fact that at the higher ratio investigated here (1:5), no crystals were observed on the substrate after 150 mins, indicating that the induction time was too long relative to the residence time. The induction time is related to the nucleation rate, which in turn is dependent upon the free energy barrier to nucleation ($\Delta g_n$). With this in mind and that the interfacial energy influences $\Delta g_n$, it could be supposed that for heterogeneous nucleation, the induction time is dependent upon the effectiveness of the substrate in causing nucleation. To test this, control experiments using the uncracked PPDMS were carried out using the same reaction conditions as those used for Figure 57. No crystals were present on the substrate after 150 mins, and so the residence time was extended. The results of this experiment are shown in Figure 58.

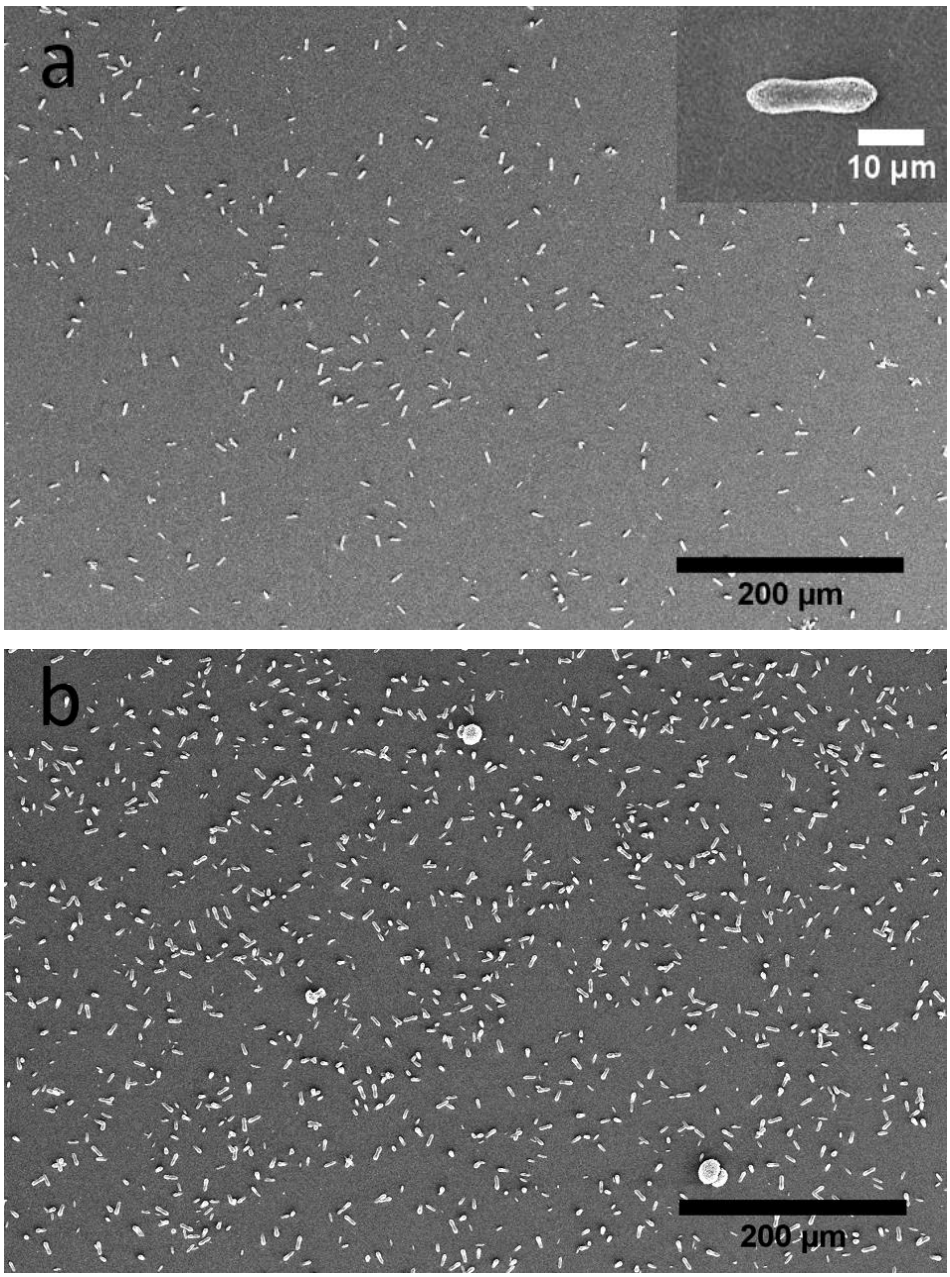


**Figure 58: Electron micrographs of calcium carbonate crystals precipitated on an uncracked PPDMS substrate that had been coated with the 16COOH thiol**

After 180 mins, calcite alone was present on the 16COOH-coated uncracked PPDMS substrate, but prior to this (150 mins), no calcite was observed. At 4 hours, both calcite and aragonite had precipitated and so a longer induction time was required compared to the cracked substrates for aragonite to be observed. When combined with the data of Figure 57, these results demonstrate that a substrate possessing a suitable topography can greatly reduce the induction time and enhance the rate of precipitation.

#### 2.5.3.5 Investigations into the Precipitation of other Crystal Systems on 16-Mercaptohexadecanoic Acid Coated PPDMS

As mentioned in Chapter 1, the ability to control nucleation and growth of crystals using surface topography and chemistry poses distinct advantages over the use of soluble additives. To determine the generality of the 16COOH-coated PPDMS substrate, other crystal systems were investigated. Carbonates were chosen, due to their obvious compositional similarity to calcium carbonate, and the biomineral calcium oxalate was also investigated. Visual Minteq was used to calculate concentrations of the chloride salt and sodium carbonate that, when combined, would produce similar supersaturations to those used so far for $CaCO_3$ in order to provide comparable conditions. Strontium and barium carbonate were chosen as they both possess an aragonitic structure, while manganese carbonate has the same structure as calcite and so was investigated. Malachite (a basic copper carbonate) and calcium oxalate both have a monoclinic structure with different space groups, which are not found in the calcium carbonate system; these were also explored. Table 7 shows each crystal system considered, along with its concentration, supersaturation, crystal structure and space group. In all instances, a residence time of 60 minutes was used:

**Table 7: Solution concentrations used for the crystallisation of various crystal systems**

| Compound | Equivalent $CaCO_3$ Concentration ($[Ca^{2+}] = [CO_3^{2-}]$) (mM) | Concentration of $MCl_2$ used (equimolar $Na_2CO_3$) (mM) | Saturation Index ($LogIAP/LogK_{sp}$) | Crystal Structure | Space Group |
|---|---|---|---|---|---|
| $SrCO_3$ (Strontianite) | 1.0 | 0.3 | 1.7 | Orthorhombic | *Pmcn* |
| | 2.0 | 0.5 | 2.1 | | |
| | 3.0 | 0.7 | 2.4 | | |
| $BaCO_3$ (Witherite) | 1.0 | 0.7 | 1.7 | Orthorhombic | *Pmcn* |
| | 2.0 | 1.25 | 2.1 | | |
| | 3.0 | 1.8 | 2.4 | | |
| $MnCO_3$ (Rhodochrosite) | 1.0 | 0.15 | 1.7 | Triganol | $R\bar{3}c$ |
| | 2.0 | 0.25 | 2.1 | | |
| | 3.0 | 0.45 | 2.4 | | |
| Basic $CuCO_3$ (Malachite) | 1.0 | 2.75 | 1.7 | Monoclinic | $P2_1/a$ |
| | 2.0 | 6.5 | 2.1 | | |
| | 3.0 | 12.5 | 2.4 | | |
| Calcium Oxalate (Monohydrate) | 1.1 | 0.6* | 1.8 | Monoclinic | 2/m |
| | 1.7 | 0.8* | 2.0 | | |
| | 3.0 | 1.0* | 2.1 | | |

***Ammonium Oxalate was used instead of a chloride salt.**

$BaCO_3$ and $SrCO_3$ only possess one polymorph each and these are aragonitic in structure. Both of these were found to nucleate at the cracks of the 16COOH coated PPDMS substrates (Figure 59).

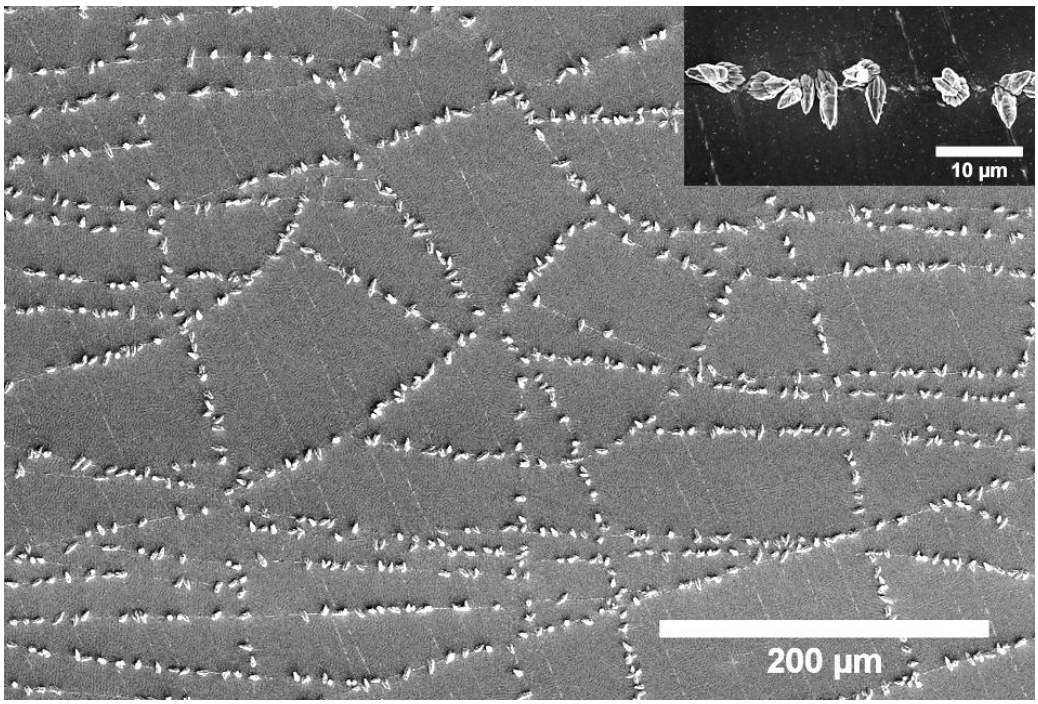


**Figure 59: Strontium carbonate crystals precipitated on a 16COOH coated PPDMS substrate**

Figure 60 shows a crack of the 16COOH coated PPDMS substrate which, over the course of two days, had become densely populated with $SrCO_3$ crystals. This demonstrates the affinity of strontium carbonate for the substrate features.

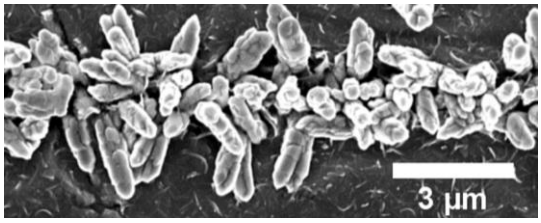


**Figure 60: High magnification image of $SrCO_3$ crystals at a crack on a 16COOH coated substrate**

Barium carbonate also demonstrated a preference for the cracks of the 16COOH PPDMS substrate (Figure 61).

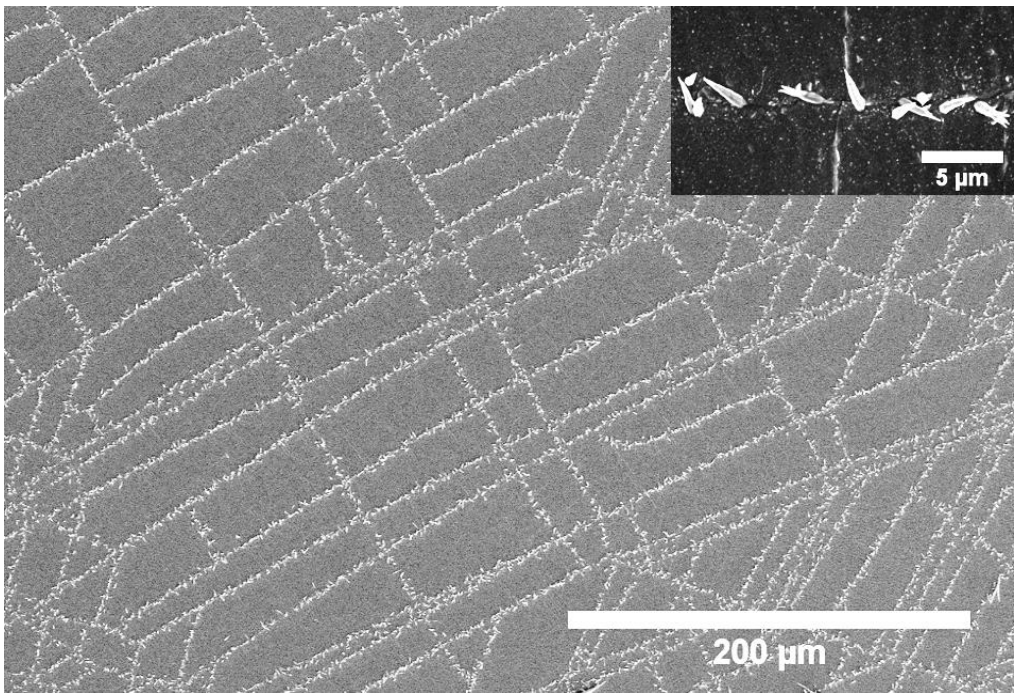


**Figure 61: Barium carbonate crystals precipitated on a 16COOH coated PPDMS substrate**

Under the conditions shown in Table 7, no manganese carbonate crystals were observed on the substrates. However, on mixing the manganese chloride and sodium carbonate solutions, a rust coloured precipitate was observed in solution. This indicated that spontaneous nucleation was taking place. To overcome this, sodium bicarbonate was used in place of sodium carbonate, forming a solution with a supersaturation slightly higher than that used for previous experiments (SI = 2.6). Observation of these substrates in the SEM revealed rhodrochrosite localised to the cracks of the substrate (Figure 62).

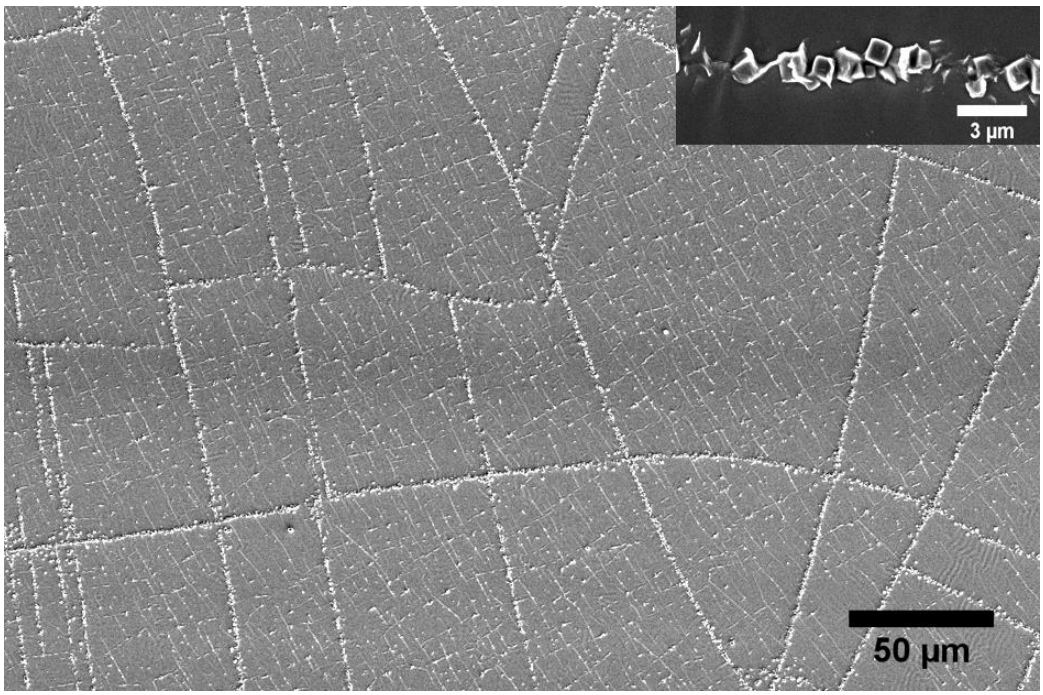


**Figure 62: SEM micrograph of $MnCO_3$ crystals precipitated on the 16COOH coated PPDMS substrate**

Table 7 provides the SI for copper (II) carbonate; on mixing the copper chloride and sodium carbonate, a teal precipitate formed in solution. Again, on removal of the substrate from solution, no crystals were observed associated with the surface, so bicarbonate was used instead of carbonate (SI = 3.6). On inspection using SEM, crystals were observed at the cracks (Figure 63).

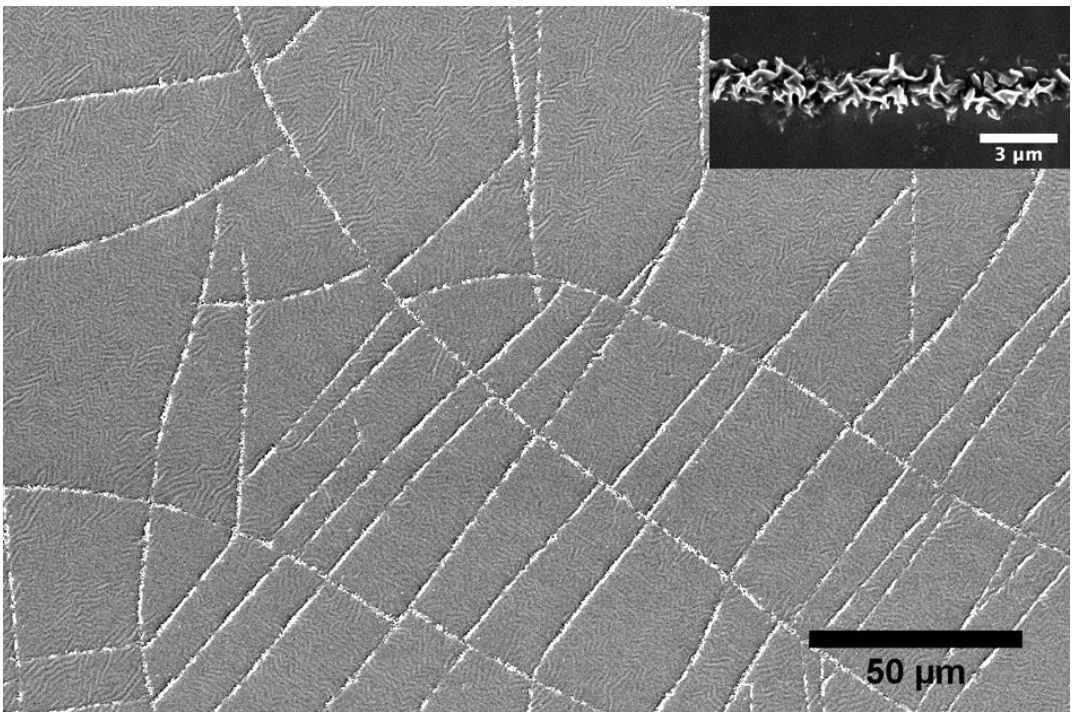


**Figure 63: SEM micrograph of $CuCO_3$ crystals precipitated on the 16COOH-coated PPDMS substrate**

There are several species which may precipitate when carbonate and copper ions are combined, namely basic $CuCO_3$, malachite ($Cu_3(CO_3)_2(OH)_2$) and azurite ($Cu_2CO_3(OH)_2$). To identify which of these phases had precipitated, IR spectroscopy was used, which indicated that it was the basic copper carbonate, malachite ($Cu_2CO_3(OH)_2$) present on the substrate.

In addition to the chosen carbonates, calcium oxalate was also precipitated in the presence of the 16COOH-coated PPDMS substrates. A supersaturation of 2.1 with respect to the monohydrate was used (Figure 64).

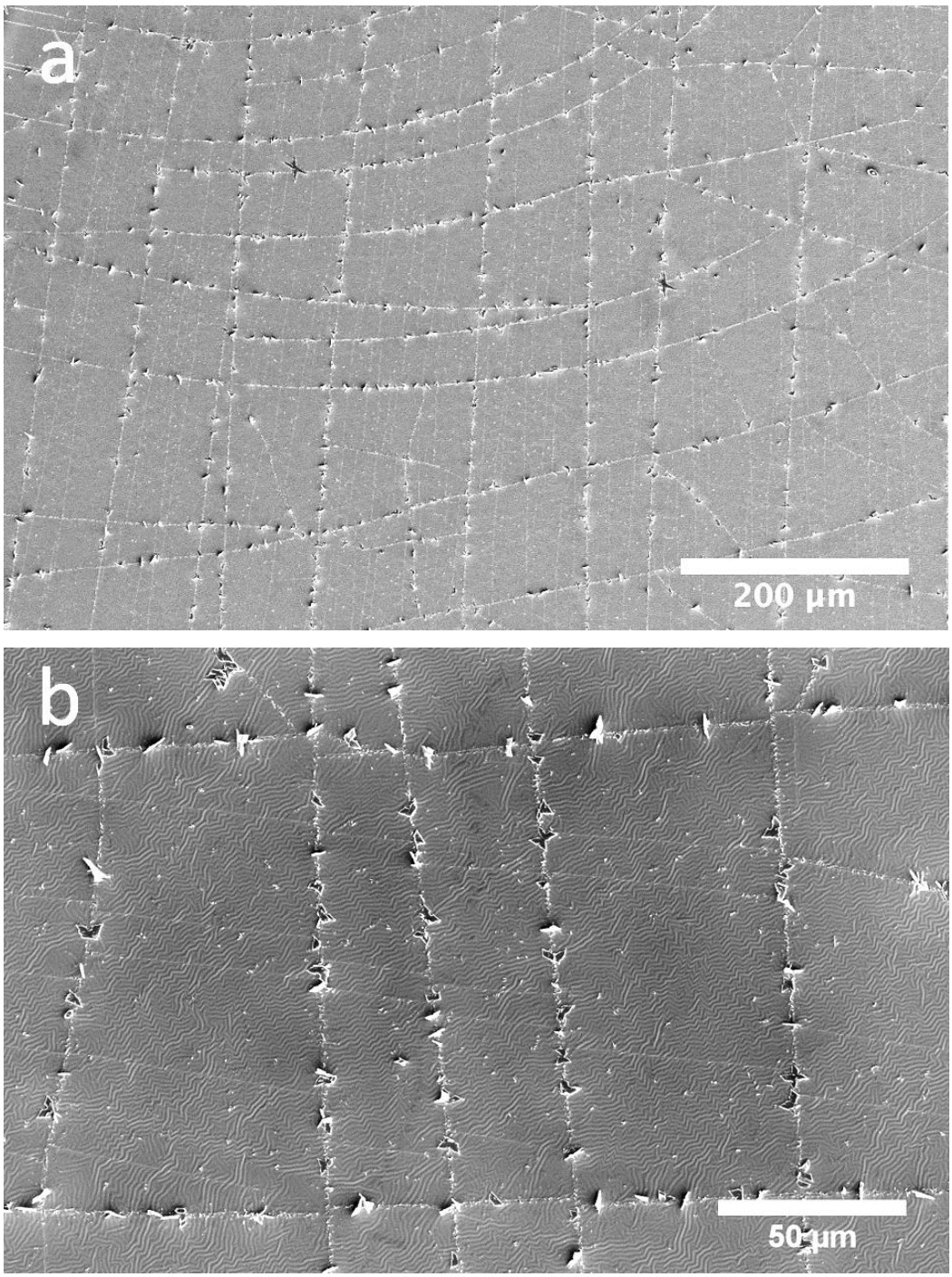


**Figure 64: SEM micrographs of calcium oxalate monohydrate crystals precipitated on a 16COOH-coated PPDMS substrate**

As with the other systems investigated, the calcium oxalate crystals preferentially precipitated at the cracks. The effectiveness of a 16COOH coated PPDMS substrate in causing the localised precipitation across a range of crystal systems is considered in the General Discussion (Section 2.6).

#### 2.5.3.6 Spatially Controlled Formation of Surface Features on Plasma-treated PDMS

Control over the location of crystallisation has been realised before through the patterning of a surface with thiol SAMs [84, 86, 100-104]. Patterning of SAMs is typically achieved through the use of microcontact printing, involving an elastomeric stamp with a relief structure [81]. The stamp is used to apply monomers to discrete regions of the substrate, the pattern of which is determined by the diameter and periodicity of the stamp structure. The 'ink' is often a thiol with a functional group associated with a low interfacial energy between the crystal/SAM interface. Once the thiol has been deposited, the interstitial regions are typically passivated using a monolayer that has a higher interfacial energy than that in the discrete regions. As such, during crystallisation, the nucleation and growth should occur preferentially at the patterned monolayer, as a lower interfacial energy is associated with a smaller energy barrier to nucleation (Section 2.4.1.1). The substrates used here differ to those described, in that the entire substrate surface is coated with a single thiol. Instead, it is the cracks of the PPDMS that are patterned.

Initial attempts at localising the formation of cracks involved the use of a PDMS contact mask (Section 2.4.1.9). After exposure to plasma and formation of the 16COOH SAM, the substrates were placed in a supersaturated solution of calcium carbonate (Figure 65).

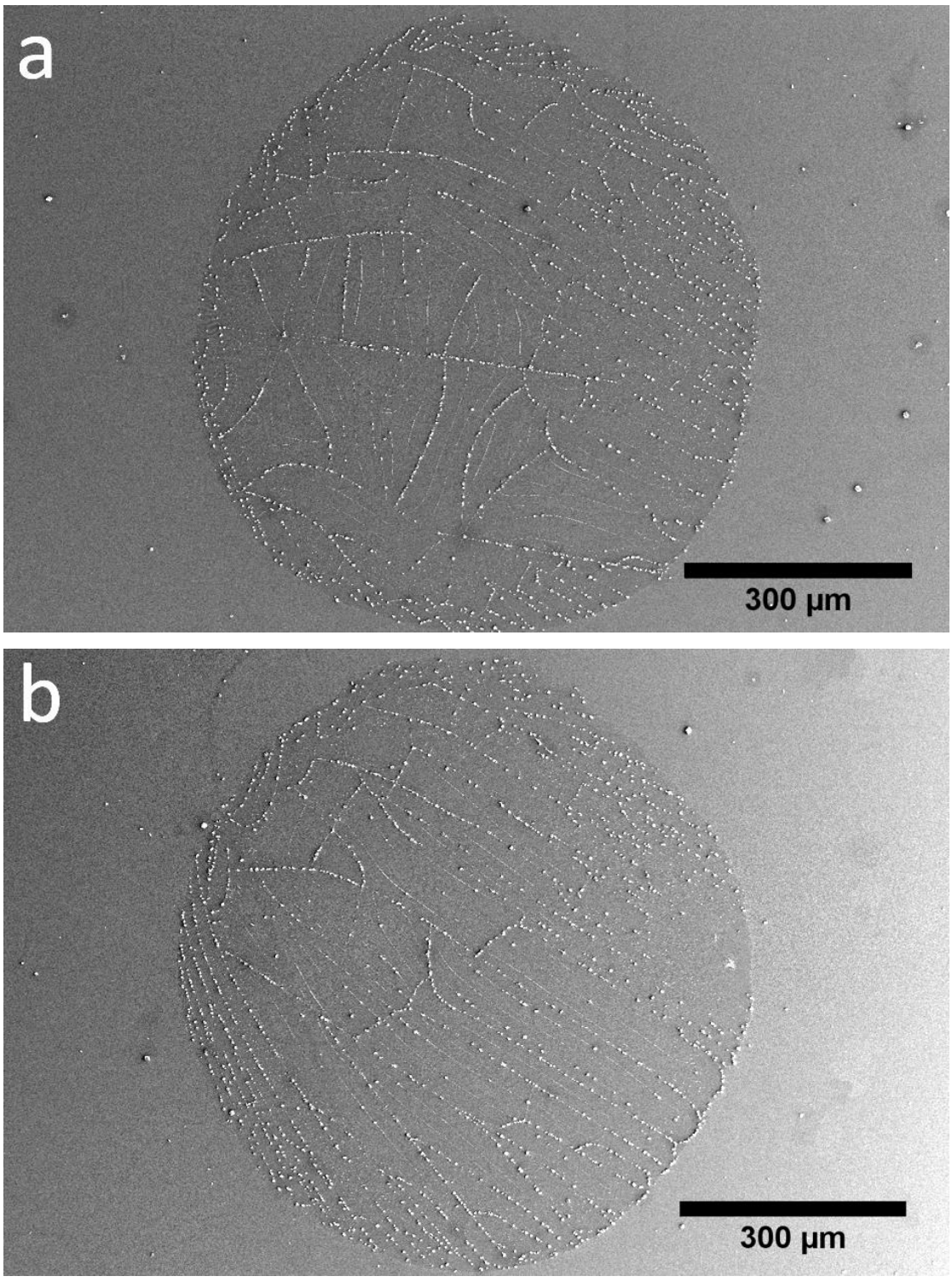


**Figure 65: Calcium carbonate crystallisation on a PDMS substrate, on which only discrete areas have been exposed to RF low pressure air plasma**

Although the entire surface is coated with the SAM, the cracks are observed to be situated only at the areas exposed to the plasma and the crystals are localised to the cracks. PDMS, used in commercial membrane-based vapour separation applications, is permeable to a range of gases, including hydrogen, oxygen and carbon dioxide [4]. Gas penetration through PDMS is possible due to its large free volume, and the permeability of a penetrant through a non-

porous polymer membrane independent of pressure is the product of the solubility and diffusivity of that gas in the polymer [105]. PDMS has a poor gas particle size selectivity, common to rubbery polymers with highly flexible polymer chains and as such, selectivity is governed by penetrant solubility. As mentioned in Section 2.4.1.1, the formation of the silica like surface layer is caused by the displacement of pendant methyl groups by radicals of oxygen and hydroxyl. Given that the depth of the cracks have been measured as 120 nm deep and the $SiO_x$ surface layer is unlikely to extend much beyond this [19], the oxygen/hydroxyl radicals are unable to penetrate the PDMS mask sufficiently to oxidise the underlying PDMS surface, hence the absence of cracks in the masked areas of the PDMS substrate.

In order to reduce the exposure area and obtain an even spatial distribution of Plasma-treated PDMS 'patches', a copper TEM grid was used as the mask. Copper is impermeable to gas and the grids were deposited onto the PDMS substrate in such a way as to maximise the contact between the two materials. Again, after the 16COOH SAM formation, the substrates were used for the crystallisation of calcium carbonate (Figure 66).

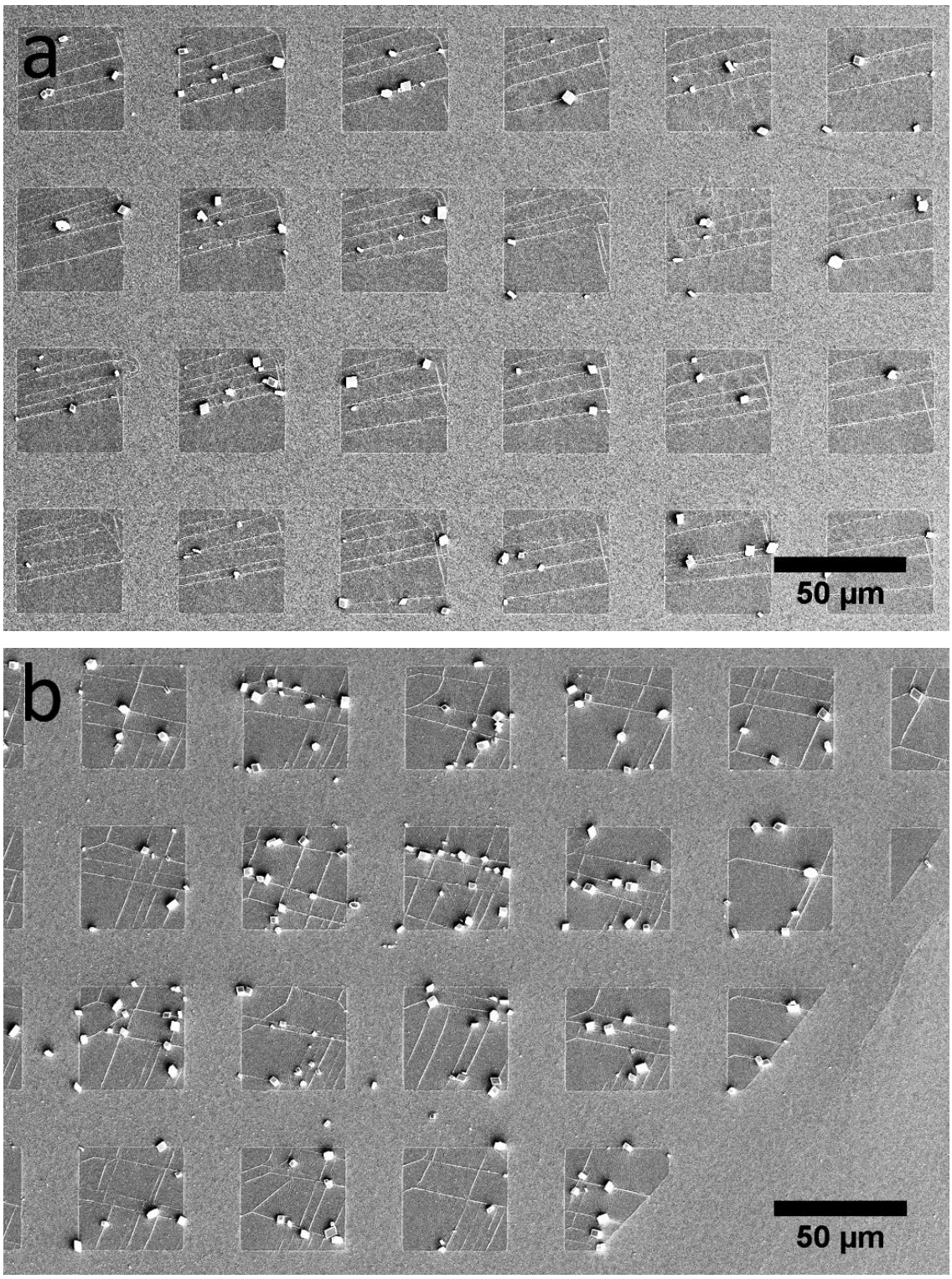


**Figure 66: Calcium carbonate crystallisation on a PPDMS substrate patterned using a copper TEM grid**

The data presented here demonstrates that it is possible to not only expose discrete regions of PDMS to RF air plasma using a PDMS mask or TEM grid, but also that, once coated with a 16COOH SAM, the resultant cracks in the windows of the mask act as nucleation sites for calcium carbonate crystallisation.

#### 2.5.3.7 Wrinkled Plasma-treated PDMS

The previous section discussed the patterning of the cracks through the use of a selective area exposure to RF air plasma. This section covers briefly another method that can be used to alter the spatial arrangement of cracks on the surface of plasma-treated PDMS, whilst still maintaining their effective nucleating capabilities. A paper by Yang et al described a method by which it was possible to obtain PDMS with a nanowrinkled surface [106]. Given that acute nanofeatures can be good nucleators [21, 107-113], the nanowrinkled PDMS substrate was investigated for calcium carbonate crystallisation. In order to obtain PDMS with such surface features, a tensile stress was applied to the PDMS during exposure to the plasma. A simple custom made piece of apparatus that involved two clamps separated by a screw was used, where the screw allowed the distance between the clamps to be varied (See Section 2.4.1.10, Figure 34). The PDMS was uni-axially stretched to an extension ratio (final length/initial length) of 1.4 prior to plasma exposure and the tensile stress was released immediately on removal by cutting the PDMS free from the jig. The resulting surface topography involved nanoscale surface undulations with an average periodicity of 450 nm. These were arranged perpendicularly to long surface cracks that extended for 100's of μm's (Figure 67).

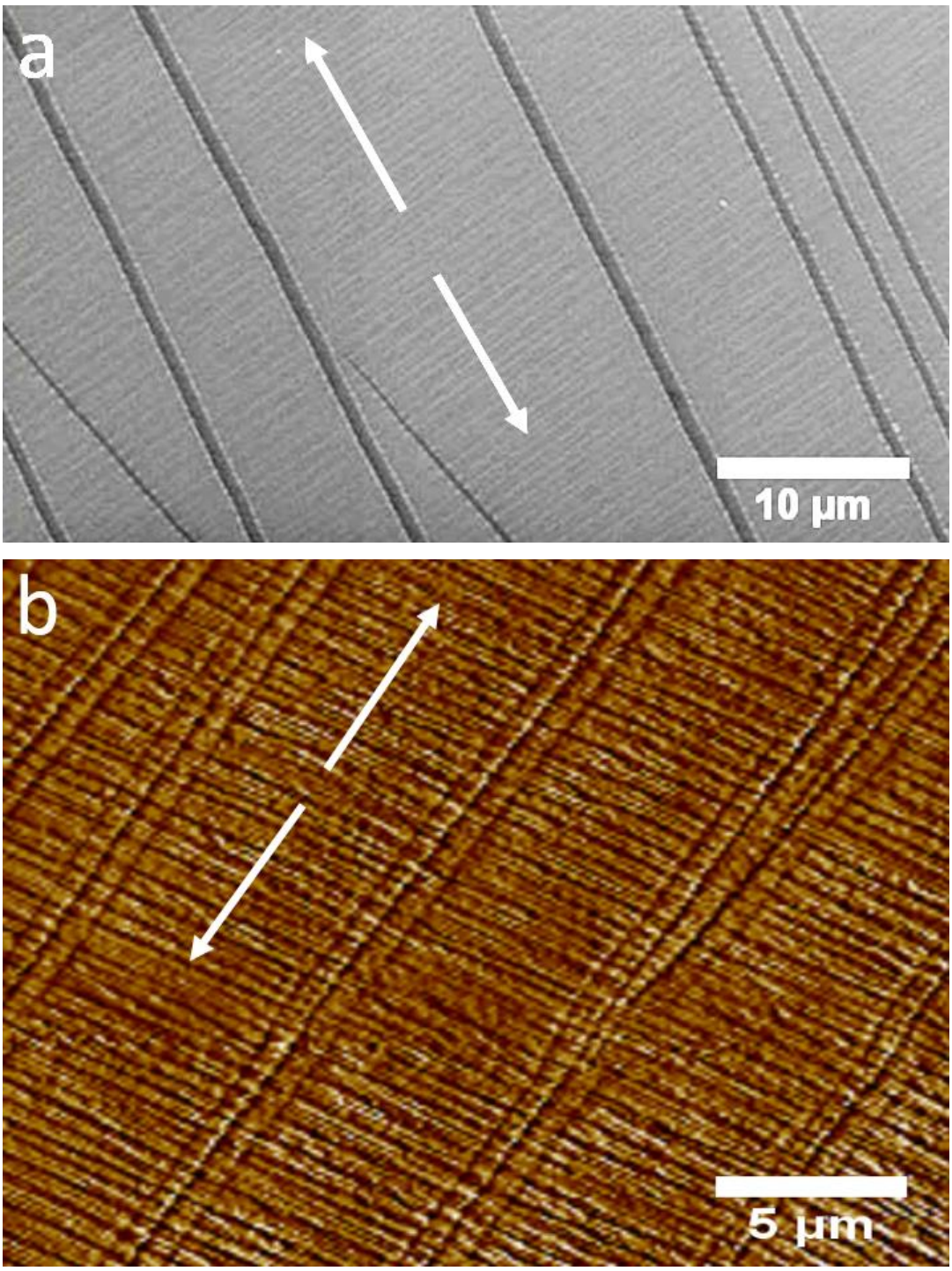


**Figure 67: Micrographs of a wrinkled PPDMS substrate**The surface structure described by Yang *et al* lacked the presence of the long, parallel cracks. However, their exposure time was significantly shorter at 60 seconds compared to the 7 minute exposure used here. The surface undulations form perpendicular to the direction of strain and the long cracks parallel to the strain. The wrinkle features originate from the difference in deformability of the silica-like surface layer and the underlying PDMS. The PDMS can be considered as a spring, and the silicate layer as a thin, hard coating. On release of the mechanical stretch, the compressive force of the substrate exceeds that of the critical threshold for buckling of the

surface layer, forcing a new equilibrium state to be achieved due to the discrepancy between the two materials. The formation of the wrinkles in the surface layer relaxes the compressive strain of the PDMS [24]. The wrinkled PPDMS was coated with Ir and the 16COOH and used as a substrate for calcium carbonate precipitation, with interesting results (Figure 68).

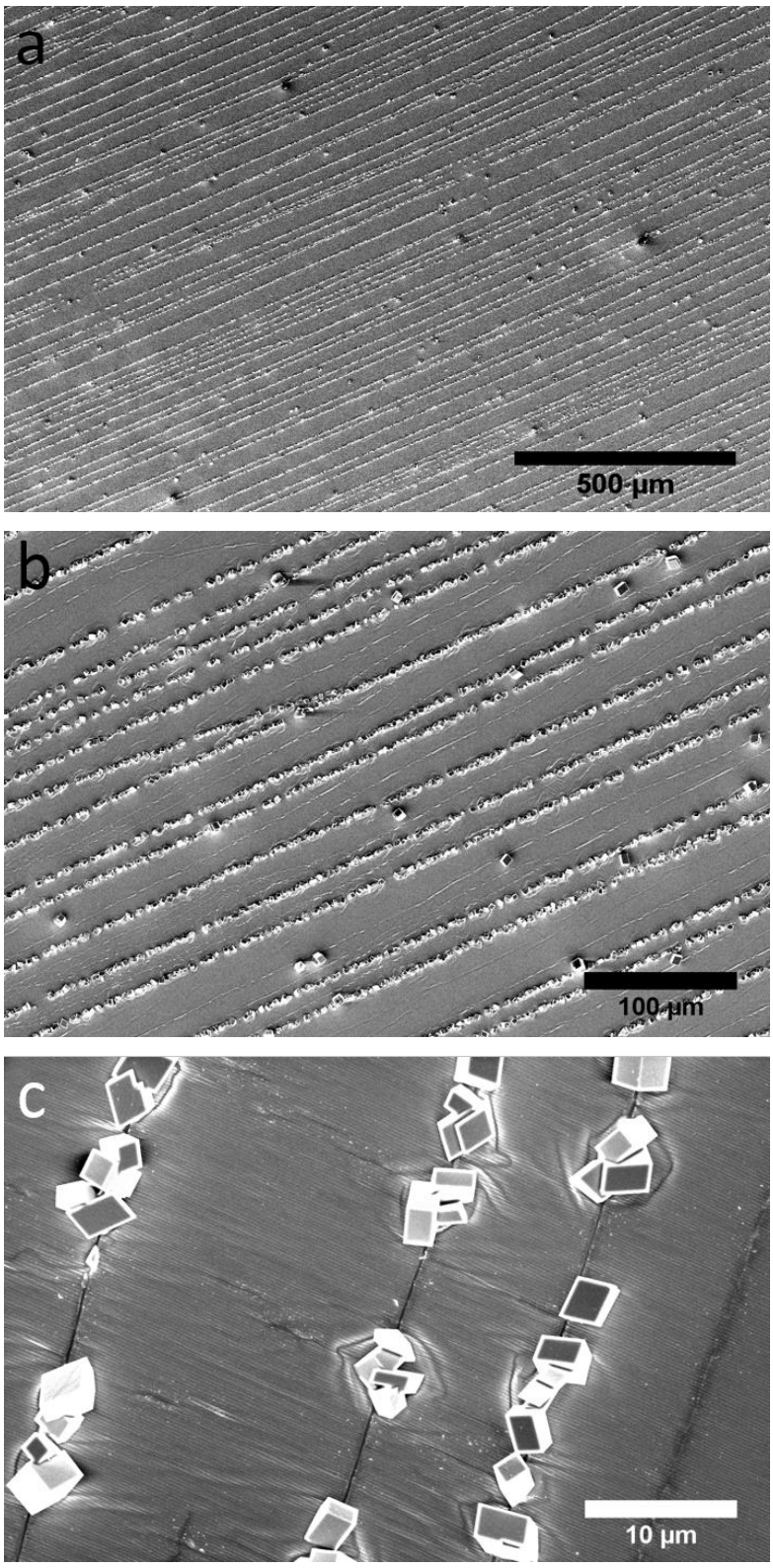


**Figure 68: SEM images of calcite crystals grown on a PPDMS substrate that had been exposed to RF plasma whilst under tensile stress, then coated with the 16COOH SAM.**

Calcite crystals precipitated at the long cracks of the substrate, forming parallel rows of crystals that stretched for millimetres. The wrinkles, in contrast, had nucleated very few crystals and so evidently their geometry was not as effective at nucleating crystals as the

cracks. This technique demonstrates a method by which the arrangement of the cracks can be controlled to produce ordered rows of crystals over large length scales.

#### 2.5.3.8 Thiol Exchange

As already described, thiol self-assembled monolayers can form densely packed, complete films on metallic substrates, allowing the interfacial properties of a surface to be modified in a facile manner. This property has made them an indispensable tool in the study of interfacial phenomena, and, aside from heterogeneous nucleation of crystals, they have proved useful in the study of tribology, adhesion, corrosion, charge transfer through organic molecules and as model surfaces for cell biology and biochemistry [114-119]. The crystallinity of the thiol SAM is dependent upon a number of factors, including the surface topography of the underlying substrate. Aizenberg *et al* demonstrated that topographies with sharp features can generate SAMs with disordered structures [22]. As established by a number of different studies, the ability of a SAM to prevent the diffusion of molecules to the surface of the underlying substrate is dependent not only on the terminal group of the SAM (electrostatic repulsion, physical obstruction etc), but also on the continuity of the film. Monomer vacancies and imperfect films can provide aqueous species with access to the metal intermediary layer, and this fact was exploited by Aizenberg *et al* in their study into the effect of local disorder on thiol SAM lability. The hypothesis of the study was that it should be possible to exchange thiol monomers present in the disordered regions of a SAM with thiol molecules in solution, due to the lack of an effective barrier in these areas. The method proved effective and as such, I briefly investigated thiol exchange using two different thiols that produce contrasting results for the crystallisation of calcium carbonate on plasma-treated PDMS. The goal was to determine if the thiol monolayer within the crack is also disordered, and to observe how the presence of a different surface chemistry at the crack to that of the adjacent areas might affect crystallisation compared to a monolayer composed of only one terminal functionality.

The chosen thiols were 16-mercaptohexadecanoic acid (16COOH) and 11-mercaptoundecanol (OH-terminated). As demonstrated in the previous sections, the 16COOH SAM causes a high population of aligned calcite to form at the cracks on a PPDMS coated substrate. Conversely, an 11-mercaptoundecanol coated substrate causes a much lower population of crystals to form at the cracks, the majority of which are vaterite (Figure 69a). The initial monolayer was formed from the 16COOH thiol, and the monomers present at the disordered regions were exchanged with the OH-terminated thiol by submersion in an

ethanolic solution of the latter. After the two-step deposition had taken place and the substrates had been washed/dried, crystallisation in a solution supersaturated with respect to calcium carbonate produced interesting results (Figure 69c and d). To act as a control and to confirm that an exchange was taking place, a substrate was placed in an equimolar mixed solution of the 16COOH and OH-terminated thiol (in which the thiols were at the same concentration as used for the thiol exchange experiment). This was then immersed in an identical crystallisation solution (Figure 69b).

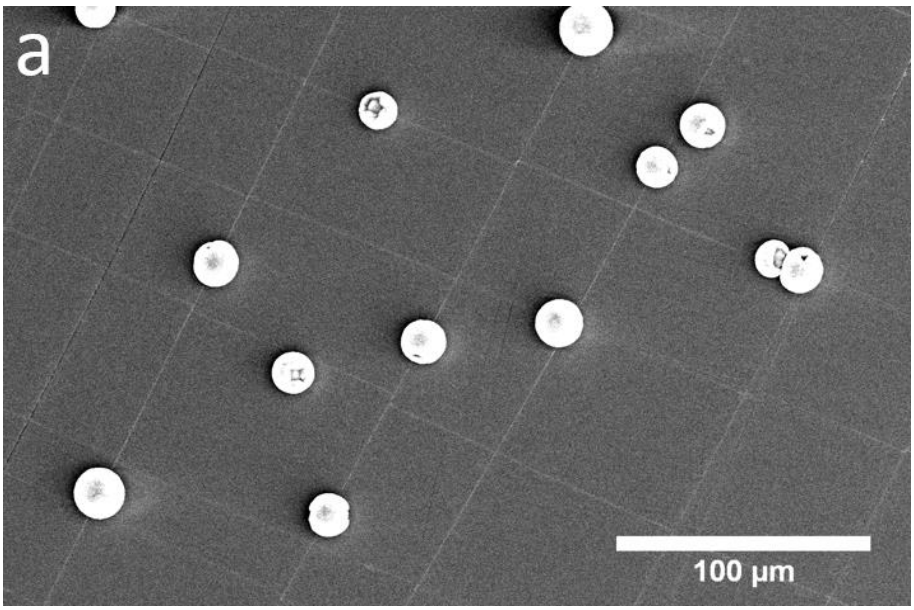
a
100 µm

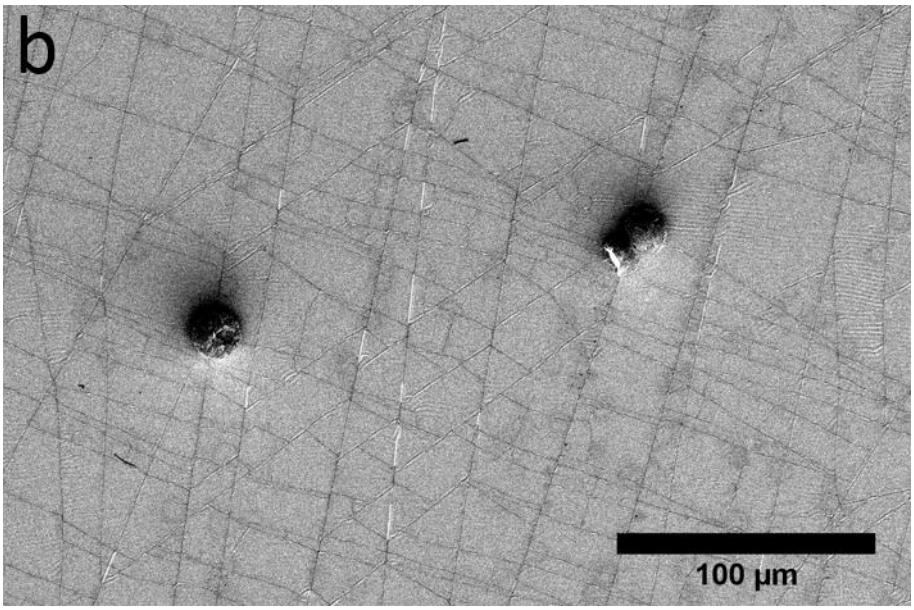
b
100 µm

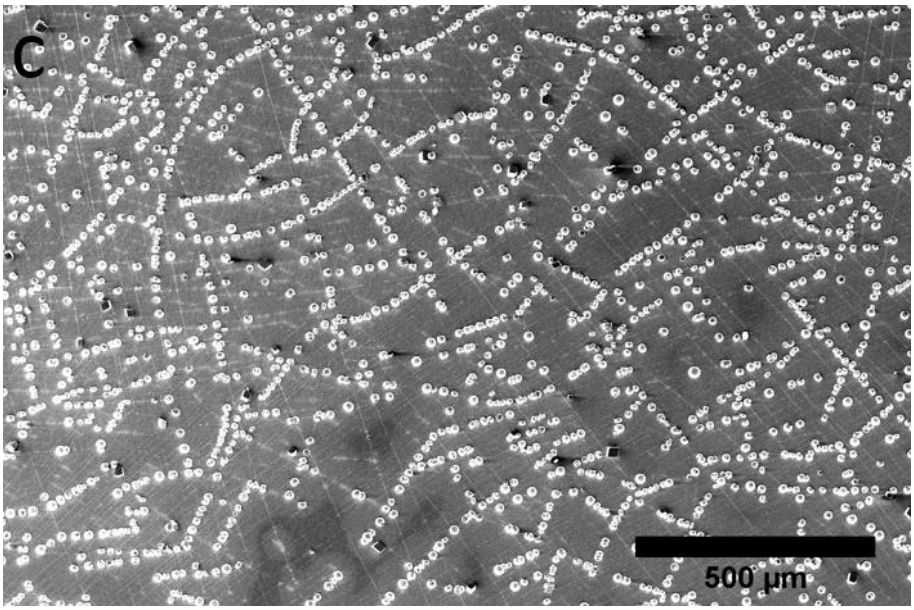
c
500 µm

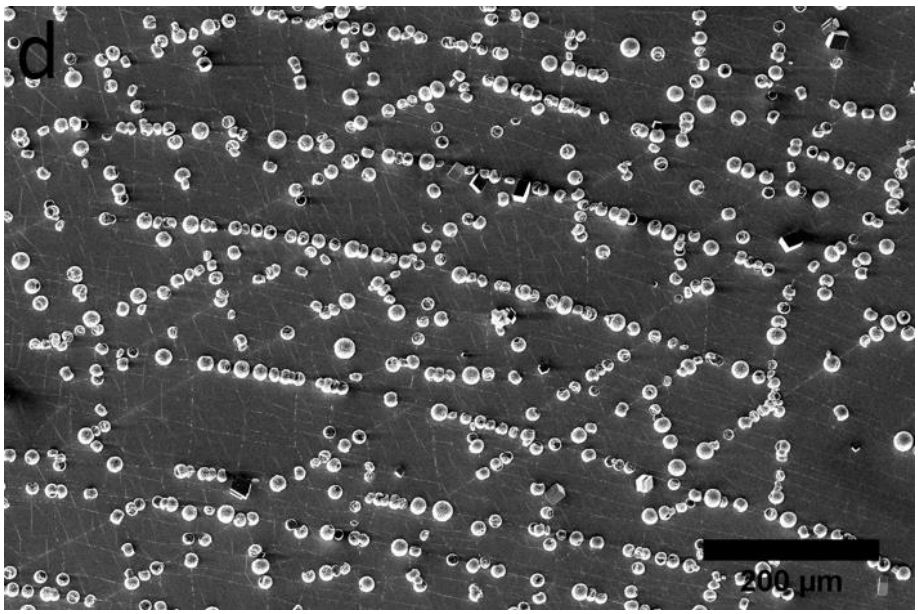


**Figure 69: Thiol exchange experiment micrographs**

Surprisingly, the substrate subjected to a thiol exchange yielded results that appeared to be a combination of the most salient traits of the individual constituents after crystallisation – a high population of crystals (16COOH), the majority of which were vaterite (OH terminated thiol). The large quantity of vaterite suggests cooperative effects and thus it is likely that both the 16COOH and OH-terminated thiols exist in the acute features. Without knowing exactly why the OH-terminated thiol causes vaterite to form, it is hard to provide an explanation for these observations. However, when the data obtained from the ammonia diffusion method (ADM) experiments (Section 2.5.3.3) is taken into consideration, it is possible to speculate. One can expect that on a carboxylic acid-terminated thiol, the COOH groups are deprotonated at the pH at which the crystallisation occurs and therefore, the Stern layer at the SAM/solution interface will be $Ca^{2+}$ rich. Calcite is always the only polymorph observed on these substrates when direct mixing of the precursors is involved, yet when the ADM is used, vaterite is present, even when the [$Ca^{2+}$] is low (Figure 52b). Carbonate is in excess in solution during the ADM experiments, as it is constantly replenished by gaseous diffusion from the decomposing solid ammonium carbonate. If, as we have seen above, a thiol exchange is applied and direct mixing is used, vaterite is present in large quantities on the substrate. Therefore, the large population of vaterite on the thiol exchanged substrate compared to a solely OH-coated substrate may be a result of a greater proportion of $Ca^{2+}$ in the Stern layer. The presence of charged $COO^-$ groups among the OH termini can electrostatically attract calcium to the surface. This combined with a greater number of $CO_3^{2-}$ ions at the interface, which are maintained by the capability of this anion to hydrogen bond to the OH groups of

11-mercaptoundecanol molecules, could cause the observed population increase [120, 121]. In any case, the fact that the crystallisation results were different for a thiol exchanged substrate compared to a random mixed monolayer gives an indication of the importance of the monolayer structure. Although the thiols were present at an equimolar concentration in the ethanolic mixture it is unlikely that they exist in the monolayer at a 1:1 ratio. Experimental and theoretical calculations have suggested that in a binary 1:1 mixture of carboxylate and alcohol thiols, the acidic monomer exists at a slightly higher proportion at the surface as domains surrounded by a continuous layer of alcohol thiol monomers [122, 123]. Based on the crystallisation data and in contrast to what might be expected, the presence of vaterite on the PPDMS-mixed thiol substrate may suggest that it is instead the OH thiols which are present at a higher surface concentration, as one might anticipate more calcite to form if the monolayer contained a higher percentage of acidic groups, based on previous data presented here ($Ca^{2+}$ rich Stern layer favours calcite).

### 2.5.4 Silane-Coated Plasma-treated PDMS

In addition to thiols, silanes can also form self-assembled monolayers. The silane monolayer formation involves vapour phase deposition directly onto the substrate surface over the course of a couple hours, and so the synthetic procedure is quicker and requires less equipment than for thiol SAM generation, as no metal intermediary layer is required or prolonged assembly time. The formation of a silane SAM on PDMS involves exposing the PDMS to an air plasma, causing $SiO_x$ groups to form on the surface. A condensation reaction then occurs between the tail group of the silane molecule and $SiO_x$ groups of PDMS, anchoring them to the surface [124]. As indicated by the data presented thus far, the carboxylate terminated thiol is effective at enhancing nucleation at the PPDMS cracks and increasing the crystal population relative to the control experiments. To investigate whether a silane with the same terminal group would have similar effects on calcium carbonate crystallisation, the carboxylate group must be formed on the terminus of the silane molecules after monolayer deposition. This is because acidic functional terminal groups are incompatible with the trimethoxy tailgroup of the monomer, and so instead the preferred route of formation is to use a monomer with an C=C terminal group, which is then oxidised to a carboxylate group using potassium permanganate solution. Once this final step had been completed, the substrates could be used for calcium carbonate crystallisation (Figure 70).

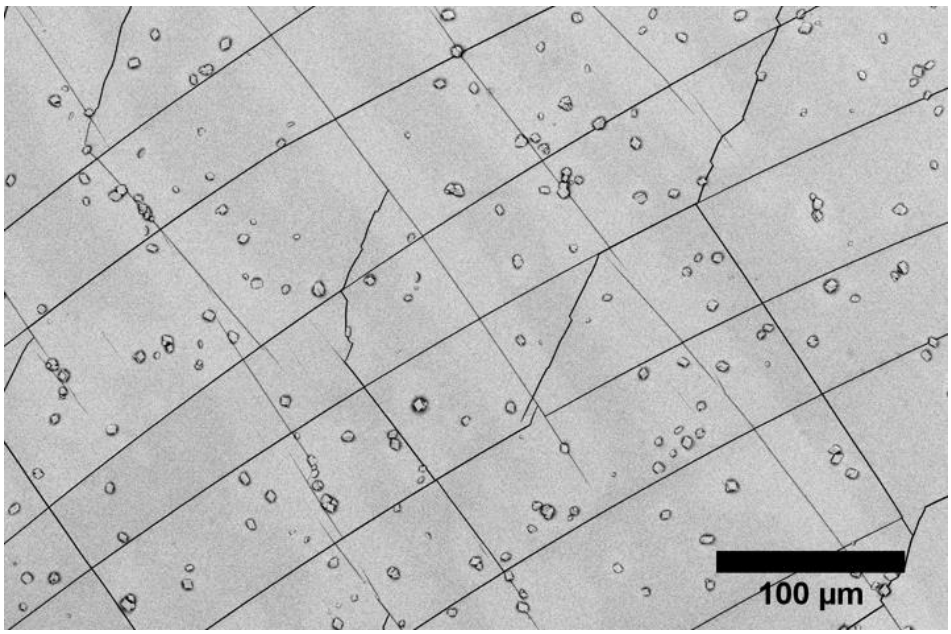


**Figure 70: Representative SEM micrograph of a crystallisation on a silane coated PPDMS substrate. The terminal group of the silane was carboxylate.**

Crystal alignment with the cracks was poor on the silane-coated PPDMS substrate compared to the 16COOH coated PPDMS substrate. It is likely that the silane is ineffective due to the poor quality of the monolayer, which arises due to the formation process and hydrophobic recovery of PDMS. Although silanol groups will exist at the PPDMS surface, not every surface silicon atom will possess an OH group, some will have retained their pendant methyl groups, others will have bonded to multiple oxygens, becoming part of the $SiO_x$ network of polymer chains [125]. Therefore, if every silanol group at the surface after plasma exposure were able to bond to a silane monomer, the monolayer would contain vacancies as not all surface silicon atoms present OH groups. In contrast, thiols form much more complete monolayers since each surface metal atom is available to bind a monomer (though it should be noted that the atom:monomer ratio is not 1:1 at the surface of a monolayer due to packing effects). In addition to this, hydrophobic recovery is likely to affect the surface coverage and ordering of the silane monolayer. The diffusion of unmodified polymer chains to the PDMS surface, migration of modified chains away from the surface and pendant group reorientation may all play a role in disrupting the monolayer, therefore reducing its effectiveness at enhancing alignment.

## 2.6 General Discussion

A typical thiol SAM (such as 16-mercaptohexadecanoic acid) will form a hexagonal close-packed lattice, due to the face-centred cubic structure of the metal intermediary layer [87].

Research elsewhere has suggested that crystals that possess a threefold symmetry axis, such as calcite (space group $R\bar{3}c$) may experience a reduction in the energy barrier to heterogeneous nucleation caused by templating effects [126]. According to this, crystals that do not crystallise in a configuration with a threefold symmetry axis, such as barium carbonate and strontium carbonate (both of the *Pmcn* space group), should not benefit from a similar reduction in energy barrier. This is most likely an oversimplification and, given the specificity required for templating to occur on a rigid monolayer i.e. correct spatial distribution and orientation of the appropriate functional groups, an alternative explanation is required. Instead, the general consensus in the biomineralisation community is that a co-templating process occurs at the crystal/SAM interface during nucleation and growth [75, 78, 80, 88, 127, 128]. Rather than the monolayer existing as a rigid entity, in which the carboxylate groups have fixed positions, packing defects provide the monomers with some freedom of movement. Therefore, it is not sufficient for the monolayer to only present an appropriate terminal group chemical functionality, structural flexibility is also necessary. This plasticity allows the monolayer to adopt the most energetically favourable configuration to promote the formation of the nucleating phase, not just at the onset of nucleation, but also as mineralisation proceeds [128, 129].

However, it is not yet fully understood whether (in all instances) the crystal nucleates directly on the monolayer or if it is preceded by the nucleation of an amorphous precursor on the organic surface, which then transforms to a more stable crystalline phase. At least for the 16COOH SAM, research by Hamm *et al* has suggested that even under conditions where the solution is supersaturated with respect to ACC, the reduction in interfacial energy barrier is sufficient to favour the direct nucleation of calcite [130]. Many inorganic crystals are thought to be capable of forming via an amorphous precursor phase, and indeed, of the crystal systems investigated here other than calcium carbonate, amorphous phases have been detected for both calcium oxalate and manganese carbonate [131, 132].

It is worth noting that the probability of nucleation not only scales with the free-energy barrier, but also with a kinetic barrier. This barrier is associated with processes such as ion desolvation and binding [133]. Calcium ions in solution have a reasonably high enthalpy of solvation ($\Delta H^{o}_{hyd}$ = -1579 KJ/Mol) [93] and their coordination fluctuates just above 7 water molecules [95]. Hence, the presence of a carboxylate monolayer at the substrate surface may facilitate removal of the hydration shell (which would also provide an entropic contribution).

The generality of the 16COOH substrate, in that the substrate features promote nucleation across a range of crystal systems, is also of interest. Effective ice nucleators have been described in which the surface structure of the substrate bears no resemblance at all to the crystal structure of the nucleating ice [99]. Instead, it has been suggested that the contact layer of water acts as a mediator between the substrate and the forming ice crystal, such that the substrate surface structure need not match that of the crystal. Although the long range order of the contact layer is also not ice-like in structure, there exists local structures that are ice-like. This layer is sufficient to template the formation of an ice-like structure in the second layer, which is then propagated throughout the rest of the crystal. A similar process may occur involving the Stern layer of ions adjacent to the monolayer surface in the case of inorganic nucleation. We believe the effectiveness of the 16COOH coated PPDMS in achieving localised nucleation and growth is caused by the presence of surface microstructures within the contact layer that are conducive to nucleation and growth past the critical size. Their formation is facilitated by the flexibility of the monolayer, and nucleation is localised to the cracks as a result of the associated reduction of the free-energy barrier at an acute surface feature (smaller $\Delta G'$ compared to flat surfaces), where the nucleation rate is greater than on the adjacent terraces.

## 2.7 Summary

This research began with preliminary studies involving the formation of surface defects in glass slides via abrasion with diamond powder. These slides were used as substrates for the crystallisation of calcium carbonate. An increase in the crystal population relative to the control slides was observed, alongside the alignment of crystals along single, extended defects. These data indicated that surface topography does indeed play a role in heterogeneous nucleation and as such, a more effective system to study the effects was sought. The cracks formed in the surface of a plasma-treated poly(dimethylsiloxane) (PPDMS) substrate, a result of the formation of a silica-like surface layer after exposure to RF air plasma, were shown to be effective nucleation sites for the formation of calcium carbonate. In order to investigate the combined effects of surface topography and surface chemistry a thiol self-assembled monolayer was formed on the PPDMS surface. 16-mercaptohexadecanoic acid (16COOH) was chosen, due to the extensive body of research on this thiol regarding its use as an organic interface for biomineralisation studies. Once deposited onto the PDMS substrate, the 16COOH thiol greatly enhanced the population of calcium carbonate crystals at the cracks and was selective for calcite. The studies described here have shown that it is possible to generate surface topographies that are highly effective at localising crystal nucleation and growth. However, the process of heterogeneous nucleation and the effect of surface topography are not yet fully understood, and more information about the dynamic interaction between nuclei, metastable phases, crystals and the substrate surface structure is required in order to form definitive conclusions.

## 2.8 References


1. Weinhold, F. and R. West, *The nature of the silicon–oxygen bond.* Organometallics, 2011. **30**(21): p. 5815-5824.
2. Roe, R.-J., *Surface tension of polymer liquids.* The Journal of Physical Chemistry, 1968. **72**(6): p. 2013-2017.
3. Fox, H., P. Taylor, and W. Zisman, *Polyorganosiloxanes...Surface Active Properties.* Industrial & Engineering Chemistry, 1947. **39**(11): p. 1401-1409.
4. Clarson, S.J. and J.A. Semlyen, *Siloxane Polymers*. 1st ed. Polymer Science and Technologies, ed. E. Horwood, T.J. Kemp, and J.E. Mark. 1993, Englewood Cliffs, New Jersey, U.S.A.: PTR Prentice Hall. 668.
5. DeKock, R.L. and H.B. Gray, *Chemical Structure and Bonding*. 1989: University Science Books.
6. Sutton, L.E., *Tables of Interatomic Distances and Configuration in Molecules and Ions: Supplement 1956-59*. 1965: Chemical Society.
7. Wu, S., *Polymer interface and adhesion*. 1982: M. Dekker.
8. Dou, Q., et al., *PDMS-Modified Polyurethane Films with Low Water Contact Angle Hysteresis.* Macromolecular Chemistry and Physics, 2006. **207**(23): p. 2170-2179.
9. Bodas, D. and C. Khan-Malek, *Formation of more stable hydrophilic surfaces of PDMS by plasma and chemical treatments.* Microelectronic Engineering, 2006. **83**(4–9): p. 1277-1279.
10. Jin, M., et al., *Super-hydrophobic PDMS surface with ultra-low adhesive force.* Macromolecular Rapid Communications, 2005. **26**(22): p. 1805-1809.
11. Paunov, V.N., *Novel Method for Determining the Three-Phase Contact Angle of Colloid Particles Adsorbed at Air−Water and Oil−Water Interfaces.* Langmuir, 2003. **19**(19): p. 7970-7976.
12. Cottrell, T.L., *The Strength of Chemical Bonds*. 1954: Butterworth's Scientific Pubs.
13. Haynes, W.M., *CRC Handbook of Chemistry and Physics, 95th Edition*. 2014: CRC Press.
14. Lötters, J., et al., *The mechanical properties of the rubber elastic polymer polydimethylsiloxane for sensor applications.* Journal of Micromechanics and Microengineering, 1997. **7**(3): p. 145.
15. Shefer, A. and M. Gottlieb, *Effect of crosslinks on the glass transition temperature of end-linked elastomers.* Macromolecules, 1992. **25**(15): p. 4036-4042.
16. Holbrough, J., et al., *Topographical control of crystal nucleation.* Crystal Growth & Design, 2012. **12**(2): p. 750-755.
17. Campbell, J.M., F.C. Meldrum, and H.K. Christenson, *Characterization of Preferred Crystal Nucleation Sites on Mica Surfaces.* Crystal Growth & Design, 2013. **13**(5): p. 1915-1925.
18. Hillborg, H., et al., *Crosslinked polydimethylsiloxane exposed to oxygen plasma studied by neutron reflectometry and other surface specific techniques.* Polymer, 2000. **41**(18): p. 6851-6863.
19. Fritz, J.L. and M.J. Owen, *Hydrophobic recovery of plasma-treated polydimethylsiloxane.* The Journal of Adhesion, 1995. **54**(1-4): p. 33-45.
20. Huck, W.T.S., et al., *Ordering of Spontaneously Formed Buckles on Planar Surfaces.* Langmuir, 2000. **16**(7): p. 3497-3501.
21. Sengupta Ghatak, A. and A. Ghatak, *Disordered nanowrinkle substrates for inducing crystallization over a wide range of concentration of protein and precipitant.* Langmuir, 2013. **29**(13): p. 4373-4380.

22. Aizenberg, J., A.J. Black, and G.M. Whitesides, *Controlling local disorder in self-assembled monolayers by patterning the topography of their metallic supports.* Nature, 1998. **394**(6696): p. 868-871.
23. Maoz, R. and J. Sagiv, *Penetration-controlled reactions in organized monolayer assemblies. 1. Aqueous permanganate interaction with monolayer and multilayer films of long-chain surfactants.* Langmuir, 1987. **3**(6): p. 1034-1044.
24. Yang, S., K. Khare, and P.-C. Lin, *Harnessing Surface Wrinkle Patterns in Soft Matter.* Advanced Functional Materials, 2010. **20**(16): p. 2550-2564.
25. Amin, G., *ZnO and CuO nanostructures: low temperature growth, characterization, their optoelectronic and sensing applications*. 2012, Linköping University Electronic Press.
26. Hawkes, P. and L. Reimer, *Scanning Electron Microscopy: Physics of Image Formation and Microanalysis*. 2013: Springer Berlin Heidelberg.
27. Spence, J.C.H., *High-Resolution Electron Microscopy*. 2013: OUP Oxford.
28. Goodhew, P.J., J. Humphreys, and R. Beanland, *Electron Microscopy and Analysis, Third Edition*. 2000: Taylor & Francis.
29. Tsougeni, K., et al., *Control of Nanotexture and Wetting Properties of Polydimethylsiloxane from Very Hydrophobic to Super-Hydrophobic by Plasma Processing.* Plasma Processes and Polymers, 2007. **4**(4): p. 398-405.
30. Riccardi, C., et al., *Surface modification of poly(ethylene terephthalate) fibers induced by radio frequency air plasma treatment.* Applied Surface Science, 2003. **211**(1–4): p. 386-397.
31. Hillborg, H. and U. Gedde, *Hydrophobicity recovery of polydimethylsiloxane after exposure to corona discharges.* Polymer, 1998. **39**(10): p. 1991-1998.
32. Morra, M., et al., *On the aging of oxygen plasma-treated polydimethylsiloxane surfaces.* Journal of Colloid and Interface Science, 1990. **137**(1): p. 11-24.
33. Bodas, D. and C. Khan-Malek, *Hydrophilization and hydrophobic recovery of PDMS by oxygen plasma and chemical treatment—An SEM investigation.* Sensors and Actuators B: Chemical, 2007. **123**(1): p. 368-373.
34. Perz, S.V., C.S. McMillan, and M.J. Owen, *Wettability of fluorosilicone surfaces*, in *Fluorinate Surfaces, Coatings and FIlms*. 2001. p. 112-128.
35. Nawrot, C.F., et al., *Dental phosphoprotein-induced formation of hydroxylapatite during in vitro synthesis of amorphous calcium phosphate.* Biochemistry, 1976. **15**(16): p. 3445-3449.
36. Weiner, S., *Organization of organic matrix components in mineralized tissues.* American zoologist, 1984. **24**(4): p. 945-951.
37. Veis, A. and B. Sabsay, *Bone and tooth formation. Insights into mineralization strategies*, in *Biomineralization and biological metal accumulation*. 1983, Springer. p. 273-284.
38. Veis, A. *chemistry and biology of mineralized connective tissues*. in *International Conference on the Chemistry and Biology of Mineralized Connective Tissues 1981: Northwestern University Dental School)*. 1981. Elsevier/North-Holland.
39. Lowenstam, H. and S. Weiner, *Mineralization by organisms and the evolution of biomineralization*, in *Biomineralization and biological metal accumulation*. 1983, Springer. p. 191-203.
40. Wilbur, K.M. and A.M. Bernhardt, *Effects of amino acids, magnesium, and molluscan extrapallial fluid on crystallization of calcium carbonate: in vitro experiments.* The Biological Bulletin, 1984. **166**(1): p. 251-259.

41. Wheeler, A., J.W. George, and C. Evans, *Control of calcium carbonate nucleation and crystal growth by soluble matrx of oyster shell.* Science, 1981. **212**(4501): p. 1397-1398.
42. Termine, J., E. Eanes, and K. Conn, *Phosphoprotein modulation of apatite crystallization.* Calcified tissue international, 1980. **31**(1): p. 247-251.
43. Rodríguez-Navarro, A.B., et al., *Amorphous calcium carbonate controls avian eggshell mineralization: A new paradigm for understanding rapid eggshell calcification.* Journal of Structural Biology, 2015. **190**(3): p. 291-303.
44. Kirboga, S. and M. Oner, *Calcium Carbonate Precipitation in the Presence of Additives.*
45. Yu, J., et al., *Effects of PAA additive and temperature on morphology of calcium carbonate particles.* Journal of Solid State Chemistry, 2004. **177**(3): p. 681-689.
46. Westin, K.-J. and Å.C. Rasmuson, *Precipitation of calcium carbonate in the presence of citrate and EDTA.* Desalination, 2003. **159**(2): p. 107-118.
47. Westin, K.J. and Å.C. Rasmuson, *Nucleation of calcium carbonate in presence of citric acid, DTPA, EDTA and pyromellitic acid.* Journal of Colloid and Interface Science, 2005. **282**(2): p. 370-379.
48. Wada, N., K. Kanamura, and T. Umegaki, *Effects of Carboxylic Acids on the Crystallization of Calcium Carbonate.* Journal of Colloid and Interface Science, 2001. **233**(1): p. 65-72.
49. Wada, N., et al., *Effect of Polyacrylic acid and Polarization on the Controlled Crystallization of Calcium Carbonate on Single-Phase Calcite Substrates.* Crystal Growth & Design, 2013.
50. Ukrainczyk, M., et al., *Influence of etidronic acid and tartaric acid on the growth of different calcite morphologies.* Journal of Crystal Growth, 2013.
51. Su, Y., et al., *Crystallization and morphological control of calcium carbonate by functionalized triblock copolymers.* Colloids and Surfaces A: Physicochemical and Engineering Aspects, 2010. **355**(1): p. 158-162.
52. Song, R.-Q. and H. Cölfen, *Additive controlled crystallization.* CrystEngComm, 2011. **13**(5): p. 1249-1276.
53. Rieger, J., J. Thieme, and C. Schmidt, *Study of Precipitation Reactions by X-ray Microscopy: CaCO3 Precipitation and the Effect of Polycarboxylates.* Langmuir, 2000. **16**(22): p. 8300-8305.
54. Reddy, M.M. and A.R. Hoch, *Calcite crystal growth rate inhibition by polycarboxylic acids.* Journal of colloid and interface science, 2001. **235**(2): p. 365-370.
55. Ravichandran, K. and S. Narayanan, *Effective screening of scaling inhibitors for cooling water systems-Development of an accelerated electrochemical method.* Corrosion reviews, 2002. **20**(1-2): p. 105-114.
56. Persinski, L.J., J.L. Walker, and B.P. Boffardi, *Synergistic scale and corrosion inhibiting admixtures containing carboxylic acid/sulfonic acid polymers*. 1987, Google Patents.
57. Packter, A. and D. Saunders, *Precipitation of sparingly soluble alkaline-earth and lead salts; the effects of chelating additives on nucleation and growth rates.* J. Chem. Soc. A, 1970: p. 725-729.
58. Neville, A. and A.P. Morizot, *A combined bulk chemistry/electrochemical approach to study the precipitation, deposition and inhibition of CaCO3.* Chemical Engineering Science, 2000. **55**(20): p. 4737-4743.
59. Morizot, A.P. and A. Neville, *Insights into electrodeposition of an inhibitor film and its inhibitive effects on calcium carbonate deposition.* Journal of colloid and interface science, 2002. **245**(1): p. 40-49.

60. Meldrum, F.C. and S.T. Hyde, *Morphological influence of magnesium and organic additives on the precipitation of calcite.* Journal of Crystal Growth, 2001. **231**(4): p. 544-558.
61. Matahwa, H., V. Ramiah, and R. Sanderson, *Calcium carbonate crystallization in the presence of modified polysaccharides and linear polymeric additives.* Journal of Crystal Growth, 2008. **310**(21): p. 4561-4569.
62. MacAdam, J. and S.A. Parsons, *Calcium carbonate scale formation and control.* Re/Views in Environmental Science & Bio/Technology, 2004. **3**(2): p. 159-169.
63. Macadam, J. and S. Parsons, *Calcium carbonate scale control, effect of material and inhibitors.* Water Science & Technology, 2004. **49**(2): p. 153-159.
64. Loy, J.E., J. Guo, and S.J. Severtson, *Role of Adsorption Fractionation in Determining the CaCO3 Scale Inhibition Performance of Polydisperse Sodium Polyacrylate.* Industrial & Engineering Chemistry Research, 2004. **43**(8): p. 1882-1887.
65. Jada, A. and S. Erlenmeyer, *Zeta Potential of Calcium Carbonate Precipitated in the Presence of Sodium Polyacrylates.* Journal of Colloid Science and Biotechnology, 2012. **1**(1): p. 129-136.
66. Jada, A., et al., *Effect of sodium polyacrylate molecular weight on the crystallogenesis of calcium carbonate.* Journal of Crystal Growth, 2007. **306**(2): p. 373-382.
67. Henderson, G.E., B.J. Murray, and K.M. McGrath, *Controlled variation of calcite morphology using simple carboxylic acids.* Journal of Crystal Growth, 2008. **310**(18): p. 4190-4198.
68. Harris, A. and A. Marshall. *The evaluation of scale control additives*. in *Proceedings of Symposium on Progress in the Prevention of Fouling in Industrial Plant*. 1981.
69. Guo, J. and S.J. Severtson, *Application of classical nucleation theory to characterize the influence of carboxylate-containing additives on CaCO3 nucleation at high temperature, pH, and ionic strength.* Industrial & engineering chemistry research, 2003. **42**(14): p. 3480-3486.
70. Didymus, J.M., et al., *Influence of low-molecular-weight and macromolecular organic additives on the morphology of calcium carbonate.* J. Chem. Soc., Faraday Trans., 1993. **89**(15): p. 2891-2900.
71. Aschauer, U., et al., *Growth modification of seeded calcite using carboxylic acids: Atomistic simulations.* Journal of colloid and interface science, 2010. **346**(1): p. 226-231.
72. Aschauer, U., et al., *Growth Modification of Seeded Calcite by Carboxylic Acid Oligomers and Polymers: Toward an Understanding of Complex Growth Mechanisms.* Crystal Growth & Design, 2010. **10**(9): p. 3956-3963.
73. Amjad, Z. and R. Zuhl, *Effect of heat treatment on the performance of deposit control polymers as calcium carbonate inhibitors.* CORROSION 2007, 2007.
74. Amjad, Z., *Kinetic study of the seeded growth of calcium carbonate in the presence of benzenepolycarboxylic acids.* Langmuir, 1987. **3**(2): p. 224-228.
75. Freeman, C.L., et al., *Surface selectivity of calcite on self-assembled monolayers.* The Journal of Physical Chemistry C, 2013. **117**(10): p. 5154-5163.
76. Quigley, D., et al., *Metadynamics simulations of calcite crystallization on self-assembled monolayers.* The Journal of chemical physics, 2009. **131**(9): p. 094703.
77. Pokroy, B. and J. Aizenberg, *Calcite shape modulation through the lattice mismatch between the self-assembled monolayer template and the nucleated crystal face.* CrystEngComm, 2007. **9**(12): p. 1219-1225.
78. Lee, J.R., et al., *Structural development of mercaptophenol self-assembled monolayers and the overlying mineral phase during templated CaCO3 crystallization from a*

*transient amorphous film.* Journal of the American Chemical Society, 2007. **129**(34): p. 10370-10381.
79. Travaille, A.M., et al., *Thermodynamics of epitaxial calcite nucleation on self-assembled monolayers.* The Journal of Physical Chemistry B, 2005. **109**(12): p. 5618-5626.
80. Duffy, D.M. and J.H. Harding, *Simulation of organic monolayers as templates for the nucleation of calcite crystals.* Langmuir, 2004. **20**(18): p. 7630-7636.
81. Aizenberg, J., *Crystallization in Patterns: A Bio-Inspired Approach.* Advanced Materials, 2004. **16**(15): p. 1295-1302.
82. Han, Y.-J. and J. Aizenberg, *Face-Selective Nucleation of Calcite on Self-Assembled Monolayers of Alkanethiols: Effect of the Parity of the Alkyl Chain.* Angewandte Chemie, 2003. **115**(31): p. 3796-3798.
83. Travaille, A.M., et al., *Aligned growth of calcite crystals on a self-assembled monolayer.* Advanced Materials, 2002. **14**(7): p. 492.
84. Lee, I., et al., *Formation of patterned continuous calcium carbonate films on self-assembled monolayers via nanoparticle-directed crystallization.* Advanced Materials, 2002. **14**(22): p. 1640-1643.
85. Aizenberg, J., A.J. Black, and G.M. Whitesides, *Oriented Growth of Calcite Controlled by Self-Assembled Monolayers of Functionalized Alkanethiols Supported on Gold and Silver.* Journal of the American Chemical Society, 1999. **121**(18): p. 4500-4509.
86. Aizenberg, J., A.J. Black, and G.M. Whitesides, *Control of crystal nucleation by patterned self-assembled monolayers.* Nature, 1999. **398**(6727): p. 495-498.
87. Kuther, J., et al., *Templated growth of calcite, vaterite and aragonite crystals onself-assembled monolayers of substituted alkylthiols on gold.* Journal of Materials Chemistry, 1998. **8**(3): p. 641-650.
88. Hu, Q., et al., *The thermodynamics of calcite nucleation at organic interfaces: Classical vs. non-classical pathways.* Faraday Discussions, 2012. **159**(1): p. 509-523.
89. Ihli, J., et al., *Elucidating Mechanisms of Diffusion-Based Calcium Carbonate Synthesis Leads to Controlled Mesocrystal Formation.* Advanced Functional Materials, 2012. **23**(15): p. 1965-1973.
90. Blue, C.R., et al., *Chemical and physical controls on the transformation of amorphous calcium carbonate into crystalline CaCO3 polymorphs.* Geochimica et Cosmochimica Acta, 2017. **196**: p. 179-196.
91. Davis, K.J., et al., *Morphological consequences of differential Mg2+ incorporation at structurally distinct steps on calcite.* American Mineralogist, 2004. **89**: p. 714-720.
92. Compton, R.G. and C.A. Brown, *The Inhibition of Calcite Dissolution/Precipitation: Mg< sup> 2+</sup> Cations.* Journal of colloid and interface science, 1994. **165**(2): p. 445-449.
93. Kaye, G.W.C. and T.H. Laby, *Tables of physical and chemical constants*. 1995: Longman.
94. Lippmann, F., *Sedimentary carbonate minerals*. Vol. 228. 1973: Springer.
95. Gale, J.D., P. Raiteri, and A.C.T. van Duin, *A reactive force field for aqueous-calcium carbonate systems.* Physical Chemistry Chemical Physics, 2011. **13**(37): p. 16666-16679.
96. McLester, M.E., D. Martin, and W. Taft, *Effects of alkaline-earth metal ions on the transformation of aragonite to calcite in aqueous solution.* Journal of Inorganic and Nuclear Chemistry, 1970. **32**(2): p. 391-399.
97. Katz, A., *The interaction of magnesium with calcite during crystal growth at 25–90 C and one atmosphere.* Geochimica et Cosmochimica Acta, 1973. **37**(6): p. 1563-1586.

98. Wada, N., K. Yamashita, and T. Umegaki, *Effects of divalent cations upon nucleation, growth and transformation of calcium carbonate polymorphs under conditions of double diffusion.* Journal of crystal growth, 1995. **148**(3): p. 297-304.
99. Pedevilla, P., et al., *Can Ice-Like Structures Form on Non-Ice-Like Substrates? The Example of the K-feldspar Microcline.* The Journal of Physical Chemistry C, 2016. **120**(12): p. 6704-6713.
100. Palms, D., et al., *Directed crystallisation of zinc oxide on patterned surfaces.* Journal of Colloid and Interface Science, 2006. **303**(2): p. 333-336.
101. Lee, A.Y., I.S. Lee, and A.S. Myerson, *Factors Affecting the Polymorphic Outcome of Glycine Crystals Constrained on Patterned Substrates.* Chemical Engineering & Technology, 2006. **29**(2): p. 281-285.
102. Lee, A.Y., et al., *Crystallization on Confined Engineered Surfaces: A Method to Control Crystal Size and Generate Different Polymorphs.* Journal of the American Chemical Society, 2005. **127**(43): p. 14982-14983.
103. Briseno, A.L., et al., *Patterned Growth of Large Oriented Organic Semiconductor Single Crystals on Self-Assembled Monolayer Templates.* Journal of the American Chemical Society, 2005. **127**(35): p. 12164-12165.
104. Aizenberg, J., et al., *Direct fabrication of large micropatterned single crystals.* Science, 2003. **299**(5610): p. 1205-1208.
105. Merkel, T.C., et al., *Gas sorption, diffusion, and permeation in poly(dimethylsiloxane).* Journal of Polymer Science Part B: Polymer Physics, 2000. **38**(3): p. 415-434.
106. Lin, P.-C., et al., *Mechanically tunable dry adhesive from wrinkled elastomers.* Soft Matter, 2008. **4**(9): p. 1830-1835.
107. Tan, L., et al., *Control of Heterogeneous Nucleation via Rationally Designed Biocompatible Polymer Surfaces with Nanoscale Features.* Crystal Growth & Design, 2015. **15**(5): p. 2176-2186.
108. Jiang, Q. and M.D. Ward, *Crystallization under nanoscale confinement.* Chemical Society Reviews, 2014. **43**(7): p. 2066-2079.
109. Kertis, F., et al., *Heterogeneous nucleation of protein crystals using nanoporous gold nucleants.* Journal of Materials Chemistry, 2012. **22**(41): p. 21928-21934.
110. Diao, Y., et al., *Surface Design for Controlled Crystallization: The Role of Surface Chemistry and Nanoscale Pores in Heterogeneous Nucleation.* Langmuir, 2011. **27**(9): p. 5324-5334.
111. Diao, Y., et al., *The role of nanopore shape in surface-induced crystallization.* Nature Materials, 2011. **10**(11): p. 867-871.
112. Ruckenstein, E. and G.O. Berim, *Kinetics of heterogeneous nucleation on a rough surface: Nucleation of a liquid phase in nanocavities.* Journal of Colloid and Interface Science, 2010. **351**(1): p. 277-282.
113. Ha, J.-M., et al., *Polymorph Selectivity under Nanoscopic Confinement.* Journal of the American Chemical Society, 2004. **126**(11): p. 3382-3383.
114. Ahn, H.-S., et al., *Effect of molecular structure of self-assembled monolayers on their tribological behaviors in nano-and microscales.* Wear, 2003. **255**(7): p. 819-825.
115. Adams, D.M., et al., *Charge transfer on the nanoscale: current status.* The Journal of Physical Chemistry B, 2003. **107**(28): p. 6668-6697.
116. Mrksich, M., *What can surface chemistry do for cell biology?* Current opinion in chemical biology, 2002. **6**(6): p. 794-797.
117. Houston, J.E. and H.I. Kim, *Adhesion, friction, and mechanical properties of functionalized alkanethiol self-assembled monolayers.* Accounts of chemical research, 2002. **35**(7): p. 547-553.

118. Burleigh, T., et al., *Tarnish protection of silver using a hexadecanethiol self-assembled monolayer and descriptions of accelerated tarnish tests.* Corrosion, 2001. **57**(12): p. 1066-1074.
119. Ostuni, E., L. Yan, and G.M. Whitesides, *The interaction of proteins and cells with self-assembled monolayers of alkanethiolates on gold and silver.* Colloids and Surfaces B: Biointerfaces, 1999. **15**(1): p. 3-30.
120. Mann, S., et al., *Crystal synthesis under langmuir monolayers.* Advanced Materials, 1990. **2**(5): p. 257-261.
121. Kumar, P.P., A.G. Kalinichev, and R.J. Kirkpatrick, *Hydrogen-Bonding Structure and Dynamics of Aqueous Carbonate Species from Car− Parrinello Molecular Dynamics Simulations.* The Journal of Physical Chemistry B, 2008. **113**(3): p. 794-802.
122. Tielens, F., et al., *Stability of Binary SAMs Formed by ω-Acid and Alcohol Functionalized Thiol Mixtures.* Langmuir, 2009. **25**(17): p. 9980-9985.
123. Tielens, F., et al., *Characterization of ω-Functionalized Undecanethiol Mixed Self-Assembled Monolayers on Au(111): A Combined Polarization Modulation Infrared Reflection–Absorption Spectroscopy/X-ray Photoelectron Spectroscopy/Periodic Density Functional Theory Study.* The Journal of Physical Chemistry C, 2008. **112**(1): p. 182-190.
124. Paz, Y., *Self-assembled monolayers and titanium dioxide: From surface patterning to potential applications.* Beilstein Journal of Nanotechnology, 2011. **2**: p. 845-861.
125. Zhou, J., A.V. Ellis, and N.H. Voelcker, *Recent developments in PDMS surface modification for microfluidic devices.* ELECTROPHORESIS, 2010. **31**(1): p. 2-16.
126. Küther, J., et al., *Templated Crystallisation of Calcium and Strontium Carbonates on Centred Rectangular Self-Assembled Monolayer Substrates.* Chemistry–A European Journal, 1998. **4**(9): p. 1834-1842.
127. Côté, A.S., R. Darkins, and D.M. Duffy, *Modeling Calcite Crystallization on Self-Assembled Carboxylate-Terminated Alkanethiols.* The Journal of Physical Chemistry C, 2014. **118**(33): p. 19188-19193.
128. Nielsen, M.H., et al., *Structural evolution, formation pathways and energetic controls during template-directed nucleation of CaCO 3.* Faraday Discussions, 2012. **159**(1): p. 105-121.
129. Berman, A., et al., *Total alignment of calcite at acidic polydiacetylene films: cooperativity at the organic-inorganic interface.* Science, 1995. **269**(5223): p. 515.
130. Hamm, L.M., et al., *Reconciling disparate views of template-directed nucleation through measurement of calcite nucleation kinetics and binding energies.* Proceedings of the National Academy of Sciences, 2014. **111**(4): p. 1304-1309.
131. Ihli, J., et al., *Precipitation of Amorphous Calcium Oxalate in Aqueous Solution.* Chemistry of Materials, 2015. **27**(11): p. 3999-4007.
132. Radha, A. and A. Navrotsky, *Manganese carbonate formation from amorphous and nanocrystalline precursors: Thermodynamics and geochemical relevance.* American Mineralogist, 2014. **99**(5-6): p. 1063-1070.
133. Smeets, P.J.M., et al., *Calcium carbonate nucleation driven by ion binding in a biomimetic matrix revealed by in situ electron microscopy.* Nat Mater, 2015. **advance online publication**.

# 3 Image Analysis of Crystallisation on Plasma-treated Poly(dimethylsiloxane)

## 3.1 Aims and Overview

Chapter 2 demonstrated that it is possible to influence the spatial distribution of crystals on a substrate through the use of surface features that act as effective nucleation promotors. The results were presented qualitatively, so this current chapter aims to provide a more rigorous examination of the combined effect of surface topography and surface chemistry on the precipitation of calcium carbonate by employing quantitative techniques.

Image analysis software makes it possible to extract crystal populations, crystal size and polymorphic ratios associated with crystallisation data. ImageJ was used to analyse the crystallisation of calcium carbonate on Plasma-treated PDMS substrates with differing surface functionalities. As in Chapter 2, the chemistry of the surface was altered by using thiol self-assembled monolayers. The fact that the molecular structure determines the properties of the monolayer, which in turn will affect crystallisation on its surface, necessitated the careful choice of thiol molecules. By choosing molecules with only minor structural differences, it was possible to gain an insight into how thiol SAMs can affect crystallisation when used in conjunction with surface topography. As such, a pair of carboxyl-terminated thiols were selected that differed only in carbon chain length. An OH-terminated thiol of the same length as the shorter carboxylate thiol was chosen, as well as a methyl-terminated thiol of the same chain length as the longer COOH-thiol. Finally, a perfluorocarbon thiol was investigated, and iridium-coated PPDMS and uncoated PPDMS to act as controls. Image analysis was then used to analyse SEM micrographs after crystallisation.

## 3.2 Experimental Methods

### 3.2.1 Image Acquisition, Correction, Analysis and Solution Conditions

Image analysis was carried out in order to quantify the effect of the substrate surface chemistry on the precipitation of calcium carbonate at the topographic features of plasma-treated poly(dimethylsiloxane). Using ImageJ, it is possible to extract data from micrographs such as crystal size, population, polymorph and crystal size frequency. The SAMs investigated and their identifiers in brackets were as follows:

- 16-mercaptohexadecanoic acid (16COOH)
- 11-mercaptoundecanoic acid (11COOH)
- 11-mercapto-1-undecanol (11OH)
- 1-hexadecanethiol ($CH_3$)
- 1H, 1H, 2H, 2H-perfluorododecanethiol ($CF_3$)
- Iridium coated PPDMS (IrPPDMS)
- Native PPDMS (PPDMS)

The intention of using two carboxylic acid-terminated SAMs of differing length (16COOH and 11COOH) was to investigate the effect of chain parity on crystallisation. The alcohol-terminated thiol, 11OH, provides a functional group comparison at the same chain length as the 11COOH. Similarly, the fact that 1-hexadecane thiol and 16COOH share the same chain length means that the only variable between them are the functional groups and so differences can be attributed to this. Finally, the PFC thiol provides a low-energy surface for contrast. The remaining two (Iridium coated PPDMS, Native PPDMS) are controls.

The micrographs were collected using a FEI Nova Nanosem 450 SEM. Twenty regions from three repeats for each condition (6 conditions) on every substrate (7 substrate types) were captured at random (avoiding the edge of the substrate). Each region comprised a 360 x 360 µm area. Table 8 contains the conditions investigated.

**Table 8: Table of the solution conditions and residence times used for the image analysis data acquisition**

| Residence time (mins) | Initial Concentrations $[Ca^{2+}] = [CO_3^{2-}]$ (mM) |
|---|---|
| 10 | 1 |
| 10 | 2 |
| 10 | 3 |
| 60 | 1 |
| 60 | 2 |
| 60 | 3 |

The micrographs were analysed using ImageJ software. Custom macros were written to facilitate the software's 'Analyse Particles' plugin and the results were verified and corrected when necessary i.e. if crystals were touching, their outline was incomplete, image artefacts etc. Image analysis using ImageJ is a time consuming process as each image is analysed individually. The general procedure is as follows:

- Using the Line tool, a line was drawn over the scale bar of the image, ensuring that the line was horizontal and covered the full width of the bar.
- The scale was set using Analyze > Set Scale, and in the pop-up box, the length of the scale bar was inserted into the Known Distance field. The unit of length was set as um (ImageJ automatically converts um to μm) and the Global checkbox was selected. Ok was then pressed.
- Using the Rectangular Selection tool, the image area was selected and the information bar at the bottom of the micrograph was omitted.
- With the Threshold function, it is possible to select only the crystals in the image and to subtract the background (ensure that the image type is 8-bit). This is done by using Image > Adjust > Threshold and then using the sliders to adjust the maximum and minimum intensities. When adjusting these parameters, the final setting should include the vast majority of crystals, and as little background as possible. Click apply to close the Threshold box.
- The image, now rendered in black and white, should only show the crystals. However, other objects may have been isolated (image artefacts such as regions of charge, for

example), which need to be removed. This is done by selecting the colour picker tool and then clicking on a white part of the image. This selects the colour white. Then click on the paint brush tool and remove any objects that are not crystals. In addition to this, any 'holes' in crystals need to be filled in. These are areas contained within the outline of a crystal that were not fully picked up by the threshold and as such have remained white. Use the colour picker to select any black area in the image, then click the paintbrush tool. Fill in any of the holes in the crystals.

- Once only solid 2-dimensional representations of the crystals remain, the data can be extracted. Click on Analyze > Analyze Particles. Set the size to 0.2 – infinity, the circularity as 0.00 – 1.00, Show: Outlines, and ensure all of the following checkboxes have been ticked: Display results, Clear results, Summarize, Exclude on Edges. Press Ok, and the data will appear in the results manager.
- The output will include the size of each individual crystal (in $\mu m^2$), the total count, total area, average size, and %area. These data can then be processed as required.
- Images that contained multiple polymorphs were processed multiple times (once for each polymorph) providing distinct data for each. In order to do this, the above process is carried out until after the threshold step has been completed. Then, using the paintbrush set on white, all crystals are removed that aren't calcite. This data is then passed through for analysis. The image is then reopened and the steps ran through till after the threshold again. This time, all the calcite crystals are removed and this image is passed through for analysis as well. This provides two distinct sets of data for the image: a calcite set and a vaterite set.

## 3.3 Results/Discussion

The greatest number density (population) of crystals observed across all substrates and conditions was achieved on substrates that had been functionalised with the 16COOH thiol; almost 140 times more crystals formed on this as compared with the next most populous, the 11OH coated substrate (Table 9).

**Table 9: Total number of crystals of all polymorphs counted across all conditions and substrates.**

| Substrate | Total Number of Crystals Counted Across all Conditions and Substrates (total area per substrate data set = 67.4 $mm^2$) |
|---|---|
| 16COOH | 52176 |
| 11OH | 375 |
| $CH_3$ | 346 |
| 11COOH | 271 |
| IrPPDMS | 123 |
| $CF_3$ | 110 |
| PPDMS | 57 |

The dominant polymorph precipitated on the carboxylated substrates was calcite, whilst on the OH, $CH_3$ and $CF_3$ substrate, it was vaterite. Figure 71 indicates the percentage of calcite/vaterite on each of the substrates at the various concentrations and residence times.

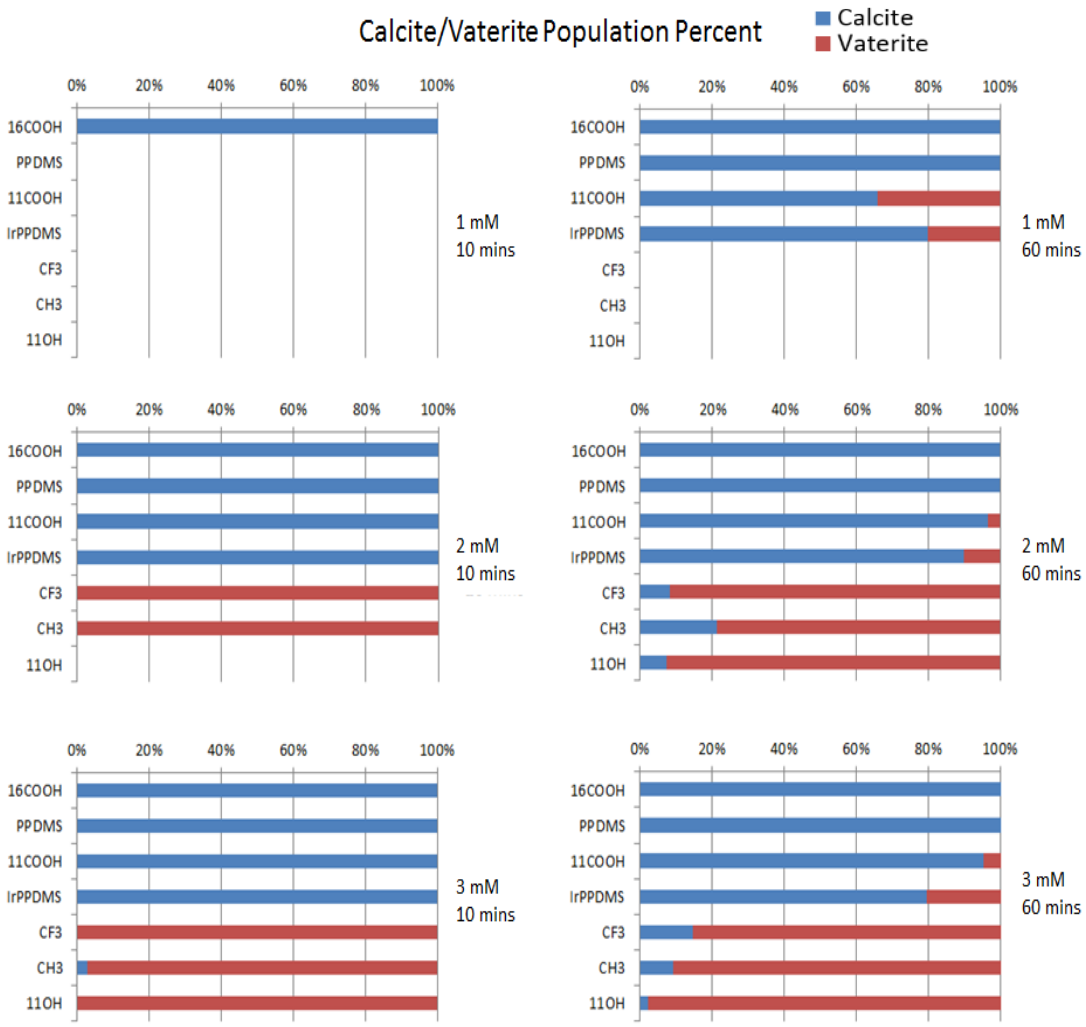


**Figure 71: Calcite/vaterite population percent at various concentrations and residence times**

At the lowest concentration and residence time displayed in Figure 71, crystals were only present on the 16COOH coated substrate (crystals were also present after $[Ca^{2+}] = [CO_3^{2-}] = 0.5$ mM, t = 60, refer to Figure 72b). For both residence times, as the initial concentration was increased, the percentage of vaterite also increased in all cases except for the $CF_3$ substrate, (a decrease in the vaterite population was observed from 2 mM to 3 mM after 60 mins, where the vaterite population was 91.7 and 85.37 respectively). Where vaterite is the dominant polymorph, a greater percentage of calcite is observed at t = 60 as compared to t = 10 at the same concentration, likely due to the transformation of vaterite that precipitated initially to the more thermodynamically stable calcite. The 11OH substrate consistently produced the lowest percentage of calcite, and interestingly, no crystals were observed on this substrate at 1 mM 10 mins, 2 mM 10 mins and 1 mM 60 mins. The 11COOH substrate supported the formation of a small fraction of vaterite crystals at 2 and 3 mM, 60 mins (3.4 % and 4.9 % respectively). This is surprising when compared to the 16COOH substrate considering they

differ only in parity and chain length. Yet vaterite was never detected on the carboxylate monolayer composed of even parity monomers. The population of each polymorph was also recorded under all conditions tested, and the data is displayed in Figure 72. The horizontal brackets below the x-axis of the graph indicate the measurements that were taken at the same initial concentration. In addition, the colour, order and position of bars are maintained throughout all of the graphs in this chapter to provide clarity, but also so that it is evident if no crystals were observed at a condition (signified by the lack of bar at the measurements allocated position).

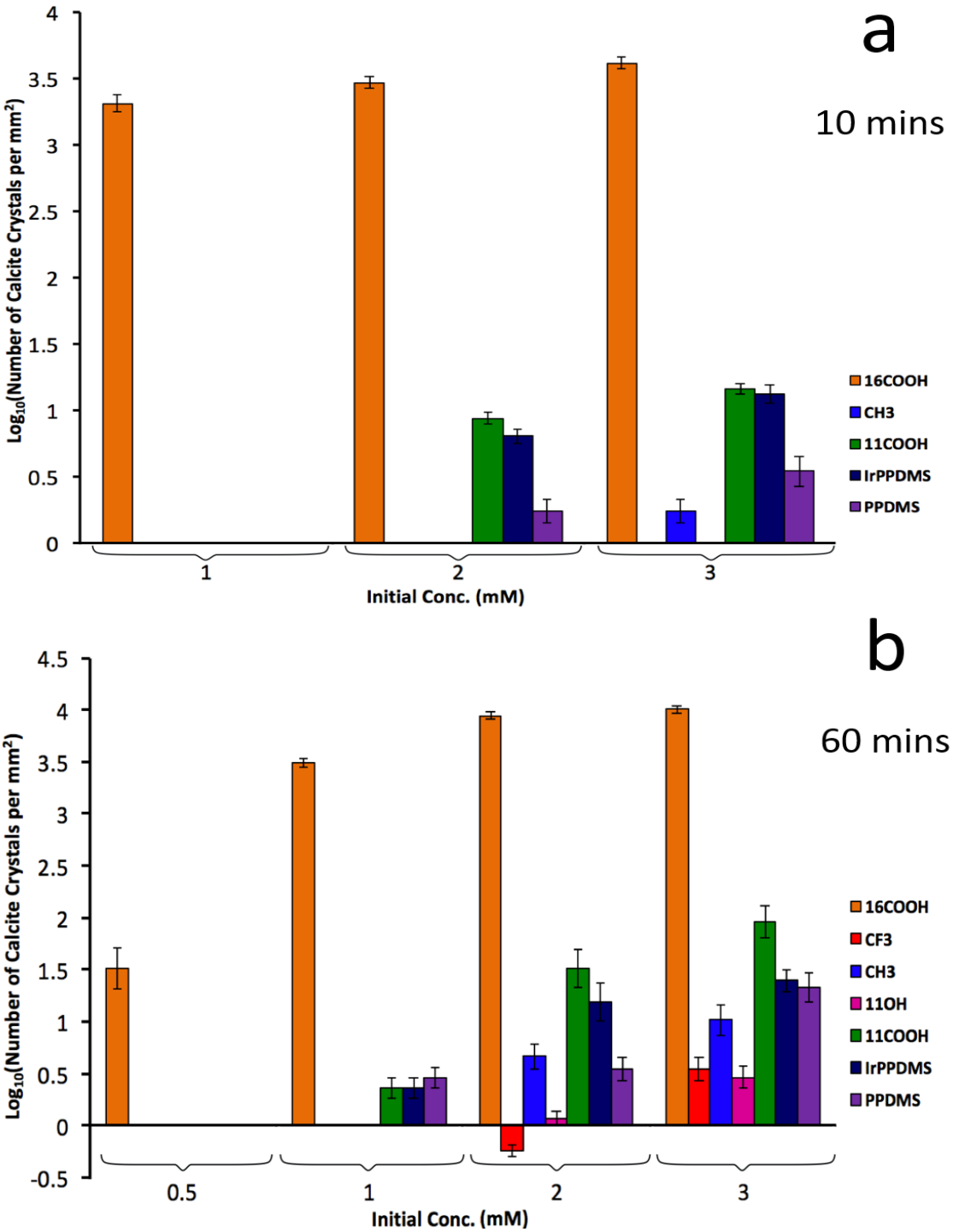


**Figure 72: Graphs of the relationship between the log of the number of calcite crystals per mm$^2$ and the initial ion concentration after the indicated residence time**

As mentioned above, the 16COOH substrate supported the formation of more calcite than any other substrate. Figure 72b indicates that the calcite population on 16COOH tends towards a maximum. This is most likely because the cracks become fully occupied and so the frequency of successful nucleation events decreased as only the terraces are left on which it can occur. Alternatively, it may simply be that the supersaturation has been depleted and so there is no longer a driving force for the phase change. The fact that the vast majority of crystals are

associated with the cracks suggests that the barrier to nucleation is reduced in the cracks, which in turn increases the nucleation rate and so more crystals are observed on this topography. The calcite population on the 11COOH and iridium-coated substrates are similar after 10 minutes at 2 and 3 mM (Figure 72a, $Population_{Calcite,11COOH,2mM,10mins}$: 8.7 ± 1.1 per $mm^2$, $Population_{Calcite,Ir,2mM,10mins}$: 6.4 ± 1.1 per $mm^2$, $Population_{Calcite,11COOH,3mM,10mins}$: 14.4 ± 1.1 per $mm^2$, $Population_{Calcite,Ir,3mM,10mins}$: 13.3 ± 1.2 per $mm^2$), though at longer residence times they diverge (Figure 72b, $Population_{Calcite,11COOH,2mM,60mins}$: 32.9 ± 1.5 per $mm^2$, $Population_{Calcite,Ir,2mM,60mins}$: 15.6 ± 1.5 per $mm^2$, $Population_{Calcite,11COOH,3mM,60mins}$: 91.1 ± 1.4 per $mm^2$, $Population_{Calcite,Ir,3mM,60mins}$: 24.8 ± 1.3 per $mm^2$), with the population of calcite on the 11COOH becoming almost 4 times greater than that on the Ir-coated substrate at 3 mM and 60 mins. Few calcite crystals were observed under all conditions on the 11OH, $CF_3$ and $CH_3$ substrates, as these substrates produced vaterite as the dominant polymorph. The size of the calcite crystals could also be quantified and is reported as a cross-sectional area in $\mu m^2$ (Figure 73)

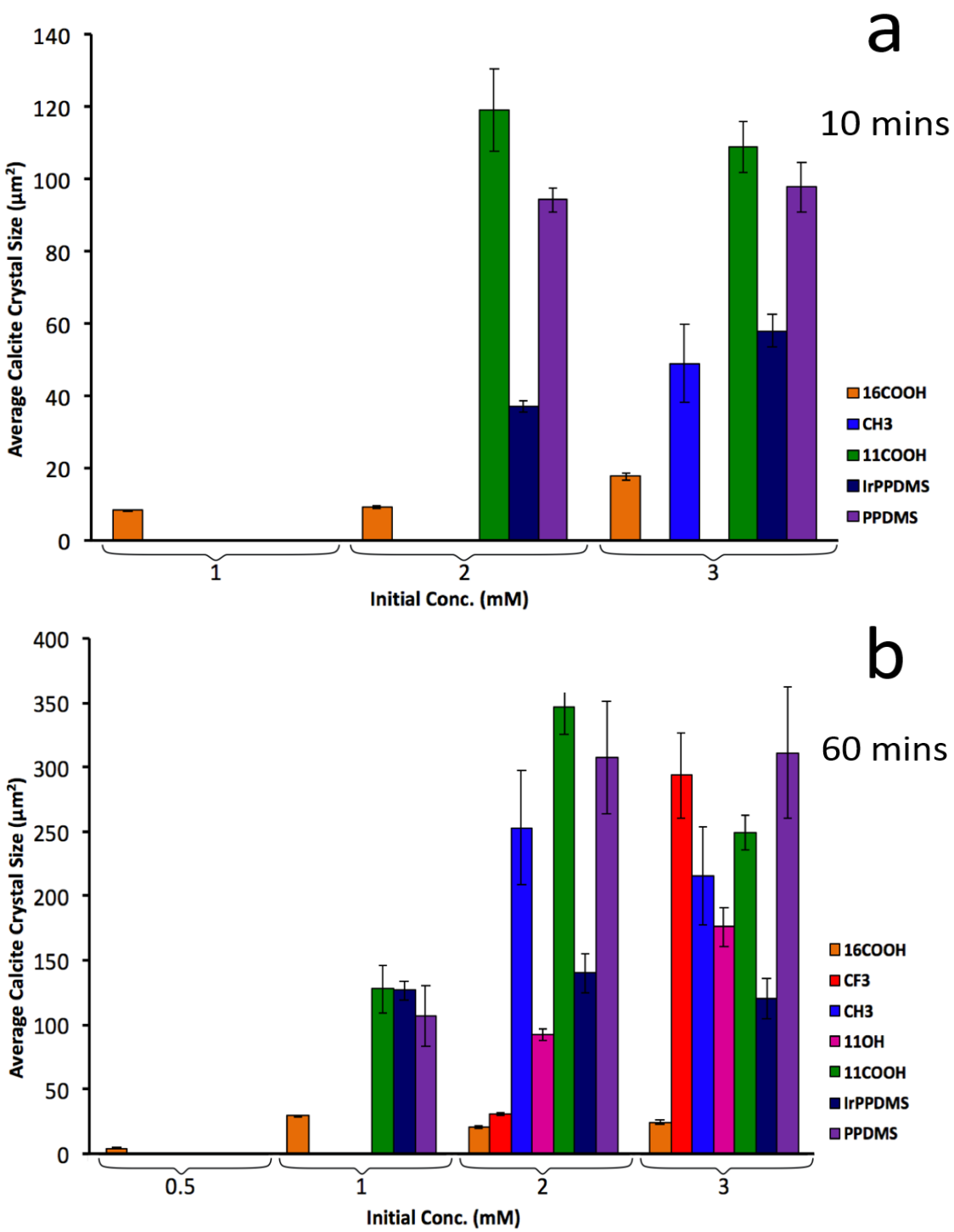


**Figure 73: Variation of calcite size with initial concentration after the indicated residence time**

At the shorter residence time and up to 2 mM and 60 mins, the largest calcite crystals were observed on the 11COOH substrate (Crystal $Size_{Calcite,11COOH,2mM,10mins}$: 119 ± 11.5 µm², Crystal $Size_{Calcite,11COOH,3mM,10mins}$: 108.71 ± 7.1 µm², Crystal $Size_{Calcite,11COOH,1mM,60mins}$: 127.5 ± 18.9 µm², Crystal $Size_{Calcite,11COOH,2mM,60mins}$: 346.6 ± 21.7 µm², Crystal $Size_{Calcite,11COOH,3mM,60mins}$: 249.2 ± 13.1 µm² ), though this decreases at 3 mM and 60 mins along with a slight reduction in calcite size from 2 mM to 3 mM at 10 mins. This decrease in average size from 2 mM to 3 mM at both

10 and 60 mins is most likely due to a greater number of nucleation events occurring over a sustained period of time at the higher supersaturation (nucleation dominating over growth), which produces a wide spread of crystal sizes. As nucleation is sustained over a longer period of time for the 3 mM condition, there are a greater proportion of small crystals compared to the 2 mM condition, which in turn decreases the mean crystal size. Large crystals were also observed on the plasma-treated PDMS substrate and $CF_3$ substrates if exposed to a sufficiently high supersaturation and residence time (3 mM, 60 mins), although, as can be seen in Figure 72b, the number of calcite crystals at these conditions was comparatively low ($Population_{Calcite,PPDMS,2mM,60mins}$: 3.5 ± 1.3 per $mm^2$, $Population_{Calcite,PPDMS,3mM,60mins}$: 21.3 ± 1.4 per $mm^2$, $Population_{Calcite,Ir,2mM,60mins}$: 32.88 ± 1.5 per $mm^2$, $Population_{Calcite,Ir,3mM,60mins}$: 91.1 ± 1.4 per $mm^2$).

These graphs also indicate that an average maximum crystal size exists on the 16COOH substrate, of approximately 23 $\mu m^2$ cross-sectional area, which is achieved between 1-3 mM, 60 mins (Figure 73b). However, the population histograms of Figure 74 below suggest that the most populous size range for the 16COOH substrate is 6 – 8 $\mu m^2$. This difference in average crystal size is indicative of the measures of central tendency that each of the graphs represent. The bar charts of Figure 73 represent the arithmetic mean of the crystal size, which can be distorted by extreme values, whilst the population histograms (Figure 74) provide the mode and is independent of extreme values. Given that the probability distribution of the population histograms below has a positive skew, the mode is a more accurate measure of the average crystal size than the arithmetic mean.

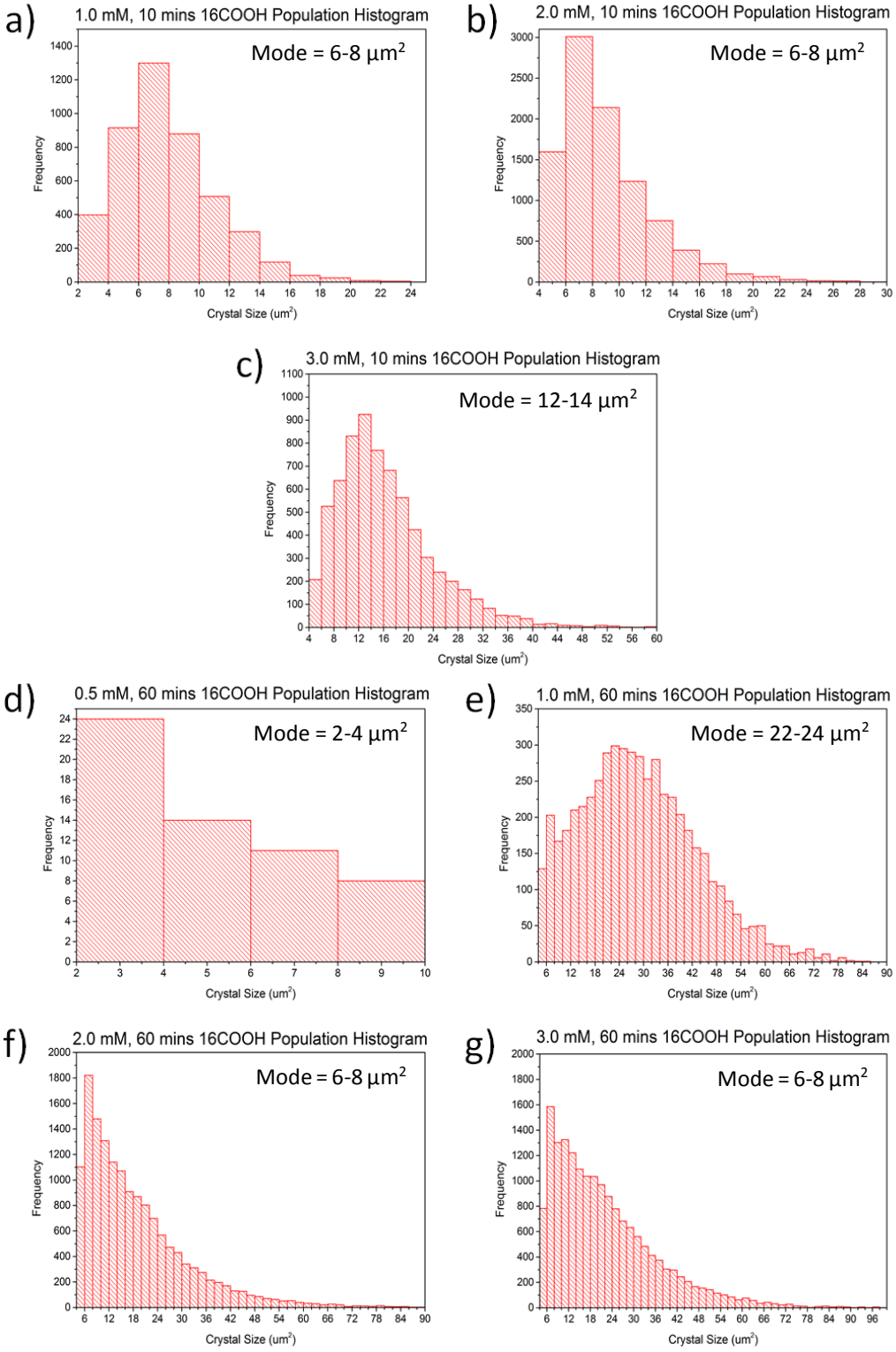


**Figure 74: Population histograms of calcite size on the 16COOH substrate at varying concentration and residence time with a 2 µm² bin size**

The population of calcite crystals present after 10 mins according to the population histograms (Figure 74a – c) suggests that at 1 mM and 2 mM, the majority of crystals are 6 –

8 $\mu m^2$ in size, likely due to the fact that the crystals nucleate at a similar time. At 3 mM, this shifts to 12 – 14 $\mu m^2$ and there is a greater spread of crystal sizes. This could be because nucleation is sustained over a longer period and growth occurs more rapidly at higher supersaturations. At the longer residence time (Figure 74d – g) the most common crystal size is again 6 – 8 $\mu m^2$ at 2 and 3 mM. However, at 0.5 mM almost half of the crystals (24 out of 57) are in the size range 2 – 4 $\mu m^2$ and at 1 mM there is a large spread of crystal sizes about the 20-22 $\mu m^2$ size bin. At 0.5 mM, 60 mins, the supersaturation was sufficient to induce nucleation, but not enough to sustain it for the duration of the residence time due to depletion of the supersaturation. The large spread of crystal size at 1 mM 60 mins might be because nucleation was continuous over the residence time, though was not sufficient to generate a crystal population that could fully occupy the cracks. When the crystals are situated in close proximity to one another along a crack, their associated depletion zones overlap, reducing their growth rates and causing them to maintain a smaller, more uniform size. At 1 mM 60 mins the isolated crystals were allowed to grow larger as they were further apart and were not competing for ions.

Vaterite had also precipitated on some of the substrates and the size and population of these crystals was quantified (Figure 75).

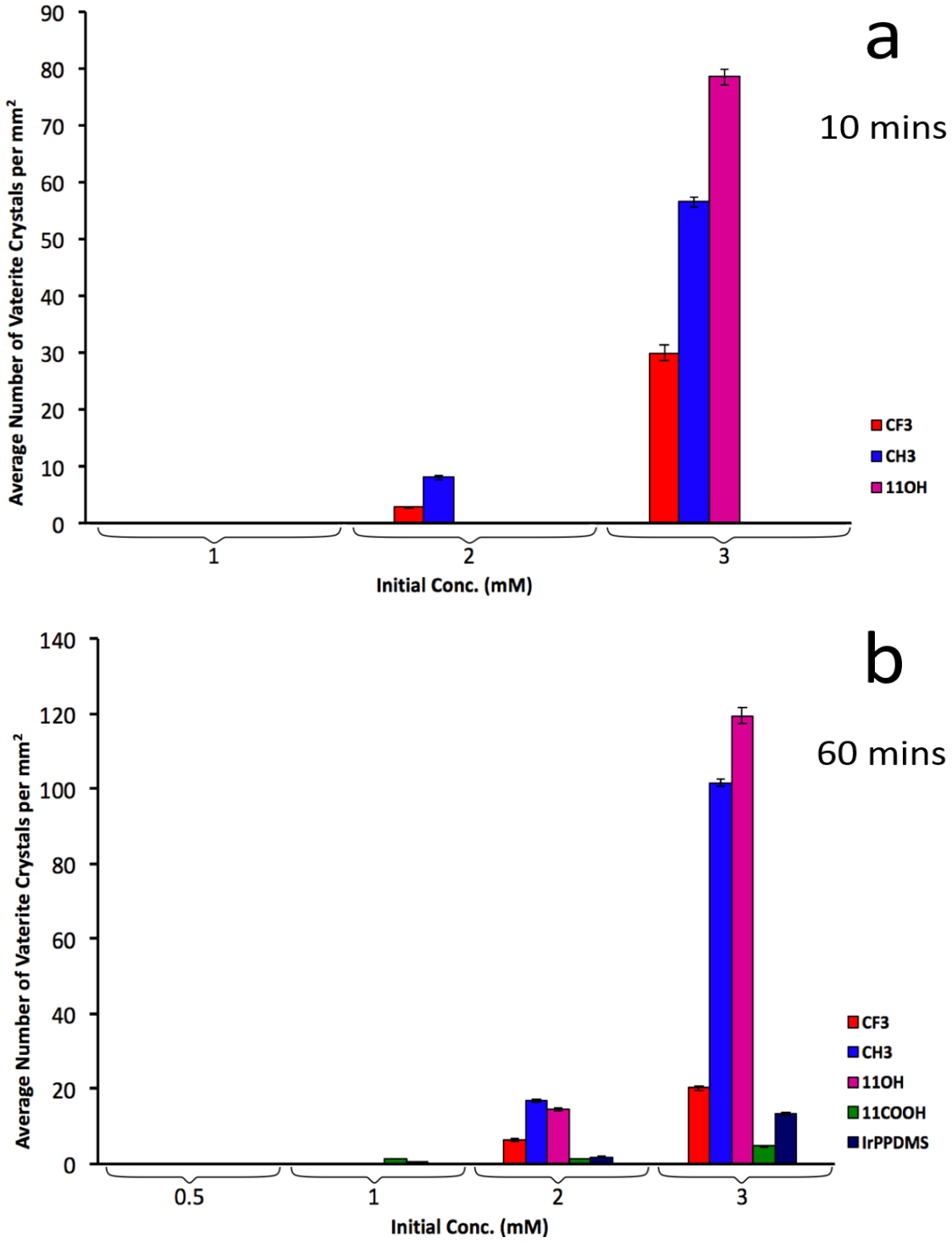


**Figure 75: Number of vaterite crystals per mm² at varying concentration after the indicated residence time**

As expected, the proportion of vaterite increased with the initial solution concentrations. Vaterite was observed on the $CF_3$ and $CH_3$ substrates after only 10 mins at 2 mM ($Population_{Vaterite,CF3,2mM,10mins}$: 2.9 ± 0.1 per mm², $Population_{Vaterite,CF3,3mM,10mins}$: 30 ± 1.5 per mm², $Population_{Vaterite,CH3,2mM,60mins}$: 8.1 ± 0.3 per mm², $Population_{Vaterite,CH3,3mM,60mins}$: 56 ± 0.9 per mm²), and at 3 mM the 11OH substrate also contained vaterite

(Population$_{Vaterite,CH3,2mM,60mins}$: 78.5 ± 1.4 per mm$^2$) (Figure 75a). The 11COOH and IrPPDMS substrate both exhibited vaterite after 60 minutes at 1 mM (Population$_{Vaterite,11COOH,1mM,60mins}$: 1.2 ± 0.1 per mm$^2$, Population$_{Vaterite,IrPPDMS,1mM,60mins}$: 0.6 ± 0.1 per mm$^2$), whilst $CF_3$, $CH_3$ and 11OH only had vaterite at 2 and 3 mM (Population$_{Vaterite,CF3,2mM,60mins}$: 6.3 ± 0.3 per mm$^2$, Population$_{Vaterite,CF3,3mM,60mins}$: 20.2 ± 0.6 per mm$^2$, Population$_{VateriteCH3,2mM,60mins}$: 16.7 ± 0.3 per mm$^2$, Population$_{VateriteCH3,3mM,60mins}$: 101.5 ± 0.9 per mm$^2$, Population$_{Vaterite11OH,2mM,60mins}$: 14.4 ± 0.3 per mm$^2$, Population$_{Vaterite11OH,3mM,60mins}$: 119.4 ± 2.1 per mm$^2$), but with a larger population at these concentrations (Figure 75b). The average vaterite crystal sizes are given below in Figure 76.

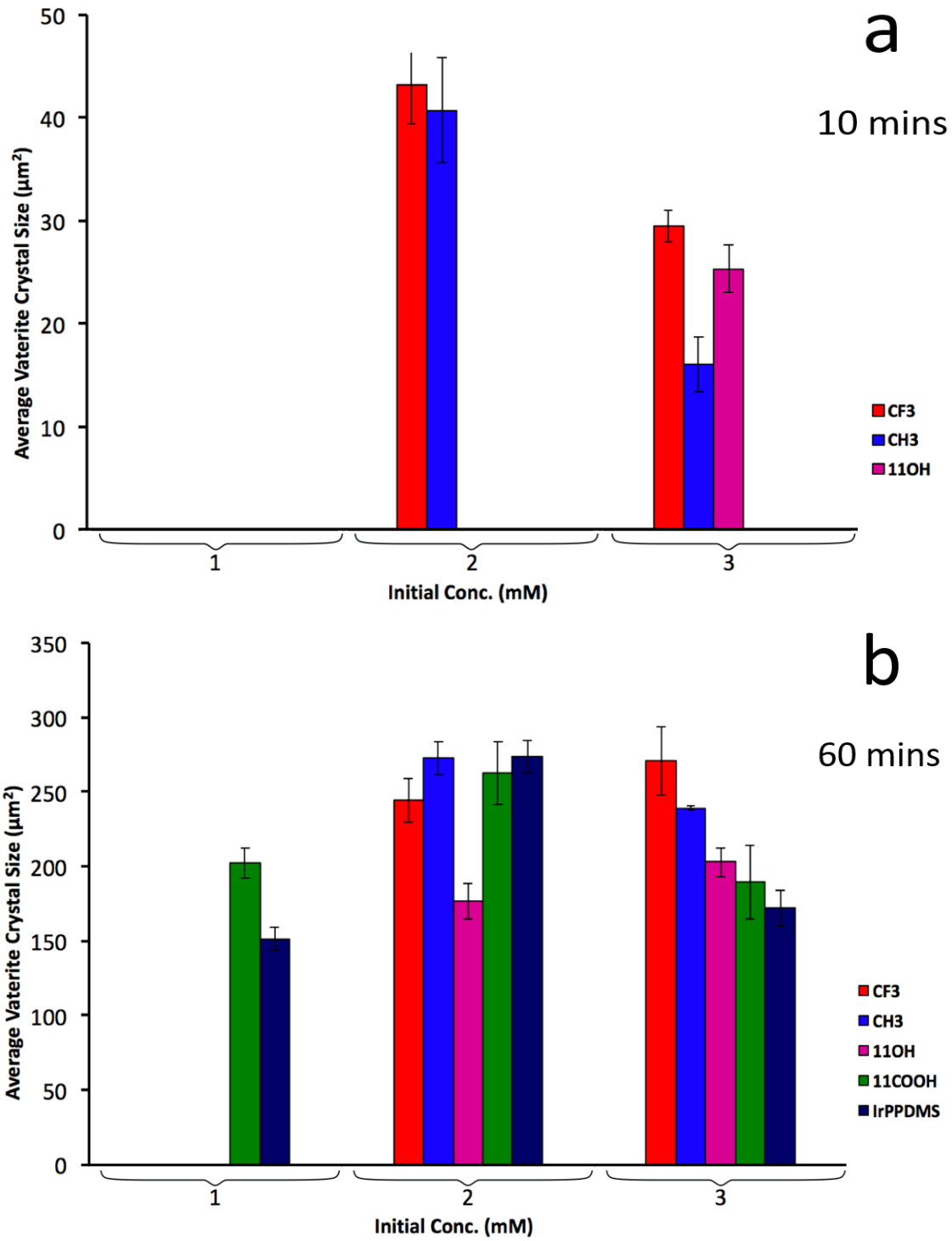


**Figure 76: Average vaterite size at varying concentration after the indicated residence time**

After 10 mins residence time, the average vaterite size is smaller for the substrates exposed to 3 mM than to 2 mM solution, with the largest crystals found on the $CF_3$ substrate (Crystal $Size_{Vaterite,CF3,2mM,10mins}$: 43.2 ± 3.8 µm$^2$, Crystal $Size_{Vaterite,CF3,3mM,10mins}$: 29.4 ± 1.5 µm$^2$) (Figure 76a). This decrease is probably due to sustained nucleation at the higher concentration, which is evident in Figure 75a. At 60 mins residence time and 2 mM initial ion concentration, the sizes of the vaterite crystals found on 11COOH, IrPPDMS and $CH_3$ substrates were similar

(Crystal $Size_{Vaterite,11COOH,2mM,60mins}$: 262.7 ± 20.7 $\mu m^2$, Crystal $Size_{Vaterite,IrPPDMS,2mM,60mins}$: 273.5 ± 11.1 $\mu m^2$, Crystal $Size_{Vaterite,CH3,2mM,60mins}$: 272.6 ± 10.9 $\mu m^2$), and all three substrates experienced a decrease in vaterite size at the higher 3 mM concentration (Crystal $Size_{Vaterite,11COOH,3mM,60mins}$: 189.2 ± 24.6 $\mu m^2$, Crystal $Size_{Vaterite,IrPPDMS,3mM,60mins}$: 172.0 ± 11.8 $\mu m^2$, Crystal $Size_{Vaterite,CH3,3mM,60mins}$: 239.3 ± 1.4 $\mu m^2$) (Figure 76b). In contrast, the vaterite crystals on the $CF_3$ and 11OH substrates increased in size from 2 mM to 3 mM (Crystal $Size_{Vaterite,CF3,2mM,60mins}$: 244.3 ± 15.0 $\mu m^2$, Crystal $Size_{Vaterite,CF3,3mM,60mins}$: 270.8 ± 22.5 $\mu m^2$, Crystal $Size_{Vaterite,11OH,2mM,60mins}$: 177.0 ± 12.0 $\mu m^2$, Crystal $Size_{Vaterite,11OH,3mM,60mins}$: 202.9 ± 9.8 $\mu m^2$), probably because Ostwald ripening had begun in both instances.

In the case of the 16COOH substrate, the vast majority of crystals were observed associated with the cracks on the substrate (79 out 52,176 were not associated with a crack; these occurred only at 2 mM and 3 mM and once there was no remaining space along the feature). However, this was not true for all substrates and so the number of crystals associated with cracks was determined. The number of crystals that were observed associated with a crack (and therefore assumed to have nucleated there) for each surface coating is shown in Figure 77. Since no crystals were observed after 1 mM, 10 minutes on any of the substrates other than 16COOH, the 10 minute bar chart only shows data for 2 and 3 mM solutions after 10 mins.

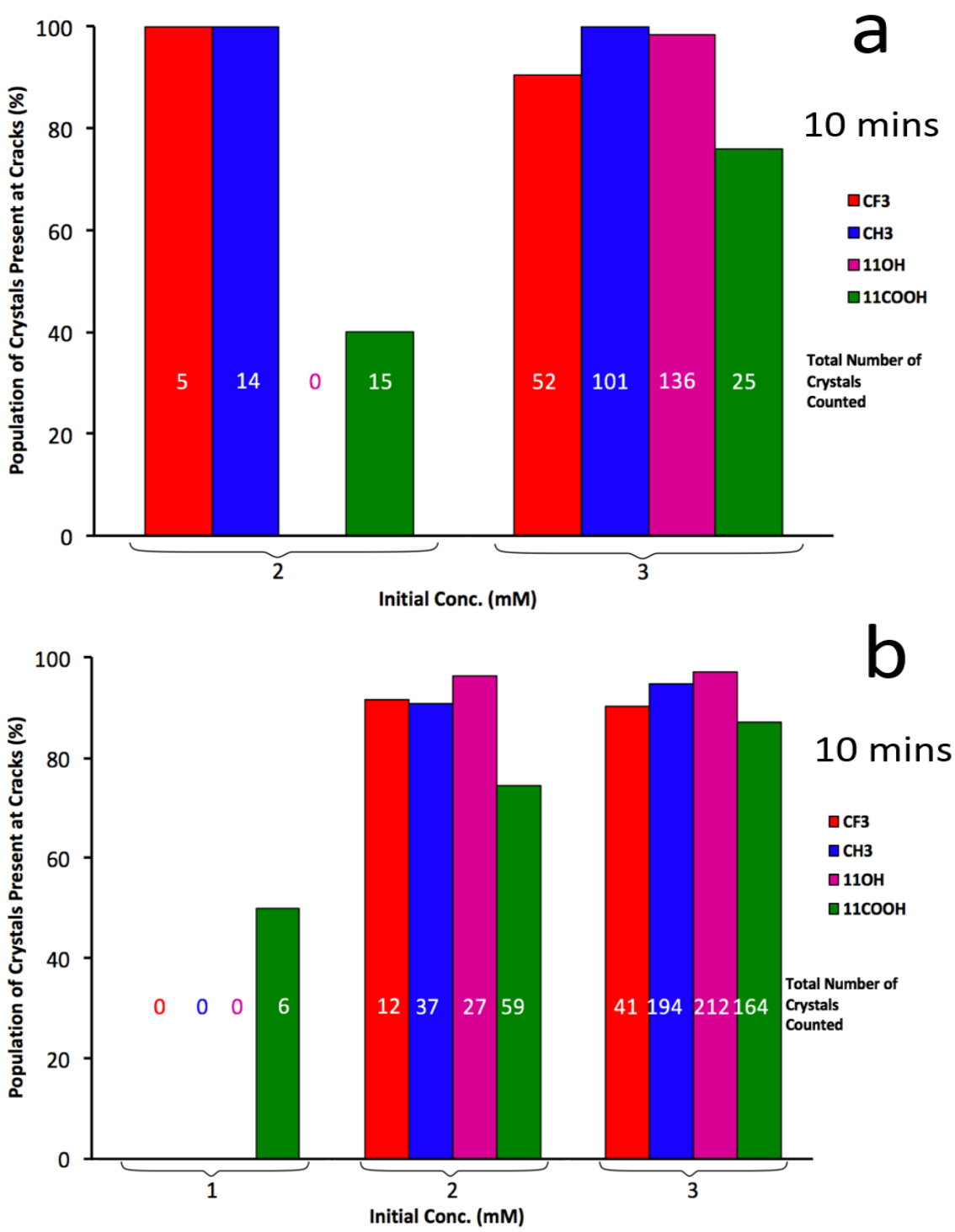


**Figure 77: Percentage of total crystal population nucleated on a surface crack at varying concentration after the indicated residence time.**

Comparing all conditions, the 11COOH substrate exhibited the lowest crystal/crack alignment as a percentage of the total crystal population, whilst the 11OH substrate, which produced mostly vaterite, demonstrated the best alignment of those substrates included in Figure 77. A significant proportion of the crystals that had precipitated on the two hydrophobic substrates, $CF_3$ and $CH_3$, also demonstrated alignment. If we compare the percentage of crystals aligned

for each of the surface modifications at 2 mM and 3 mM initial concentration, it is evident that the values are quite consistent (except for 11COOH, Figure 77b).

### 3.3.1 ImageJ Analysis Discussion

The difference in crystal/substrate interaction observed between the two carboxylate thiols can be explained by the orientation of the $COO^-$ terminal group. Simulations have suggested that the vector between oxygen atoms within a $COO^-$ group of an even parity thiol is oriented at an average inclination of $0^o$ relative to the underlying substrate (Figure 78), leading to a six-member nearest neighbour shell (Figure 79a).

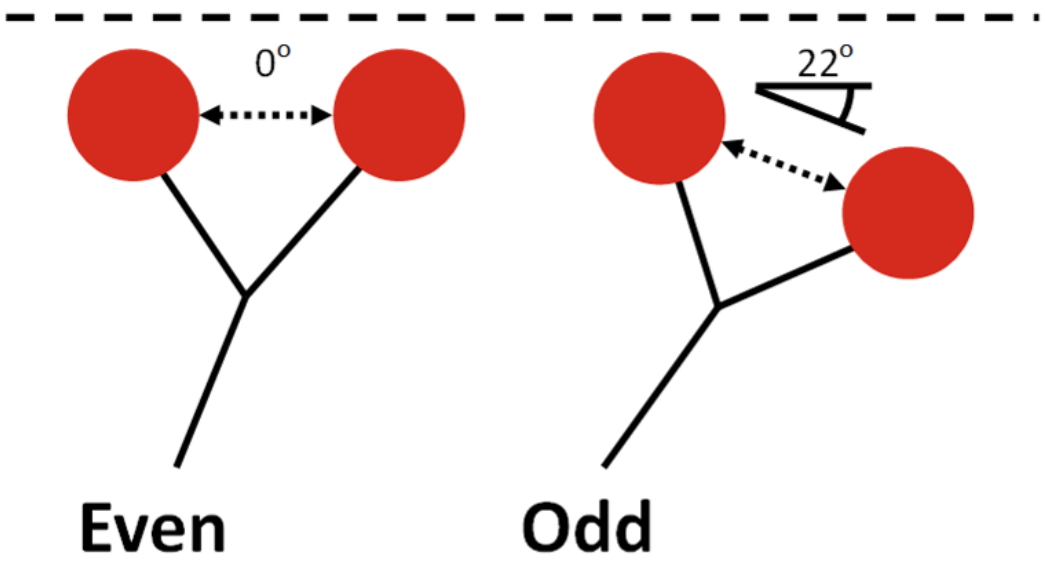


**Figure 78: Schematic of the relationship between the carbon chain parity of a thiol monomer and the terminal group orientation relative to the substrate**

Conversely, an odd parity carboxylate will have an O-O atom vector of approximately $22^o$, and as such one of the oxygen atoms will be contained within the plane of the monolayer, as opposed to pointing out into the solution. When two oxygen atoms on adjacent monomers point towards one another, Coulombic repulsion will push them apart. This interaction will momentarily disrupt the hexagonal shell, causing a 5 + 1 arrangement (Figure 79) [1].

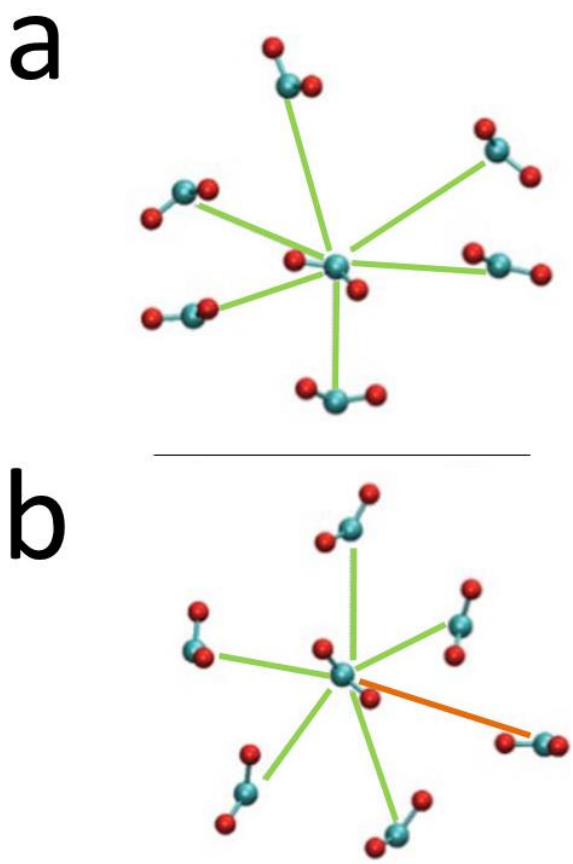


**Figure 79: Snapshot from simulations carried out by Hu *et al***

Research has suggested that this disorder contributes towards a higher free energy barrier for 11COOH as compared to 16COOH, where this could be the explanation for the difference in crystal populations observed here [2]. With regards to the 16COOH SAM, an O-O vector that is parallel to the substrate surface would result in a greater charge density compared to the 11COOH SAM and so one could expect a larger number of interactions per unit area between the terminal groups and the $Ca^{2+}$ ions of the solution/SAM interface. A low free energy barrier to nucleation would be accompanied by more successful nucleation events and therefore, a greater crystal population after a set period of time. The fact that the crystal population on the 16COOH substrates was significantly larger than on any other substrate after a residence time of both 10 and 60 mins suggests that the free energy barrier is smaller than those associated with the other substrates (Table 9). A larger nucleation rate at a defined supersaturation suggests a smaller effective interfacial energy and a smaller critical nucleus size for the crystal/substrate system [3].

Under the conditions studied here, the carboxylic acid groups would be deprotonated [4] and would therefore possess a negative charge. As mentioned above, the orientation of these

terminal groups would determine their interaction with calcium ions. The 16COOH SAM, with its better oriented array of functional groups, would induce a $Ca^{2+}$ rich stern layer, allowing direct nucleation of calcite, whilst the stern layer of the disordered 11COOH would contain fewer $Ca^{2+}$ ions and a very different charge distribution.

Studies elsewhere have suggested that the Stern layer plays an important role in determining calcium carbonate polymorph selectivity at surfaces [5], but also the degree of organisation of the monolayer, with highly disordered monolayers favouring the metastable phases [5-9]. In the present study, vaterite occurs as the dominant polymorph on the 11OH, $CH_3$ and $CF_3$ substrates (Figure 71). At the solution pH of the precipitation experiments, these three monolayers would be neutral in charge, and so co-ion/counter-ion ordering adjacent to the monolayer would be limited. Few calcite crystals were observed on these substrates under any condition (Figure 72). The lack of a highly ordered Stern layer could possibly play a role in selecting polycrystalline vaterite over calcite as the dominant polymorph. This idea is supported by the small fraction of vaterite observed on the 11COOH substrate (Figure 75), which would also lack a highly ordered Stern layer due to its 5 + 1 arrangement of monomer terminal groups.

Reports in the literature suggest that 11OH SAMs and 11COOH SAMs promote the formation of ACC at the SAM/liquid interface [2, 10-12] and dissolution-reprecipitation phase transformations have been observed for ACC to vaterite [13, 14]. The substrates that yield vaterite could be retarding the transformation to calcite; it is likely that if left in solution for an extended period of time, calcite would be the dominant polymorph. These observations are supported by data in Sections 2.5.3.3 and 2.5.3.8 of Chapter 2. Substrates crystallised on using the ammonia diffusion method produced vaterite at low [$Ca^{2+}$], and substrates that have undergone a thiol exchange yield vaterite in large quantities at the cracks. In both of these instances, a greater proportion of carbonate ions relative to calcium would be expected at the SAM solution interface, and therefore a Stern layer deficient in $Ca^{2+}$ compared to that of a 16COOH substrate crystallised on via direct mixing. However, further analysis is required to confirm this.

No crystals were present on the 11OH substrate after 1 mM 10 mins, 2 mM 10 mins and 1 mM 60 mins (Figure 72). The formation of a $CaCO_3$ phase from a supersaturated solution through heterogeneous nucleation involves the replacement of a substrate/solution interface with a

calcium carbonate/solution interface. The net surface free energy of the growing nuclei can be written as Equation 20 [15].

$$\boldsymbol{\alpha_{het} = \alpha_{nuc/sol} + h(\alpha_{nuc/sub} - \alpha_{sub/sol})} \qquad \text{Equation 20}$$

where h is a shape factor and $\alpha_{x/y}$ are the interfacial energies. According to this equation, a substrate that would inhibit calcium carbonate precipitation would be one that is hydrophilic (low $\alpha_{sub/sol}$), and therefore forms strong bonds with water, but must also not form strong bonds with the precipitating material (high $\alpha_{nuc/sub}$). The 11OH substrate satisfies both of these requirements. The polarity of the OH bond, brought about due to the difference in electronegativity between the oxygen and hydrogen atoms (3.44 and 2.20, respectively [16]), and the fact that hydroxy groups and water are $sp^3$ hybridised [17] and thus share similar structures, causes hydrogen bonds to form between the 11OH substrate surface and the water molecules. The formation of these hydrogen bonds would be more favourable than interactions between the OH groups and the $Ca^{2+}$ or $CO_3^{2-}$ ions. This would result in a comparatively long induction time (hence why no crystals at 1 mM, 10 mins and 2 mM, 10 mins). A smaller critical nucleus is associated with a higher supersaturation, and therefore a reduced nucleus/substrate contact area and enhanced nucleation rate, which is why crystals were observed at both 3 mM residence times.

## 3.4 Summary

The present work has demonstrated that it is possible to promote precipitation at surface features and simultaneously control the polymorphism through surface modification. Negatively charged monolayers produce calcite as the dominant polymorph and neutral substrates yield vaterite. The greatest crystal/feature alignment and population was observed on the monolayer which, as indicated in the literature, forms the strongest interactions with the calcium carbonate crystals: 16-mercaptohexadecanoic acid. The neutral, OH substrate caused vaterite to precipitate, which also exhibited good alignment with the cracks.

## 3.5 References


1. Freeman, C.L., et al., *Surface selectivity of calcite on self-assembled monolayers.* The Journal of Physical Chemistry C, 2013. **117**(10): p. 5154-5163.
2. Hu, Q., et al., *The thermodynamics of calcite nucleation at organic interfaces: Classical vs. non-classical pathways.* Faraday Discussions, 2012. **159**(1): p. 509-523.
3. Li, Q., et al., *Interfacial energies for heterogeneous nucleation of calcium carbonate on mica and quartz.* Environmental science & technology, 2014. **48**(10): p. 5745-5753.
4. Garcia-Manyes, S., G. Oncins, and F. Sanz, *Effect of Ion-Binding and Chemical Phospholipid Structure on the Nanomechanics of Lipid Bilayers Studied by Force Spectroscopy.* Biophysical Journal, 2005. **89**(3): p. 1812-1826.
5. Popescu, D.C., et al., *Template Adaptability Is Key in the Oriented Crystallization of CaCO3.* Journal of the American Chemical Society, 2007. **129**(45): p. 14058-14067.
6. Lee, I., et al., *Formation of patterned continuous calcium carbonate films on self-assembled monolayers via nanoparticle-directed crystallization.* Advanced Materials, 2002. **14**(22): p. 1640-1643.
7. Fricke, M., et al., *Vaterite Polymorph Switching Controlled by Surface Charge Density of an Amphiphilic Dendron-calix[4]arene.* Crystal Growth & Design, 2006. **6**(5): p. 1120-1123.
8. Küther, J., et al., *Mercaptophenol-Protected Gold Colloids as Nuclei for the Crystallization of Inorganic Minerals: Templated Crystallization on Curved Surfaces.* Chemistry of Materials, 1999. **11**(5): p. 1317-1325.
9. Küther, J., et al., *Templated Crystallisation of Calcium and Strontium Carbonates on Centred Rectangular Self-Assembled Monolayer Substrates.* Chemistry–A European Journal, 1998. **4**(9): p. 1834-1842.
10. Nielsen, M.H., et al., *Structural evolution, formation pathways and energetic controls during template-directed nucleation of CaCO 3.* Faraday Discussions, 2012. **159**(1): p. 105-121.
11. Han, Y.J., et al., *Template-dependent morphogenesis of oriented calcite crystals in the presence of magnesium ions.* Angewandte Chemie, 2005. **117**(16): p. 2438-2442.
12. Aizenberg, J., et al., *Direct fabrication of large micropatterned single crystals.* Science, 2003. **299**(5610): p. 1205-1208.
13. Nielsen, M.H., S. Aloni, and J.J. De Yoreo, *In situ TEM imaging of CaCO3 nucleation reveals coexistence of direct and indirect pathways.* Science, 2014. **345**(6201): p. 1158-1162.
14. Pouget, E.M., et al., *The development of morphology and structure in hexagonal vaterite.* Journal of the American Chemical Society, 2010. **132**(33): p. 11560-11565.
15. Mullin, J.W., *Crystallization*. 2001: Elsevier Science.
16. Haynes, W.M., *CRC Handbook of Chemistry and Physics, 95th Edition*. 2014: CRC Press.
17. Atkins, P. and J. de Paula, *Atkins' Physical Chemistry*. 2010: OUP Oxford.

# 4 Control of Crystallisation through the use of Layered Materials

## 4.1 Introduction

### 4.1.1 Aims and Overview

In this chapter, surface topographies generated by the spin coating of carbon nanostructures onto silicon wafers and their effect on the heterogeneous crystallisation of calcium carbonate were investigated. The materials explored were carbon nanotubes, carboxylated-carbon nanotubes, graphene oxide and reduced-graphene oxide (rGO). Only the latter formed a sufficiently adhesive surface coating that allowed it to remain on the substrate for the duration of the experiment, and it was also this that produced an unexpected, interesting result. It was found that when the rGO was spin coated onto a silicon wafer and submerged in a solution supersaturated with respect to calcium carbonate, the metastable phase aragonite would form on the substrate surface, and in vast quantities compared to an uncoated, control wafer. Aragonite can be produced through the addition of soluble chemicals, and no other surface coating presented in the literature has been as effective at producing this polymorph. As such, this surface coating was investigated further. To determine if this observation was unique to the rGO provided by this supplier, material purchased from a commercial supplier was also investigated. Again, aragonite was the dominant polymorph observed on the substrate. To identify if the presence of impurities was the cause, a number of experiments were conducted. Energy-dispersive X-ray analysis revealed that both samples were contaminated with transition metals, and thermogravimetric analysis suggested that approximately 4 mass% was composed of inorganic impurities. However, crystallisation in the presence of the isolated impurities failed to produce aragonite. X-ray photoelectron spectroscopy indicated that the samples were oxidised to different extents, and using Raman spectroscopy it was possible to calculate the average domain size of the $sp^2$ carbon clusters. Dropcasting was investigated as an alternative method of forming the surface coating. This technique generates a very different surface topography to spin coating. Interestingly no aragonite was produced on a wafer that had been coated using this method. Free-floating rGO flakes and a surface coating formed from agglomerated rGO also

failed to cause aragonite to form. Each of these experiments suggest that it was a topographical effect that was promoting aragonite precipitation. Further experiments aimed to determine if this was unique to rGO spin coated wafers, and so surface coatings formed from other layered materials were investigated. However, these experiments were inconclusive as the materials provided by the suppliers were of poor quality and ultrasonication failed to delaminate the agglomerations. Finally, an experiment is described in which wedges were formed between graphitic flakes and a silicon wafer. After calcium carbonate crystallisation, calcite crystals were often observed at these structures, providing further evidence that topographies formed using graphitic materials can indeed influence crystallisation.

## 4.1.2 Background

### 4.1.2.1 Graphene/GO

Prior to the 1960's, only two carbon allotropes were known, including their polymorphic modifications: graphite and diamond [1]. The discovery of the remaining allotropes of carbon that we are aware of today and the associated materials facilitated the emergence and realisation of nanotechnology. A number of landmark events in the discovery of carbon allotropes (carbon nanotubes, fullerenes and graphene [2]) can be identified. In 1960, Bacon successfully synthesised carbon tubes with graphite layer structures (termed 'graphite whiskers') [3], in 1980 the first carbon nanotubes were observed by Iijima [4] and in 1985, Harry Kroto *et al* detected $C_{60}$ in the mass spectrum of laser-evaporated graphite [5]. By the early 21$^{st}$ century, forty years after carbon tubes were first discovered, large scale production of single walled carbon nanotubes (SWNT) was possible [6], as well as the formation of ordered single crystals of SWNT's of micron sizes [7]. In 2004, Andre Geim and Konstantin Novoselov released their seminal paper on the isolation of graphene, and this two-dimensional crystal became the focus of much attention due to its many exceptional properties [8]. Incredibly, at the time of writing, this paper has over 34,000 citations.

Few material discoveries have excited the scientific community as much as graphene. Before its discovery, it was confined to the abstract realm, existing initially as a starting point for understanding the electronic properties of graphite and later as a suitable condensed matter model for (2+1)-dimensional quantum electrodynamics [9]. For many years, physicists and chemists agreed that 2-dimensional crystals could not exist, the belief fortified by theory and

a collection of empirical data. Two-dimensional crystals were perceived as thermodynamically unstable, as it had been shown that as the number of atomic layers of a 3D material decreased, the melting point rapidly declined until, at a thickness typically well above a single monolayer, the film would decompose and segregate into islands [10]. The isolation of graphene and since then, other two-dimensional materials, has opened up a new exciting field of research that promises to effect change in a range of disciplines. Graphene can be considered as a large aromatic molecule [11] and is a densely packed monolayer of $sp^2$ hybridised carbon atoms arranged in a honeycomb lattice. Strictly from a topological viewpoint, it forms the most basic unit from which all other graphitic materials can be constructed. As shown in Figure 80, it can be wrapped-up to form a fullerene, rolled to produce a carbon nanotube, or stacked to give graphite [12].

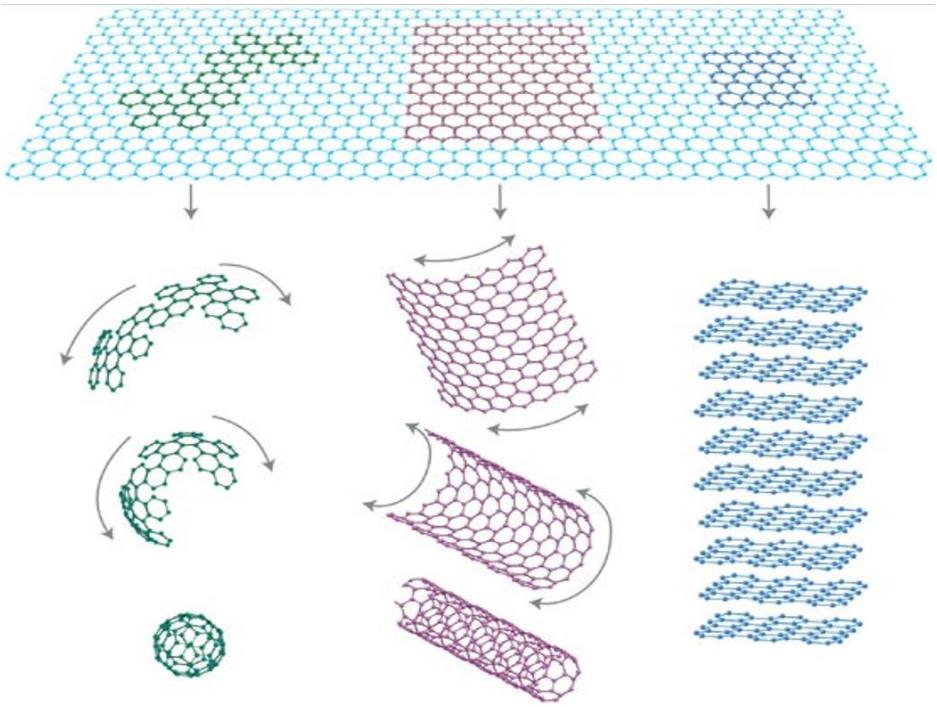

**Figure 80: Schematic indicating the relationships between graphene and other graphitic materials**

A layer of graphene is extraordinarily thin, at only 0.345 nm thick [13]. An individual carbon atom shares σ-bonds with each of its three neighbours ($l_{c-c}$ = 1.42 Å) and also possesses a π-bond oriented out of the plane. These π-bonds become hybridised together to form the π-band and π*-band. It is these bands that endow graphene with its interesting electronic properties [14], including a pronounced ambipolar electric field effect and quantum Hall effect, both of which are beyond the scope of this document (for further reading, see [15-20]).

As graphene is composed of strongly bonded light atoms, vibrational conduction in-plane is exceptional, such that graphene has remarkably high thermal [21] and acoustic conductivity [22]. Both of these properties have been investigated extensively [21, 23-30].

Although isolated graphene has only been accessible for 12 years, it has found a number of applications, with many more predicted. Its large surface area and high electrical conductivity have lead it to be used in super capacitors [31-37], and its novel electron-hole symmetric band structure and high carrier mobility/thermal velocity makes it suitable for field-effect transistors [38-44]. Graphene-based materials have also been investigated for water remediation via the adsorption of hazardous materials [45, 46] and photocatalysis [47, 48], for the removal of atmospheric pollutants via gas adsorption and gas phase separation [49-54], and also in perhaps more unexpected applications, such as in radio-frequency communications [55], chemotherapy [56-60], drug delivery [61-64] and biosensors [65-70].

Aside from the mechanical exfoliation method that Geim and Novoselov used, there are a number of different ways in which graphene and its related compound graphene oxide (which contains a range of reactive oxygen groups, including epoxy, carboxylic acid and hydroxyl functionalities [71]) can be synthesised. Their method of mechanical exfoliation of graphene involved baking highly-oriented pyrolytic graphite flakes into the surface of a photoresist and then repeated delamination of the graphite through the use of scotch tape [8]. The thin flakes were then released in acetone and then a silicon wafer with a 300 nm $SiO_2$ surface layer was dipped into the solution. On removal, some of the flakes adhered to the surface of the wafer and the largest were removed by sonication in propanol. Identification of graphitic flakes with thicknesses less than 50 nm was possible using optical microscopy due to the added optical path that shifts the interference colours of the wafer (Figure 81).

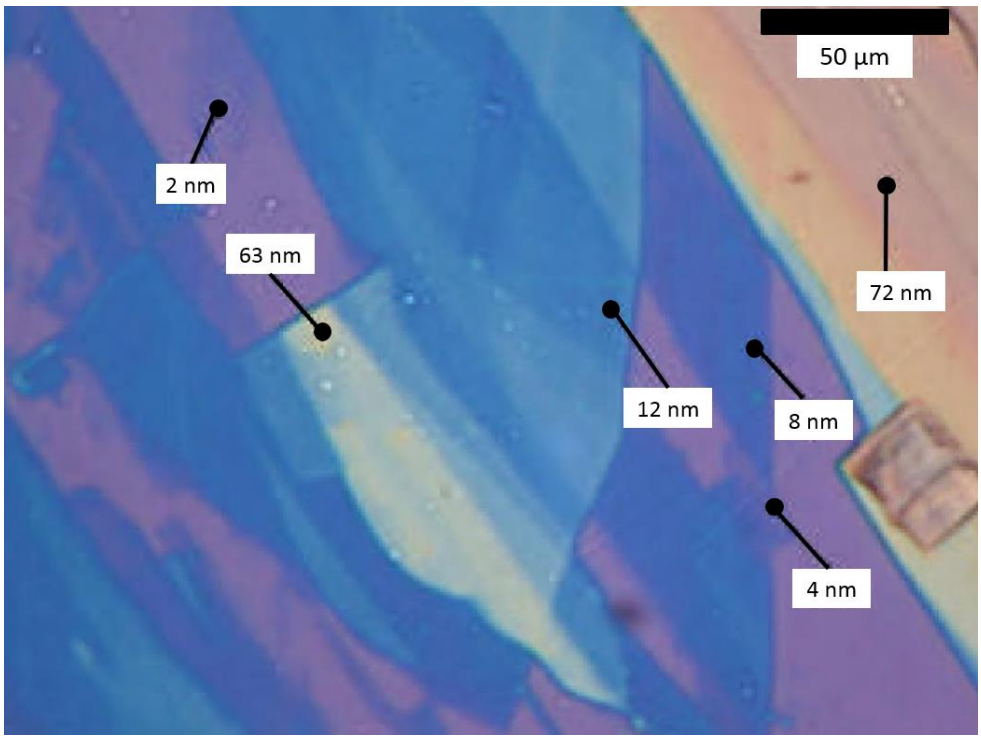


**Figure 81: The 'colour reference' used by Geim and Novoselov to estimate the thickness of graphitic flakes**

Flakes with thicknesses less than 1.5 nm are invisible in the optical microscope, though are visible in the SEM. Therefore, to identify flakes thinner than 1.5 nm, SEM micrographs must be compared with optical micrographs to identify material that can be seen in the former, but not in the latter. Finally, to determine whether or not the candidates are few-layer graphene or single layer graphene, atomic force microscopy is used. The primary problem with the synthetic route used by Geim and Novoselov was the scalability and yield [13], therefore inhibiting its use in industry or for research that requires considerable material. Hence, a method to produce significant quantities of high quality graphene became a hot topic of research [72]. There have been a number of attempts over the years, including heating a mixture of calcium carbonate and magnesium powder to high temperatures [73], the simultaneous exfoliation and reduction of graphite oxide to graphene via detonation [74], and 'unzipping' carbon nanotubes [75-77]. However, the most successful method was developed by Ruoff *et al* in 2006, which involved the modification of the Hummer's method and permitted the synthesis of large quantities of graphene [78]. Today, this is the most commonly used synthetic route for obtaining considerable amounts of graphene (referred to as reduced graphene oxide, rGO, via this and similar methods) where the overall crystal quality is not of main concern [79], for example in conductive inks/paints, battery electrodes and for some types of sensor [80]. The oxidation/reduction procedure results in alteration of the basal plane

of graphene in the form of defects and broken symmetry, though some groups suggest that nonconjugated $sp^3$ carbon constitutes most of the defects, with only a small fraction caused by residual oxygen species [81, 82]. However, high-resolution TEM has discounted this theory and revealed that the basal plane of rGO is decorated with regions of $sp^2$ carbons, amorphous oxidised ($sp^3$) carbons, and even holes that disrupt the continuity of the sheet. A more detailed account of the structure of rGO is given in the General Discussion (Section 4.4). When high quality graphene is required, for example in complementary metal-oxide semiconductor research, substrate-based methods are used. Chemical vapour deposition and epitaxial growth of graphene provides a distinct advantage over solution-based synthesis and exfoliated graphene in that the graphene can be produced on a prepatterned substrate, allowing electrical contacts to be formed between the film and the features of the surface [83].

The research presented here is primarily concerned with the use of reduced-graphene oxide as a surface topography modifier on a silicon substrate. The details of the experimental procedures used are provided in the following section.

## 4.2 Experimental Methods

The Experimental Methods section contains information regarding the methodologies used to carry out the investigations into the formation of aragonite on a silicon wafer spin coated with rGO. The initial materials were provided by a colleague at Sichuan University. These, alongside the rGO that was purchased from elsewhere as a comparison, are described in Section 4.2.1. Section 4.2.2 lists the other layered materials that were investigated as surface coatings due to their structural similarity to rGO. Section 4.2.3, General Substrate Preparation describes the process used for forming the dispersions and then applying them to the silicon substrates. Dropcasting was investigated as an alternative to spin coating and this methodology is described in Section 4.2.3.2. In another set of experiments, the rGO that consistently produced the greatest proportion of aragonite was washed in order to remove as many of the contaminants as possible. Section 4.2.3.3 describes this. Finally, there is a section that describes the analytical techniques that are unique to this chapter and how they were carried out. These are energy-dispersive X-ray analysis, thermogravimetric analysis, X-ray photoelectron spectroscopy and Raman spectroscopy.

### 4.2.1 Materials for Carbon Nanostructures Experiments

The carbon nanostructured materials that were investigated as surface coatings are described below. These were:

- CNT: Carbon nanotubes (length = approx. 100 μm, diameter = approx. 50 nm). Supplied by Sichuan University.
- CNTCOOH: COOH-functionalised carbon nanotubes (length = approx. 2 μm, diameter = 10 nm). Supplied by Sichuan University.
- GO: Graphene oxide (diameter = 3 μm, thickness = 3 nm). Supplied by Sichuan University.
- gG rGO: Reduced-graphene oxide (average diameter = 3 μm, thickness = 3 nm). Supplied by Sichuan University.
- TN rGO: Reduced-graphene oxide (diameter = 0.5 - 3 μm, thickness = 0.7 - 3 nm). Supplied by Timesnano.

Each of these materials were made into dispersions in Millipore water. The concentration used for each one was 0.1 mg/ml. Initially, polyvinylpyrrolidone was used as a dispersant. In later

experiments, to ensure that PVP was not affecting the crystallisation results, dispersions were made without a dispersant (where stated).

### 4.2.2 Other Layered Materials

The rGO's provided by Sichuan University and Timesnano had produced some interesting results, and so to test if this was unique to these materials, other compounds with a similar structure were also investigated. These were:

- Molybdenum disulphide (Sigma-Aldrich, 6 µm width in plane).
- Tungsten disulphide (Sigma-Aldrich. 2 µm width in plane).
- Graphitic carbon nitride (Fairland Technology. 30 um width in plane).

Dispersions of each were made using Millipore water (no dispersant), at concentrations of 0.1 mg/ml.

### 4.2.3 Substrate Preparation

#### 4.2.3.1 General Substrate Preparation

The general substrate preparation methodology described here was used for all experiments in which spin coating was involved. A Si (100) wafer was cut into 10 x 10 mm squares using a diamond pen. These were rinsed repeatedly with water, then ethanol, and then sonicated in water for 5 mins to remove silicon fragments from the cutting process. Next, the surface was thoroughly cleaned using fine tipped cleanroom swabs and alternating washes of ethanol and acetone. These were then placed into clean glass petri dishes and exposed to 300 $^{o}$C in a Nabertherm P300 furnace for two hours. The wafer pieces were kept in the furnace afterwards to allow them to cool gradually, but were not removed until required (to reduce contamination from air particulates). Prior to use, the dispersions were sonicated (unless otherwise stated) in a 20 ml glass vial using a sonication probe (Bandelin HD 2200 and titanium flat tip with Sonopuls controller set on 44% power) for 2 minutes. The vial containing the dispersion was semi-submerged in an ethanol/dry ice bath to reduce the heating effect of the sonication process. When needed, individual substrates were removed from the furnace (after cooling to room temperature) and placed onto a Chemat Technology KW4-A spin coater using an aluminium 8 mm grooved vacuum chuck (Pi-Kem Ltd). 300 µl of the selected dispersion was then pipetted onto the surface. The spin program involved an initial spin at 400 rpm for 9 seconds, then 2000 rpm for 60 seconds. After coating, the substrates were heated in the

furnace at 300 $^{o}$C for two hours, allowed to cool to room temperature, and then used as is for crystallisation studies. Substrates were always used the day they were produced to reduce contamination and for consistency. A direct mixing method was used for crystallisation, as described in Chapter 2, where the crystallisation conditions were $[Ca^{2+}] = [CO_3^{2-}] = 1$ mM, residence time = 60 mins.

#### 4.2.3.2 Dropcast Coating Formation

In order to examine if the surface topography formed via spin coating of the rGO's onto a silicon wafer was necessary for aragonite to form, an alternative method of forming a surface coating was used. This was achieved using dropcasting, which is a very simple procedure. After sonication for 2 mins using the probe sonicator as described in the General Substrate Preparation section, 300 µl of the gG suspension was pipetted onto the surface of a silicon wafer. This was placed into a furnace at 60 $^{o}$C for 45 mins until the water had evaporated. A circular deposit of material was left behind on the surface. In order to be consistent with the spin coating procedure, the temperature was increased to 300 $^{o}$C for two hours and then allowed to cool gradually to room temperature. The substrate was used as is for crystallisation.

#### 4.2.3.3 Washing of gG rGO

In an attempt to remove as many of the contaminants as possible in the gG rGO sample, it was washed thoroughly. This was done by vacuum filtration with a 220 nm pore size membrane. Firstly, the vacuum was turned on and ethanol was added to the Büchner funnel to wet the membrane. The vacuum was then turned off, ethanol was added (about 100 ml) and then 10 mg of the gG rGO was introduced. The vacuum was turned on, the ethanol was reduced in volume to a third, and then 150 ml of Millipore water was added. Each time the liquid was again reduced to a third in volume, it was topped up with 150 ml of Millipore water. This process was repeated until a litre of Millipore water had been washed through, then all of the water was allowed to evacuate the flask. Next, the material was washed thoroughly with ethanol, ensuring that all of the material was removed from the walls of the flask and was on the membrane. After this, the membrane was removed and the rGO was placed into a glass vial and warmed in the oven at 80 $^{o}$C for five hours to remove as much surface-associated liquid from the washing procedure as possible. This was necessary as a TGA analysis was carried out without the drying step, and 90% of the mass loss occurred before 150 $^{o}$C,

indicating that a lot of water was present in the sample. Once removed from the furnace, the material was ready for use.

#### 4.2.3.4 Mechanical Exfoliation of Graphite for Graphitic Flakes on Silicon

At the end of this chapter is included a piece of research conducted at the start of my PhD. Here, instead of spin coating the graphitic flakes onto the silicon wafer, they were applied using a mechanical exfoliation technique similar to that used by Novoselov and Geim.

Mechanical exfoliation of a layered material is a simple procedure that involves the repeated separation of the lamellae. Here, a slightly modified version was used to delaminate graphite. "Flaggy flakes" (chemically cleaned natural graphenium flakes with a carbon content in the range of 99-99.9%) with a diameter of 30 mm were obtained from NGS Natugraphit GmbH and acted as the source for the graphitic flakes of the experiment. A flaggy flake was pressed against a gloved finger that had been wrapped in Scotch tape. Separately, a long strip of scotch tape (approx. 100 cm) was secured to a flat surface, sticky-side up. Starting at one end of this strip, the flake was repeatedly cleaved between the pieces of scotch tape, progressing towards the other end of the strip such that the flake was not pressed in the same location twice. This was repeated at least 150 times, until visual inspection of the tape that was wrapped around the finger appeared sparsely populated with material. This was then pressed against a (100) Si wafer, applying the graphitic material to the surface. Initially, crystallisations were performed using these substrates as-is, but visual inspection in the SEM revealed residual glue on the wafer surface. This was removed in further experiments to ensure that it wasn't interfering with the crystallisation data. The removal involved placing the wafers, after deposition of the graphitic material, into a furnace at 300 $^{o}$C for two hours. This would eradicate any organic glue residue by thermal decomposition.

### 4.2.4 Analytical Techniques

In order to characterise the morphology and chemistry of the rGO's, a number of analytical techniques were used. These are described in the following section.

#### 4.2.4.1 Energy-Dispersive X-ray Analysis (EDXA)

The EDXA was carried out using the same scanning electron microscope as that used for imaging (FEI Nova NanoSEM 450 with Amatek Materials EDAX attachment for EDXA). The analysis involved the rGO provided by Sichuan University (sample referred to as gG) and from Timesnano (sample referred to as TN). For sample preparation, the graphene was drop cast

onto the silicon wafer, so that sufficient material was present to form a thicker layer than that possible by spin coating. This was placed in the furnace for 2 hours at 300 $^{o}$C. Using this methodology it was not possible to generate a strong enough signal from the sample for EDX analysis, so an alternative preparation procedure was used. Again, the material was dropcast onto the silicon wafer, though this time water from the suspension in the dropcast droplet was removed from the surface by heating the wafer to 60 $^{o}$C in the furnace for 45 mins. This step was repeated multiple times until a thick layer of material had been deposited on the wafer surface. Finally, the wafer was heated in the furnace at 600 $^{o}$C for six hours. This caused the decomposition and removal of the graphitic material from the wafer surface, leaving behind only the inorganic contaminants, which could now be analysed using EDX. The SEM high voltage was set to 30 kV and multiple point analyses on each of the graphene samples was carried out, as well as EDX mapping.

#### 4.2.4.2 Thermogravimetric Analysis (TGA)

TGA was carried out using a TA Instruments Q600 SDT in air. The rGO was placed in an alumina crucible and heated at a rate of 10 $^{o}$C/min from room temperature to 900 $^{o}$C. The mass (mg) and derivative mass% (%/$^{o}$C) were plotted against the temperature. By plotting the derivative mass, it is possible to see the mass loss steps that occur on heating, which can then be assigned to thermal decompositions or removal of surface water/gases.

#### 4.2.4.3 X-ray Photoelectron Spectroscopy (XPS)

XPS spectra were obtained using a Thermo Scientific ESCA Lab 250 with a chamber pressure maintained below 1 x $10^{-9}$ mbar during acquisition. A monochromated Al K-alpha X-ray source (15 kV, 150 W) irradiated the samples, with a spot diameter of approximately 0.5 mm. The spectrometer was operated in Large Area XL magnetic lens mode using pass energies of 150 and 20 eV for survey and detailed scans, respectively. All of the spectra were obtained with an electron take off angle of 90° and a step size of 0.1 eV. High resolution spectra were fitted using CasaXPS peak fitting algorithms.

#### 4.2.4.4 Raman Spectroscopy

The Raman measurements were conducted using a Renishaw InVia with a laser excitation wavelength of 514 nm. The measurements were run at 5% laser power, with a 20 second acquisition time, running 5 accumulations.

## 4.3 Results/Discussion

### 4.3.1 Carbon Nanostructures: Formation of Surface Coatings and Crystallisations of Calcium Carbonate

Materials provided by Sichuan University were investigated as surface coatings on silicon wafers where their effects on the heterogeneous nucleation of calcium carbonate were determined. The supplied samples were labelled as carbon nanotubes (CNT), COOH-functionalised carbon nanotubes (COOHCNT), graphene oxide (GO), and reduced-graphene oxide (gG). Each was dispersed in Millipore water, with PVP used as a dispersant and spun onto a silicon substrate. SEM micrographs were taken of the substrates before and after crystallisation to inspect the film formation and the effects of the surface coating on calcium carbonate nucleation and growth. The CNT dispersion had formed an incomplete film on the surface of the wafer, though agglomerations of CNT's could also be seen (Figure 82).

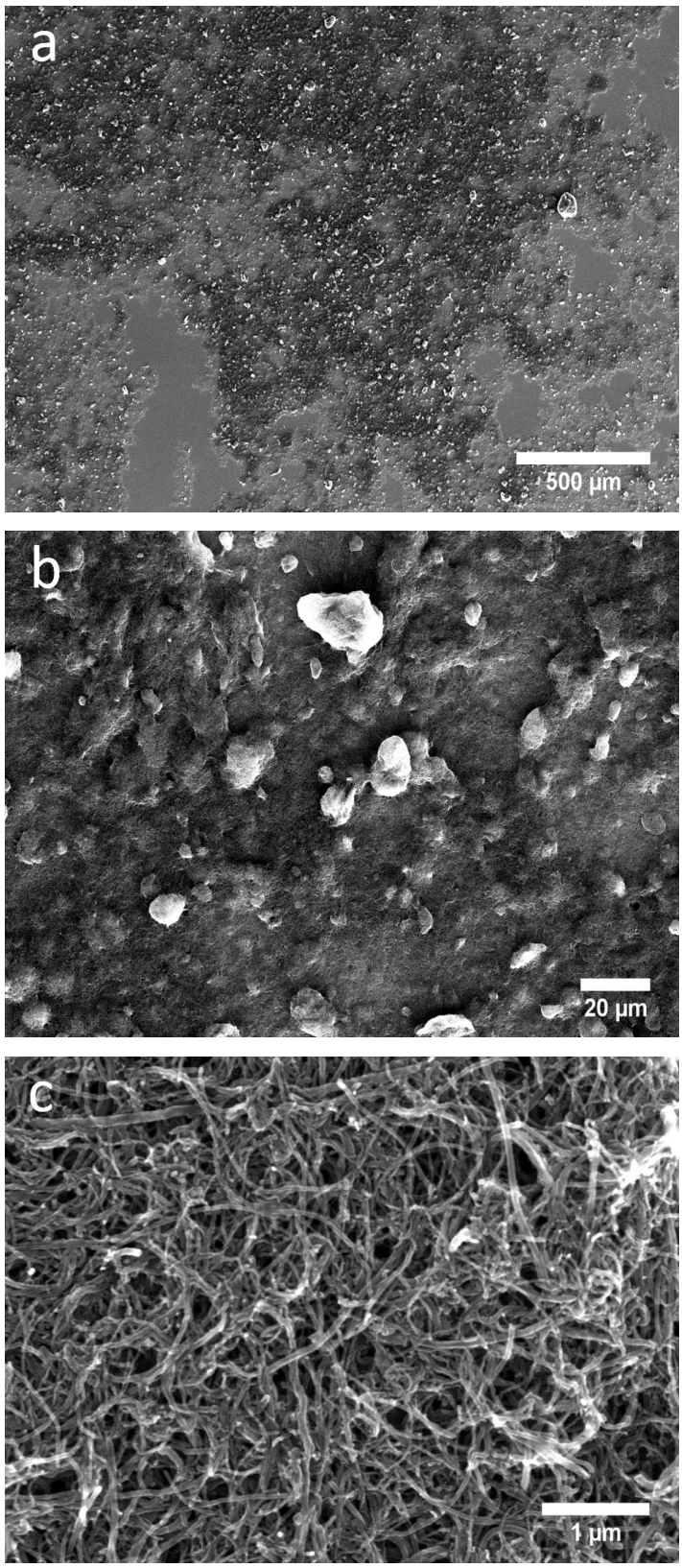


**Figure 82: SEM micrographs of a carbon nanotube surface coating on a silicon wafer**

The same was true for COOHCNT. These nanotubes were much finer than the CNT's and the film was comprised of rounded aggregations of COOHCNT's (Figure 83).

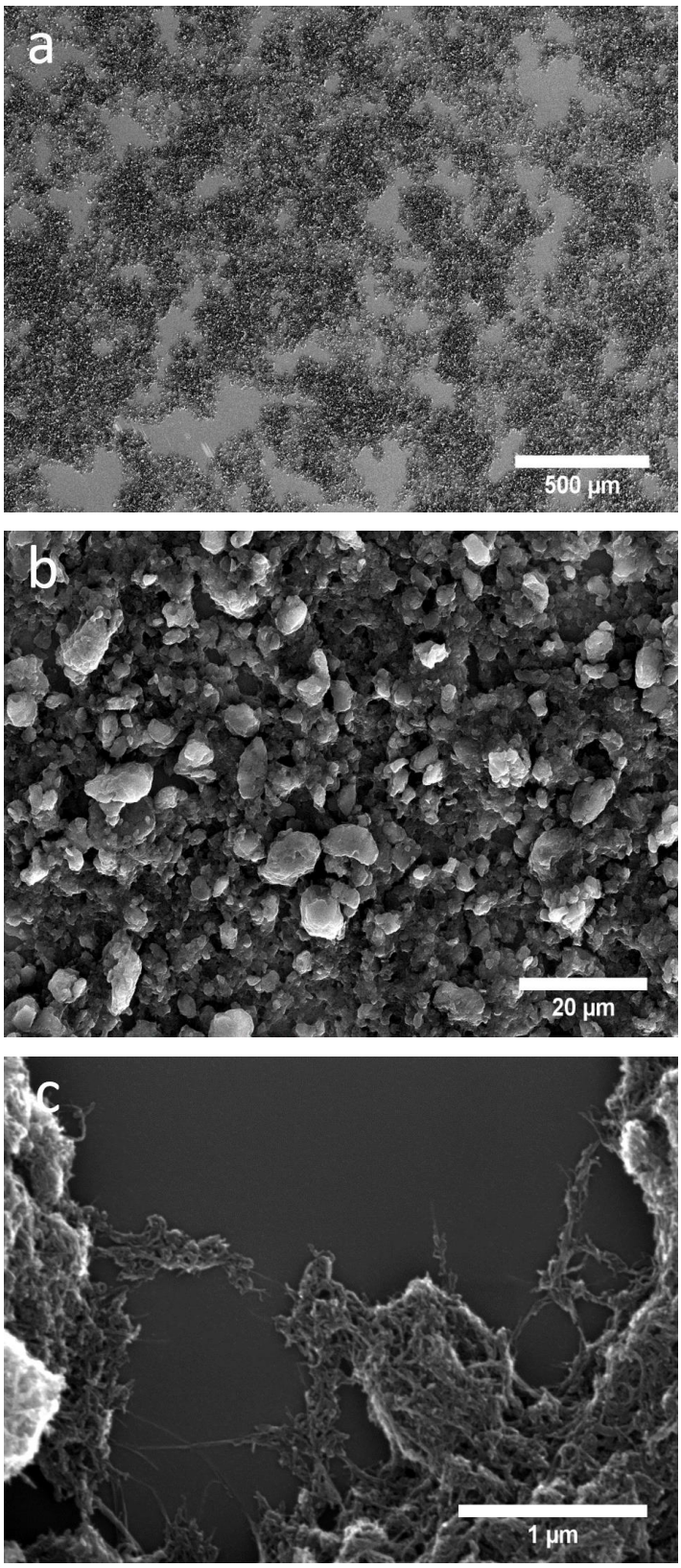


**Figure 83: Images of the COOHCNT film formed on a silicon wafer**

After crystallisation, the vast majority of the film in both instances had been removed from the substrate. This had occurred on submersion of the wafer in the crystallising solution, but

also on removal and after gentle washing. What little remained contained a sparse population of crystals (Figure 84).

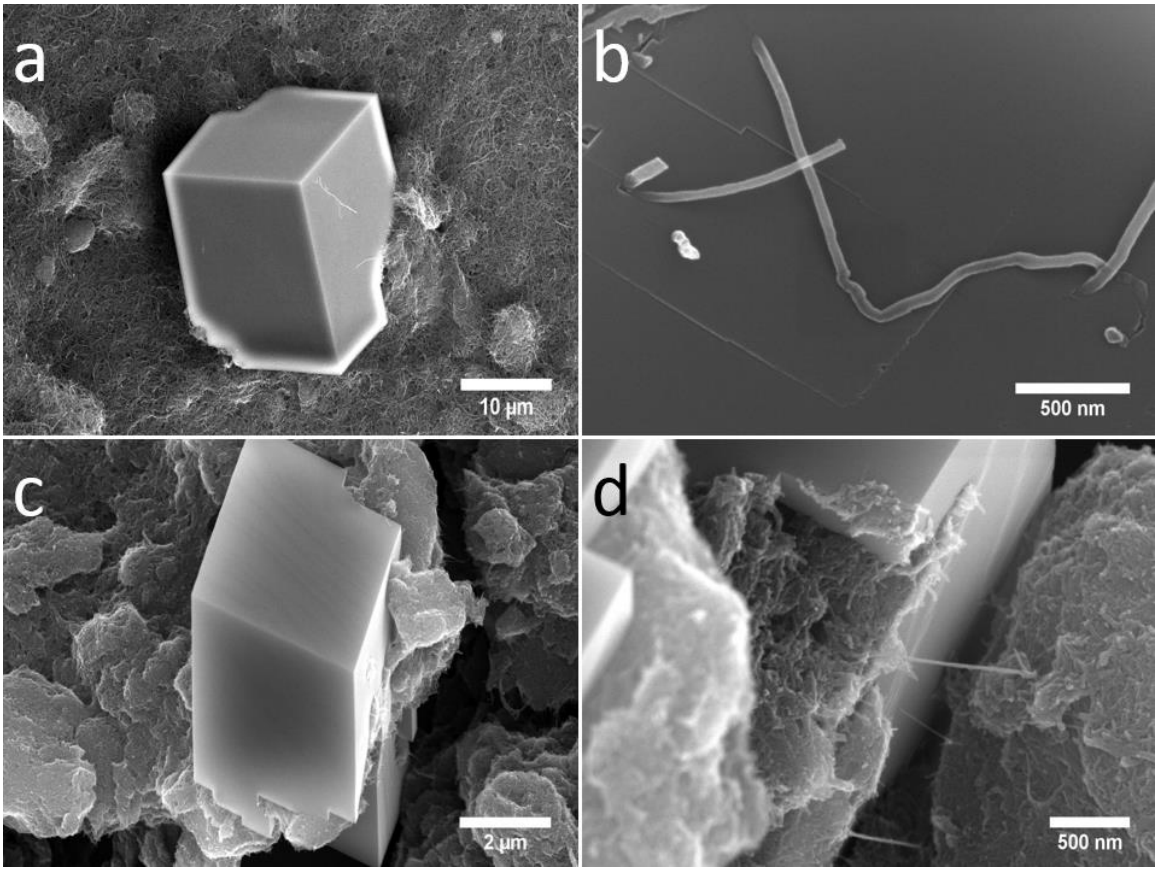


**Figure 84: Image of crystallisations on the CNT and CNTCOOH coated substrates after washing**Although the population of crystals found on the remaining film was small, the calcite crystals that were present had encapsulated nanotubes in both cases (Figure 84). This is not unusual and has been documented in the literature [84-87]. The graphene oxide (GO) and reduced-graphene oxide provided by Sichuan University were also investigated. As

expected, the coatings formed by these materials were different to the nanotubes (Figure 85).

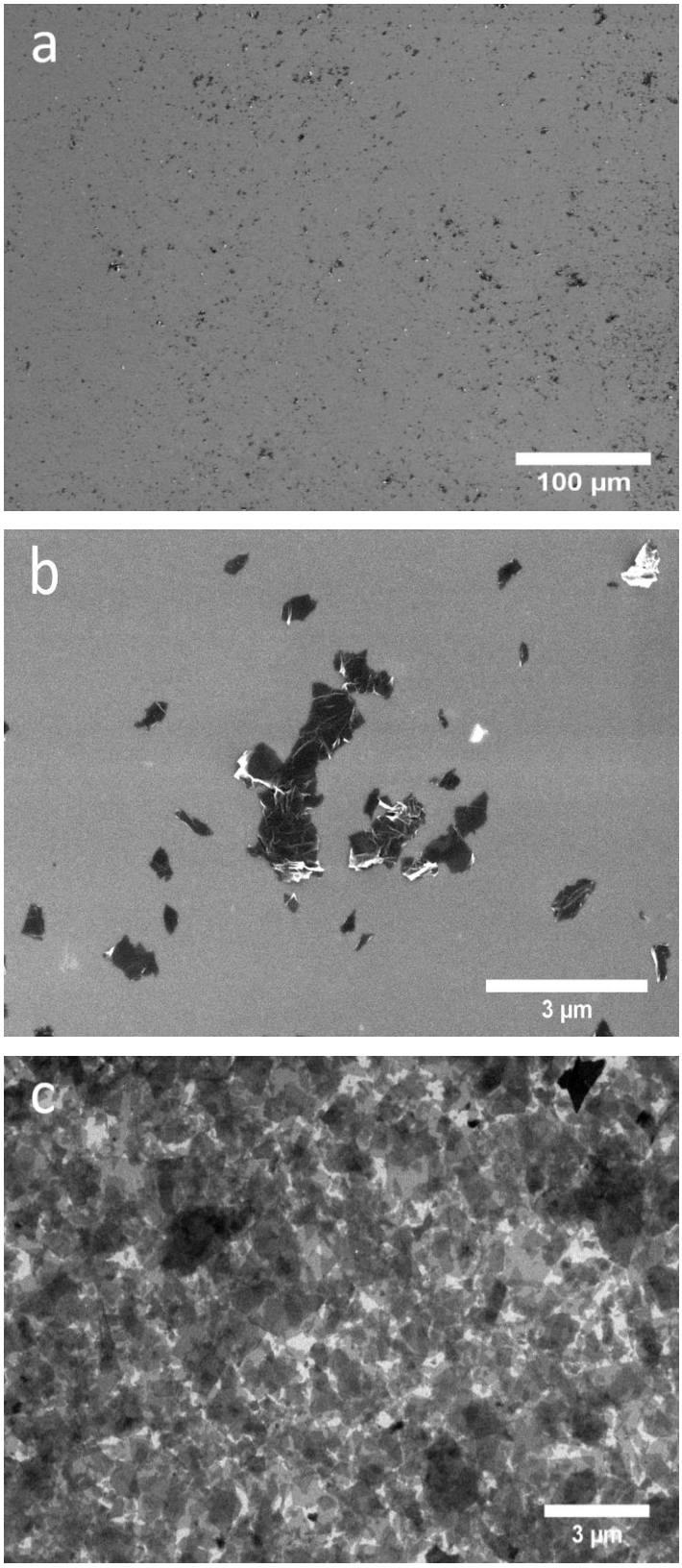


**Figure 85: SEM micrograph of a film formed by graphene supplied by Sichaun University.** The gG rGO coating was composed of a sporadic covering of flakes, whilst the GO film was

ubiquitous across the substrate. The GO flakes appeared to lie much flatter against the substrate than the gG flakes, which is most likely a result of the hydrophilic nature of graphene oxide and the surface of a silicon wafer (which possesses a thin silica surface layer that is also hydrophilic). After crystallisation, the SEM revealed that the GO coating had been completely removed and the crystal population was similar to the control (Figure 86a), indicating that the film had become detached on submersion, probably due to infiltration of water between the flakes and silicon surface. On the other hand, the distribution and quality of the gG coating appeared unchanged after crystallisation. Interestingly though, vast quantities of aragonite were present, with a minor fraction of calcite (Figure 86b-j).

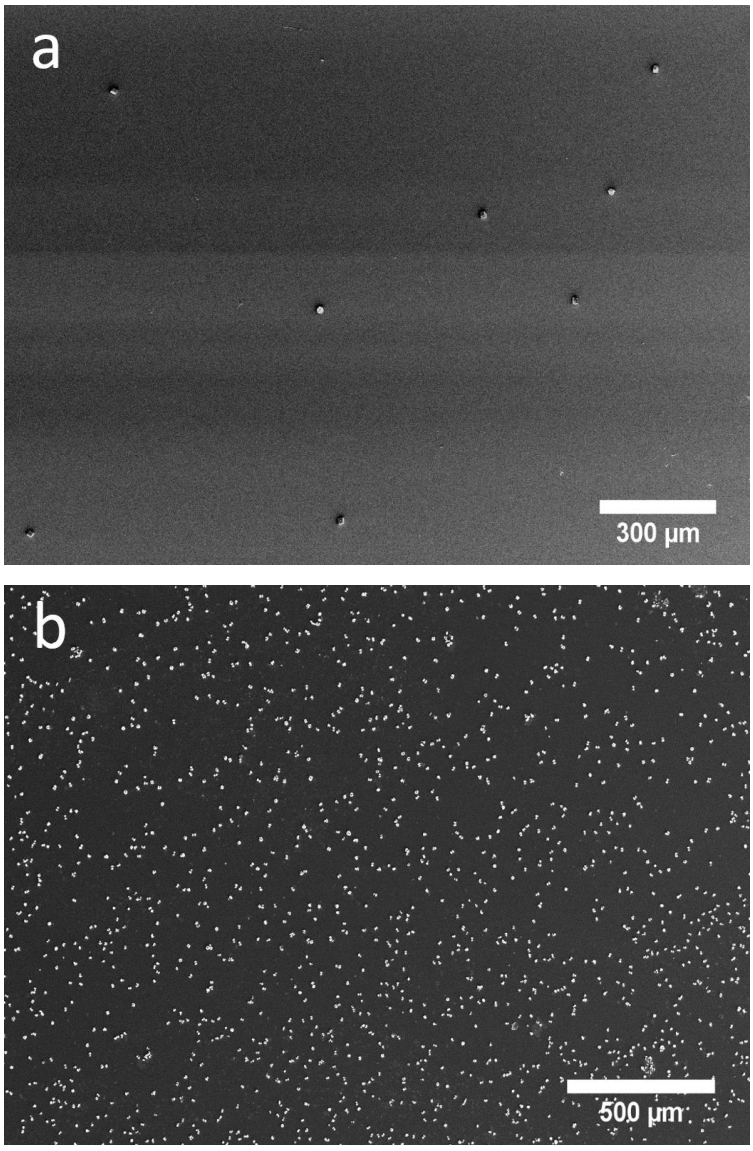

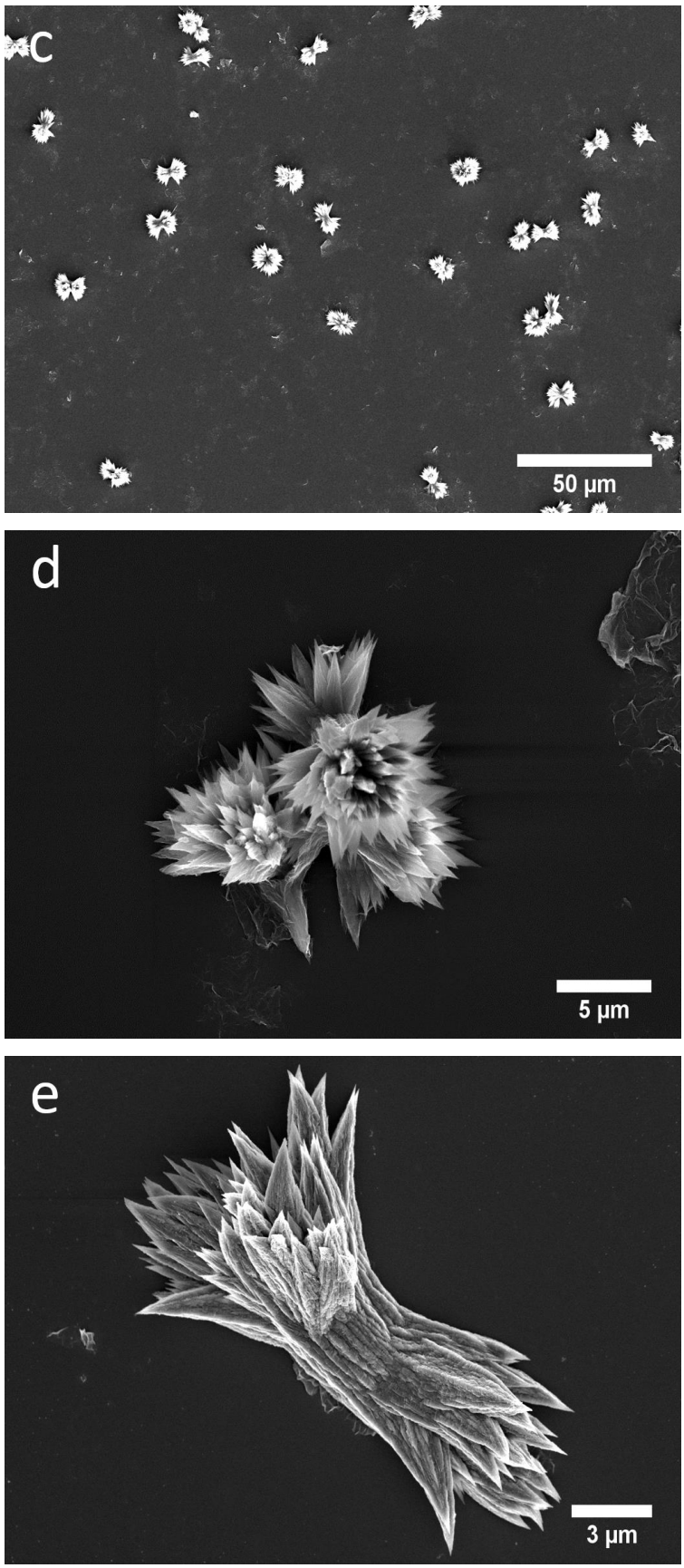
c
50 µm
d
5 µm
e
3 µm

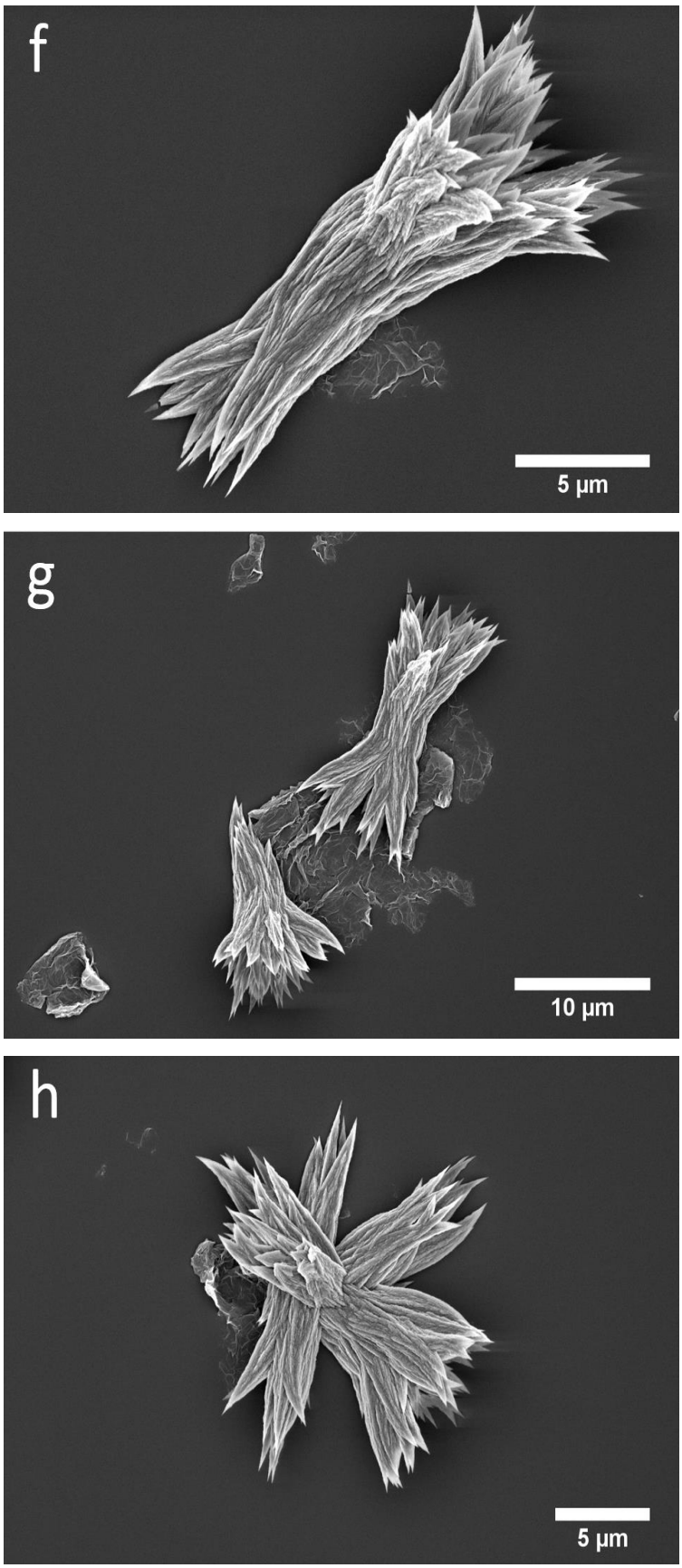
f
5 µm
g
10 µm
h
5 µm

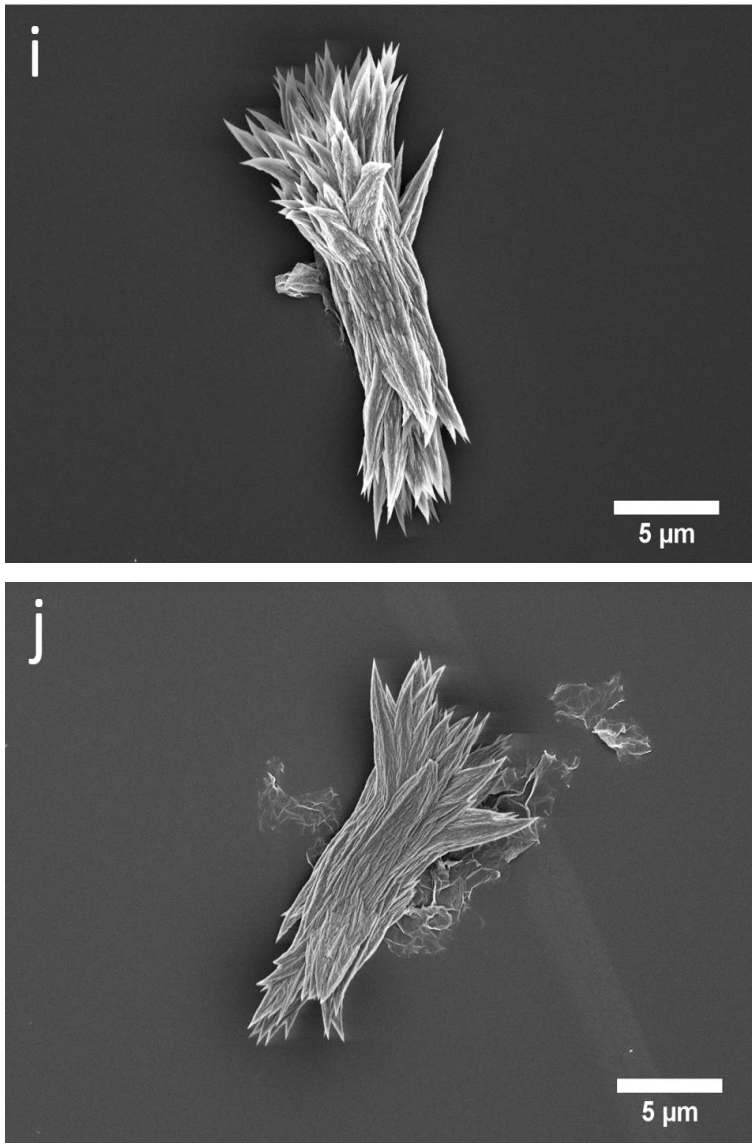


**Figure 86: Crystallisations on silicon wafers with and without a gG rGO surface coating**Obtaining a large fraction of aragonite has only been shown in the literature to be possible by crystallising in the presence of soluble additives. Thus, if the formation of aragonite was due to surface topography, then this would be a novel find and so was worth investigating further.

## 4.3.2 Investigations into the Formation of Aragonite on Silicon Wafers Coated with Reduced-Graphene Oxide

### 4.3.2.1 Introduction

There were a number of issues that needed to be addressed in order to ascertain if the formation of aragonite was the result of a surface topography effect. The questions that needed to be answered were as follows: Firstly, is it possible to produce aragonite using the same methodology, but with an rGO material purchased elsewhere? Was it the presence of

soluble contaminants or solids left over from the preparation procedure that was causing aragonite to form? Do other methods of forming an rGO coating also produce aragonite? And finally, can other layered materials such as transition metal dichalcogenides or graphitic-carbon nitride etc. also yield aragonite? The following sections contain data that was produced in order to answer these questions, in the hope of elucidating why the gG rGO causes aragonite to precipitate.

#### 4.3.2.2 Research into an Alternative Reduced-Graphene Oxide

To provide comparative data that might help identify the cause of aragonite precipitation, rGO was purchased from a different supplier. This rGO was obtained from Timesnano and the provided material is referred to as TN in this chapter (4.2.1). Using the TN sample, substrates were prepared using exactly the same methodology as that used for the gG samples. Like gG, TN also yielded aragonite when spin coated on a Si wafer. However, a smaller percentage of aragonite was observed and a greater proportion of calcite. Comparative micrographs of crystallisations carried out at the same concentration and residence time are given in Figure 87.

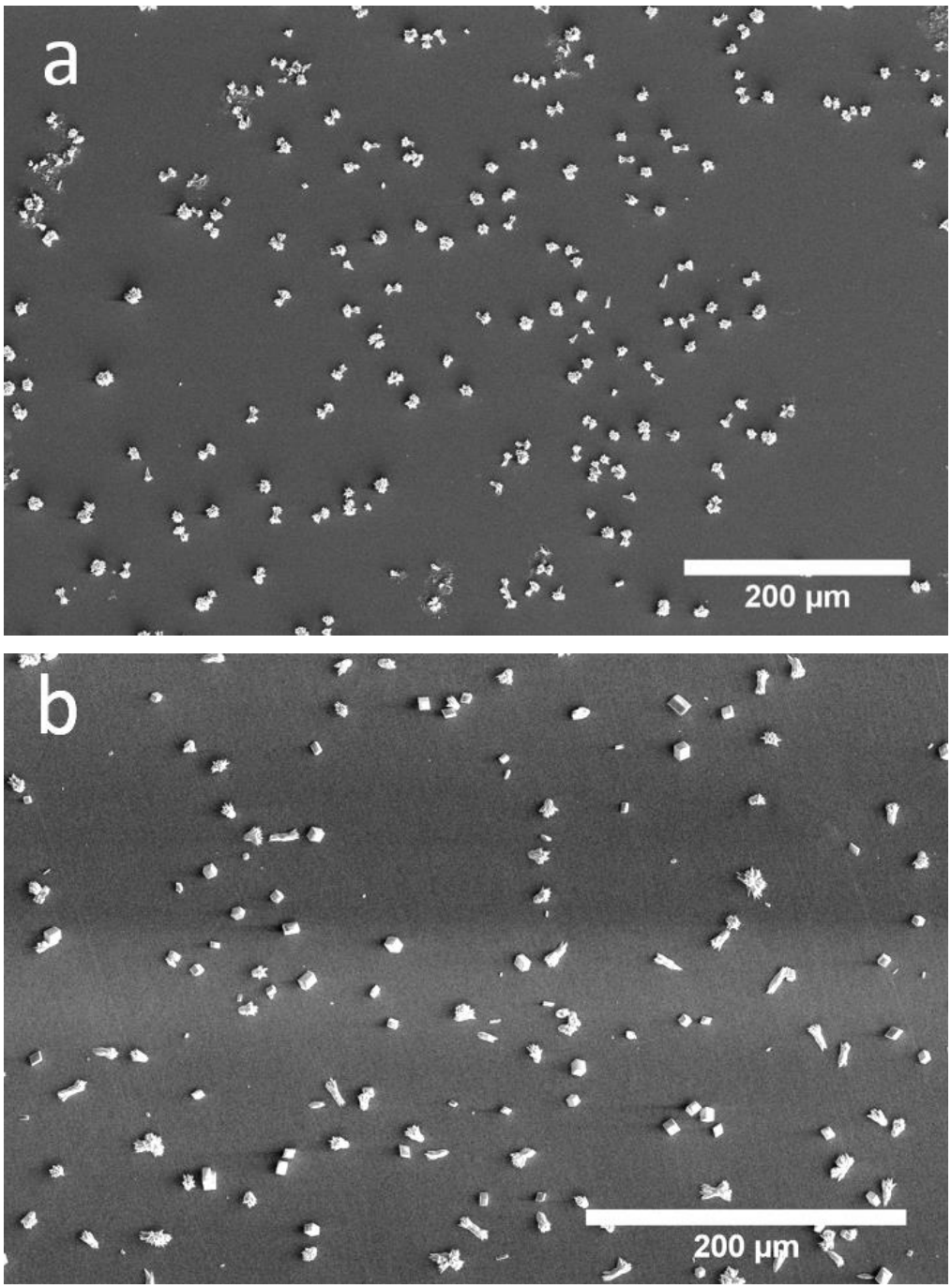


**Figure 87: Electron micrographs of the silicon wafers spin coated with gG rGO or TN rGO**

To provide an estimate for the percentage of calcite or aragonite present, each sample was analysed using powder x-ray diffraction and TOPAS analysis. This revealed that that more than 89% of crystals present on a gG coated Si wafer were aragonite, while on a TN coated wafer, 66% were aragonite (in both cases the remaining fraction was calcite).

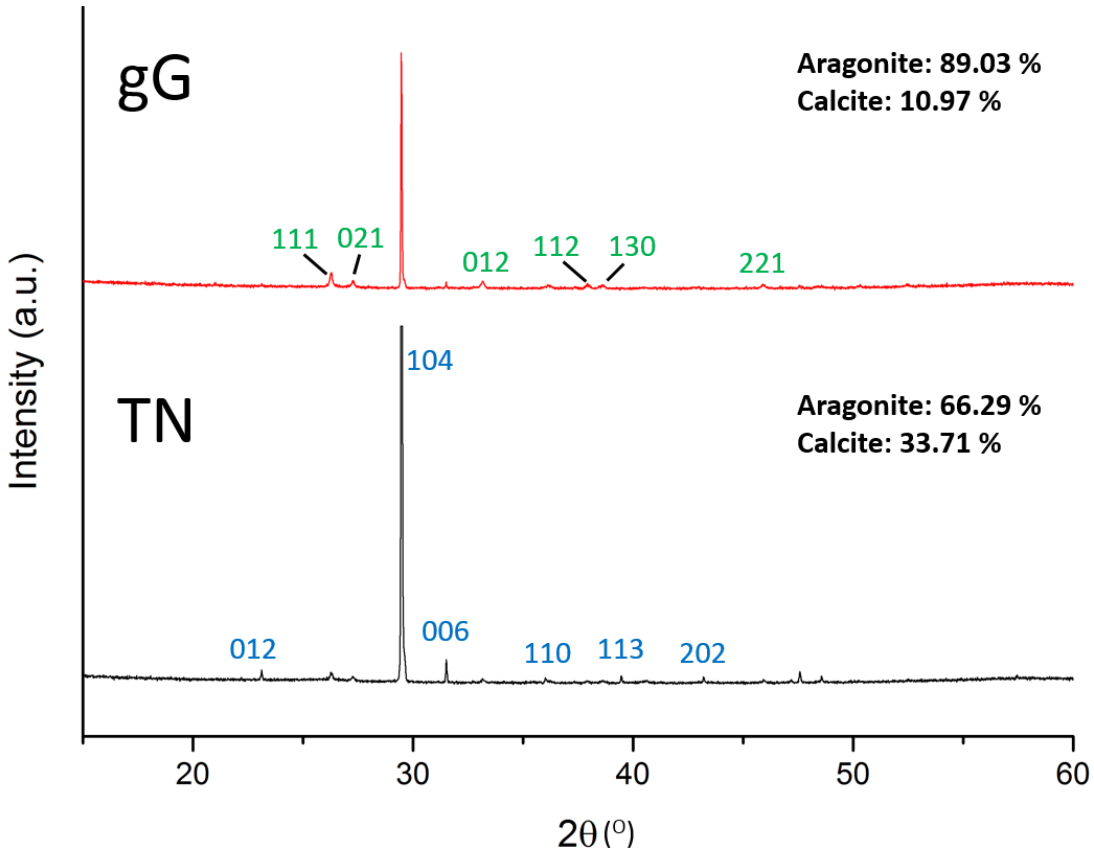


**Figure 88: XRD analysis of the calcium carbonate crystal polymorph populations precipitated on a silicon wafer either spin coated with gG rGO or TN rGO**

The samples were also imaged in the SEM and atomic force microscope, to provide insight on any topographical differences between the samples (Figure 89).

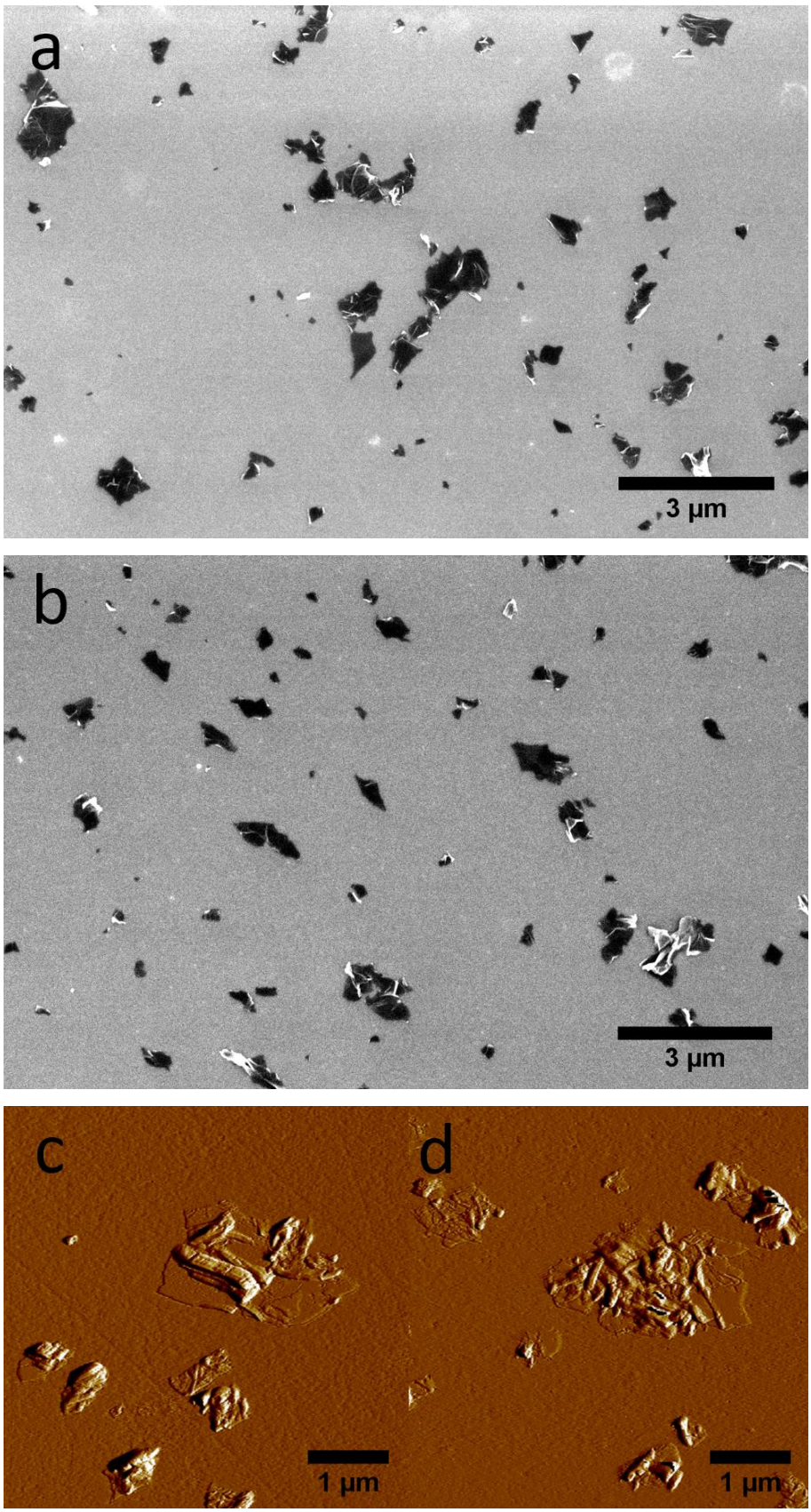


**Figure 89: Electron micrograph of silicon wafer spin coated with gG rGO**

Figure 9 shows how the surface coatings formed by the two rGO's are indistinguishable. In both cases, no flakes were measured with a height over 70 nm, with most falling in between

15 and 40 nm high. The flakes were highly folded and as such the thickness of a single flake would vary significantly. Considering the rGO flakes on the surface of the wafer formed similar topographies in both samples, the difference in polymorphic populations between the samples may be a result of contaminants associated with each of the materials, or the chemistry of the surface of the flakes. The following sections aim to investigate this.

#### 4.3.2.3 Identification of Contaminants: Crystallisations in the absence of the Dispersant

Thus far, all of the dispersions had contained poly(vinylpyrrolidone) (PVP) as a dispersing agent.

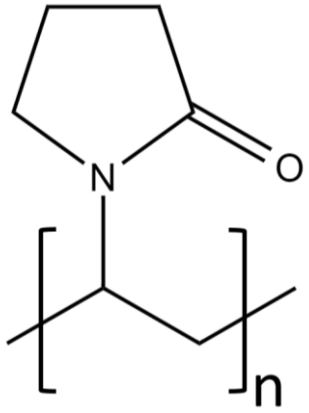


**Figure 90: Chemical structure of poly(vinylpyrrolidone), the dispersing agent that had been used thus far to stabilise the suspensions of carbon nanostructures**

The literature regarding the effect of polymer additives on the crystallisation of calcium carbonate is extensive, and a number of studies have investigated the effects of PVP [91-95]. All data in the literature indicates that PVP has no effect on the polymorphism of calcium carbonate and in each study, aragonite was not detected. In my experiments, aragonite was only present on substrates coated with rGO, and not on any of the other substrates that had surface coatings. All of the dispersions of the different carbon nanostructured materials used to form the surface coatings contained PVP as a dispersant, so the fact that aragonite was only detected on the rGO coated substrates suggests that it was not the PVP that caused aragonite to form. Regardless, to investigate the topographical effect of the gG material further with as few variables as possible, dispersions of gG were made without PVP. The substrate preparation and crystallisation were carried out in the same manner as before. Images of the crystallisation results are shown in Figure 91.

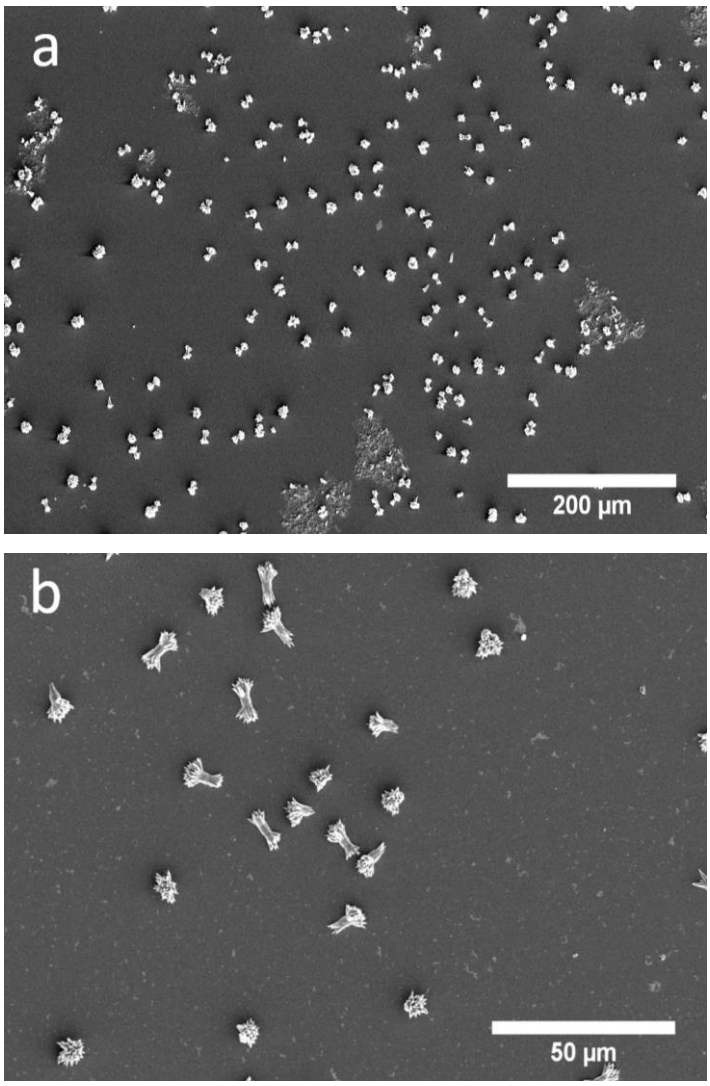


**Figure 91: Micrographs of aragonite crystals precipitated on a film of gG on a silicon wafer**

Aragonite was observed on the substrate in the absence of PVP, indicating that this polymer does not promote this phase. However, in order to establish if it is the topography of the spin coated flakes that cause the formation of aragonite, it is necessary to determine if the rGO's are associated with any impurities. The following sections contain data obtained using a variety of analytical techniques to examine this.

#### 4.3.2.4 Characterisation of the rGO's and Identification of Contaminants: Energy Dispersive X-ray Analysis

Energy Dispersive X-ray Analysis (EDXA) involves measuring the energy of X-rays that are emitted from a sample after irradiation with a high energy beam of particles, in this case, electrons generated within the SEM. The beam electrons are able to interact with inner shell electrons of atoms at the surface, causing them to be ejected and an associated release of X-rays [96]. In the resultant X-ray spectra, there are two sources of X-rays that are produced as

a result of interactions between the electron beam with the specimen atoms. Continuum (Bremsstrahlung) X-rays are caused by the inelastic interaction of an incident electron with the coulomb field of an atomic nucleus. As the path of the electron is redirected, some of the energy of the electron is emitted in the form of X-ray radiation. These contribute towards the background of the X-ray spectrum of the sample. The other type of X-rays are called characteristic X-rays and they are produced by the electronic rearrangement of an atom. Primary electrons can dislocate an inner shell electron, causing them to be ejected from the atom. An electron from a higher valence shell fills the shell of the displaced electron, emitting an X-ray photon in the process. The amount of energy lost is characteristic of the atom, and thus their presence can be identified. These X-rays reveal themselves as peaks in the X-ray spectrum of the sample [97] and are used for the spectral analysis.

To ascertain if there were any contaminants present in the samples that may be influencing the crystallisation of calcium carbonate, an EDX analysis was carried out. Initially, the samples were prepared by dropcasting the rGO suspension onto the wafer (see Section 4.2.3). However, only carbon and silicon (from the wafer) were detected. To concentrate any contaminants that may exist in the sample, an alternative preparation method was used (4.2.4). This involved repeated dropcasting and evaporation of the water from the suspension to build up a thick layer of the rGO. The graphitic material was then removed via thermal decomposition by heating to 600 $^{o}$C for an extended period of time. The residue left on the surface was composed of inorganic contaminants. Both of the rGO samples (gG and TN) were prepared and analysed using this methodology. The residual material formed from each of the samples was very different in appearance in each case, as demonstrated by the electron micrographs below (Figure 92).

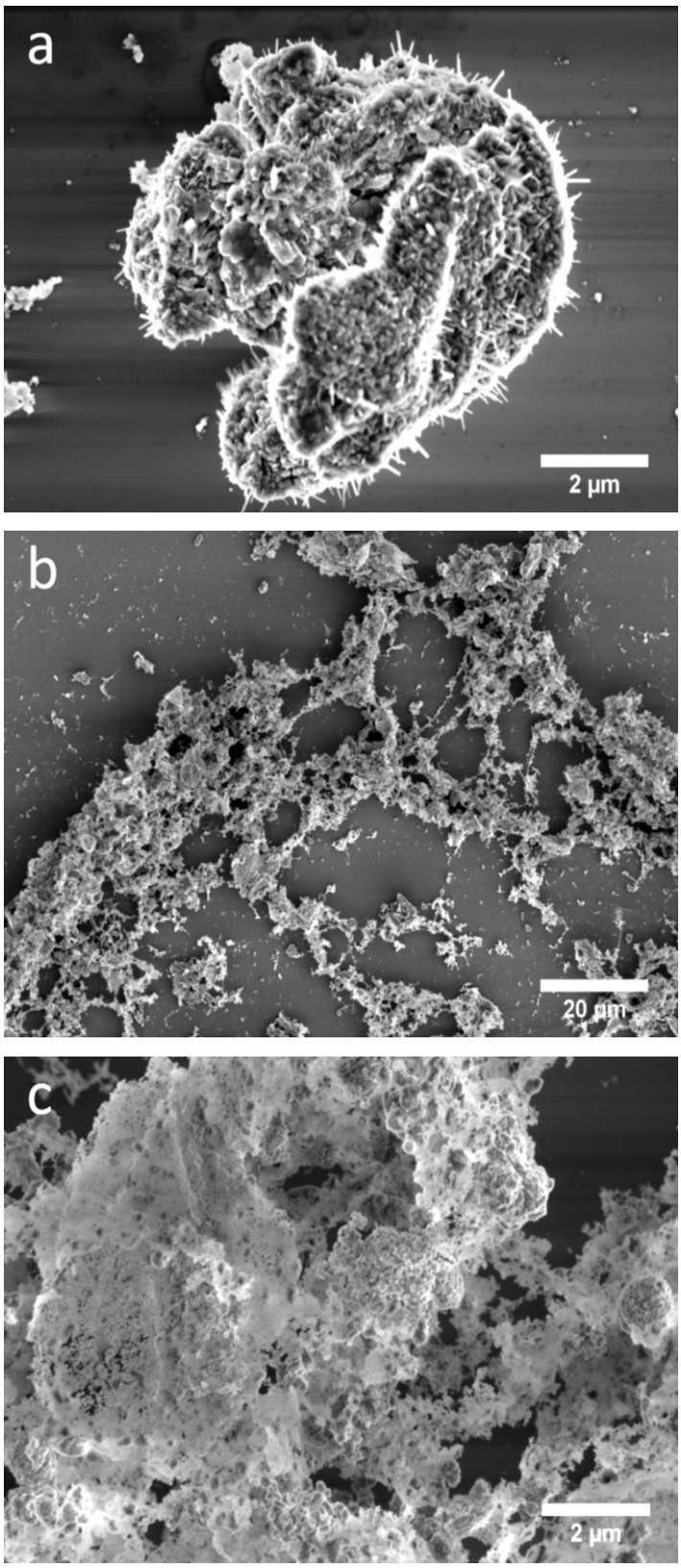


**Figure 92: Images of the residual material left on the Si wafer after exposure of the gG and TN samples to 600 °C for 5h**

The gG residual material was composed of discrete particles (as seen in Figure 92a), while larger deposits formed from many small particles were present on the TN sample after

burning. A selected area analysis of a particle from the gG sample revealed its composition (Figure 93, Table 10).

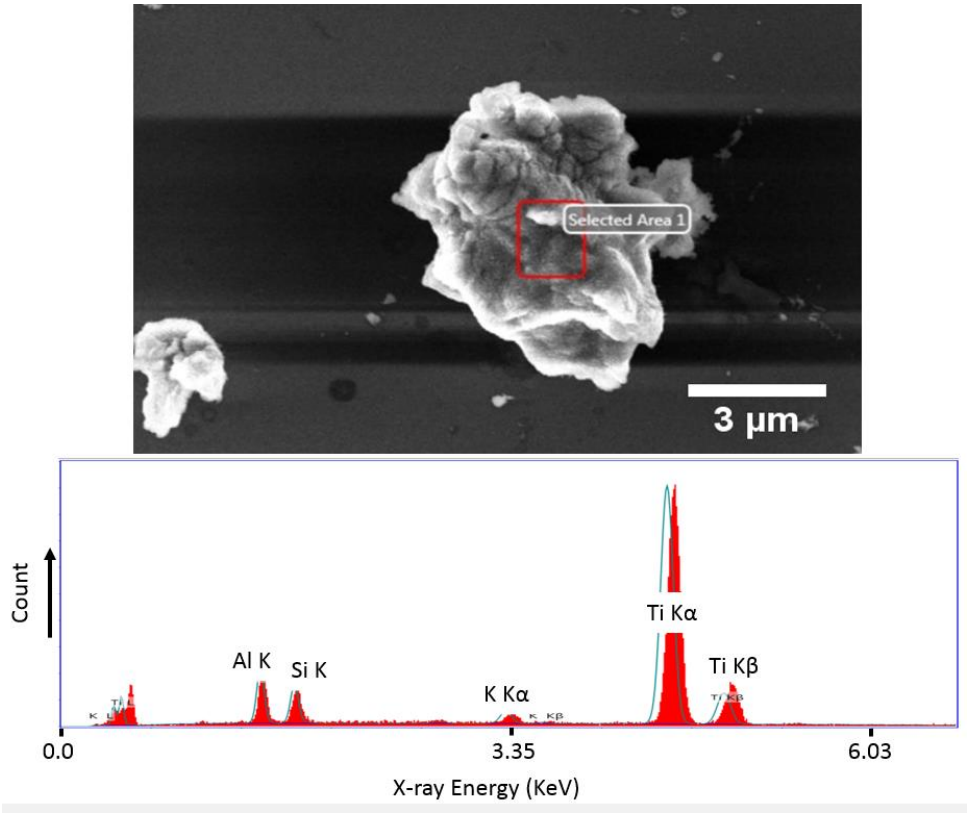


**Figure 93: Selected area EDX analysis of a particle on the gG sample after exposure to 600 °C for 5 hours**

**Table 10: Measured atomic percentages of the elements identified in Figure 93 via EDX analysis.**

| Element | Atomic % |
|---|---|
| Al | 4.72 |
| Si | 3.35 |
| K | 2.10 |
| Ti | 89.83 |

As can be seen from Figure 93 and Table 10, the particle is composed of aluminium, titanium and potassium. The silicon peak likely originates from the silicon wafer. Potassium permanganate is used as an oxidising agent in one of the steps of the Hummer's method [98, 99], and so it is possible that this is where the potassium contamination is from. Titanium, which is the most abundant impurity according to Table 10, is most likely from the sonicator horn used to ultrasonicate the samples, as this is composed of high purity titanium. It's

possible that the high vibrational frequency has caused titanium particles to be released into the sample dispersion. The presence of aluminium could be accounted for by the reducing agent used to transform the graphene oxide into rGO for the gG sample. Lithium aluminium hydride is a commonly used strong reducing agent in synthetic chemistry and is capable of converting oxygen functionalities via a well-understood reduction mechanism [100]. The use of $LiAlH_4$ for the reduction of GO has been documented [101]. However, as stated above, the synthetic protocol for producing the gG sample has not been confirmed and so it is not certain that this is the cause of the presence of aluminium. In addition, an EDX analysis map was made of an agglomeration of particles on the gG surface (Figure 94).

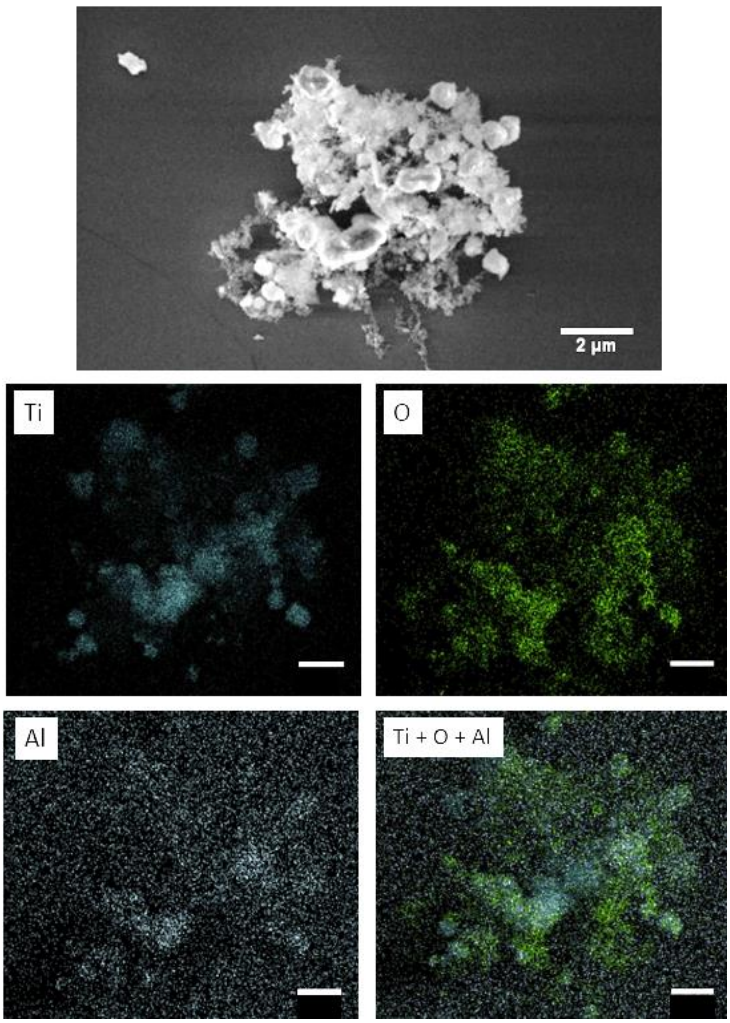


**Figure 94: SEM micrograph of the particle that was analysed for the EDX map.**

**Table 11: Measured atomic percentages of the elements identified in Figure 94 via EDX mapping.**

| Element | Atomic% |
|---|---|
| O | 32.02 |

| | |
|---|---|
| Al | 6.36 |
| Ti | 61.62 |

The EDX map (Figure 94) and atomic percentages (Table 11) suggested that this agglomeration was particles of $TiO_2$. As stated above, the titanium was most likely introduced via the sonication step, which was then oxidised due to exposure to 600 $^{o}$C for 6 hours [102]. There was also a small amount of aluminium present, possibly vestigial reducing agent.

A selected area analysis of a particle on the TN sample indicated that, as well as titanium, aluminium and oxygen (as seen in the gG sample), iron and nickel were present as contaminants (Figure 95).

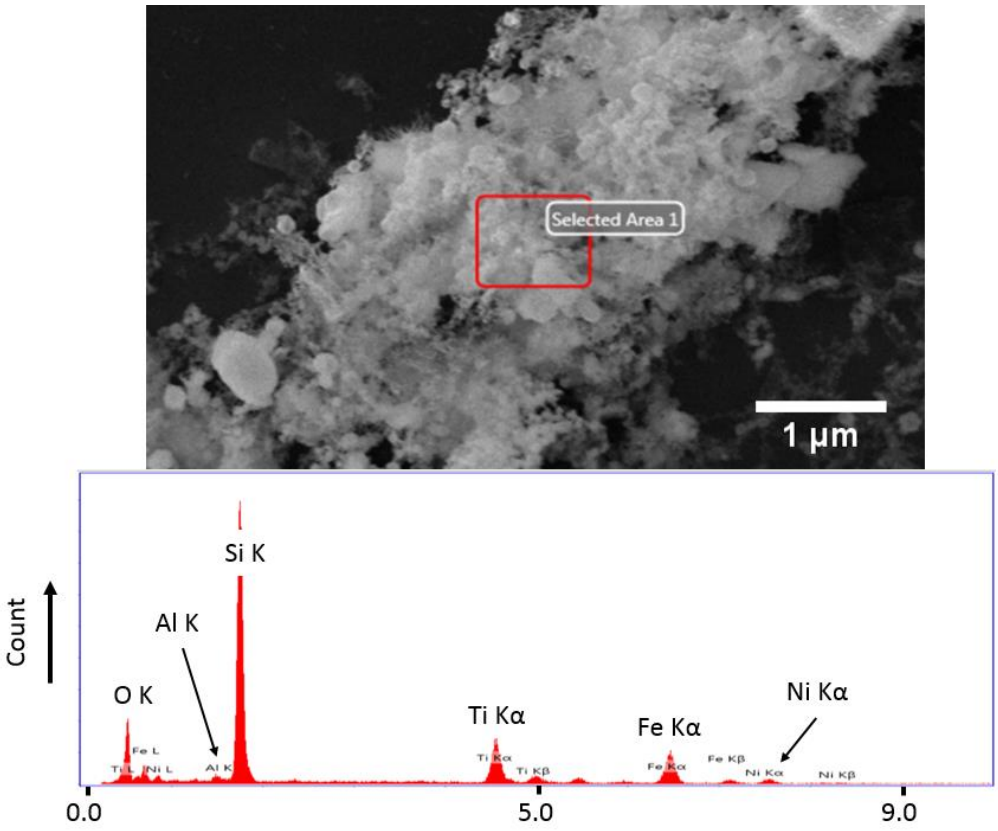


**Figure 95: Selected area EDX analysis of TN residual material after exposure to 600 $^{o}$C for 5 hours**

**Table 12: Measured atomic percentages of the elements identified in Figure 95 via EDX analysis.**

| Element | Atomic % |
|---|---|
| O | 20.97 |
| Fe | 1.45 |

| | |
|---|---|
| Ni | 0.09 |
| Al | 0.29 |
| Si | 33.8 |
| Ti | 43.4 |

An EDX analysis map was also taken of a different particle (Figure 96).

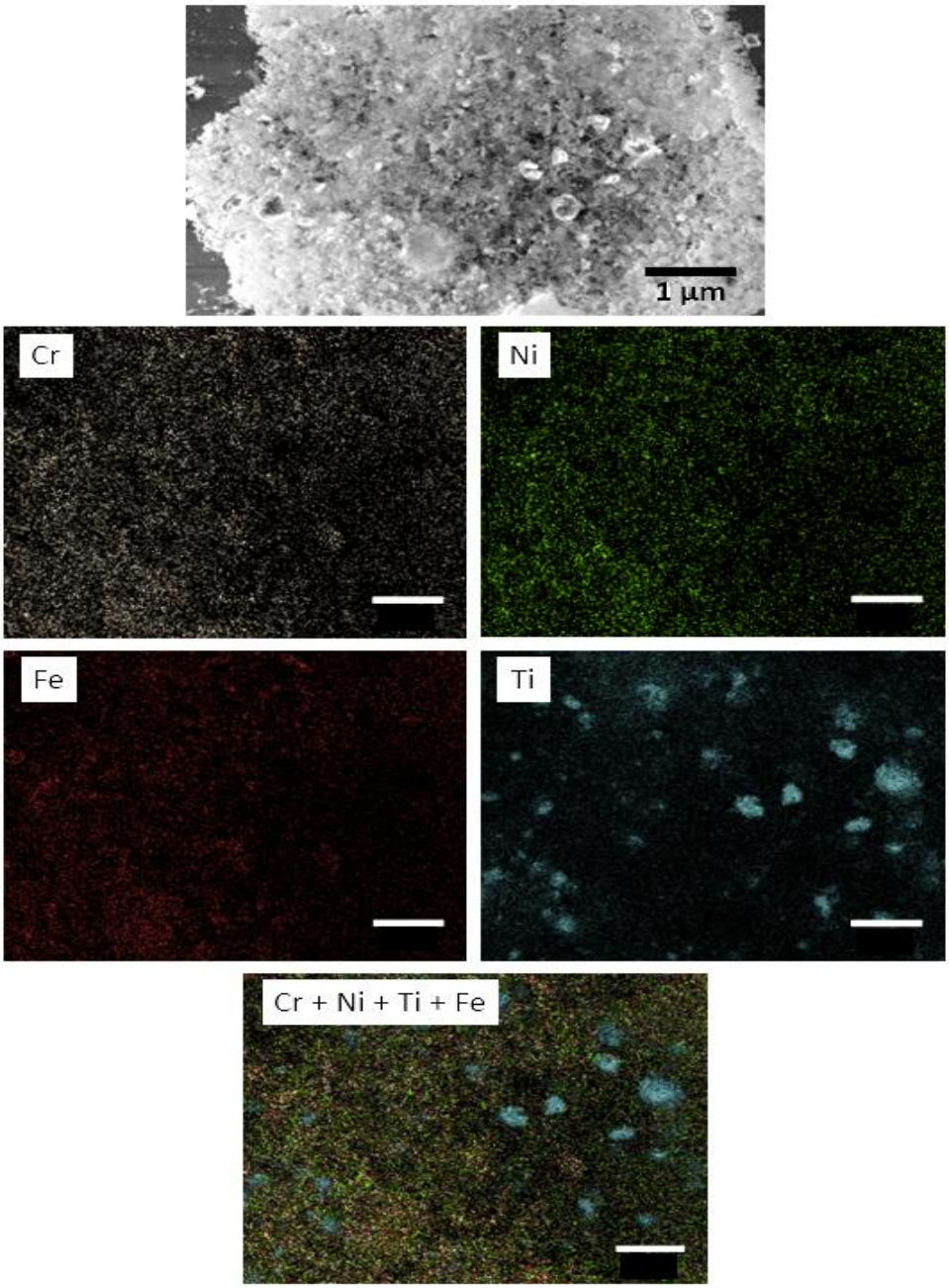


**Figure 96: EDX analysis map of TN residual material after exposure to 600 °C for 6 hours**

**Table 13: Measured atomic percentages of the elements identified in Figure 96 via EDX mapping.**

| Element | Atomic% |
|---|---|
| Cr | 17.19 |
| Fe | 0.74 |
| Ni | 0.00 |
| Ti | 82.07 |

The EDX analysis and atomic percentages suggested that although both graphene samples contain impurities, the TN sample is contaminated with a greater range of elements. Given the elemental signatures detected in the TN sample, it is possible that iron, nickel and chromium are caused by a stainless steel contaminant, the origin of which is unknown. This may be 304 stainless steel, which typically contains both chromium and nickel. Again, the titanium likely originates from the sonicator horn used to ultrasonicate the samples. Now that the contaminants had been isolated, concentrated and analysed using EDX, the next logical step was to use the silicon wafers on which they were situated as substrates for the crystallisation of calcium carbonate. The reasoning was that if aragonite was observed on these substrates, then it must be these contaminants that had been causing it to form. Crystallisations were carried out using the same methodology as that used for the graphene-coated wafers (Section 4.2.3.1). In addition, a substrate of high purity titanium was also crystallised on, since this element was found to be the most prevalent impurity (Figure 97).

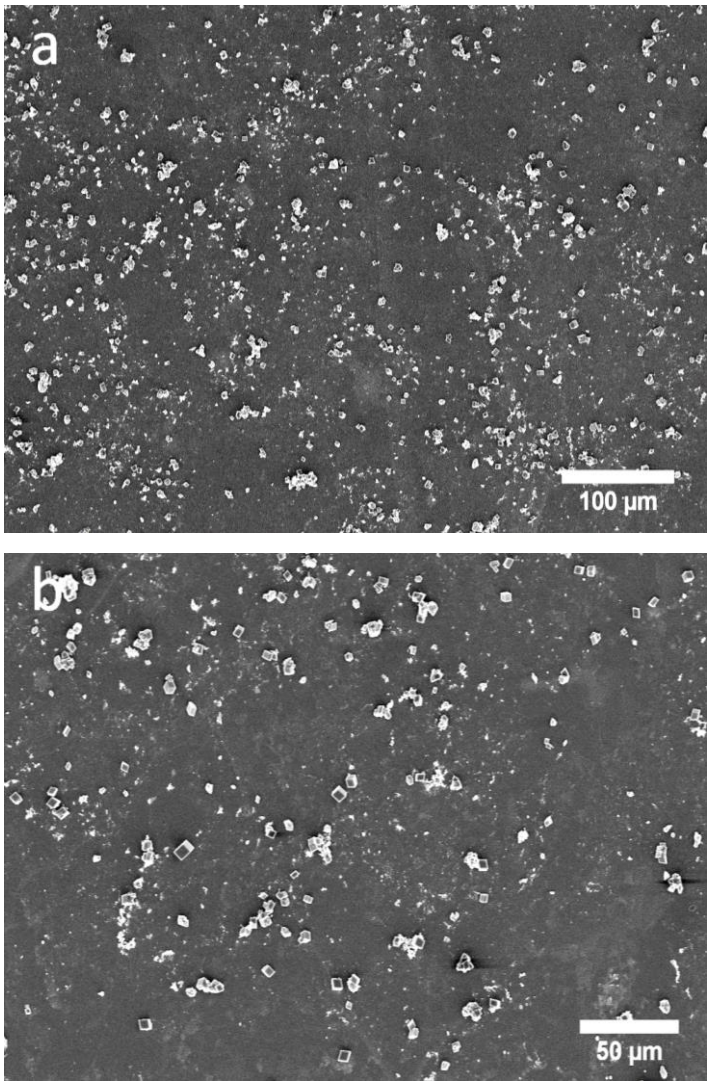

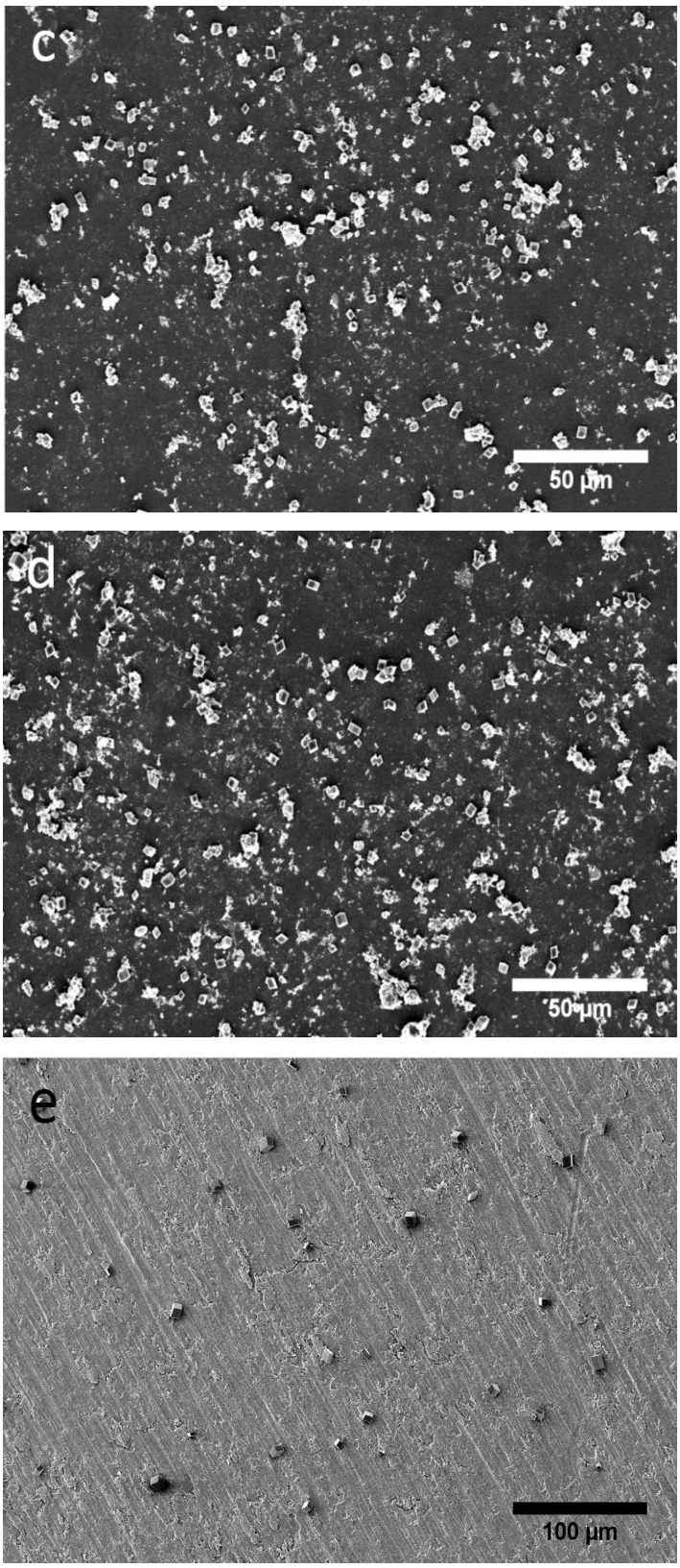


**Figure 97: SEM images of calcium carbonate crystallisation carried out on the gG residual material after graphene removal, on TN residual material after graphene removal, high purity titanium substrate**

In all experiments, no aragonite was detected. Only calcite was observed on the silicon wafers that had the concentrated contaminants on the surface, and both calcite and a few vaterite

had precipitated on the titanium plate. Although aragonite was not observed, it may be still possible that the impurities detected here were causing its precipitation on the spin coated substrates. Heating to 600 $^{o}$C may change the 'active' impurity chemically and physically in such a way that it is no longer able to promote aragonite formation. In order to determine the mass percent of impurities present in each of the samples, thermogravimetric analysis was conducted.

#### 4.3.2.5 Characterisation of the rGO's and Identification of Contaminants: TGA Analysis

Thermogravimetric analysis (TGA) is a simple technique in which the mass of a sample is monitored as it is exposed to a controlled heating program. By using this technique, it will be possible to determine the mass percent of impurities present in my samples. This is because at about 600 $^{o}$C, the rGO will thermally decompose into carbon dioxide and carbon monoxide, leaving behind any inorganic matter. TGA may also provide an insight into which of the two samples is oxidised to a greater extent, as the sample with the higher oxygen content should decompose at a lower temperature. TGA was conducted on both the gG and the TN sample. It was also used to analyse a sample of gG that had been thoroughly washed, in an attempt to remove as much contamination as possible (see 4.2.3.4). The derivative of the mass is plotted in each case, revealing the mass loss steps for each sample. Below are the three TGA traces (Figure 98).

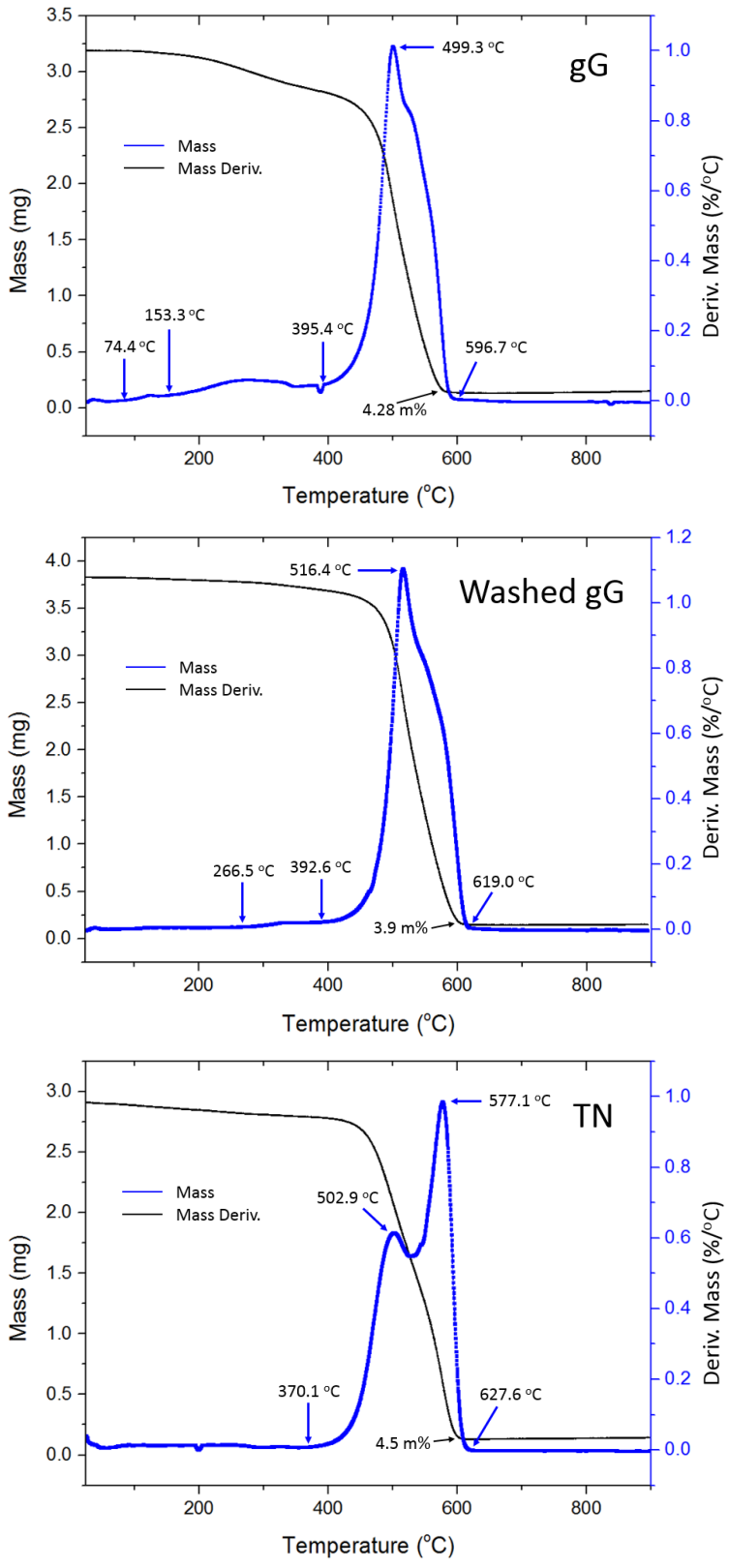


**Figure 98: Thermogravimetric analyses of gG rGO, Washed gG rGO and TN rGO**

When comparing the two gG samples (unwashed gG and washed gG), there are a number of features of the graphs that are noticeable. The first is that for the unwashed sample, there is an initial mass loss at 74.4 °C followed by another at 153.3 °C. The mass loss at the lower temperature will be caused by loosely bound water and this is absent in the washed sample

because after washing, it was placed in the oven at 80 $^{o}$C for five hours to dry it out (otherwise the washed sample would lose 90% of its mass up to 150 $^{o}$C due to this water). The second change in mass (153.3 $^{o}$C) is a result of the liberation of water that is more intimately bound to the rGO flakes, existing intercalated between sheets that have agglomerated. Desorption of gas molecules will also contribute [103]. The associated mass loss for the washed sample is at 266.5 $^{o}$C. A significant proportion of water will have been driven off by the drying step, which is why the mass loss occurs at a higher temperature for this material. This step is almost undefinable in the TN sample, indicating that there was very little bound water or gases. At gG: 395.4 $^{o}$C, washed gG: 392.6 $^{o}$C and TN 370.1 $^{o}$C, the thermal decomposition of the rGO begins. This is quite low for these materials, as carbon oxidation of rGO's is expected to occur about at about 650 $^{o}$C [104, 105]. The lower associated temperature for the TN sample compared to the two gG samples suggests that this material is more oxidised than the other rGO's, as pristine graphene thermally decomposes at 800 $^{o}$C [106]. The fact that the process began at similar temperatures for the washed and unwashed gG indicates that the oxidation of these two are the same (as expected). The decomposition process reaches a maximum at 499.3 $^{o}$C, 516.4 $^{o}$C and 577.1 $^{o}$C for the gG, washed gG and TN samples, though there is another process that occurs within the rGO decomposition for TN. This may be the thermal decomposition of one of the impurities, though it is difficult to say for certain. Finally, if we compare the residual masses left after all of the rGO has burnt away, the TN sample has the greatest mass percent of material remaining, indicating that impurities make up a greater proportion of this sample. The smaller residual mass of the washed gG sample means that some of the impurities were removed by washing, either because they were soluble or there were also nanoparticles that were small enough to be removed through the filter membrane (220 nm pore size).

#### 4.3.2.6 Characterisation of the rGO's and Identification of Contaminants: XPS Analysis

To provide further information regarding the composition of the gG and TN graphitic material, X-ray photoelectron spectrosopy was used (XPS). XPS is similar to EDX, except that instead of irradiating with electrons and detecting emitted X-rays, it excites with X-rays and measures ejected photoelectrons. XPS is a surface sensitive technique that can analyse the surface of a sample to a depth of <10 nm, revealing the chemical and electronic states of superficial atoms [107]. The process involves irradiating the surface with X-rays, and if the energy of the X-ray is equal to or greater than the binding energy of the electron, then it will be ejected. The kinetic energy of these photo-ejected electrons is measured by an electron analyser,

producing data that allows the intensity (number of photoelectrons detected per unit time) to be plotted against the binding energy. Using this information, it is possible to identify and quantify the elements present at the surface [108].

A survey scan for each sample (gG and TN) was conducted first (Figure 99). This broad scan is carried out initially as it identifies all the elements that are present on the silicon wafer surface. The information can then be used for high resolution scans, allowing specific ranges of binding energy to be analysed in more detail.

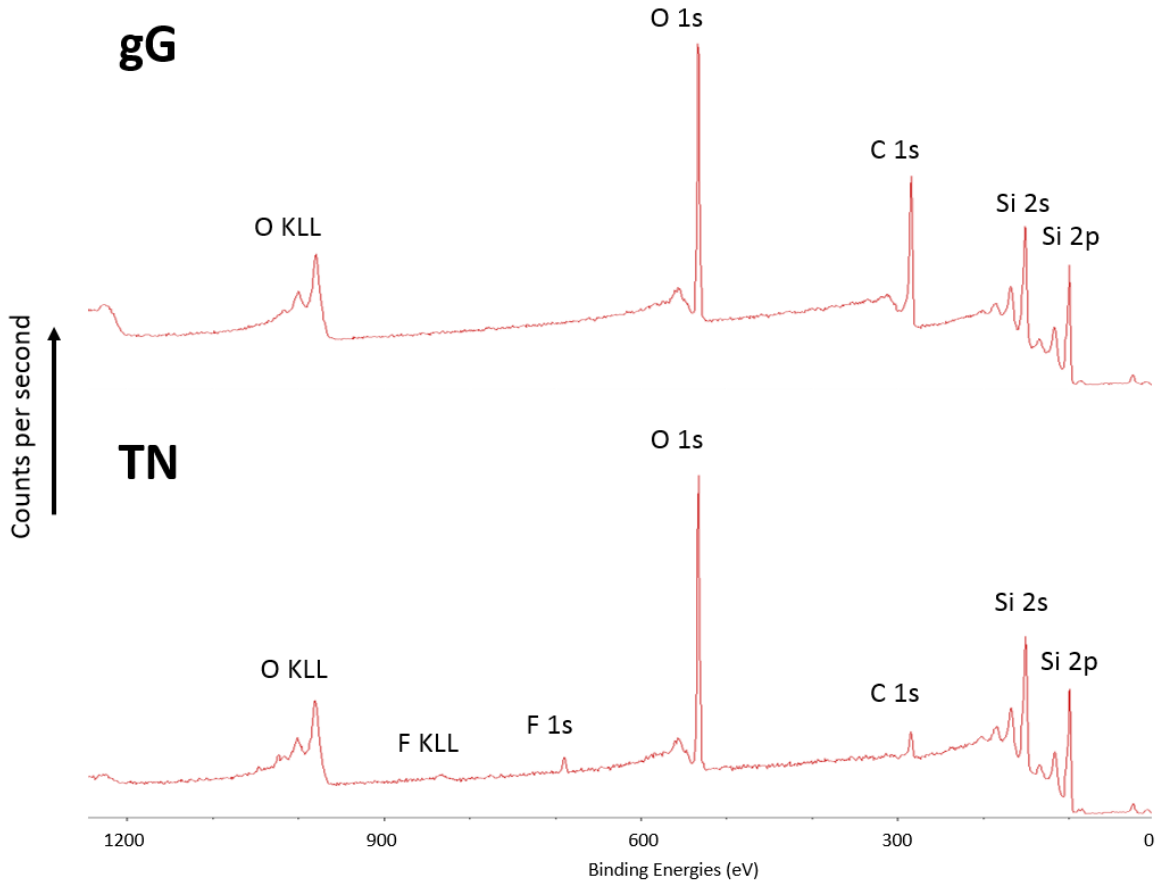


**Figure 99: Survey scans for the gG rGO sample and TN rGO sample**

The first quality of the spectra that was immediately noticeable was the lack of peaks associated with Cr, Ni, Al, Fe and Ti, the contaminants identified in the EDX analysis. Their absence could be attributed to the fact that the detection limit for XPS is parts per thousand and so since the material was deposited on the wafer via spin coating (rather than drop casting as was the case for the EDX analysis), these elements may not exist at a high enough concentration to generate a detectable signal. However, a contaminant that has been identified in the XPS spectrum of the TN sample is fluorine, though the exact cause of this is unknown, and may be confined to only this particular TN sample that was analysed. The

presence of the Si 2s and 2p emissions indicates that the film was indeed not continuous across the surface (confirmed by SEM and AFM, Figure 85 and Figure 89c, d), as XPS is only sensitive to the top 10 nm of the illuminated surface. Present in both spectra was an intense oxygen peak (O 1s), caused by the oxygen of the silica surface layer, with some contribution from the oxygen functionalities of the rGO. The KLL peaks associated with the oxygen and fluorine emissions are known as the Auger peaks. Auger electrons are generated by autoionisation, and their emission involves a three-electron process [109, 110]. The process is initiated by the photoemission of an electron from the core shell, in this case, the K shell. This creates a core hole and an unstable electronic state, and so an electron from an outer shell (L) fills the hole and emits energy that is equal to the difference between the two orbital energies. This emitted energy from the second electron that filled the hole can be transferred to a third electron, situated in the outer L shell. If the energy is greater than the orbital binding energy, the electron is ejected from the atom, which is now doubly ionised, and the photoemitted Auger electron is picked up by the detector [109, 110]. Once the survey scan had been collected, scan ranges could be chosen based on the binding energies of the elements of interest. The C 1s peak was chosen for further analysis, as this is of interest from a graphitic material viewpoint. The high resolution C 1s scans are shown below (Figure 100).

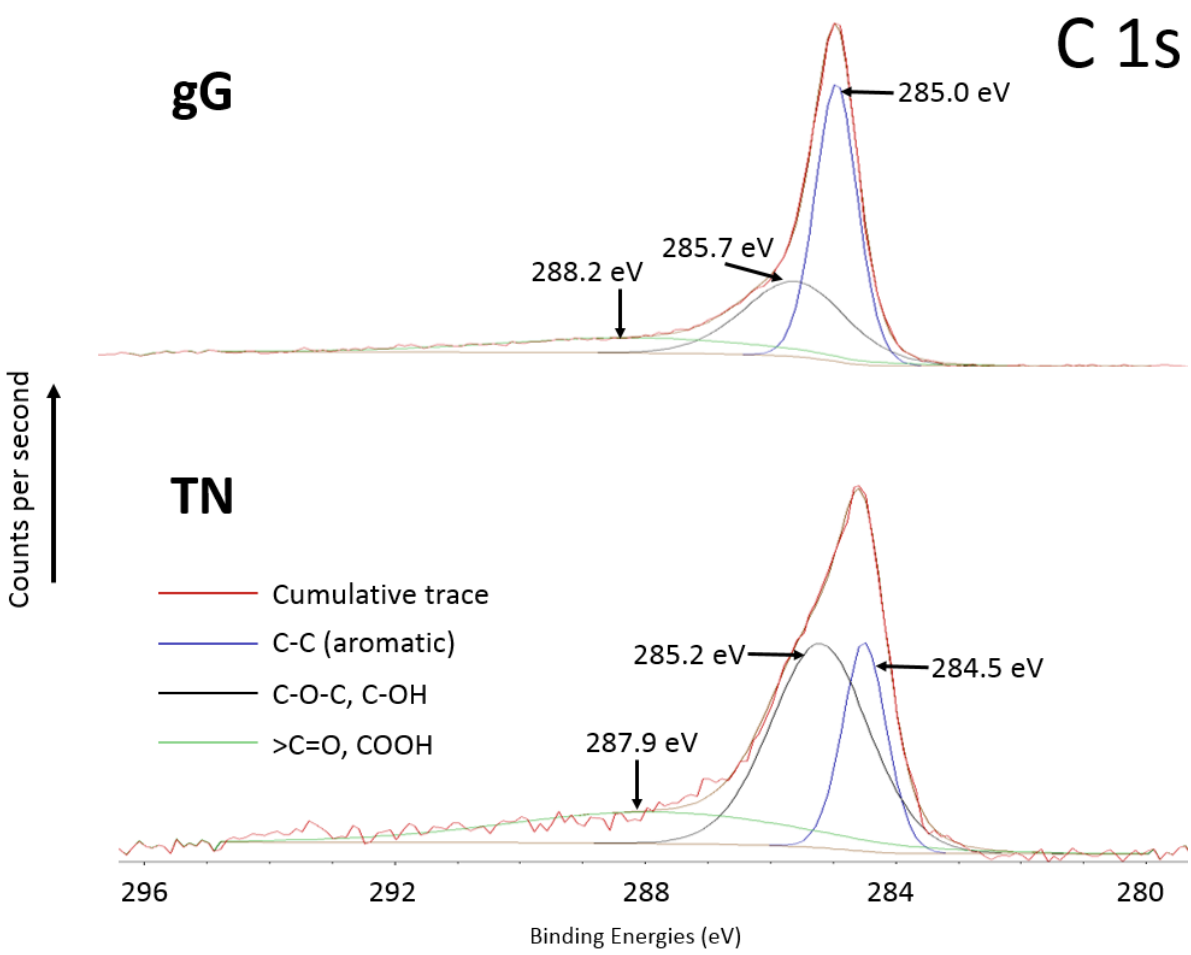


**Figure 100: High-resolution XPS C 1s scans for the gG and TN samples**

The XPS C1s scans revealed that each of the samples is oxidised to a different extent. An immediately noticeable difference between the scans are the ratios between the aromatic carbon peak (gG: 285.0 eV, TN: 284.5 eV) and the epoxide/hydroxyl (C-O-C) peaks (gG: 285.7, TN: 285.2) and the greater intensity of the TN carbonyl/carboxy peak relative to the aromatic and epoxide elements, compared to the same peaks of the gG sample. By considering the shape of the cumulative traces and comparing them to data obtained in the literature, we can form some conclusions related to the oxygen content of the samples (Figure 101).

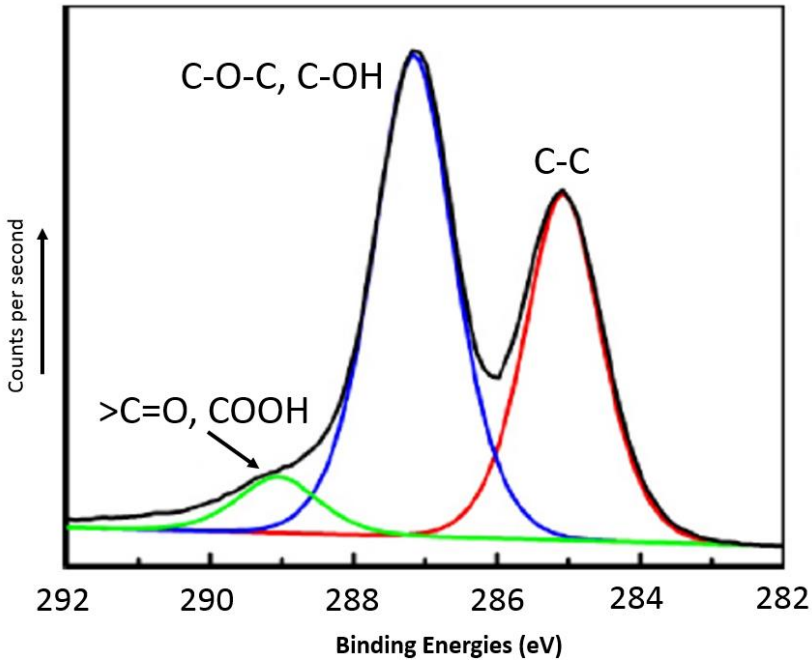


**Figure 101: XPS spectrum of the C 1s peak of graphene oxide**

The double peak structure present in Figure 101 (with a contribution at approx. 289 eV) is characteristic of highly oxidised graphene oxide. As the oxygen content increases, the C-O-C/C-OH peak intensity also increases as the proportion of these groups rises, while the C-C peak intensity decreases [112]. If we consider the TN and gG C 1s spectra of Figure 100, a shoulder on the TN spectrum is present, caused by the relatively high intensity of the 285.2 eV peak. This suggests that the TN rGO was more oxidised than the gG sample, indicating that the reductive process employed for this material was not as effective as that used for gG, as more oxygen groups remain. Using Raman spectroscopy, it is possible to learn more about the oxygen content of the reduced graphene oxide and the disorder this imposes on the sheets of rGO.

#### 4.3.2.7 Characterisation of the rGO's and Identification of Contaminants: Raman Analysis

Raman spectroscopy was also used to analyse the rGO samples. This technique is a standard non-destructive tool for the characterisation of crystalline, nanocrystalline and amorphous carbons [82]. Using visible Raman spectroscopy it is possible to deduce the amount of disorder (or deviation from perfect graphene) present in graphitic material caused by the oxidation of $sp^2$ carbon atoms. This is because the spectra are fundamentally dependent upon the carbon $sp^2$ domain sizes that are present, but also indirectly on the fraction of $sp^3$ sites [113]. Therefore, as the number of functional groups added to the basal plane increases, the number of $sp^3$ sites also increases as $sp^2$ atoms are converted to $sp^3$. The region of interest of the

Raman spectrum in which this information is contained is the range 1150 to 1750 $cm^{-1}$. Found here are the D and G peaks, which correspond to the Raman active vibrational modes $A_{1g}$ and $E_{2g}$, respectively [114]. These are depicted in Figure 102.

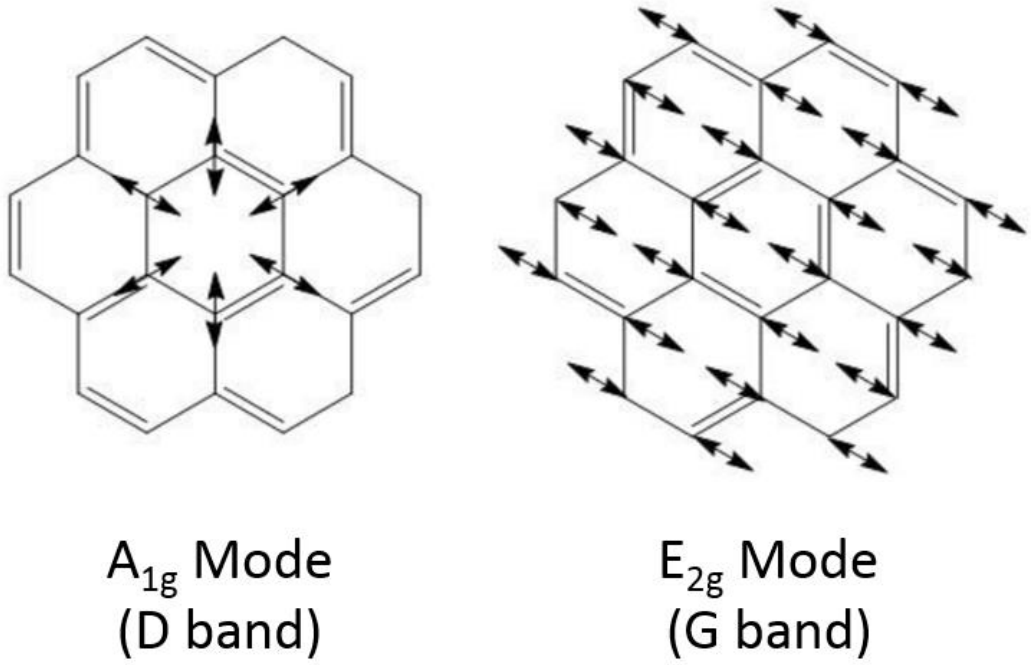


**Figure 102: Schematic of the vibrational modes A1g and E2g**

The A1g mode corresponds to the breathing mode of a six-membered aromatic ring. This is represented by the D band, typically observed about 1350 $cm^{-1}$. Perfect graphene will not exhibit this form of molecular vibration as it is forbidden and only exists in the presence of disorder [103, 115]. This mode occurs at defect sites and at the edges of the $sp^2$ regions. On the other hand, the G peak, present between 1580-1600 $cm^{-1}$, is active for all $sp^2$ hybridised carbon sites and does not require the presence of six-fold rings [116]. Hence, by calculating the ratio between the intensity of the D and G peaks, it is possible to estimate the size of continuous $sp^2$ carbon areas present in the sample. The Tuinstra and Koenig (TK) equation (Equation 21) describes the relationship between the peak intensities and the average $sp^2$ domain size [114]:

$$\frac{I_D}{I_G} = \frac{C(\lambda)}{L_a} \qquad \text{Equation 21}$$

where $I_D$ and $I_G$ correspond to the intensities of the D band and the G band respectively, C represents a constant that is dependent on the wavelength of the laser used for the measurement and $L_a$ is the average cluster size of defect free graphene ($sp^2$ carbon). At a fixed

wavelength, $I_D/I_G$ varies inversely with $L_a$ i.e. as the ratio increases, as does the size of the amorphous regions. However, the TK equation only applies to $sp^2$ domain sizes larger than 20 Å because the intensity of the D peak reduces as the average cluster size falls below this value [114]. The cause of this is that as $L_a$ decreases below 2 nm, the 6-membered rings are disrupted by the high level of disorder and so there exists fewer of them. The intensity of the G peak will remain unchanged as it only relates to the bond stretching of $sp^2$ pairs, and so as the amorphisisation increases, $I_D/I_G$ will decrease. Another indication of an increase in disorder is the broadening of the D and G peaks, which is caused by an increase in the stress on $sp^2$ clusters surrounded by oxygen rich regions [117]. Under these conditions, the TK equation fails and so for samples with a greater proportion of amorphous area, a modified equation is required. A variation of Equation 21 that accounts for this is given below (Equation 22) [114]:

$$\frac{I_D}{I_G} = C'(\lambda){L_a}^2 \qquad \text{Equation 22}$$

where C' is a different constant that also depends on the experimental wavelength of the laser. After taking into consideration the effect of disorder on the basal plane as well as $I_D/I_G$, Ferrari *et al* proposed a relationship between the average cluster size and the ratio between the intensities of the D and G peaks according to Equation 21 and 22 (Figure 103) [114].

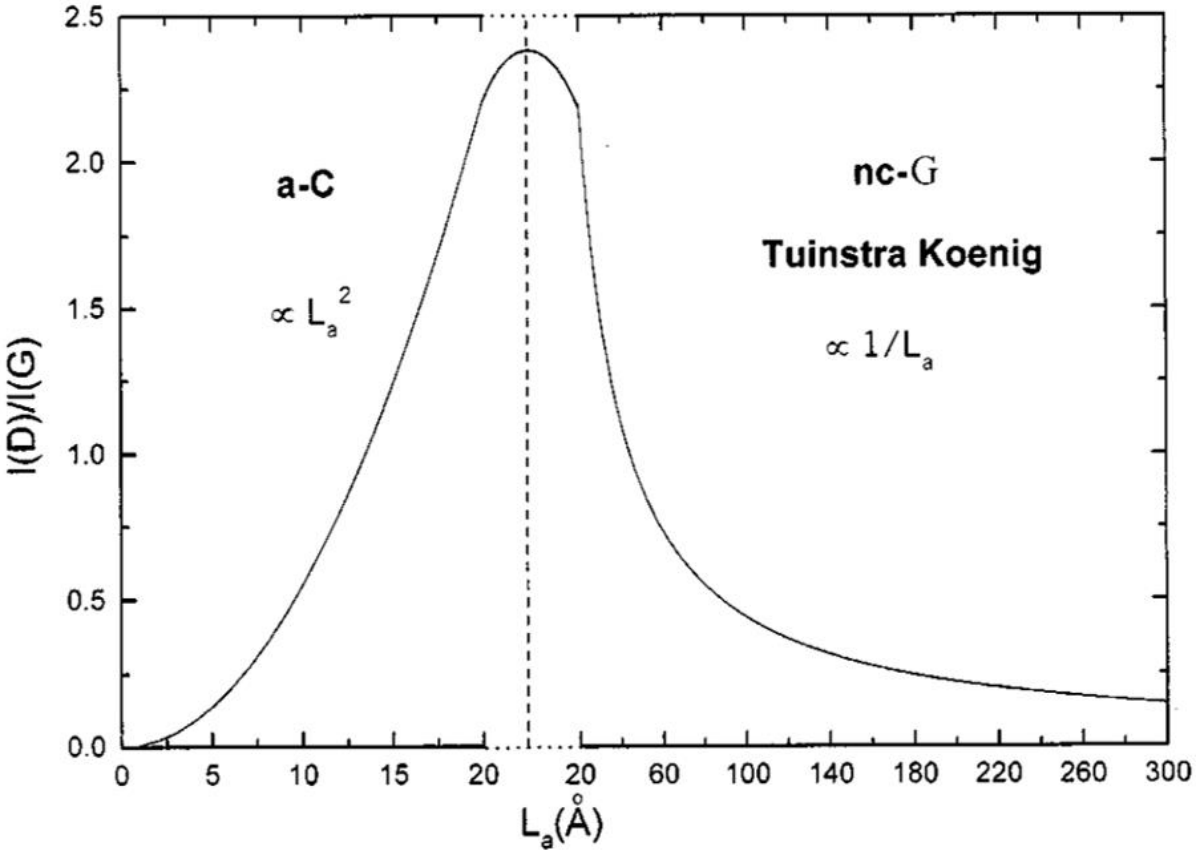


**Figure 103: Relationship between the ratio of the D and G peaks and the average cluster size, $L_a$**

The left hand region of Figure 103, labelled a-C, relates to Equation 22 and is appropriate for amorphisised carbon, such as rGO. The right hand side, labelled nc-G is applicable to nanocrystalline graphene and relates to Equation 21. Using this and the properties of the peaks from the Raman spectra obtained for my rGO samples, it is possible to produce an estimate of the average $sp^2$ cluster size. The Raman spectra of the 1150 to 1750 $cm^{-1}$ regions are below in Figure 104.

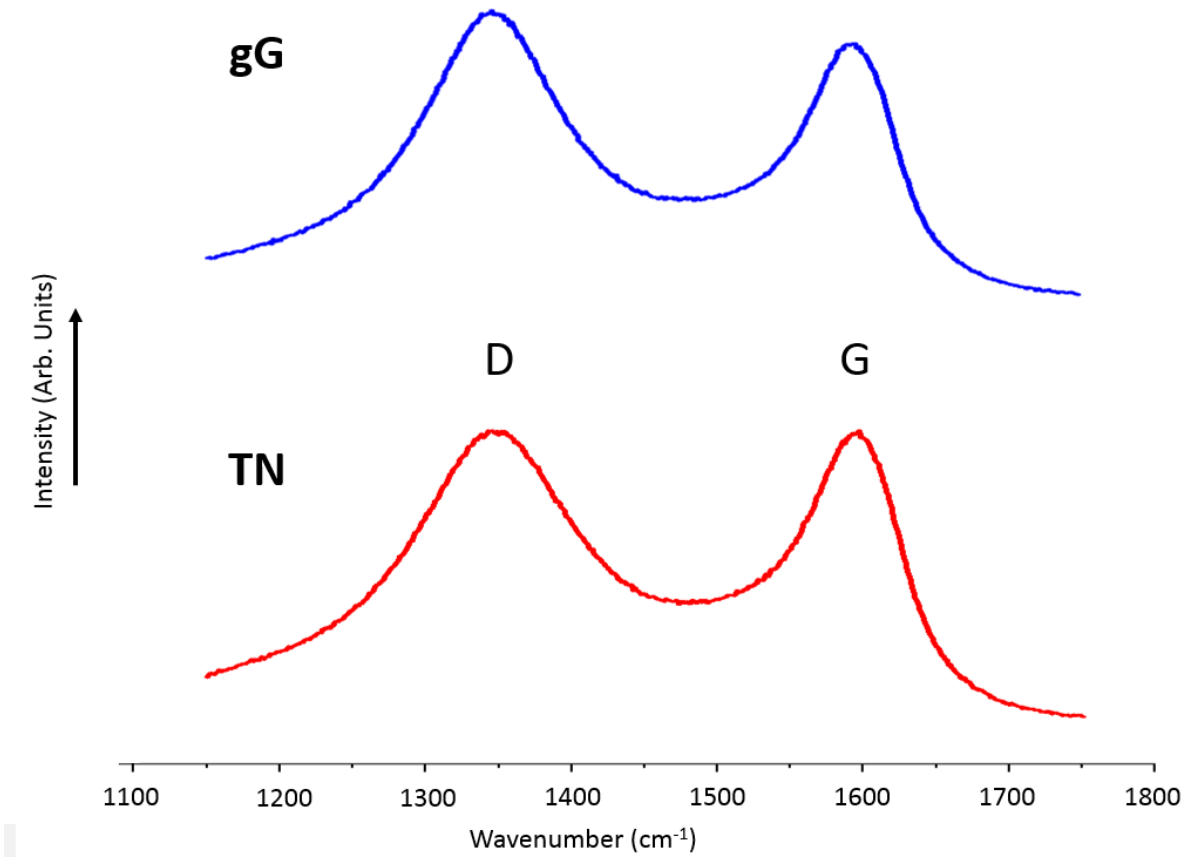


**Figure 104**: **Raman spectra of the gG and TN samples taken from 1150 to 1750 $cm^{-1}$**

The peak positions, full width at half maximum (FWHM), and $I_D/I_G$ ratio are presented in Table 14.

**Table 14: D/G Raman peak analysis for the gG and TN samples**

| Sample | Peak Position ($cm^{-1}$) | | FWHM ($cm^{-1}$) | | $I_D/I_G$ |
|---|---|---|---|---|---|
| | D Peak | G Peak | D Peak | G Peak | |
| **gG** | 1346.75 | 1590.59 | 156.2 | 81.35 | 1.18 |
| **TN** | 1347.72 | 1590.83 | 189.3 | 85.1 | 1.04 |

The positions of the D and G peaks were similar between samples. The greater value for the peak ratio of the gG sample ($I_D/I_G$ = 1.18) indicates that this was a more crystalline sample than TN ($I_D/I_G$ = 1.04), which is supported by the smaller FWHM measurements for gG. By comparing the FWHM values to those in the literature for argon bombarded graphene [113], it is possible to determine whether it is the a-C or nc-G regions of Figure 103 that should be considered when analysing these rGO samples. This is important because, as already mentioned, this will influence the value obtained for $L_a$ as the TK equation (Equation 21)

breaks down at cluster sizes smaller than 2 nm. The authors state that values below 40 $cm^{-1}$ for the $FWHM_D$ and $FWHM_G$ are caused by average $sp^2$ cluster sizes above 20 Å. The values obtained here are far greater than this and so the samples should be analysed using the a-C region of the graph (Figure 103). This correlates with the XPS data, which suggested that the oxygen content of both samples was relatively high (Figure 100) and as such, the $sp^2$ domain size will be small. Using Equation 22 ($ID/IG = C'(\lambda)L_a^2$) and values for C' in the literature for a Raman laser wavelength of 514 nm (C' = 0.0055 Å [114]), the peak ratio was plotted against the average cluster size (Figure 105).

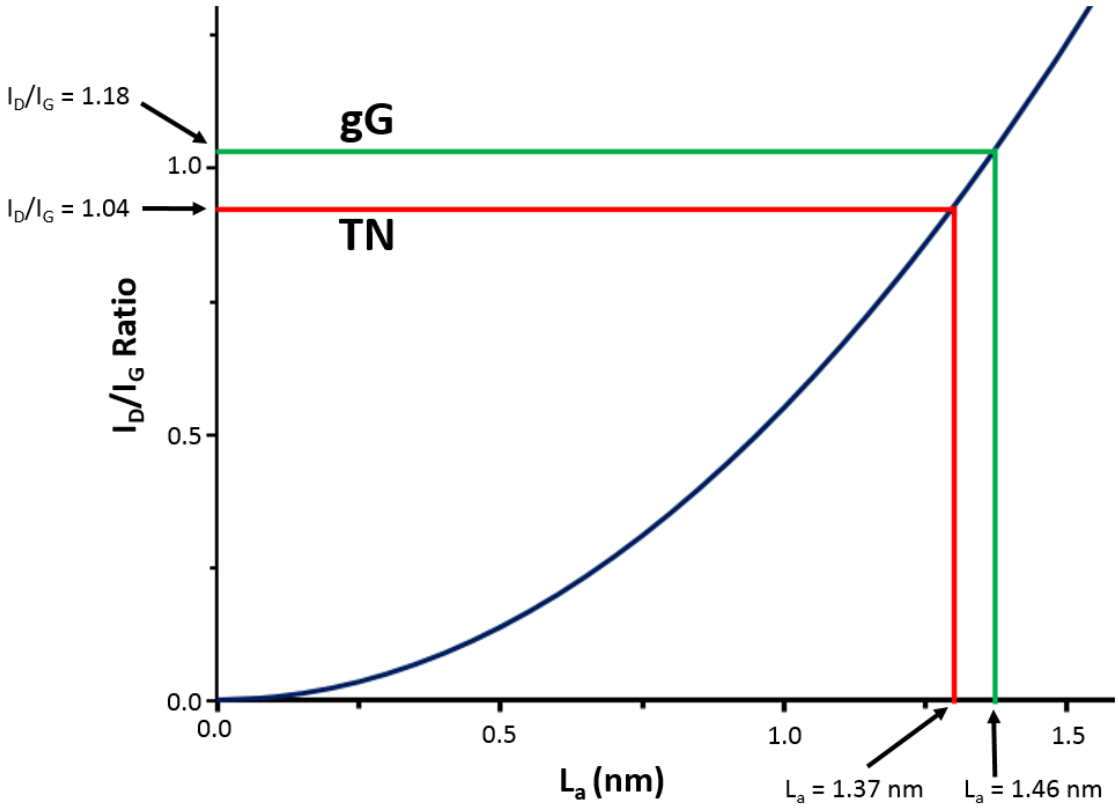


**Figure 105: Plot of $I_D/I_G$ ratio against the average $sp^2$ cluster size, $L_a$**

Using the relationship between the peak ratio and average $sp^2$ cluster size proposed by Ferrari *et al* [114], values of $L_a$ for the gG and TN sample were calculated to be 1.46 and 1.37 nm, respectively. It has been suggested elsewhere that the FWHM of the D peak can provide a comparative assessment of the range of $sp^2$ cluster sizes between samples. According to this, the greater $FWHM_D$ value indicates a broader range of cluster sizes for the TN sample than the gG sample ($FWHM_D$ gG = 156.2 $cm^{-1}$, $FWHM_D$ TN = 189.3 $cm^{-1}$).

#### 4.3.2.8 Effect of rGO Film Preparation on the Crystallisation of Calcium Carbonate: Dropcasting

Dropcasting is the simplest film preparation procedure since it requires only pipetting a drop of a material's dispersion onto a surface, followed by evaporation. Dropcasted films are often heterogeneous in thickness and distribution of material, and as such spin coating is typically preferred were film continuity and consistency are important [118]. The purpose of this investigation was to reveal if the topography generated by spin coating was necessary for aragonite to form. Given the different solution dynamics involved in spin coating and dropcasting, the resultant surface coatings of rGO are very different from a topographical viewpoint. Micrographs of a dropcasted gG coating on a silicon wafer are included below (Figure 106a-c), and also a spin coated surface for comparison (Figure 106d).

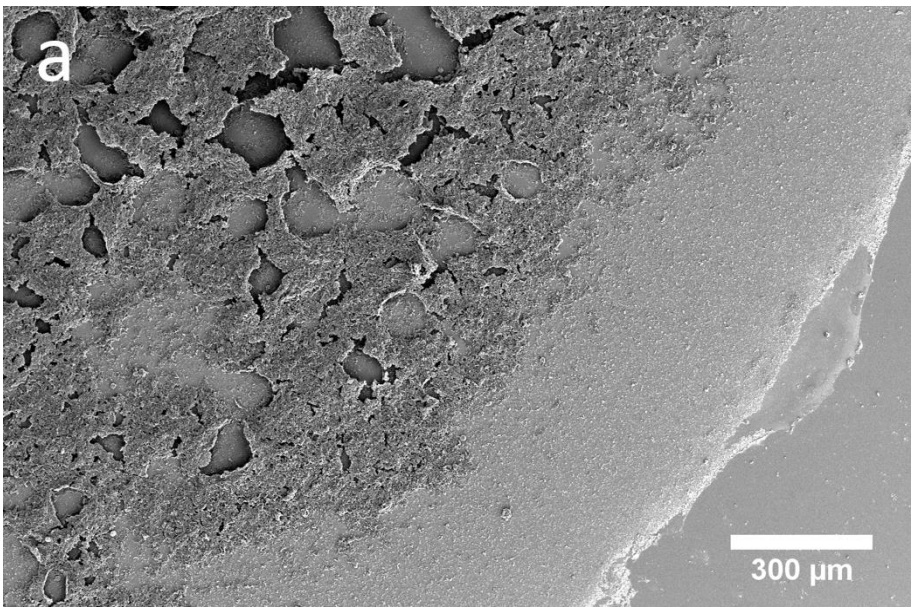
a
300 µm

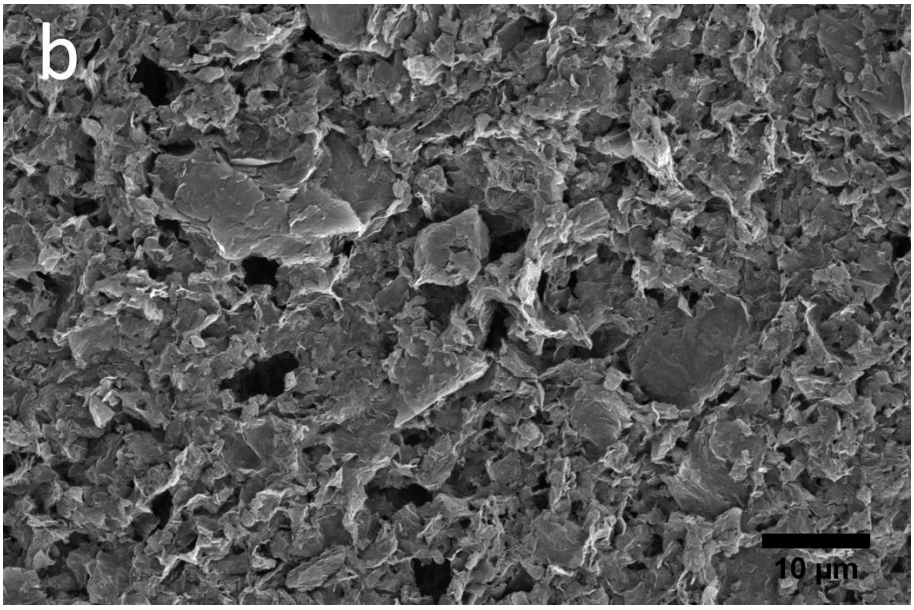
b
10 µm

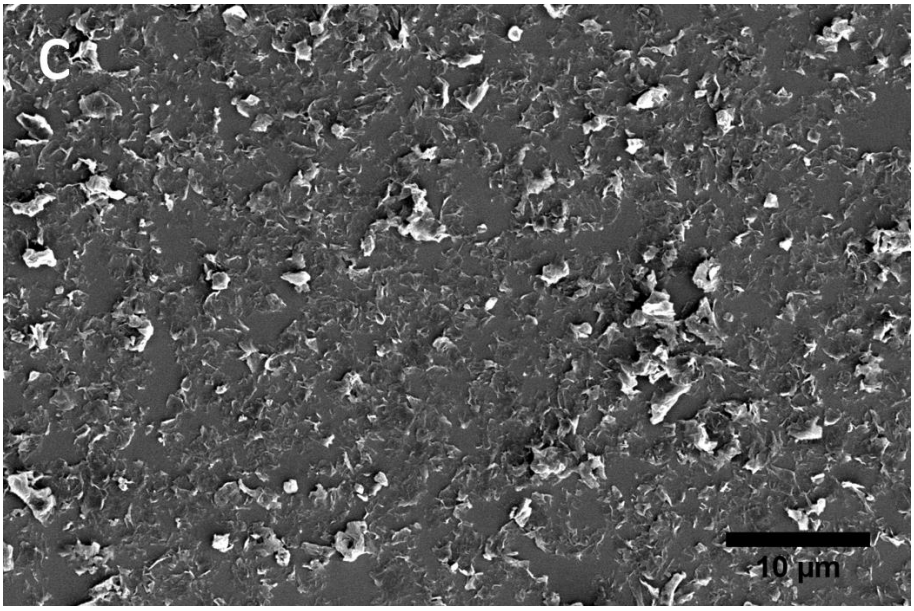
c
10 µm

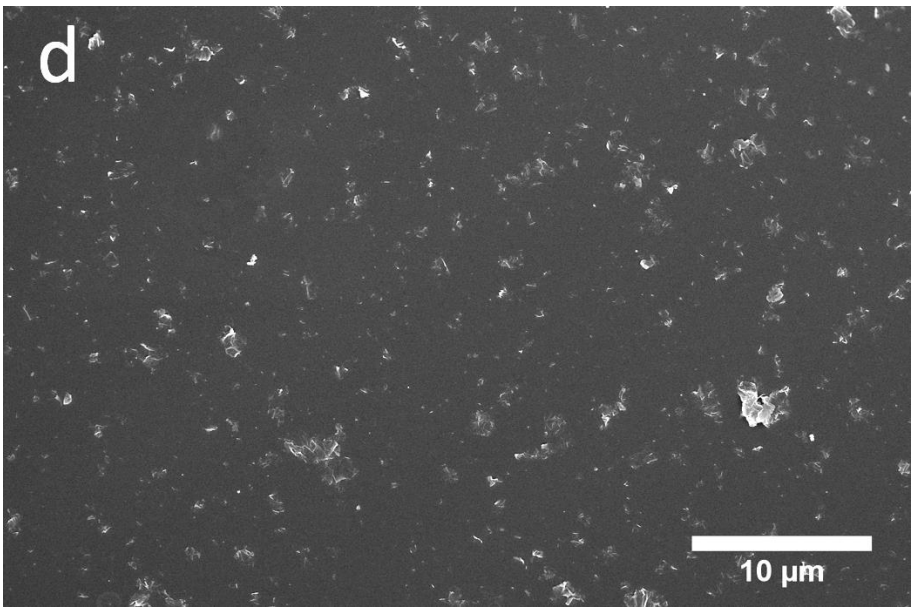


**Figure 106: Electron micrographs of a film of gG rGO deposited on a silicon wafer via dropcasting**

As expected, the topography varied significantly from the perimeter of the film to the centre. The deposited material was composed of two distinct regions. A dense, central mass was surrounded by a thinner ring of material, their arrangement dictated by the receding contact line and associated increase in rGO concentration as the water evaporates and the contact area of the droplet reduces [119]. The topography of these two regions are significantly different both from each other and from the spun rGO, as indicated by Figure 106. On crystallisation, the total crystal population was comparatively low compared to spin-coated rGO, and calcite was observed both within the outer ring and atop the aggregated central mass (Figure 107). Interestingly, no aragonite was observed on the deposited material.

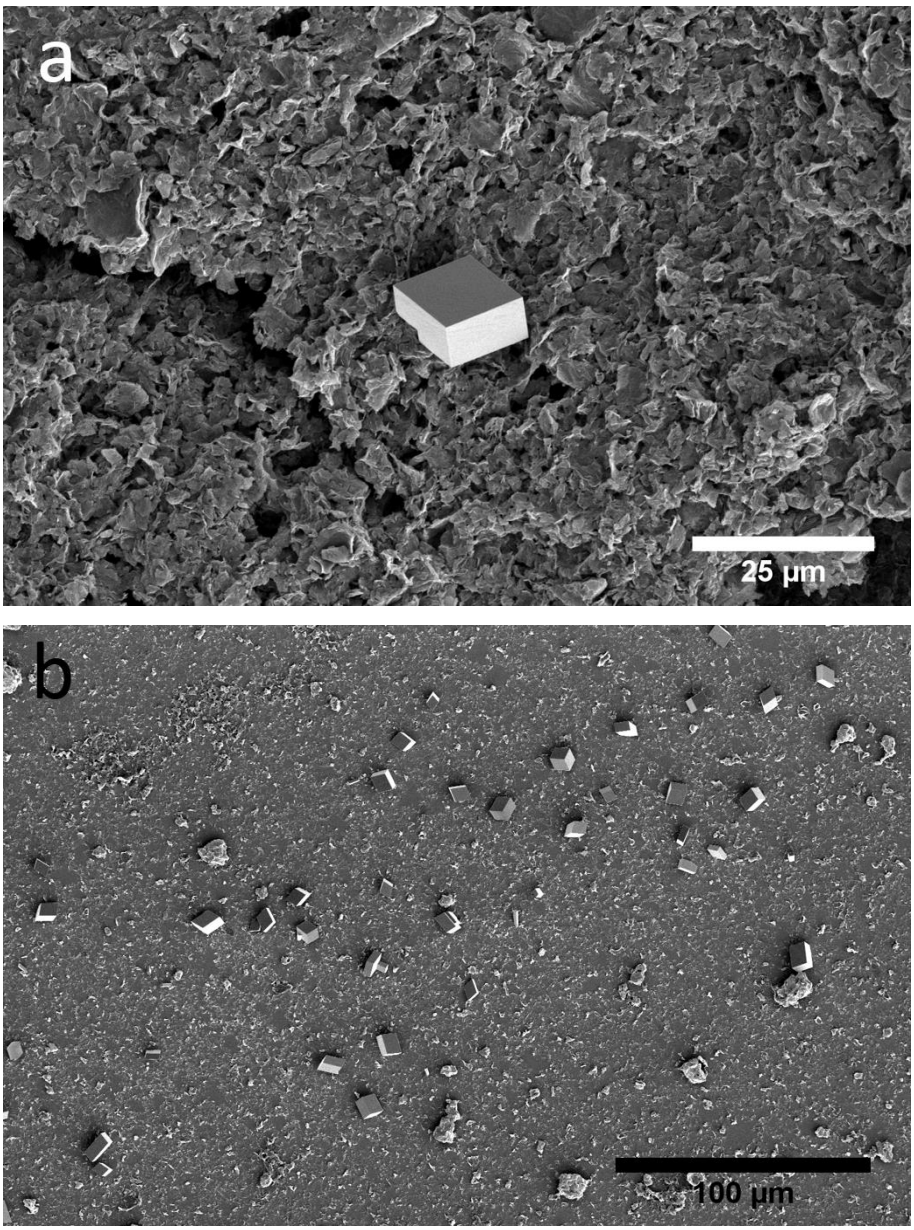


**Figure 107: Electron micrographs of calcium carbonate crystals precipitated on the dropcasted gG rGO film**

Only a small number of crystals were observed in the central mass of material, the crystal population was much lower here than inside the outer ring, though, as stated above, in both areas only calcite was observed. The atomic force micrographs provide an insight into the topographies present at each of the sites (Figure 108).

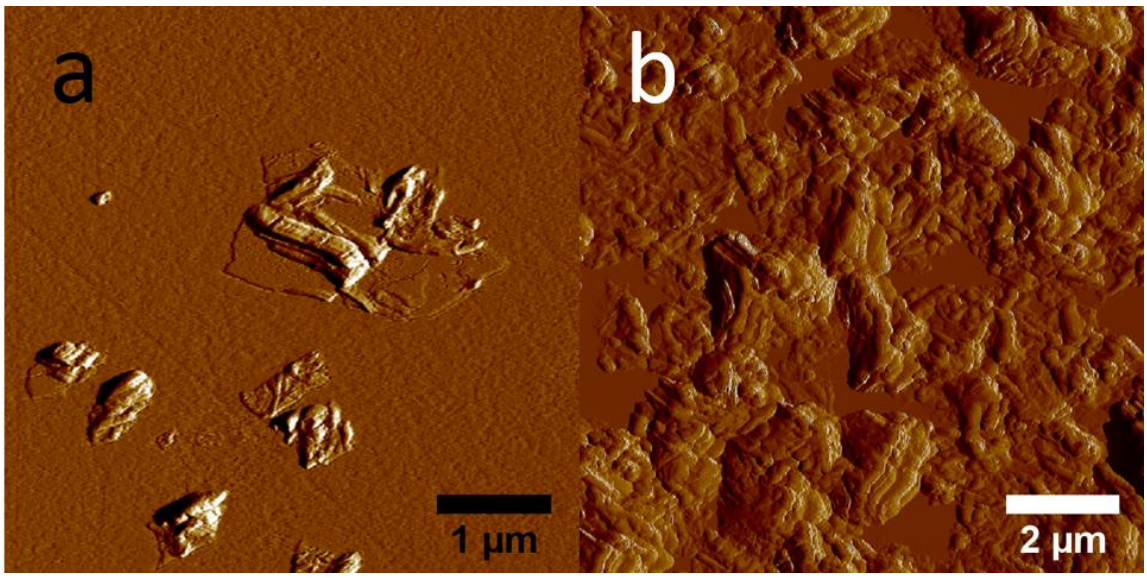


**Figure 108: Atomic force micrographs of gG rGO spin coated onto a silicon wafer and dropcasted onto a wafer**

The difference between the coatings is striking. A much denser surface coverage is achieved by dropcasting and the flakes form tangled masses. The maximum feature height measured on this substrate was 2.2 microns, compared to the 70 nm of the spin coated sample. There was also a much greater spread of heights recorded on the dropcasted substrate. As a further test to determine whether it was the topography causing aragonite to form on the spin coated substrate, and that it wasn't the presence of impurities inhibiting its formation on the dropcast substrate, the gG rGO was washed thoroughly in an attempt to remove as much contamination as possible (Section 4.2.3.4). Crystallisations were carried out on substrates where this washed gG had been spun onto the substrate or dropcasted. Micrographs of the crystallisations are shown below (Figure 109).

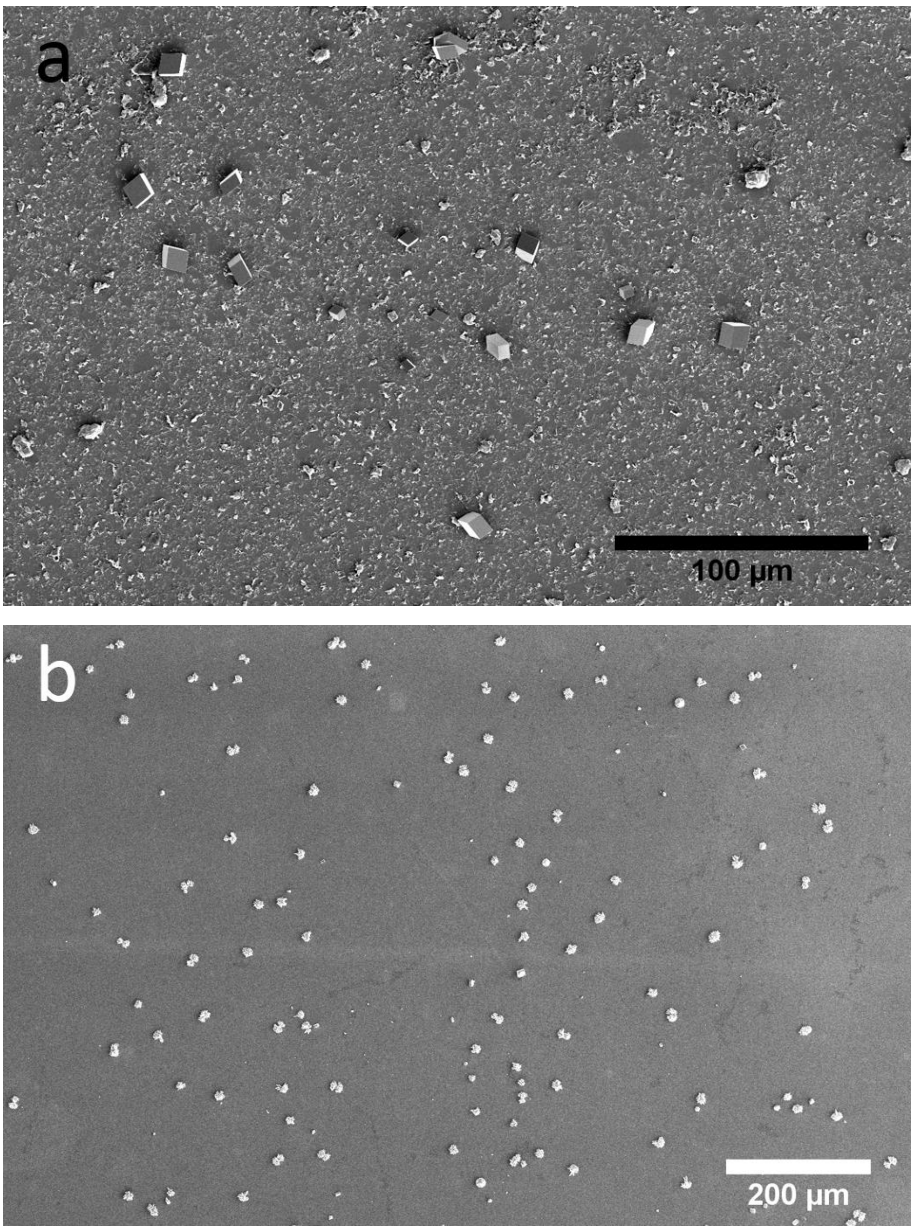


**Figure 109: Crystallisation on silicon wafers coated with washed gG rGO**

Aragonite was observed on the spin coated substrate, but was absent from the substrate that had been coated with gG rGO using dropcasting. The fact that the coatings that are formed by each technique are so different from one another is compelling evidence that it is indeed the surface topography that causes aragonite to form.

#### 4.3.2.9 Effect of rGO Film Preparation on the Crystallisation of Calcium Carbonate: Delamination Through Ultrasonication

The next investigation was aimed at determining if delamination of the graphitic sheets via sonication was necessary for aragonite to form. This is another topographical test, since a coating formed from agglomerations will have a significantly different surface topography to a spincoated film. Sonication of graphitic dispersions is a commonly used method to separate

the stacks of rGO [81]. Although this method is a fast exfoliation method, it should be noted that its vigorous nature can cause physical damage to individual sheets and break them into smaller fragments [117]. The fact that sonication is required in order for a surface coating to form was confirmed via SEM, as inspection revealed that very little material was present on the wafer surface after deposition of the gG rGO that hadn't been sonicated. The material that was present existed as agglomerations, and failed to produce aragonite on crystallisation (Figure 110).

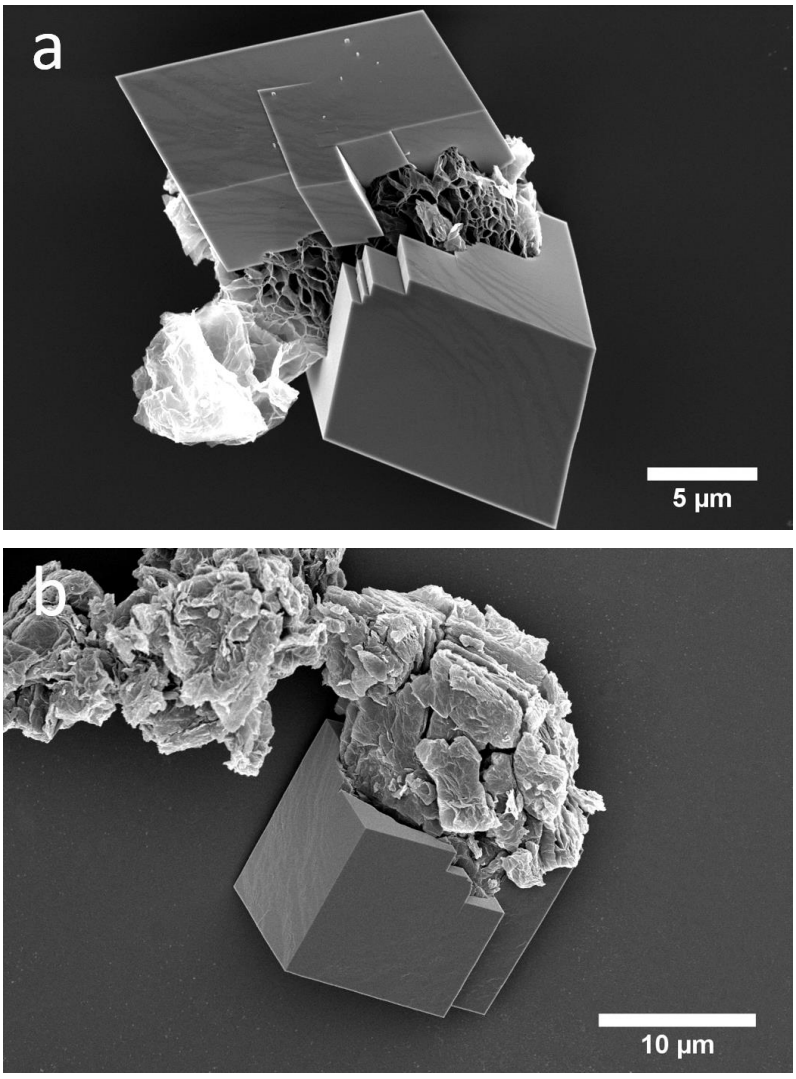


**Figure 110: Calcite crystals nucleated on a graphitic particle that was deposited from a gG rGO dispersion that had not been sonicated**

This data combined with the previous experiment suggests that the presence alone of rGO on the wafer surface is not sufficient to cause aragonite precipitation. It is also possible though that the resultant topography formed on the silicon surface by spin coating is not required, instead, only the presence of rGO post-sonication within the solution is needed. The next

experiment investigates whether free-floating exfoliated reduced-graphene oxide within the bulk of the solution that has detached from the surface can promote aragonite formation.

#### 4.3.2.10 Effect of rGO Film Preparation on the Crystallisation of Calcium Carbonate: Isolation of Crystals from Bulk Solution

So far, the experimental data have suggested that it is necessary to sonicate the rGO dispersion prior to film formation, and that spin coating is required for aragonite to form. On submersion of the spin coated substrate in the crystallising solution, some flakes will inevitably be removed from the surface as water infiltrates the gaps between the material and the silicon wafer. These flakes have undergone both sonication and spin coating and so are a good comparison to those that remain on the surface. The aim of this experiment was to determine if these free-floating flakes are able to cause aragonite to form. If so, this would suggest that, rather than the surface topography generated by surface coating being the cause, it may be the surface of the sonicated rGO flakes instead. To test this, the crystallisation was executed using the normal procedure, though after completion, the solution was removed from the crystallisation dish using a syringe and then vacuum filtered using a 220 nm pore size membrane. The membrane was then imaged in the SEM to determine which crystal polymorphs were present (Figure 111).

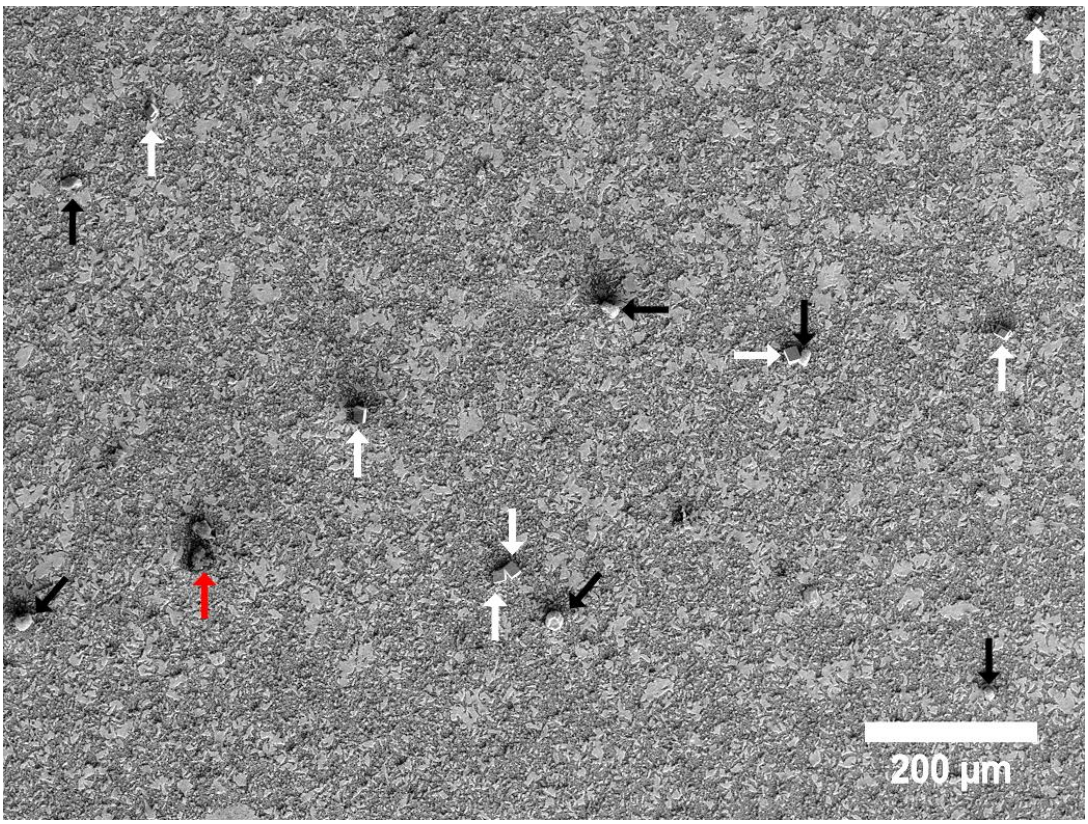


**Figure 111: SEM image of the 220 nm pore size membrane used to filter the solution after crystallisation with a rGO coated Si wafer present**

The number of crystals observed on the membrane was much smaller than that typically found on the substrate surface, indicating that crystallisation preferentially occurred on the rGO film than on free-floating material. Inspection of the membrane with the SEM revealed no aragonite, only calcite and vaterite. The fact that no aragonite was detected away from the substrate surface suggests that a rGO spin-coated surface is required, and free-floating agglomerations are ineffective at inducing aragonite formation.

### 4.3.3 Investigations into the Precipitation of Calcium Carbonate on Silicon Substrates coated with Other Atomically Layered Materials

After obtaining aragonite by spin coating reduced-graphene oxide onto a silicon wafer, the next step was to determine if it was possible to produce a high yield of this polymorph using other atomically layered materials.

Since the isolation of graphene in 2004, research into atomically layered materials has grown exponentially [79]. The revelation of the exciting electrical properties of graphene opened the door for a new area of study: two-dimensional electronics. A rapid expansion of this field occurred, as researchers searched for other layered materials that could be isolated into

atomically thin sheets. This exploration was fueled by the limited scope of electronic device applications that graphene, a zero gap semiconductor [120], can realise, as its absence of a bandgap means it cannot be used in transistors in its pristine state [121]. Alternative 2D semiconductor components would permit the fabrication of truly two-dimensional electronic devices, suitable for unique applications, particularly in sensing and actuation [122].

Shortly after their paper on graphene, Novoselov and Geim released an article documenting their success at isolating other 2D crystals [123]. Their method of isolation was even simpler than that used to acquire graphene; the layered crystal bulk was simply rubbed against a silicon wafer (according to the authors, "*virtually any solid surface is suitable"*), leaving a variety of flakes adhered to the surface, among which single layers were always found. The process of isolating and identifying potential 2D crystals was quick, taking only half an hour. Many researchers had tried previously to isolate two-dimensional materials, with no success, and it was a serendipitous observation that allowed Novoselov and Geim to do so. They realised that 2D crystallites could be identified on an oxidised silicon wafer as even these infinitesimally thin materials add sufficiently to the optical path of reflected light such that a different interference colour is perceived relative to an empty substrate. Using this methodology, Novoselov and Geim presented data in their paper on the isolation of four new atomically thin crystals: hexagonal boron nitride, molybdenum disulhpide, niobium disulphide and $Bi_2Sr_2CaCu_2O_x$. Since then, the number of isolated 2D materials has expanded and now includes black phosphorene (2D allotrope of black phosphorous) [124], silicene (2D allotrope of silicon) [125] and germanene (2D allotrope of germanium) [126]. Indeed, most group IV and V elements have been predicted to have one or more stable 2D allotropes [127].

Although there now exists a range of materials that can be produced with structures similar to graphene, not all of them are as easy to isolate. For my research, it was important to use materials that could be easily obtained. The materials that were chosen were the transition metal dichalcogenides $MoS_2$ and $WS_2$, and graphitic carbon nitride, all of which can be exfoliated via ultrasonication, as documented in the literature [128, 129]. Each of these could be purchased from a supplier in powder form. Further information regarding these materials is provided below, alongside data from my very brief investigation.

#### 4.3.3.1 Transition Metal Dichalcogenides

Transition metal dichalcogenides (TMDs) possess the formula $MX_2$, where M is a group IV, V or VI transition metal and X is a chalcogen atom such as sulphur. Their structure involves metal

atoms with octahedral or triganol prismatic coordination sandwiched between layers of chalcogen atoms. When viewed from above, a hexagonal lattice is formed with alternating M and X atoms (Figure 112). For this research, surface coatings on a silicon wafer of molybdenum disulphide and tungsten disulphide were formed.

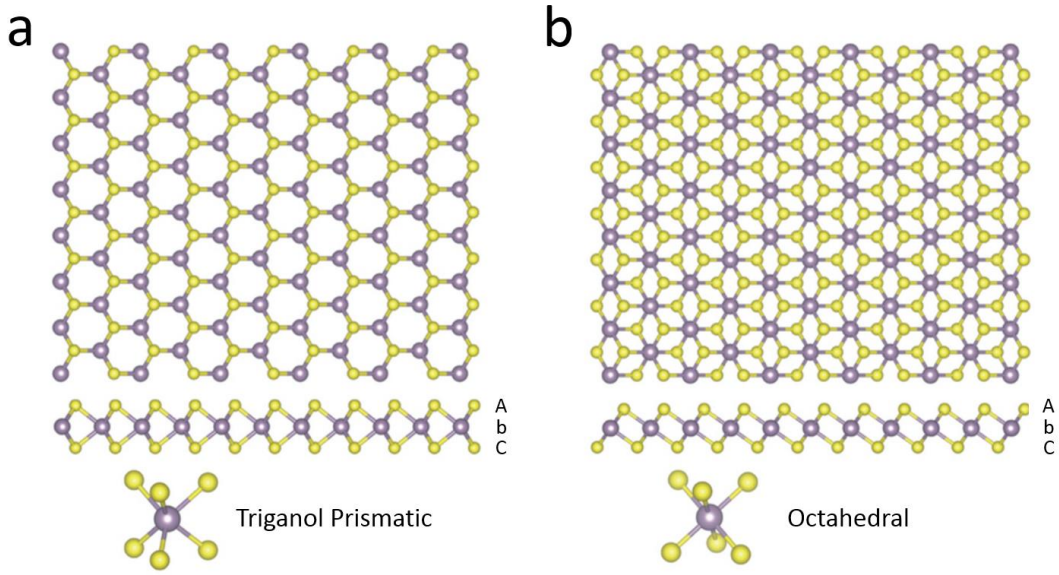


**Figure 112: Schematic of the structure of transition metal dichalcogenides**

As detailed in Section 4.2.3, mechanical exfoliation was used to separate the stacks of layers present in the powder form. The dispersion was sonicated and then spin coated onto a silicon wafer using the same procedure as that used for the rGO suspensions. Micrographs of the resultant coatings are given in Figure 113.

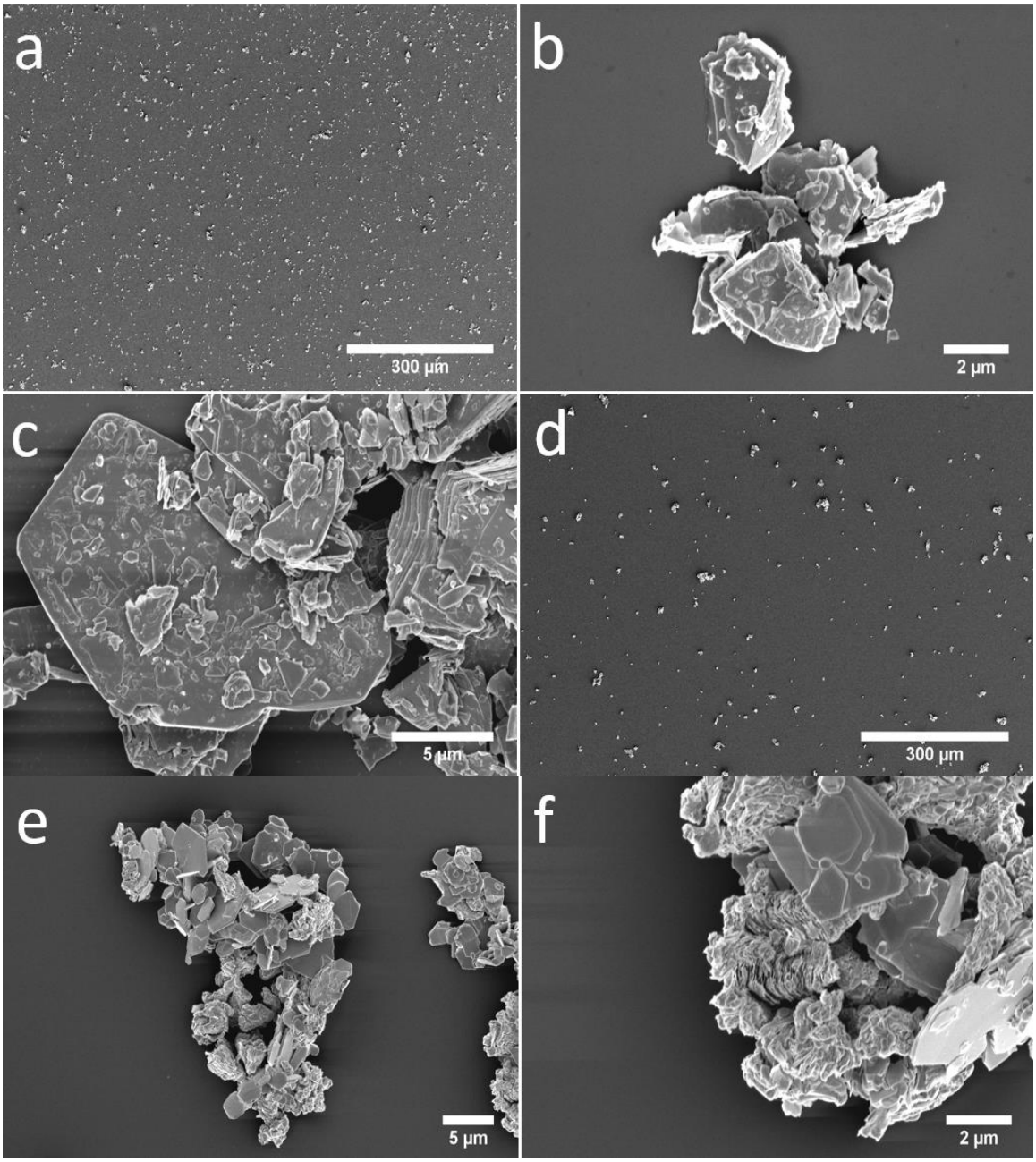


**Figure 113: Electron micrographs of the surface coatings formed on silicon wafers by spin coating molybdenum disulphide or tungsten disulphide.**

On visual inspection, many more molybdenum disulphide particles remained on the surface after spin coating compared to tungsten disulphide (Figure 113a and d). In both cases the particle size range was large and ultrasonication appeared to be a poor method of exfoliation. This is evident in Figure 113c and f, where material can be seen still tightly bound together. Although the surface coating appeared very different to those achieved by spin coating the rGO's, a calcium carbonate crystallsiation was carried out (Figure 114).

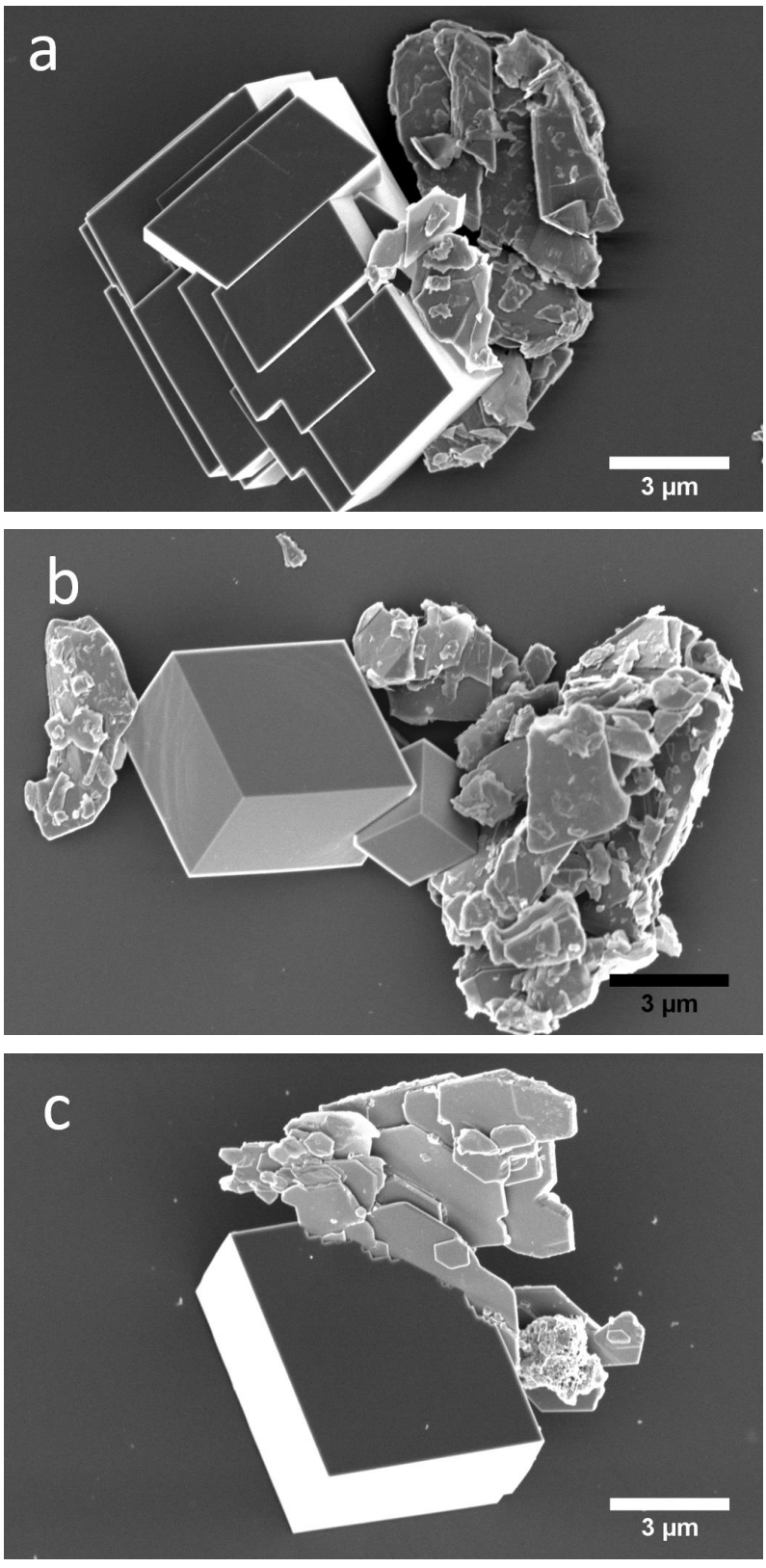
a
3 µm
b
3 µm
c
3 µm

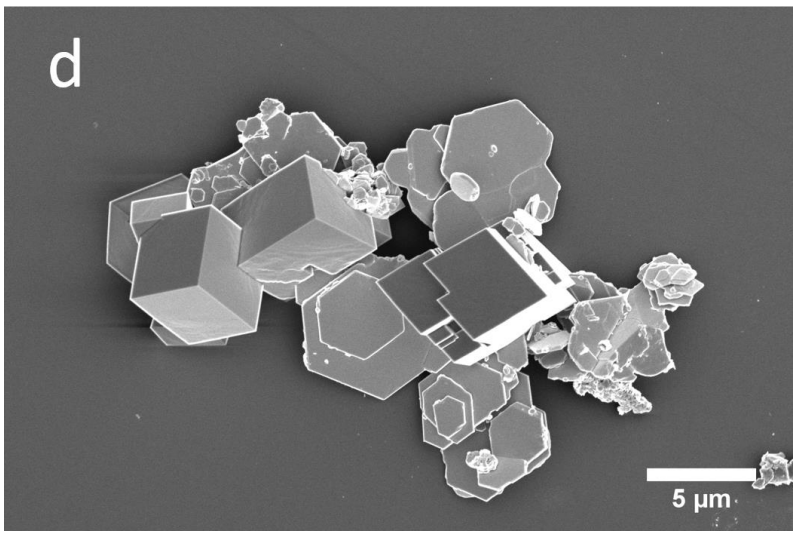


**Figure 114: Images of the $MoS_2$ and $WS_2$ particles after crystallisation of calcium carbonate**

Unfortunately, the crystallisation results were quite uninteresting and no aragonite had precipitated associated with the particles. No further experiments were conducted, with these materials, though it may have been interesting to form a coating from material that had been better exfoliated. One such method that has been proposed as quite effective for the delamination of TMDs involves the use of lithium [130]. A powder of the TMD is submerged in a solution of n-butyl lithium in hexane. Over the course of 48 hours, lithium ions intercalate between the lamellae of the TMD. The powder is then removed and submerged in water, which reacts violently with the intercalated lithium. Hydrogen gas is evolved, its expansion pushing the layers apart and effectively delaminating the TMD. Perhaps a coating formed from a suspension of TMDs exfoliated in this manner may have produced more interesting results.

#### 4.3.3.2 Graphitic Carbon Nitride

Graphitic carbon nitride (g-$C_3N_4$) is a polymeric sheet of carbon and nitrogen atoms and is the most stable allotrope of the carbon nitrides. It has high thermal stability and resistance to chemical attack, a result of the strong C-N bonds and its structure. The interlayer distance has been recorded as 0.326 nm, compared to 0.333 nm of graphite [131, 132]. There are two structural isomers of g-$C_3N_4$ and these differ according to the size of the intervallic vacancies in the sheet plane [133]. The first isomer of g-$C_3N_4$ is composed of s-triazine subunits and has a periodic array of single carbon vacancies, while the second isomer is composed of tri-s-triazine subunits and has larger vacancies (Figure 115) [134].

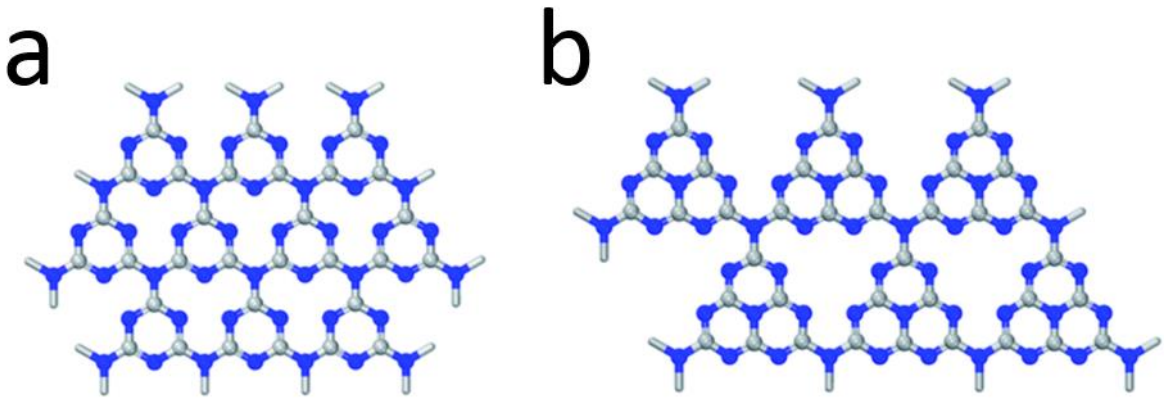


**Figure 115: The two structural isomers of graphitic carbon nitride**

The material was provided by the supplier as a powder, and, like the transition metal dichalcogenides and rGOs, the suspensions were sonicated to exfoliate the material. The same spin coating process was involved and the surface was inspected using electron microscopy.

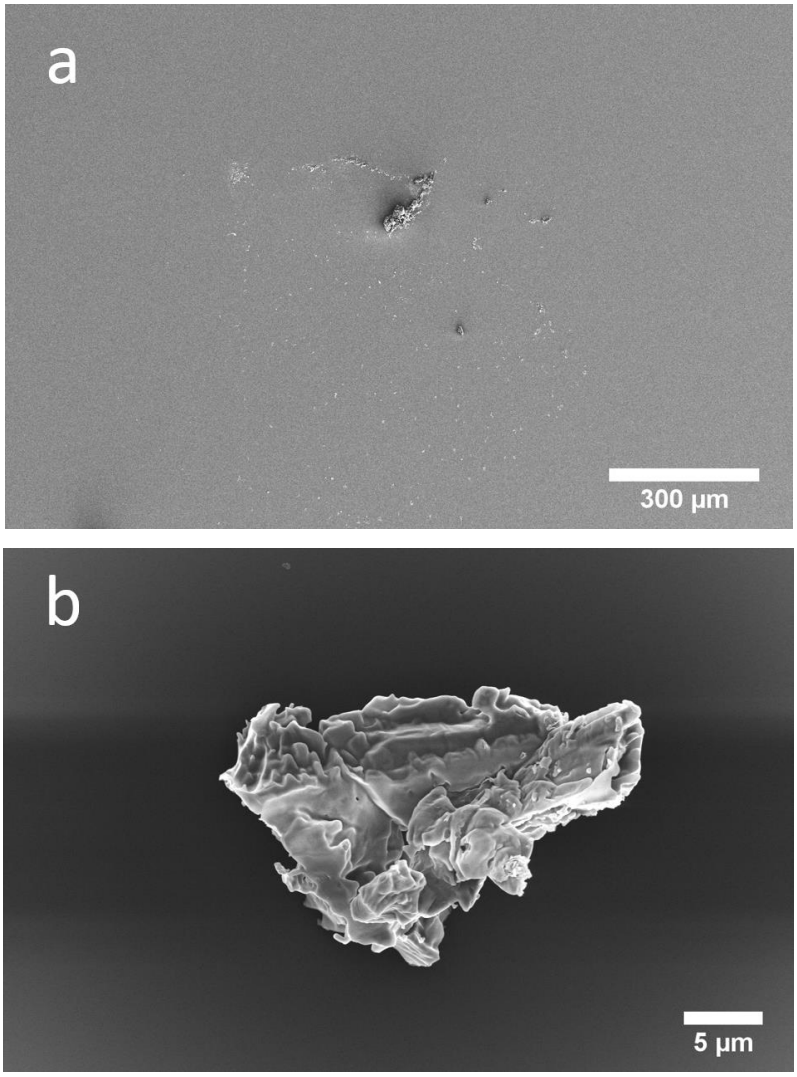

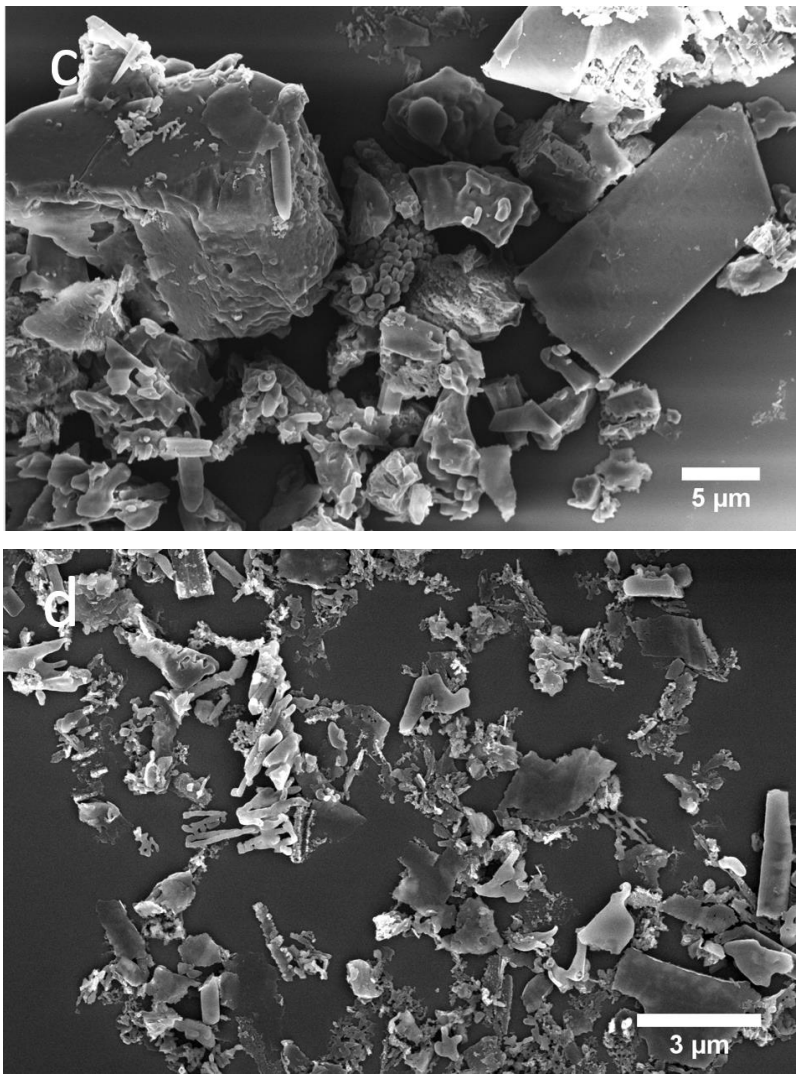


**Figure 116: Electron micrographs of the residual material present on a silicon wafer after spin coating with a suspension of graphitic carbon nitride**

Very little material was present on the substrate after spin coating and a huge variety of particle morphologies were observed. The fact that the shapes of the particles were so variable and very little flake-like or stacked material was observed may be an indication of heavy contamination or an ineffective synthetic procedure used by the supplier. To produce a sample with more material, allowing better inspection of the particles, a suspension was made in ethanol that was dropcasted onto a silicon wafer. This was imaged in the SEM (Figure 117).

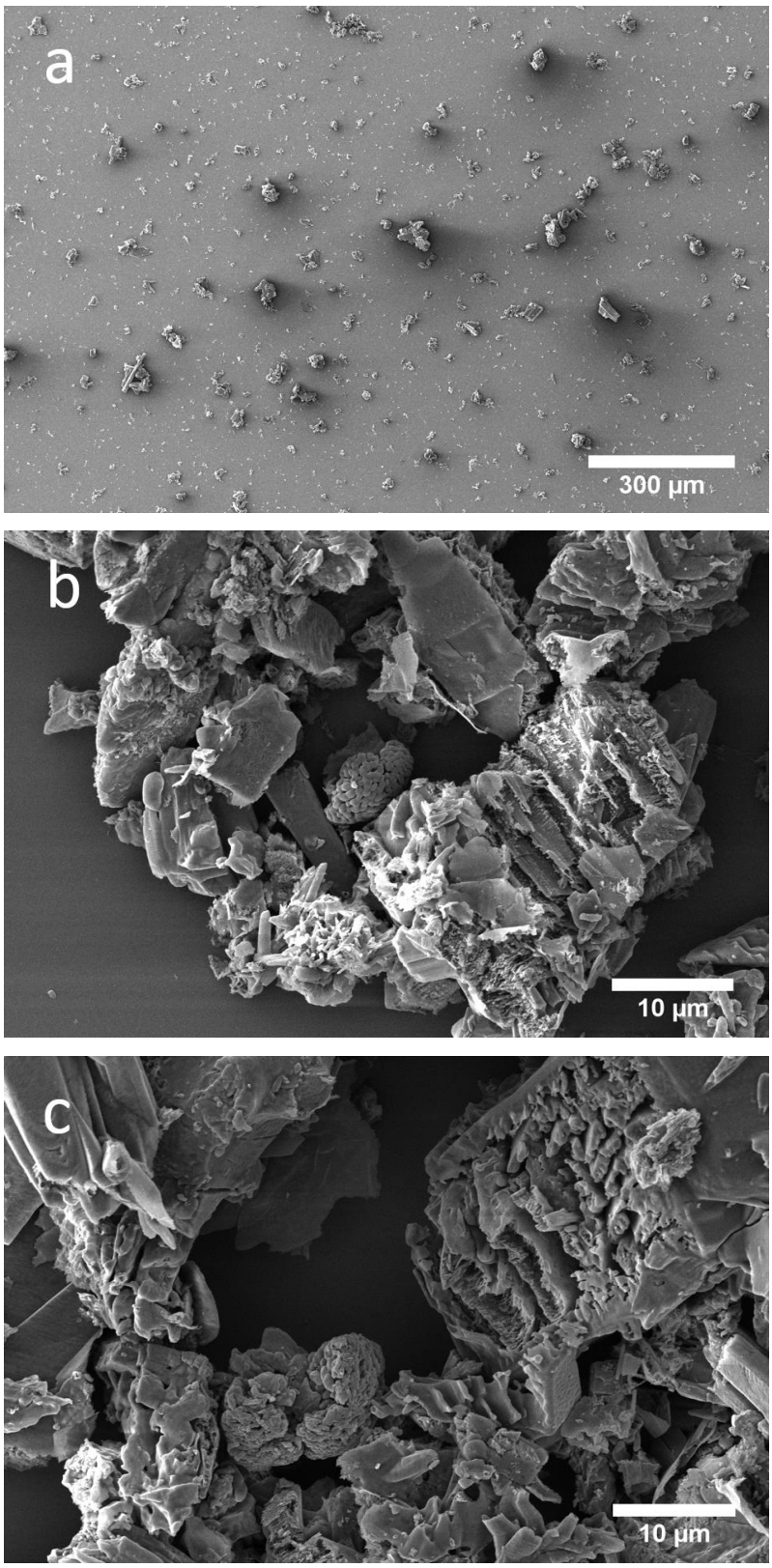


**Figure 117: (a-c) Electron micrographs of material sold as g-$C_3N_4$ dropcast onto a silicon wafer**

As before, the particles did not possess the morphology one would expect of atomically layered materials. Both substrates (spin coated and dropcast) were used for crystallisation,

and in both cases no material could be found on the surface after removal from the crystallising solution.

### 4.3.4 Wedge Structures formed by Graphitic Flakes on Silicon: A Related Study

The final experiment of this section details one of the first experiments I carried out as a graduate student. I have included it in this chapter as it relevant to the systems described so far. The work here dates back to the early stages of my PhD, when I was searching for interesting microstructures that could be used to study the effects of topography on crystallisation. The project began after reading a paper by Calado *et al*, in which the authors developed a procedure that allowed the precise redeposition of graphene produced via Novsoleov and Geim's procedure [135]. The issue was that mechanical exfoliation of graphene produced an arbitrary distribution of flakes across a surface [136] that was not much use for the fabrication of intricate electronic structures. Calado *et al* tackled this by coating the flakes on the silicon surface with a hydrophobic polymer that forms a solid film after evaporation of the solvent at room temperature. The substrate containing the polymer/graphene was then lowered into DI water at a $30^{o}$ angle to the water's surface. The polymer/graphene was 'wedged' off the substrate as the capillary force exerted by the water infiltrated the space between the hydrophilic/hydrophobic interface of the Si wafer and polymer. By using a probe needle that was controlled in two-dimensions by micrometric screws, they were able to accurately deposit the graphene onto a second substrate at the bottom of the vessel through draining the water and positioning the flake with the needle (Figure 118).

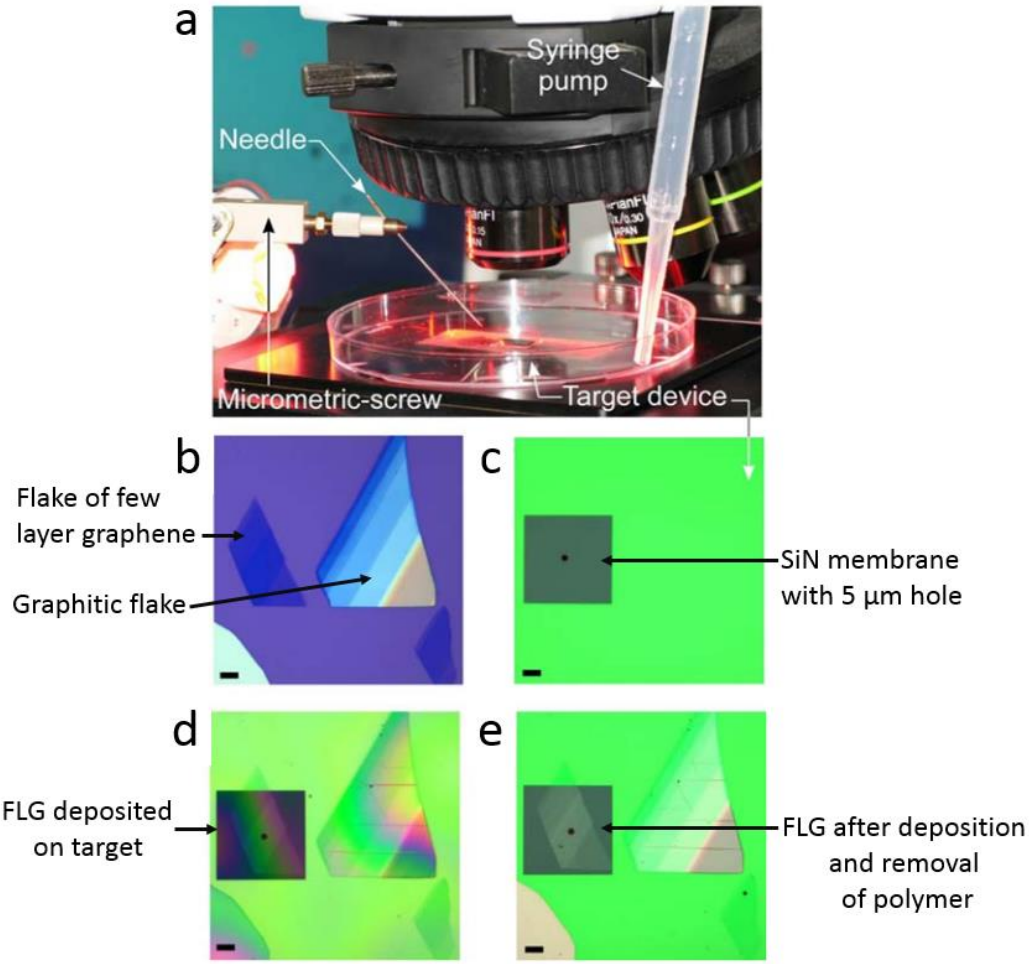


**Figure 118: Experimental setup used by Calado et al to achieve redeposition of mechanically exfoliated graphene**

Once the graphene was in contact with the wafer and the vessel was drained further, water was evacuated from between the substrate and graphene via corrugations in the flake. The technique was of interest from a topographical view point because after the water had been removed, the corrugations remained as surface wrinkles. These structures had a mean height of 3.3 ± 0.4 nm and full width at half maximum of 6.8 ± 2.2 nm, so exist on the same length scale typical of critical nuclei [137]. As such, I made an attempt at replicating these structures, the hypothesis being that the wrinkles would act as nucleation sites for calcium carbonate crystals, demonstrating topographical control of crystal nucleation. The process proved difficult to reproduce, but the mechanical exfoliation of the graphite produced graphitic structures that had interesting topographies.

A modified version of the mechanical exfoliation technique used by Novoselov and Geim was employed to deposit the graphitic flakes on a silicon wafer (described in Section 4.2.3). Optical microscopy of the silicon wafer confirmed the presence of graphitic flakes (so-called as their

thickness was unknown, though single-layer and few layer graphene are invisible in the optical microscope without phase contrast [8]) (Figure 119a). Inspection in the scanning electron microscope revealed that a proportion of the flakes did not lie perfectly flat against the substrate (as seen in Figure 119b), but instead presented a wedge formed between the flake and the Si (Figure 119c and d).

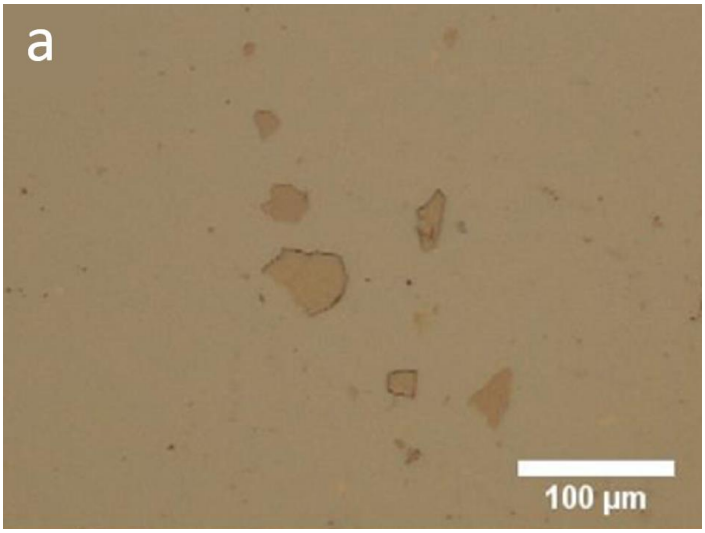


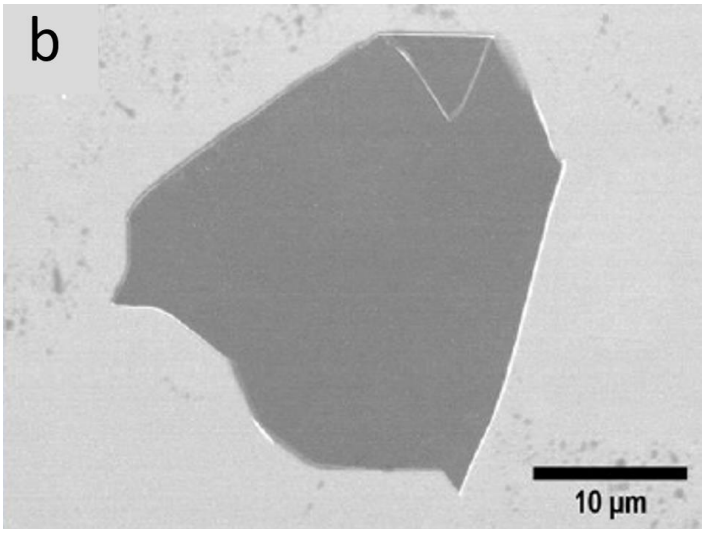

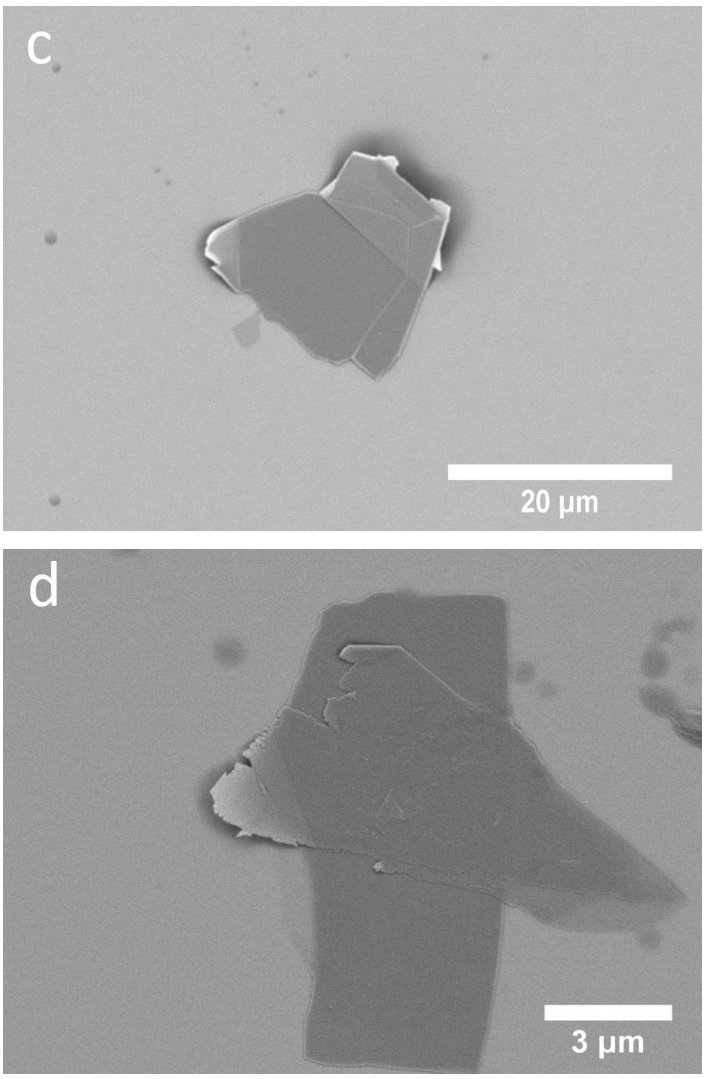


**Figure 119: Optical micrograph of graphitic flakes on a Si substrate.**

A broad range of size and shapes of the graphitic flakes were observed, though most were between 5 and 30 microns in diameter. Research by Campbell *et al* revealed that surface structures that possess acute geometries are often favourable sites for nucleation [138]. Considering this, it may be supposed that the wedges of the graphitic flake/Si substrate could act as preferential sites for the nucleation of calcium carbonate. To investigate this, the substrates were exposed to a solution supersaturated with respect to calcium carbonate using the direct mixing method ($SI_{calcite}$ = 2.1) (Figure 120).

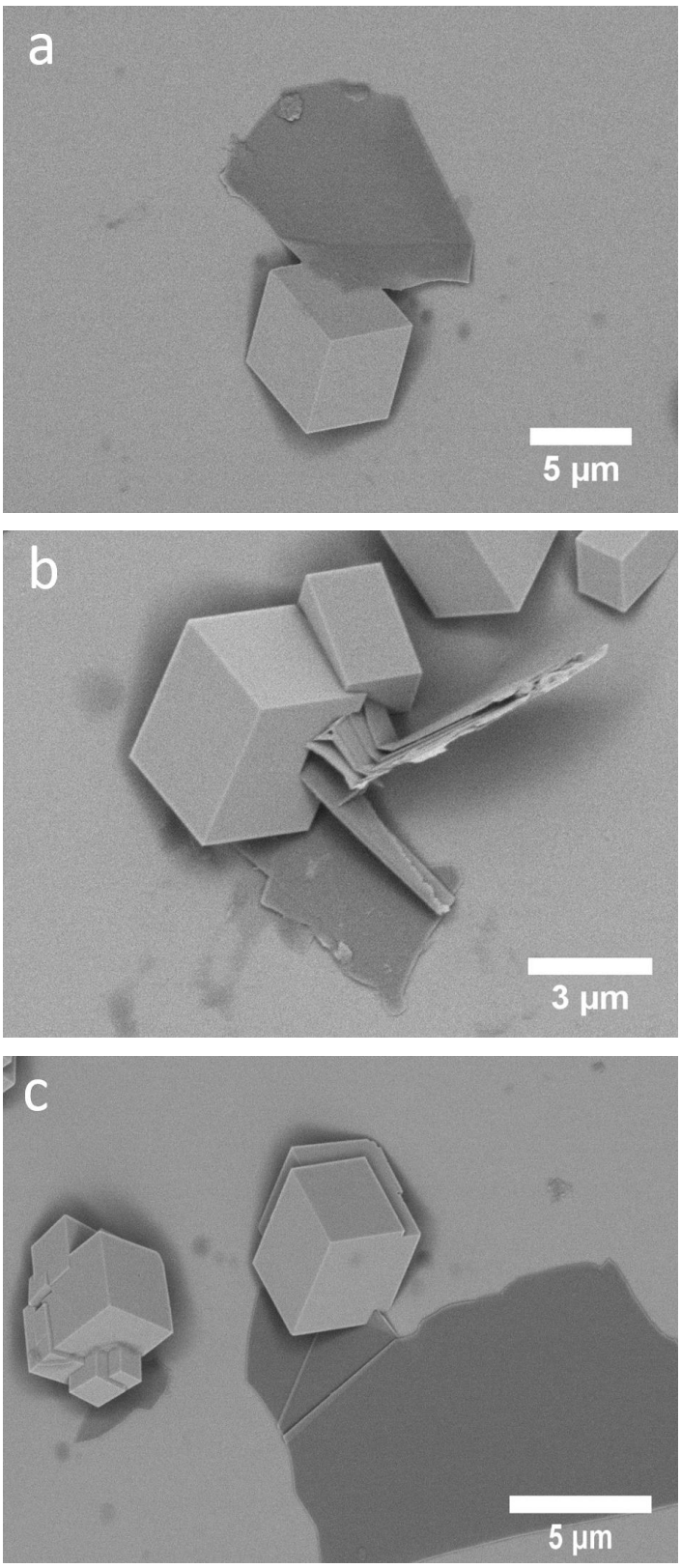


**Figure 120: SEM images of calcite crystals that had nucleated in a wedge formed by the flake and the Si substrate**

Only a fraction of the flakes on the Si surface had formed acute wedges with the substrate, and no unoccupied wedges were observed after crystallisation. On closer inspection of the micrographs presented in Figure 120, residual glue from the scotch tape can be seen on the

silicon wafer. To avoid any influence the glue may have on the crystallisation results, it was removed from the substrate. After the graphitic flakes had been deposited on the wafer, the substrates were placed into a furnace at 300 $^{o}$C for two hours, then sonicated in acetone for five minutes. The SEM revealed that the residual organics had been removed, and flakes with acute wedges still existed on the surface (Figure 121).

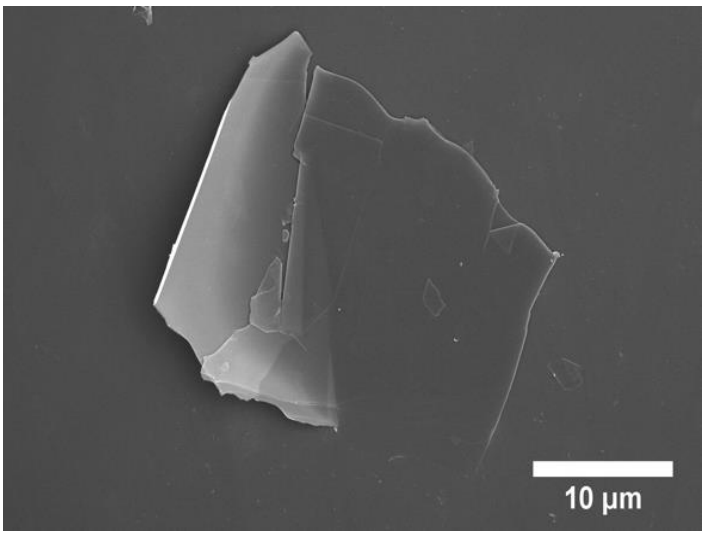


**Figure 121: Graphitic flake on a silicon wafer after exposure to 300 $^{o}$C and sonication in acetone to remove organics**

After treatment, the substrates were again used for the crystallisation of calcium carbonate, with similar results as before (Figure 122).

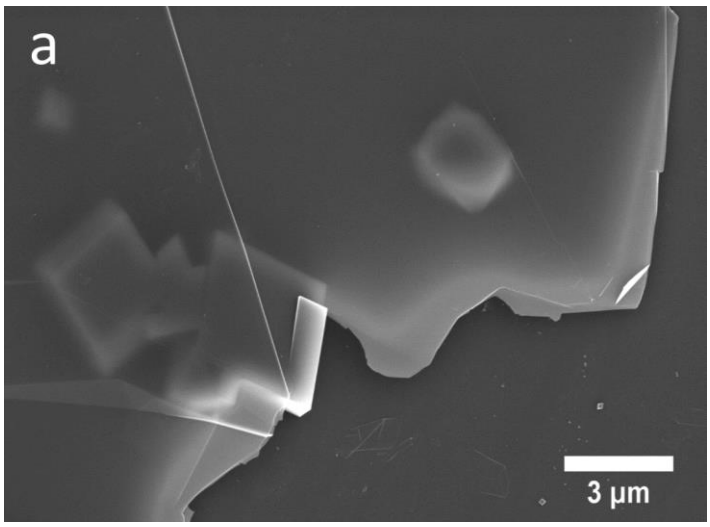
a
3 µm

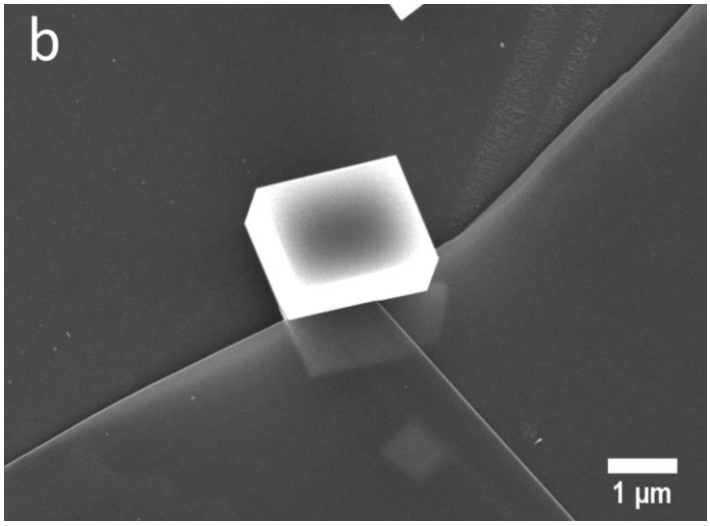
b
1 µm

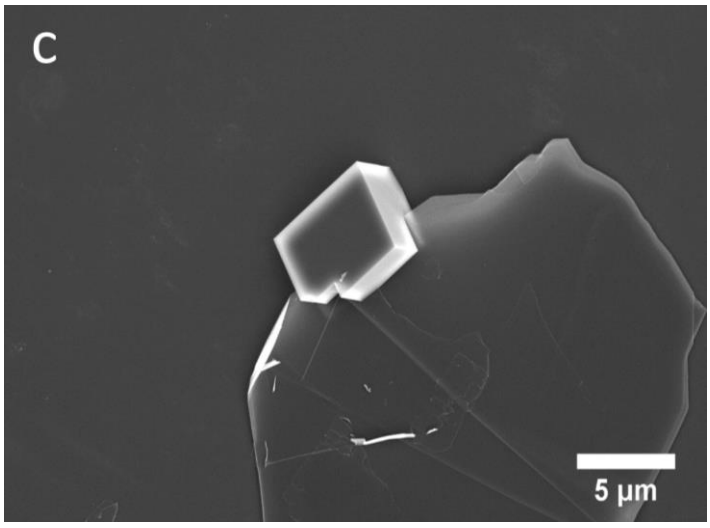
c
5 µm

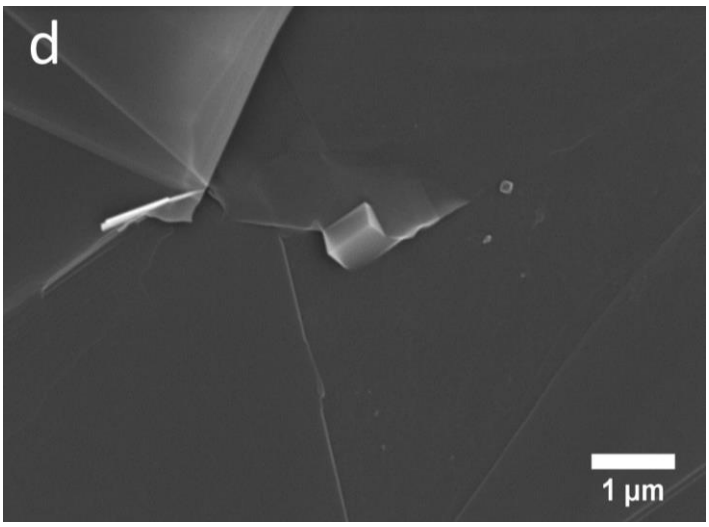


**Figure 122: SEM images of the acute wedges of graphitic flakes occupied by calcite crystals**

The existence of crystals at the wedge after removal of the glue suggests that it was indeed the acute geometry of the flake that caused the crystal to nucleate at this feature. No measurements of determining how effective these structures are at causing nucleation were taken, though the data are still interesting when considered alongside the spin coated rGO work.

## 4.4 General discussion

Despite the data presented here, it is difficult to explain why reduced-graphene oxide that has been spin coated onto a silicon wafer causes aragonite to form. This is a complex system with a lot of unknowns. To begin, we must first consider the structure of reduced graphene oxide in more detail.

Aberration-corrected ultra-high resolution transmission electron microscopy has arguably been the most revealing technique employed for the elucidation of the structure of graphene oxide and reduced-graphene oxide [139]. Although previously used analytical techniques, including spectroscopy, diffraction and structural deduction based on reactivity [140-144], had led researchers to propose basal plane arrangements, being able to 'see' the graphitic network of carbon and oxygen has been most insightful. Micrographs revealed that both GO and rGO are composed of $sp^2$ carbon regions, highly oxidised amorphous areas and holes (Figure 123).

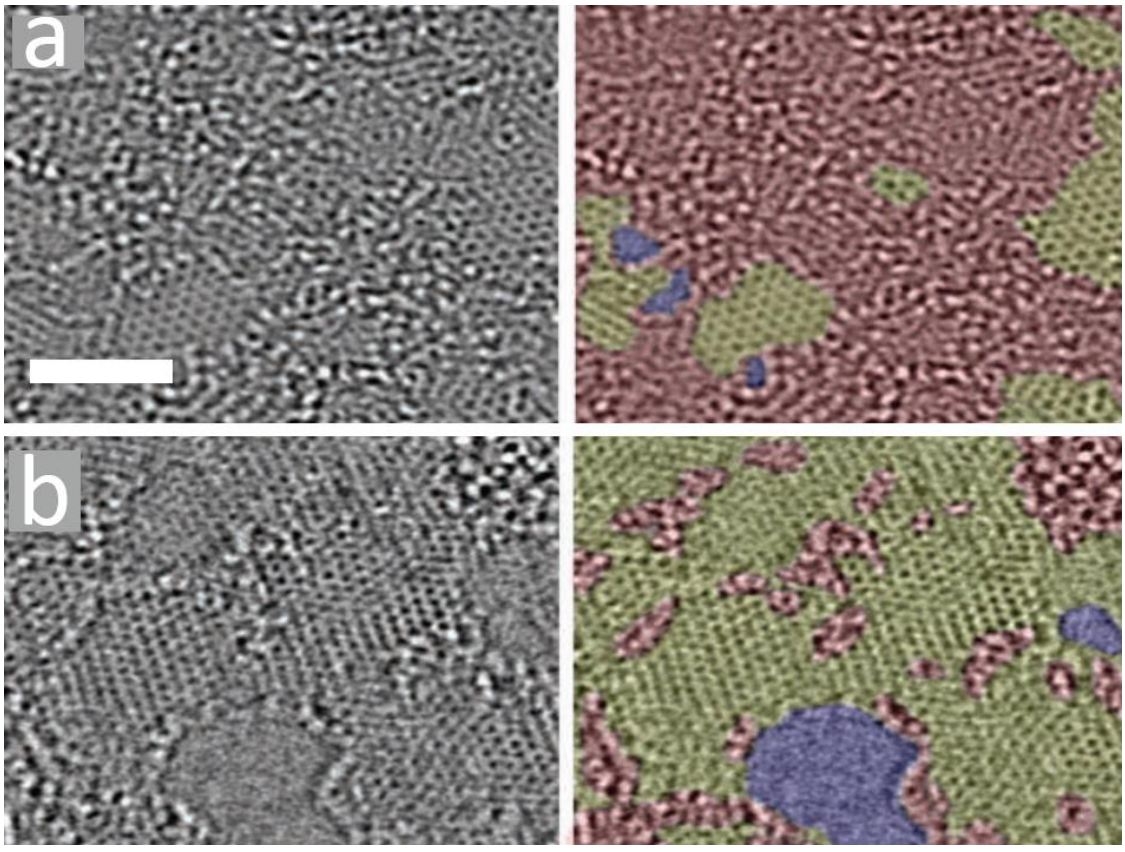


**Figure 123: High resolution TEM micrographs of the basal plane of graphene oxide and reduced-graphene oxide**

As suggested by Figure 123, the relative proportions of the oxidised and $sp^2$ regions differ between the two materials (a consequence of the reduction step involved in the production

of rGO), though perhaps not as obvious is that the surface coverage of holes will be fairly similar (assuming rGO was formed using the same material and oxidation process as the GO). During the synthetic procedure of graphene oxide from graphite, the first step involves the intercalation of sulphuric acid between the lamellae [145]. After this, oxygen functionalities are introduced by the oxidising agent (often $KMnO_4$ is used), increasing the separation between sheets and allowing the subsequent infiltration of water forming a dispersion. During the oxidation step, the oxidising agent accesses the sheets either from the edge of the flakes or by 'drilling' down through the stack [146]. The 'drilling' process involves the conversion of the carbon network into carbon dioxide gas, which is the origin of the effervescence during GO synthesis. This is the cause of the holes in the basal plane of GO, which remain after reduction to rGO, as the reduction does not involve the reintroduction of carbon into the sheet [139]. There are methods available however that can be used to reconstruct the $sp^2$ network and therefore reduce the number and size of the holes [147-150]. Alongside the holes there are the $sp^2$ regions and areas of clustered oxygen functionalities. These oxidised areas are highly disordered and are believed to be composed of mostly hydroxyl, ketone and phenol groups, as well a smaller portion of carbonyl and carboxyl groups [151, 152]. On the other hand, carbonyl and carboxyl groups are thought to be in the majority at the edges of holes and the sides of flakes. It should be noted that the terms graphene oxide and reduced-graphene oxide are rather broad, since the degree of oxidation (and reduction in the case of rGO) is dependent upon the graphite source and the procedures involved. After considering the structure of these materials, we can now turn our attention to the use of GO and rGO as a crystallisation additive.

The literature regarding calcium carbonate and GO/rGO has been dominated by attempts at emulating naturally occurring biomineral structures such as nacre (Figure 124) [153-157]. Here, the authors identified the opportunity of producing a material with alternating layers of GO and calcium carbonate (Figure 124).

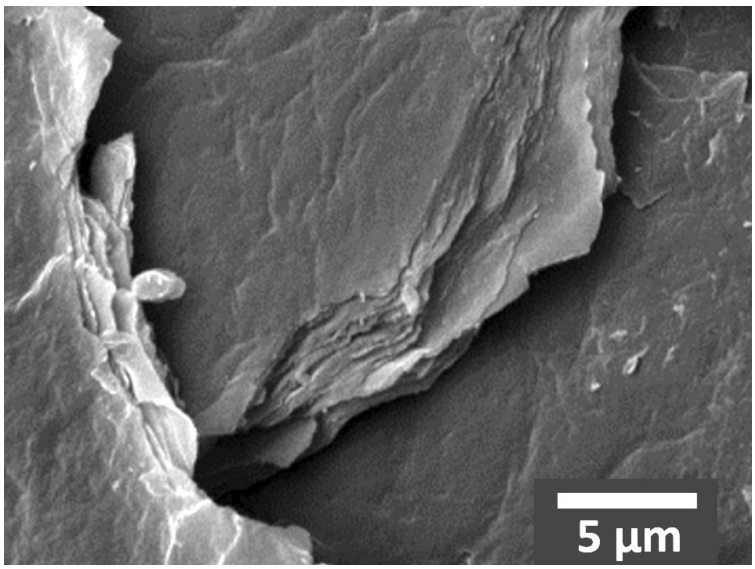


**Figure 124: The nacre like material achieved by Li *et al* using carboxylated-graphene oxide and calcium carbonate [153]. Much of the $CaCO_3$/graphitic material literature is centred around producing biomimetic materials.**

The nacre-related studies focus on the later stages of crystal growth (structural characterisation of the composite material) and investigations into its mechanical properties. As such, they are of little use in the context of my research, where an understanding of how graphitic materials may act as nucleants and influence the early stages of crystal growth are more pertinent. Therefore, it is necessary to look at the influence of GO/rGO on crystallisation elsewhere in the literature.

The high surface area and presence of oxygen functionalities on GO/rGO have led many groups to investigate the use of this material as a support for functional nanocomposites. Carboxyl, carbonyl, hydroxyl, epoxy and phenol groups not only aid in the dispersion of these graphitic materials, but also provide the sites for chemical functionalisation via known carbon chemistry. By grafting polymers onto the basal plane, it has proven possible to produce nanomaterials involving a plethora of metal nanoparticles and proteins for applications in catalysis, conducting adhesives, photovoltaics, energy generation and storage, and sensors [158-174]. Decoration of GO/rGO sheets with metal nanoparticles via bridging polymers has been achieved by numerous research groups (Figure 125).

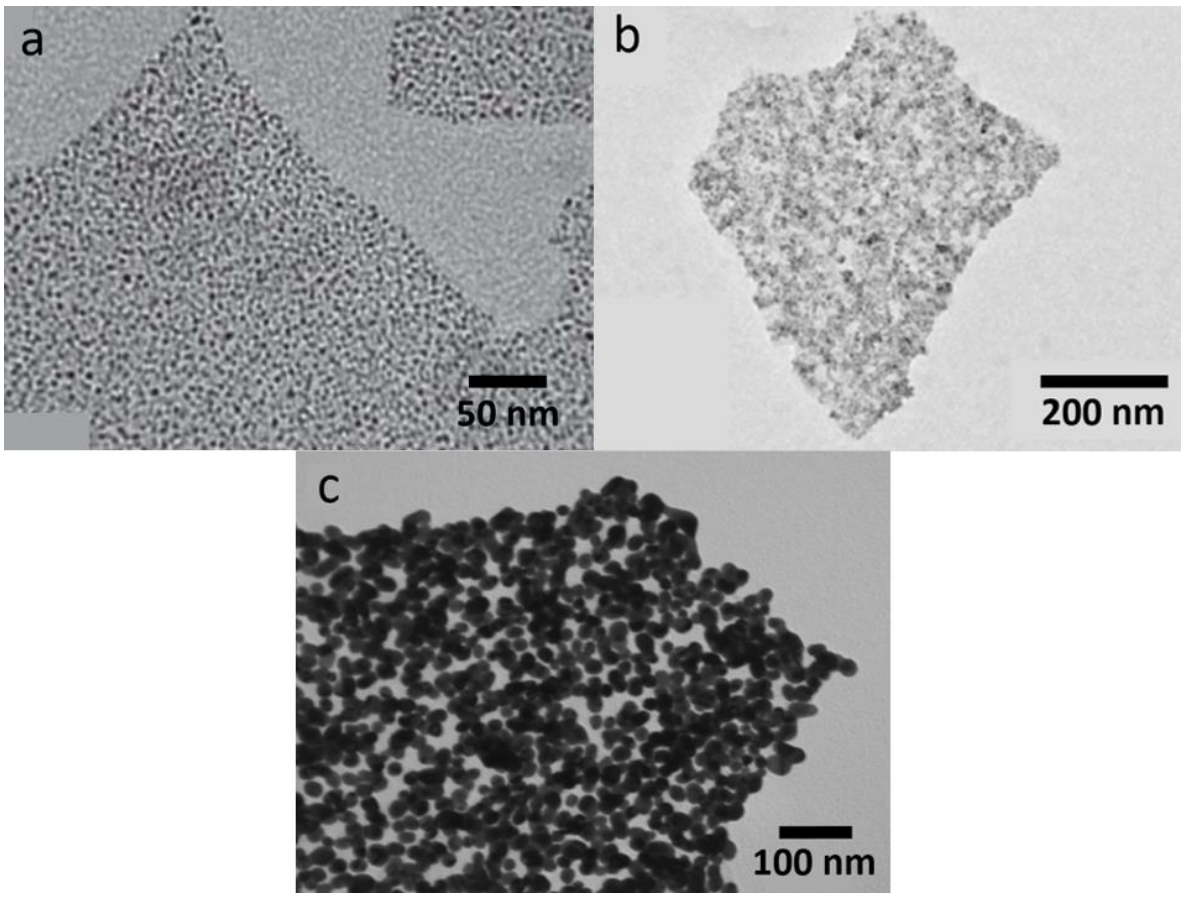


**Figure 125: TEM images of metal particle/rGO composites formed through the use of bridging polymers**

Although modification of the rGO surface with polymers has proven successful in nucleating nanoparticles and a significant portion of the literature is dedicated to these methods, my system is quite different as the rGO only contains residual oxygen functionalities left over from the conversion of graphite to graphene oxide. However, there still exists some examples in which the authors have been able to produce rGO associated with metal nanoparticles without surface modification [164, 165, 177, 178] (Figure 126).

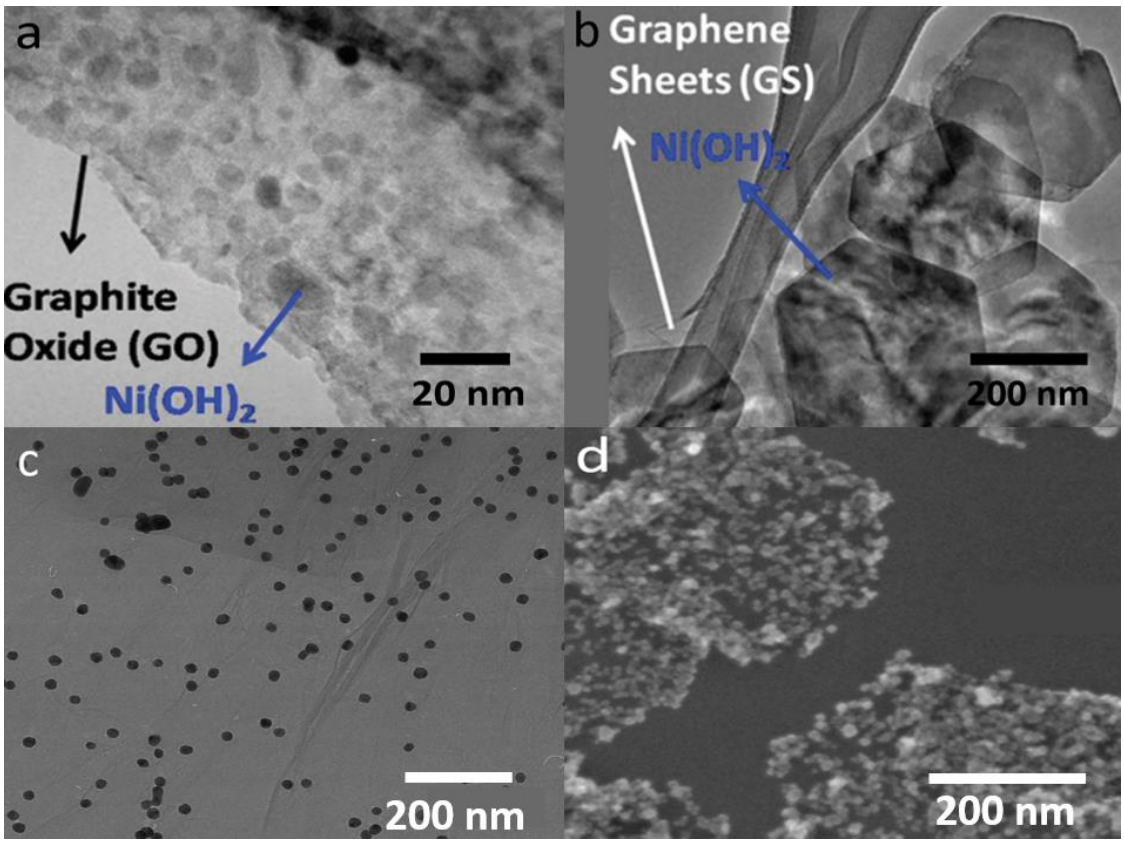


**Figure 126: TEM micrographs of metal particle/rGO composites in which the nanocrystals nucleate directly on the flakes.**

In each case, the authors agree that it is the oxygen groups that promote the nucleation of the metal nanoparticles on the flake surface. Several research groups have conducted experiments that support this hypothesis. Wang *et al* synthesized hexagonal nanoplates of $Ni(OH)_2$ on graphitic nanosheets with different extents of oxidation [164]. They found that graphene oxide, with its high density of functional groups and defects would produce many small $Ni(OH)_2$ crystallites (Figure 126a). On the other hand, rGO has a much lower density of surface oxygen species, a result of their removal via the reduction process. This is evidenced by the number and size of the $Ni(OH)_2$ crystals that form on the rGO surface under the same conditions. These were found to be much fewer in number and also larger in size (Figure 126). A similar study was conducted by Goncalves *et al*, though this time gold nanoparticles were grown instead on the surface of GO or rGO [177]. Again, fewer nanocrystals were observed on the rGO than on the GO, though in each case the authors confirm that it is the oxygen groups that are most likely causing nucleation and growth.

After consideration of the arguments proposed in the literature for the observed effects of rGO on crystallisation, it is evident that the surface chemistry of the flakes is often suggested as the cause. However, there are a number of experiments in this chapter that suggest that

this is not the dominant factor in my system. For example, in Sections 4.3.2.9 and 4.3.2.10, agglomerated flakes and flakes that had detached from the surface both failed to cause aragonite to form. Further, surface coatings formed by dropcasting did not produce aragonite. In each case, the surface chemistry of the rGO flakes would be the same as that of the spin coated rGO since no chemical modification had taken place. Chemical analyses of the rGO samples revealed the presence of some contaminants, however, it is unlikely that it was these causing aragonite to form. This is because although the impurities made up 4.28 and 4.5 percent of the total mass of the gG and TN rGO's, respectively, when the impurities were isolated on a wafer that was used as a substrate for calcium carbonate crystallisation, no aragonite was observed. It is also worth considering that the rGO dispersions used for spin coating were made to a concentration of 1 mg/ml and the volume pipetted onto the surface was 300 µl. Assuming that both the flakes and impurities were homogeneously dispersed, this would mean that approximately 13 µg of contaminants had been introduced to the wafer. This 13 µg is composed of a number of different compounds and so each exists at a mass less than the total sum. In addition, spin coating would likely remove most of the material as it is evacuated from the surface with the water due to centrifugal motion. The fact that surface contamination is low was confirmed by XPS. The samples used for this analysis was spin coated with rGO, and none of the contaminants that had been identified by EDX, where the wafer was coated by dropcasting, could be detected. Further, there exists no examples in the literature of the detected contaminants causing aragonite to form when used as additives to the crystallising solution. All of the data presented in this chapter suggests that aragonite forms on the rGO spin coated wafers because of a topographical effect. However, explaining why these substrates are selective for aragonite is difficult, and requires further investigation to do so.

## 4.5 Summary

Initially, the surface topographies generated by spin coating silicon wafers with carbon nanostructured materials were explored. Carbon nanotubes, carboxylated carbon nanotubes, graphene oxide and reduced graphene oxide (gG rGO) were investigated. After deposition, the wafers were used as substrates for calcium carbonate crystallisation. The nanotubes and

graphene oxide were mostly removed from the substrate prior to crystallisation and so their investigation was not pursued. Conversely, the rGO was maintained on the substrate and caused a large increase in crystal population relative to the control substrate and the vast majority of the crystals were aragonite. To determine if this was unique to the rGO provided by Sichuan University, a second reduced-graphene oxide was purchased from a separate supplier (TN rGO). When prepared in the same way as the previous rGO sample, aragonite was again the dominant polymorph. Analytical procedures were employed to identify any contaminants. Energy-dispersive X-ray analysis (EDX) revealed that a number of different transition metals were present in the samples. Using thermogravimetric analysis, these were found to contribute approximately 4.2 and 4.5 m% to the gG and TN samples, respectively. X-ray photoelectron spectroscopy (XPS) suggested that the TN rGO sample was more oxidised than the gG rGO. Further, the contaminants identified by EDX could not be detected by XPS. For EDX analysis, the impurities had been concentrated onto the Si wafer, whereas for XPS, spin coating was used (the same coating procedure that is associated with aragonite formation). Their absence in the XPS spectra indicates that they are mostly removed by spin coating. Free-floating flakes in the crystallising solution and agglomerated flakes failed to produce aragonite. In addition, dropcasting was used instead of spin coating, as these techniques cause surface coatings with quite different structures to form. The fact that only spin coated rGO produces aragonite suggests that it is a topographical effect that causes this phase to precipitate. Other layered materials were investigated as surface coatings to reveal if they too could produce aragonite when spin coated onto a silicon wafer. These were graphitic-carbon nitride as well as the transition metal dichalcogenides molybdenum disulphide and tungsten disulphide. In the case of $MoS_2$ and $WS_2$, the exfoliation technique employed (ultrasonication) proved ineffective and so the coating was formed of agglomerated masses, which failed to cause aragonite to form. The graphitic-carbon nitride appeared heavily contaminated, and the coating formed from it was removed on submersion in the crystallising solution. Finally, an experiment was described in which graphitic flakes were deposited on a silicon wafer such that it was possible to form wedge structures. The wedge existed between the flake and the silicon wafer. When these substrates were used for calcium carbonate crystallisation, calcite crystals were observed having nucleated within the wedges, which reinforces the idea that structures formed by graphitic flakes can indeed exert a topographical effect on crystallisation.

## 4.6 References


1. Shenderova, O., V. Zhirnov, and D. Brenner, *Carbon nanostructures.* Critical Reviews in Solid State and Material Sciences, 2002. **27**(3-4): p. 227-356.
2. Hirsch, A., *The era of carbon allotropes.* Nat Mater, 2010. **9**(11): p. 868-871.
3. Bacon, R., *Growth, structure, and properties of graphite whiskers.* Journal of Applied Physics, 1960. **31**(2): p. 283-290.
4. Iijima, S., *High resolution electron microscopy of some carbonaceous materials.* Journal of Microscopy, 1980. **119**(1): p. 99-111.
5. Kroto, H.W., et al., *C 60: buckminsterfullerene.* Nature, 1985. **318**(6042): p. 162-163.
6. Thess, A., et al., *Crystalline ropes of metallic carbon nanotubes.* Science, 1996. **273**(5274): p. 483.
7. Schlittler, R., et al., *Single crystals of single-walled carbon nanotubes formed by self-assembly.* Science, 2001. **292**(5519): p. 1136-1139.
8. Novoselov, K.S., et al., *Electric Field Effect in Atomically Thin Carbon Films.* Science, 2004. **306**(5696): p. 666-669.
9. Geim, A.K., *Graphene prehistory.* Physica Scripta, 2012. **2012**(T146): p. 014003.
10. Yang, C.C. and Y.-W. Mai, *Thermodynamics at the nanoscale: A new approach to the investigation of unique physicochemical properties of nanomaterials.* Materials Science and Engineering: R: Reports, 2014. **79**: p. 1-40.
11. Geim, A.K., *Random walk to graphene.* International Journal of Modern Physics B, 2011. **25**(30): p. 4055-4080.
12. Geim, A.K. and K.S. Novoselov, *The rise of graphene.* Nat Mater, 2007. **6**(3): p. 183-191.
13. Allen, M.J., V.C. Tung, and R.B. Kaner, *Honeycomb Carbon: A Review of Graphene.* Chemical Reviews, 2010. **110**(1): p. 132-145.
14. Zhang, Y., et al., *Experimental observation of the quantum Hall effect and Berry's phase in graphene.* Nature, 2005. **438**(7065): p. 201-204.
15. Ando, T., *The electronic properties of graphene and carbon nanotubes.* NPG Asia Mater, 2009. **1**: p. 17-21.
16. Nilsson, J., et al., *Electronic Properties of Graphene Multilayers.* Physical Review Letters, 2006. **97**(26): p. 266801.
17. Goerbig, M.O., *Electronic properties of graphene in a strong magnetic field.* Reviews of Modern Physics, 2011. **83**(4): p. 1193-1243.
18. Choi, S.-M., S.-H. Jhi, and Y.-W. Son, *Effects of strain on electronic properties of graphene.* Physical Review B, 2010. **81**(8): p. 081407.
19. Castro Neto, A.H., et al., *The electronic properties of graphene.* Reviews of Modern Physics, 2009. **81**(1): p. 109-162.
20. Novoselov, K.S., et al., *Electronic properties of graphene.* physica status solidi (b), 2007. **244**(11): p. 4106-4111.
21. Balandin, A.A., et al., *Superior thermal conductivity of single-layer graphene.* Nano letters, 2008. **8**(3): p. 902-907.
22. Bandhu, L. and G.R. Nash, *Controlling the properties of surface acoustic waves using graphene.* Nano Research, 2016. **9**(3): p. 685-691.
23. Hwang, E. and S.D. Sarma, *Acoustic phonon scattering limited carrier mobility in two-dimensional extrinsic graphene.* Physical Review B, 2008. **77**(11): p. 115449.
24. Bonini, N., J. Garg, and N. Marzari, *Acoustic phonon lifetimes and thermal transport in free-standing and strained graphene.* Nano letters, 2012. **12**(6): p. 2673-2678.
25. Arsat, R., et al., *Graphene-like nano-sheets for surface acoustic wave gas sensor applications.* Chemical Physics Letters, 2009. **467**(4): p. 344-347.

26. Ghosh, S., et al., *Dimensional crossover of thermal transport in few-layer graphene.* Nature materials, 2010. **9**(7): p. 555-558.
27. Ghosh, S., et al., *Heat conduction in graphene: experimental study and theoretical interpretation.* New Journal of Physics, 2009. **11**(9): p. 095012.
28. Balandin, A.A., *Thermal properties of graphene and nanostructured carbon materials.* Nature materials, 2011. **10**(8): p. 569-581.
29. Ghosh, S., et al., *Extremely high thermal conductivity of graphene: Prospects for thermal management applications in nanoelectronic circuits.* Applied Physics Letters, 2008. **92**(15): p. 151911.
30. Nika, D.L., et al., *Phonon thermal conduction in graphene: Role of Umklapp and edge roughness scattering.* Physical Review B, 2009. **79**(15): p. 155413.
31. Zhang, L.L., R. Zhou, and X. Zhao, *Graphene-based materials as supercapacitor electrodes.* Journal of Materials Chemistry, 2010. **20**(29): p. 5983-5992.
32. Wang, Y., et al., *Supercapacitor devices based on graphene materials.* The Journal of Physical Chemistry C, 2009. **113**(30): p. 13103-13107.
33. Liu, C., et al., *Graphene-based supercapacitor with an ultrahigh energy density.* Nano letters, 2010. **10**(12): p. 4863-4868.
34. Xie, Y., et al., *Stretchable all-solid-state supercapacitor with wavy shaped polyaniline/graphene electrode.* Journal of Materials Chemistry A, 2014. **2**(24): p. 9142-9149.
35. Cao, J., et al., *High voltage asymmetric supercapacitor based on MnO 2 and graphene electrodes.* Journal of Electroanalytical Chemistry, 2013. **689**: p. 201-206.
36. Le, L.T., et al., *Graphene supercapacitor electrodes fabricated by inkjet printing and thermal reduction of graphene oxide.* Electrochemistry Communications, 2011. **13**(4): p. 355-358.
37. Guo, C.X. and C.M. Li, *A self-assembled hierarchical nanostructure comprising carbon spheres and graphene nanosheets for enhanced supercapacitor performance.* Energy & Environmental Science, 2011. **4**(11): p. 4504-4507.
38. Muraviev, A., et al., *Plasmonic and bolometric terahertz detection by graphene field-effect transistor.* Applied Physics Letters, 2013. **103**(18): p. 181114.
39. Matsumoto, K., et al. *Graphene field-effect transistor for biosensor*. in *Active-Matrix Flatpanel Displays and Devices (AMFPD), 2016 The 23rd International Workshop on Active-Matrix Flatpanel Displays and Devices*. 2016. FTFMD.
40. Vicarelli, L., et al., *Graphene field-effect transistors as room-temperature terahertz detectors.* Nature materials, 2012. **11**(10): p. 865-871.
41. Britnell, L., et al., *Field-effect tunneling transistor based on vertical graphene heterostructures.* Science, 2012. **335**(6071): p. 947-950.
42. Georgiou, T., et al., *Vertical field-effect transistor based on graphene-WS2 heterostructures for flexible and transparent electronics.* Nature nanotechnology, 2013. **8**(2): p. 100-103.
43. Kim, S., et al., *Realization of a high mobility dual-gated graphene field effect transistor with Al2O3 dielectric.* arXiv preprint arXiv:0901.2901, 2009.
44. Reddy, D., et al., *Graphene field-effect transistors.* Journal of Physics D: Applied Physics, 2011. **44**(31): p. 313001.
45. Georgakilas, V., et al., *Functionalization of Graphene: Covalent and Non-Covalent Approaches, Derivatives and Applications.* Chemical Reviews, 2012. **112**(11): p. 6156-6214.

46. Machida, M., T. Mochimaru, and H. Tatsumoto, *Lead (II) adsorption onto the graphene layer of carbonaceous materials in aqueous solution.* Carbon, 2006. **44**(13): p. 2681-2688.
47. Zhang, X.-F. and Q. Xi, *A graphene sheet as an efficient electron acceptor and conductor for photoinduced charge separation.* Carbon, 2011. **49**(12): p. 3842-3850.
48. Kim, S.R., M.K. Parvez, and M. Chhowalla, *UV-reduction of graphene oxide and its application as an interfacial layer to reduce the back-transport reactions in dye-sensitized solar cells.* Chemical Physics Letters, 2009. **483**(1–3): p. 124-127.
49. Carrillo, I., E. Rangel, and L.F. Magaña, *Adsorption of carbon dioxide and methane on graphene with a high titanium coverage.* Carbon, 2009. **47**(11): p. 2758-2760.
50. Shan, M., et al., *Influence of chemical functionalization on the CO2/N2 separation performance of porous graphene membranes.* Nanoscale, 2012. **4**(17): p. 5477-5482.
51. Wood, B.C., et al., *Methane and carbon dioxide adsorption on edge-functionalized graphene: a comparative DFT study.* The Journal of chemical physics, 2012. **137**(5): p. 054702.
52. Garcia-Gallastegui, A., et al., *Graphene Oxide as Support for Layered Double Hydroxides: Enhancing the CO2 Adsorption Capacity.* Chemistry of Materials, 2012. **24**(23): p. 4531-4539.
53. Ning, G., et al., *High capacity gas storage in corrugated porous graphene with a specific surface area-lossless tightly stacking manner.* Chemical Communications, 2012. **48**(54): p. 6815-6817.
54. Srinivas, G., J. Burress, and T. Yildirim, *Graphene oxide derived carbons (GODCs): synthesis and gas adsorption properties.* Energy & Environmental Science, 2012. **5**(4): p. 6453-6459.
55. Palacios, T., A. Hsu, and H. Wang, *Applications of graphene devices in RF communications.* IEEE Communications Magazine, 2010. **48**(6): p. 122-128.
56. Zhang, L., et al., *Enhanced chemotherapy efficacy by sequential delivery of siRNA and anticancer drugs using PEI-grafted graphene oxide.* Small, 2011. **7**(4): p. 460-464.
57. Yang, K., et al., *Graphene in mice: ultrahigh in vivo tumor uptake and efficient photothermal therapy.* Nano letters, 2010. **10**(9): p. 3318-3323.
58. Markovic, Z.M., et al., *In vitro comparison of the photothermal anticancer activity of graphene nanoparticles and carbon nanotubes.* Biomaterials, 2011. **32**(4): p. 1121-1129.
59. Huang, Z., et al., *Photodynamic therapy for treatment of solid tumors—potential and technical challenges.* Technology in cancer research & treatment, 2008. **7**(4): p. 309-320.
60. Zhang, W., et al., *Synergistic effect of chemo-photothermal therapy using PEGylated graphene oxide.* Biomaterials, 2011. **32**(33): p. 8555-8561.
61. Mintzer, M.A. and E.E. Simanek, *Nonviral vectors for gene delivery.* Chemical reviews, 2008. **109**(2): p. 259-302.
62. Feng, L., S. Zhang, and Z. Liu, *Graphene based gene transfection.* Nanoscale, 2011. **3**(3): p. 1252-1257.
63. Chen, B., et al., *Polyethylenimine-functionalized graphene oxide as an efficient gene delivery vector.* Journal of Materials Chemistry, 2011. **21**(21): p. 7736-7741.
64. Bao, H., et al., *Chitosan-functionalized graphene oxide as a nanocarrier for drug and gene delivery.* Small, 2011. **7**(11): p. 1569-1578.
65. Chang, H., et al., *Graphene fluorescence resonance energy transfer aptasensor for the thrombin detection.* Analytical Chemistry, 2010. **82**(6): p. 2341-2346.

66. Dong, X., et al., *Graphene as a novel matrix for the analysis of small molecules by MALDI-TOF MS.* Analytical chemistry, 2010. **82**(14): p. 6208-6214.
67. He, Q., et al., *Centimeter-long and large-scale micropatterns of reduced graphene oxide films: fabrication and sensing applications.* Acs Nano, 2010. **4**(6): p. 3201-3208.
68. Wang, Y., et al., *Application of graphene-modified electrode for selective detection of dopamine.* Electrochemistry Communications, 2009. **11**(4): p. 889-892.
69. Wang, Y., et al., *Aptamer/graphene oxide nanocomplex for in situ molecular probing in living cells.* Journal of the American Chemical Society, 2010. **132**(27): p. 9274-9276.
70. Wang, Y., et al., *Nitrogen-doped graphene and its application in electrochemical biosensing.* ACS nano, 2010. **4**(4): p. 1790-1798.
71. Dreyer, D.R., et al., *The chemistry of graphene oxide.* Chemical Society Reviews, 2010. **39**(1): p. 228-240.
72. Cooper, D.R., et al., *Experimental review of graphene.* ISRN Condensed Matter Physics, 2012. **2012**.
73. Zhao, J., et al., *An approach for synthesizing graphene with calcium carbonate and magnesium.* Carbon, 2012. **50**(13): p. 4939-4944.
74. Wang, C., et al., *Preparation of graphene nanosheets through detonation.* New Carbon Materials, 2011. **26**(1): p. 21-25.
75. Kosynkin, D.V., et al., *Longitudinal unzipping of carbon nanotubes to form graphene nanoribbons.* Nature, 2009. **458**(7240): p. 872-876.
76. Jiao, L., et al., *Narrow graphene nanoribbons from carbon nanotubes.* Nature, 2009. **458**(7240): p. 877-880.
77. Cano-Márquez, A.G., et al., *Ex-MWNTs: graphene sheets and ribbons produced by lithium intercalation and exfoliation of carbon nanotubes.* Nano letters, 2009. **9**(4): p. 1527-1533.
78. Stankovich, S., et al., *Stable aqueous dispersions of graphitic nanoplatelets via the reduction of exfoliated graphite oxide in the presence of poly (sodium 4-styrenesulfonate).* Journal of Materials Chemistry, 2006. **16**(2): p. 155-158.
79. Singh, V., et al., *Graphene based materials: Past, present and future.* Progress in Materials Science, 2011. **56**(8): p. 1178-1271.
80. Shams, S.S., R. Zhang, and J. Zhu, *Graphene synthesis: a Review.* Materials Science-Poland, 2015. **33**(3): p. 566-578.
81. Li, D., et al., *Processable aqueous dispersions of graphene nanosheets.* Nature nanotechnology, 2008. **3**(2): p. 101-105.
82. Stankovich, S., et al., *Synthesis of graphene-based nanosheets via chemical reduction of exfoliated graphite oxide.* carbon, 2007. **45**(7): p. 1558-1565.
83. Choi, W., et al., *Synthesis of Graphene and Its Applications: A Review.* Critical Reviews in Solid State and Materials Sciences, 2010. **35**(1): p. 52-71.
84. Calvaresi, M., et al., *Morphological and mechanical characterization of composite calcite/SWCNT–COOH single crystals.* Nanoscale, 2013. **5**(15): p. 6944-6949.
85. Ford, W.E., A. Yasuda, and J.M. Wessels, *Microcrystalline composite particles of carbon nanotubes and calcium carbonate.* Langmuir, 2008. **24**(7): p. 3479-3485.
86. Tasis, D., et al., *Growth of calcium carbonate on non-covalently modified carbon nanotubes.* Materials Letters, 2007. **61**(28): p. 5044-5046.
87. Li, W. and C. Gao, *Efficiently Stabilized Spherical Vaterite CaCO3 Crystals by Carbon Nanotubes in Biomimetic Mineralization.* Langmuir, 2007. **23**(8): p. 4575-4582.
88. Fu, G., et al., *CaCO3 biomineralization: acidic 8-kDa proteins isolated from aragonitic abalone shell nacre can specifically modify calcite crystal morphology.* Biomacromolecules, 2005. **6**(3): p. 1289-1298.

89. Kontoyannis, C.G. and N.V. Vagenas, *Calcium carbonate phase analysis using XRD and FT-Raman spectroscopy.* Analyst, 2000. **125**(2): p. 251-255.
90. Green, D.C., et al., *3D visualization of additive occlusion and tunable full-spectrum fluorescence in calcite.* Nature Communications, 2016. **7**: p. 13524.
91. Wei, H., et al., *Effect of anionic surfactant–polymer complexes on the crystallization of calcium carbonate.* Journal of Crystal Growth, 2004. **264**(1–3): p. 424-429.
92. Shen, Q., et al., *Crystallization and Aggregation Behaviors of Calcium Carbonate in the Presence of Poly(vinylpyrrolidone) and Sodium Dodecyl Sulfate.* The Journal of Physical Chemistry B, 2005. **109**(39): p. 18342-18347.
93. Kim, I.W., R.E. Robertson, and R. Zand, *Effects of Some Nonionic Polymeric Additives on the Crystallization of Calcium Carbonate.* Crystal Growth & Design, 2005. **5**(2): p. 513-522.
94. Wei, H., et al., *Crystallization habit of calcium carbonate in presence of sodium dodecyl sulfate and/or polypyrrolidone.* Journal of Crystal Growth, 2004. **260**(3–4): p. 545-550.
95. Wei, H., et al., *Influence of polyvinylpyrrolidone on the precipitation of calcium carbonate and on the transformation of vaterite to calcite.* Journal of Crystal Growth, 2003. **250**(3): p. 516-524.
96. Russ, J.C., *Fundamentals of Energy Dispersive X-ray Analysis*. 1984: Butterworths.
97. Shindo, D. and T. Oikawa, *Energy Dispersive X-ray Spectroscopy*, in *Analytical Electron Microscopy for Materials Science*. 2002, Springer Japan: Tokyo. p. 81-102.
98. Chen, J., et al., *An improved Hummers method for eco-friendly synthesis of graphene oxide.* Carbon, 2013. **64**: p. 225-229.
99. Hummers Jr, W.S. and R.E. Offeman, *Preparation of graphitic oxide.* Journal of the American Chemical Society, 1958. **80**(6): p. 1339-1339.
100. Clayden, J., *Organic Chemistry*. 2001: Oxford University Press.
101. Ambrosi, A., et al., *Lithium Aluminum Hydride as Reducing Agent for Chemically Reduced Graphene Oxides.* Chemistry of Materials, 2012. **24**(12): p. 2292-2298.
102. Kofstad, P., *High-temperature oxidation of titanium.* Journal of the Less Common Metals, 1967. **12**(6): p. 449-464.
103. Smith, C., *Graphene Oxide Material Interfaces in Electronics, Energy and Environmental Membranes*, in *Nanoelectronics Centre*. 2016, University of Surrey.
104. Marcano, D.C., et al., *Improved Synthesis of Graphene Oxide.* ACS Nano, 2010. **4**(8): p. 4806-4814.
105. Wang, Y., et al., *High-quality reduced graphene oxide-nanocrystalline platinum hybrid materials prepared by simultaneous co-reduction of graphene oxide and chloroplatinic acid.* Nanoscale Research Letters, 2011. **6**(1): p. 241.
106. Klusek, Z., P. Datta, and W. Kozlowski, *Nanoscale studies of the oxidation and hydrogenation of graphite surface.* Corrosion science, 2003. **45**(7): p. 1383-1393.
107. Agarwal, B.K., *X-ray spectroscopy: an introduction*. 1991: Springer-Verlag.
108. Leng, Y., *Materials Characterization: Introduction to Microscopic and Spectroscopic Methods*. 2009: Wiley.
109. Oura, K., et al., *Surface Science: An Introduction*. 2013: Springer Berlin Heidelberg.
110. Carlson, T.A., *Photoelectron and Auger spectroscopy*. 1975: Plenum Press.
111. de Moraes, A.C.M., et al., *Graphene oxide-silver nanocomposite as a promising biocidal agent against methicillin-resistant Staphylococcus aureus.* International journal of nanomedicine, 2015. **10**: p. 6847.
112. Ganguly, A., et al., *Probing the Thermal Deoxygenation of Graphene Oxide Using High-Resolution In Situ X-ray-Based Spectroscopies.* The Journal of Physical Chemistry C, 2011. **115**(34): p. 17009-17019.

113. Cançado, L.G., et al., *Quantifying Defects in Graphene via Raman Spectroscopy at Different Excitation Energies.* Nano Letters, 2011. **11**(8): p. 3190-3196.
114. Ferrari, A.C. and J. Robertson, *Interpretation of Raman spectra of disordered and amorphous carbon.* Physical review B, 2000. **61**(20): p. 14095.
115. Kaniyoor, A. and S. Ramaprabhu, *A Raman spectroscopic investigation of graphite oxide derived graphene.* Aip Advances, 2012. **2**(3): p. 032183.
116. Schwan, J., et al., *Raman spectroscopy on amorphous carbon films.* Journal of Applied Physics, 1996. **80**(1): p. 440-447.
117. Chua, C.K. and M. Pumera, *Chemical reduction of graphene oxide: a synthetic chemistry viewpoint.* Chemical Society Reviews, 2014. **43**(1): p. 291-312.
118. Chan, Y.Y., et al., *Assessments of Surface Coverage after Nanomaterials are Drop Cast onto Electrodes for Electroanalytical Applications.* ChemElectroChem, 2015. **2**(7): p. 1003-1009.
119. Shelton, J. *Spin-coating*. Spin-coating 2017 26/01/17]; Available from: https://www.ossila.com/pages/spin-coating.
120. Geim, A.K., *Graphene: status and prospects.* science, 2009. **324**(5934): p. 1530-1534.
121. Baugher, B.W.H., *Electronic transport in atomically thin layered materials*. 2014, Massachusetts Institute of Technology.
122. Song, X., J. Hu, and H. Zeng, *Two-dimensional semiconductors: recent progress and future perspectives.* Journal of Materials Chemistry C, 2013. **1**(17): p. 2952-2969.
123. Novoselov, K.S., et al., *Two-Dimensional Atomic Crystals.* Proceedings of the National Academy of Sciences of the United States of America, 2005. **102**(30): p. 10451-10453.
124. Liu, H., et al., *Phosphorene: a new 2D material with high carrier mobility.* arXiv preprint arXiv:1401.4133, 2014.
125. Vogt, P., et al., *Silicene: Compelling Experimental Evidence for Graphenelike Two-Dimensional Silicon.* Physical Review Letters, 2012. **108**(15): p. 155501.
126. Dávila, M., et al., *Germanene: a novel two-dimensional germanium allotrope akin to graphene and silicene.* New Journal of Physics, 2014. **16**(9): p. 095002.
127. Zhang, Y., A. Rubio, and G. Le Lay, *Emergent elemental two-dimensional materials beyond graphene.* Journal of Physics D: Applied Physics, 2017. **50**(5): p. 053004.
128. Yang, S., et al., *Exfoliated Graphitic Carbon Nitride Nanosheets as Efficient Catalysts for Hydrogen Evolution Under Visible Light.* Advanced Materials, 2013. **25**(17): p. 2452-2456.
129. Chhowalla, M., et al., *The chemistry of two-dimensional layered transition metal dichalcogenide nanosheets.* Nat Chem, 2013. **5**(4): p. 263-275.
130. Joensen, P., R.F. Frindt, and S.R. Morrison, *Single-layer MoS2.* Materials Research Bulletin, 1986. **21**(4): p. 457-461.
131. Bojdys, M.J., et al., *Ionothermal synthesis of crystalline, condensed, graphitic carbon nitride.* Chemistry–A European Journal, 2008. **14**(27): p. 8177-8182.
132. Hod, O., *Graphite and Hexagonal Boron-Nitride have the Same Interlayer Distance. Why?* Journal of Chemical Theory and Computation, 2012. **8**(4): p. 1360-1369.
133. Thomas, A., et al., *Graphitic carbon nitride materials: variation of structure and morphology and their use as metal-free catalysts.* Journal of Materials Chemistry, 2008. **18**(41): p. 4893-4908.
134. Zheng, Y., et al., *Graphitic carbon nitride materials: controllable synthesis and applications in fuel cells and photocatalysis.* Energy & Environmental Science, 2012. **5**(5): p. 6717-6731.
135. Calado, V., et al., *Formation and control of wrinkles in graphene by the wedging transfer method.* Applied Physics Letters, 2012. **101**(10): p. 103116.

136. Schneider, G.g.F., et al., *Wedging Transfer of Nanostructures.* Nano Letters, 2010. **10**(5): p. 1912-1916.
137. Horsch, M., J. Vrabec, and H. Hasse, *Modification of the classical nucleation theory based on molecular simulation data for surface tension, critical nucleus size, and nucleation rate.* Physical Review E, 2008. **78**(1): p. 011603.
138. Campbell, J.M., F.C. Meldrum, and H.K. Christenson, *Characterization of Preferred Crystal Nucleation Sites on Mica Surfaces.* Crystal Growth & Design, 2013. **13**(5): p. 1915-1925.
139. Erickson, K., et al., *Determination of the Local Chemical Structure of Graphene Oxide and Reduced Graphene Oxide.* Advanced Materials, 2010. **22**(40): p. 4467-4472.
140. Lerf, A., et al., *Structure of Graphite Oxide Revisited.* The Journal of Physical Chemistry B, 1998. **102**(23): p. 4477-4482.
141. He, H., et al., *Solid-State NMR Studies of the Structure of Graphite Oxide.* The Journal of Physical Chemistry, 1996. **100**(51): p. 19954-19958.
142. Mermoux, M., Y. Chabre, and A. Rousseau, *FTIR and 13C NMR study of graphite oxide.* Carbon, 1991. **29**(3): p. 469-474.
143. Szabó, T., et al., *Evolution of Surface Functional Groups in a Series of Progressively Oxidized Graphite Oxides.* Chemistry of Materials, 2006. **18**(11): p. 2740-2749.
144. Lerf, A., et al., *13C and 1H MAS NMR studies of graphite oxide and its chemically modified derivatives.* Solid State Ionics, 1997. **101**: p. 857-862.
145. Dimiev, A.M. and J.M. Tour, *Mechanism of graphene oxide formation.* ACS nano, 2014. **8**(3): p. 3060-3068.
146. Dimiev, A.M. and S. Eigler, *Graphene Oxide: Fundamentals and Applications*. 2016: Wiley.
147. Liang, Y., et al., *Transparent, highly conductive graphene electrodes from acetylene-assisted thermolysis of graphite oxide sheets and nanographene molecules.* Nanotechnology, 2009. **20**(43): p. 434007.
148. Li, X., et al., *Highly conducting graphene sheets and Langmuir–Blodgett films.* Nature nanotechnology, 2008. **3**(9): p. 538-542.
149. López, V., et al., *Graphene Monolayers: Chemical Vapor Deposition Repair of Graphene Oxide: A Route to Highly-Conductive Graphene Monolayers (Adv. Mater. 46/2009).* Advanced Materials, 2009. **21**(46): p. n/a-n/a.
150. Su, Q., et al., *Composites of graphene with large aromatic molecules.* Advanced materials, 2009. **21**(31): p. 3191-3195.
151. Rourke, J.P., et al., *The Real Graphene Oxide Revealed: Stripping the Oxidative Debris from the Graphene-like Sheets.* Angewandte Chemie, 2011. **123**(14): p. 3231-3235.
152. Gómez-Navarro, C., et al., *Atomic structure of reduced graphene oxide.* Nano letters, 2010. **10**(4): p. 1144-1148.
153. Li, J., et al., *A bio-inspired nacre-like layered hybrid structure of calcium carbonate under the control of carboxyl graphene.* CrystEngComm, 2015. **17**(3): p. 520-525.
154. Yao, C., et al., *Nacre-like calcium carbonate controlled by ionic liquid/graphene oxide composite template.* Materials Science and Engineering: C, 2015. **51**: p. 274-278.
155. Calvaresi, M., et al., *Morphological changes of calcite single crystals induced by graphene–biomolecule adducts.* Journal of Crystal Growth, 2017. **457**: p. 356-361.
156. Kim, S., et al., *Graphene–biomineral hybrid materials.* Advanced Materials, 2011. **23**(17): p. 2009-2014.
157. Rianasari, I., et al., *A Chemical Template for Synthesis of Molecular Sheets of Calcium Carbonate.* Scientific Reports, 2016. **6**: p. 25393.

158. Venkatesan, B.M., et al., *Stacked graphene-Al2O3 nanopore sensors for sensitive detection of DNA and DNA–protein complexes.* ACS nano, 2011. **6**(1): p. 441-450.
159. Mao, S., et al., *Specific Protein Detection Using Thermally Reduced Graphene Oxide Sheet Decorated with Gold Nanoparticle-Antibody Conjugates.* Advanced Materials, 2010. **22**(32): p. 3521-3526.
160. Leese, H.S., et al., *Reductively PEGylated carbon nanomaterials and their use to nucleate 3D protein crystals: a comparison of dimensionality.* Chemical Science, 2016. **7**(4): p. 2916-2923.
161. Sheng, Z., et al., *Protein-assisted fabrication of nano-reduced graphene oxide for combined in vivo photoacoustic imaging and photothermal therapy.* Biomaterials, 2013. **34**(21): p. 5236-5243.
162. Hu, S.H., et al., *Photoresponsive Protein–Graphene–Protein Hybrid Capsules with Dual Targeted Heat-Triggered Drug Delivery Approach for Enhanced Tumor Therapy.* Advanced Functional Materials, 2014. **24**(26): p. 4144-4155.
163. Scheuermann, G.M., et al., *Palladium nanoparticles on graphite oxide and its functionalized graphene derivatives as highly active catalysts for the Suzuki− Miyaura coupling reaction.* Journal of the American Chemical Society, 2009. **131**(23): p. 8262-8270.
164. Wang, H., et al., *Ni(OH)2 nanoplates grown on graphene as advanced electrochemical pseudocapacitor materials.* Journal of the American Chemical Society, 2010. **132**(21): p. 7472-7477.
165. Wang, H., et al., *Mn3O4− graphene hybrid as a high-capacity anode material for lithium ion batteries.* Journal of the American Chemical Society, 2010. **132**(40): p. 13978-13980.
166. Rodrigo, D., et al., *Mid-infrared plasmonic biosensing with graphene.* Science, 2015. **349**(6244): p. 165-168.
167. Tang, X.-Z., et al., *Growth of silver nanocrystals on graphene by simultaneous reduction of graphene oxide and silver ions with a rapid and efficient one-step approach.* Chemical communications, 2011. **47**(11): p. 3084-3086.
168. Viswanathan, S., et al., *Graphene–protein field effect biosensors: glucose sensing.* Materials Today, 2015. **18**(9): p. 513-522.
169. Lu, Y., et al., *Graphene-protein bioelectronic devices with wavelength-dependent photoresponse.* Applied Physics Letters, 2012. **100**(3): p. 033110.
170. Yang, X., et al., *Graphene uniformly decorated with gold nanodots: in situ synthesis, enhanced dispersibility and applications.* Journal of Materials Chemistry, 2011. **21**(22): p. 8096-8103.
171. Xu, C., X. Wang, and J. Zhu, *Graphene− metal particle nanocomposites.* The Journal of Physical Chemistry C, 2008. **112**(50): p. 19841-19845.
172. Zhao, H., et al., *Fabrication of a palladium nanoparticle/graphene nanosheet hybrid via sacrifice of a copper template and its application in catalytic oxidation of formic acid.* Chemical Communications, 2011. **47**(7): p. 2014-2016.
173. Ohno, Y., et al., *Electrolyte-gated graphene field-effect transistors for detecting pH and protein adsorption.* Nano Letters, 2009. **9**(9): p. 3318-3322.
174. Guo, C.X., et al., *Biointerface by cell growth on layered graphene–artificial peroxidase–protein nanostructure for in situ quantitative molecular detection.* Advanced Materials, 2010. **22**(45): p. 5164-5167.
175. Su, Y., et al., *Two-Dimensional Carbon-Coated Graphene/Metal Oxide Hybrids for Enhanced Lithium Storage.* ACS Nano, 2012. **6**(9): p. 8349-8356.

176. Fang, Y., et al., *Self-assembly of cationic polyelectrolyte-functionalized graphene nanosheets and gold nanoparticles: a two-dimensional heterostructure for hydrogen peroxide sensing.* Langmuir, 2010. **26**(13): p. 11277-11282.
177. Goncalves, G., et al., *Surface modification of graphene nanosheets with gold nanoparticles: the role of oxygen moieties at graphene surface on gold nucleation and growth.* Chemistry of Materials, 2009. **21**(20): p. 4796-4802.
178. Chen, S., et al., *Graphene oxide− MnO2 nanocomposites for supercapacitors.* ACS nano, 2010. **4**(5): p. 2822-2830.

# 5 Localisation of Calcium Carbonate Crystallisation using Gold Microstructures

## 5.1 Introduction

This short chapter documents an attempt at fabricating surface topographies using microlithography that have the capacity to spatially control crystallisation. To this end, gold structures were formed on a gold-coated silicon wafer. The entire surface was composed of the same material, therefore decoupling surface chemistry and surface topography, such that any topographical effects could be observed. By depositing the gold at an angle to the surface, it was possible to construct features that had an overhang, consequently producing a wedge geometry between the structure and the substrate. The procedure required to achieve this is documented in the experimental methods, where the wafer preparation, spincoating, photolithography and electron beam evaporation steps are described. Once prepared, the substrates were used for the crystallisation of calcium carbonate. On inspection in the optical and electron microscopes, calcite crystals were observed localised to the gold features. The results clearly demonstrate that it is possible to design substrates with features that can lower the energy barrier to nucleation relative to adjacent areas, therefore promoting crystallisation at their location.

## 5.2 Experimental Methods

The Experimental Methods is separated into two sections in order to communicate the Ledge Overhang Array fabrication procedure effectively. The first section, General Overview, provides a synopsis of the procedure and some of the principles involved. The second, Detailed Overview, describes the process with sufficient information such that the substrates could be reproduced.

### 5.2.1 General Overview

The process begins with photolithography, in which two layers of polymer are spincoated onto a clean silicon wafer that has been coated with gold. The polymer adjacent to the gold surface is a lift-off resist polymer (LOR), while the outermost is a positive photoresist. The polymer is then exposed to ultraviolet radiation in discrete areas. This alters the extent of crosslinking in these regions [1], such that when placed in a developer solution, the polymer is removed only in these locations (this corresponds to the white bars of Figure 127). The mask and therefore exposure pattern used for this step is given below in Figure 127.

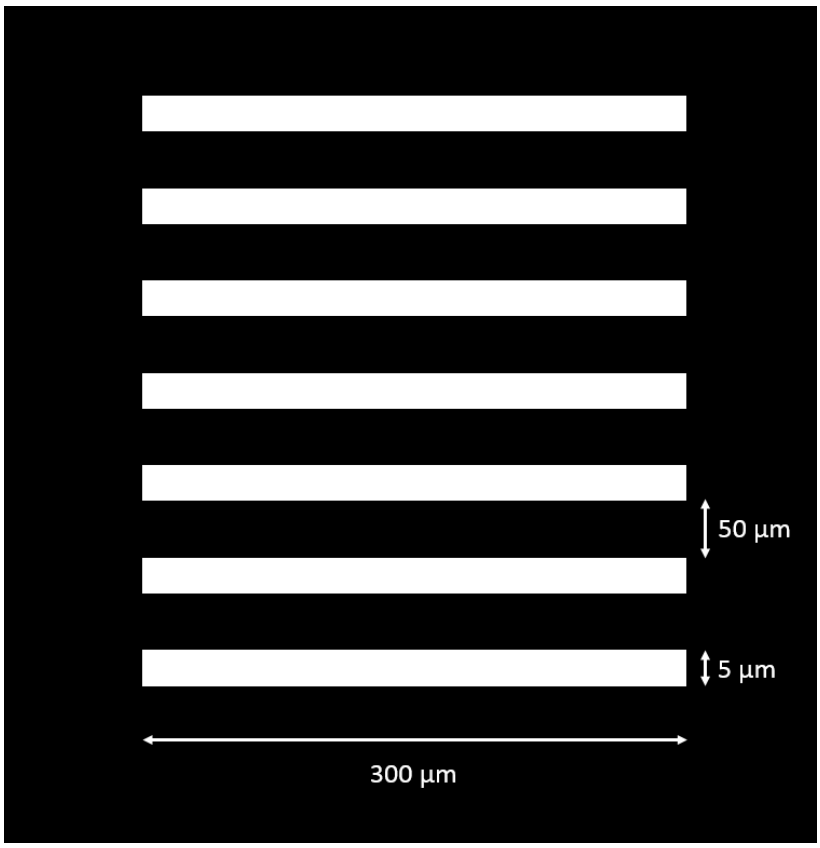


**Figure 127: Schematic of the mask that was used for the ultraviolet exposure step of the photolithography process.**

The mask was simple and involved transparent bars that were 300 x 5 µm and separated by 50 µm. Therefore, after exposure to UV radiation and removal of the resist in the exposed regions, the photoresist would contain voids. When viewed from above, these holes would have dimensions that matched that of the mask, but a cross section would reveal that under the top layer of polymer, the voids were slightly larger. This is because the LOR has a different solubility to the positive photoresist, and so an undercut structure forms as more of the LOR has been removed [2]. An illustration of this is given in Figure 128.


**Figure 128: Illustration of the substrate structure after development of the photoresist layers**

The structure that is formed on the gold surface coating is also composed of gold, and involves a bar that on one side has an overhang. This forms an acute wedge with the substrate. As indicated by my previous chapters and research elsewhere, acute features are effective at promoting nucleation [3-8], which is why this geometry was chosen. To produce the overhang, it was necessary to orient the substrate at an angle to the gold vapour source during deposition. By positioning the substrate in this way, a bar with a rhomboidal cross-section should hypothetically be obtained. To achieve this orientation in the electron beam evaporator, the wafer was secured into a jig that allowed the angle between two plates to be varied. These plates are the base plate, which is secured into the evaporator via screws, and the wafer plate that holds the silicon wafer that has been coated with gold. This custom made jig is shown in Figure 129.

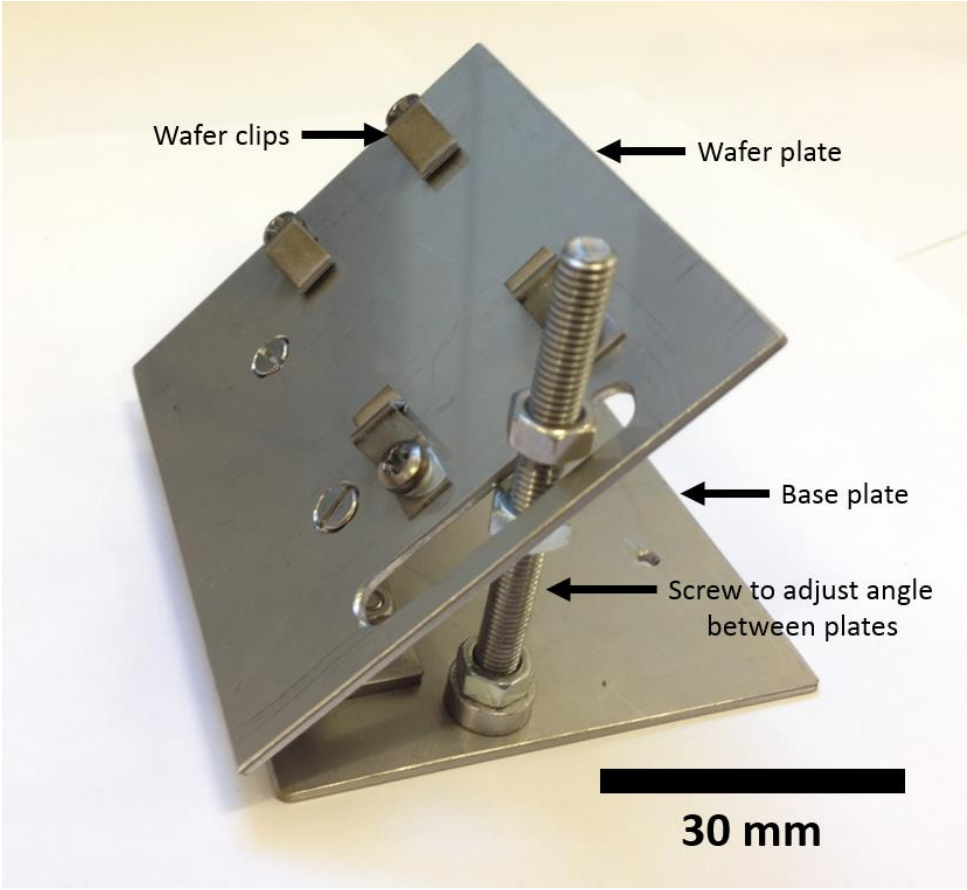


**Figure 129: Photograph of the angle jig used to fabricate the ledge overhang structures.**

The wafer was clipped into the jig and by altering the height of the nuts on the screw, the angle between the base plate and the plate holding the substrate could be adjusted. By doing so, it was possible to produce substrates with different feature angles. The chosen angles between the substrate and feature (wedge angles) were 35°, 45° and 55°. These were investigated to provide a range of angles with the hypothesis that the most acute of the three, the 35° angle, would be the most effective at promoting nucleation. Also, the fabrication process limits the acuteness of the angle, because if the angle between the gold source and substrate it too small, the photoresist blocks access to the substrate and so contact between the deposited gold and surface gold is not made.

Once the wafer had been secured, the jig was placed into the electron beam evaporator for the gold deposition step. This involved superheating a tungsten crucible containing gold in a high-vacuum chamber until the gold was vaporised and deposited on any nearby surfaces. After this, the photoresists were dissolved, leaving the gold overhang structure on the surface of the wafer. A schematic of this process is given in Figure 130.

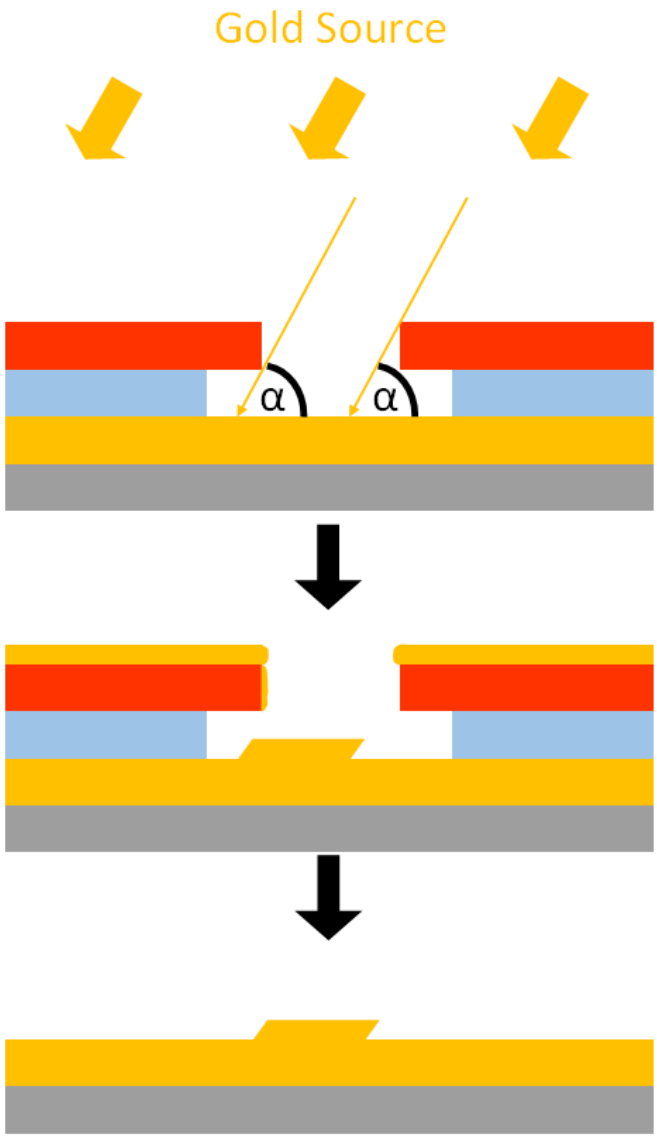


**Figure 130: Schematic of the formation of the gold overhang structure.**

As mentioned above, by altering the angle of the jig, it's possible to control the angle between the substrate and the feature, labelled as α in Figure 130. After deposition, the wafer was cleaned and was then ready for crystallisation studies.

### 5.2.2 Detailed Overview

#### Wafer Preparation

The fabrication of the substrate with gold microstructures was carried out in a class 100 cleanroom. Using a Loadpoint Microace 66 wafer saw, a 6 inch (100) silicon wafer was cut into 25 mm squares. These were then cleaned thoroughly using alternating washes of isopropyl alcohol and acetone, whilst wiping with a fine tipped cleanroom swab. The washing process was complete once the surface was free of dust/contaminants on visual inspection under the

microscope. Next, the wafer section was exposed to UV ozone in a Jelight UVO-Cleaner Model 42-220 for fifteen minutes, then dry baked on a hotplate at 200 $^{o}$C for ten minutes.

**Spincoating of Photoresists**

After being placed on a vacuum truck and secured into a Süss Microtec spincoater, MicroChem Lift Off Resist LOR3A was pipetted onto the surface and the wafer rotated at 2000 rpm for 40 seconds, generating a ~ 400 nm thick surface coating. The wafer was removed and baked at 180 $^{o}$C for 2 mins 30, then placed back into the spincoater on the truck and MicroChem S1813 (positive) photoresist was pipetted onto the surface. After spinning at 4000 rpm for 40 seconds, a top layer that was ~ 1.4 µm thick was formed. The total resist thickness should therefore be approximately 1.8 µm thick. Finally, the wafer was baked for 1 minute at 115 $^{o}$C.

**Photolithography**

The photolithography was carried out using a Karl Süss MJB3 mask aligner. After ensuring the resist surface was in contact with the mask, it was exposed for five seconds to a super-pressure mercury discharge bulb that emits a broad wavelength radiation consisting of 365, 405 and 436 nm.

**Photoresist Development**

Approximately 30 ml of MicroChem MF319 Developer solution was poured into a glassware dish, the patterned wafer added and the dish swirled for 90 seconds. After removal, it was washed with deionised water and dried with a nitrogen air jet to obtain the desired photoresist pattern as shown in Figure 127.

**Electron Beam Evaporation**

The electron beam evaporation was carried out using a Univex 350 Ebeam evaporator. The patterned sample was clamped onto the custom jig, which was attached onto a sample holder. After securing the whole sample holder assembly into the vacuum chamber, the system was pumped down into high vacuum. The gold film was deposited onto the surface with recipe control. After cooling down, the system was vented into air. Next, the sample was removed from the assembly.

**Lift-off**

The sample was soaked into Microposit remover 1165 at 65°C to remove the resist, as well as metal that had deposited on top of the resist (and therefore was not in contact with the gold surface). Finally, the sample was rinsed and blown dry, then ready for testing.

## 5.3 Results/Discussion

### 5.3.1 Characterisation of the Feature

**Ledge Overhang Array: LOA35**

The first Ledge Overhang Array that was investigated was the LOA35, so called because the angle of the wedge between the substrate and feature should be 35°. A low magnification electron micrograph of the features are given below (Figure 131). For clarity and consistency, the overhang will be located at the top side of the feature in images when the features are horizontal in the micrographs, and on the right side when vertical. In micrographs where this is not true, the position of overhang is visually obvious (i.e. Figure 136 and Figure 139).

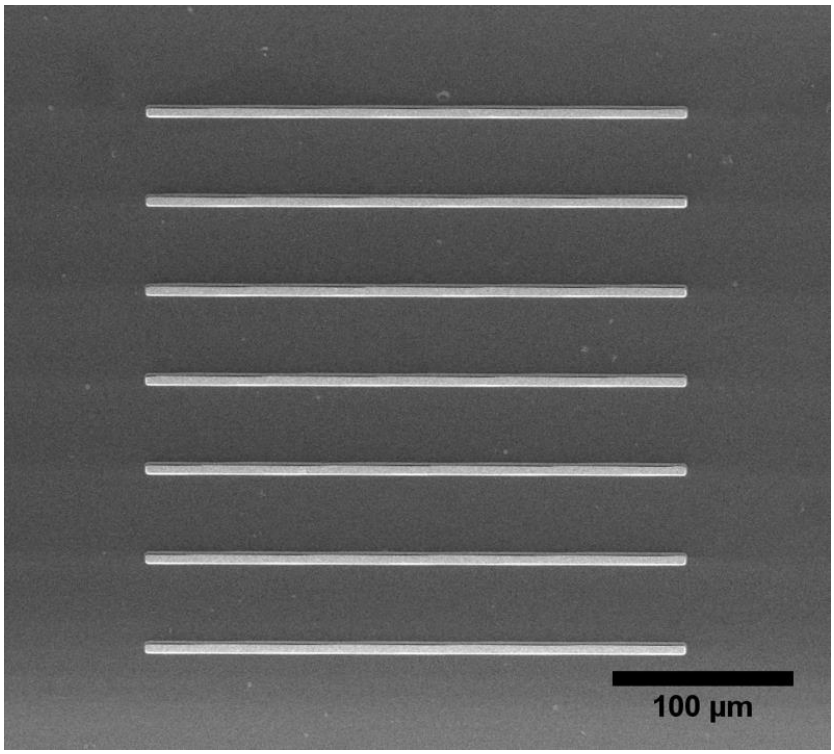


**Figure 131: Top down-view electron micrograph of a series of overhang features on the LOA35 substrate.**

The features were 300 µm long as intended. However, observation at higher magnification in the SEM and imaging in the AFM revealed artefacts from the patterning process (Figure 132).

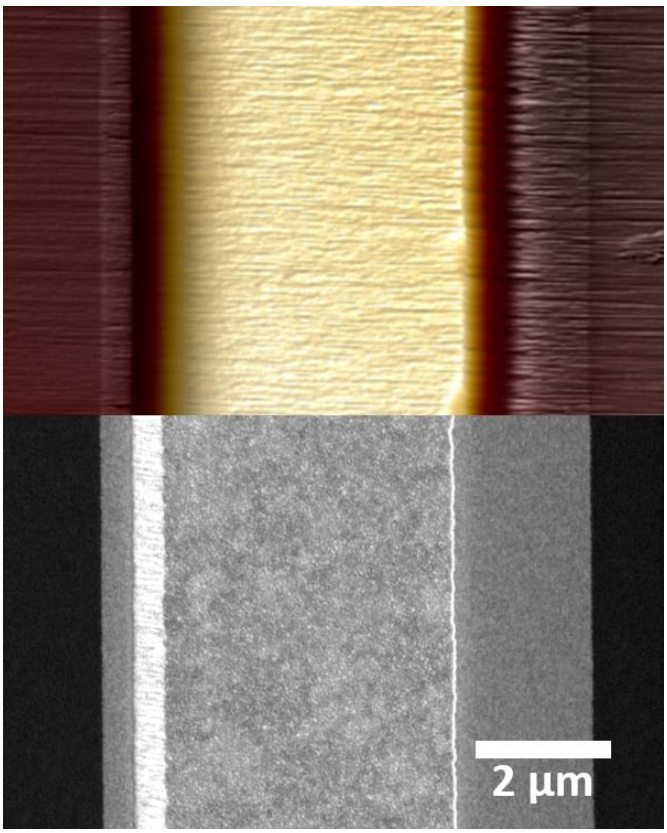


**Figure 132: (Top) AFM micrograph of a feature on the LOA35 substrate. (Bottom) SEM micrograph of a feature the LOA35 substrate.**

Although the structure appeared well-formed, the micrographs indicated that there was residual photoresist with a height of 4 nm located either side of the feature. This can be seen in the SEM micrograph of Figure 132 as the dark regions on each side. This was easily removed by leaving the substrate in acetone overnight (Figure 133).

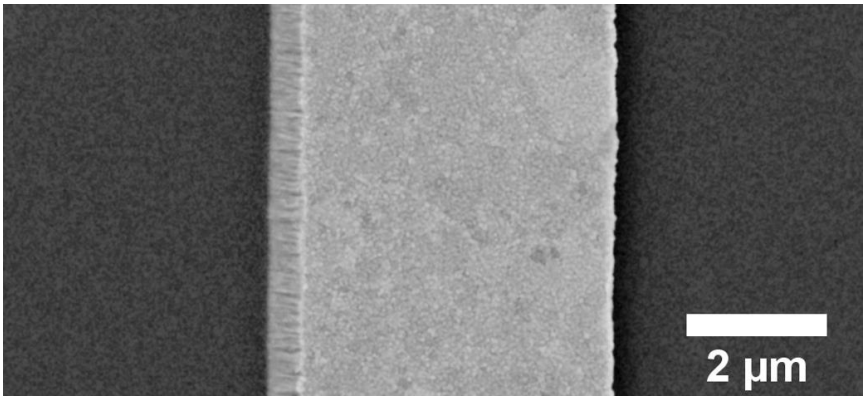


**Figure 133: SEM micrograph of the LOA S1 substrate after submersion in acetone for 24 hours to remove residual photoresist.**

The jig angle that had been used for the gold deposition process was 55$^{o}$, and so the angle between the substrate surface and the feature should be 35$^{o}$. To confirm this indirectly, the surface was visualised using atomic force microscopy (Figure 134).

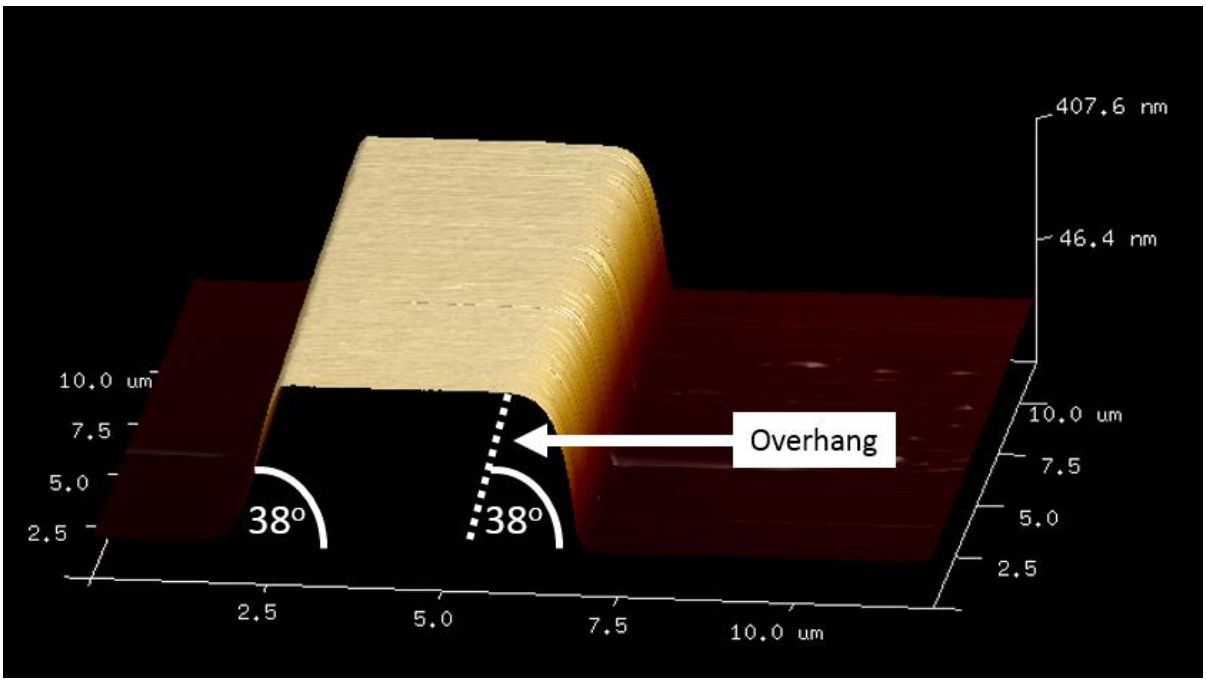


**Figure 134: Atomic Force Micrograph of the LOA35 substrate. The overhang angle was calculated to be 38°**

Since the AFM tip is held perpendicular to the plane of the surface, it unable to access the interior region of the overhang. To calculate the overhang angle, it was assumed that this would be the same as the angle of the ramp on the opposite side of the feature (left hand ramp in Figure 134). Using the atomic force micrograph, the angle of the ramp and therefore the overhang was calculated as 38° (Figure 134, note that this is not to scale). However, this is a tentative approximation as without electron micrographs of the feature profile, it is impossible to provide an accurate value. The height of the feature was measured at approximately 400 nm, and the feature width was 4.8 µm.

**Ledge Overhang Array: LOA45**

The next substrate was fabricated with a jig angle of 45° and was called LOA45. This means that the angle between the substrate and feature should also be 45°. On imaging in the SEM and AFM, structural defects were evident indicating the feature had not formed as intended.

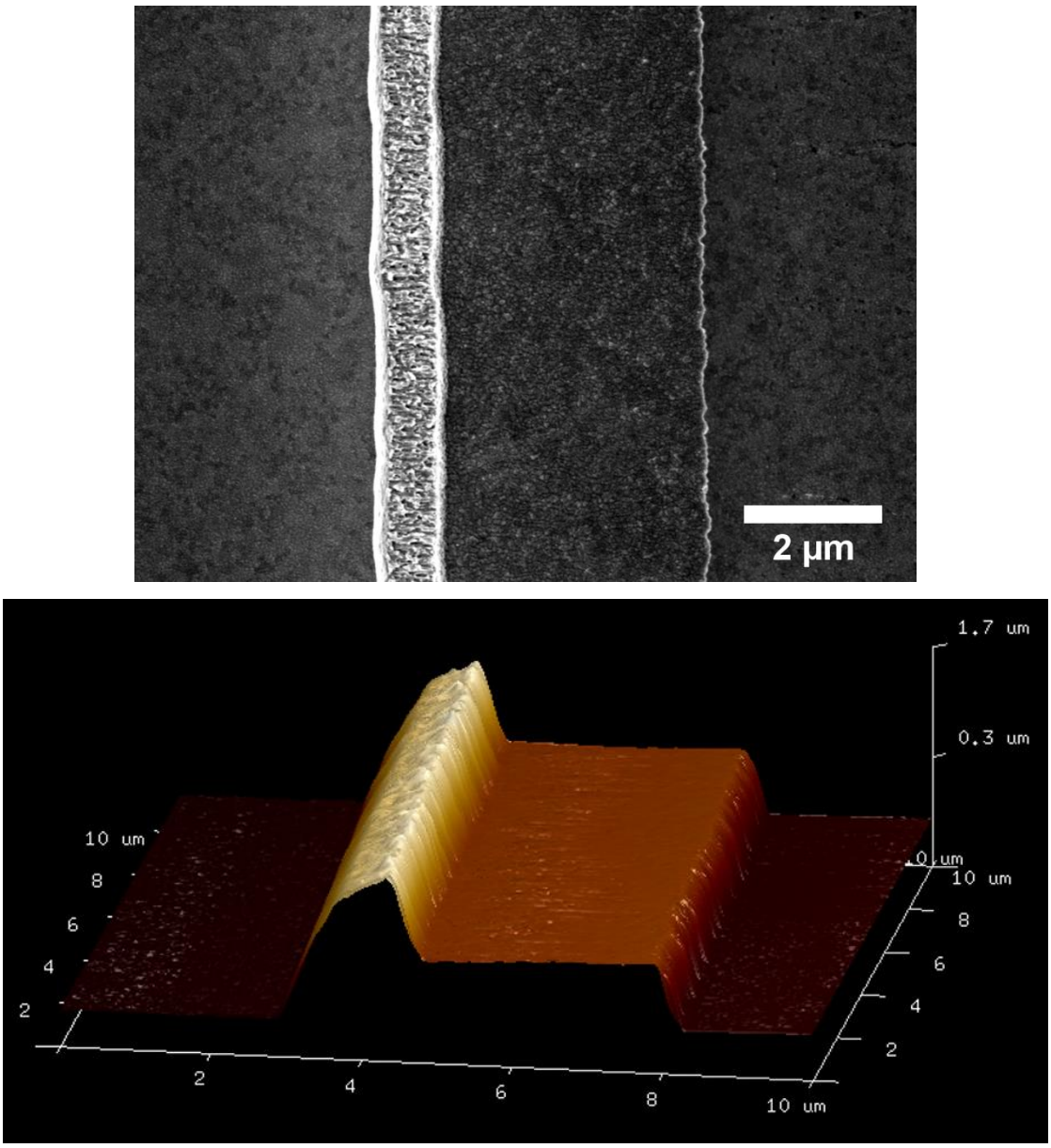


**Figure 135: Micrographs of the LOA45 substrate**

The feature possessed a ridge that ran the length of the structure on the side opposite to that where the overhang was expected. According to the AFM, the ramp opposite the feature was curved, and so a reasonable estimate of the angle at the overhang cannot be given using this data. The height (relative to the flat substrate) of the ridge and the adjacent plateau was measured as 1.7 and 0.75 µm, respectively. In reality, the ridge walls are almost vertical, and the curvature seen in the AFM image is due to tip convolution, which occurs because the AFM tip did not have a high enough aspect ratio to accurately reproduce the surface. This was confirmed using the SEM, in which the substrate was imaged with a tilt angle, allowing the features to be visualised in detail.

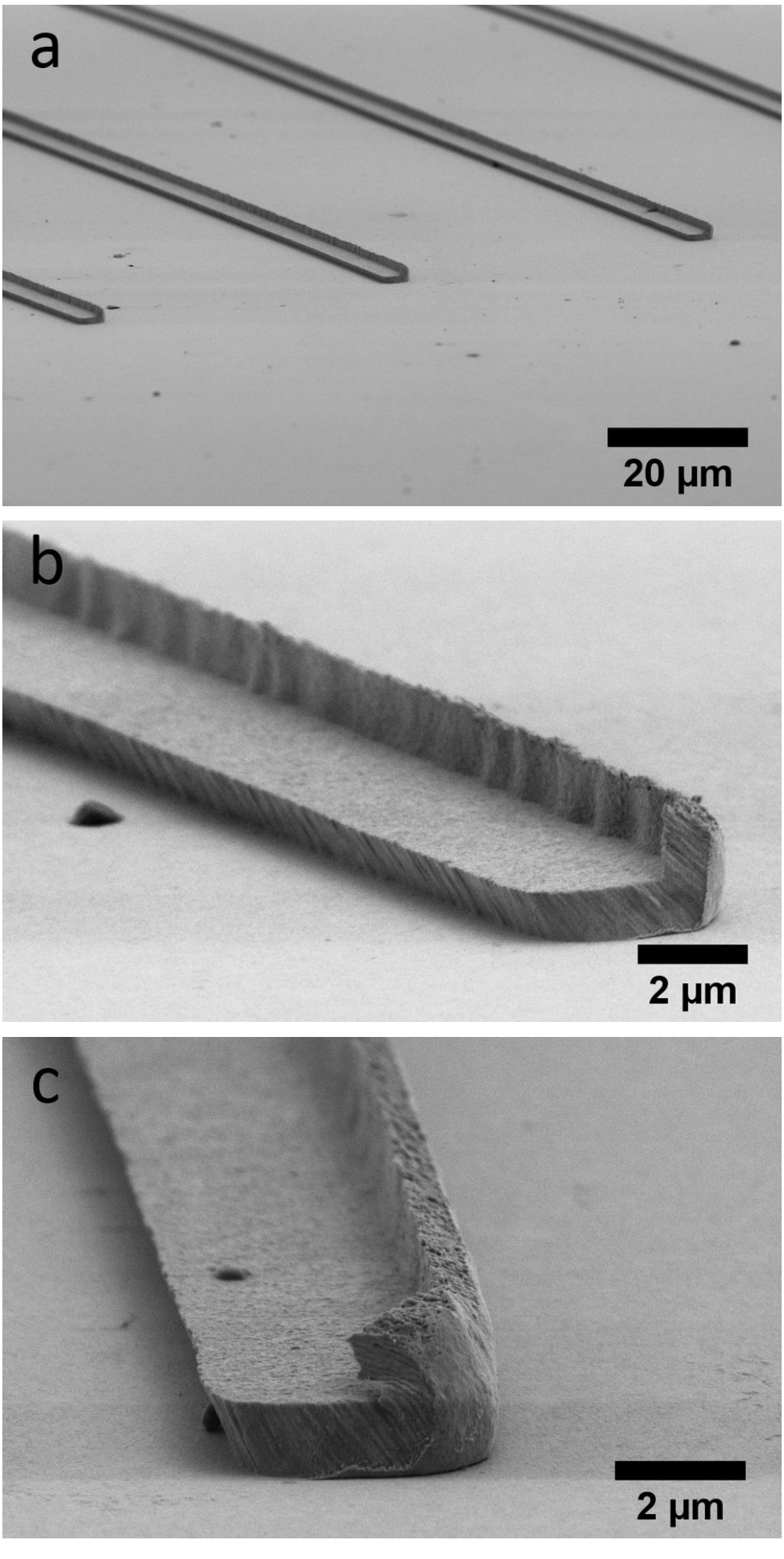
a
20 µm
b
2 µm
c
2 µm

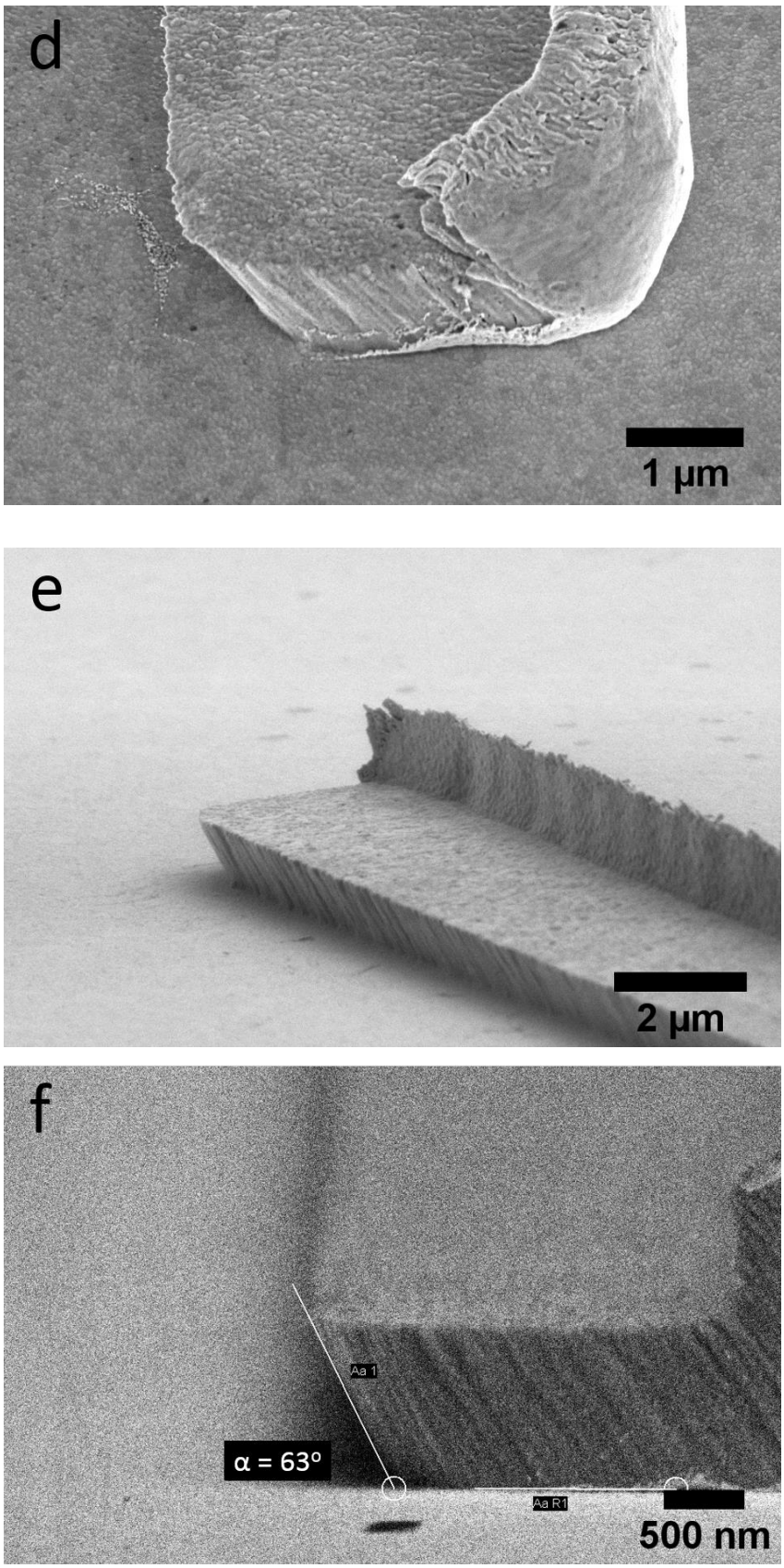


**Figure 136: Scanning electron micrographs of gold over hang structures on the LOA45 substrate taken at varying tilt angle.**

The electron micrographs of Figure 136 prove that the walls of the ridge are almost vertical. The overhang was measured as approximately 63°, an unexpected increase of 18° over the

intended 45°. The reason for this is most likely because the substrate was not positioned directly over the crucible, and the paths of vapourised atoms are radially distributed from the source, therefore increasing the deposition angle. On inspection of Figure 136c and d, a smooth back wall on the ridge can be seen. This gives an indication of how the ridge was formed, and why the morphology is so different to that seen in LOA35. A schematic representation of the deposition process is given in Figure 137.

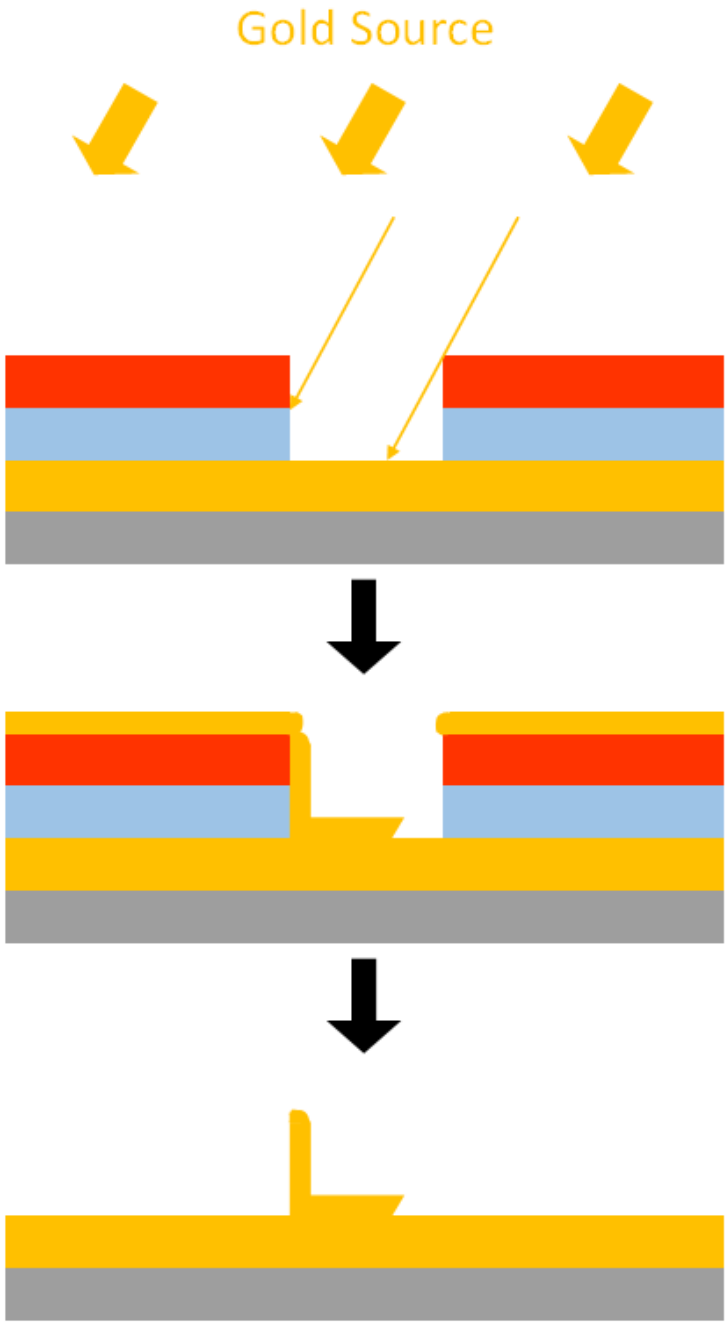


**Figure 137: Schematic of ridge formation on the LOA45 substrate.**

Figure 137 illustrates the formation of the ridge on the features of the LOA45 substrate. An underdeveloped undercut in the LOR causes a buildup of deposited gold material, which accumulates into a ridge. In some instances, this ridge may make sufficient contact with the gold deposited on the top surface of the resists, such that once the polymers are removed, this material remains on the substrate and adheres via Van der Waals interactions. Examples of such a structure are given in Figure 138.

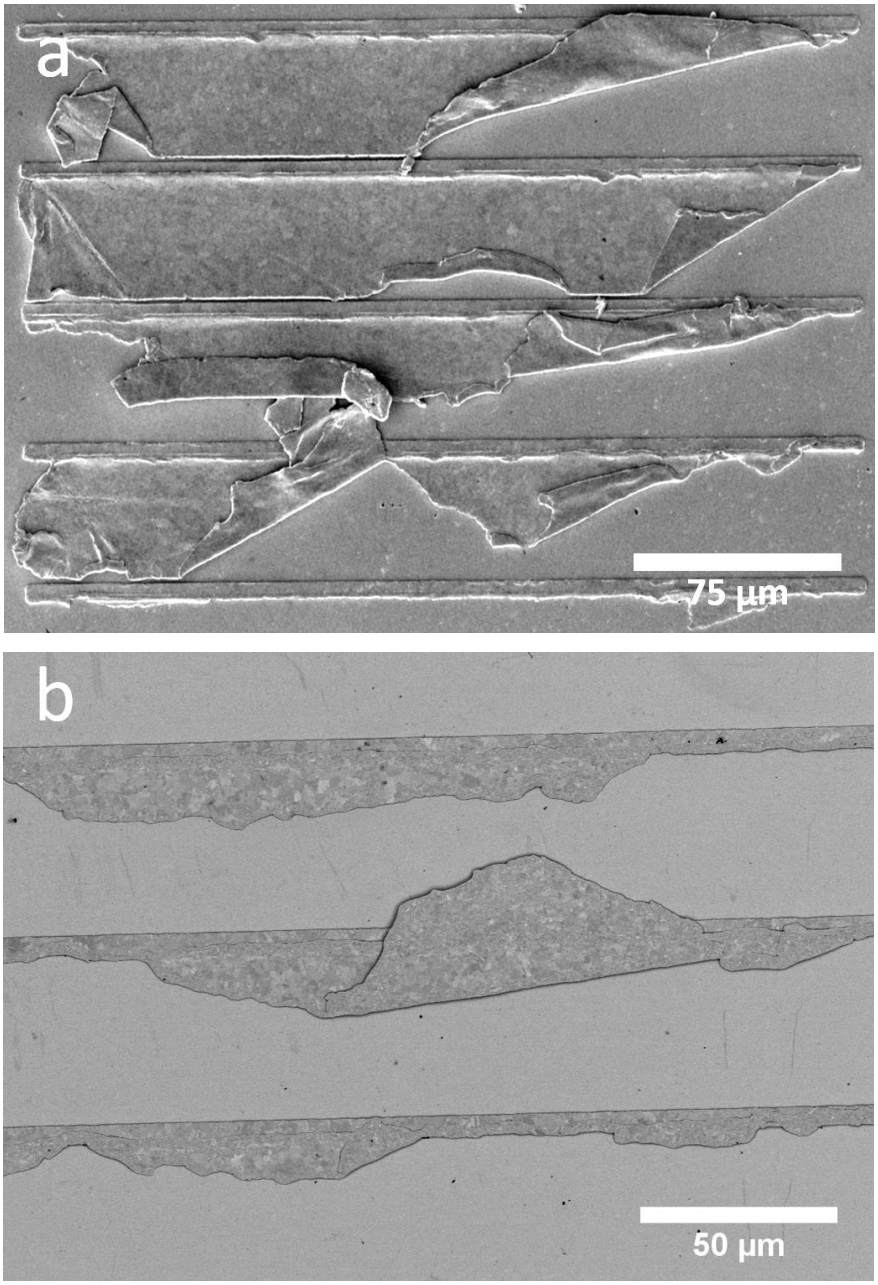


**Figure 138: SEM micrographs of poorly formed structures on the LOA 45 substrate.**

Sometimes, the wall may even collapse under its own weight or be mechanically deformed by an external source. This is demonstrated in the micrographs of Figure 139.

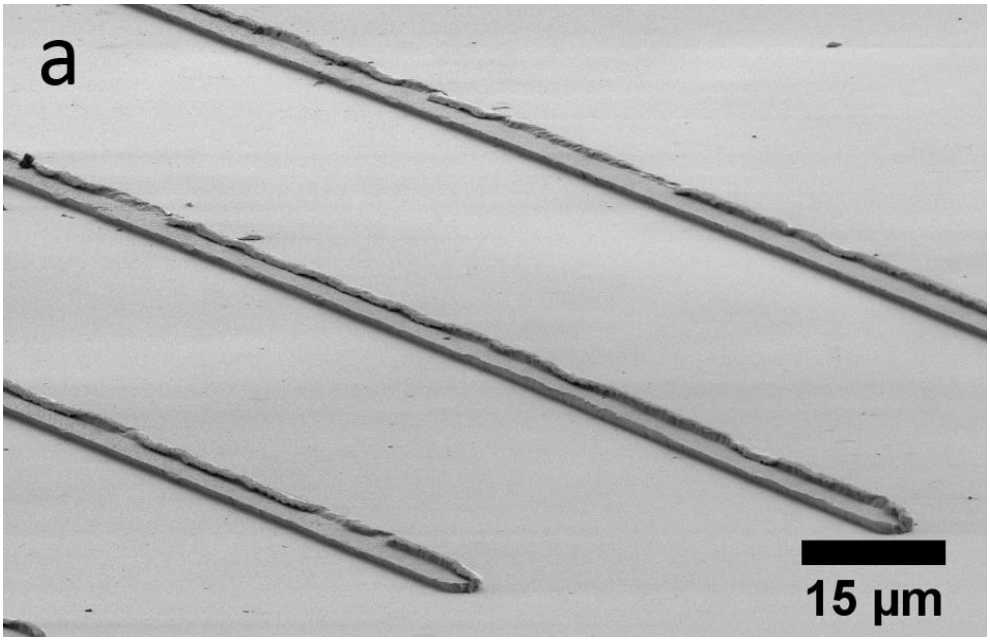
a
15 µm

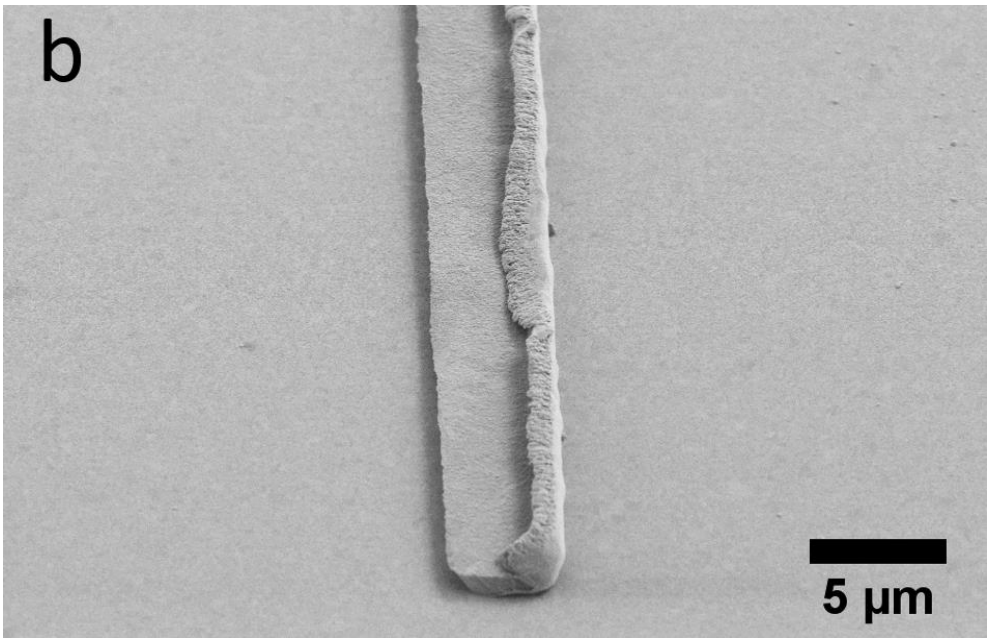
b
5 µm

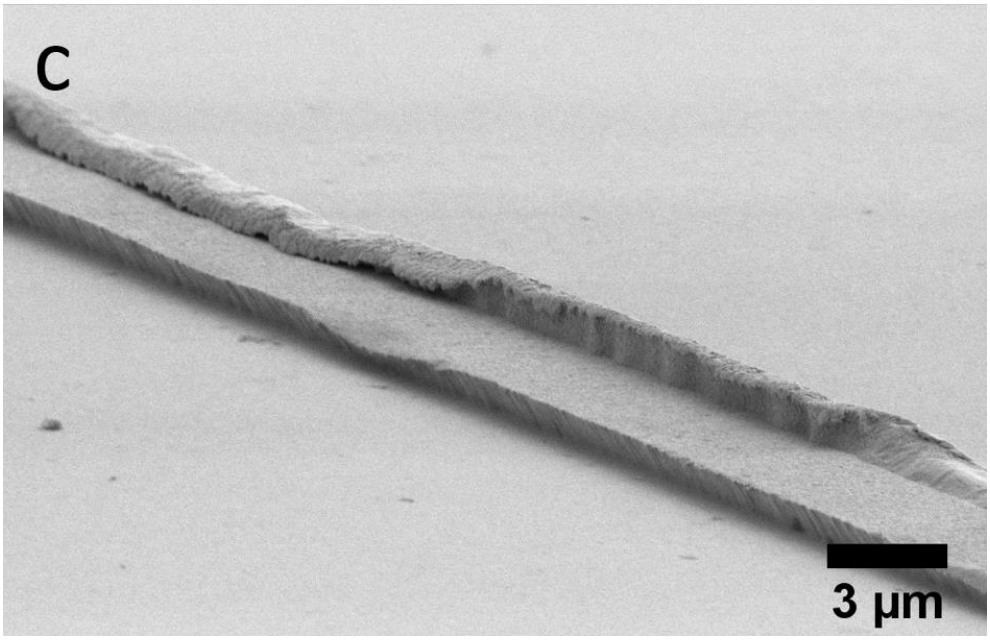
c
3 µm

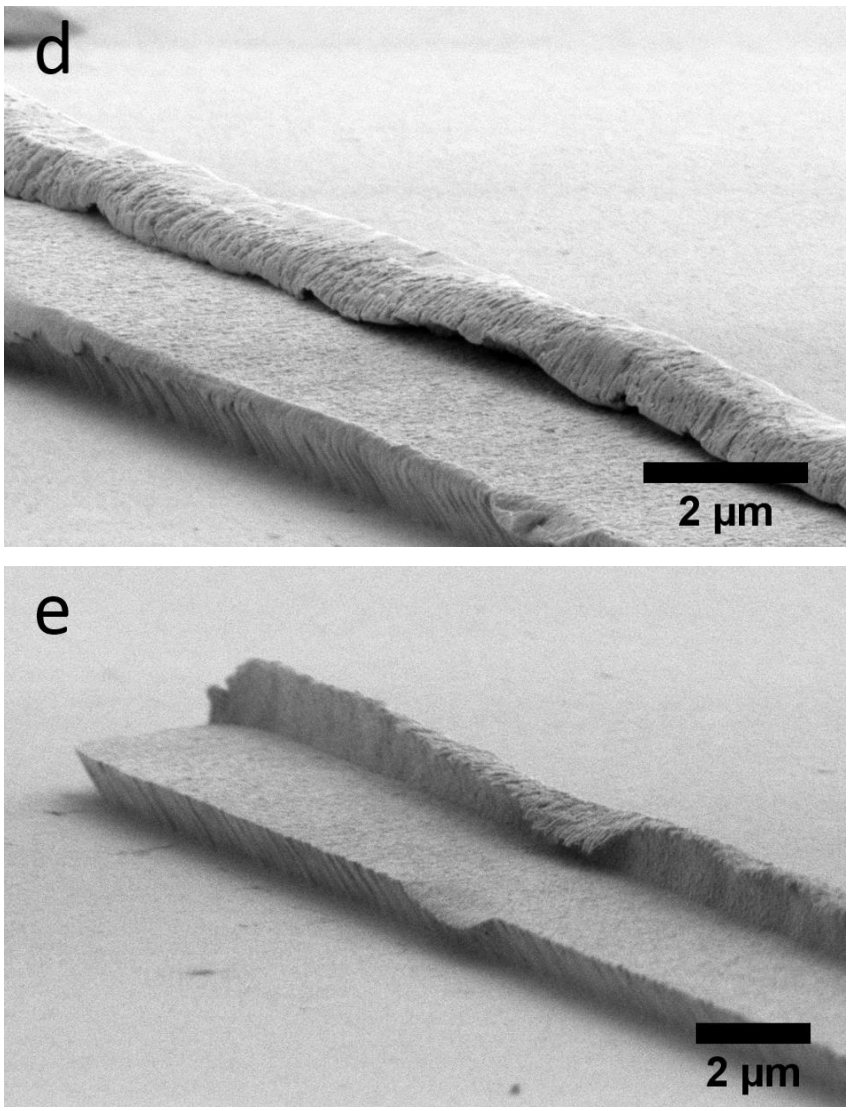


**Figure 139: Electron micrographs of some features on the LOA45 substrate in which the ridge has either collapsed or mechanically deformed.**

Despite the unintended morphology of these overhang structures, the LOA45 substrate was used for crystallisation studies. The results are shown in Section 5.4.2.

**Ledge Overhang Array: LOA55**

For the final Ledge Overhang Array, the angle jig was set to 35°, which was expected to give a feature angle of 55°. The SEM and AFM data suggested that again, the features had not formed as envisioned.

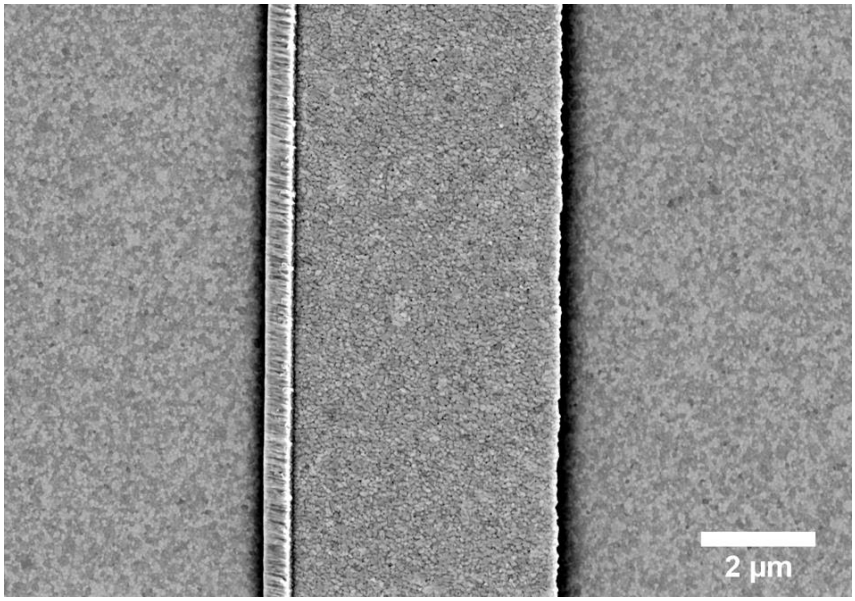


**Figure 140: Scanning electron micrograph of a feature on the LOA55 substrate.**

Although the structures on the LOA55 substrate in the SEM appeared very similar to those found on LOA35, the AFM micrographs implied that their morphologies were closer to the features of LOA45.

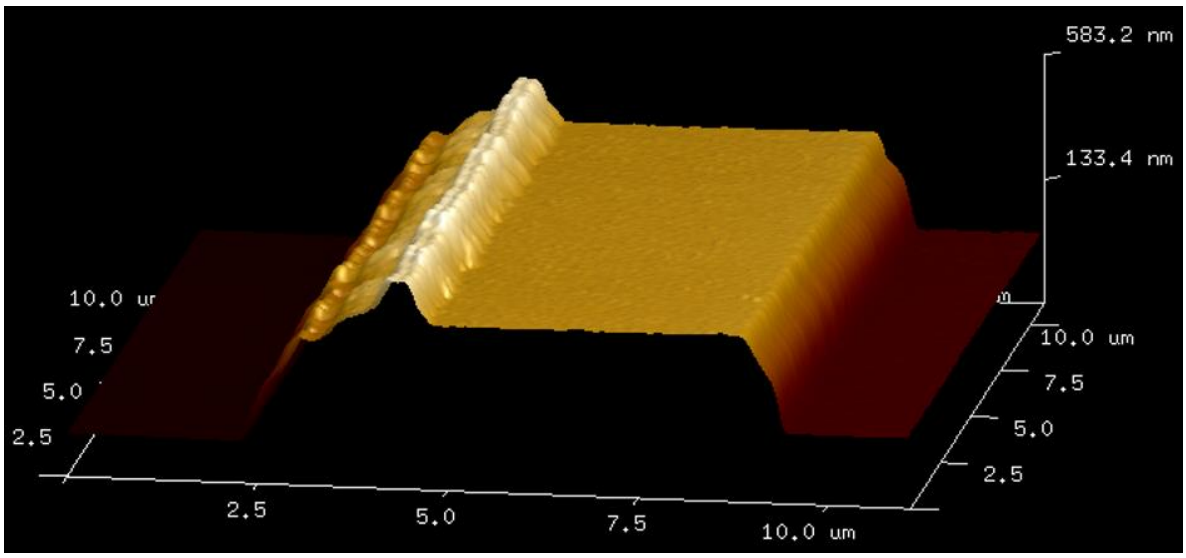


**Figure 141: Atomic force micrograph of a feature on the LOA55 substrate.**

Without electron micrographs of the LOA55 taken with a tilt angle, a measurement of the overhang angle is not yet possible or visualization of the ridge. However, it is likely that the curvature of the ridge indicated by the AFM micrograph is not real, but due to tip convolution. The top of the ridge appears much narrower than that seen on the features of the LOA45 substrate. Using the AFM and SEM data, it is possible to suggest how this structure formed.

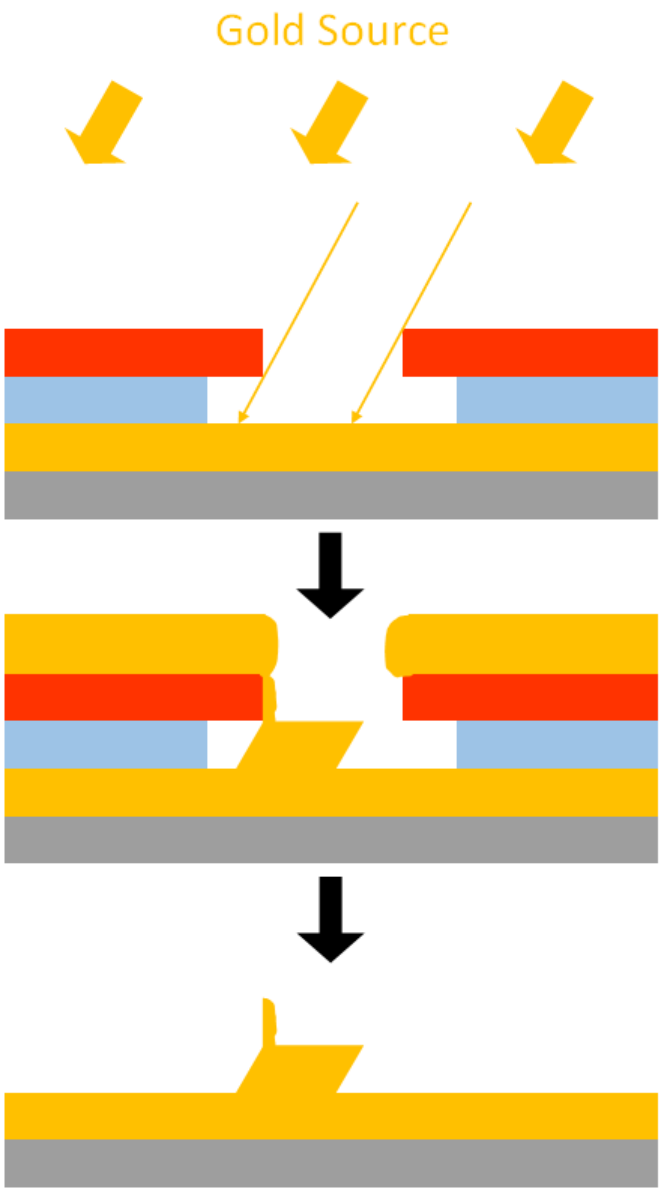


**Figure 142: Schematic of how the ridge structure may have formed on the features of the LOA55 substrate.**

In the case of LOA55, the undercut may have been present, but the layer of gold deposited was too thick. As such, the structure came into contact with gold coated on the sidewall of the resist, which remained after the processing steps. As with the LOA45 substrate, although the LOA55 feature morphology was incorrect, it was still used for crystallisation studies.

## 5.4 Crystallisation Data

### 5.4.1 LOA35

The initial crystallisation experiments were conducted using the LOA35 substrate prior to removal of the residual photoresist. This meant that the vast majority of the substrate was still coated with photoresist, and voids in this layer only existed in the immediate vicinity of the structures (see Figure 132). The substrate was submerged in an ethanolic solution of 16-mercaptohexadecanoic acid to form a carboxylate-terminated self-assembled monolayer (SAM). Since the flat areas were coated with photoresist, the SAM would form only at the features and on the flat areas immediately adjacent to the structure, which were both formed from gold. After crystallisation at $[Ca^{2+}] = [CO_3^{2-}] = 1$ mM for 10 minutes, the majority of crystals had precipitated either at the overhang or on the ramp on the opposite side (Figure 143). The arrows in Figure 143 are to aid the viewer and indicate where the crystals had precipitated. The green box is presented at a higher magnification in Figure 143b.

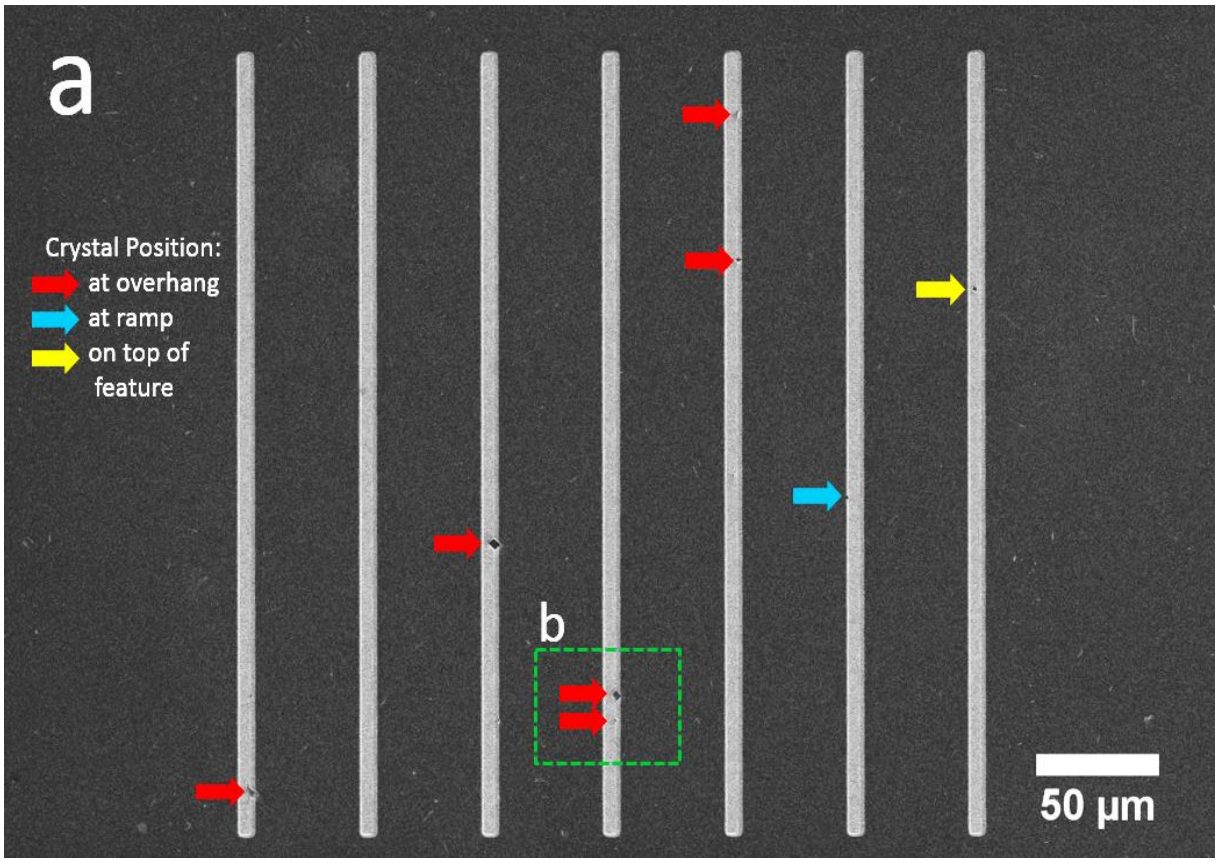

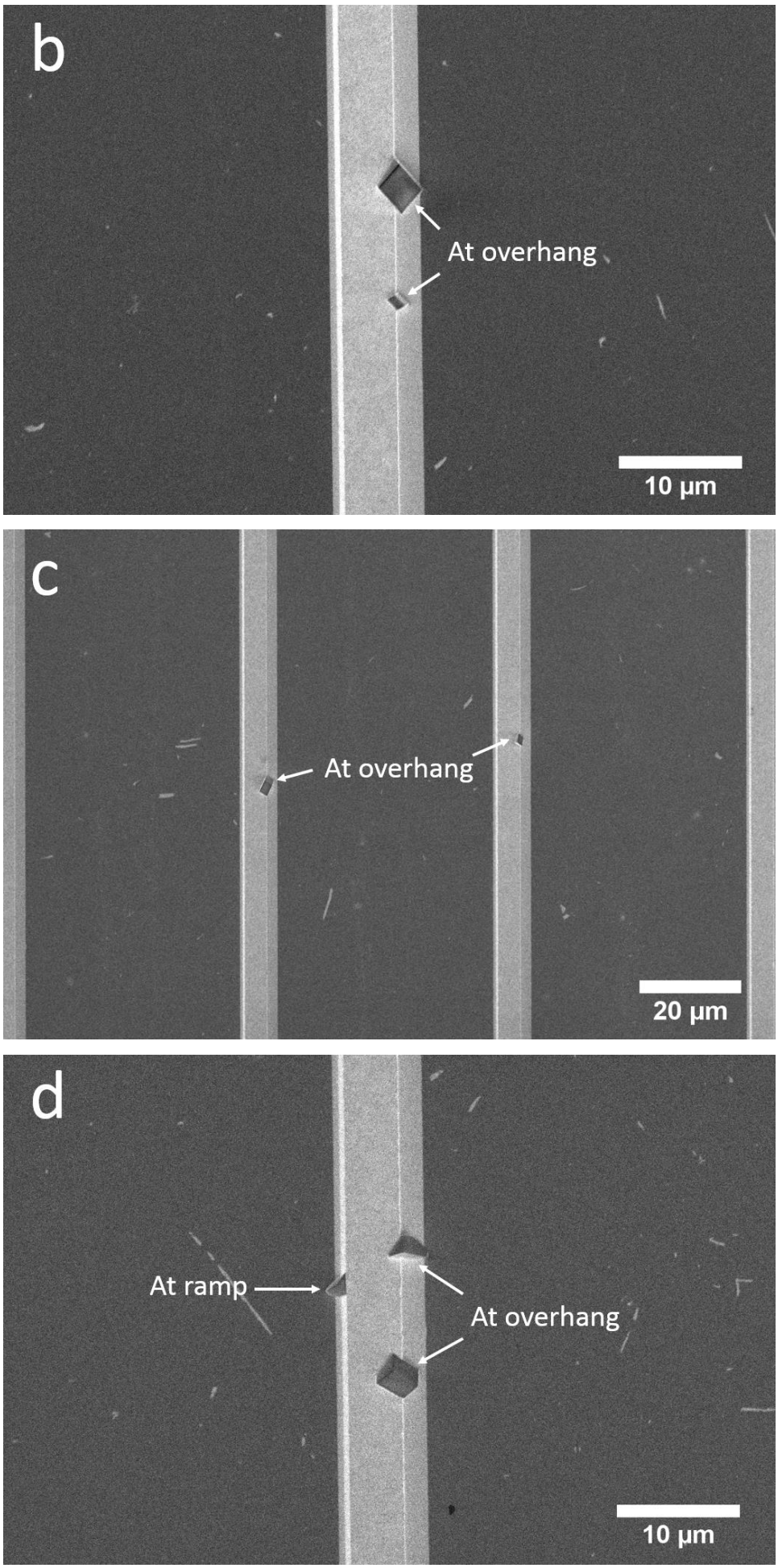
b
At overhang
10 µm
c
At overhang
20 µm
d
At ramp
At overhang
10 µm

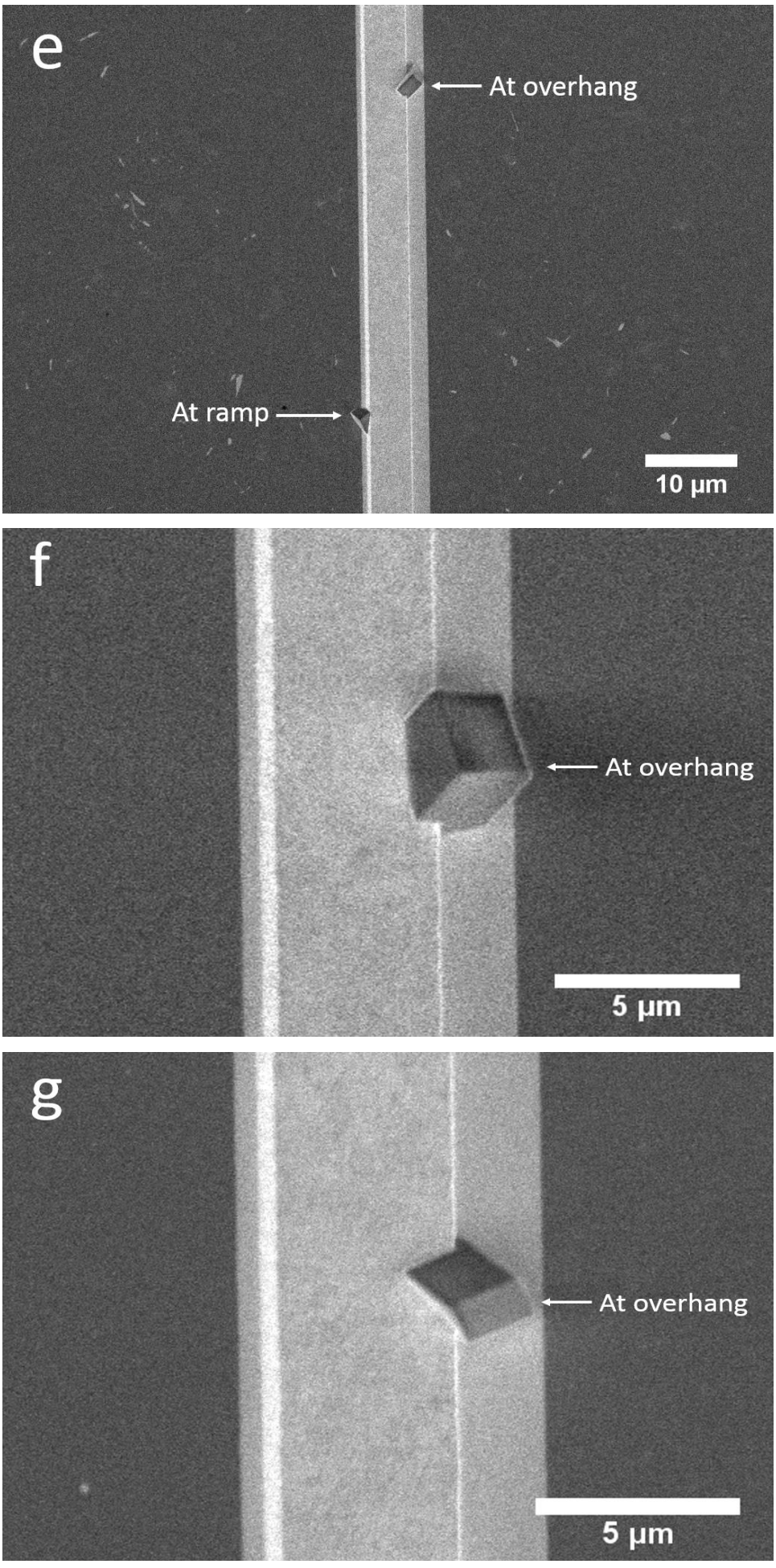
e
At overhang
At ramp
10 µm
f
At overhang
5 µm
g
At overhang
5 µm

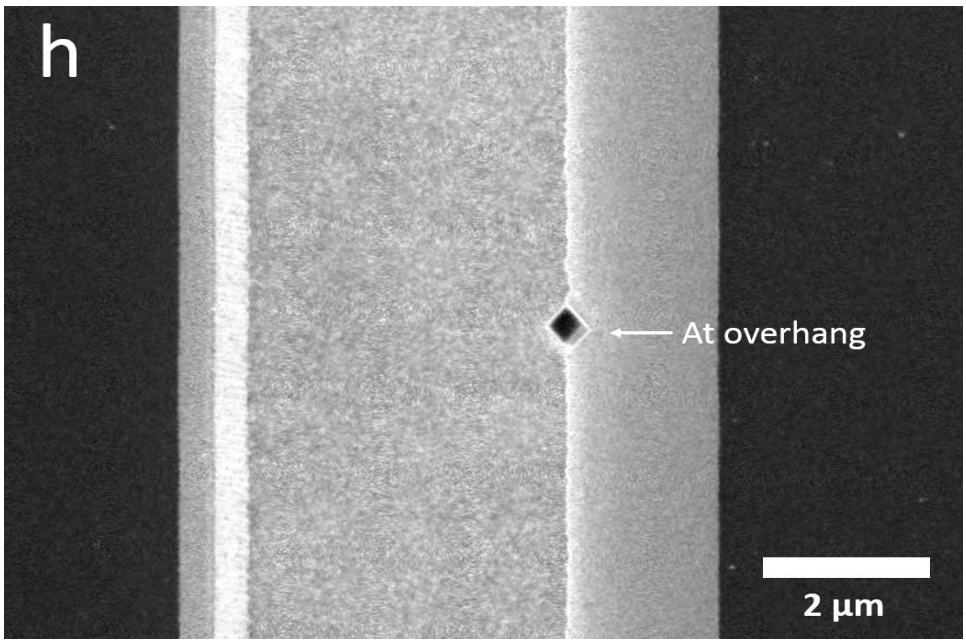


**Figure 143: SEM micrographs of calcium carbonate crystals precipitated on the LOA35 substrate before removal of the residual photoresist and after formation of a carboxylate terminated SAM**

As stated above, the majority of the region between features was coated with photoresist. This meant that the carboxylate-terminated SAM would only form on the feature and the substrate in proximity, as these are made of gold. If the feature did not influence crystallisation at all, then we would expect to see crystals that have precipitated indiscriminately across the surface of the structure and adjacent areas. Conversely, the crystals clearly show a preference for the overhang, but also a tendency to nucleate at the ramp as well (Figure 143d and e). The fact that crystals were observed at both of these locations was interesting, as it suggests that the angle does not necessarily have to be acute to promote nucleation. An alternative explanation may simply be that the deposition process produces structures on the ramp and the wall of the overhang that are conducive to nucleation. Specifically, it is not the angle that stabilises the nucleus, but rather the surface topography that is generated in these areas via an angled deposition, as was used here. By referring back to Figure 136e, in which it is possible to see the wall of the overhang, this surface appears to be quite rough. Research has suggested that rough surfaces can indeed increase crystal populations [5, 9-11], supporting this suggestion.

After the photoresist had been removed by prolonged submersion in acetone, a series of crystallisations were carried out at $[Ca^{2+}] = [CO_3^{2-}]$ = 1, 2 or 3 mM for 10 minutes. At 1 mM, 10 mins, very few unaligned crystals were observed and at 2 mM, 10 minutes a random

distribution of crystals were present and there appeared to be no preference for the feature. However, the results at 3 mM were quite different (Figure 144).

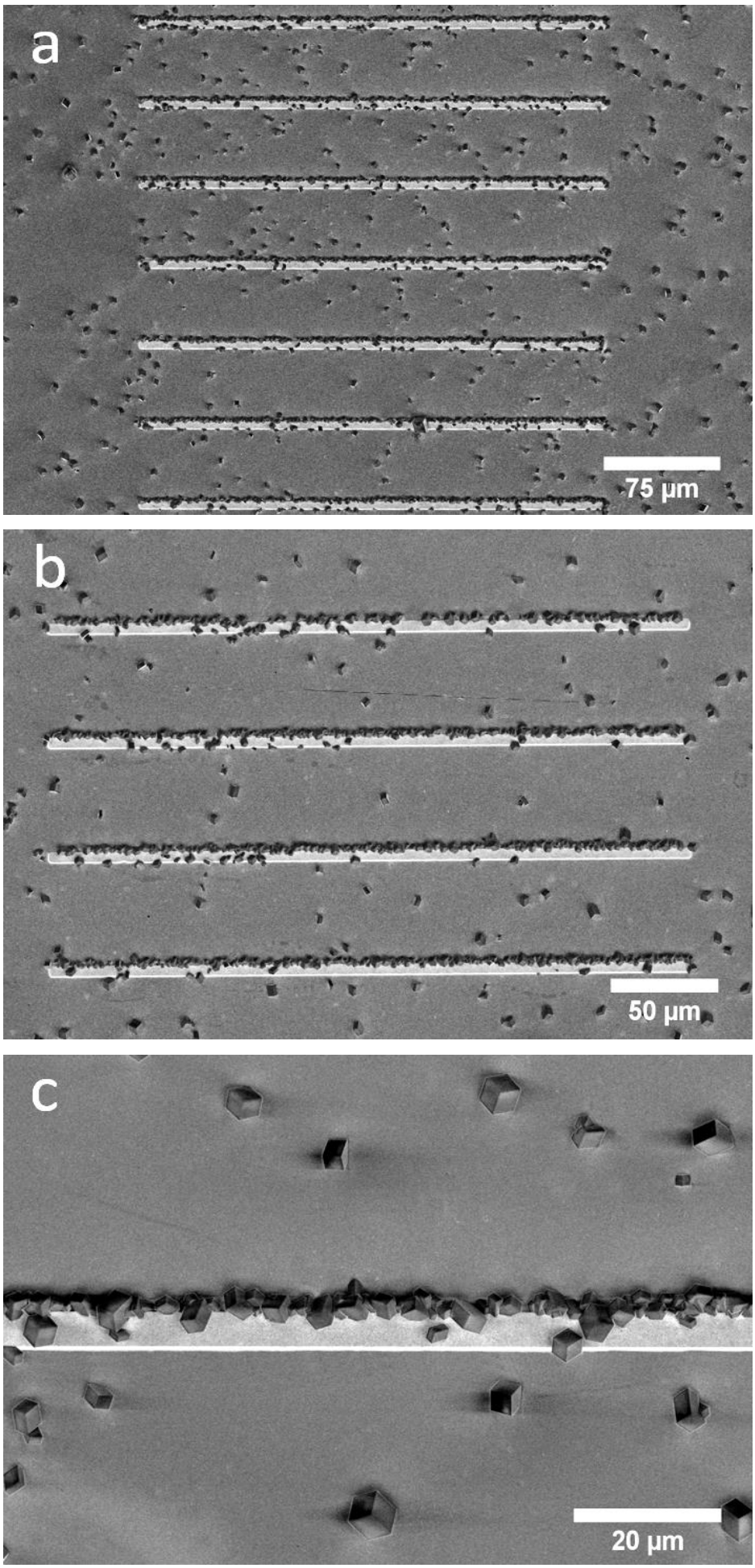
a
75 µm
b
50 µm
c
20 µm

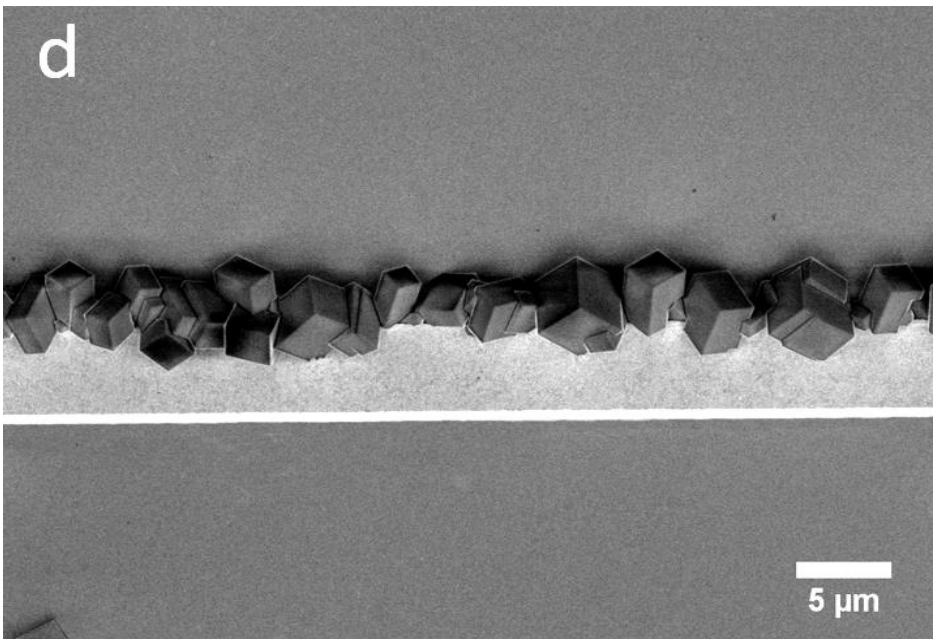


**Figure 144: Electron micrographs of calcite crystals precipitated on the LOA35 substrate**

Although no alignment with the features was observed at 1 and 2 mM after a residence time of 10 minutes, at 3 mM a significant number of crystals had precipitated at the gold structures. The majority of these had formed on the side on which the overhang was, a smaller portion on the ramp on the opposite side, and fewer still on top of the feature. A longer residence time at an equimolar concentration of 1 mM was also investigated (Figure 145).

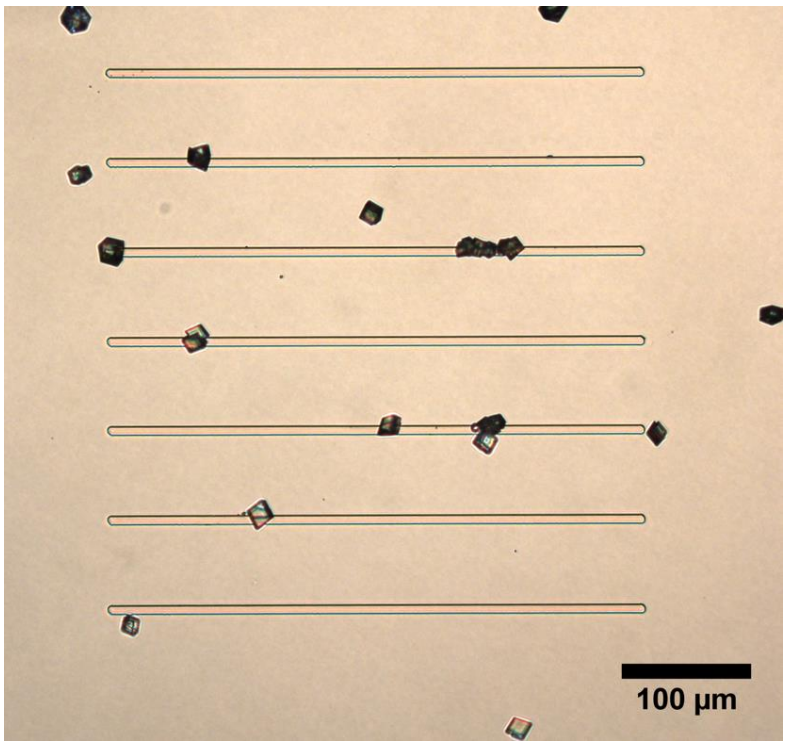


**Figure 145: Optical micrograph of the LOA35 substrate after calcium carbonate crystallisation. [$Ca^{2+}$] = [$CO_3^{2-}$] = 1 mM, residence time = 60 minutes.**

The fact that no crystals were observed at 1 mM, 10 mins, yet crystals were present at 3 mM, 10 mins and 1 mM 60 mins may be explained by mass transport effects. If the most acute part of the overhang penetrates far enough back into the structure and this is where the crystals nucleate, then one might expect that the initial growth of a crystal that had precipitated here would be limited by mass transport. This is because the solution that the nascent crystal has access to is limited, as it is almost enclosed by the surrounding structure. While the crystal would exist underneath the overhang, it could not be seen by the microscope and so would not be detected at 1 or 2 mM and 10 minutes. At 3 mM, 10 mins, the supersaturation is high enough for the crystal to grow beyond the overhang after this short residence time, and at 1 mM, 60 mins, the residence time is sufficiently long for crystals to grow to a large enough size to be observed.

### 5.4.2 LOA45

As with LOA35, LOA45 was also coated with 16-mercaptohexadecanoic acid. However, no residual photoresist was present on the surface and so the self-assembled monolayer should exist both at the features and the interstitial regions. Again, an equimolar concentration of 1 mM and 10 minutes residence time was used (Figure 146).

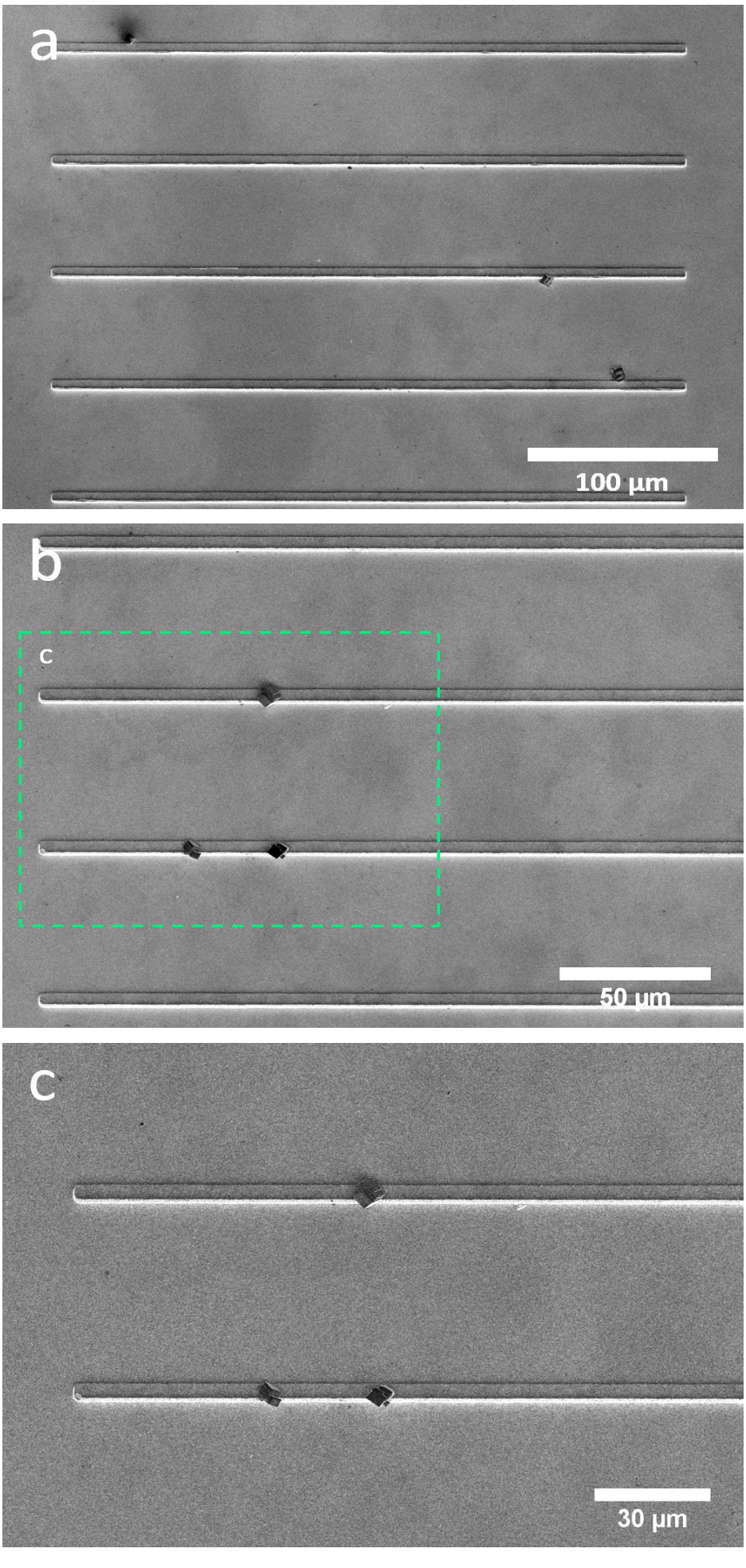
a
100 µm
b
c
50 µm
c
30 µm

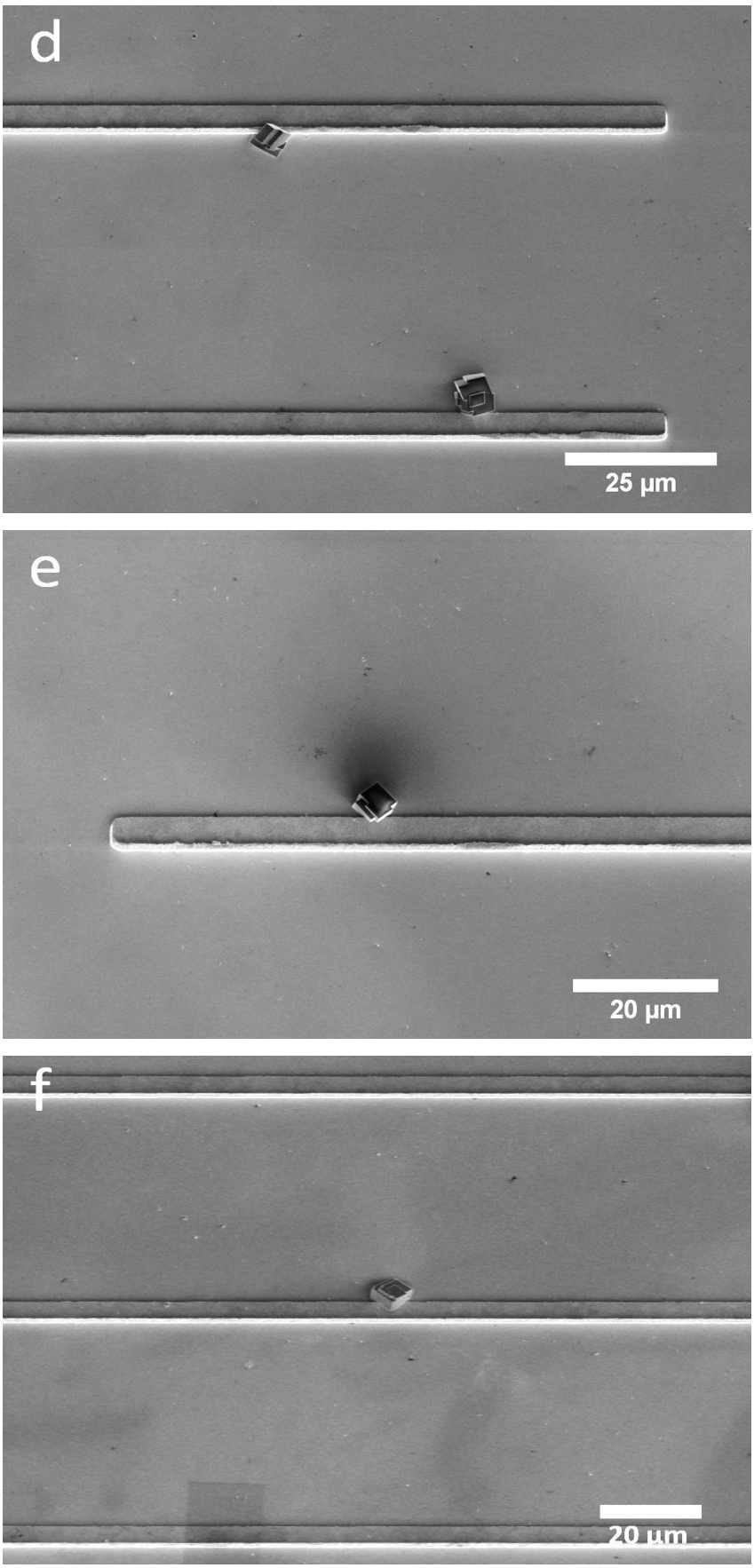


**Figure 146: Electron micrographs of calcite crystals precipitated on the LOA45 substrate after it had been coated with 16-mercaptohexadecanoic acid**

As before, the features were effective at localising crystallisation. The features of the LOA45 substrate not only possess an overhang and a ramp, but also an additional ridge-like feature, as described in Section 5.2.1. Crystals were also found to have precipitated here, as indicated by Figure 146b and c. Further crystallisation experiments were conducted with this substrate, but without the carboxylate SAM coating. 1, 2 and 3 mM and 10 minute residence time was used (Figure 147). At 1 and 2 mM, a random distribution was observed and at 3 mM, there was some evidence of localisation.

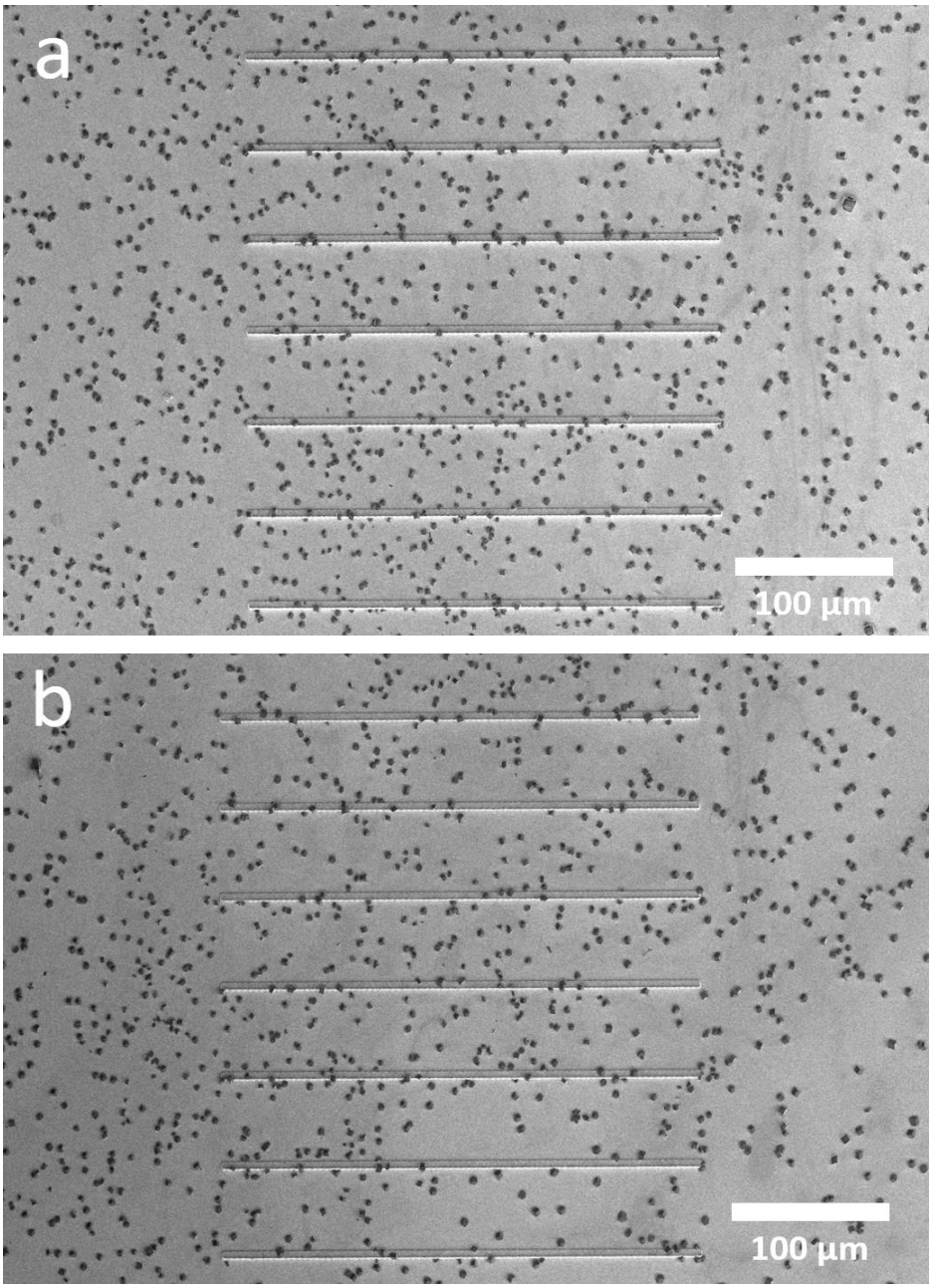

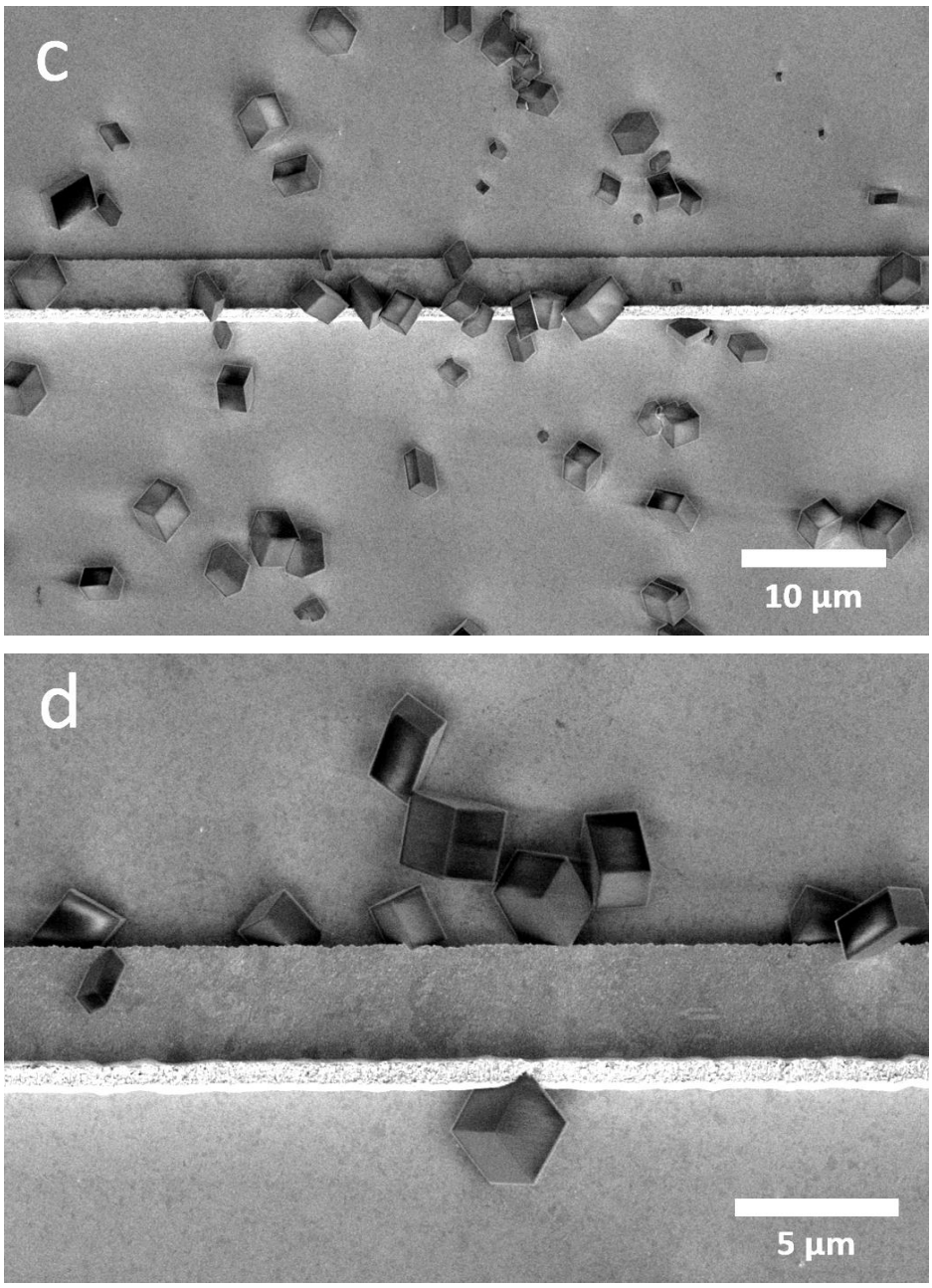


**Figure 147: Electron micrographs of calcite crystals precipitated on the LOA45 substrate. $[Ca^{2+}] = [CO_3^{2-}] = 3$ mM, residence time = 10 minutes.**

The large population of crystals and their apparent random distribution makes it difficult to conclude that there was a preference for the gold structures. Though not immediately obvious from Figure 147a and b, there did appear to be some instances where the crystals had precipitated at the overhangs and ramps of the features (Figure 147c and d). As mentioned above in Section 5.3.1, the patterning in some areas was of poorer quality than in others (Figure 138). Interestingly though, crystals were associated with some of these amorphic structures (Figure 148).

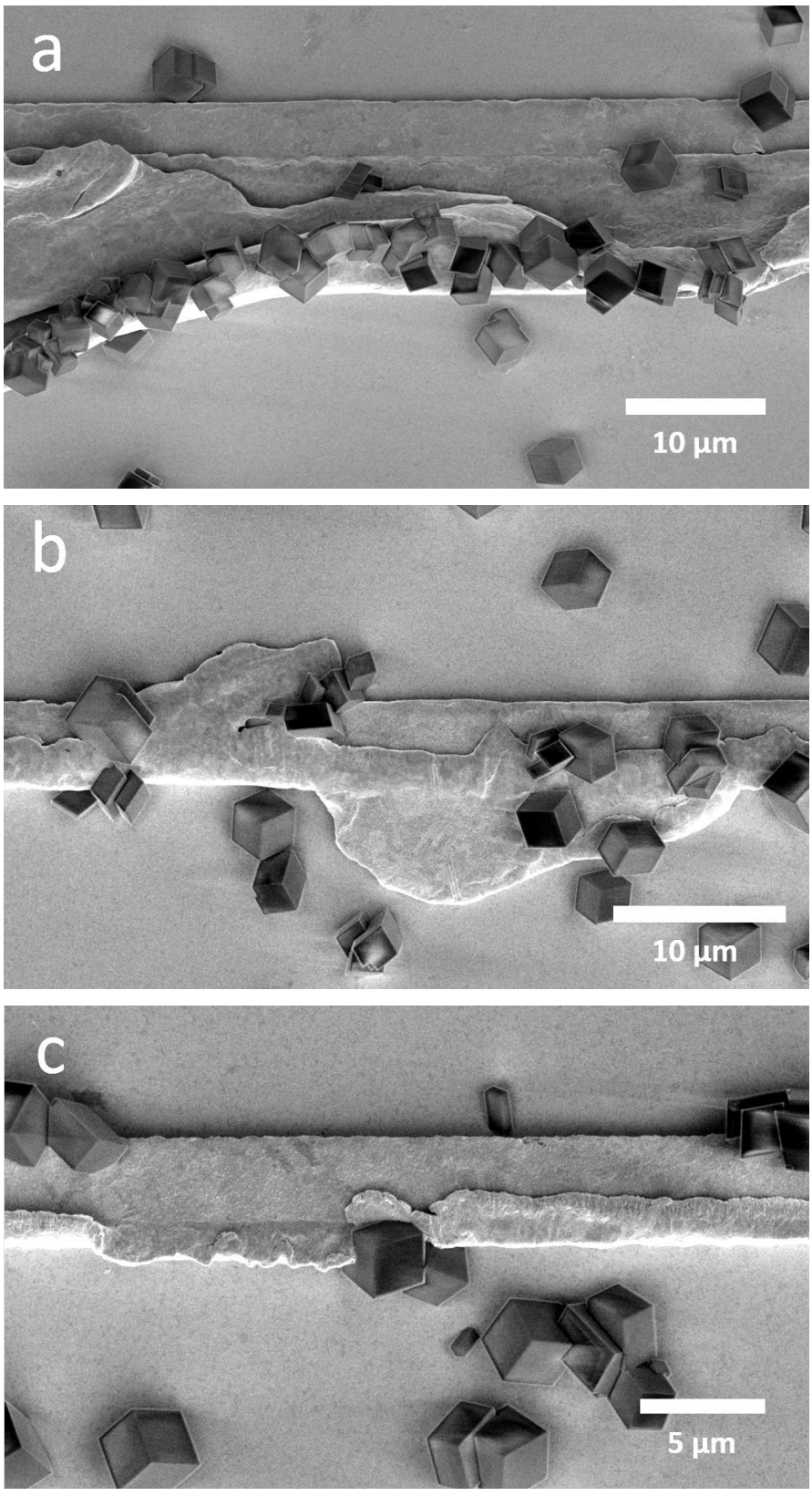


**Figure 148: Electron micrographs of calcite crystals precipitated on some poorly formed structures of the LOA45 substrate. $[Ca^{2+}] = [CO_3^{2-}] = 3$ mM, residence time = 10 minutes.**

The LOA45 substrate is interesting because of its range of surface structures. The micrographs further support the idea that angular geometries are favourable for nucleation, as crystals had

precipitated not only at the overhang/ramp of some of the structures, but also at the folds of material of some of the malformed features.

### 5.4.3 LOA55

Crystallisation experiments were carried out using the LOA55 substrate without a SAM coating. A low supersaturation was used and optical micrographs were taken initially, then the SEM was used to investigate areas of the substrate further. The green boxes of Figure 149a (scale bar = 50 µm) are the areas that were imaged in the SEM and are presented as high-magnification micrographs in Figure 149b-i.

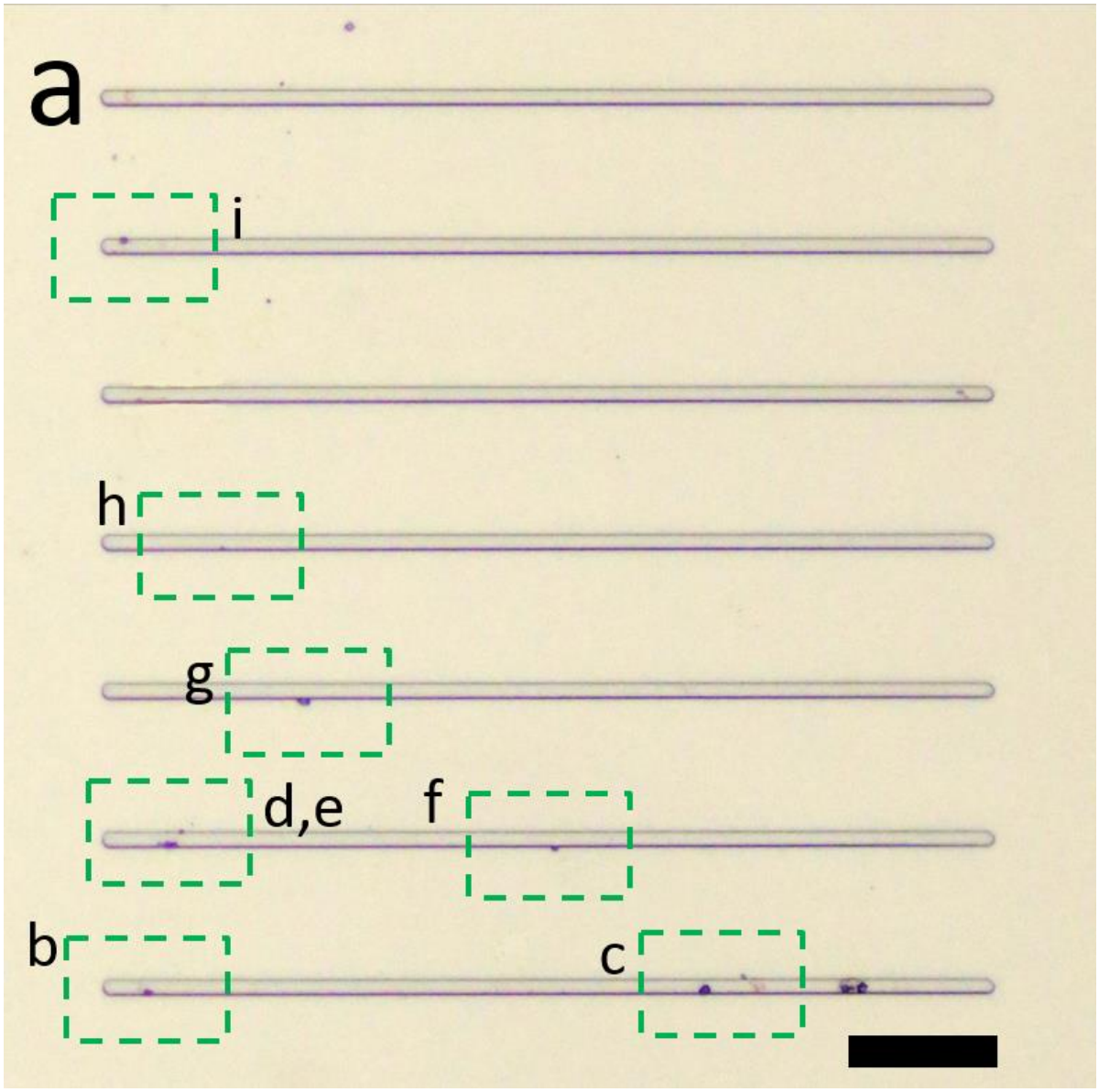

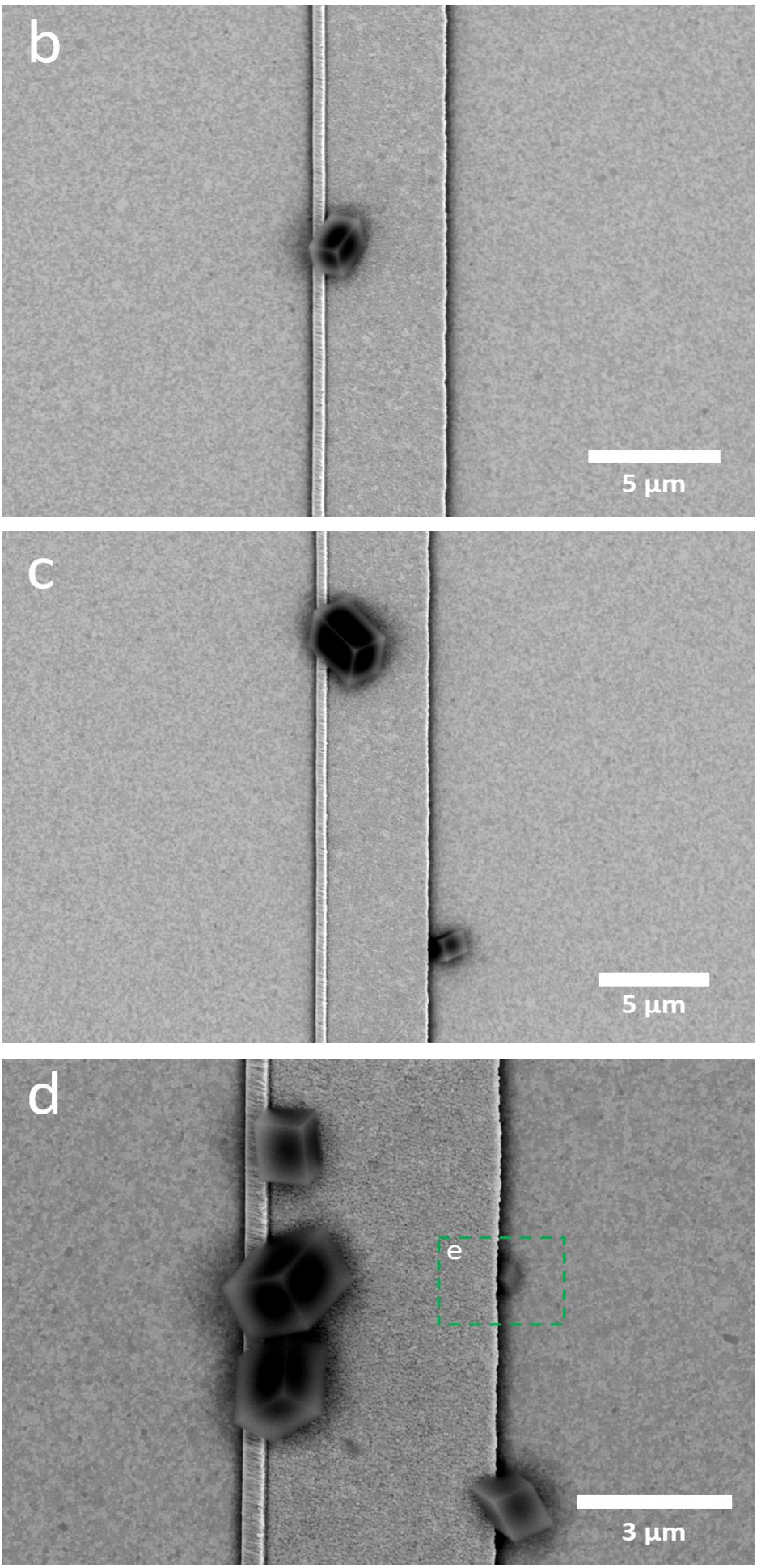
b
5 µm
c
5 µm
d
e
3 µm

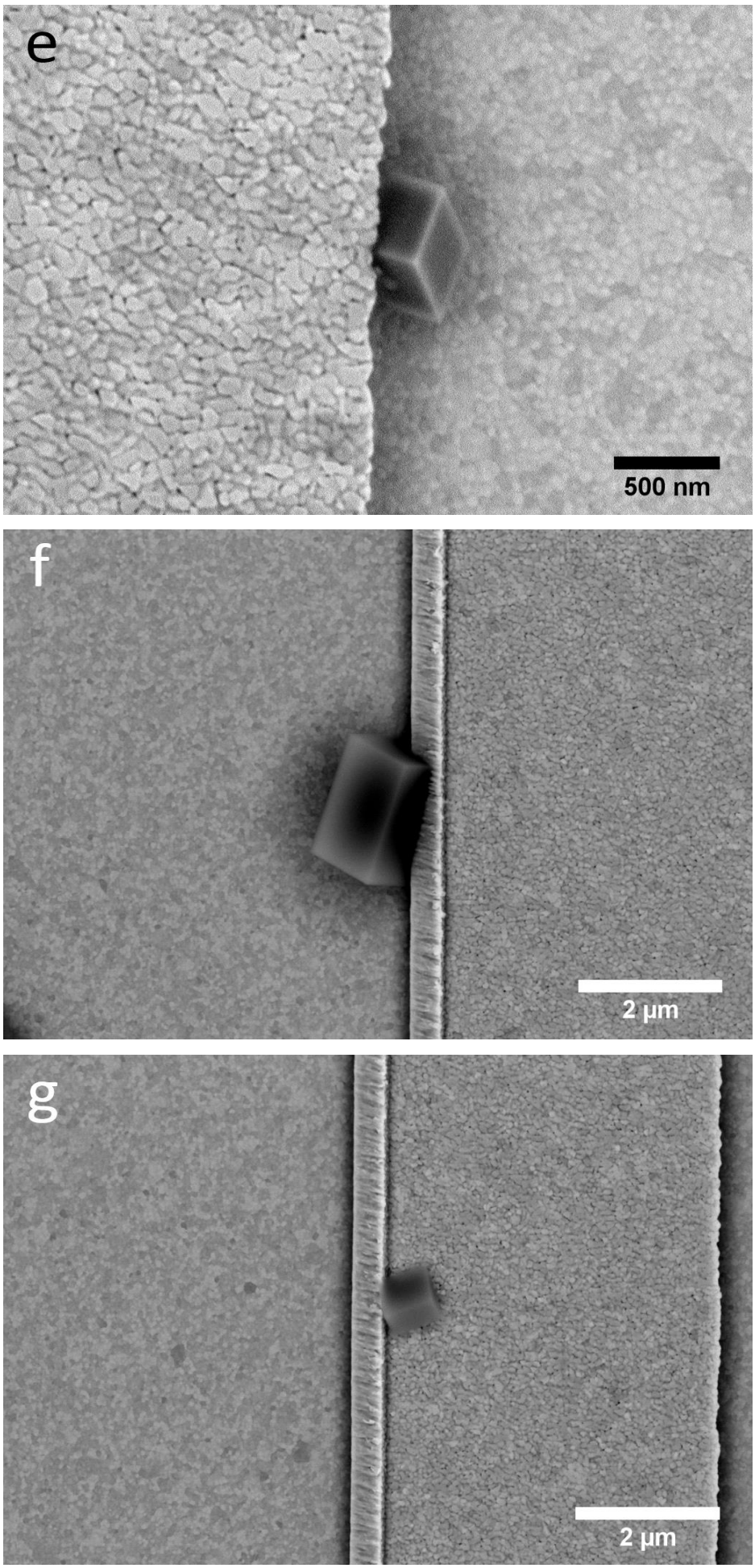
e
500 nm
f
2 µm
g
2 µm

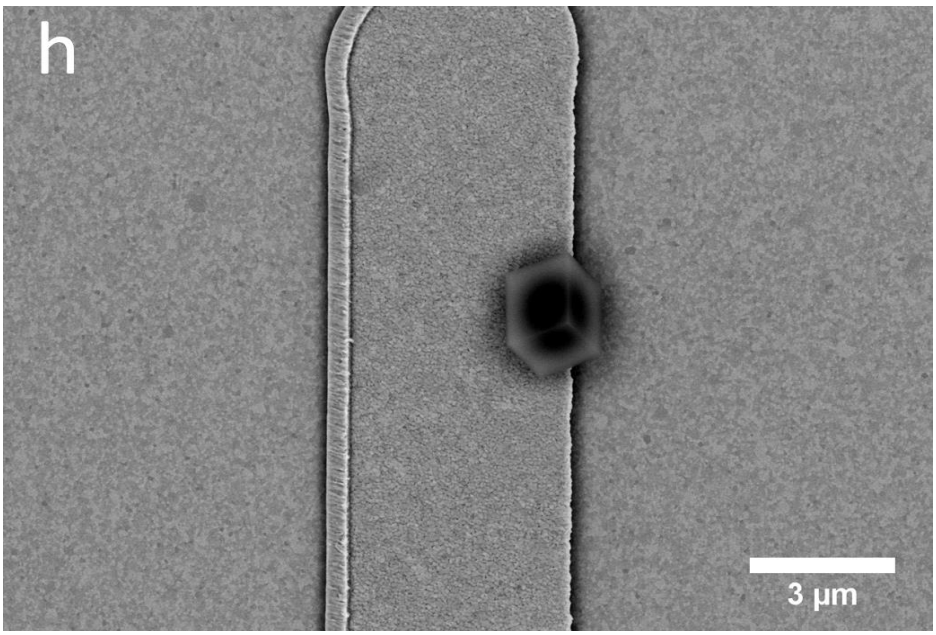


**Figure 149: Micrographs of calcite crystals precipitated on the features of the LOA55 substrate**

The experiment depicted in Figure 149 demonstrates the influence that topographical features can have on crystallisation. That the majority of the crystals were observed at the overhang or either side of the ramp is intriguing. It suggests that at this supersaturation, the energy barrier associated with nucleation on the flat spaces is often too large to be overcome. By nucleating at the angular geometries of the gold structure, the topographically-reduced energy barrier can be surmounted; hence why almost all of the crystals are present at this location.

## 5.5 Summary

The aim of this brief research project was to demonstrate that it is possible to fabricate structures that can be used to topographically control crystallisation. To achieve this, gold

microstructures were formed on a gold-coated silicon wafer. The fact that the entire surface was composed of gold was an attempt to create topographical features with homogeneous surface chemistry. The structures were produced by depositing gold using electron beam evaporation. The substrate was held at an inclination to the gold source, such that an overhang should form on one side between the feature and the surface. In practice, obtaining this particular structure was difficult, with only one successful attempt, though the structures formed unintentionally were interesting nonetheless. Regardless, all of the substrates were used for calcium carbonate crystallisation and the crystals showed a clear preference for either the overhang or the ramp on the opposite side. Though the structures were quite crude, their ability to localise crystallisation is indisputable.

## 5.6 References


1. Levinson, H.J., *Principles of Lithography*. 2010: Society of Photo Optical.
2. Rai-Choudhury, P., *Handbook of Microlithography, Micromachining, and Microfabrication: Microlithography*. 1997: SPIE Optical Engineering Press.
3. Carter, P.W. and M.D. Ward, *Topographically directed nucleation of organic crystals on molecular single-crystal substrates.* Journal of the American Chemical Society, 1993. **115**(24): p. 11521-11535.
4. Holbrough, J., et al., *Topographical control of crystal nucleation.* Crystal Growth & Design, 2012. **12**(2): p. 750-755.
5. Campbell, J.M., F.C. Meldrum, and H.K. Christenson, *Is ice nucleation from supercooled water insensitive to surface roughness?* The Journal of Physical Chemistry C, 2015. **119**(2): p. 1164-1169.
6. Dennig, P.A. and D.A. Stevenson, *Influence of substrate topography on the nucleation of diamond thin films.* Applied physics letters, 1991. **59**(13): p. 1562-1564.
7. Aizenberg, J., A.J. Black, and G.M. Whitesides, *Controlling local disorder in self-assembled monolayers by patterning the topography of their metallic supports.* Nature, 1998. **394**(6696): p. 868-871.
8. Campbell, J.M., F.C. Meldrum, and H.K. Christenson, *Characterization of Preferred Crystal Nucleation Sites on Mica Surfaces.* Crystal Growth & Design, 2013. **13**(5): p. 1915-1925.
9. Asanithi, P., *Surface porosity and roughness of micrographite film for nucleation of hydroxyapatite.* Journal of Biomedical Materials Research Part A, 2014. **102**(8): p. 2590-2599.
10. Liu, Y., et al., *Investigation of adhesion of CaCO3 crystalline fouling on stainless steel surfaces with different roughness.* International Communications in Heat and Mass Transfer, 2011. **38**(6): p. 730-733.
11. Keysar, S., et al., *Effect of Surface Roughness on the Morphology of Calcite Crystallizing on Mild Steel.* Journal of Colloid and Interface Science, 1994. **162**(2): p. 311-319.

# 6 General Discussion

The data presented in this thesis have proven that surface topography can be used to control crystallisation. The purpose of this chapter is to discuss the possible origins of this phenomenon. However, it should be made clear that the proposed mechanism is speculative, as it is impossible to be certain given the data that has been obtained and the assumptive nature of classical nucleation theory.

According to classical nucleation theory, heterogeneous nucleation will be favoured over homogenous nucleation, so long as the contact angle between the nucleus and surface is less than 180$^{o}$. The relationship between the surface tensions and the contact angle is described by the three phase energy diagram (Figure 150) and Young's equation (Equation 23):

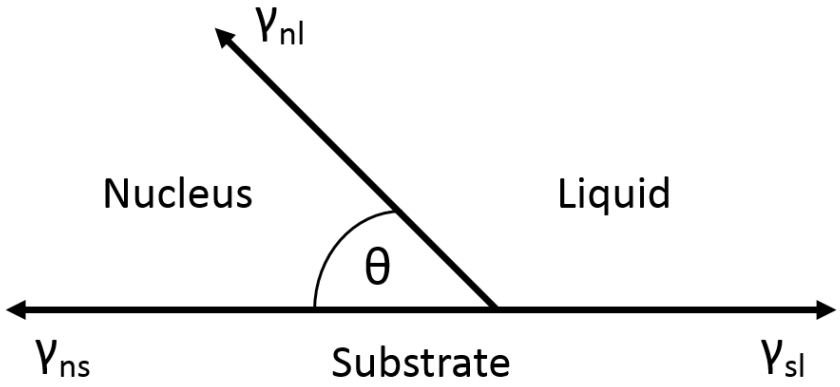


**Figure 150: Interfacial energy diagram for three phases in contact.**

$$cos\theta = \frac{\gamma_{sl} - \gamma_{ns}}{\gamma_{nl}} \qquad \text{Equation 23}$$

where θ is the contact angle between the substrate and nucleus, and the interfacial tensions are as follows:

- $\gamma_{ns}$: Interfacial tension between nucleus and substrate.
- $\gamma_{nl}$: Interfacial tension between nucleus and liquid.
- $\gamma_{sl}$: Interfacial tension between substrate and liquid.

The interplay between the interfacial tensions influences the value of a factor, ϕ, which is dependent upon the contact angle of the system. ϕ has a value less than or equal to one and

determines by how much the energy barrier will be reduced relative to that for homogenous nucleation:

$$\phi = \frac{(2 + cos\theta)(1 - cos\theta)^2}{4} \qquad \text{Equation 24}$$

$$\Delta G' = \phi \Delta G^* \qquad \text{Equation 25}$$

Where ΔG' is the energy barrier to heterogeneous nucleation and ΔG* the energy barrier to homogeneous nucleation [1]. By consideration of Equations 23, 24 and 25, we can describe the effect of the surface tensions on the energy barrier to nucleation. The smallest contact angles between the nucleus and the substrate are associated with values for the right-hand side of Equation 23 that are close to 1 (cosθ can't be larger than 1). If the value of *x* is close to 1, then through $\cos^{-1}(x) = \theta$, a small angle for θ will be obtained, and ϕ will be less than 1. A situation where this would be true is if both of the interactions between the nucleus and solution ($\gamma_{nl}$) and the nucleus and substrate ($\gamma_{ns}$) are favourable (i.e. little work is required to form these new surfaces) and the interface between the substrate and solution is unfavourable (large $\gamma_{sl}$). Also, if $\gamma_{sl} = \gamma_{ns}$, then the contact angle will be 90° and the energy barrier for heterogeneous nucleation will be half that for homogeneous nucleation. Finally, if $\gamma_{sl} - \gamma_{ns} << \gamma_{nl}$, then the contact angle will be 180° and there will be no reduction in the energy barrier. However, this is rarely the case as the interactions between the nucleus and the surface are often stronger than the bonds of solvation, and so heterogeneous nucleation is almost always favoured [2].

Now, let us consider nucleation within a surface feature in the context of classical nucleation theory. This scenario is illustrated in Figure 151, where, for simplicity, the nuclei have equal radii and the contact angle in both instances is 90°.

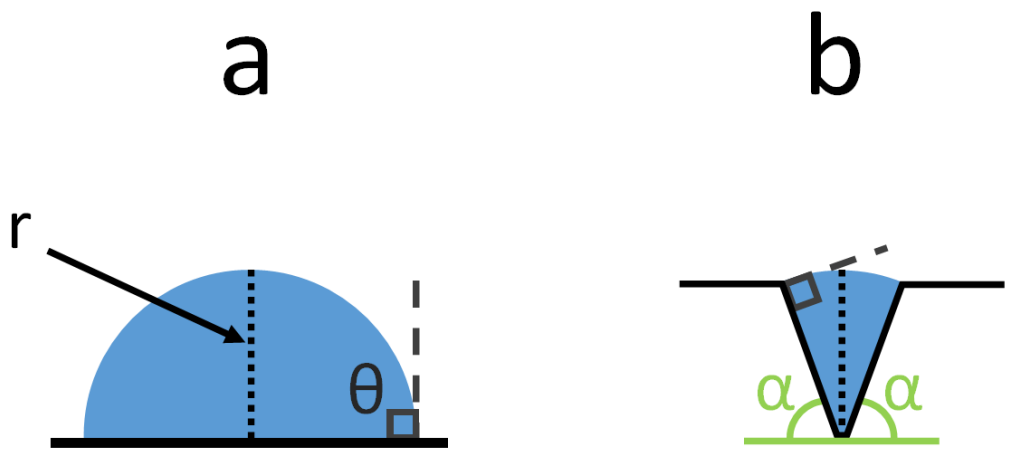


**Figure 151: Schematic of nucleation on a flat surface and in an acute wedge.**

By consideration of Figure 151a, it becomes evident as to why the nucleation barrier to homogeneous nucleation is halved if the contact angle is 90°. In this configuration, the nucleus becomes a hemispherical cap on the surface and so the volume and the surface area have been halved. In Figure 151b, the nucleus is confined by two flat surfaces that each make an angle α with a common plane, so that the internal angle of the wedge is 180 - 2α. By nucleating in the feature, the surface area of the nucleus exposed to the solution has been reduced and the majority of the nucleus' interface is in contact with the surface [3], and therefore in a more favourable condition. According to Sholl and Fletcher, for the nucleation of a material in a wedge, the energy barrier to homogeneous nucleation is reduced by the wedge factor, $\phi_w(\theta, \alpha)$ [4]. The mathematical definition of this factor is beyond the scope of this thesis, though the relationship between homogeneous nucleation and heterogeneous nucleation in a wedge is described in Equation 22.

$$\Delta G'_W = \phi_W(\theta, \alpha)\Delta G^* \qquad \text{Equation 22}$$

There are some significant implications of this relationship, as described by Sear [3]. If the angle α = 0°, then the wedge factor will be equal to the heterogeneous nucleation factor, ϕ. If α > 0°, the wedge factor will always be less than ϕ, though the difference tends to 0 as the contact angle approaches 180°. Therefore, nucleation will always be more favourable in a wedge. Further, $\phi_W$ approaches 0 as the contact angle tends towards the value of α. Importantly, if θ < α, then there will be no barrier to nucleation. This means that for a very acute wedge, where α is large, there exists a broad range of contact angles where there is no energy barrier to nucleation. It should be noted that although CNT suffers from a number of

limitations, this model is sufficient to aid in the explanation of why my topographical systems are effective at promoting nucleation.

When plasma-treated PDMS was used as a substrate for the crystallisation of calcium carbonate, the majority of crystals nucleated at the cracks in the surface (Figure 152a). The crystal population could be hugely increased relative to the uncoated substrate at the same supersaturation by coating the surface with a carboxylate-terminated thiol (Figure 152b), with near-perfect alignment to the cracks (99.85% of crystals detected in the image analysis were aligned with a crack out of a total of 52,176 crystals, see Section 3.3). A huge increase in crystal population was observed on silicon wafers spin coated with reduced-graphene oxide compared to an uncoated silicon wafer (Figure 152c), and the vast majority of these crystals were the metastable polymorph, aragonite. Acute wedges formed between the surface of a graphitic flake and a silicon wafer were found to be effective at nucleating calcite (Figure 152d), and numerous crystals were present at microfabricated structures on silicon wafers after crystallisation (Figure 152e).

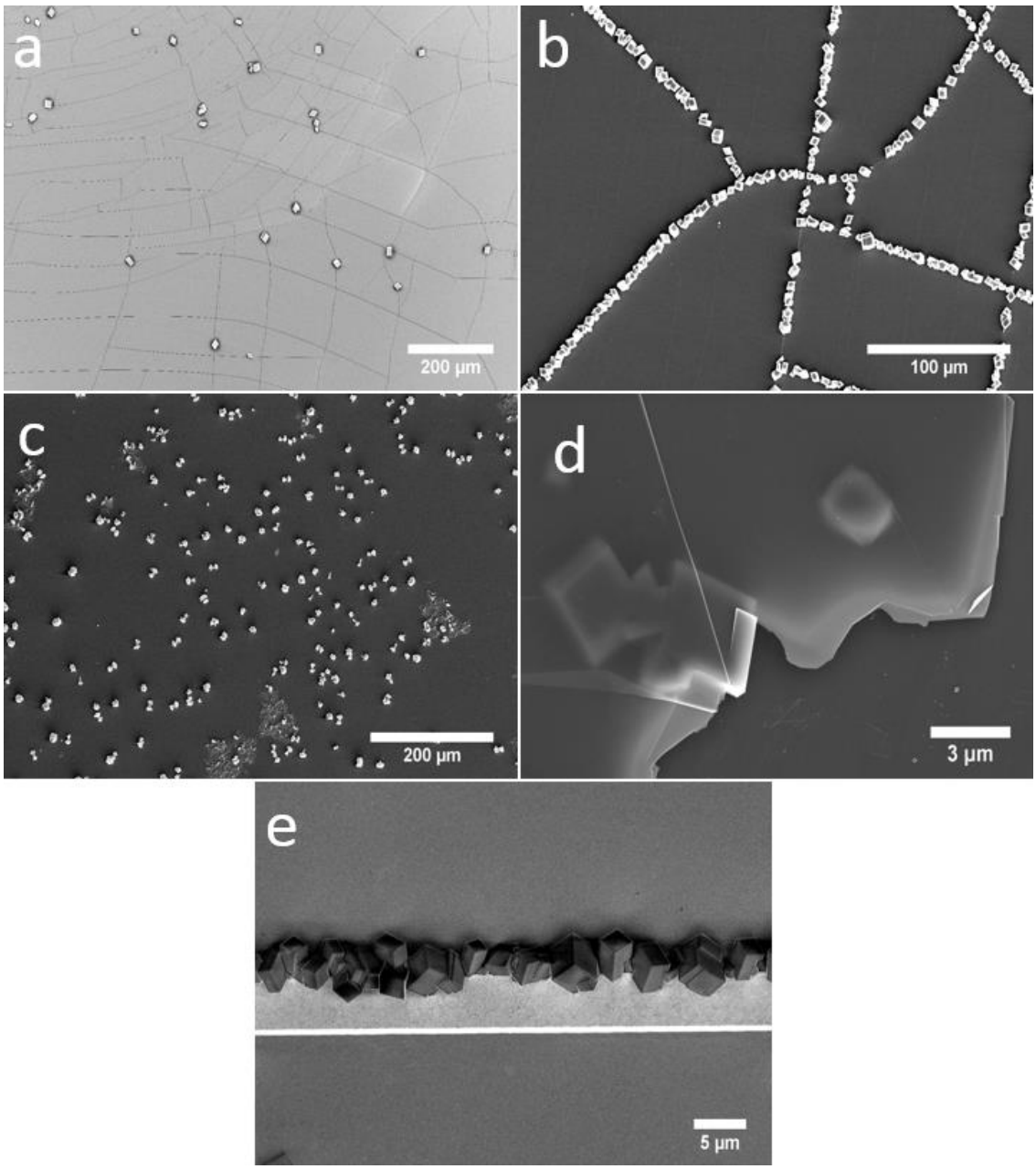


**Figure 152: Electron micrographs of examples of topographical manipulation of crystallisation demonstrated within this thesis.**

The control experiments for the plasma-treated PDMS substrates (coated and uncoated) and the rGO coated Si wafers (Figure 153) provide clear evidence that surface topography can play a critical role in the crystallisation of a material when compared to Figure 152.

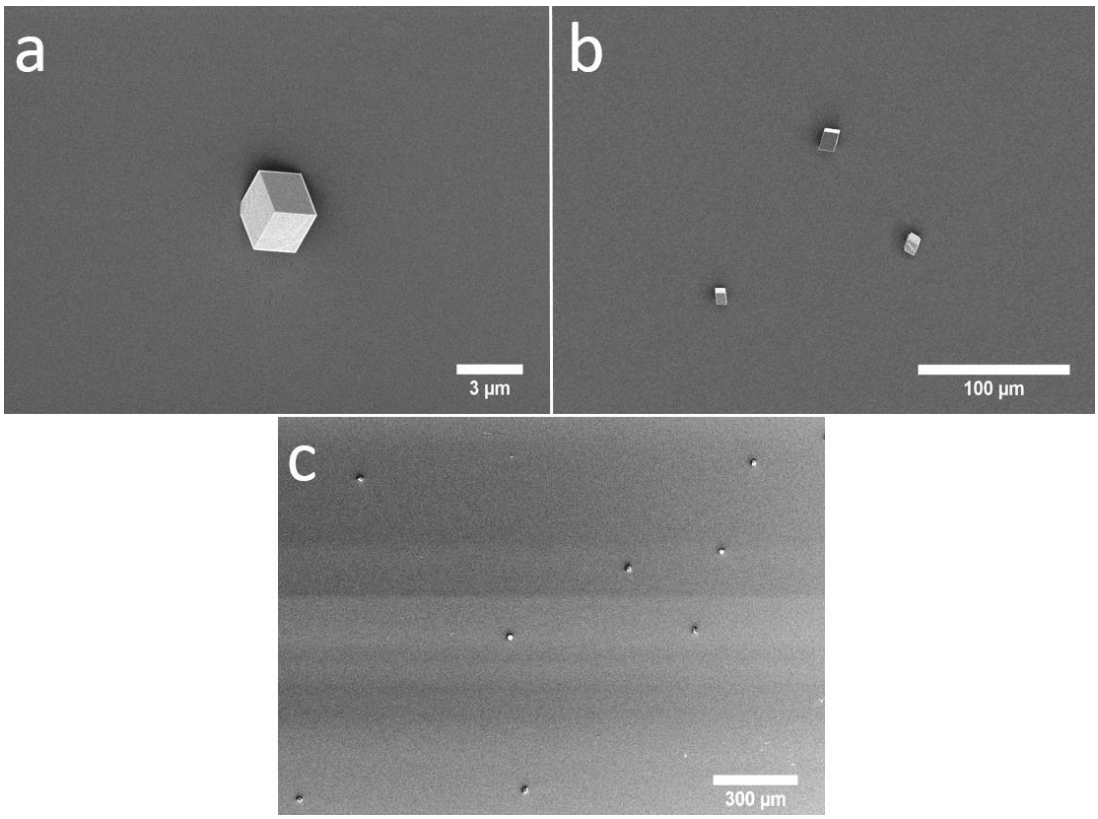


**Figure 153: Control experiments for the data presented in Figure 152.**

The substrates represented in Figure 153 were exposed to exactly the same crystallisation conditions as those used for the corresponding experiments of Figure 152, where Figure 153a is the control experiment for Figure 152a and so on. The introduced surface topographies cause a visually striking difference in crystallisation results, and in each case, the structures that enhance nucleation share a common trait (Figure 154).

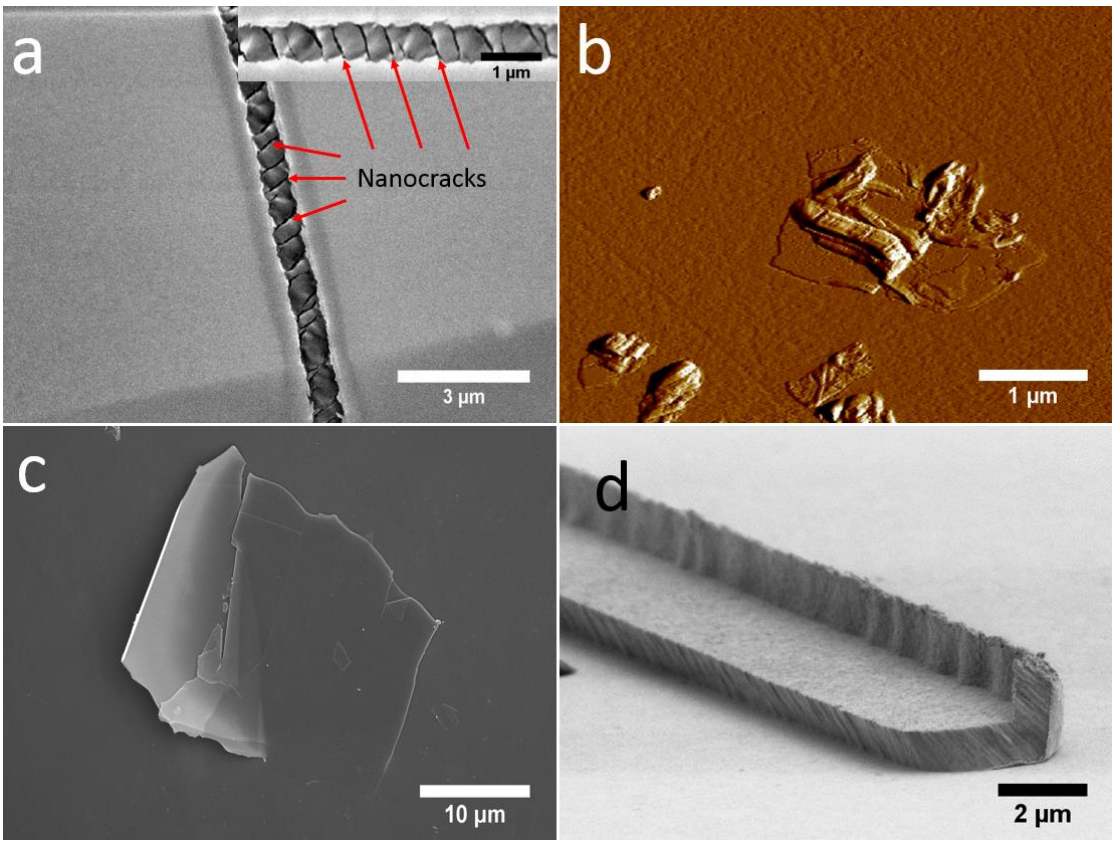


**Figure 154: Electron micrographs of the topographical features of each system that are believed to promote nucleation**

The structures all possess acute wedges, which according to classical nucleation theory will provide a lower energy barrier to nucleation compared to that associated with nucleation on a flat surface. In the plasma-treated PDMS system, the nanocracks (highlighted in Figure 154a and inset) have a maximum width of 90 nm. This becomes significantly narrower as the nanocrack opening approaches the edge of the microcrack, where it becomes highly acute as the two surfaces recombine. It is most likely that the nucleation event occurs here, rather than deeper within the crack. This is because of the acuteness of the feature in this location, and also mass transport will be greater here than deep within the confines of the crack. Coating this substrate with iridium and then forming a carboxylate self-assembled monolayer on the surface greatly enhances the crystal population at the cracks. Though one can expect that depositing iridium on the surface will alter the surface topography, the observed effect of the carboxylate coated substrate on crystallisation is not because of this topographical modification. This is proven by the image analysis data in Chapter 3, where a total of 52,176 crystals were detected on the carboxylate coated PPDMS, compared to only 123 on the Ir coated PPDMS across the same surface area.

The difference between the uncoated PPDMS and the carboxylate-coated PPDMS is an illustration of the effect that surface chemistry combined with surface topography can have on the energy barrier to nucleation. According to De Yoreo *et al*, the effective interfacial energy between a calcite crystal and the solution is 109 mJ $m^{-2}$. The interfacial energy between the surface of a calcite crystal and a 16-mercaptohexadecanoic SAM (the same monomer as that used here) is 72 mJ $m^{-2}$ [5]. The SAM that this value was calculated for was formed on a gold intermediary layer, while the SAM used in this research was formed on an iridium layer. Although the crystalline structure of the underlying metal influences the packing of the SAM monomers (and therefore the value of the interfacial tension), one can reasonably expect that the calcite/SAM interfacial tension will be lower than the calcite/solution interfacial tension. The interfacial tension between the nucleus and substrate influences the contact angle, θ, between the substrate and the nucleus. According to Equation 22, if θ is less than the wedge angle (α), then there will be no energy barrier to nucleation. The nucleation rate is directly related to this energy barrier and so if the barrier is low, then the nucleation rate will be high and there will be a large population of crystals. The combination of the highly acute regions of the nanocracks and the low interfactial tension due to the presence of the SAM could therefore be suggested as the reason why the substrate is so effective. Of course, CNT is a simplification and in actuality doesn't compensate for all real-world parameters. The angle that a crystal face makes with the substrate is not trivially defined by the surface energies, though CNT as described here provides a basis for understanding the experimental observations. Further, there is no evidence that suggests that the crystallisation of calcium carbonate in the cracks of the carboxylate-coated PPDMS substrate proceeds via an amorphous precursor. In their AFM studies of the heterogeneous nucleation of calcium carbonate, De Yoreo *et al* only observed direct nucleation of calcite onto a SAM formed from the same monomer as that used here [5]. In addition, the ability of the cracks to localise the crystals of other materials, as demonstrated in Chapter 3, may support this hypothesis (Figure 155).

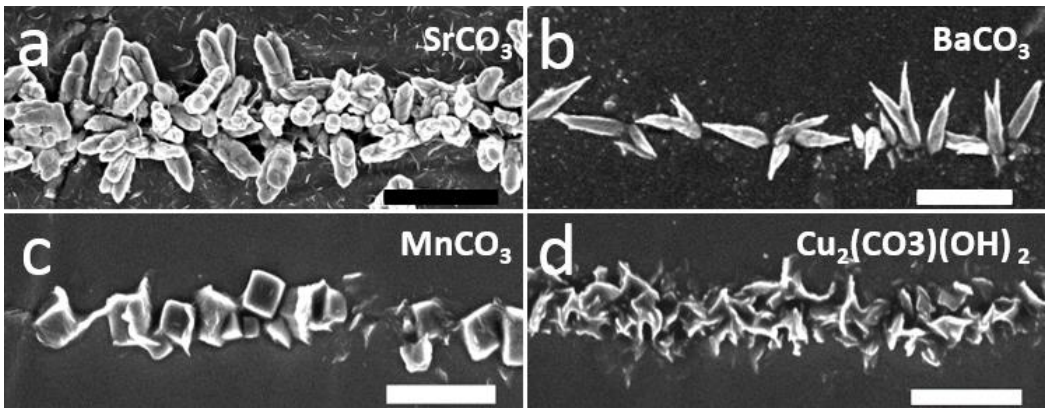


**Figure 155: Electron micrographs of various crystalline materials precipitated at the cracks of a carboxylate-coated plasma-treated poly(dimethylsiloxane) polymer**

The fact that the crystals of other carbonates are found associated with the cracks at relatively low supersaturation ($SI_{SrCO_3}$ = 2.4, $SI_{BaCO3}$ = 2.4, $SI_{MnCO_3}$ = 2.6, $SI_{Cu_2(CO_3)(OH)_2}$ = 3.6) also suggests that direct nucleation of the crystalline phase at the crack may occur. The amorphous phases of the investigated materials have only been obtained under conditions very different to those used here or in the presence of soluble additives [6-11]. However, we cannot rule out an amorphous precursor formation mechanism for this system given the limited mechanistic data at hand.

Although acute wedge geometries were not directly observed for the rGO/Si wafer system (Figure 154b), it is likely that they exist, formed either between the wafer and flake surfaces, or as 'cave-like' openings between the rGO lamellae. The topography formed by spin coating rGO onto a silicon wafer is unique in its ability to promote the heterogeneous nucleation of aragonite, and further data is required to explain this.

The hypothesis that acute geometries promote nucleation is corroborated by the data obtained for crystallisation experiments in the presence of the graphitic flakes/Si wafer (Figure 154c) and the fabricated microstructured substrates (Figure 154d). However, it is worth mentioning that not all surface topographies involving acute wedges are effective at promoting the nucleation of crystals from solution. Campbell *et al* had some success with calcium carbonate nucleation on mica defects, though the data was irreproducible and thus inconclusive [1]. The effects of confinement on calcium carbonate crystallisation of $CaCO_3$ has been investigated using annular wedges [12] and track etch membranes [13], though there currently exists no examples in the literature of systems that exhibit such a strong effect on nucleation as those presented in this thesis.

## 6.1 References


1. Campbell, J.M., *On topography and crystal nucleation*, in *School of Physics and Astronomy*. 2014, University of Leeds: Leeds. p. 232.
2. De Yoreo, J.J. and P.G. Vekilov, *Principles of crystal nucleation and growth.* Reviews in mineralogy and geochemistry, 2003. **54**(1): p. 57-93.
3. Sear, R.P., *Nucleation: theory and applications to protein solutions and colloidal suspensions.* Journal of Physics: Condensed Matter, 2007. **19**(3): p. 033101.
4. Sholl, C. and N. Fletcher, *Decoration criteria for surface steps.* Acta Metallurgica, 1970. **18**(10): p. 1083-1086.
5. Hamm, L.M., et al., *Reconciling disparate views of template-directed nucleation through measurement of calcite nucleation kinetics and binding energies.* Proceedings of the National Academy of Sciences, 2014. **111**(4): p. 1304-1309.
6. Wolf, S.E., et al., *Carbonate-coordinated metal complexes precede the formation of liquid amorphous mineral emulsions of divalent metal carbonates.* Nanoscale, 2011. **3**(3): p. 1158-1165.
7. Sondi, I. and E. Matijević, *Homogeneous precipitation by enzyme-catalyzed reactions. 2. Strontium and barium carbonates.* Chemistry of materials, 2003. **15**(6): p. 1322-1326.
8. Li, W., et al., *Controlling the morphology of BaCO3 aggregates by carboxymethyl cellulose through polymer induced needle-stacking self-assembly.* Crystal Growth & Design, 2010. **10**(6): p. 2685-2692.
9. Homeijer, S.J., R.A. Barrett, and L.B. Gower, *Polymer-Induced Liquid-Precursor (PILP) process in the non-calcium based systems of barium and strontium carbonate.* Crystal Growth & Design, 2010. **10**(3): p. 1040-1052.
10. Guo, X.-H., et al., *Mineralization of unique barium carbonate crystal superstructures controlled by a liquid crystalline phase polymer.* CrystEngComm, 2012. **14**(9): p. 3213-3219.
11. Chen, L., et al., *Bacteria-mediated synthesis of metal carbonate minerals with unusual morphologies and structures.* Crystal Growth and Design, 2008. **9**(2): p. 743-754.
12. Loste, E., et al., *Precipitation of Calcium Carbonate in Confinement.* Advanced Functional Materials, 2004. **14**(12): p. 1211-1220.
13. Stephens, C.J., et al., *Amorphous Calcium Carbonate is Stabilized in Confinement.* Advanced Functional Materials, 2010. **20**(13): p. 2108-2115.

# Conclusions and Future Work

The work in this thesis proves that surface topography is a viable tool for the control of crystallisation. This can be extended by modification of the surface chemistry, allowing not only the spatial distribution of crystals to be determined, but also the polymorph, their size and number. The effectiveness of each of the topographical systems was attributed to the presence of surface features with acute geometries. The ability to control crystallisation using surface topography has applications in a huge number of fields, as so many modern technologies are reliant on the fabrication of crystals with predictable properties.

In the first experimental chapter, plasma-treated poly(dimethylsiloxane) was used as a substrate for the crystallisation of calcium carbonate. The surface cracks, formed due to the conversion of the surface layer to $SiO_x$, were ideal nucleation sites for calcium carbonate crystals and the two were often found in association. By coating the surface with a carboxylate-terminated alkylthiol, the population of crystals at the cracks could be significantly enhanced, whilst maintaining the low population that had nucleated on the featureless, intervening surfaces. Further control over the population could be afforded by adjustment of the initial ion ratio, while the addition of magnesium ions caused the precipitation of aragonite at the surface features. The use of contact masks or application of a tensile stress during plasma exposure can be used to alter the arrangement of cracks, and therefore the distribution of crystals. Finally, a two-step surface modification procedure in which labile alkylthiol monomers at acute geometries were swapped for monomers with a different terminal group functionality was also used. This method allowed large populations of metastable vaterite to be obtained.

The second experimental chapter involved the plasma-treated poly(dimethylsiloxane) substrates of the first chapter, but a number of different self-assembled monolayers as surface coatings were investigated. Crystallisations of calcium carbonate were performed, using the surface modified PPDMS as a substrate. ImageJ, which is an image analysis software, was used to extract the sizes and populations of crystals present on each of the substrates. This chapter demonstrated that by altering the surface chemistry, polymorphs could be selected and the size and number of crystals controlled.

Further work regarding the first two research chapters would involve working towards a comprehensive description of the structure of the cracks. This is necessary as it is here that the crystals grow. Knowledge of these features that are so effective at promoting nucleation would therefore advance understanding of how topography exerts control over crystallisation. Also, the surface features could be used to achieve the patterned crystallisation of crystals that have industrial relevance, such as semiconductors, perhaps providing a synthetic route that has advantages over the conventional methods used to fabricate these materials. It may even be possible to use the substrates to select for a particular pharmaceutical polymorph. Hypothetically, the surface topography could be used to obtain monodisperse crystals of the desired polymorph, which could be removed from the substrate by a shear flow and then processed downstream.

The third research chapter described a system where surface topography could be used to promote the formation of metastable aragonite. This polymorph was only obtained on silicon wafers that had been spin coated with reduced-graphene oxide. Although chemical analyses identified contaminants, none of these have been shown to promote aragonite formation. Their concentration in the dispersion from which the coating was formed and the fact that most of the contaminant material would be removed by spin coating suggests that it is not these that are causing aragonite to precipitate, but the topography formed via the coating process. Other layered materials ($MoS_2$, $WS_2$ and g-$C_3N_4$) failed to produce the same effect, though this may be due to the poor quality of the materials provided by the supplier or the fact that exfoliation was unsuccessful. In addition, work was presented in which acute wedges formed between graphitic flakes and the surface of a silicon wafer were found to promote calcite nucleation.

Further research for the third research chapter would involve producing data that supported the conclusion that the formation of aragonite on the rGO spin coated wafers was due to topography. This could be provided by investigating other coating forming techniques that produce different topographies, such as spray coating. Physical modification of discrete areas of the rGO spin coated material may also provide good evidence. This would involve spin coating the rGO onto the wafer in the usual way, and then physically disturbing the flakes in specific locations such that the topography had been disrupted. If aragonite precipitated in the undisturbed areas and was absent in the regions that had been altered, then this would suggest that it was indeed a topographical effect. With regards to the formation of coatings

from the other layered materials, more effective exfoliation techniques (and for the g-$C_3N_4$, higher quality material) would be required. It may then be possible to spin coat these materials onto Si wafers and determine if these can also cause aragonite to form.

In the final research chapter, surface topographies were generated using cleanroom microfabrication techniques. The structures that were formed could be used to localise crystallisation, proving that surface features can be designed to promote nucleation. Further work for this chapter would involve refining the fabrication process and investigating if they are effective for other crystal systems. In addition, focused ion beam milling could be used to generate surface features in a gold substrate. The advantage of producing features using this technique is that numerous gold structures that each form a different angle with the surface could exist on a single substrate. This would allow multiple feature angles to be tested simultaneously.